Compilation of Supersonic Configurations at Low Speeds (SCALOS) Final Report & Appendices A – F

NASA Point of Contact: Sarah L. Langston

Configuration Aerodynamics Branch

NASA Langley Research Center, Hampton, VA

sarah.langston@nasa.gov

NASA's Commercial Supersonics Technology (CST) project identified a need for more detailed study into the design drivers for low-speed stability and control and performance of low-boom commercial supersonic transports. To aid in addressing this research gap, CST funded a research proposal from the University of Washington and partners in 2019 to study this area. The grant was awarded in 2019 under NASA award number 80NSSC19K1661 and completed in 2024. This publicly released report serves as a publicly releasable version of the grant final report. Copies of already published papers and Appendices G – J included in the grant final report have been removed. The only modifications to the grant final report are the removal of the noted previously published papers and appendices.

Contents:

Modified From Original - See Cover Sheet - Cover Sheet Must Remain Attached

Innovation in Commercial Supersonic Aircraft

- NASA CST -

The NASA **SCALOS** Project

Supersonic Configurations at Low Speeds

NASA Award Number: 80NSSC19K1661

Final Report

University of Washington
Eli Livne, Chester P. Nelson, Reza M. Soltani,
Kuang-Ying Ting, Nicolas Mavriplis, Kenneth Wiersema

University of Michigan
Carlos E.S. Cesnik, Ilya Kolmanovsky, Joaquim R.R.A. Martins,
Thiago A. M. Guimaraes, Torbjørn Cunis, Guilherme C. Barbosa, Rafael Bertolin,
Dr. Sabet Seraj, Bernardo B. Monteiro

Stanford University
Juan J. Alonso, Ilan Kroo, Tejal K. Shanbhag, Yiren Shen

Boeing Research and Technology
Todd E. Magee, Patrick J. Hayes, Andrew J. Dorgan, Abdollah Khodadoust

Contacts:
PIs:
Eli Livne: eli@aa.washington.edu
Carlos Cesnik: cesnick@umich.edu
Juan Alonso: jjalonso@stanford.edu
Todd Magee: todd.magee@boeing.com

12/17/2024

Summary

The report describes work carried out at the University of Washington in Seattle, the University of Michigan, Ann Arbor, Stanford University, and Boeing Research and Technology on the low-speed characteristics of long-range supersonic configurations. The work includes substantial low-speed wind tunnel testing in an effort to ”map” and cover the related configuration shape design space, water tunnel testing for dynamic stability derivatives, the development of CFD simulation and optimization technology that would make the simultaneous optimization of supersonic configurations for both low and high speed flight practical, contributions to the development of required multidisciplinary design optimization technology (MDO), the control of such configurations at low speeds, and contributions to the practical simulation of associated airplane noise. The report is accompanied by wind tunnel and water tunnel test results data sets, CAD definitions of parts and selected full wind tunnel model tested, and data that cover key aspects of the conceptual design of a representative reference commercial supersonic aircraft (RSAC).

Contents

1 Introduction

Major resources have been dedicated in the last 25-30 years to the development of simulation, design, and testing technologies that would tackle the sonic boom, supersonic aerodynamic performance efficiency, and propulsion challenges and overcome them in the pursuit of efficient, environmentally-acceptable, commercial supersonic aircraft. The **Supersonic Configurations at Low Speeds (SCALOS)** project was launched to contribute to commercial supersonic aircraft technology development by focusing on the low-speed aspects of such designs.

Much has been done already in this area over the years, including significant work on the low speed characteristics of supersonic fighter jets, the commercial Concorde and Tu-144 of the 1960s/1970s, The NASA High Speed Civil Transport (HSCT) effort of the 1990s and follow on research and technology development studies, the NASA funded N+2/N+3 studies by Boeing and Lockheed, and other conceptual design studies at various levels of detail. The slenderness and other aerodynamic shaping features of emerging new configurations, especially those shaped for some optimal tradeoffs between low-boom, supersonic performance, and low-speed performance, call for more work in the low-speed area, and the SCALOS project was conceived to add information, insights, and lessons, shared with the aerospace engineering community, in those areas that previous efforts did not cover.

Figure 1 shows the building blocks of supersonic commercial MDO technology and those areas that still require work. Figure 2 shows the areas that the SCALOS project covered and the project's work plan and flow. Figure 3 shows what each project team (University of Washington (UW), University of Michigan (UM), Stanford University (SU), and Boeing Research and Technology) focused on during the project.

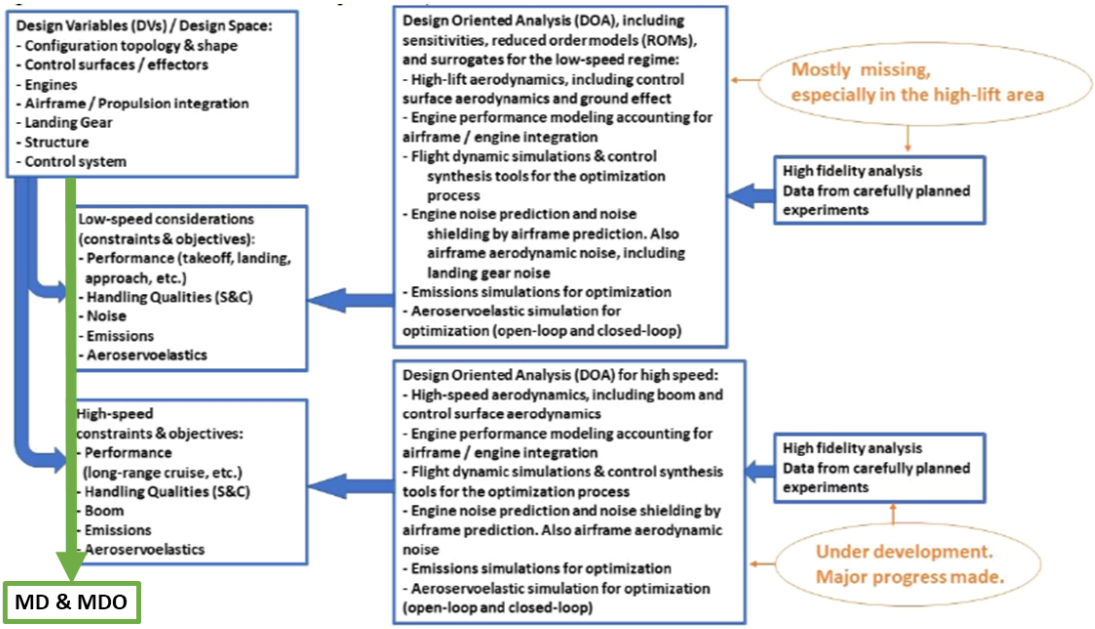

Figure 1: The MDO of Supersonic Long Range Configurations

Descriptions of work progress by the project teams in the years 2020-2024 can be found in References: [1–18] by the University of Michigan, references [19–31] by the University of Washington, References [32–34] by Stanford University, and References [35–37] by Boeing Research & Technology.

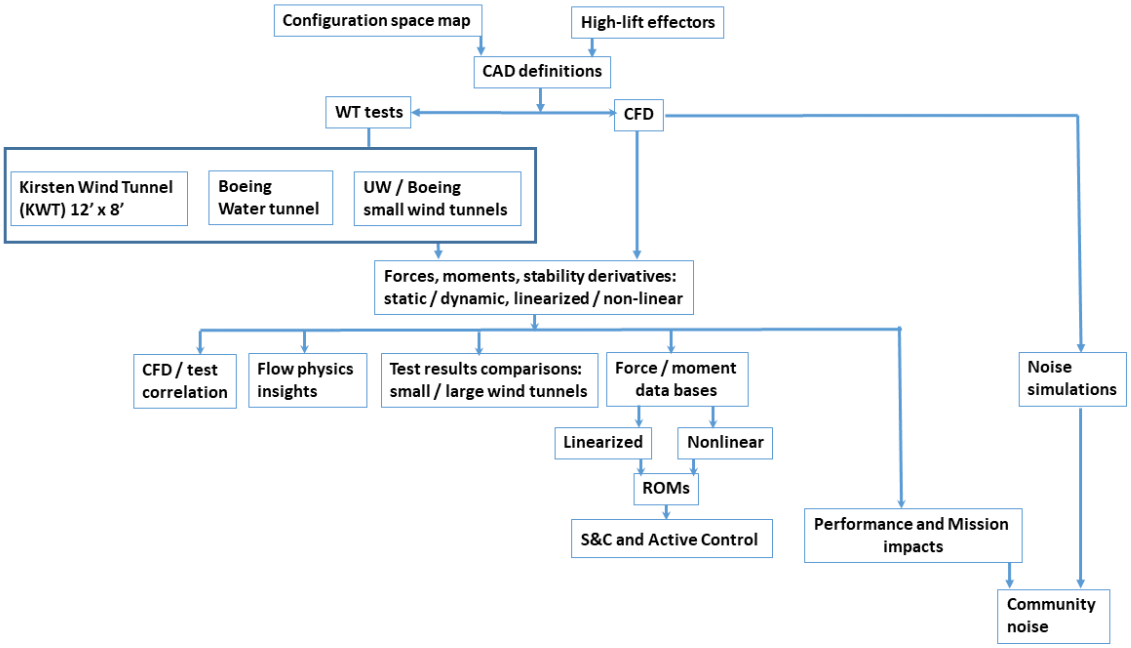

Figure 2: The SCALOS Project - A Flow Diagram

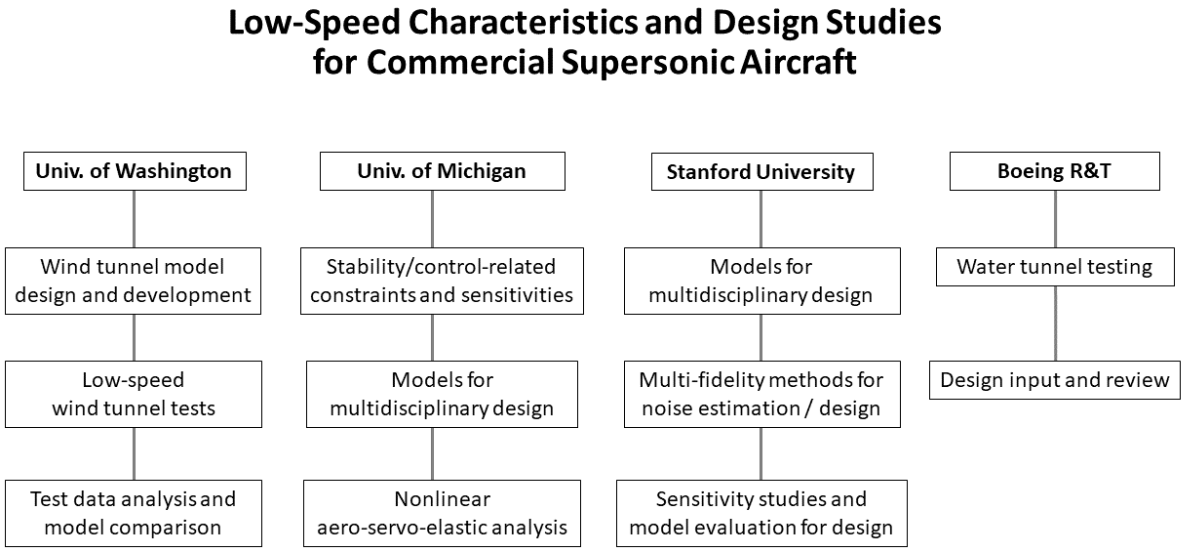

Figure 3: The SCALOS Project - Team Member Roles

The AIAA SciTech2025 papers (Refs. [29–31, 33, 34, 37]) have been completed and submitted. They will be assigned AIAA Paper numbers by the AIAA. At the time of concluding this final report these AIAA

paper numbers have not been received yet.

The structure of this report is as follows: Final reports by each of the member teams will be presented, covering:

By the University of Michigan: its work on aerodynamic, aeroelastic and MDO developments, the flight control constraint development, and the integrated subsonic/supersonic CFD optimization.

By the University of Washington (UW): The low-speed Kirsten Wind Tunnel (KWT) testing campaign, including the development of WT corrections, selected test results, a user's guide to delivered databases that include test results (case run by case run) and CAD definitions of model parts and selected complete models, as well as the wind tunnel test section and the model support system used. Additional work by the UW team includes CFD simulations of the KWT tests, flow-visualization in the UW's low-speed 3'x3' wind tunnel, and a conceptual design of a reference supersonic airplane concept (RSAC).

A Report from Stanford University (SU) covers its work on the noise problem and on the MDO challenge.

A final report from Boeing covers its flow-visualization water tunnel (FVWT) effort, launched to gather dynamic stability derivatives for configurations of interest.

Because of the substantial scope of the work completed for this project and in order to keep the final report user-friendly and simple to navigate, it is includes a brief overall presentation, supported by a set of appendices which contain project summaries by the project's teams as well as guides to the test databases that were created. More details in each of the areas covered by the project can be found in the published papers (Refs. [1] to [37]).

The report will conclude with a discussion of collaboration, during the project, among the project teams and a summary of key accomplishments, as well as key insights and lessons gained during the project.

Several appendices, which constitute important parts of this report, include

A. UM - The final report from the University of Michigan.

B. SU - The final report from Stanford University.

C. Boeing - The final report from Boeing R&T.

D. UW - An overview of the Kirsten Wind Tunnel test program at the University of Washington

E. UW - Selected Lateral-Directional Kirsten Wind Tunnel Test Results

F. UW - RSAC (Reference Supersonic Airliner Concept) - a conceptual design study of a supersonic commercial airplane.

G. UW - A User Guide to the Kirsten Wind Tunnel Test Data.

H. UW - A data reduction (DR) guide for the Kirsten Wind Tunnel results database.

I. UW - A guide to the geometry of parts and selected models tested in the Kirsten Wind Tunnel.

J. UW - A list of parts of the models tested in the Kirsten Wind Tunnel.

Detailed presentations of the project's accomplishments, lessons, and insights, together with recommendations for future work can be found in Appendices A, B, C, D, E, and F.

2 University of Michigan

A number of challenges guided the University of Michigan's SCALOS project work:

- Evaluate the capability of current CFD tools to accurately "capture" the aerodynamic behavior of SCALOS-type configurations, especially at low speeds;
- Advance CFD-based aerodynamic optimization technology to include subsonic and supersonic constraints simultaneously in the shape optimization of supersonic commercial aircraft;
- Develop variable fidelity aerodynamic modeling methods that would make the shaping of supersonic aircraft for performance as well as stability and control at low speeds practical;

  and

- Contribute to the development of integrated trajectory / control/ vehicle shaping of SCALOS-type configurations for the low-speed flight regime.

A final report by the University of Michigan is included here as **Appendix A**. Contributions by the University of Michigan are documented in Refs. [1–18].

The University of Michigan's team addressed the definition of a low-order aerodynamic model for control design and control co-design in aircraft MDO. The vortex-based codes provide adequate fidelity, capturing the prevalent physics phenomena involved in steady/unsteady simulations of high angles of attack and low-speed maneuvers. It also enabled the development of the non-intrusive PCE surrogate model. The surrogate model generates continuous equations formed by Hermite polynomials guaranteed computational efficiency. A set of parameterized flight simulations covering a wide range of supersonic design parameters, gust amplitudes, and trimming conditions was presented and analyzed.

A methodology was proposed to evaluate sensitivity metrics and to generate linearized aerodynamic co-efficients for command of surface deflections based on the combination of the linearized UVLM with the additional linearized effect from the vortex lift derived from the Polhamus method. This approach enabled the exploration of parametric variations of the SCALOS aircraft for sensitivity analysis and the generation of linearized control surface derivatives. The developed approach enabled obtaining the control surface derivatives about the reference condition, which were considered for different angles of attack, and this is ready to be integrated into the control modeling. Additionally, given that the linearized model is obtained directly from the analytical derivatives, including the states and inputs of interest, the linearized aerodynamic model allows integration with the aeroelastic flight-dynamic model and can be used for studying the aircraft's stability.

An integrated framework was developed for simulating the coupled aeroelastic-flight-dynamics behavior of supersonic aircraft flying at low speeds and high angles of attack. The UVLM code, enhanced with the Polhamos method with corrections from the water tunnel experiments, provided adequate fidelity while capturing the prevalent physical vortex phenomena involved in high angles of attack and low-speed maneuvers. Including elastic modes from the finite element model into the UM/HSV simulation framework enabled the simulation of the longitudinal dynamic behavior of the aircraft considering different gust amplitudes and allowed for a comparison between the rigid and flexible vehicles.

The open-loop simulation results confirmed that aeroelastic effects are non-negligible and must be accounted for when designing supersonic vehicles and their flight control system during low-speed flight. Special attention needs to be paid to the impact of flexibility of long and slender fuselages when determining flight dynamics stability characteristics.

To properly model the impact of vortex breakdown on the Longitudinal Flight Behavior of SCALOS configurations, corrections were developed for the baseline aircraft and were included in the UM/HSV framework to further analyze the aircraft's response in gust conditions. The modeling methodology for accounting for variations of the LE-flap deflections were also assessed to simulate the aircraft's dynamic response.

The effort on computational fluid dynamics (CFD) technology for optimization of SCALOS-type configurations focused first on establishing which CFD methods could be reliably used to predict the flight conditions of interest. Reynolds-averaged Navier–Stokes (RANS) and delayed detached eddy simulations (DDES) were studied for the subsonic, high angle of attack condition. It was found that RANS was suitable for moderate angles of attack where the flow was separated but not unsteady. It was then found that RANS accurately captured the subsonic pitch-up behavior of the UW-S-20A configuration. This motivated work on accurate and efficient RANS solvers for low and high Mach number flow and RANS-based shape optimization, where we minimized supersonic drag with a constraint on the subsonic static margin. Shape optimization was shown to increase the wing thickness and leading edge radius to design a cranked arrow wing that is stable at subsonic speeds at the cost of a 5.8% increase in supersonic drag.

Some limitations of RANS-based optimizations were encountered. In particular, mesh warping poses restrictions on the design space that can be explored. To study configuration-level tradeoffs without mesh-related restrictions, a supersonic buildup model was formulated and used to optimize the configuration's trim surface sizing. The University of Michigan's final report and associated publications provide more details.

3 Stanford University

The Stanford University effort focused on two major tasks:

- The aeroacoustic modeling of supersonic aircraft jet exhausts based on RANS simulations, including both the modeling and the use in design optimization.

- Endow conceptual design tools for supersonic configurations with the ability to predict low-speed stability & control so that proper constraints can be imposed. Since VLM (Vortex Lattice Methods) cannot predict the nonlinear behavior of the pitching moment at large angle of attack, the Stanford University team ended up developing a ML (machine learning) capability to learn the discrepancy in force and moment coefficients between RANS and VLM for SCALOS-type configurations. The method was named VortexNet, and one of the main contributions is the development of this kind of discrepancy modeling that can be embedded into a conceptual design tool like SUAVE (ongoing work). Such "discrepancy modeling" can be very useful in an MDO environment that is based on variable-fidelity modeling of the aerodynamics of the configurations being optimized. Of course, $V\&V$'ing this new capability and understanding the accuracy for actual supersonic wings (and how much high-fidelity data will be needed to train these low-fidelity or medium fidelity models) is critical. The Stanford University work addresses both of these contributions.

The Stanford University final report is attached as **Appendix B**. The associated references can be found in [32–34].

4 Boeing Research & Technology

The major elements of the Boeing R&T effort contribution to the SCALOS project include:

- Carry out systematic unsteady tests in the Flow Visualization Water Tunnel (FVWT) to measure dynamic stability derivatives of SCALOS-type configurations and gain insight into key flow field features using flow visualization techniques.

- Carry out exploratory Vortex Lattice and CFD simulation studies to evaluate their capabilities to "capture" by analysis the dynamic physical behavior of the configurations tested.

The Boeing SCALOS effort was comprised of a series of dynamic stability water tunnel tests at the Boeing Flow Visualization Water Tunnel (FVWT) of the University of Washington 2020, 2017 and 2015 supersonic configurations. There was also commensurate vortex lattice and CFD conducted to compare with the FVWT results. The work is documented in **Appendix C** and in three American Institute for Aeronautics and Astronautics (AIAA) conference papers.

Reporting Boeing's work, Ref. [35] focused on studying the dynamic stability characteristics of supersonic configurations through forced oscillation testing in the Boeing Flow Visualization Water Tunnel (FVWT). It included some initial parametric trade studies focused on nose length, pitch frequency, and comparisons with CFD. Ref. [36] showed forced oscillation test results for additional configuration trades, which included trades on wing planform, nacelle location, horizontal tail location, leading-edge flap deflection and canard-on versus off. It also showed the effect of frequency on the yaw and roll dynamic stability derivatives, as well as repeatability in the dynamic stability derivative data gathered in the Boeing FVWT. The third reference, [37], shows two additional configuration trades, which include a new supersonic configuration and the effect of a forebody chine on dynamic stability derivative coefficients. Additional repeat runs for pitch(q), yaw(r), and roll(p) forced oscillation runs are included at reduced frequencies of 0.05, 0.1, and 0.2. Yaw forced oscillation amplitudes of 5º and 10º are also investigated. Single-point and integral forced oscillation data reduction methods are compared. A rough uncertainty analysis of FVWT data is conducted to determine the agreement between test and CFD data.

Together with University of Washington's Kirsten Wind Tunnel (KWT) test results, the FVWT test results for the same configurations provide complete sets of stability derivatives (static and dynamic) for flight dynamic simulations and for control synthesis. Like the KWT test effort, the FVWT test results add to the understanding of the aerodynamics of SCALOS-type configurations at low speeds and to the associated test experience with these particular configurations (including issues such as model support, tunnel effects, uncertainty, noise, and repeatability).

5 University of Washington

The major elements of the University of Washington's (UW) contributions are:

- A configuration design space survey to identify candidate supersonic commercial configurations of interest based on the history of supersonic aircraft research and development, including recent developments that study tradeoffs between supersonic performance and low-boom characteristics.

- A substantial number of Kirsten Wind Tunnel (KWT) low-speed tests planned for generating a rich database of aerodynamic performance and S&C results for SCALOS-type configurations that aerodynamicists (including CFD experts) and designers will benefit from.
- The development of wind tunnel "corrections" for the tested configurations to remove wind tunnel support and wall effects and transform the raw data into results for the models in free flight.
- The development of certain insights into the physics of the aerodynamic flow fields involved and the effects of configuration geometry and arrangement variations.
- An exploratory evaluation of the capability of current state of the art RANS simulation techniques to "capture", by analysis, the measured behavior.
- The conceptual design of a Reference Supersonic Airliner Concept (RSAC) that would serve as a starting point for future more detailed design studies.

An important goal of the University of Washington's SCALOS research effort was to engage as many undergraduate students as possible in the effort so that they would gain conceptual design as well as solid wind tunnel testing experience. About 60 seniors, in five two-quarter capstone airplane design projects in the years 2020-2024, worked on the conceptual design of supersonic commercial aircraft and supported wind tunnel tests in both the UW's Kirsten and 3x3 wind tunnels. For an overview of the scope and level of technical depth in the UW's capstone senior airplane design courses prior to the SCALOS project years, see Ref. [38]. Three graduate students contributed significantly to the UW's SCALOS effort.

The work done by the University of Washington is documented in Refs. [19–31] and **Appendices D to J** of this report.

- **Appendix D** presents an overview of the SCALOS Kirsten Wind Tunnel Test effort. It includes lists of the test runs and configurations tested and their geometries. Including KWT tests of SCALOS-type configurations that were carried out at the University of Washington (2015-2018) as part of its capstone airplane design program prior to the SCALOS project, 2400 test runs were completed overall. Appendix D includes a presentation of some key insights regarding the longitudinal performance, stability, and control of the numerous configurations tested, including the effects of wing planform, canard, tail, and fuselage shape variations and the effects of configuration arrangement.
- **Appendix E** extends the presentation of results and insights to the lateral-directional case, including the effects of several control effector variations.
- **Appendix F** presents the conceptual design of a reference supersonic airliner configuration (RSAC) - the conclusion of a multi-year capstone design educational effort with capstone airplane design seniors at the University of Washington's William E. Boeing Department of Aeronautics and Astronautics.

An important element of the SCALOS project at the University of Washington was the supersonic airliner conceptual design work done by teams of capstone airplane design seniors. The result is the conceptual design of a Reference Supersonic Airliner Concept (RSAC) (see **Appendix F**).

The primary focus of the RSAC conceptual design was for UW capstone senior design classes and graduate students, working with instructors and advisors, to develop a credible "straw horse" representation of a supersonic airliner that could be brought to market within 12 years or so. It is intended to be technically feasible using mostly off-the-shelf technology, requiring technology commercial-use maturation and development efforts not greater than those expended on the 787 or A380 programs a decade or so ago. The sizing and proportions of RSAC's wing and propulsion components would coincide with those

used to define model parts for the SCALOS modular model testing. The RSAC's external aerodynamic lines would provide a realistic starting point for those wishing to exercise or further develop aero shape optimization tools. The conceptual internal arrangement would provide representative integration features and "packaging" dimensions / volume allowances to guide the development of OML shape constraints. A detailed weights breakdown, representative propulsion system and structures concepts and engine performance estimates, combined with information from the SCALOS wind tunnel testing database, would provide academia, industry, and researchers with a common non-proprietary point-of-departure for design trades, MDO development, and calibration of various predictive tools. To the maximum extent possible, within the limitations of the academic program and the time and resources of the SCALOS grant program, it is believed that the above objectives have been achieved. Like all concept level designs, the RSAC-E still contains many "place-holders" and assumptions and is far from the "perfect design". The RSAC-E does satisfy the original configuration intents.

The following appendices serve to document the contents of the KWT test database provided at the end of the project, in order to guide future users of this database.

- **Appendix G** is a general users' guide.
- **Appendix H** describes the data reduction process (DR) used to generate the "corrected" wind tunnel results (test results adjusted for removing the effects of test section and model support geometry from test data to generate aerodynamic characteristics of the models "in free flight").
- **Appendix I** includes lists of all KWT model parts that were used to assemble the tested configurations.
- **Appendix J** is a guide to the geometry of the tested models. A CAD database is provided to NASA with the final wind tunnel test package.

6 Key Lessons

The research work that has been completed by the SCALOS project is substantial, and there are many insights and lessons to learn from that should guide future work. Those can be found in the appendices and in the papers that have been published. Much more than what the text and figures of the appendices and papers present can be learned by working directly with the databases that the project has generated: The database of Kirsten Wind Tunnel test results and the Boeing Flow Visualization Water Tunnel test database - both with the geometry and arrangements of the configurations that were tested.
In the following we summarize some key accomplishments, insights and lessons:

From the **University of Michigan's** SCALOS CFD work:

Summary of high-angle-of-attack CFD:

- RANS captures steady vortex flows.
- DDES is more accurate for unsteady flows, including vortex breakdown.
- RANS is appropriate for optimizing the SCALOS aircraft.

Summary of aerodynamic shape optimization:

- The stable wing design is thicker and has larger leading-edge flap deflections.
- The design changes reduce leading-edge vortex strength, which improves stability.
- There is a supersonic drag penalty of 0.5% for neutral stability and 0.85% for a 10 % static margin.

Summary of trim surface optimization:

- The buildup method avoids mesh-related limitations.
- Optimizing for minimum supersonic drag results in a canard configuration.
- The optimized configuration is unstable at subsonic speeds.

SCALOS CFD research at the **University of Michigan** - Key accomplishments:

- Validated RANS against UW wind tunnel tests
- Performed the first RANS-based supersonic aircraft optimization with variable wing-fuselage intersection
- Included leading and trailing-edge flap deflections in the shape optimization

The University of Michigan's work on the nonlinear aeroelastic modeling of low-speed flight of SCALOS-type configurations:

- Vortex-based aerodynamic models can accurately and effectively simulate the complex physics of operating a supersonic aircraft at low speeds.
- Limited steady experimental data were used to adjust the VLM models to better capture the vortex breakdown effect.
- The experimental data from water and wind tunnel tests, both steady and unsteady, were used to validate The fine-tuned VLM models' accuracy, including in the separation region at high angles of attack (AoAs). The University of Michigan's developed framework based on the UM/HSV was fundamental to enabling the aeroelastic-flight dynamic analysis under gust disturbances.
- To explore the design space, the use of sensitivity methods, both analytical and numerical, enabled the identification of important trade-offs aimed at improving the controllability of the aircraft. The use of analytical linearized aerodynamic models (UVLM + Polhamus) was effective for design exploration, and it can enable a rapid connection with MDO problems and control-oriented models.
- Initial analysis of the ride quality metric indicates that discomfort levels increase with greater fuselage flexibility, particularly in long, slender fuselages.
- The flight dynamics simulation revealed instability due to vortex breakdown, indicating the need to account for it during the vehicle design process.

In the area of technology development for the control-aware multidisciplinary design optimization of SCALOS-type vehicles approaches and metrics were defined for control-aware (and specific controller-agnostic) MDO:

- Avoid committing to a specific control design early in the development cycle.
- Exploit bi-level optimization with inner loop optimization with respect to
  - Control trajectory as a function of time given disturbance scenarios ("optimal control route") – extends the classical controllability Grammian analysis to systems with constraints and disturbances
  - or
  - Sensitivity function parameters ("fundamental limitations of performance and frequency domain risk metrics route") - captures the effects of a feedback controller without explicitly designing the controller.
- Risk metrics that depend on the moments of the PSD were defined based on the novel application of Rice's formula and their use demonstrated in case studies (Probability of exceedance, frequency of exceedance, . . .)
- Approaches and metrics are compatible with gradient-based optimization: Procedures to compute derivatives of the metrics were developed leading to fast, accurate, and memory efficient derivatives.

Conclusions from the case studies have design guideline implications, e.g., risk metrics for landing of the supersonic configuration aircraft are very sensitive to the CG position.

From **Stanford University** in the area of variable fidelity CFD/VLM aerodynamic modeling using neural net fine-tuning:

1. In the current study, the concept of using graph neural network to build multi-fidelity surrogate models was investigated to infer high-fidelity field data from low-fidelity field data input.
2. The predicted field variable and the computed functionals of interests showed reasonably good quality for the purpose of conceptual design.
3. Artifacts exist in the predicted results, which shall be mitigated by adding physical constraints and regularization in the neural net architecture.

In the area of RANS based methods for the prediction and reduction of jet noise:

- Wavepacket jitter modeling:
  - A predictive model form of acoustic line source cross spectral density was proposed, based on eddy-viscosity resolvent analysis to deduce wavepacket structure.
  - Expressive model capturing physical complexity with minimal tuning parameters.
  - Shallow angle acoustic prediction was demonstrated.
- Turbulent scales modeling:
  - Characteristic turbulent scales against true velocity correlations obtained from LES data at M = 0.5 and M = 0.9 were compared.
  - A predictive model based on radial weight distribution was proposed - with comparable accuracy to industry codes with fewer correction terms and tuning constants.

  - Sideline angle acoustic prediction was demonstrated.

- Adjoint-based chevron optimization:

  - Ribner acoustic source model with geometric acoustics for far field propagation was implemented - acoustic prediction was validated against experiments.
  - AD-enabled acoustic design tool with SU2 discrete adjoint solver were coupled to perform computationally efficient design optimization of nozzle geometries.
  - The objective agnostic implementation can be used with any acoustic module.

A summary of key accomplishments and lessons from the **University of Washington's** Kirsten Wind Tunnel test program:

- Data from 85.5 test days at the KWT was gathered, including pre-SCALOS tests 2015-2018.
- 2400 test runs of numerous configurations were completed, covering various wing planforms, tail geometries, canard geometries, aft-decks, arrangements of configuration components including engine nacelle location, high-lift devices leading to a treasure of experimental data.
- New wind tunnel "corrections" for T&I effects were developed because of the unique nature of the SCALOS-type configurations. With new configurations that are out of the configuration space that a wind tunnel has raw data to free flight "corrections" for dedicated T&I "corrections" should be developed.
- The sampling of configuration design space, because of the large number of shape parameters involved, cannot be exhaustive. The selection of SCALOS-type configurations for testing was based on engineering / aerodynamic experience and is believed to answer key questions well enough.
- Important insights, regarding the effects of configuration shapes and configuration arrangements were gained. Lists of major insights in this area can be found in **Appendix D** and **Appendix E** and the associated conference papers. Direct work with the KWT test results database (and the companion Boeing FVWT test results database) will allow designers and aerodynamicists (including CFD technology developers) to study more configuration variations than those that were discussed in the papers and Appendices.

Additional accomplishments and lessons from **University of Washington** SCALOS work:

- RANS simulations that were carried out so far captured lift well overall, but "struggled" especially with pitching moment predictions. The SCALOS-type configurations, with their long fuselages, cranked-delta wings, and various engine nacelle locations exhibit complex "vortex action" in the flow field, including vortex burst at high angles of attack and sideslip angles. Capturing the flow physics in the leading edge areas, around highly swept subsonic leading edges and around thin supersonic leading edges is a challenge, as it is a challenge to capture by a RANS CFD model the complex flow field behind a model and its wind tunnel support system, especially at high angles of attack. Because of the slenderness and length of the model any CFD modeling accuracies in the nose and tail area or any area that has a large moment arm to the CG would translate to inaccuracies in the prediction of pitching and yawing moments. A detailed list of CFD analysis to test results correlation insights is presented in [30].
- Tests of SCALOS-type models in the UW's 3x3 led to useful data, including flow-vis images (see Ref. [29]) that added understanding of the flow fields involved. It is believed that after additional investments in 3x3 calibration and wind tunnel corrections, it can be a very useful and cost effective tool in the configuration development of aircraft regarding their low-speed characteristics.

Regarding the RSAC development: As has already stated above, the RSAC's external aerodynamic lines would provide a realistic starting point for those wishing to exercise or further develop aero shape optimization tools. The conceptual internal arrangement would provide representative integration features and "packaging" dimensions / volume allowances to guide the development of OML shape constraints. A detailed weights breakdown, representative propulsion system and structures concepts and engine performance estimates, combined with information from the SCALOS wind tunnel testing database, would provide academia, industry, and researchers with a common non-proprietary point-of-departure for design trades, MDO development, and calibration of various predictive tools. To the maximum extent possible, within the limitations of the academic program and the time and resources of the SCALOS grant program, it is believed that the above objectives have been achieved. Like all concept level designs, the RSAC-E still contains many "place-holders" and assumptions and is far from the "perfect design". The RSAC-E does satisfy the original configuration intents.

The **Boeing** Flow Visualization Water Tunnel work:

The goal here was to measure dynamic stability derivatives at a range of angles of attack and reduced frequencies. The test models were equipped with dye injection capabilities for flow visualization. Numerous test runs were completed. The resulting test database, together with the UW KWT test database, cover both static and dynamic stability derivatives of SCALOS-type configurations based on which the mathematical models of such configurations for flight dynamics and control research and development work can be created.

Several data issues were observed and investigated during Part I and II of the FVWT project work and continued to be investigated in Part III of the work (see **Appendix C**). These included data repeatability, noisy forced oscillation data and issues with low-pass filtering. Unfortunately, pitch and yaw plunge testing was not able to be conducted to determine the $\dot{\alpha}$ and $\dot{\beta}$ angular rate dynamic stability derivative components. The FVWT work conducted on this project has furthered the understanding of how unique low-boom and conventional supersonic aircraft configuration perform at low-speed takeoff and landing flight conditions. It also shows the accuracy, utility, and cost effectiveness of using the Boeing FVWT for acquiring dynamic stability derivative data through forced oscillation testing.

7 Teams Collaboration

The project benefited from strong collaboration among its UM, SU, UW, and Boeing teams.

- UW configuration geometries were shared with Boeing, UM, and Stanford and used for their work.
- UW KWT test results were shared with Boeing, UM, and Stanford and were used for validation of simulation and test results.
- KWT and Boeing test results were used by UM and SU to improve low-fidelity nonlinear aerodynamic models and study the accuracy of CFD simulations.
- UM aerodynamic simulation tools, fine-tuned by UW and Boeing test results, were used at UM for the flight dynamic simulations driving the UM handling qualities and trajectory control studies.

8 Recommendations

Much more work is needed in each of the areas that the SCALOS project covered. In what follows we use the term "SCALOS-type configurations" to denote the slender configurations that the SCALOS project has covered, including different tradeoffs between low-boom and supersonic performance considerations. More detailed recommendations are presented in **Appendices A,B,C,D,E, and F**. //

- The CFD aspect of the work: Additional work is required to understand the sources of modeling difficulty and to guide **practical** CFD modeling of SCALOS-type configurations at low speeds over the relevant range of angles of attack and sideslip angles as well as the range of operation of control and high lift devices. A few open questions that need addressing:

  - The capability of RANS CFD to capture aerodynamic characteristics at the high AOA and beta range where the unsteadiness of the flow becomes very important. Although commercial aircraft flight enveloped will be limited in order to keep them within well-behaved and well-modeled operations, there must be reliable modeling of beyond-limits dynamic behavior since cases of angle of attack (AOA) and beta beyond-limits flight conditions are expected.
  - The capability of CFD-based modeling to generate accurate predictions in the transonic flight regime for SCALOS-type configurations.
  - The differences in predictions that comparisons of state of the art CFD tools show and their theoretical and numerical implementation sources.

- It is important to continue to develop CFD-based shape optimization of supersonic commercial configurations with constraints that cover both the low-speed and high speed flight regimes, including the capability for tradeoff studies and multi-objective optimization. In such shape and arrangement optimization studies the transonic flight regime should be covered in addition to the supersonic and low-speed regimes.

- Aeroelastic effects, static and dynamic, play an important role in the flight dynamics of SCALOS-type configurations. It is important to develop computationally-efficient and accurate flight dynamic models for elastic SCALOS-type configurations capable of capturing both linear and nonlinear unsteady aerodynamic behavior.

- More work dedicated to the development of control strategies for SCALOS-type aircraft in the takeoff, early climb, approach, and landing phases of their flight, including handling qualities, ride comfort, dynamic loads, and noise.

- More water tunnel tests are recommended to cover cases that were not tested during the SCALOS project and to expand the configuration design space for which dynamic stability derivatives will be available. More CFD work needs to be carried out to evaluate how well time-domain CFD modeling tools can capture the measured aerodynamic behavior of dynamically moving models. More should be invested in trying to identify and understand the high noise levels in the FVWT measurements and to reduce them.

- Much more work is required to develop aeroacoustic computational design tools for predicting community noise generated by SCALOS-type vehicles the that are accurate and practical.

- An effort should be made to integrate the KWT and FVWT test results databases and create a user-friendly database in which finding the aerodynamic data for the SCALOS configurations will be automated and which will allow interpolation between the KWT / FVWT configuration sample points to find estimates of the aerodynamic characteristics of similar but different configurations. In a way, create a "Digital DATCOM"-like database using appropriate machine learning and graphic techniques.

- More wind tunnel testing with large models is recommended to cover cases and areas that have not been covered yet and for:

  - More in-dept understanding of test / CFD-prediction discrepancies and their sources. Such tests should include flow field surveys and, if budgets allow, pressure distribution measurements.
  - Studying the effects of additional aerodynamic design shaping features such as fences, LE gaps, vortex generators, TE fins, vortilons, etc. With such aerodynamic shaping "tools", it may be possible to stabilize the flow field at higher angles of attack and delay the appearance of buffet and major unsteadiness. This may allow RANS CFD simulations to stay accurate at higher angle of attack and sideslip angles.

- Continue to develop 3x3 low-speed tunnel test capabilities (for the UW's 3x3 tunnel or similar tunnels) for SCALOS-type configurations for fast, cost-effective, configuration research and development.

- Continue to improve the conceptual design of the RSAC configuration, with more support by analysis (from low to medium to high fidelity modeling), more detail, and the necessary design improvements that would make it meet all design requirements. As a part of this effort, continue to provide senior level aircraft design educational experience to as many aerospace engineering students, exposing them to the challenges of designing supersonic aircraft (where today most of the capstone design experience of undergraduate students is focused on low-speed UAVs and low-speed aircraft of all types).

- Beyond what the SCALOS project tackled, add propulsion and propulsion integration to the mix of design requirements and constraints for the low-speed, subsonic, and supersonic flight regimes.

References

[1] Seraj, S., and Martins, J. R. R. A., "Predicting the High Angle of Attack Characteristics of a Delta Wing at Low Speed," *AIAA Aviation Forum*, 2021. doi:10.2514/6.2021-2612.

[2] Seraj, S., and Martins, J. R. R. A., "Aerodynamic Shape Optimization of a Supersonic Transport Considering Low-Speed Stability," *AIAA SciTech Forum*, 2022. doi:10.2514/6.2022-2177.

[3] Seraj, S., and Martins, J. R. R. A., "Predicting the High-Angle-of-Attack Characteristics of a Delta Wing at Low Speed," *Journal of Aircraft*, Vol. 59, No. 4, 2022, pp. 1071–1081. doi:10.2514/1.C036618.

[4] Seraj, S., Yildirim, A., Anibal, J. L., and Martins, J. R. R. A., "Improving the Performance of a Compressible RANS Solver for Low and High Mach Number Flows," *Eleventh International Conference on Computational Fluid Dynamics*, 2022.

[5] Seraj, S., and Martins, J. R. R. A., "Minimum Trim Drag for a Three-Surface Supersonic Transport Aircraft," *AIAA Aviation Forum*, 2023. doi:10.2514/6.2023-3472.

[6] Seraj, S., Yildirim, A., Anibal, J. L., and Martins, J. R. R. A., "Dissipation and time step scaling strategies for low and high Mach number flows," *Journal of Computational Physics*, Vol. 491, 2023, p. 112358. doi:10.1016/j.jcp.2023.112358.

[7] Anibal, J. L., Seraj, S., Yildirim, A., and Martins, J. R. R. A., "Mixed continuation methods for robust CFD Newton solvers," *AIAA SciTech Forum*, 2023. doi:10.2514/6.2023-2296.

[8] Hajdik, H. M., Yildirim, A., Wu, N., Brelje, B. J., Seraj, S., Mangano, M., Anibal, J. L., Jonsson, E., Adler, E. J., Mader, C. A., Kenway, G. K. W., and Martins, J. R. R. A., "pyGeo: A geometry package for multidisciplinary design optimization," *Journal of Open Source Software*, Vol. 8, No. 87, 2023, p. 5319. doi:10.21105/joss.05319.

[9] Seraj, S., "Aerodynamic Design Optimization of a Supersonic Transport Aircraft Considering Low-Speed Stability," Ph.D. thesis, University of Michigan, 2024. doi:10.7302/22987.

[10] Guimarães, T. A., Cesnik, C., and Kolmanovsky, I., "Low Speed Aerodynamic Modeling for Control-related Considerations in Supersonic Aircraft Design," *AIAA Aviation 2021 Forum*, AIAA Paper 2021-2531, 2021. doi:10.2514/6.2021-2531.

[11] Guimarães, T. A., Cesnik, C., and Kolmanovsky, I. V., "An Integrated Low-Speed Aeroelastic-Flight-Dynamics Framework for Modeling Supersonic Aircraft," *AIAA SciTech 2022 Forum*, AIAA Paper 2022-2175, 2022. doi:10.2514/6.2022-2175.

[12] Guimarães, T. A., Cesnik, C., and Kolmanovsky, I., "Unsteady Vortex Lattice Linearization and Sensitivity Analyses for Control Models in Supersonic Aircraft Design," *AIAA SciTech 2023 Forum*, AIAA Paper 2023-0416, 2023. doi:10.2514/6.2023-0416.

[13] Guimarães, T. A., Cesnik, C., and Kolmanovsky, I., "Flexibility Assessment of the Aeroelastic-flight-dynamic Behavior for Supersonic Aircraft," *AIAA SciTech 2023 Forum*, AIAA Paper 2023-0417, 2023. doi:10.2514/6.2023-0417.

[14] Guimarães, T. A., and Cesnik, C., "The Impact of Vortex Breakdown on the Longitudinal Flight Behavior of the SCALOS Aircraft," *AIAA SciTech 2024 Forum*, 2024.

[15] Cunis, T., Kolmanovsky, I. V., and Cesnik, C., "Control Co-Design Optimization: Integrating nonlinear controllability into a multidisciplinary design process," *AIAA SciTech 2022 Forum*, AIAA Paper 2022-2176, 2022. doi:10.2514/6.2022-2176.

[16] Bertolin, R., Chaves Barbosa, G., Cunis, T., Kolmanovsky, I. V., and Cesnik, C., "Gust Rejection of a Supersonic Aircraft During Final Approach," *AIAA SciTech 2022 Forum*, AIAA Paper 2022-2174, 2022. doi:10.2514/6.2022-2174.

[17] Monteiro, B. B., Kolmanovsky, I., and Cesnik, C., "Controller Agnostic Design Metrics for Stochastic Disturbance Rejection," *AIAA SciTech 2024 Forum*, 2024. doi:10.2514/6.2024-0901.

[18] Monteiro, B. B., "Control Related Metrics for Multidisciplinary Design Optimization," Ph.D. thesis, University of Michigan, 2024. doi:10.7302/23748.

[19] Nelson, C. P., Ting, K.-Y., Mavriplis, N., Soltani, R., and Livne, E., "Supersonic Configurations at Low Speeds (SCALOS): Project Background and Progress at University of Washington," *AIAA SciTech 2022 Forum*, AIAA Paper 2022-1803, 2022. doi:10.2514/6.2022-1803.

[20] Ting, K.-Y., Mavriplis, N., Soltani, R. M., Nelson, C. P., and Livne, E., "Supersonic Configurations at Low Speeds (SCALOS): Model Geometry and Aerodynamic Results," *AIAA SciTech 2022 Forum*, AIAA Paper 2022-1800, 2022. doi:10.2514/6.2022-1800.

[21] Mavriplis, N., Ting, K.-Y., Moustafa, A., Hill, C., Soltani, R. M., Nelson, C. P., and Livne, E., "Supersonic Configurations at Low Speeds (SCALOS): Test / Simulation Correlation Studies," *AIAA SciTech 2022 Forum*, AIAA Paper 2022-1801, 2022. doi:10.2514/6.2022-1801.

[22] Mavriplis, N., "RANS-CFD Based Assessment of Corrections Applied to the Measured Characteristics of Supersonic Configurations in a Low Speed Wind Tunnel," Master's thesis, University of Washington, 2022. URL http://hdl.handle.net/1773/49591.

[23] Nelson, C. P., Ting, K.-Y., Ignacio, J., Mavriplis, N., Soltani, R., and Livne, E., "Supersonic Configurations at Low Speeds (SCALOS): Configuration Comparison of SCALOS to Existing Designs," *AIAA SciTech 2023 Forum*, AIAA Paper 2023-0228, 2023. doi:10.2514/6.2023-0228.

[24] Ting, K.-Y., Mavriplis, N., Soltani, R. M., Nelson, C. P., and Livne, E., "Supersonic Configurations at Low Speeds (SCALOS): The Aerodynamic Effects of Control Surfaces," *AIAA SciTech 2023 Forum*, AIAA Paper 2023-0229, 2023. doi:10.2514/6.2023-0229.

[25] Ting, K.-Y., Mavriplis, N., Soltani, R. M., Nelson, C. P., and Livne, E., "Supersonic Configurations at Low Speeds (SCALOS) Longitudinal Aerodynamics: Configuration Variations and Control Surfaces Effects," *AIAA SciTech 2023 Forum*, AIAA Paper 2023-0230, 2023. doi:10.2514/6.2023-0230.

[26] Mavriplis, N., Ting, K.-Y., Soltani, R. M., Nelson, C. P., and Livne, E., "Supersonic Configurations at Low Speeds (SCALOS): CFD Aided Wind Tunnel Data Corrections," *AIAA SciTech 2023 Forum*, AIAA Paper 2023-0231, 2023. doi:https://doi.org/10.2514/6.2023-0231.

[27] Ting, K.-Y., Nelson, C. P., and Livne, E., "Supersonic Configurations at Low Speeds (SCALOS): Tare & Interference Corrections for SCALOS Configurations Tested at the University of Washington's Kirsten Wind Tunnel," *AIAA SciTech 2024 Forum*, 2024. doi:10.2514/6.2024-0899, AIAA Paper 2024-0899.

[28] Ting, K.-Y., Nelson, C. P., Wiersema, K., and Livne, E., "Supersonic Configurations at Low Speeds (SCALOS): Progress at the University of Washington," *AIAA SciTech 2024 Forum*, 2024. doi:10.2514/6.2024-0898, AIAA Paper 2024-0898.

[29] Ting, K.-Y., Soltani, R. M., Wiersema, K., Nelson, C. P., and Livne, E., "Lateral-directional Aerodynamics: Configuration Variations and Control Surface Effects," *AIAA SciTech 2025 Forum*, AIAA Paper, 2025.

[30] Wiersema, K., Ting, K.-Y., Nelson, C. P., and Livne, E., "Supersonic Configurations at Low Speeds(SCALOS): Correlation of CFD / Wind Tunnel Test Results," *AIAA SciTech 2025 Forum*, AIAA Paper, 2025.

[31] Ting, K.-Y., Wiersema, K., Soltani, R. M., Nelson, C. P., and Livne, E., "Supersonic Configurations at Low Speeds (SCALOS): Wind Tunnel Tests at the University of Washington - an Overview and Some Key Insights," *AIAA SciTech 2025 Forum*, AIAA Paper, 2025.

[32] Shanbhag, T. K., Zhou, B. Y., Molina, E., and Alonso, J., "A Comparison of Jet Acoustic Analysis Methods," *AIAA Aviation 2021 Forum*, AIAA Paper 2021-2102, 2021. doi:10.2514/6.2021-2102.

[33] Shen, Y., and J., A. J., "Performance Evaluation of a Graph Neural Network-Augmented Multi-Fidelity Workflow for Predicting Aerodynamic Coefficients on Delta Wings at Low Speed," *AIAA SciTech 2025 Forum*, 2025. Session APA-82/SPSN-04, Supersonic Aerodynamics I.

[34] Shen, Y., Needels, J. T., and Alonso, J. J., "VortexNet: A Graph Neural Network-Based Multi-Fidelity Surrogate Model for Field Predictions," *AIAA SciTech 2025 Forum*, 2025. Session APA-22, Special Session: Applied Surrogate Modeling III.

[35] Magee, T. E., Hayes, P. J., Dorgan, A. J., and Khodadoust, A., "Dynamic Stability Characteristics for Commercial Supersonic Configurations at Low-Speed Flight Conditions," *AIAA SciTech 2022 Forum*, AIAA Paper 2022-1802, 2022. doi:10.2514/6.2022-1802.

[36] Magee, T. E., Hayes, P. J., Dorgan, A. J., and Khodadoust, A., "Dynamic Stability Characteristics for Commercial Supersonic Configurations at Low-Speed Flight Conditions – Part II," *AIAA SciTech 2024 Forum*, 2024. doi:10.2514/6.2024-0900.

[37] Magee, T. E., Hayes, P. J., and Khodadoust, A., "Dynamic Stability Characteristics for Commercial Supersonic Configurations at Low-Speed Flight Conditions – Part III," *AIAA SciTech 2025 Forum*, 2025.

[38] Livne, E., and Nelson, C., "From Blank Slate to Flight Ready New Small Research UAVs in Twenty Weeks-Undergraduate Airplane Design at the University of Washington," *AIAA Paper 2012-845*, 2012. doi:10.2514/6.2012-845, 50th AIAA Aerospace Sciences Meeting including the New Horizons Forum and Aerospace Exposition.

Supersonic Configurations at Low Speeds (SCALOS)

Final Report

December 15, 2024

Appendix A

University of Michigan

NASA's Commercial Supersonic Technology Project.

Project Prime: University of Washington's Low-Speed Flight Characteristics and Noise Design Tools for the Integrated Configuration Shaping of Commercial Supersonic Aircraft

Final Report

Modeling of Low-Speed Flight Characteristics for Integrated Configuration Shaping of Commercial Supersonic Aircraft

Carlos E. S. Cesnik (PI),
Ilya Kolmanovsky (co-I), Joaquim R. R. A. Martins (co-I),
Thiago A. M. Guimarães, Bernardo B. Monteiro, Sabet Seraj,
Torbjørn Cunis, Rafael M. Bertolin, and Guilherme C. Barbosa

October 2023

MICHIGAN ENGINEERING
UNIVERSITY OF MICHIGAN

Executive Summary

The work conducted by the University of Michigan team during the project focused on the assessment of the integration challenges and understanding of the couplings of the nonlinear aerodynamic interactions with the aircraft dynamics for deriving control-oriented models. It involved several investigations addressed in published papers [1, 2, 3, 4, 5, 6, 7, 8, 9, 10, 11, 12, 13, 14] and the previous annual reports.

Figure 1 outlines the organization of the internal teams at the University of Michigan (UM), highlighting its connection with the project framework. The aerodynamic modeling efforts provided input data for control metrics formulation and evaluations. In addition, exploring low-order methods enabled the capture of complex vortex interactions and the creation of surrogate models ready for control applications.

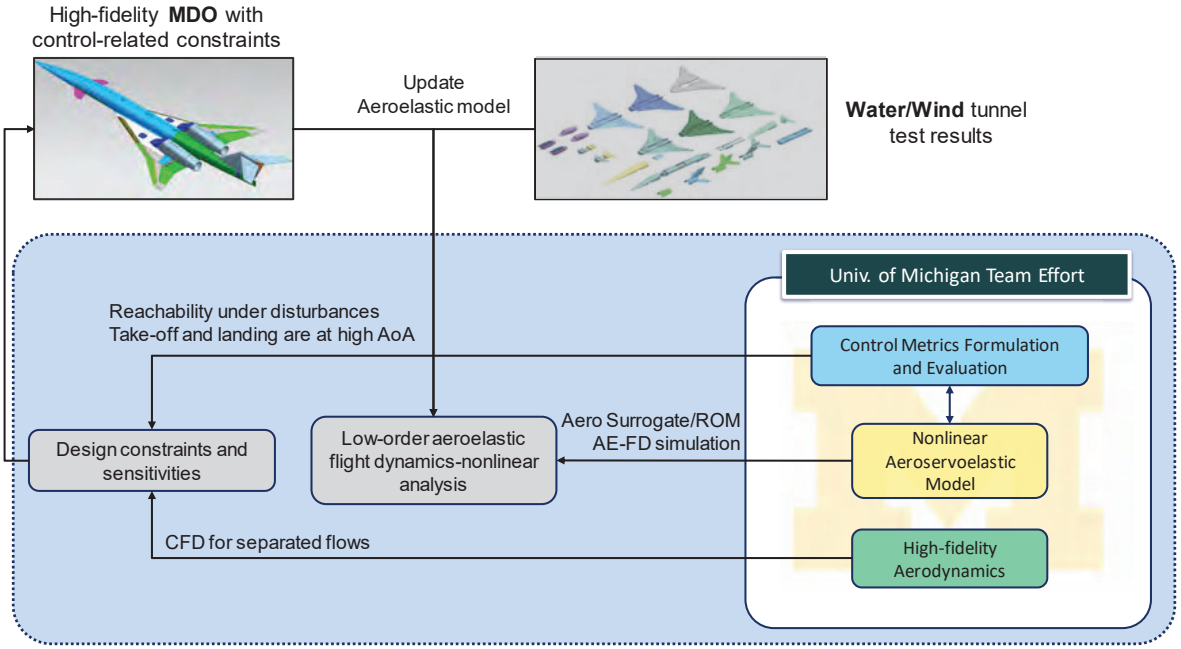

Figure 1: University of Michigan (UM) team's organization and synergisms in support to the advancement of low-speed modeling characteristics for supersonic aircraft configuration design.

The plan was originally for the high-fidelity aerodynamics group and the low-order modeling techniques group to collaborate on correcting the vortex-breakdown phenomenon at high angles of attack. However, due to the phenomenon's complexity and the need for dedicated models, the tasks were reorganized. As a result, the necessary corrections were obtained solely through experimental data.

In what follow we describe progress on the aerodynamic and aeroelastic modeling and evaluation in Sec. 1, the developments related to optimal control in Sec. 2, and progress on CFD analysis and design optimization in Sec. 3.

1 Aerodynamic and aeroelastic modeling and simulation

This section summarizes the developments in aerodynamic and aeroelastic modeling and simulation. The main focus is determining the appropriate level of model fidelity needed to capture the physics involved in the operation of supersonic aircraft at low speeds and high angles of attack, aiming to provide data suitable for control evaluations.

During the first year, the aerodynamic modeling effort focused on finding a low-order model to be used in modeling previous configurations and understanding the physics involved in operating a supersonic aircraft at low speeds and high angles of attack. The VORSTAB code [15] was selected, and due to its capability of modeling the effect of vortex lift and accounting for the effect of vortex breakdown, it was used to generate an initial reduced-order model built considering a polynomial chaos expansion, summarized in Sec. 1.2. This model was used first to generate a simplified model for controls regarding the baseline Scalos model and later to explore design alternatives by expanding geometrical parameters as discussed in the paper, "Low Speed Aerodynamic Modeling for Control-related Considerations in Supersonic Aircraft Design," which was presented at the 2021 Aviation Conference [1]. Additionally, sensitivity analyses were also investigated based on the global sensitivity method regarding the aerodynamic coefficients.

The following year, we focused on generating an in-house lower-order code to explore steady and unsteady aerodynamic simulations of the full vehicle configuration. We selected the UVLM method, combined with the Polhamos vortex lift method and the source panel method for modeling non-lifting surfaces, as the initial aerodynamic framework, as shown in Fig. 2. Details about the theoretical model and its integration in the aeroelastic framework are described in the paper, "An Integrated Low-Speed Aeroelastic-Flight Dynamics Framework for Modeling Supersonic Aircraft", published in annals of 2022 Scitech Conference [3] and summarized in Sec. 1.3

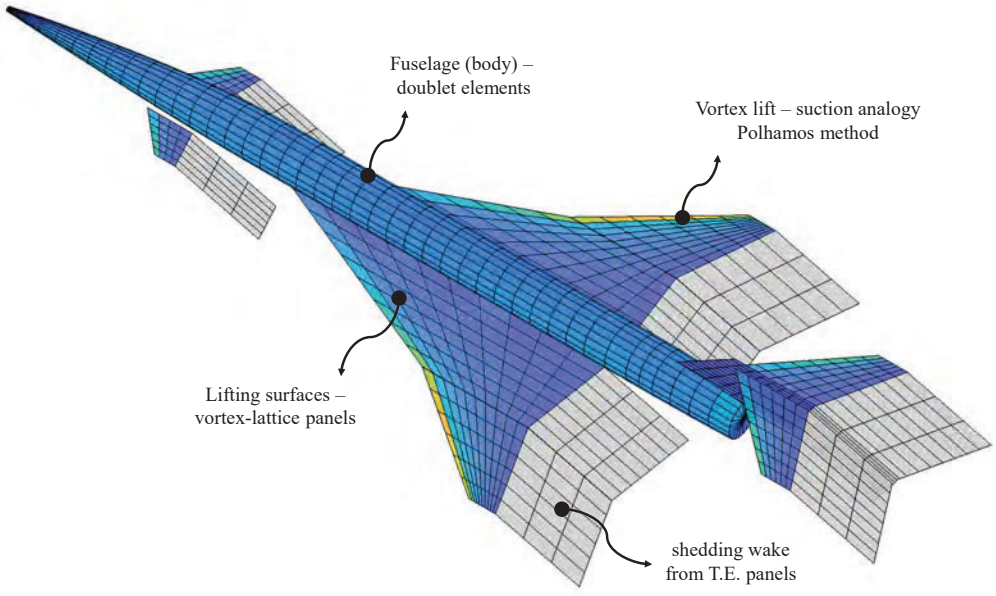

Figure 2: Aerodynamic model description.

Aiming to reduce the number of states of the aerodynamic model and to investigate sensitivity analysis of geometrical parameters, during the third year of the project, a dedicated effort was raised to bring the linearized UVLM to the developed framework, which also enabled obtaining the values sensitivity values that

could be used for optimization studies. To conduct this investigation, we also proposed a linearization of the vortex lift term, and the main findings are discussed in the paper published in the 2023 Scitech conference, "Unsteady Vortex Lattice Linearization and Sensitivity Analyses for Control Models in Supersonic Aircraft Design" [3]. A summary of the verification of the linearized model is presented in Sec. 1.4.

The impact of flexibility on the aeroelastic-flight dynamic behavior of a supersonic aircraft flying at low speeds and high angles of attack under gust continuous gust disturbances is also investigated and three distinct, flexible configurations are assessed to identify the impact of slender fuselages on the overall dynamic behavior of the aircraft. Using the previously mentioned enhanced UM/HSV framework [2], the coupled aeroelastic flight dynamic characteristics were investigated, as well as the riding quality metrics. The initial findings of this study were published in the 2023 Scitech conference, "Flexibility Assessment of the Aeroelastic-flight-dynamic Behavior for Supersonic Aircraft" [4] and are summarized in Sec. 1.5.

1.1 Scalos Model description

The Scalos aircraft model is based on the 2020 supersonic configuration developed by the University of Washington [16]. The configuration incorporates design features typically present in low-boom aircraft and business jet designs, as well as traditional supersonic configurations that do not prioritize low sonic boom. These design features include over-wing mounted nacelles, extended fuselage noses, T-tail arrangements, and 3-surface canard configurations.

The Kirsten Wind Tunnel at the University of Washington (UW) was used for all wind tunnel tests, with a test section of 12ft x 8ft x 10ft and two sets of 14' 9" -diameter seven-bladed propellers. Raw data from the external balance required correction for obtaining final force and moment values, with standard correction protocols applied for mechanical interaction of forces and moments in the balance system, weight tare, strut tare, blockage, flow angularity, and wall effects. Additional CFD and test work was done to improve wind tunnel corrections, but the data presented in the paper is based on historically used corrections. Tests were mainly conducted at 40 psf and later lowered to 32 psf to prevent severe buffeting of the model at high angles of attack [16].

The Water Tunnel model [17] is based on the UW 2020 and 2017 supersonic configurations with features commonly found on low-boom and business jet configurations and traditional supersonic configurations. The objective of the test was to determine how these features affect the low-speed dynamic stability of the aircraft through a modular model, which includes variations on nose length, wing planform, nacelle location, tail location, canard on/off, and leading-edge flap deflection. The model was constructed using additive manufacturing methods, with dye ports built-in for flow visualization during testing, as depicted in Fig. 3.

1.2 Reduced Order Model

The classical polynomial chaos expansions (PCEs) model, which are well-known non-intrusive metamodels, was selected in our case due to its capability of dealing with a high number of parameters using a set of sparse orthonormal polynomials to approximate the aerodynamic global behavior of the reference model.

The PCE representation of a given output parameter f is given by

$$f(\xi_1, \xi_2, ..., \xi_n) = u_0 \mathbf{H}_0 + \sum_{i=1}^{n} u_i \mathbf{H}_1(\xi_i) + \sum_{i=1}^{n} \sum_{j=1}^{i} u_{ij} \mathbf{H}_2(\xi_i, \xi_j) + \sum_{i=1}^{n} \sum_{j=1}^{j} \sum_{k=1}^{j} u_{ijk} \mathbf{H}_3(\xi_i, \xi_j, \xi_k) + \ldots, \tag{1}$$

where $u_i \ldots u_n$ are the deterministic coefficients to be determined and $\xi_i \ldots \xi_n$ are input variables. The projection basis is formed by Hermite polynomials $\boldsymbol{H}_0$, $\boldsymbol{H}_1(\xi_i)$, $\boldsymbol{H}_2(\xi_i, \xi_j), \ldots$ up to order p, so that the

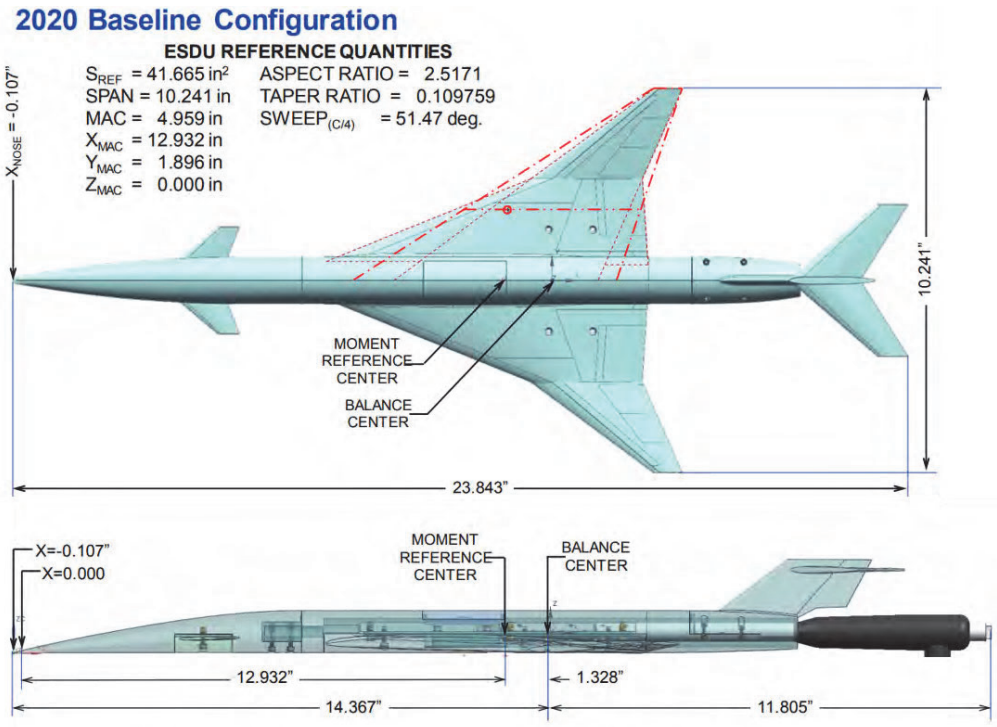

Figure 3: WT- Scalos baseline configuration [17].

total number of terms in Eq. 1 is:

$$N = \frac{(n+p)!}{n!p!}. \tag{2}$$

The number of parameters and the polynomial order needs to be set properly to avoid over-fitting and guarantee efficiency to be suitable for a control model.

The generation of two surrogate models for the Scalos baseline aircraft was conducted using the output for the aerodynamic coefficient values: lift coefficient (C_L), drag coefficient (C_D), pitching moment coefficient (C_m), lift coefficient due to pitch rate (C_{Lq}), and pitching moment damping derivative coefficient (C_{mq}). The verification of the surrogate model is presented in Figure 4, which compares the results obtained from the ROM with those obtained from the direct VORSTAB solution for the baseline SCALOS aircraft. Both sets of results exhibit excellent agreement in general. Furthermore, the PCE model is much faster, more robust to run, and better suited to support the evaluation of control metrics and constraints in future design optimization problems.

The SCALOS wind tunnel model described in Sec. 1.1 was used as the reference configuration for our studies, expanding our design space considering an expanded envelope of supersonic configurations. Its layout is shown in Fig. 4, where one can also see the parametrization variables. There are 16 input parameters considered. They comprise the aircraft angle of attack, flaps, canard and elevator deflection, wing, flaps, canard, horizontal tail, vertical tail, and elevator geometry–as detailed in Table 1.

The Latin-hypercube sampling (LHS) technique was selected to construct a database of $50,000$ individuals inside the design space that allows exploring different polynomial orders aiming at better data fitting.

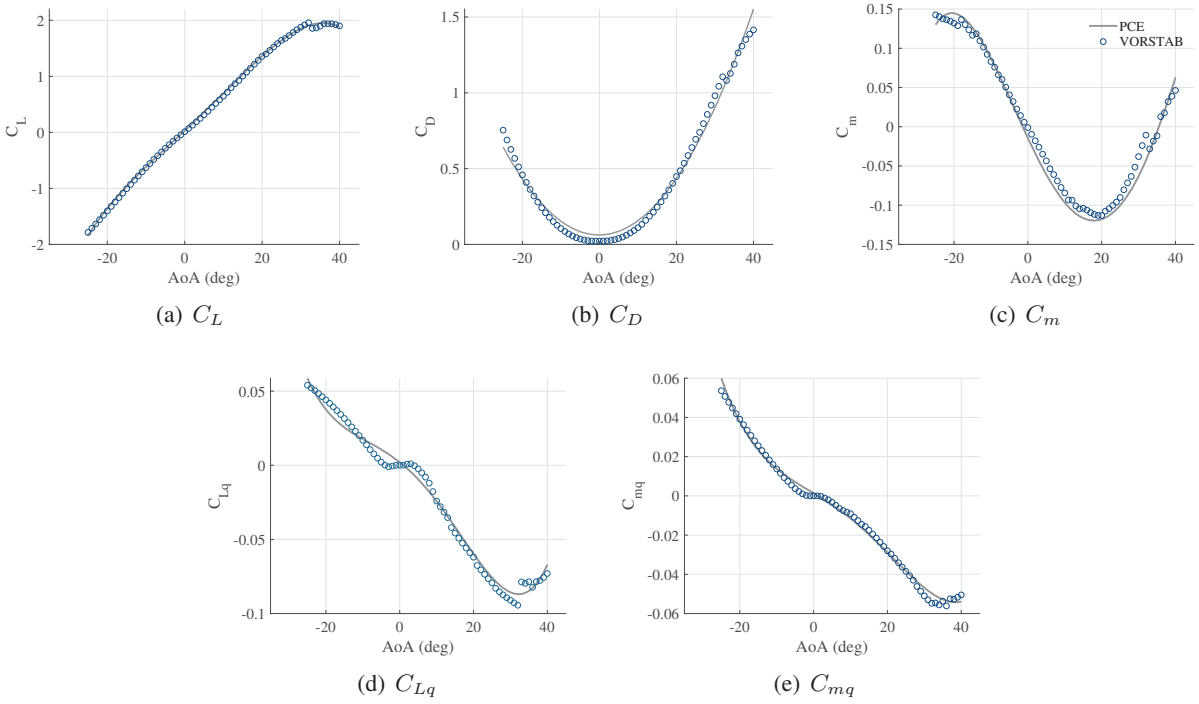

(a) C_L (b) C_D (c) C_m

(d) C_{Lq} (e) C_{mq}

Figure 4: PCE model verification with VORSTAB results.

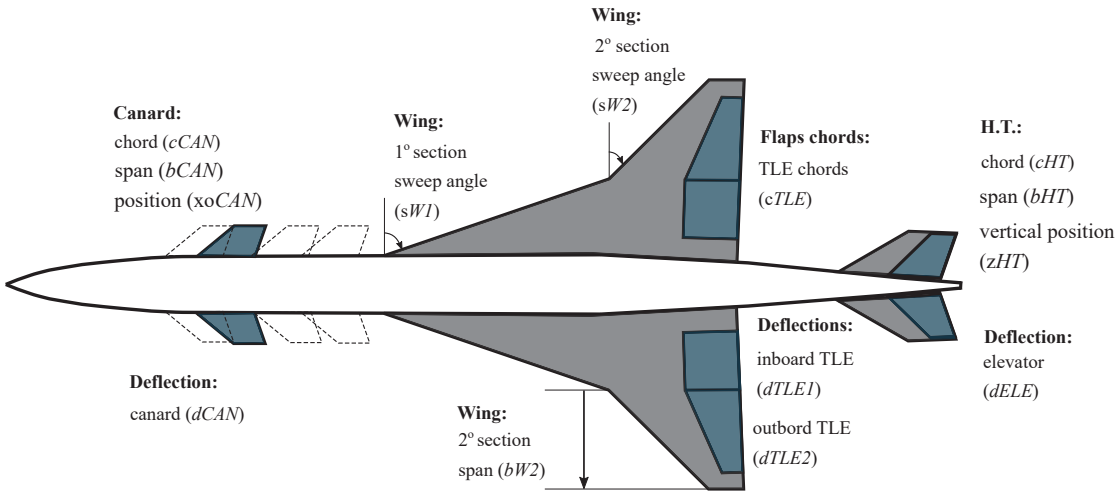

Figure 5: Input variables definitions for surrogate model generation.

1.3 Aerodynamic modeling based on vortex methods

The developed aerodynamic model based on the UVLM with the additional contribution of the vortex lift effect modeled following the Polhamos correction [18] is validated against the water tunnel experimental data [17] under the same steady conditions. To account for the separation effects, the aerodynamic coefficients are updated using, and the comparison using the proposed method with and without experimental corrections are highlighted in Fig. 6.

The box-plot data for each discrete angle of attack was gathered from the water tunnel test to measure the

Table 1: Input variables and their range for the SCALOS configurations

		Bounds		
Parameter name	Baseline	Lower	Upper	Unit/Scaling factor
Trailing edge flaps chord	0.1	0.1	0.2	root chord
Wing sweep angle (1st section)	67.3	63.0	73.0	°
Wing sweep angle (2nd section)	40.8	35.0	40.8	°
Wing span (2nd section)	1.0	0.6	1.2	reference wing span
Canard span	1.0	0.6	1.4	reference canard span
Canard chord	1.0	0.6	1.4	reference canard chord
Canard position	0.0	0.0	1.5	m (from reference canard position)
Horizontal tail (HT) span	1.0	0.6	1.4	reference HT span
Horizontal tail (HT) chord	1.0	0.6	1.4	reference HT chord
Elevator chord	0.7	0.3	0.7	reference HT chord
Horizontal tail vertical position	0.5	0.0	2.0	m (from reference HT position)
Inboard trailing edge flap	–	−15.0	35.0	°
Outboard trailing edge flap	–	−15.0	35.0	°
All-movable canard	–	−15.0	20.0	°
Elevator deflection	–	−20.0	20.0	°
Aircraft angle-of-attack	–	−25.0	40.0	°

aerodynamic coefficients at the steady condition. The UVLM combined with the Polhamos method shows a good agreement for angles of attack below 16 degrees. This was expected, considering the attached flow in this condition. However, for higher angles of attack, the mean values from the experimental test were considered to correct the K_v term from Polhamos correction and account for separation effects. Based on the single correction for the lift coefficient (C_L), the drag coefficient was consequently affected and showed a good agreement for higher angles of attack with the experimental values. To update the pitching moment, the new K_v values and the actuation point ($\bar{x}_{le}$) parameter were determined from experimental data.

Additionally, the results obtained with our proposed approach are compared with CFD results based on RANS equations [19], depicted in Fig. 7.

Interestingly, the UVLM approach has shown similar outcomes to those obtained through CFD simulations. This is a noteworthy finding as it indicates that the UVLM method can provide reliable results while saving computational time. Furthermore, the UVLM modeling approach allows for unsteady simulations that can capture the added mass effect, thereby enhancing the accuracy and fidelity of the aerodynamic model, as presented in the following discussion.

This research is planned to be published in the AIAA Journal [6] after expansion.

1.4 Aerodynamic linearization methods

This section explores the aerodynamic responses of the SCALOS aircraft based on the water tunnel geometry [17] using the linearized UVLM framework in combination with the linearized contribution from the leading edge vorteces. The SCALOS layout is assembled considering a canard, lower wing without deflecting the leading edge flap, short nose, and a vertical T-tail.

Three distinct configurations were selected to be investigated, considering geometric variations of the baseline aircraft, as proposed by Guimarães et al. [1] and depicted in Fig. 8. These configurations were chosen considering variations in span for the canard, wing, and HT surfaces. It is worth mentioning that the

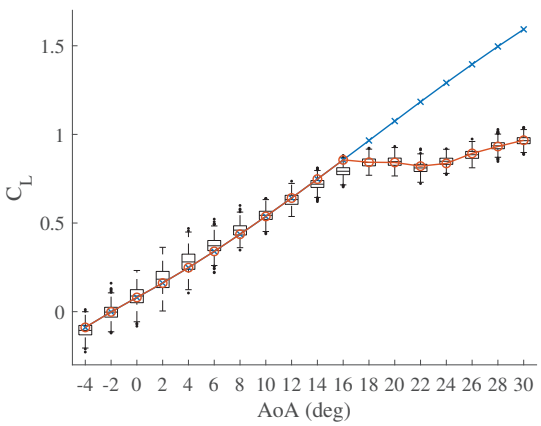

(a) Lift coefficient

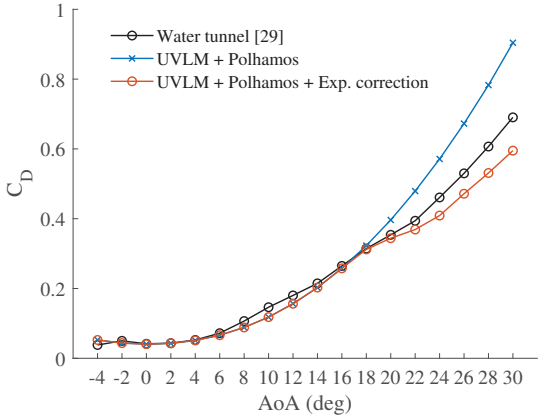

(b) Drag coefficient

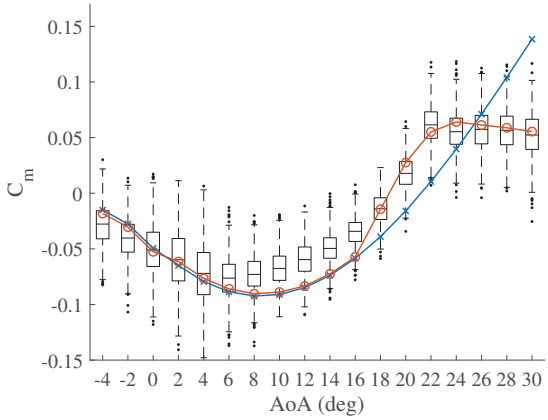

(c) Pitching moment coefficient

Figure 6: C_L, C_D, and C_m results comparison of SCALOS configuration with water tunnel experimental data.

fuselage effects were not considered in the following results, and all linearized results were obtained for the baseline configuration with no control surface deflection.

The verification comprises the configuration with variation in the wing span, considering results from the NL-UVLM solution against those obtained with the linearized version. For a flight condition at a high Angle-of-Attack case (AoA = 17deg.), the differences in the aerodynamic coefficients related to the variation of the potential forces and the vortex lift components are highlighted in Fig. 9.

The study is going to be expanded and published in the AIAA Journal [7].

1.5 Aeroelastic-flight-dynamic response

The water tunnel SCALOS aircraft geometry [17] is used to support the creation of a FE model to mimic the structural behavior of flexible supersonic aircraft. Three configurations are selected based on the geometry and definitions of the SCALOS aircraft. First, the baseline configuration (BL) considers the geometry and structural descriptions described in the authors' previous work [2]. The second configuration is similar to the first one, but the fuselage is considered rigid, and only the flexibility of the lifting surfaces is accounted for in further investigations. Finally, the third configuration is defined considering an extended nose (EN)

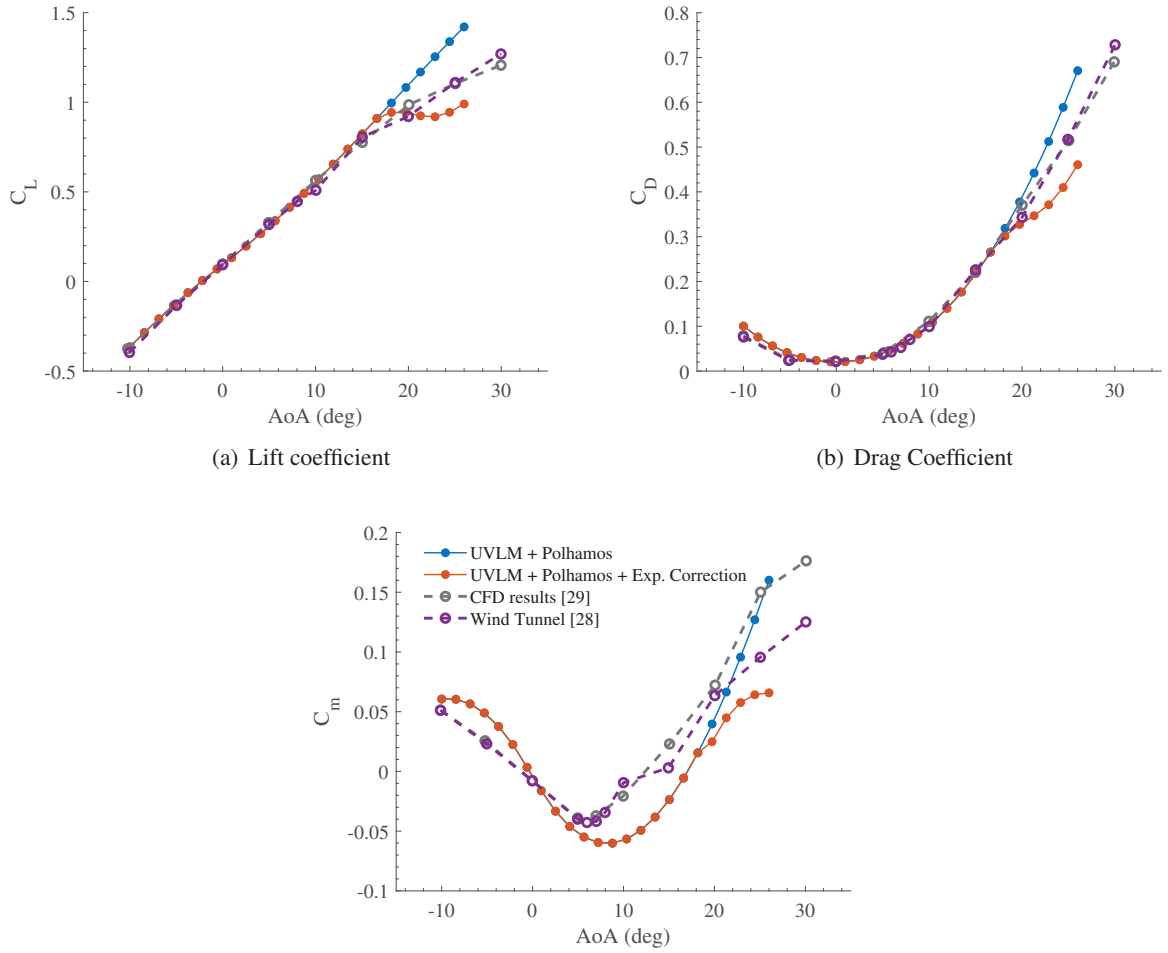

(a) Lift coefficient

(b) Drag Coefficient

(c) Pitching moment coefficient

Figure 7: C_L, C_D, and C_m Comparison for baseline SCALOS configuration with CFD and wind tunnel experimental data.

aiming to simulate the aeroelastic effect of a more slender and flexible fuselage. In Fig 10, the modes shapes for each configuration are depicted.

A geometric comparison between the baseline and the extended nose configuration is shown in Fig. 11. It is worth mentioning that the position of all lifting surfaces was considered the same, and only the length of the aircraft was modified by increasing the nose length. Additionally, the impact of the extended nose was considered negligible on the overall mass of the aircraft and in the center of gravity position of the aircraft.

The following studies consider a penetrative continuous gust input. Figure 12 shows the time signal associated with the vertical gust applied to the aircraft trimmed for level flight. We selected a moderate condition for the reference turbulence velocity starting after the first second with a gust duration of 10 seconds. The flight condition represents a low speed and high angle of attack case ($M_\infty = 0.25$, H = 2000m).

Figure 13 highlights the effect of fuselage flexibility on the flight dynamics behavior, in which the temporal response of the angle-of-attack and the pitch rate is shown. For the cases investigated, the fuselage flexibility affects the trimmed states. However, no significant difference between BL and EN configuration responses was noted. On the other hand, the dynamic behavior on the pitch rate response (ω_y) has a similar

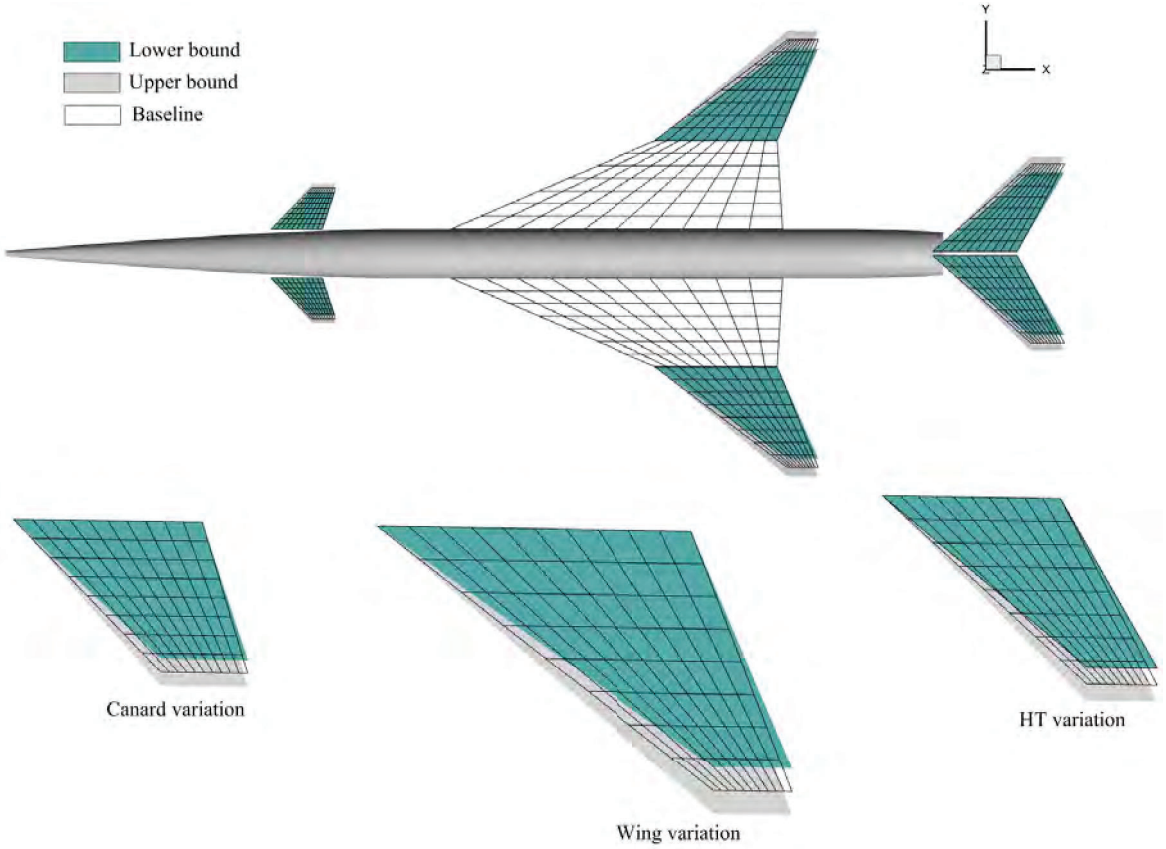

Figure 8: Span parametric variations of the SCALOS baseline aircraft.

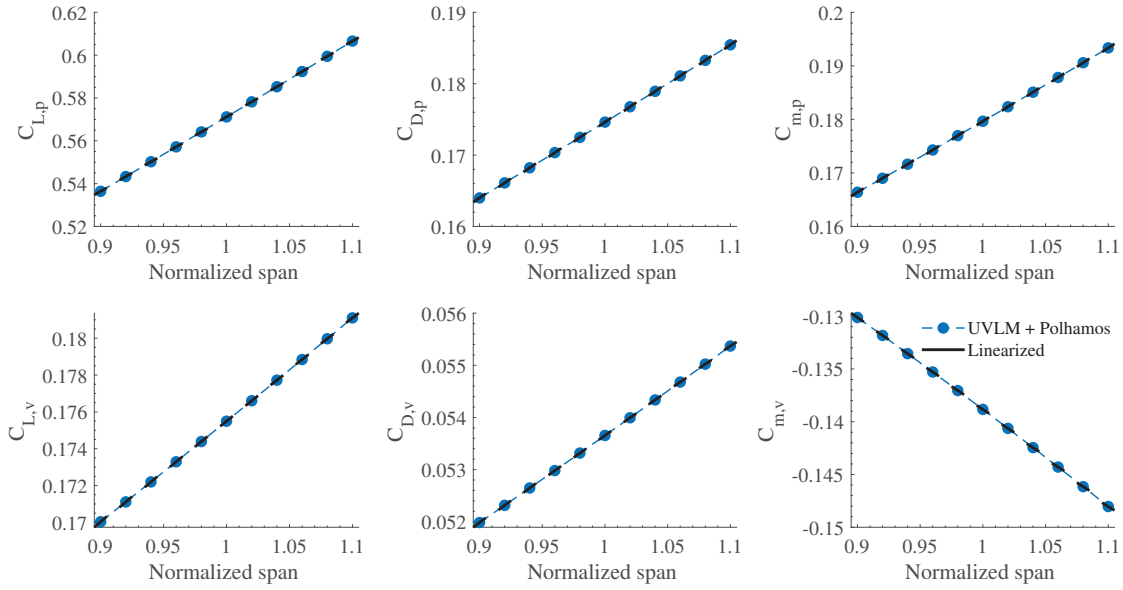

Figure 9: Results comparison for wing span variation.

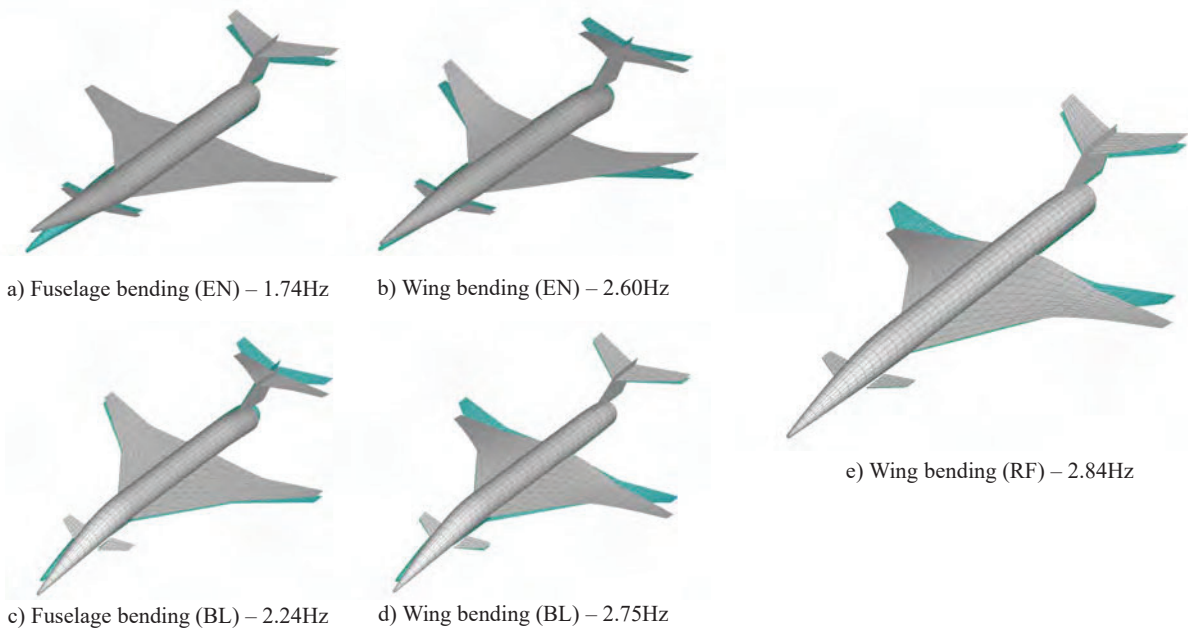

Figure 10: Elastic modes shapes for configurations BL, RF, and EN.

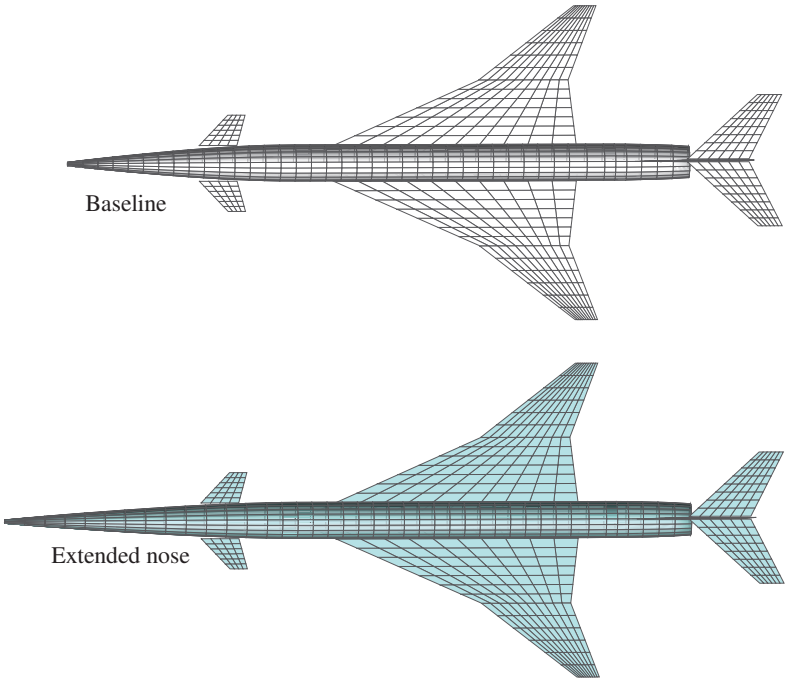

Figure 11: Geometry comparison between baseline and the extended nose configurations.

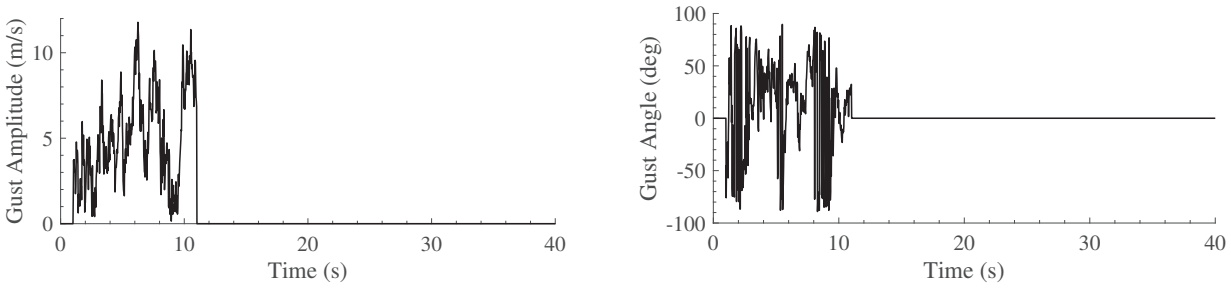

Figure 12: Von Kármán gust - Amplitude and angle profiles.

pattern among the configurations. Still, it is different in terms of amplitude, as highlighted in the detail of Figure 13.

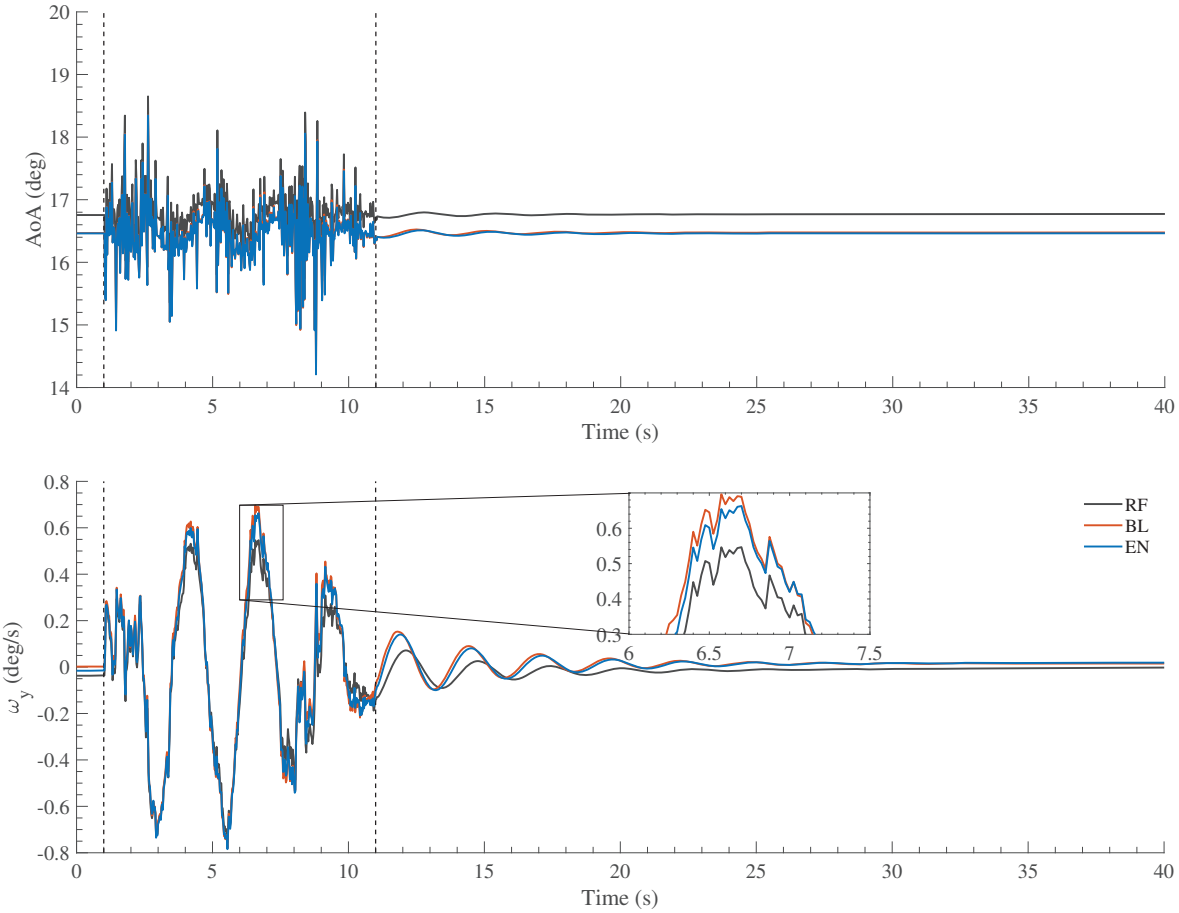

Figure 13: Results comparison of gust encounter - AoA and pitch rate states.

The open-loop simulation results confirmed that aeroelastic effects are non-negligible and must be accounted for when designing supersonic vehicles and their flight control system during low-speed flights.

Additional discussion regarding the linearized model used to generate the state-space representation of vehicle dynamics is provided in our paper [3], as well as the results related to ride quality analyses. The study is being expanded and is set to be published in the AIAA Journal of Aircraft [8].

1.6 Summary

We addressed the definition of a low-order aerodynamic model for control design and control co-design in aircraft MDO. The vortex-based codes provide adequate fidelity, capturing the prevalent physics phenomena involved in steady/unsteady simulations of high angles of attack and low-speed maneuvers. It also enabled the development of the non-intrusive PCE surrogate model. The surrogate model generates continuous equations formed by Hermite polynomials guaranteed computational efficiency. A set of parameterized flight simulations covering a wide range of supersonic design parameters, gust amplitudes, and trimming conditions was presented and analyzed.

We proposed a methodology to evaluate sensitivity metrics and to generate linearized aerodynamic coefficients for command of surface deflections based on the combination of the linearized UVLM with the additional linearized effect from the vortex lift derived from the Polhamus method. This approach enabled the exploration of parametric variations of the SCALOS aircraft for sensitivity analysis and the generation of linearized control surface derivatives. The developed approach enabled obtaining the control surface derivatives about the reference condition, which were considered for different angles of attack, and it is ready to be integrated into the control modeling. Additionally, given that the linearized model is obtained directly from the analytical derivatives, including the states and inputs of interest, the linearized aerodynamic model allows integration with the aeroelastic flight-dynamic model and can be used for studying the aircraft's stability.

We developed an integrated framework to simulate the coupled aeroelastic-flight-dynamics behavior of supersonic aircraft flying at low speeds and high angles of attack. The UVLM code enhanced with the Polhamos method with corrections from the water tunnel experiments provided adequate fidelity while capturing the prevalent physical vortex phenomena involved in high angles of attack and low-speed maneuvers. Including elastic modes from the finite element model into the UM/HSV simulation framework enabled the simulation of the longitudinal dynamic behavior of the aircraft considering different gust amplitudes and allowed for a comparison between the rigid and flexible vehicles. The open-loop simulation results confirmed that aeroelastic effects are non-negligible and must be accounted for when designing supersonic vehicles and their flight control system during low-speed flight. Special attention goes to the impact of flexibility from long and slender fuselages while determining flight dynamics stability characteristics.

Our upcoming work, to be presented at the next Scitech Conference, "The Impact of Vortex Breakdown on the Longitudinal Flight Behavior of the Scalos Aircraft," [5], focuses on the effect of vortex breakdown on aerodynamic coefficients. We have developed corrections for the baseline aircraft and included them in the UM/HSV framework to further analyze the aircraft's response under gust conditions. We have enhanced our modeling methodology, and variations of the LE-flap deflections were also assessed to simulate the aircraft's dynamic response. Future investigations should compare the impact of proper dynamic modeling of the vortex breakdown effects.

2 Aircraft maneuverability under gust disturbance for MDO

In this part of the report, we highlight the progress made in the formulation, evaluation, and optimization of control-related yet controller-agnostic (in the sense that a controller is not designed) metrics for airframe design. The main developments include applying the classical modal analysis and controllability Gramian-based analysis, followed by the extension of the latter to define optimal control-based metrics for aircraft maneuverability under a chosen wind disturbance scenario [12]. It covers the progress in establishing approaches for integrating optimal control-based metrics into airframe design optimization [13, 14]. Finally, the discussion focused on evaluating the airframe response to continuous turbulence in the frequency domain and through the probability and frequency of exceedence of operational constraints of the SCALOS aircraft during the final approach to landing. Specifically, exceedance of the envelopes of glideslope deviation, angle-of-attack, elevator deflection and elevator deflection rate were considered.

2.1 Controllability into a multidisciplinary design process

We propose a bilevel optimization framework, detailed in Fig. 14, where the outer loop represents a generic MDO algorithm exploiting gradients of the cost function and design constraints. We then propose an approach to nonlinear controllability constraints in terms of value functions of lower-level optimal control problems, which characterize the ability to perform specified maneuvers and will be solved depending on the design parameters as input from MDO. Unlike control-related metrics previously used for MDO [20, 21, 22, 23, 24], our framework is not limited to linearized dynamics and thus allows for controllability constraints spanning over a range of operating conditions. We develop an approach to compute the sensitivity of the nonlinear controllability constraint with respect to design parameters based on dual optimization variables.

We analyze and address potential nondifferentiability of the optimal value function using a concept of a generalized derivative, the subdifferential. This extension is important as value functions of the optimal control problems can be expected to be Lipschitz continuous but not differentiable everywhere. Instead, subdifferentials could possibly be integrated into a nonsmooth outer optimization scheme. Finally, we illustrate an implementation of the proposed approach for a supersonic wing-shaping case study. Overall, the proposed framework, supported by the analysis in this paper, enables the integration of control-related constraints into MDO in a way that is controller-agnostic yet ensures the existencee of a control input history that meets overall system targets.

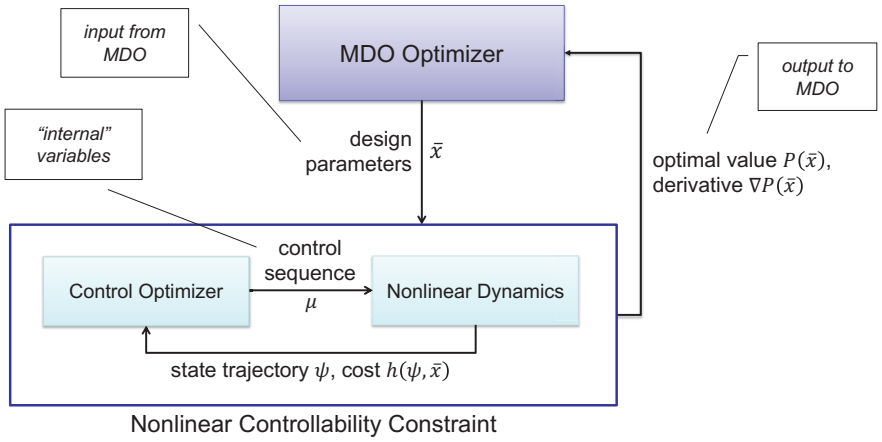

Figure 14: Structure of the proposed control-aware, controller-agnostic design optimization. Adapted from [14] with permission.

The proposed approach uses the dynamic model of a supersonic aircraft described in [14]. The results

for a control-agnostic design optimization example that integrated a discrete-time nonlinear controllability problem into a simplified optimal design of the aircraft's wing shape were obtained using the optimization process depicted in Fig. 15.

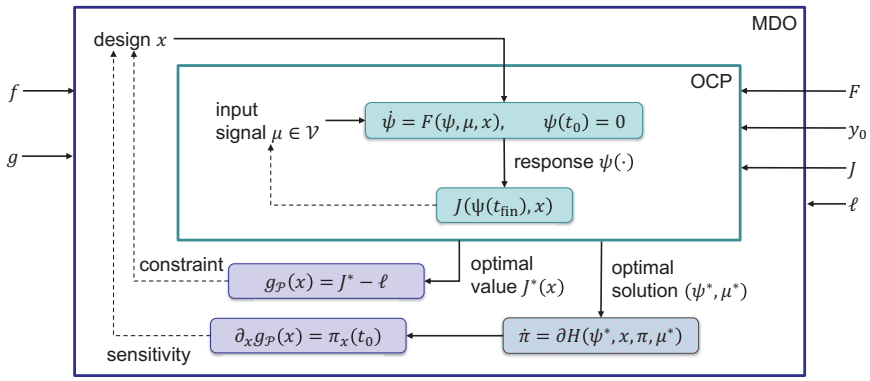

Figure 15: Details of the control-agnostic design optimization process [14]

We consider the problem of designing a supersonic aircraft with minimal wing area subject to the aircraft's ability to reject a sharp gust wind disturbance. Here, we chose the aircraft's wing area as a substitute for reducing energy consumption, as a smaller wing typically reduces both the overall aerodynamic drag as well as structural mass, thereby requiring less thrust to maintain level flight. According to Figure 16, the wing area can be computed as

$$f(x) = b_{\text{W1}}^2 \tan \varsigma_{\text{W1}} + 2 b_{\text{W1}} c_{\text{W2}} + b_{\text{W2}}(2 c_{\text{W2}} - b_{\text{W2}} \tan \varsigma_{\text{W2}}) \tag{3}$$

where the vector of design parameters x consists of first and second section sweep angles ς_{W1} and ς_{W2}, respectively, and the second section half-wing span b_{W2}; the first section half-wing span $b_{\text{W1}} = 1.615\,\text{m}$ and the wing chord length at the junction $c_{\text{W2}} = 2.43\,\text{m}$ are given as constants. The feasible design is constrained to a compact and convex set $X \subset \mathbb{X}$ given by Table 2.

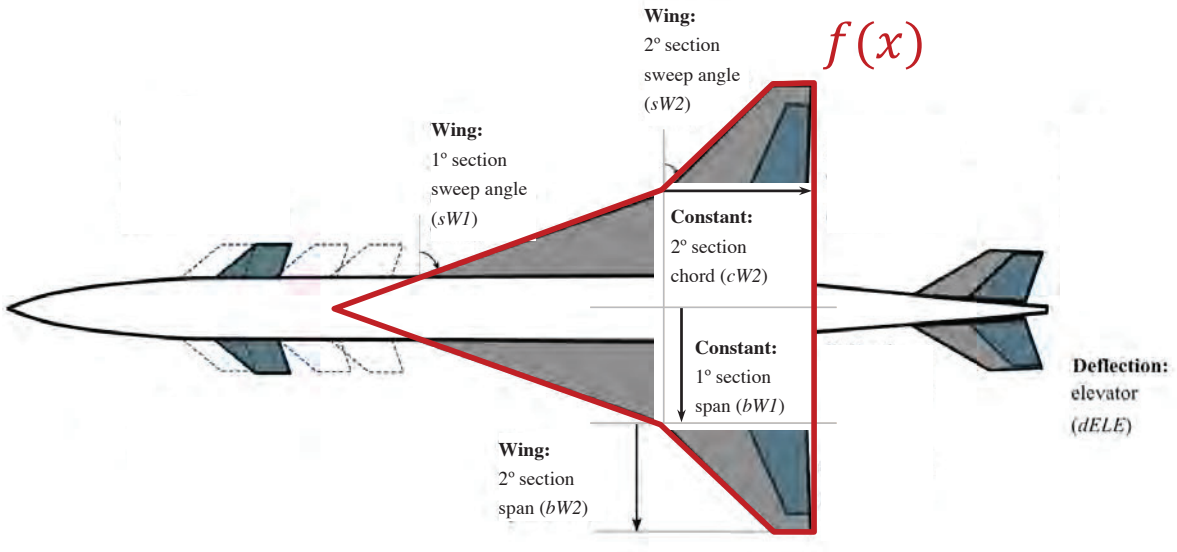

Figure 16: Aircraft geometry and details of the design optimization

Geometric	label	parameters	lower bound	upper bound	baseline	unit
Wing sweep angle 1st section	sW1	ς_{W1}	63	73	67.8	(°)
Wing sweep angle 2nd section	sW2	ς_{W2}	35	40.76	40.76	(°)
Wing span 2nd section	bW2	b_{W2}	1.344	2.688	2.24	(m)

Table 2: Design parameters of the design optimization.

Having defined the design objective and constraints, we proceed with detailing the controllability problem: The notion of gust rejection and the nonlinear aerodynamic model for a supersonic aircraft are detailed in [14]. For the purpose of this example, the longitudinal aerodynamics are characterized by a continuous-time nonlinear ordinary differential equation

$$\dot{y} = F_{\text{ODE}}(y, v, x)$$

where $F_{\text{ODE}} : \mathbb{Y} \times \mathbb{V} \times \mathbb{X} \to \mathcal{R}$ is computed with rational, polynomial, and trigonometric functions in (y, v) and polynomials in x; the state vector y comprises the path speed V_{K}, path inclination angle γ_{K}, pitch rate q, and pitch angle Θ; and the input vector v comprises the elevator deflection η and thrust force F. We consider the gust disturbance to be rejected if the aircraft returns sufficiently close to its desired flight path within a given finite time $T > 0$. Hence, to define the parametrized controllability problem, the control cost function $h : \mathbb{Y} \to \mathbb{R}$ determines the relative distance of $(V_{\text{K}}, \gamma_{\text{K}})$ to the desired flight path y^{SP}, i.e.,

$$h : y = (V_{\text{K}}, \gamma_{\text{K}}, q, \Theta) \mapsto \frac{||(V_{\text{K}}, \gamma_{\text{K}}) - (V_{\text{K}}, \gamma_{\text{K}})^{\text{SP}}||}{||(V_{\text{K}}, \gamma_{\text{K}})^{\text{SP}}||} \tag{4}$$

and the limit $\ell = 0.02$ corresponds to a $2\,\%$ terminal deviation. In other words, the aircraft is sufficiently close to the desired flight path if the relative distance does not exceed $2\,\%$, that is, $h(y) \leq \ell$. The aircraft is initially trimmed to a $-5°$-descent at $75\,\text{m}\,\text{s}^{-1}$, the desired flight path ($y_0 = y^{\text{SP}}$) without wind. At time t_0, the aircraft is subjected to a vertical up-wind step to $V_{\text{W}} = 25\,\text{m}\,\text{s}^{-1}$. The aircraft dynamics are discretized over the horizon $T = 25\,\text{s}$ into a grid of $N = 200$ control intervals $\mathcal{T}$ using a trapezoidal integration scheme, yielding the implicit discrete dynamics $G : \mathbb{Y}^2 \times \mathbb{V} \times \mathbb{X} \to \mathcal{R}$ defined as

$$G : (y_{k+1}, y_k, v_k, x) \mapsto y_{k+1} - \frac{T}{2N}\big(F_{\text{ODE}}(y_k, v_k, x) - F_{\text{ODE}}(y_{k+1}, v_k, x)\big) - y_k \tag{5}$$

for all $k \in [0, N)$. The viable inputs are restricted to the compact set

$$V = [-30°, +30°] \times [0, 50\,\text{kN}]$$

and the set of viable input sequences $\mathcal{V}$ contains all functions $\mu : \mathbb{N}_0 \to \mathbb{V}$ satisfying $\mu(k) \in V$ for all $k \in [0, N]$.

Remark 1. Although in our example, only elevator deflections and thrust force are constrained, further restrictions, such as limits on the rate of change of the controls, can be integrated into the proposed framework as additional constraints.

Clearly, V is locally closed (by compactness), normally regular (by convexity), and sequentially normally compact (by finite dimension). We assume that for any feasible design $\bar{x} \in X$ and viable input sequence $\mathbf{v} \in \mathcal{V}$, the solution $\mathbf{y} \subset \mathbb{Y}$ of the initial value problem defined by (5) and y_0 is contained by some compact set $Y \subset \mathbb{Y}$ for all $k \in [0, N)$, where F_{ODE} is nonsingular on $Y \times V \times X$. This can be assured be restricting $F_{\text{ODE}}(y, v)$ to the tangent cone of Y unless $y \in \operatorname{int} Y$. Hence, the continuous-time initial

value problem is unique and G and h are strictly differentiable (a fortiori, locally Lipschitz continuous) on $Y \times V \times X$. We thus have that for any feasible design $\bar{x} \in X$,

If $P(\bar{x}) \leq \ell$, then the designed aircraft can be kept within $2\,\%$ of the desired slope $25\,\mathrm{s}$ into the disturbance

where $P(\bar{x})$ is the optimal control value

$$P : x \mapsto \min_{\substack{\mathbf{y}\in\mathbb{Y}^N \\ \mathbf{v}\in\mathbb{V}^N}} h(y_N) \quad \text{s.t. } v_k \in V \text{ and } G(y_{k+1}, y_k, v_k, x) = 0 \text{ for all } k \in [0, N)$$

Assuming that the implicit equations of motion given by $G(\cdot)$ are an accurate discretization of F_{ODE}, that is, uniqueness and continuity of the feasible state trajectory for any input sequence are preserved, then the sufficient condition is equivalent to a unique solution $\bar{\mathbf{v}}$ of $P(\bar{x})$. This assumption is particularly justified if $\bar{x}$ is either on the boundary or the exterior of the ℓ-sublevel set of $P(\cdot)$, that is, the desired flight condition y^{SP} is barely reachable under the specified disturbance. Hence, we assume that the solution map $\Sigma(\cdot)$ is P-inner semicontinuous at the optimal solution, and sensitivities of the discrete-time optimal control cost can be obtained by solving for the Lagrange multipliers, as detailed in [13].

Encoding the feasibility and controllability constraints as g_X, $g_{\mathcal{P}}$, respectively, as

$$g_X : x \mapsto (x_{\text{lb}} - x, x - x_{\text{ub}}) \tag{6a}$$

$$g_{\mathcal{P}} : x \mapsto P(x) - \ell \tag{6b}$$

we obtain the design optimization problem

$$\mathcal{P}_{\text{CCDO}} : \quad \text{Minimize } \min_x f(x) \text{ subject to } g_X(x) \leq 0 \text{ and } g_{\mathcal{P}}(x) \leq 0$$

Since, by the assumptions made, $P(\cdot)$ is continuously differentiable almost everywhere on X, the optimization $\mathcal{P}_{\text{CCDO}}$ can be solved using standard nonlinear solver that relies on gradients for a search direction.

We have solved the described control-agnostic design optimization problem executing `Ipopt` [25] and Matlab's `fmincon` for the inner and outer optimization, respectively. Figure 17(d) illustrate the wing shapes corresponding to the initial guess, intermediate feasible solution, near-optimal design, and final solution, as well as the respective system responses to the sharp gust wind disturbance (all wing lengths are drawn relative to baseline b_{W2}). It is important to note, however, that the latter represent the 'best' responses subject to the control cost and, except for the initial and infeasible design, do not necessarily reflect on the aircraft's performance for disturbance rejection.

Additional discussion regarding the proposed methodology in our paper [13], as well as additional investigation of the optimization results.

2.2 Gust Rejection

This subsection presents a methodology based on optimal control to characterize the ability of a supersonic aircraft to reject atmospheric disturbances during its final approach to land. A longitudinal flight dynamics model is considered for which a set of rejectable disturbances is defined based on the values of three proposed barrier functionals. The problem of finding an admissible control input is then converted into a discrete nonlinear optimal control problem (NOCP) by defining an objective function based on augmented discretized nonlinear dynamics that considers the disturbance models. It uses the Kreisselheimer-Steinhauser aggregation function to apply gradient-based optimization methods. As an illustration, such an approach is applied to three different configurations of a supersonic business jet in the landing flight phase and under gust and turbulence disturbances. The detailed study was published in the paper, "Gust Rejection of a Supersonic Aircraft During Final Approach," which was presented at the 2022 Scitech Conference [12].

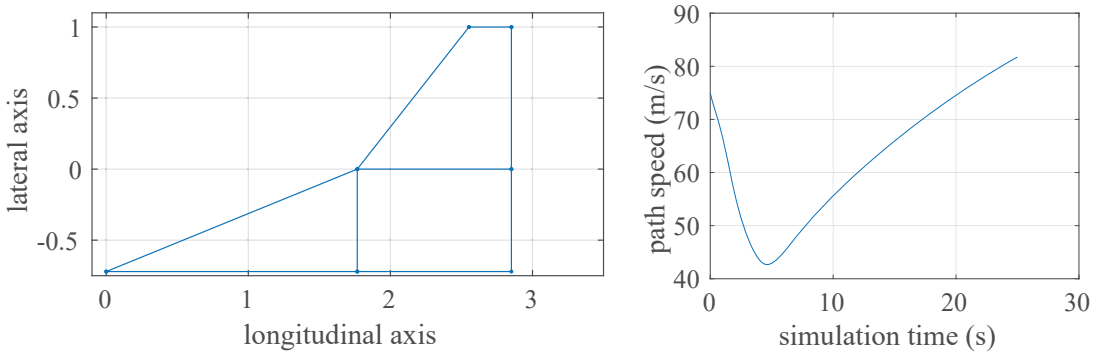

(a) Wing shape and system response at initial guess.

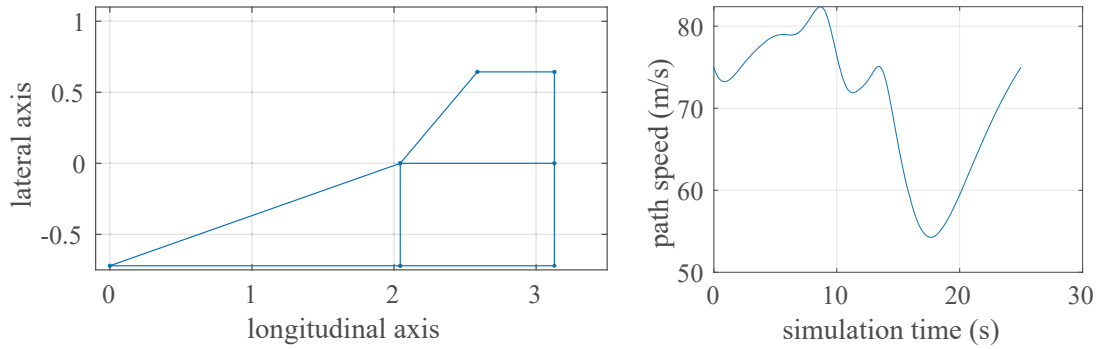

(b) Wing shape and system response after 10 iterations.

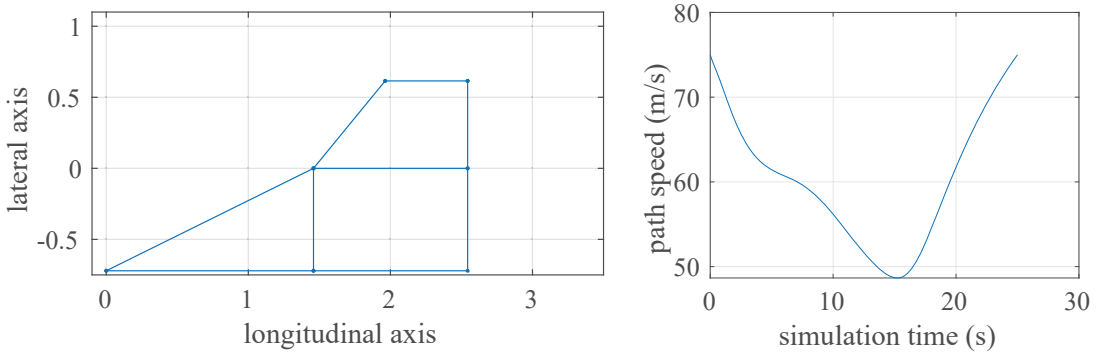

(c) Wing shape and system response after 16 iterations.

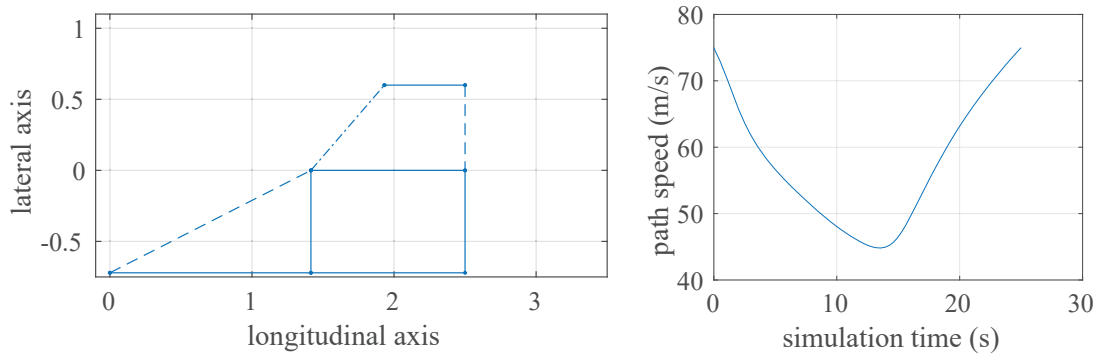

(d) Wing shape and system response at the optimal solution.

Figure 17: Candidate design and its constraint satisfaction at selected iterations. Adapted from [14]

2.2.1 Problem Statement

Consider the equations of motion of a supersonic aircraft given by the nonlinear ordinary differential equations

$$\dot{x}(t) = f(x(t), u(t), w(t)) \tag{7a}$$
$$y(t) = h(x(t)) \tag{7b}$$

that are assumed to hold for almost all $t \in \mathbb{R}_{\geq 0}$, where $x(\cdot) \in \mathbb{R}^{n_x}$ corresponds to the state vector, $u(\cdot) \in \mathbb{R}^{n_u}$ denotes the vector of control inputs, $w(\cdot) \in \mathbb{R}^{n_w}$ is the vector of disturbance inputs, and $y(\cdot) \in \mathbb{R}^{n_y}$ is the system output vector. f and h are Lipschitz-continuous mappings $f : \mathbb{R}^{n_x} \times \mathbb{R}^{n_u} \times \mathbb{R}^{n_w} \to \mathbb{R}^{n_x}$ and $h : \mathbb{R}^{n_x} \to \mathbb{R}^{n_y}$.

In addition, denote the set of constrained states, viable inputs, and potential disturbances by $\mathcal{C} \subseteq \mathbb{R}^{n_x}$, $\mathcal{U} \subseteq \mathbb{R}^{n_u}$, $\mathcal{W} \subseteq \mathbb{R}^{n_w}$, respectively, and consider that a steady-state flight condition is characterized by

$$f(x^*, u^*, 0) = 0 \tag{8a}$$
$$y^{\text{SP}} = h(x^*) \tag{8b}$$

with $x^* \in \mathcal{C}$ and $u^* \in \mathcal{U}$ corresponding to an equilibrium point, and $0 \in \mathcal{W}$.

Given y^{SP}, and considering the controlled system response to a disturbance over a finite horizon $T > 0$, the following three *barrier* functionals are proposed in this paper:

$$K = \sup_{t \in (0,T]} e^{-\lambda(T-t)} \|h(x(t)) - y^{\text{SP}}\|^2 \tag{9a}$$
$$L = \frac{1}{T} \int_0^T \|h(x(t)) - y^{\text{SP}}\|^2 \, \mathrm{d}\, t \tag{9b}$$
$$H = \|h(x(T)) - y^{\text{SP}}\|^2 \tag{9c}$$

They represent the discounted maximum squared (Eq. (9a)), average (Eq. (9b)), and final (Eq. (9c)) deviations from the desired flight path. In these expressions, $x(\cdot)$ denotes the state evolution under controls $u \in \mathscr{U} \subset \{[0, T] \to \mathcal{U}\}$ and disturbance $w \in \mathscr{W} \subset \{[0, T] \to \mathcal{W}\}$; the factor $\lambda \geq 0$ is added to discount an initial, potentially abrupt response to step-wise disturbances and emphasize deviations later in the horizon; and $\| \cdot \|$ stands for the Euclidean norm.

The problem addressed here aims to formulate a nonlinear optimal control problem, based on the barrier functionals defined in Eqs. (9), able to verify that a viable control input signal exists such that a given disturbance can be successfully rejected. If allowed maximum values of the barrier functionals are denoted by $\delta\kappa, \ell, \hbar > 0$, then the set of *rejectable disturbances* is defined as

$$\mathcal{R} = \{w \in \mathscr{W} \mid \exists u \in \mathscr{U}, \quad K(u, w) \leq \delta\kappa,\ L(u, w) \leq \ell,\ H(u, w) \leq \hbar\} \tag{10}$$

Different system configurations can be compared based on a measure of the set $\mathcal{R}$ or on whether it contains certain typical disturbance profiles.

2.2.2 Numerical Results

The three configurations of a supersonic business jet described in [2], depicted in Fig. 18 are considered for the following investigations derived from the baseline SCALOS aircraft, described in Sec. 1.1.

The von Kármán wind turbulence model [26] is considered in the rejectability analysis. The von Kármán model treats the translational and angular velocity components of continuous gusts as spatially varying stochastic processes.

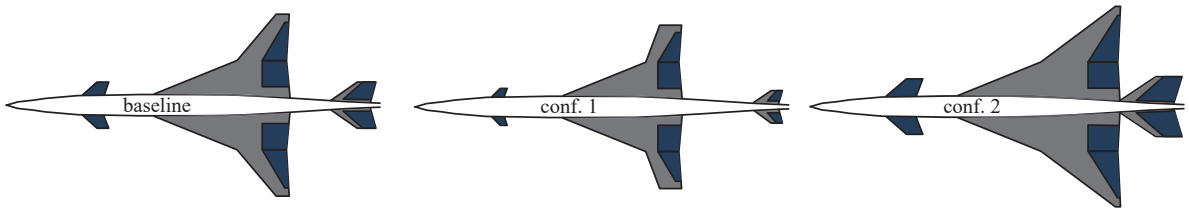

Figure 18: Three configurations considered considered in the case studies of this paper [2].

Typically, the aircraft speed is much higher than that of the wind disturbances, and for that reason, it is reasonable to assume a frozen turbulence profile, that is, a constant velocity field in space with the aircraft flying through it. In that case, the turbulence velocity components are usually generated a priori and then accessed in simulations using lookup tables.

As for the gust case, an analytical representation of the turbulence model is necessary in the NOCP. To accomplish that, the von Kármán Simulink block was first used to generate the turbulence velocity components according to the MIL-F-8785C standard [26], and later, such components were analytically modeled utilizing a cubic spline interpolation method combined with fuzzy logic, thus avoiding the use of lookup tables or any other nonanalytical data access method.

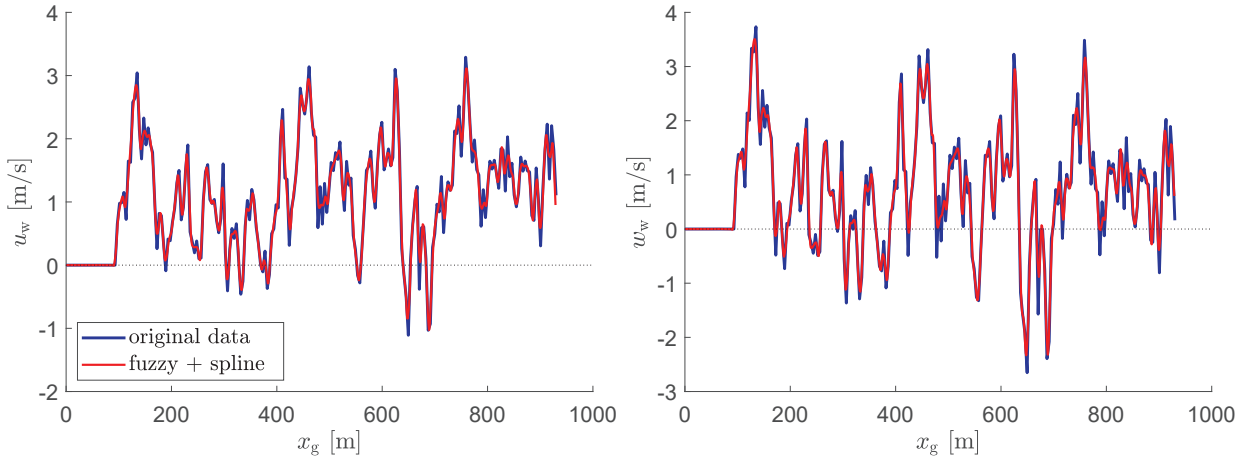

Figure 19: Longitudinal linear velocity components of the turbulent wind generated considering a wind speed of $23\,\mathrm{m\,s^{-1}}$ and seed equal to 0.

Specifically, the cubic spline method provides piecewise third-order polynomial coefficients that represent each $x_{g1} - x_{g0}$ discretized spatial segment of the turbulence components and then those coefficients are interpolated over the total turbulent space using the following Gaussian fuzzy membership functions:

$$\mathfrak{m}(x) = e^{-(x-c)^2/(2\sigma^2)} \tag{11}$$

where c corresponds to the longitudinal position (the segment indices) for each set of generated coefficients, and σ is a parameter that defines the spread of this coefficient among its neighbors.

Twelve turbulent scenario samples were evaluated for all aircraft configurations. The Simulink parameters of interest used to generate each sample are the reference wind speed, related to the turbulence intensity, and the random noise seed, typically used to generate "pseudorandom" signals. In the former, three values were considered: 23 m/s (reference value for severe turbulence, according to the MIL-F-8785C [26]), 38 m/s and 53 m/s; in the latter case, four values were taken into account: 0, 23341, 46682, and 70023. The twelve scenarios correspond to a combination of them.

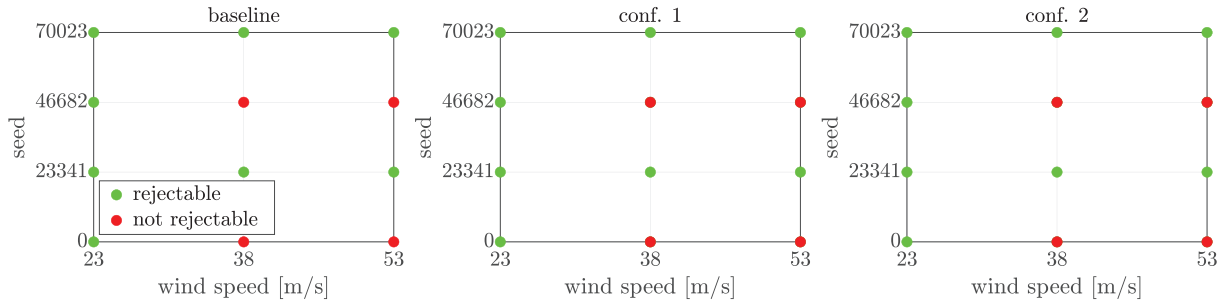

Figure 20: Rejectability analysis for the 12 sampled turbulent scenarios during the landing flight phase for all aircraft configurations.

Figure 19 shows the turbulent wind components (only the longitudinal linear velocities) generated considering a wind speed reference of 23 m/s and seed equal to 0. The figure compares the original data, that is, the one directly drawn from the Simulink block, with the data from the analytic model combining the cubic spline method with fuzzy logic interpolation. A good agreement level between both data is achieved.

Figure 20 presents the results of the rejectability analysis for the 12 turbulent cases applied to all aircraft configurations during the landing flight phase. All configurations performed equally and could not reject four turbulence samples (for wind speeds of 38 and 53 m/s and seeds equal to 0 and 46682.)

Figure 21 presents the results for the wind speed equal to $38\,\mathrm{m\,s^{-1}}$ and seed 46682. The former corresponds to a rejectable sample, while the latter to a not rejectable one.

2.3 Stochastic control metrics

Gusts are random processes frequently modeled as random Gaussian processes (*i.e.*, colored noised) for certification and analysis [27], even though that approximation is found to yield non-conservative results in some cases [28]. However, this type of model, which can be fully described by the spectrum of atmospheric turbulence, such as the ones by von Kármán [29], Kaimal [30], and Mann [31], has been well validated in practice and made their way into the certification procedure for aircraft (*e.g.*, 14 CFR 25.341(b) Continuous Turbulence Design Criteria) and wind turbines (*e.g.*, IEC 61400-1, 2005), as opposed to more recent models based on large-eddy simulation (LES) [32, 33, 34]. Furthermore, Gaussian processes have been extensively studied in the mathematical literature and offer a very tractable framework, both in the time and frequency domain.

The performance of the system is evaluated by the probability and frequency of exceedance (calculated using Rice's formula [35]) of the operational envelope of signals of interest. It uses a linearized aircraft model and the control architecture shown in Figure 22, where u is the elevator deflection, y is the glideslope deviation and z is the angle-of-attack. The feedback loop is closed between angle of attack and glideslope deviation.

To maintain the controller-agnostic approach favored by this project, the controller $K(s)$ is not designed. Instead, the sensitivity function, defined as $S(s) = \frac{1}{1+G_{yu}(s)K(s)}$, is considered as a design variable. Furthermore, for an open-loop stable linear time-invariant system, the sensitivity function must satisfy the Bode integral relation [36]:

$$\int_0^\infty \log|S(j\omega)|\,\mathrm{d}\omega = 0 \tag{12}$$

This approach was applied for a model of the SCALOS aircraft consisting of the longitudinal rigid-body equations of motions combined with the ROM aerodynamical model described in Section 1.2. This model was trimmed at the final approach to land condition, which resulted in an open-loop system with the

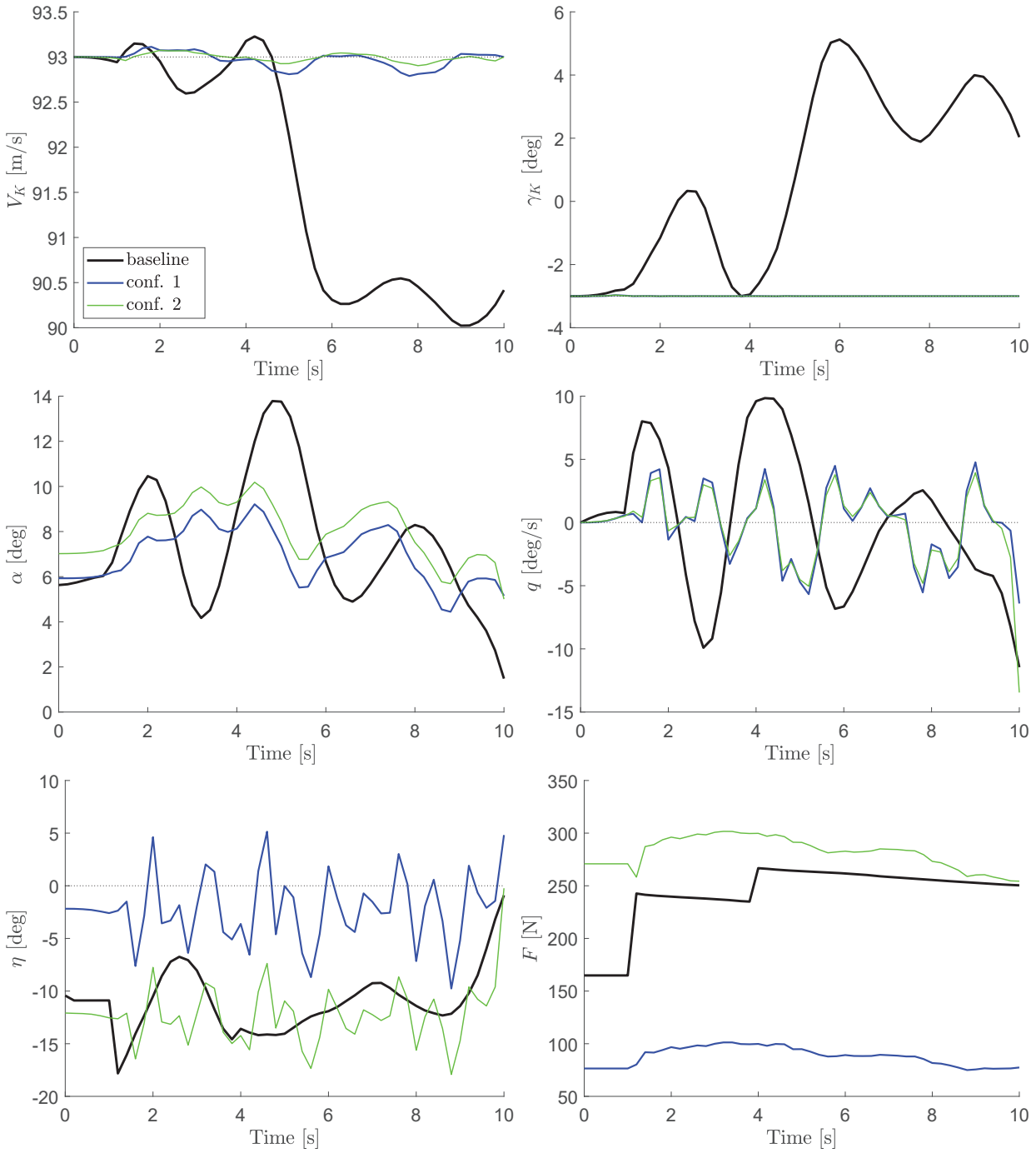

Figure 21: Flight path resulting from the optimization process for the turbulence sample whose wind speed is equal to $38\,\mathrm{m\,s^{-1}}$ and seed is 46682 – nonrejectable sample.

following poles:

$$\lambda_1 = (-0.19 + 0.40\mathrm{i})\,\mathrm{rad\,s^{-1}}$$
$$\lambda_2 = (-0.19 - 0.40\mathrm{i})\,\mathrm{rad\,s^{-1}}$$
$$\lambda_3 = (-0.02 + 0.12\mathrm{i})\,\mathrm{rad\,s^{-1}}$$
$$\lambda_4 = (-0.02 - 0.12\mathrm{i})\,\mathrm{rad\,s^{-1}}$$

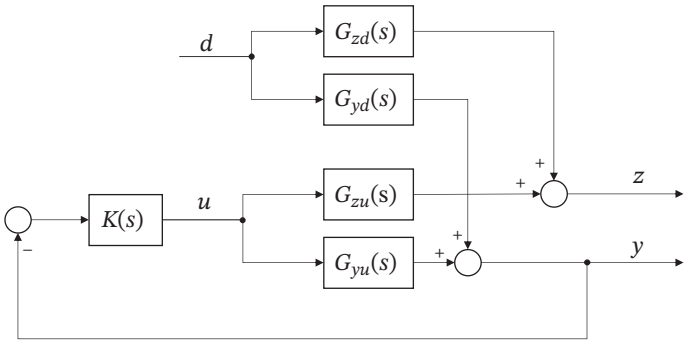

Figure 22: Block diagram showing the open-loop transfer functions with a controller $K(s)$.

where the first conjugate pair corresponds to the short-period mode and the second is related to the phugoid mode. Figure 23 shows the Bode plots for the open-loop linearized system.

the sensitivity function was parameterized by considering a series arrangement of a second-order Butterworth high-pass filter and one peaking filter, *i.e.*,

$$S(s) = \underbrace{\frac{s^2}{s^2 + \sqrt{2}\omega_c s + \omega_c^2}}_{\text{high-pass filter}} \underbrace{\frac{s^2 + g_0\omega_0/q_0 + {\omega_0}^2}{s^2 + \omega_0/q_0 + {\omega_0}^2}}_{\text{peaking filter}} \tag{14}$$

The parameters of the sensitivity function are the high-pass filter's cutoff frequency ω_c, and the peaking filter's gain g_0, center frequency ω_0, and quality factor q_0.

The calculated landing metrics for the trim condition and sensitivity function defined by $\omega_c = 1.26\,\mathrm{rad\,s^{-1}}, \omega_0 = 0.20\,\mathrm{rad\,s^{-1}}, g_0 = 4.00, q_0 = 0.34$ are shown in Table 3, along with relevant statistical parameters and the design limits for each quantity of interest. This choice of parameters for the sensitivity function satisfies the Bode integral relation but is otherwise arbitrary.

Table 3: Design metrics, design limits, mean and standard deviation for the quantities of interest

	Probability of exceedance (-)	Frequency of Exceedance (1/s)	Frequency of zero crossings (1/s)	Lower limit	Upper limit	Mean	Standard deviation	Units
Glideslope deviation	0.15	0.06	0.14	-10.00	10.00	0.00	6.99	(m)
Angle-of-attack	0.04	1.55	6.55	-10.00	40.00	20.00	11.12	(°)
Elevator deflection	0.08	0.25	0.82	-30.00	30.00	-19.48	7.56	(°)
Elevator rate	0.00	0.22	3.30	-60.00	60.00	0.00	19.49	(°/s)

More insight into the calculated metrics can be obtained from analyzing the closed-loop Bode plots in Figure 24 and the probability density functions (PDF) in Figure 25. The chosen sensitivity function adds

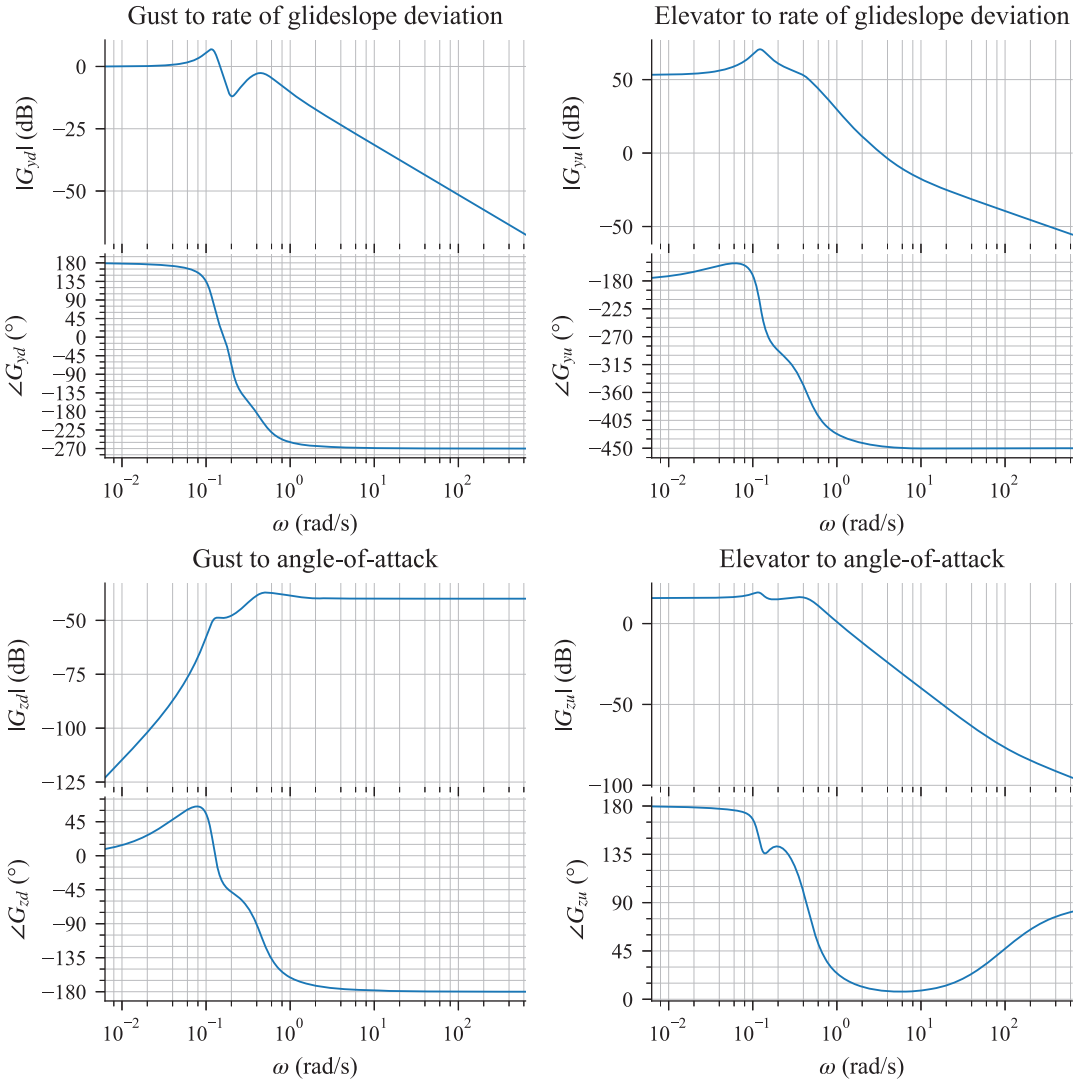

Figure 23: Open-loop Bode plots for longitudinal aircraft plant

two (closed-loop) zeros at the origin of the gust to glideslope deviation transfer function, one that cancels the integrator from the deviation velocity and another one that removes the steady state error, as can be seen in its PSD, which is zero at zero frequency and has peaks at the phugoid and short-period modes. The angle-of-attack PSD shows very high spectral content in low frequencies and another peak for the short-period mode, which contributes to the relatively high frequency of exceedance and zero-crossings for this quantity.

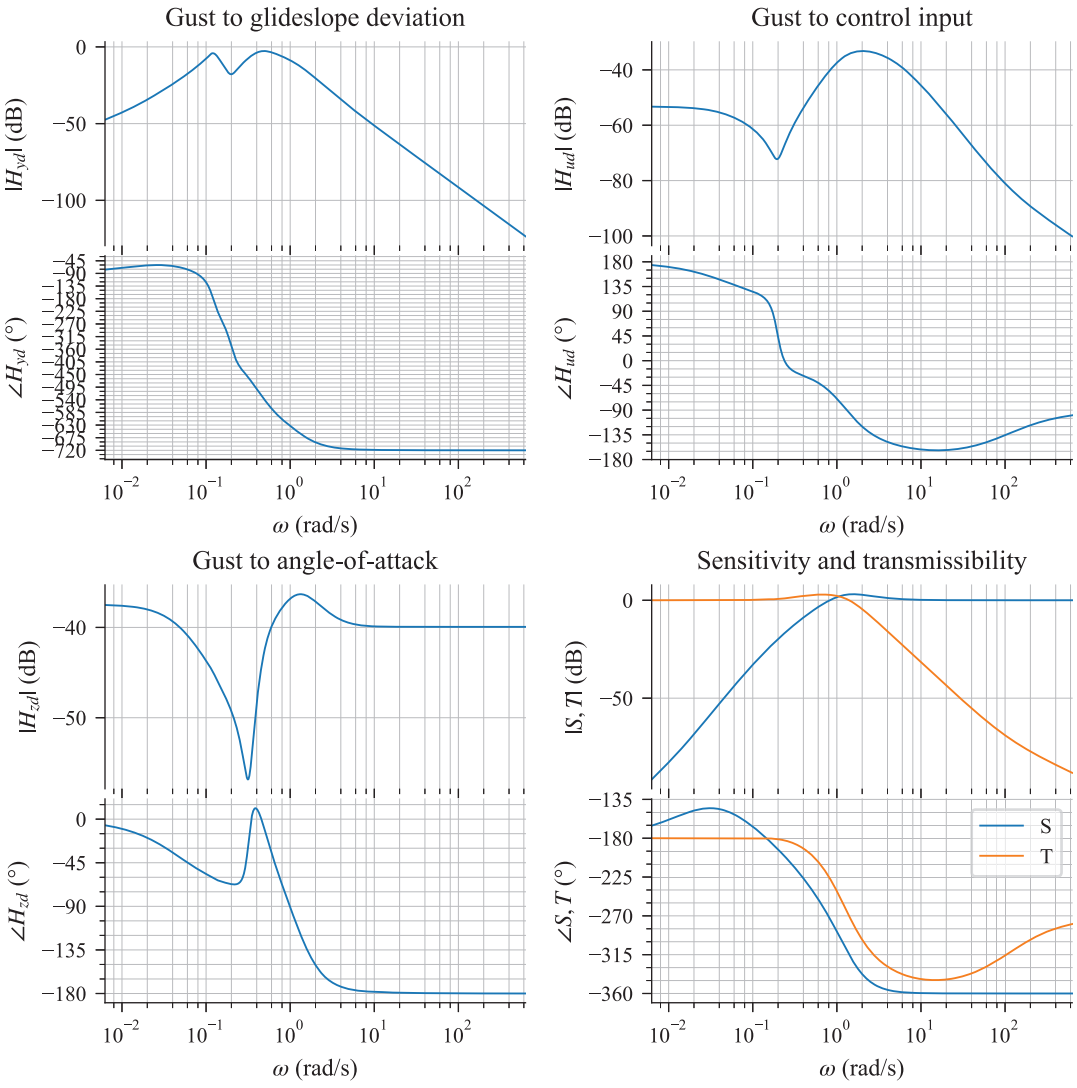

Figure 24: Closed-loop Bode plots for longitudinal aircraft plant

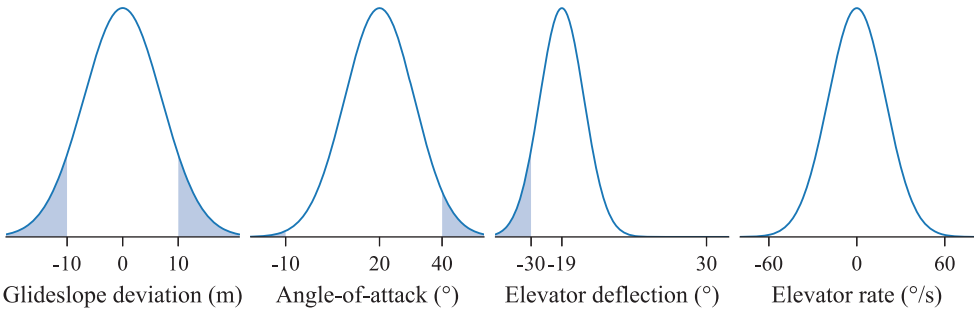

Figure 25: Probability density functions for the quantities of interest. The portion outside the design limits is highlighted, and the values shown correspond to the trim value and the upper and lower limits.

3 CFD analysis and aerodynamic design optimization

The effort on using computational fluid dynamics (CFD) for optimization first focused on establishing which CFD methods could be reliably used to predict the flight conditions of interest. We studied Reynolds-averaged Navier–Stokes (RANS) and delayed detached eddy simulations (DDES) for the subsonic, high angle of attack condition (Sec. 3.1). We found that RANS was suitable for moderate angles of attack where the flow was separated but not unsteady. We then found that RANS accurately captured the subsonic pitch-up behavior of the UW-S-20A configuration. This motivated our work on accurate and efficient RANS solvers for low and high Mach number flow (Sec 3.2 and RANS-based shape optimization (Sec. 3.3), where we minimized supersonic drag with a constraint on the subsonic static margin. We showed that shape optimization increases the wing thickness and leading edge radius to design a cranked arrow wing that is stable at subsonic speeds at the cost of a 5.8% increase in supersonic drag. We also ran into some limitations of RANS-based optimizations. In particular, mesh warping poses restrictions on the design space that can be explored. To study configuration level tradeoffs without mesh-related restrictions, we formulated a supersonic buildup model and used in to optimize the configuration's trim surface sizing. More details on each of these developments are given below.

3.1 Predicting high-angle-of-attack aerodynamics

Supersonic transport (SST) aircraft commonly use thin, highly swept wings to reduce supersonic wave drag. This design decision also influences the aircraft's low-speed aerodynamic characteristics, particularly during takeoff and landing when flying at high angles of attack. The flow over highly swept wings at high angles of attack is unsteady, separated, and characterized by leading-edge vortices [37]. Leading-edge vortices can be advantageous in some cases. The Concorde relied on leading-edge vortices instead of high-lift devices to generate lift during subsonic flight [38]. On the other hand, these vortices can contribute to unstable pitch-up behavior at moderate to high angles of attack [39], conditions that fall within the aircraft's flight envelope. Accurately predicting high-angle-of-attack aerodynamics is essential to designing the next generation of SSTs. The key contributions of our work are: 1) evaluating the accuracy of RANS and DDES models at predicting the low-speed aerodynamics of a delta wing over multiple angles of attack, including angles up to and past stall; and 2) formulating a metric to quantify how steady the flow is at a given angle of attack.

We show select DDES results in this report. The full set of results can be found in Seraj and Martins [9]. For DDES, we use pimpleFoam, a time-accurate, incompressible finite volume flow solver that is part of the OpenFOAM toolbox [40]. We use the SA-DDES formulation [41], a hybrid RANS/LES model that uses the Spalart–Allmaras turbulence model near the wall and a subgrid scale model away from the wall. We run DDES with a 24 million cell mesh (denoted 24M) for angles of attack from 0 to 40 deg. From 25 to 40 deg, we also run DDES with a 69 million cell mesh (denoted 69M) because these are the most challenging flow conditions to resolve accurately. The aerodynamic characteristics near the point of maximum lift are dominated by unsteady vortex effects, such as vortex breakdown [37]. Figure 26 shows how vortex breakdown causes the vortex structure to become progressively less coherent as the angle of attack increases and the vortex breakdown location moves closer to the apex.

The predicted coefficient values match the experimental data well up to 25 deg (Fig. 27). There are some discrepancies at higher angles of attack. The lift and drag at 30 deg are underpredicted by 4–6%. Refining the mesh from 24M to 69M does not improve the accuracy at this condition. This suggests that the DDES model does not fully resolve the unsteady vortex effects near the point of maximum vortex strength. The 40 deg condition is the most sensitive to mesh refinement. The 69M mesh correctly predicts a break in the pitching moment between 35 and 40 deg, whereas the 24M mesh does not.

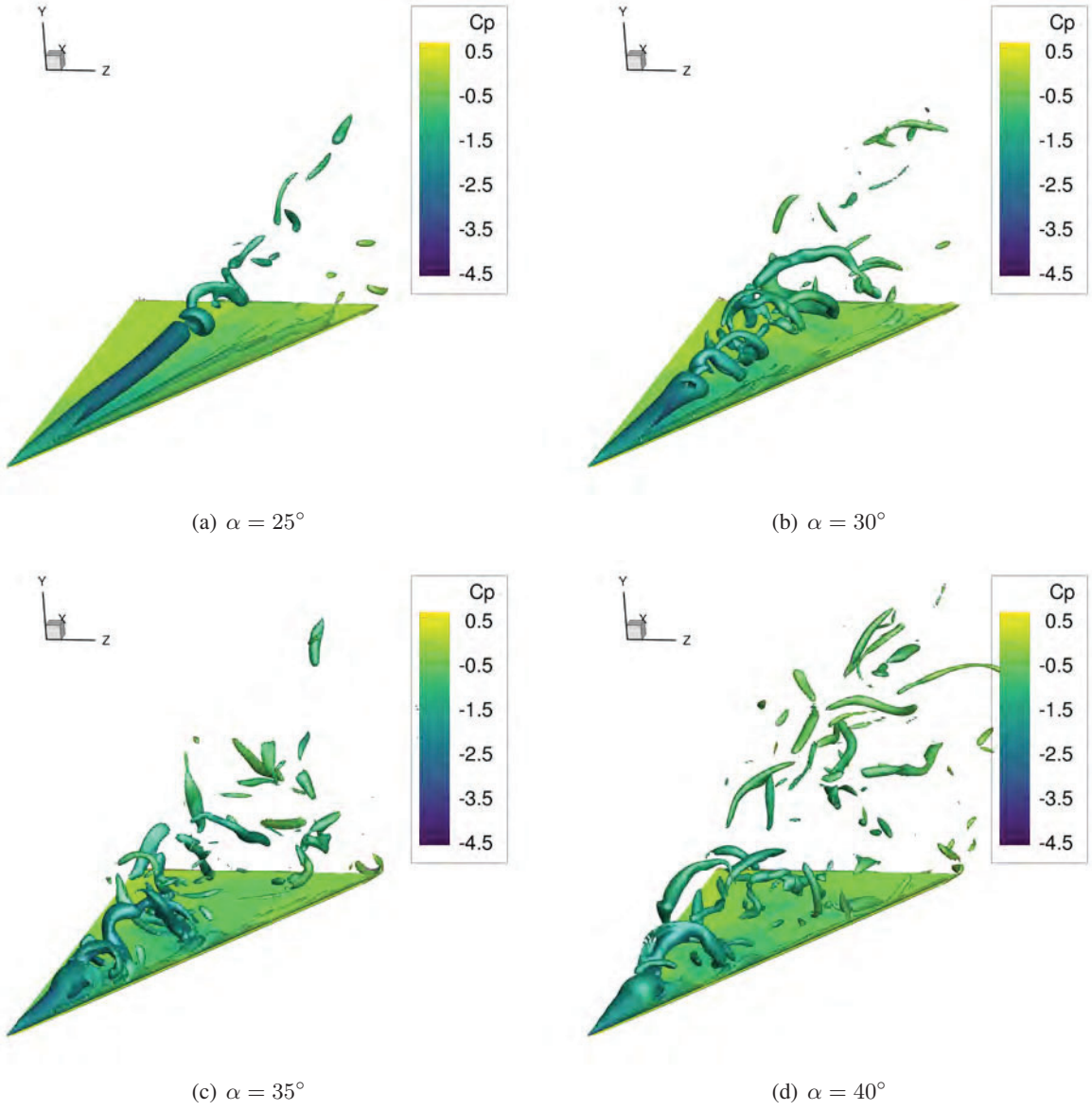

(a) $\alpha = 25°$ (b) $\alpha = 30°$

(c) $\alpha = 35°$ (d) $\alpha = 40°$

Figure 26: DDES (24M) Q-criterion isosurfaces for $Q = 10^7$ at $t = 1.2\,\mathrm{s}$

3.2 Strategies for solving low and high Mach number flows

The flight envelope of a supersonic transport aircraft can span Mach numbers from 0.25 to 2.0 [43]. Appropriately modeling the aircraft's characteristics over the entire flight envelope with computational fluid dynamics (CFD) requires solvers that are accurate and efficient at low and high Mach numbers. In theory, compressible flow solvers represent the actual physics across all Mach numbers, making them a natural choice for aerodynamic design. In practice, these solvers commonly suffer from reduced accuracy and speed at low Mach numbers. In addition, supersonic flows can be difficult to converge with second-order schemes compared to more dissipative first-order schemes. This motivates our work to improve the efficiency and accuracy of compressible Reynolds-averaged Navier–Stokes (RANS) solver at both low and high Mach number. We present some of the important outcomes of this work in this report. The full methodology and results can be found in Seraj et al. [11].

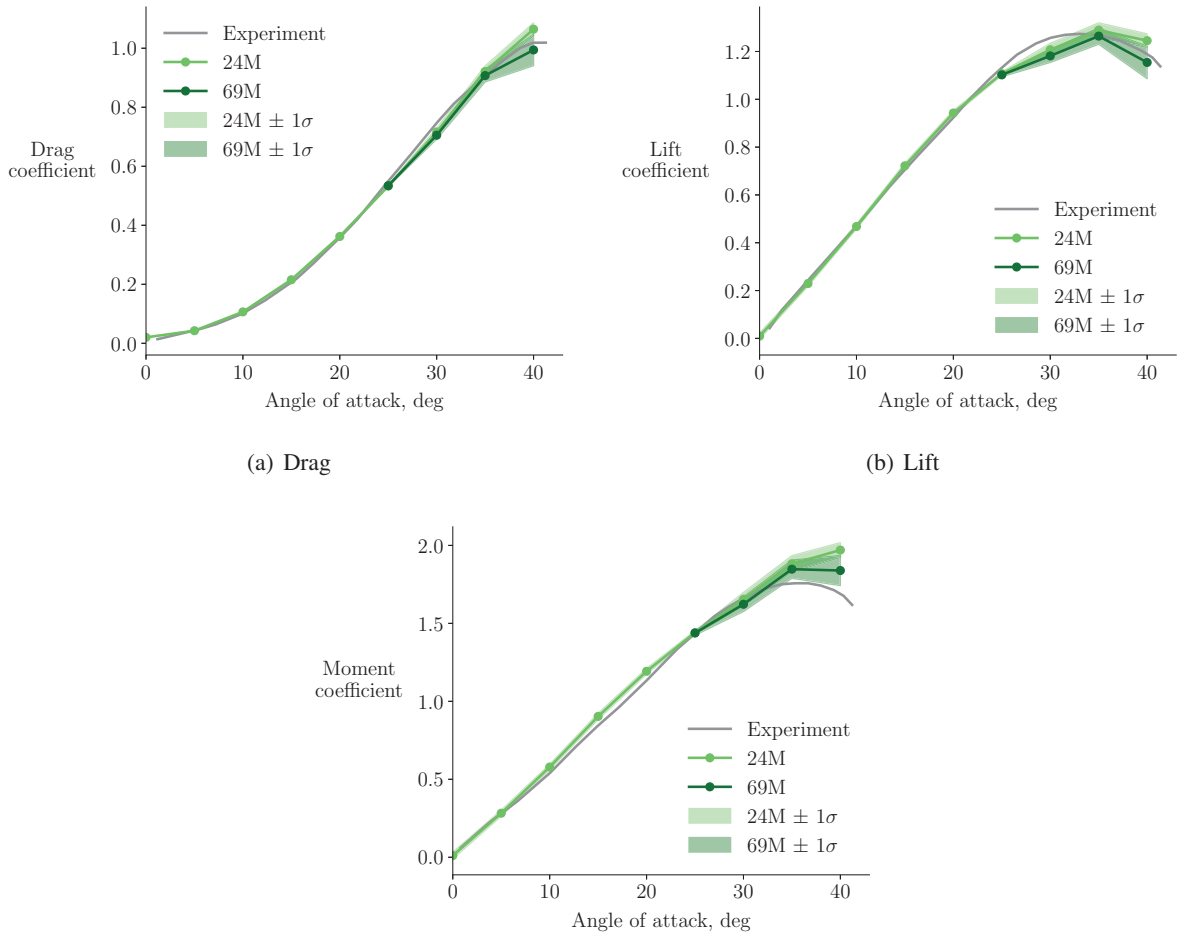

(a) Drag

(b) Lift

(c) Pitching moment

Figure 27: Comparison of DDES force and moment coefficients with experimental data from Jarrah and Ashley [42]

3.2.1 Scaling artificial dissipation to improve accuracy at low Mach numbers

Artificial dissipation is essential for nonlinear convergence but can compromise accuracy. The JST scalar dissipation scheme is generally more dissipative than second-order upwind schemes [44]. Central schemes that are less dissipative than scalar dissipation include matrix dissipation [44] and the convective-upstream-split-pressure scheme [45]. However, these central and upwind schemes are primarily designed for transonic flows and run into accuracy issues at low Mach numbers because of improperly scaled artificial dissipation [46]. One common approach to scale the dissipation is to multiply the flux Jacobian by a local preconditioning matrix. For JST, this modifies the spectral radius and, consequently, the dissipation. To improve low-speed accuracy, we opt to modify the spectral radius directly. The advantage of this approach over prior ones is that it requires minimal changes to the JST scalar dissipation formulation.

In the low Mach number limit, the advective contribution to the spectral radius is $O(1)$, whereas the acoustic contribution is $O(1/M)$ [46, 47]. Rieper [48] showed that artificial dissipation must be independent of the Mach number for accuracy in the incompressible limit. To scale the artificial dissipation for low Mach numbers, we introduce the acoustic scaling factor ζ in the isotropic spectral radius:

$$\Lambda^I = \vec{U} \cdot \vec{n}^I + \zeta c |\vec{n}^I|. \tag{15}$$

Using this formulation, we can select values for ζ that reduce or eliminate the dependence of artificial dissipation on the Mach number. Similar dissipation scaling approaches have been proposed in the context of upwind schemes [49] and kinetic energy preserving schemes [50].

To study the effect of ζ on low-speed accuracy, we consider a NACA 0012 airfoil at a Reynolds number of 10^6, 3° angle of attack, and Mach numbers from 0.01 to 0.4. To evaluate accuracy at different values of ζ, we compare the RANS results with predictions using XFOIL [51], a 2D panel method coupled with an integral boundary layer model. Fig. 28(a) compares the drag for the baseline ($\zeta = 1$), no acoustic contribution ($\zeta = 0$), and scaling the acoustic contribution by the freestream Mach number ($\zeta = M_\infty$). With no scaling, drag diverges as the Mach number is reduced. Scaling by the freestream Mach number yields the most accurate drag predictions compared to XFOIL.

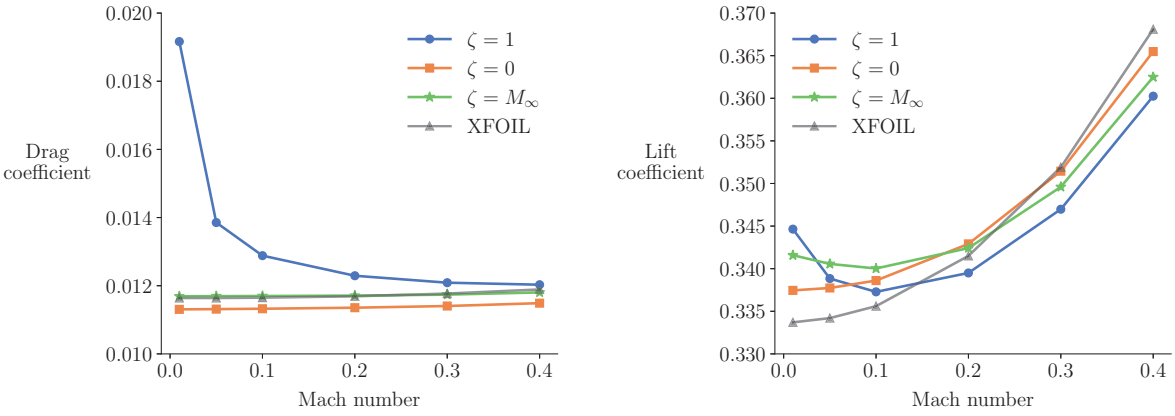

(a) (b)

Figure 28: Scaling artificial dissipation improves accuracy

3.2.2 Dissipation-based continuation for flows with shocks

Flows with shocks pose different challenges for solvers than the low Mach number flows we have discussed. Shocks can move within the domain as the solution converges, causing significant changes in cells' states. To improve robustness, Newton-based solvers can employ a physicality check that limits the update step size such that the density and energy do not change by more than 20% in any cell. A critical outcome of this approach is that the density and energy cannot become negative. Despite this added robustness, the solver can still perform poorly or fail to converge when the step sizes become small.

One approach to accelerating convergence is to loosen the physicality check to accept larger changes in the states. However, this reduces the robustness of the solver and can often lead to stalled convergence. Another approach is to increase the second-difference artificial dissipation constant, κ_2. This improves convergence by reducing the spatial gradient in the states but has the disadvantage of reducing solution accuracy. To accelerate convergence while preserving accuracy, we propose a dissipation-based continuation (DBC) method where κ_2 starts high and is continuously reduced as the solution converges.

We write the DBC formulation as

$$\kappa_2^{(n)} = \kappa_2 + f_c^{(n)} \kappa_2^c, \tag{16}$$

where $\kappa_2^{(n)}$ is the dissipation constant at nonlinear iteration n, κ_2 is the desired final dissipation constant, κ_2^c is the initial value of the additional dissipation, and $f_c^{(n)}$ is the continuation parameter at iteration n. We

require that the continuation parameter starts at 1 and approaches 0 as the solution converges. We choose to compute the continuation parameter using a generalized sigmoid function:

$$f_c^{(n)} = \frac{1}{1 + e^{-\sigma\left(\log_{10}\left(\eta_{\text{rel}}^{(n)}\right)+\lambda\right)}}, \tag{17}$$

where σ is the sharpness parameter, λ is the midpoint parameter, and $\eta_{\text{rel}}^{(n)}$ is the relative convergence at iteration n. The parameters σ and λ determine the shape of the sigmoid. Larger values of σ will result in a steeper drop in dissipation. We call λ the midpoint parameter because the additional dissipation is equal to $0.5\kappa_2^c$ at a relative residual of $10^{-\lambda}$. We use $\sigma = 3$ and $\lambda = 3$. When the solution is converged, the additional dissipation is small enough to recover the solution of the original problem. The shape parameters generally do not need to be tuned for each case. However, the appropriate value for κ_2^c depends on the Mach number. We find that $\kappa_2^c = 0.2M_\infty$ works well, and we use this value for all cases presented here.

We now apply DBC to the analysis of the SCALOS configuration with a cranked arrow wing, T-tail, and canard. We consider flow at Mach numbers of 1.8 and 0.95, representing supersonic and transonic cruise conditions for the next generation of SSTs [43]. Both cases have a 4° angle of attack. DBC converges both cases, whereas the baseline solver does not converge either (Fig. 29). We also compare DBC to the baseline solver with κ_2 increased from the default value of 0.25 to the initial DBC value of $0.25 + 0.2M_\infty$. For Mach 1.8, increasing κ_2 converges faster than DBC. However, this solution is also less accurate because of the increased dissipation near shocks. For Mach 0.95, the solver still stalls with the higher κ_2, albeit after about three more orders of convergence.

In some cases, such as in aerodynamic shape optimization, robustness is more valuable than faster convergence. Reliably converging the flow at different design points is essential for a well-behaved optimization [52]. DBC offers more robustness than the baseline solver for complex geometries at high Mach numbers, making it more suitable for many-query scenarios such as parameter sweeps or design optimization.

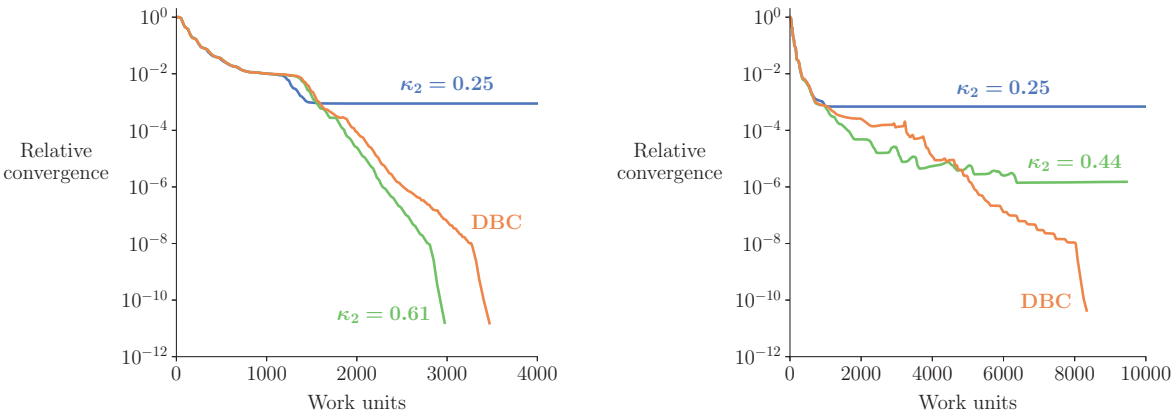

(a) Mach 1.8

(b) Mach 0.95

Figure 29: DBC converges the SST cases without sacrificing accuracy

3.3 Aerodynamic shape optimization with a subsonic static margin constraint

Supersonic transport (SST) aircraft must be designed with high-speed and low-speed flight regimes in mind. Efficiency and stability across different flight conditions are often competing objectives. For example, dou-

ble delta or cranked arrow wings are known for providing a balance between supersonic and transonic performance. However, the same wings often exhibit inadequate pitch stability at low-speed, high angle of attack conditions [39]. Designing for subsonic stability is complicated by the leading edge vortices that are characteristic of flow over highly swept wings at high angles of attack [37].

Computational fluid dynamics (CFD) combined with numerical optimization presents the opportunity to resolve flow features across different flight conditions and capture the trade-offs between competing design objectives. The goal of this paper is to use RANS-based optimization to study the effect of aerodynamic shape on the subsonic pitch stability of an SST and to quantify the supersonic drag penalty associated with enforcing a subsonic stability constraint. We first describe the aircraft geometry and evaluate the accuracy of RANS at low-speed, high angle of attack conditions in Sec. 3.3.1. We then present the optimization formulation and optimized aircraft designs in Sec. 3.3.2. The full optimization formulation and results can be found in Seraj and Martins [53]. Ongoing work involves extending these optimizations to include fuselage shape variables and flap deflections at the subsonic condition.

3.3.1 Validation at subsonic conditions

Figure 30 shows a comparison between RANS results and wind tunnel data for angles of attack from -10 deg to 25 deg for the UW-S-20A configuration. All RANS solutions are converged to a total residual of 10^{-7} or tighter relative to the freestream residual. The fine mesh provides an excellent match for the lift and drag across the entire angle of attack range. The coarse mesh is nearly as accurate from -10 to 10 deg but is slightly less accurate at higher angles of attack. The discrepancies between the experiment and CFD are most pronounced for the pitching moment. However, we are mostly interested in capturing the shape of the pitching moment curve, especially around the pitch-up angle, because this determines the pitch stability of the aircraft. The fine mesh predicts the shape of the pitching moment accurately up to 15 deg, which includes the pitch-up onset. The coarse mesh has a similar shape as the fine mesh but underpredicts the pitch-up angle by about one degree. Overall, the coarse mesh provides reasonable accuracy at about 3% of the computational cost of the fine mesh. Therefore, we use the coarse mesh for all optimizations.

3.3.2 Shape optimization formulation and results

The framework we use to perform aerodynamic shape optimization is MACH-Aero. MACH-Aero has been used extensively for aerodynamic shape optimization of wings and full aircraft configurations [52]. We are interested in evaluating the supersonic drag penalty associated with enforcing a subsonic stability constraint. To formulate this optimization problem, we first define a supersonic cruise condition and a subsonic takeoff condition in Table 4.

Table 4: Flight conditions

	Mach number	Altitude, m	Altitude, ft	Reynolds number	C_L^*	K_n^*
Supersonic	1.8	16764	55000	80.4×10^6	0.2	
Subsonic	0.3	0	0	101.8×10^6	0.7	5%

We run two supersonic drag minimization problems: one without a subsonic stability constraint (K_n unconstrained) and one with a subsonic stability constraint (K_n constrained). Each flight condition has separate angle of attack, tail rotation, and canard rotation variables to trim the aircraft. The wing twist and shape variables are shared across the supersonic and subsonic conditions. Table 5 shows the supersonic drag, subsonic static margin, and trim variables for the baseline and optimized designs.

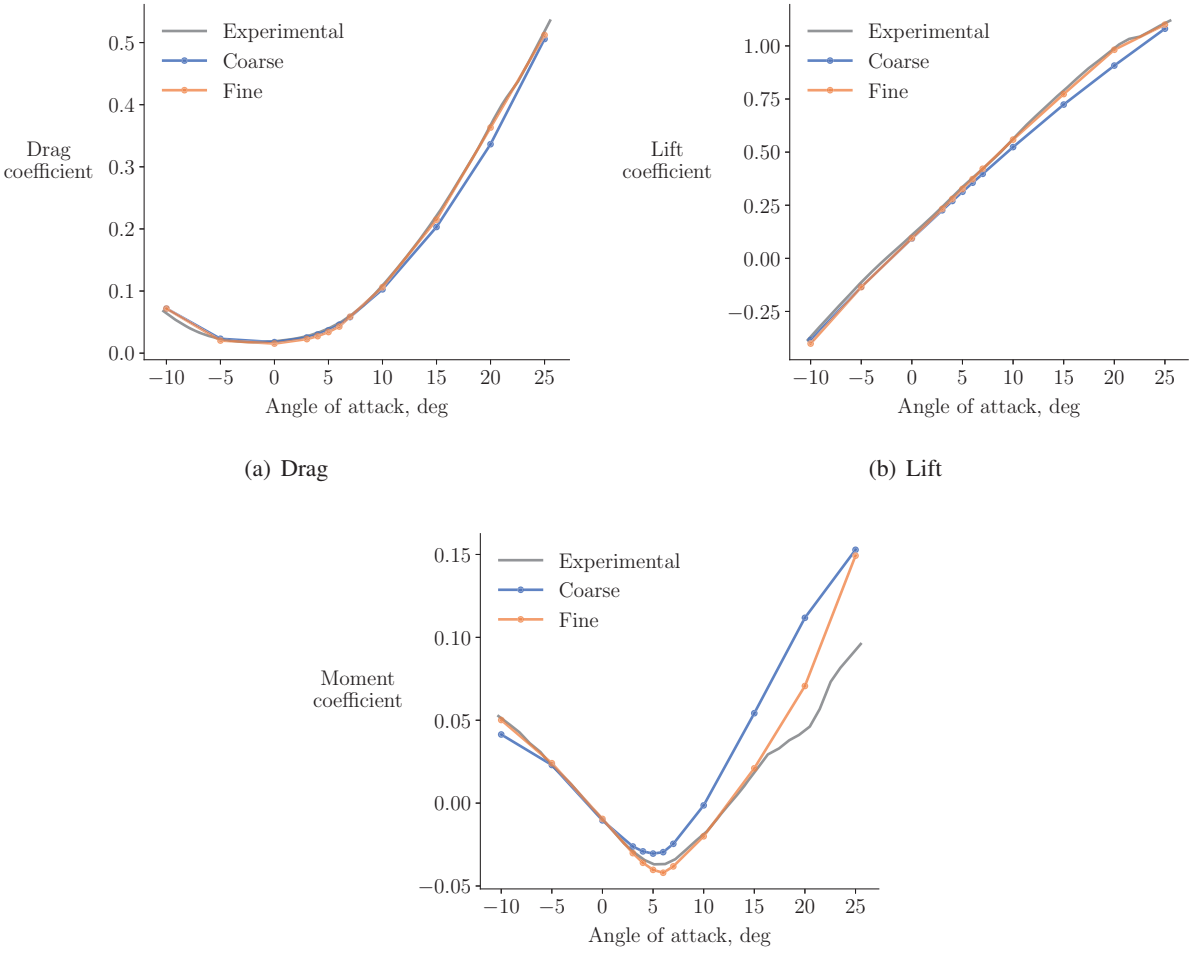

(a) Drag

(b) Lift

(c) Pitching moment

Figure 30: Angle of attack sweep

The baseline design is unstable at the subsonic condition, which is expected because of the early pitch-up tendencies shown in Fig. 30. The K_n unconstrained optimization decreases the drag from the baseline by 77.6 counts or 18.5% but is unstable with a more negative static margin than the baseline. This demonstrates the need for a low-speed stability constraint when performing supersonic shape optimization. The K_n constrained design is stable at the subsonic condition, showing that it is possible to use aerodynamic shape optimization to enforce subsonic stability for supersonic wing design. Relative to the K_n unconstrained design, there is a 5.8% drag penalty associated with adding the low-speed stability constraint.

The optimized designs are shown in Fig. 31. The K_n unconstrained design primarily uses twist to minimize the supersonic drag. The subsonic characteristics of the K_n unconstrained design are similar to the baseline because the washout is counteracted by the increased angle of attack at the subsonic condition. The two optimized designs have similar supersonic pressure and spanwise lift distributions. The difference in supersonic drag comes from the increased wing thickness of the K_n constrained design. The thickness is also responsible for the difference in pitch stability. Increasing the leading edge radius and wing thickness between 50% span and 80% span weakens the inboard leading edge vortex and improves pitch stability. This is consistent with trends reported in prior experimental and theoretical studies [39, 54, 55]. The decrease in

Table 5: Optimization results and convergence

	Baseline	K_n unconstrained	K_n constrained
Feasibility		1.9×10^{-5}	5.9×10^{-5}
Initial optimality		5.3×10^{-2}	9.0×10^{-2}
Final optimality		6.7×10^{-3}	1.9×10^{-2}
Supersonic			
Drag counts	398.0	320.4	339.1
Angle of attack	4.19°	8.19°	7.03°
Tail rotation	−5.64°	−3.09°	−2.28°
Canard rotation	6.79°	−4.46°	−1.99°
Subsonic			
Static margin	−31.4%	−33.7%	5.0%
Angle of attack	13.3°	18.8°	17.3°
Tail rotation	1.72°	4.02°	7.47°
Canard rotation	−0.42°	−5.50°	10.0°

lift near the wing break is compensated by increased camber and twist in the outboard section and more lift from the canard and tail.

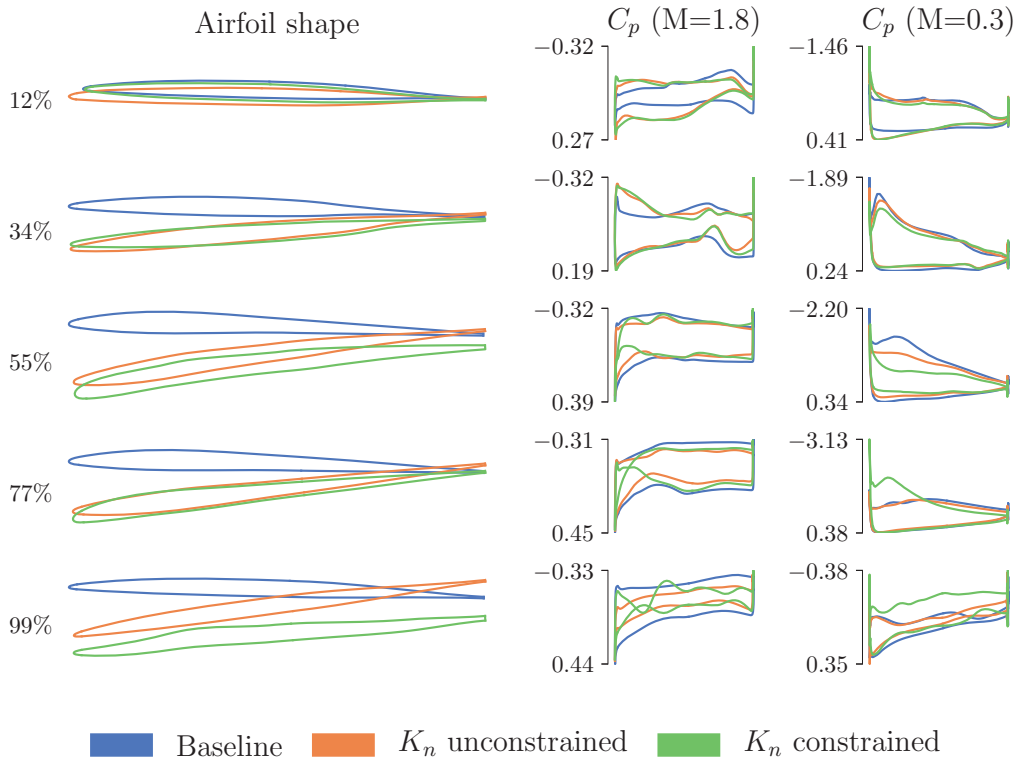

Figure 31: Sectional shape and pressure distributions of baseline and optimized wing designs

3.4 Trim surface configuration optimization

The SCALOS project has mainly focused on a three-surface configuration with a canard and tail. Three-surface aircraft have a theoretical advantage over canard and conventional two-surface configurations because three lifting surfaces allow for the aircraft to achieve minimum induced drag for any center of gravity location [56]. However, practical considerations have limited the use of three-surface configurations for subsonic aircraft. Kroo [57] used a linear vortex-based method and an analytic viscous drag model to determine that three-surface designs offer no obvious benefits over conventional configurations for subsonic aircraft. Selberg and Rokhsaz [58, 59] used a vortex lattice method to study trim for a general aviation aircraft and found that a three-surface configuration achieves a trimmed lift-to-drag ratio that is higher than a canard configuration but lower than a conventional configuration.

Different trim configurations have also been studied for supersonic aircraft. Lacey [60] conducted wind tunnel tests on a fighter-type aircraft with different trim surface geometries. They found that the three-surface configuration has lower drag at high angles of attack but that a conventional configuration is more effective at lower angles. In supersonic wind tunnel tests, Covell [61] found that a conventional fighter configuration has lower trim drag than a canard configuration. They also found that a linear aerodynamic model was unable to accurately compare canard, conventional, and tailless configurations at supersonic speeds.

Our work here makes two main contributions to the study of three-surface supersonic aircraft. The first is studying different trim configurations for an SST rather than a fighter-type aircraft. The second is using nonlinear aerodynamic models for trim analysis and optimization. We formulate a supersonic buildup model to optimize the aircraft with trim surface sizing variables. The design space for this optimization includes the option to remove either trim surface and consequently achieve the best tradeoff between parasite and induced drag.

We construct the buildup model using a combination of RANS data and analytic functions. We start with running RANS on the trimless configuration at angles of attack from -6 to 6 deg. We then construct a quartic least-squares fit on the lift, drag, and moment curves. The trim surfaces and the interactions between components are modeled analytically based primarily on the approach presented by Raymer [62].

We verify the buildup model by comparing the buildup results to RANS. We compare the buildup to RANS on the three-surface configuration at angles of attack from -6 to 6 deg (Fig. 32). The buildup drag matches RANS well but slightly underpredicts drag at higher angles of attack and negative angles of attack. The buildup lift and moment match RANS well at positive angles of attack but are only slightly better than the trimless configuration at negative angles of attack. The trim condition for the aircraft occurs at a low positive angle of attack, so we expect the buildup to perform well despite the discrepancies at negative angles.

We wrap the buildup model in OpenMDAO [63] to facilitate optimization. We minimize drag with respect to the canard span, tail span, trim rotation varialbes and angle of attack. This optimization is multimodal. Figure 33 shows the best optimized planform. The optimized planform has almost no horizontal stabilizer and a canard that is more than twice the span of the baseline. The canard has a lower lift penalty for a positive moment increment than the tail. Increasing the canard's size allows for trim at a lower angle of attack, which reduces the drag by 10.4% compared to the baseline.

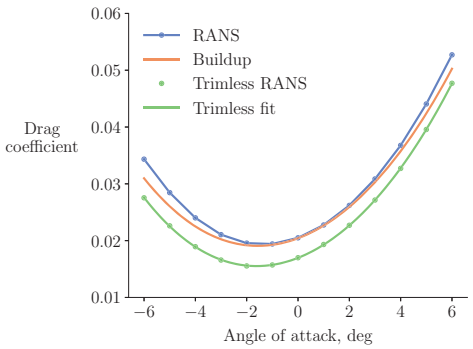

(a) Drag

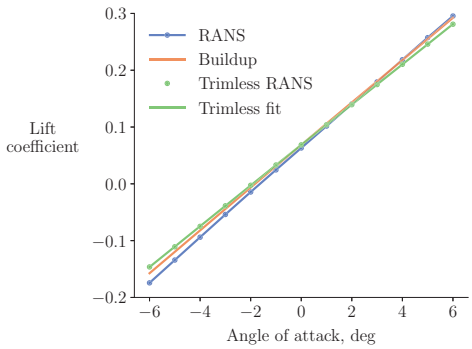

(b) Lift

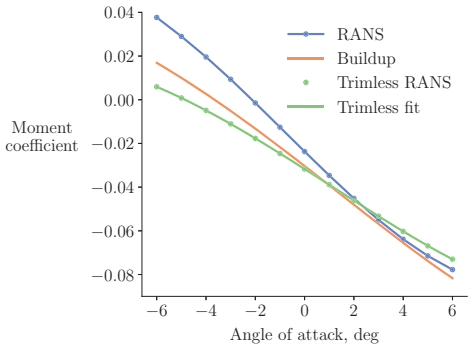

(c) Pitching moment

Figure 32: Angle of attack sweep

(a) Baseline (329.9 counts) (b) Best minimum (295.5 counts)

Figure 33: Planforms for the trim surface sizing optimization

References

[1] Guimarães, T. A., Cesnik, C. E. S., and Kolmanovsky, I., "Low Speed Aerodynamic Modeling for Control-related Considerations in Supersonic Aircraft Design," *AIAA Aviation 2021 Forum*, 2021. https://doi.org/10.2514/6.2021-2531.

[2] Guimarães, T. A. M., Cesnik, C. E. S., and Kolmanovsky, I., "An Integrated Low-Speed Aeroelastic-Flight-Dynamics Framework for Modeling Supersonic Aircraft," *AIAA SciTech 2022 Forum*, 2022. https://doi.org/10.2514/6.2022-2175.

[3] Guimarães, T. A., Cesnik, C. E. S., and Kolmanovsky, I., *Flexibility Assessment of the Aeroelastic-flight-dynamic Behavior for Supersonic Aircraft*, 2023. https://doi.org/10.2514/6.2023-0417.

[4] Guimarães, T. A. M., Cesnik, C. E. S., and Kolmanovsky, I., "Unsteady Vortex Lattice Linearization and Sensitivity Analyses for Control Models in Supersonic Aircraft Design," *AIAA SCITECH 2023 Forum*, 2023. https://doi.org/10.2514/6.2023-0416.

[5] Guimarães, T. A. M., and Cesnik, C. E. S., "The Impact of Vortex Breakdown on the Longitudinal Flight Behavior of the Scalos Aircraft," *AIAA SCITECH 2024 Forum*, Accepted for presentation - 2024.

[6] Guimarães, T. A. M., and Cesnik, C. E. S., "Aerodynamic Modeling of Supersonic Aircraft at Low Speeds and High Angles of Attack - Under preparation," *AIAA Journal*, 2024.

[7] Guimarães, T. A. M., and Cesnik, C. E. S., "Aerodynamic Linearization for Supersonic Aircraft Configurations Flying Low Speeds - Under Preparation," *AIAA Journal*, 2024.

[8] Guimarães, T. A. M., and Cesnik, C. E. S., "Aeroelastic-flight-dynamic Behavior for Supersonic Aircraft Flying Low Speeds - Under Preparation," *Journal of Aircraft*, 2024.

[9] Seraj, S., and Martins, J. R. R. A., "Predicting the High-Angle-of-Attack Characteristics of a Delta Wing at Low Speed," *Journal of Aircraft*, Vol. 59, No. 4, 2022, pp. 1071–1081. https://doi.org/10.2514/1.C036618.

[10] Seraj, S., and Martins, J. R. R. A., "Minimum Trim Drag for a Three-Surface Supersonic Transport Aircraft," *AIAA Aviation Forum*, 2023. https://doi.org/10.2514/6.2023-3472.

[11] Seraj, S., Yildirim, A., Anibal, J. L., and Martins, J. R. R. A., "Dissipation and time step scaling strategies for low and high Mach number flows," *Journal of Computational Physics*, Vol. 491, No. 4, 2023, p. 112358. https://doi.org/10.1016/j.jcp.2023.112358.

[12] Bertolin, R., Barbosa, G. C., Cunis, T., Kolmanovsky, I. V., and Cesnik, C. E. S., *Gust Rejection of a Supersonic Aircraft During Final Approach*, 2022. https://doi.org/10.2514/6.2022-2174.

[13] Cunis, T., Kolmanovsky, I., and Cesnik, C. E. S., "Integrating Nonlinear Controllability into a Multidisciplinary Design Process," *Journal of Guidance, Control, and Dynamics*, Vol. 46, No. 6, 2023, pp. 1026–1037. https://doi.org/10.2514/1.G007067.

[14] Cunis, T., Kolmanovsky, I., and Cesnik, C. E. S., "Control Co-Design Optimization: Integration nonlinear controllability into a multidisciplinary design process," *AIAA SciTech Forum*, San Diego, California, 2022. https://doi.org/10.2514/6.2022-2176.

[15] Lan, C. E., *VORSTAB, A computer program for calculating lateral-directional stability derivatives with vortex flow effect*, National Aeronautics and Space Administration, Langley Research Center, Hampton, Va., 1985.

[16] Ting, K.-Y., Mavriplis, N., Soltani, R., Nelson, C. P., and Livne, E., "Supersonic Configurations at Low Speeds (SCALOS): Model Geometry and Aerodynamic Results," *AIAA Scitech 2022 Forum*, 2022. https://doi.org/10.2514/6.2022-1800.

[17] Magee, T. E., Hayes, P. J., Dorgan, A. J., and Khodadoust, A., "Dynamic Stability Characteristics for Commercial Supersonic Configurations at Low-Speed Flight Conditions," *AIAA Scitech 2022 Forum*, 2022. https://doi.org/10.2514/6.2022-1802.

[18] Polhamus, E. C., "Predictions of vortex-lift characteristics by a leading-edge suction analogy," *Journal of Aircraft*, Vol. 8, No. 4, 1971, pp. 193–199. https://doi.org/10.2514/3.44254.

[19] Seraj, S., and Martins, J. R., "Aerodynamic Shape Optimization of a Supersonic Transport Considering Low-Speed Stability," *AIAA Scitech 2022 Forum*, 2022. https://doi.org/10.2514/6.2022-2177.

[20] Anderson, M., and Mason, W., "An MDO approach to Control-Configured-Vehicle design," *6th AIAA, NASA, and ISSMO, Symposium on Multidisciplinary Analysis and Optimization*, Bellevue, WA, 1996, pp. 734–743. https://doi.org/10.2514/6.1996-4058.

[21] Mader, C. A., and Martins, J. R. R. A., "Stability-constrained aerodynamic shape optimization of flying wings," *Journal of Aircraft*, Vol. 50, No. 5, 2013, pp. 1431–1449. https://doi.org/10.2514/1.c031956.

[22] Welstead, J., "Conceptual Design Optimization of an Augmented Stability Aircraft Incorporating Dynamic Response Performance Constraints," Ph.D. thesis, Auburn University, 2014.

[23] Welstead, J., and Crouse, G. L., "Conceptual Design Optimization of an Augmented Stability Aircraft Incorporating Dynamic Response and Actuator Constraints," *52nd Aerospace Sciences Meeting*, 2014. https://doi.org/10.2514/6.2014-0187.

[24] Niewoehner, R. J., and Kaminer, I. I., "Integrated aircraft-controller design using linear matrix inequalities," *Journal of Guidance, Control, and Dynamics*, Vol. 19, No. 2, 1996, pp. 445–452. https://doi.org/10.2514/3.21638.

[25] "Introduction to IPOPT: A tutorial for downloading, installing, and using IPOPT," Software documentation Revision 2617, Maintained by Stefan Vigerske and Andreas Wächter, 2016. URL https://www.coin-or.org/Ipopt/documentation/.

[26] Moorhouse, D., and Woodcock, R., "US military specification MIL-F-8785C," *US Department of Defense*, 1980.

[27] Hoblit, F. M., *Gust loads on aircraft: concepts and applications*, AIAA, 1988.

[28] Deskos, G., del Carre, A., and Palacios, R., "Assessment of low-altitude atmospheric turbulence models for aircraft aeroelasticity," *Journal of Fluids and Structures*, Vol. 95, 2020, p. 102981. https://doi.org/10.1016/j.jfluidstructs.2020.102981.

[29] von Kármán, T., "Progress in the Statistical Theory of Turbulence," *Proceedings of the National Academy of Sciences*, Vol. 34, No. 11, 1948, pp. 530–539. https://doi.org/10.1073/pnas.34.11.530.

[30] Kaimal, J. C., Wyngaard, J. C., Izumi, Y., and Coté, O. R., "Spectral characteristics of surface-layer turbulence," *Quarterly Journal of the Royal Meteorological Society*, Vol. 98, No. 417, 1972, pp. 563–589. https://doi.org/10.1002/qj.49709841707.

[31] Mann, J., "The spatial structure of neutral atmospheric surface-layer turbulence," *Journal of Fluid Mechanics*, Vol. 273, 1994, pp. 141–168. https://doi.org/10.1017/s0022112094001886.

[32] Porté-Agel, F., Meneveau, C., and Parlange, M. B., "A scale-dependent dynamic model for large-eddy simulation: application to a neutral atmospheric boundary layer," *Journal of Fluid Mechanics*, Vol. 415, 2000, pp. 261–284. https://doi.org/10.1017/s0022112000008776.

[33] Bou-Zeid, E., Meneveau, C., and Parlange, M., "A scale-dependent Lagrangian dynamic model for large eddy simulation of complex turbulent flows," *Physics of Fluids*, Vol. 17, No. 2, 2005, p. 025105. https://doi.org/10.1063/1.1839152.

[34] Deskos, G., Laizet, S., and Palacios, R., "WInc3D: A novel framework for turbulence-resolving simulations of wind farm wake interactions," *Wind Energy*, Vol. 23, No. 3, 2020, pp. 779–794. https://doi.org/10.1002/we.2458.

[35] Rice, S. O., "Mathematical Analysis of Random Noise," *Bell System Technical Journal*, Vol. 24, No. 1, 1945, pp. 46–156. https://doi.org/10.1002/j.1538-7305.1945.tb00453.x.

[36] Bode, H. W., "Network analysis and feedback amplifier design," 1945.

[37] Luckring, J. M., "The discovery and prediction of vortex flow aerodynamics," *The Aeronautical Journal*, Vol. 123, No. 1264, 2019, pp. 729–804. https://doi.org/10.1017/aer.2019.43.

[38] Torenbeek, E., *Essentials of Supersonic Commercial Aircraft Conceptual Design*, John Wiley & Sons Ltd., 2020. https://doi.org/10.1002/9781119667063.

[39] Nelson, C. P., "Effects of Wing Planform on HSCT Off-design Aerodynamics," *Proceedings of the 10th Applied Aerodynamics Conference*, 1992. https://doi.org/10.2514/6.1992-2629.

[40] Weller, H. G., Tabor, G., Jasak, H., and Fureby, C., "A tensorial approach to computational continuum mechanics using object-oriented techniques," *Computers in Physics*, Vol. 12, No. 6, 1998, pp. 620–631. https://doi.org/10.1063/1.168744.

[41] Spalart, P. R., Deck, S., Shur, M. L., Squires, K. D., Strelets, M. K., and Travin, A., "A New Version of Detached-eddy Simulation, Resistant to Ambiguous Grid Densities," *Theoretical and Computational Fluid Dynamics*, Vol. 20, No. 3, 2006, pp. 181–195. https://doi.org/10.1007/s00162-006-0015-0.

[42] Jarrah, M. A., and Ashley, H., "Impact of flow unsteadiness on maneuvers and loads of agile aircraft," *30th Structures, Structural Dynamics and Materials Conference*, 1989. https://doi.org/10.2514/6.1989-1282.

[43] Morgenstern, J., Buonanno, M., Yao, J., Murugappan, M., Paliath, U., Cheung, L., Malcevic, I., Ramakrishnan, K., Pastouchenko, N., Wood, T., Martens, S., Viars, P., Tersmette, T., Lee, J., Simmons, R., Plybon, D., Alonso, J., Palacios, F., Lukaczyk, T., and Carrier, G., "Advanced Concept Studies for Supersonic Commercial Transports Entering Service in the 2018-2020 Period Phase 2," Tech. Rep. NASA/CR—2015-218719, NASA, Glenn Research Center, Cleveland, OH, 2015.

[44] Swanson, R. C., and Turkel, E., "On central-difference and upwind schemes," *Journal of Computational Physics*, Vol. 101, No. 2, 1992, pp. 292–306. https://doi.org/10.1016/0021-9991(92)90007-L.

[45] Jameson, A., "Analysis and Design of Numerical Schemes for Gas Dynamics 1—Artificial Diffusion, Upwind Biasing, Limiters and Their Effect on Accuracy and Multigrid Convergence," *International Journal of Computational Fluid Dynamics*, Vol. 4, No. 3–4, 1995, pp. 171–218. https://doi.org/10.1080/10618569508904524.

[46] Turkel, E., "Preconditioning techniques in computational fluid dynamics," *Annual Review of Fluid Mechanics*, Vol. 31, No. 1, 1999, pp. 385–416. https://doi.org/10.1146/annurev.fluid.31.1.385.

[47] Gustafsson, B., "Unsymmetric hyperbolic systems and the Euler equations at low Mach numbers," *Journal of Scientific Computing*, Vol. 2, No. 2, 1987, pp. 123–136. https://doi.org/10.1007/BF01061482.

[48] Rieper, F., "A low-Mach number fix for Roe's approximate Riemann solver," *Journal of Computational Physics*, Vol. 230, No. 13, 2011, pp. 5263–5287. https://doi.org/10.1016/j.jcp.2011.03.025.

[49] Liou, M.-S., "A sequel to AUSM, Part II: AUSM+-up for all speeds," *Journal of Computational Physics*, Vol. 214, No. 1, 2006, pp. 137–170. https://doi.org/10.1016/j.jcp.2005.09.020.

[50] Berberich, J. P., and Klingenberg, C., "Entropy Stable Numerical Fluxes for Compressible Euler Equations Which Are Suitable for All Mach Numbers," *Recent Advances in Numerical Methods for Hyperbolic PDE Systems*, 2021. https://doi.org/10.1007/978-3-030-72850-2_8.

[51] Drela, M., "XFOIL: An Analysis and Design System for Low Reynolds Number Airfoils," *Low Reynolds Number Aerodynamics*, edited by T. J. Mueller, Springer Berlin Heidelberg, Berlin, Heidelberg, 1989, pp. 1–12. https://doi.org/10.1007/978-3-642-84010-4_1.

[52] Martins, J. R. R. A., "Aerodynamic Design Optimization: Challenges and Perspectives," *Computers & Fluids*, Vol. 239, 2022, p. 105391. https://doi.org/10.1016/j.compfluid.2022.105391.

[53] Seraj, S., and Martins, J. R. R. A., "Aerodynamic Shape Optimization of a Supersonic Transport Considering Low-Speed Stability," *AIAA SciTech Forum*, 2022. https://doi.org/10.2514/6.2022-2177.

[54] Kulfan, R. M., "Wing Airfoil Shape Effects on the Development of Leading Edge Vortices," *5th Atmospheric Flight Mechanics Conference for Future Space Systems*, 1979. https://doi.org/10.2514/6.1979-1675.

[55] Kulfan, R. M., "Wing Geometry Effects on Leading Edge Vortices," *Aircraft Systems and Technology Meeting*, 1979. https://doi.org/10.2514/6.1979-1872.

[56] Kendall, E. R., "The theoretical minimum induced drag of three-surface airplanes in trim," *Journal of Aircraft*, Vol. 22, No. 10, 1985, pp. 847–854. https://doi.org/10.2514/3.45214.

[57] Kroo, I., "A General Approach to Multiple Lifting Surface Design and Analysis," *Aircraft Design Systems and Operations Meeting*, 1984. https://doi.org/10.2514/6.1984-2507.

[58] Selberg, B. P., and Rokhsaz, K., "Aerodynamic Tradeoff Study of Conventional, Canard, and Trisurface Aircraft Systems," *Journal of Aircraft*, Vol. 23, No. 10, 1986, pp. 768–774. https://doi.org/10.2514/3.45379.

[59] Rokhsaz, K., and Selberg, B. P., "Three-Surface Aircraft – Optimum vs Typical," *Journal of Aircraft*, Vol. 26, No. 8, 1989, pp. 699–704. https://doi.org/10.2514/3.45827.

[60] Lacey, D. W., "Aerodynamic Characteristics of the Close-Coupled Canard as Applied to Low-to-Moderate Swept Wings. Volume 3. Transonic-Supersonic Speed Regime," Tech. rep., Naval Ship Research and Development Center, Bethesda, Maryland, USA, 1979.

[61] Covell, P. F., "Supersonic Aerodynamic Characteristics of Canard, Tailless, and Aft-Tail Configurations for Two Wing Planforms," Tech. Rep. NASA-TP-2434, NASA Langley Research Center, Hampton, Virginia, USA, 1985.

[62] Raymer, D. P., *Aircraft Design: A Conceptual Approach*, 5th ed., AIAA, Reston, VA, 2012.

[63] Gray, J. S., Hwang, J. T., Martins, J. R. R. A., Moore, K. T., and Naylor, B. A., "OpenMDAO: An open-source framework for multidisciplinary design, analysis, and optimization," *Structural and Multidisciplinary Optimization*, Vol. 59, No. 4, 2019, pp. 1075–1104. https://doi.org/10.1007/s00158-019-02211-z.

Supersonic Configurations at Low Speeds (SCALOS)

Final Report

December 15, 2024

Appendix B

Stanford University

NASA SCALOS Project - Stanford University Final Report

Project Lead Investigator

Juan J. Alonso
Vance D. and Arlene C. Coffman Professor
James and Anna Marie Spilker Chair of Aeronautics & Astronautics
Department of Aeronautics & Astronautics
Stanford University
Stanford, CA 94305
Phone: (650) 723-9954
E-mail: *jjalonso@stanford.edu*

Investigation Team

The investigation team is made up of the faculty, graduate and undergraduate students, and collaborators listed below with their respective areas of expertise / areas of contribution:

1) **Prof. Juan J. Alonso** (PI, Stanford Aeronautics & Astronautics): overall responsibility for the project and its technical and administrative elements.
2) **Mr. Yiren Shen** (Graduate Student, Stanford Aeronautics & Astronautics): responsible for research and publications of all elements of the conceptual design work for low-speed stability and control of low aspect ratio wings, including AI/ML methodologies, verification, implementation, and interface with the SUAVE conceptual design framework.
3) **Dr. Tejal Shanbhag** (Former Graduate Student, Stanford Aeronautics & Astronautics): responsible for the supersonic aircraft jet aeroacoustic prediction methodologies (including ray tracing), adjoint implementations, and interface with SU2 design optimization framework for the development of improved jet mixer designs.
4) **Prof. Ilan Kroo** (Co-PI, Stanford Aeronautics & Astronautics): advisor in conceptual design approaches for supersonic aircraft configurations.

I. Project Overview

The NASA Supersonic Configurations at Low Speeds (SCALOS) project was a collaboration between the University of Washington (lead university), the University of Michigan, the Boeing Company, and Stanford University that focused on the design, configuration aerodynamics, wind- and water-tunnel testing, control systems, and aeroacoustics of supersonic aircraft with a focus on the relevant design considerations that arise from the low-speed performance of such aircraft. This report describes the contributions in two major tasks from the portion of the team at Stanford University, with strong collaborations with the University of Washington.

Task 1: Hybrid RANS-based methods for aeroacoustic jet noise predictions and optimization

The first task that was pursued focused on the development of relatively inexpensive jet noise aeroacoustics predictions, derived from mean flow Computational Fluid Dynamics (CFD) predictions using Reynolds-averaged Navier-Stokes (RANS) turbulence modeling techniques. Existing approaches to numerical noise prediction vary widely in cost and fidelity, spanning from empirical database interpolation to expensive LES or DNS calculations. In the

context of design optimization, where repeated evaluations of a flow field are required, it is highly desirable to develop methods that minimize computational time and expense while retaining sufficient accuracy. The hybrid methodologies based on steady RANS simulations of the jet flow, which are the subject of our work in this task, are widely recognized as a well-suited alternative for this purpose. These methods post-process mean flow quantities available from RANS calculations to construct an approximate model of the jet's equivalent acoustic field. In our work in this task, initially funded by the SCALOS project (for the first 2 years of effort) and later on continued under FAA funding (ASCENT Project 59), we conducted a detailed study of hybrid computational aeroacoustic methods applied to computing the noise generated by subsonic and transonic free jets. The research focused on three areas within this field. The first area was focused on the low-frequency global source modeling. We proposed a wavepacket-based line source reconstruction method, using eddy viscosity augmented resolvent analysis and an explicit model of coherence decay effects. In several publications, we demonstrated that this approach can accurately compute the acoustic directivity field of round jets at low frequencies. The second area was focused on the fine-scale modeling of the distributed noise sources. We leveraged available LES data to compute the turbulent correlation functions typically appearing in acoustic analogy source terms and investigated the validity of RANS-derived characteristic turbulent scales at different points in the flow field. Using this information, we proposed modifications to the standard model of turbulent scales and demonstrated the improvement in far-field SPL accuracy computed using these changes. Once the modeling improvements were developed and V&V's, the third area of our work in this task focused on adjoint-based nozzle geometry optimization, based on a geometric method for far-field propagation. We implemented a modular acoustic prediction tool with the JAX library to enable GPU acceleration, greatly exceeding the computational performance of existing CPU-based tools. Using the associated automatic differentiation capabilities to couple with SU2's discrete adjoint solver, we performed preliminary constrained shape optimization of two nozzle geometries to minimize far-field noise. This work will continue for one more year under ASCENT 59 and we intend to take 2 of the optimized nozzle shapes (using the RANS-based aeroacoustic prediction modules) and validate their acoustic performance using wall-modelled LES (WMLES) techniques. This work will be reported at a later time.

Section II includes the latest publication that resulted from this work and goes into more details of the modeling strategy but, in particular, of the design optimization approach and the results obtained using our RANS-based aeroacoustics modeling strategy. The work presented represents the PhD work of Dr. Tejal Shanbhag, who completed her degree at Stanford University during the Spring of 2024 and who is now an engineer working at Siemens Digital Industries Software.

Task 2: AI/ML-based Surrogate Modeling Strategies for Conceptual Design with Low-speed Stability Constraints

The second task that we pursued under the NASA SCALOS project focused on two novel components to improve the low-speed stability predictions that are typically used in conceptual design tools for supersonic configurations.

Aircraft design typically relies on accurate aerodynamic predictions. High-fidelity (HF) methods, such as

computational fluid dynamics (CFD), provide accurate aerodynamic analyses but are computationally expensive for early-stage design. Conversely, low-fidelity (LF) methods, such as the vortex lattice method (VLM), offer cost-effective solutions but struggle to capture complex flow phenomena, limiting their predictive accuracy. The conceptual design process thus presents a fidelity-cost trade-off, requiring a balance between high-fidelity (HF) and LF data in early design phases. In order to tackle this challenge, in Task 2 we pursued the development of `VortexNet`, a graph neural network (GNN)-based surrogate model designed to bridge the fidelity gap between LF and HF aerodynamic predictions. `VortexNet` learns corrections to LF panel-wise local loading coefficient field data using data-driven insights from HF RANS CFD simulations, enabling pressure coefficient field predictions across a range of Delta wing geometries and free-stream conditions. The model demonstrates strong prediction accuracy and generalizability across configurations, effectively capturing nonlinear flow features under geometric variations. A hyper-parameter sensitivity study and a preliminary prediction mechanism explanation, leveraging the latent space ablation technique, are conducted to rationalize the model's predictive capabilities and provide guidance for future improvements in `VortexNet`-like surrogate modeling. The results we obtained indicate that `VortexNet` has potential as a valuable tool for conceptual design in multidisciplinary design optimization (MDO), while emphasizing the need for further validation and refinement.

In particular, the conceptual design of a stable and efficient supersonic transport (SST) aircraft during takeoff and landing, where higher angle-of-attack (AOA) induces complex aerodynamic phenomena such as vortex lift and flow separation, can be challenging. Existing analysis methods face the same fidelity-cost trade-off described earlier. To address this gap, the latest work we conducted in this Task 2 proposed a multi-fidelity conceptual design analysis workflow that integrates a graph neural network (GNN)-based surrogate model into VLM to augment the analysis fidelity of LF tools. The surrogate model learns the discrepancies between LF and HF pressure fields, enabling accurate and efficient aerodynamic analyses on arbitrary quantities of interest. When evaluated on a dataset with various Delta wing geometries, the proposed workflow achieves an approximately five-fold reduction in the normalized root mean square error (NRMSE) for the predicted lift, drag, and pitching moment coefficients compared to using VLM alone. The results also highlight the proposed workflow's generalizability across new flow conditions and wing geometries, while identifying its limitations in prediction accuracy variance across the test dataset. Overall, the proposed workflow provides an efficient and effective framework for aerodynamic assessment in conceptual design with improved fidelity.

A more detailed description of the work carried out in Task 2 of this project can be found in Sections IV and III of this final report.

II. An Automatic-differentiation Framework for Jet Noise Minimization Using Geometrical Acoustics

In this work, we present a computational aeroacoustics prediction tool based on Lighthill's acoustic analogy and a geometrical method for far field propagation. Both the source model and refraction model use information obtained from a standard RANS $k-\epsilon$ simulation of the jet flow. This implementation makes very few simplifying assumptions about the flow field geometry, allowing this method to be applied to complicated nozzle configurations that result in inherently three-dimensional propagation effects. The computed spectra show good agreement with experimental data at various polar angles. We have further coupled our AD-enabled Jax implementation of this acoustic prediction tool with the adjoint capability in SU2, creating an integrated framework to perform constrained shape optimization of jet nozzles. In this paper, we use the SMC006 chevron nozzle as a test case to validate the computed gradients of far field noise with respect to relevant shape design parameters. The gradient values show good agreement against both finite difference tests and adjoint-based gradients obtained from SU2 native objective functions.

A. Introduction

The high current projection for yearly growth in air traffic, and the simultaneous rapid expansion of urban populations, have created a demand for significant reduction in the noise emitted by civil and military aircraft. Jet mixing noise is one of the most significant components of aircraft noise overall, particularly at take-off condition. The calculation of this noise component has received increased research interest in recent years, as the development of reliable and computationally affordable tools for this purpose represents a considerable theoretical and computational challenge. Significant jet noise reductions have hitherto been achieved by the increase of engine bypass ratios. Experimental studies have highlighted a number of promising design concepts with potential to achieve further reductions, such as asymmetric, beveled and chevron nozzles. These designs introduce geometrical complexity and inherently three-dimensional flow features - therefore, acoustic prediction tools with sufficient robustness to account for these features are required.

The approaches to numerical prediction of jet mixing noise are widely varied in cost and fidelity, spanning from empirical database interpolation to expensive FWH calculations reliant on LES or DNS data. In the context of design optimization, where repeated aeroacoustic evaluations of a flow field are required, it is highly desirable to develop a method that minimizes computational time and expense while retaining the necessary accuracy. Hybrid methodologies based on RANS simulations of the jet flow conditions are widely recognized as an alternative well suited to this purpose. These methods post-process mean flow quantities available from RANS calculations (time-averaged velocities, pressure,

turbulent kinetic energy etc.) to construct models representing the turbulent correlation functions that appear in the source term of Lighthill's equation.

Early examples of this method type were presented by Balsa and Gliebe [3], who modeled the acoustic sources based on analytic representations of the mean flow. The MGBK method [15]builds upon this approach, replacing the use of analytic fits with a numerical $k-\epsilon$ turbulence solution. In this method, Lilley's equation is solved for a convecting source emitting a single frequency using the high frequency Green's function for an axisymmetric jet. Further exploration of acoustic analogy based methods was conducted by Tam and Auriault [20], whose proposed framework used an analogy between molecular and turbulent pressures to derive a form for the two-point correlations, and Morris and Farassat [17], who showed that such a 'kinetic theory' approach is equivalent to the standard Goldstein acoustic analogy assuming a consistent form for the source term and Green's function are used. Other efforts to model the two point correlations on the basis of RANS quantities have focused on accurately capturing the characteristic turbulent length and time scales at different locations in the jet flow. Self and Azarpeyvand [2] [19] demonstrated the importance of accounting for frequency dependence in these scales when modeling turbulent statistics for acoustic calculations. These authors have also shown that inclusion of time scales based on different turbulent mechanisms, such as dissipation, production and energy transfer, results in significantly more accurate predictions overall, and in particular at low and high frequencies.

In this paper, we use as a test case the SMC006 chevron nozzle geometry, which has frequently been used in aeroacoustics studies and CAA benchmarking. We apply a source model based on Lighthill's acoustic analogy. The resulting far field SPL predictions show good agreement with experimental data at a polar angle of 90^o. In order to handle far field propagation, and incorporate the effects of sound refraction by the mean flow field, we apply a geometrical acoustics method. This ray tracing approach, demonstrated by Ilario et al. [14], interpolates flow field variables from a RANS simulation to integrate along the path of many rays from numerically distributed source locations to the far field observer locations. We demonstrate that coupling the source modeling approach with this ray tracing methodology results in accurate prediction of far field SPL at inclined polar observer angles. The sound-flow interaction effects at different points in the jet flow are studied via the spatial distribution of the flow factor. Our implementation of both the acoustic source and propagation modeling tools in Jax allows the native Python and Numpy-based code to be automatically differentiated. We utilize the AD capability in conjunction with the discrete adjoint solver in the open source simulation suite SU2 to obtain the gradients of computed far field noise with respect to shape parameters describing the nozzle. In order to validate this coupled adjoint system, we demonstrate the agreement of these shape gradient values with those obtained by finite differencing.

The paper is organized as follows. Section II gives details of the acoustic source model, the ray tracing methodology used for far field propagation, and the AD framework used to compute gradients for shape optimization. Section III outlines the validation of the RANS mean flow quantities against experiments, observed refraction effects obtained using our acoustic prediction tool and a comparison of far field SPL against experimental results at different polar

observer angles. In addition, we present a validation of the gradients obtained from Jax of far field noise with respect to RANS simulation state variables, and a validation of AD gradient computation against finite differences obtained from the overall coupled framework. Section IV describes our intended future work on AD-enabled shape optimization for noise reduction of different nozzle configurations.

B. Methodology

1. Source model

We apply Ribner's formulation [18] of the Lighthill equation [16] as a starting point for the acoustic source model. The far-field spectrum can then be written as:

$$P(\mathbf{x},\omega) = \frac{1}{(4\pi r)^2}\frac{1}{a_0^3}\bar{\rho}^2 D_f^{-5} d_{ijkl}\int \Phi\mathcal{F}[I_{ijkl}]d^3\mathbf{y}, \tag{1}$$

where $\mathbf{x}$ and $\mathbf{y}$ are respectively the observer and source locations, and $r = |\mathbf{x}|$ is the distance to the far field. a_0 is the reference speed of sound and $\bar{\rho}$ is the time-averaged flow field density. The Doppler factor D_f is calculated as $1 - M_c\cos(\theta)$. The convective Mach number M_c is defined as follows:

$$M_c = \frac{1}{4}\left(\frac{U_1}{a}\right) + \frac{1}{3}M, \tag{2}$$

where U_1 is the local time-averaged axial flow speed, a is the local speed of sound, and M is the jet exit Mach number. d_{ijkl} is a tensor quantity representing the effects of quadrupole directivity. The effects of flow refraction are accounted for via the flow factor Φ, defined below.

$\mathcal{F}[I_{ijkl}]$ denotes the Fourier transform of the fourth order correlation of turbulent velocity fluctuations. We require a model for this tensor quantity:

$$I_{ijkl}(\tau) = \int \frac{\partial^4}{\partial\tau^4}\overline{v_i v_j v_k' v_l'}d^3\xi = \int \frac{\partial^4}{\partial\tau^4}\overline{u_i u_j u_k' u_l'}d^3\xi \tag{3}$$

Here $v_i = U_i + u_i$ is the instantaneous velocity, sum of the mean and fluctuating components. Here the prime is used to indicate evaluation at a different spatial and temporal location, separated by $\xi = (\xi_1, \xi_2, \xi_3)$ and τ respectively. We may neglect the mean components, as only the fluctuating components of velocity are considered as efficient sources of turbulent mixing noise. Assuming isotropic and locally homogeneous turbulence, it follows that u_i and u_j' are linked by a joint normal probability distribution. The fourth order correlation may then be rewritten in terms of second order quantities:

$$\overline{u_i u_j u_k' u_l'} = \overline{u_i u_j}\,\overline{u_k' u_l'} + \overline{u_i u_k'}\;\overline{u_j u_l'} + \overline{u_i u_l'}\;\overline{u_j u_k'}. \tag{4}$$

As $\overline{u_i u_j}$ and $\overline{u'_k u'_l}$ are independent of temporal separation τ, the first of these three terms does not appear in the expression for I_{ijkl}. A model for the second order correlations is then required. We follow the form suggested by Ribner [18], in which the spatial and temporal contributions may be considered independently:

$$\overline{u_i u'_j}(\xi, \tau) = R_{ij}(\xi) g(\tau). \tag{5}$$

For homogeneous and isotropic turbulence, the spatial correlation takes the form:

$$R_{ij}(\xi) = \overline{u_1^2} \left[\left(f + \frac{1}{2}|\xi| f' \right) - \frac{1}{2} f' \frac{\xi_i \xi_j}{|\xi|} \right]. \tag{6}$$

The prime in this case denotes differentiation with respect to the argument. The function $f(\xi)$ can take many different forms; we choose a Gaussian distribution:

$$f(\xi) = \exp\left(-\pi \frac{\xi^2}{L^2} \right), \tag{7}$$

where L is the characteristic turbulent length scale at the source location. Integrating the fourth order correlation tensor over the spatial source region gives:

$$I(\tau) = \frac{\partial^4 g}{\partial \tau^4} \int (R_{ik} R_{jl} + R_{il} R_{jk}) d^3\xi = \frac{\rho}{2\sqrt{2}} k^2 L^3 \frac{\partial^4 g}{\partial \tau^4}. \tag{8}$$

To reflect the isotropy of the modeled sources, the index $ijkl$ is dropped from the notation at this point. The effects of far field directivity are then accounted for entirely by the Doppler factor, and by the flow factor computed in the next section as a function of observer and source location.

A Gaussian model is also chosen for the temporal correlation:

$$g(\tau) = \exp\left(-\frac{\tau^2}{\tau_0^2} \right), \tag{9}$$

giving the following explicit form for the Fourier transform of the modeled fourth order correlation tensor:

$$I(\Omega) = \frac{\sqrt{\pi}}{4} k^2 L^3 \tau_0 \Omega^4 \frac{\sqrt{2\pi}}{2} \exp\left(-\frac{\tau_0^2 \Omega^2}{8} \right). \tag{10}$$

Here the modified frequency is given by $\Omega = \omega \sqrt{(1 - M_c \cos\theta)^2 + (\alpha k^{1/2}/a_0)^2}$, where α is an experimental parameter taken to be 0.5. The term $(1 - M_c \cos\theta)$ accounts for the Doppler shift as the source is convected, while the term $(\alpha k^{1/2}/a_0)$ accounts for the finite lifetime of an eddy as it moves downstream.

The characteristic turbulent scales L and τ_0 are calculated from the standard RANS-derived quantities k and ϵ as

follows:

$$L = c_l \frac{k^{3/2}}{\epsilon}, \qquad \tau_0 = c_\tau \frac{k}{\epsilon}, \tag{11}$$

where c_l and c_τ are empirical constants. We use the improved time scale proposed by Azarpeyvand and Self [2], which accounts for the transfer of turbulent energy between different wavenumbers; this time scale naturally reduces to the conventional scales associated with turbulent production and dissipation in the areas of the jet where these are the dominating mechanisms for noise generation:

$$\tau_0^* = \tau_0 \left(\frac{L}{D} \right)^{2/3}, \tag{12}$$

where D is the nozzle diameter. Replacing τ_0 with the improved scale τ_0^* and substituting into equation (1) gives:

$$I(\Omega) = \frac{\sqrt{\pi}}{4} \frac{c_l^3}{c_\tau^3} k^{7/2} \rho^2 \tau_0^{*4} \Omega^4 \exp\left(-\frac{\tau_0^{*2} \Omega^2}{8} \right). \tag{13}$$

$$\Rightarrow \quad P(\mathbf{x}, \omega) = \frac{1}{64\pi^{3/2}} \frac{1}{r^2 a_0^4} \frac{c_l^3}{c_\tau^3} \int \Phi(\mathbf{x}, \mathbf{y}) D_f^{-5} \rho^2 k^{7/2} \tau_0^{*4} \Omega^4 \exp\left(-\frac{\Omega^2 \tau_0^{*4}}{8} \right) d^3\mathbf{y}. \tag{14}$$

Equation 13 represents the spectrum of the far field sound radiated by a single correlated volume of turbulence within the jet, located at $\mathbf{y}$ and neglecting refraction by the jet mean flow. These refraction directivity effects are captured by $\Phi(\mathbf{x}, \mathbf{y})$, whose calculation is presented in the next section.

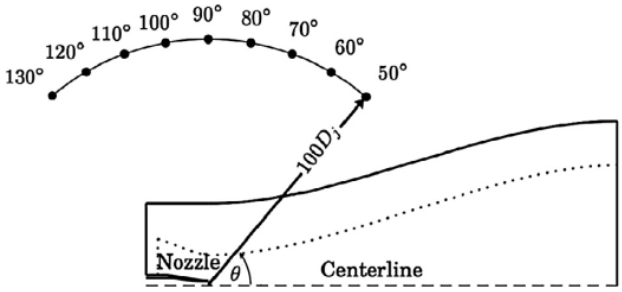

Fig. 1 Position of observer locations relative to jet orientation (reproduced from Engel et al.[12]).

2. Far-field propagation model

The inclusion of non-zero flow velocity and spatial gradients in the speed of sound, particularly across shear layers, have a significant effect on the refraction of sound waves reaching the far field. In order to account for these effects, we compute the flow factor $\Phi(\mathbf{x}, \mathbf{y})$ [14], which represents the ratio of the pressure amplitude measured at location $\mathbf{x}$ due to a source at location $\mathbf{y}$ with and without the jet flow being present. $\Phi(\mathbf{x}, \mathbf{y})$ may be calculated by a number of

different methods, such as an adjoint Green's function or asymptotic solution of Lilley's equation. In this work, we apply the geometrical ray tracing method employed to describe high-frequency wave propagation in non-uniform media. This method does not require the solution of an additional PDE over a domain extending to the far field, and may be used to study the effects of flow refraction in complex and possibly asymmetric jet configurations without resorting to azimuthal mode decomposition or similar techniques to maintain reasonable computational cost.

We follow the ray tracing formulation presented by Pierce [1]. A point x_p^{ray} on the wavefront that defines the position of a ray moves with velocity:

$$\frac{d\mathbf{x}_p^{\text{ray}}}{dt} = \mathbf{v}(\mathbf{x}_p^{\text{ray}}, t) + \mathbf{n}(\mathbf{x}_p^{\text{ray}}, t)a(\mathbf{x}_p^{\text{ray}}, t), \tag{15}$$

where $\mathbf{n}$ is the unit normal vector to the wavefront. Instead of constructing the full local wavefront surface, we do not work with $\mathbf{n}$ and instead use the wave slowness vector $\mathbf{s}$:

$$\mathbf{s} = \frac{\mathbf{n}}{a + \mathbf{v}.\mathbf{n}}. \tag{16}$$

The ray tracing equations are written in Cartesian coordinates as six coupled ordinary differential equations for the components of ray position and wave slowness:

$$\frac{dx_i^{\text{ray}}}{dt} = U_i + \frac{a^2 s_i}{1 - U_j s_j} \tag{17}$$

$$\frac{ds_i}{dt} = -\frac{1 - U_j s_j}{a}\frac{\partial a}{\partial x_i} - s_j \frac{\partial U_j}{\partial x_i} \tag{18}$$

Equations 17 and 18 are numerically integrated using a fourth-order Runge-Kutta method with a subroutine to perform spatial interpolation of the quantities U_i and a from the RANS simulation data. Each ray is integrated forward in time until it exits the RANS domain - beyond the domain the flow variables are considered to be spatially uniform, and it follows that the ray path is then a straight line to the far field.

The ratio of pressure amplitude at the source and far field locations cannot be determined from the ray tracing solution alone. We use the Blokhintsev invariant [5] to compute this quantity:

$$\frac{\overline{p^2} V A}{(1 - U_i s_i)\rho a^2} = \text{constant}, \tag{19}$$

where $V = |d\mathbf{x}^{\text{ray}}/dt|$ and A is the ray tube area. Applying equation 19 to a ray that begins at the source location and ends at the observer location gives the ratio of pressure amplitudes as follows:

$$\frac{\overline{p^2}|_{\mathbf{x}}}{\overline{p^2}|_{\mathbf{y}}} = \frac{\left.\frac{V}{(1-U_i s_i)\rho a^2}\right|_{\mathbf{y}}}{\left.\frac{V}{(1-U_i s_i)\rho a^2}\right|_{\mathbf{x}}} \frac{A|_{\mathbf{y}}}{A|_{\mathbf{x}}}. \tag{20}$$

The flow factor as we defined it is the ratio between the pressure amplitude in the far field between a ray traced through the jet flow and a ray traced from the same source but through a quiescent medium:

$$\Phi(\mathbf{x}, \mathbf{y}) = \frac{\overline{p^2}|_{\mathbf{x},\text{flow}}}{\overline{p^2}|_{\mathbf{x},\text{quiescent}}}. \tag{21}$$

In order to calculate Φ from equation 19, we make the following further assumptions: that the pressure amplitude and ray tube area at the source itself remains unchanged by the presence of a jet flow, and that for a quiescent flow, the quantity $V/(1 - U_i s_i)\rho a^2$ is equal at the source and observer locations. With these assumptions the following expression for the flow factor may be derived:

$$\Phi(\mathbf{x}, \mathbf{y}) = \frac{\left.\frac{V}{(1-U_i s_i)\rho a^2}\right|_{\mathbf{y},\text{flow}}}{\left.\frac{V}{(1-U_i s_i)\rho a^2}\right|_{\mathbf{x},\text{flow}}} \frac{A|_{\mathbf{x},\text{quiescent}}}{A|_{\mathbf{x},\text{flow}}}. \tag{22}$$

As the ray area cannot be found directly from the ray tracing solution, we approximate the ratio of tube areas using ray densities. The far field is represented as a spherical shell discretized into approximately 10^4 equal bins. A large number of rays (approximately 6×10^5 for the results in this paper) are launched from each source location. In order to ensure even coverage over space, the launch angles are chosen to intersect the vertices of a geodesic sphere with a suitably high subdivision frequency. The number of rays intersecting the far field bin closest to the far field location of interest is compared for the ray tracing solution with jet flow (N_{flow}) and without ($N_{\text{quiescent}}$). The flow factor is then finally calculated as:

$$\Phi(\mathbf{x}, \mathbf{y}) = \frac{\left.\frac{V}{(1-U_i s_i)\rho a^2}\right|_{\mathbf{y},\text{flow}}}{\left.\frac{V}{(1-U_i s_i)\rho a^2}\right|_{\mathbf{x},\text{flow}}} \frac{N|_{\mathbf{x},\text{flow}}}{N|_{\mathbf{x},\text{quiescent}}}. \tag{23}$$

$\Phi(\mathbf{x}, \mathbf{y})$ is calculated for each of the finite number of source locations (approximately 10^3 for the results in this paper). The sources are non-uniformly distributed through the jet flow, with the highest density of source placement in areas of high velocity gradient and turbulent kinetic energy.

3. AD-based framework for shape optimization

In this section we present the discrete adjoint framework developed in the context of the SU2 solver [10]. The discrete adjoint implementation makes use of automatic differentiation (AD), eliminating potential errors from hand-differentiation of the governing equations. AD is based on the observation that any simulation code may be represented

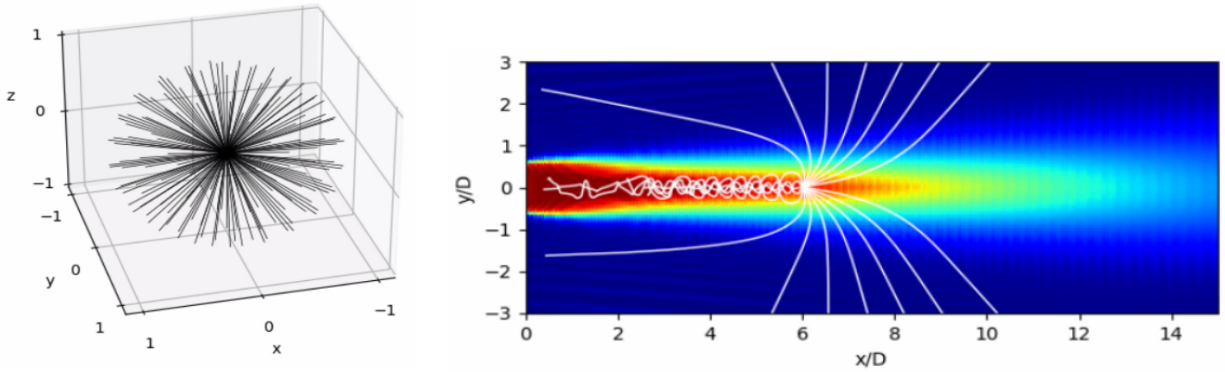

Fig. 2 Ray tracing method: (a) geodesic launch angles for 162 rays from a single source, (b) ray paths through SMC006 mean flow (Mach number contours).

as a sequence of elementary computing operations upon a set of inputs, the differentiation rules of which are known. Repeated application of the chain rule through the simulation code therefore allows us to compute both the simulation output and the gradient of this output quantity with respect to any input of interest. Furthermore, due to the way in which AD is implemented within the code, the computed derivatives are accurate to machine precision. Automatic differentiation is already integrated into the SU2 code used for the RANS computation. The acoustic source and ray tracing codes are implemented using Jax [6], an Autograd-supported framework that allows automatic differentiation of native Python code. In this paper, we use this framework to efficiently compute the gradients of far field radiated sound with respect to design variables chosen to parameterize the SMC006 chevron nozzle [8]. However, the implementation is intended to be fully generalizable to any objective function computed in a Jax functional program as the post processing of an SU2 CFD output, and any set of shape design variables described via the SU2 DOT/DEF workflow.

We represent the design configuration by a vector of design variables α. A perturbation in one of the variables results in a linear elastic mesh deformation, resulting in a new mesh X. The optimization problem of interest is then written as follows:

$$\min_{\alpha} J(U(\alpha), X(\alpha)) \quad \text{subject to} \quad R(U(\alpha), X(\alpha)) = 0. \tag{24}$$

Here J is our far field noise objective function, U is the vector of state variables, and R is the spatially discretized residual vector. This residual includes not only the flow governing equation residual but that of any coupled governing equations, such as a RANS turbulence model. A dual time stepping method may be applied to march forward in pseudo-time τ to a converged steady state solution; we assume that time marching is implemented using an implicit forward Euler scheme:

$$\frac{dU}{d\tau} + R(U) = 0 \quad \Rightarrow \quad U^{n+1} - U^n + \Delta\tau R(U^{n+1}) = 0 \qquad n = 1, ..., N. \tag{25}$$

Linearizing around the state U^n gives:

$$U^{n+1} - U^n + \Delta\tau \left[R(U^n) + \left.\frac{\partial R}{\partial U}\right|^n (U^{n+1} - U^n) \right] = 0 \qquad n = 1, ..., N. \tag{26}$$

This can be expressed as a fixed point iteration:

$$U^{n+1} = G(U^n) \qquad n = 1, ..., N. \tag{27}$$

Thus the optimization problem may be written as:

$$\min_{\alpha} J(U(\alpha), X(\alpha)) \;\text{ subject to }\; U(\alpha) = G(U(\alpha), X(\alpha)), \qquad X(\alpha) = M(\alpha). \tag{28}$$

The Lagrangian representing this optimization problem is:

$$L(\alpha, U, X, \overline{U}, \overline{X}) = N(U, \overline{U}, X) - U^T\overline{U} + [M(\alpha) - X]^T\overline{X} \tag{29}$$

where N is the shifted Lagrangian $J(U, X) + G^T(U, X)\overline{U}$. We choose the adjoint variables $\overline{U}$ and $\overline{X}$ in order to eliminate the sensitivities $\partial U/\partial\alpha$ and $\partial X/\partial\alpha$:

$$\overline{U} = \frac{\partial}{\partial U} J^T(U, X) + \frac{\partial}{\partial U} G^T(U, X)\overline{U} \tag{30}$$

$$\overline{X} = \frac{\partial}{\partial X} J^T(U, X) + \frac{\partial}{\partial X} G^T(U, X)\overline{U} \tag{31}$$

The derivatives on the right hand side of these adjoint equations are computed automatically using AD in the flow and acoustic codes. The sensitivity of the objective J to the flow state variables U is communicated via the term $\partial J^T/\partial U$, which is accumulated to the adjoint fixed-point iterator at each sub-iteration used to solve the coupled adjoint system. Once the adjoint variables are converged, this gives the total derivative of our objective function J as:

$$\frac{dJ^T}{d\alpha} = \frac{d}{d\alpha} M^T(\alpha)\overline{X} \tag{32}$$

The complete coupled SU2-Jax workflow is shown schematically in Figure 3. Solid blocks in the diagram refer to primal calculations, while outlined blocks refer to adjoint calculations; SU2 (C++) modules, Jax (Python) modules and user inputs are shown in blue, orange and green respectively.

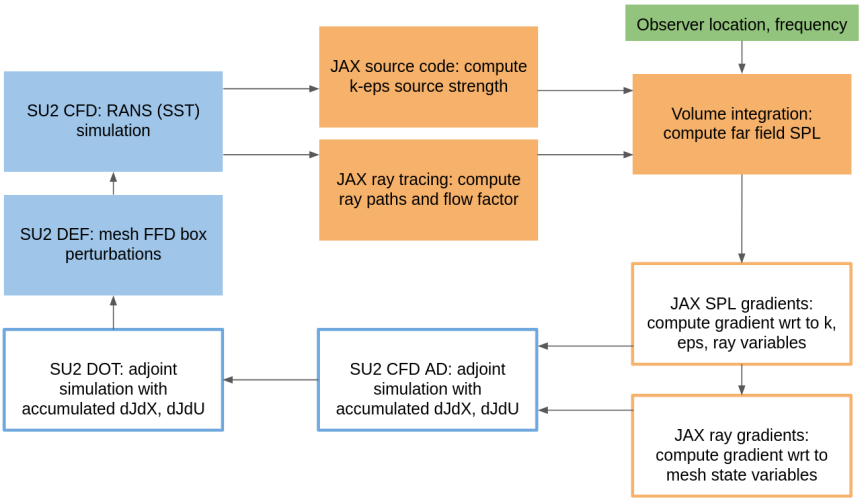

Fig. 3 Overall coupled workflow for primal, adjoint and shape gradient calculation.

C. Results

1. RANS mean flow solution

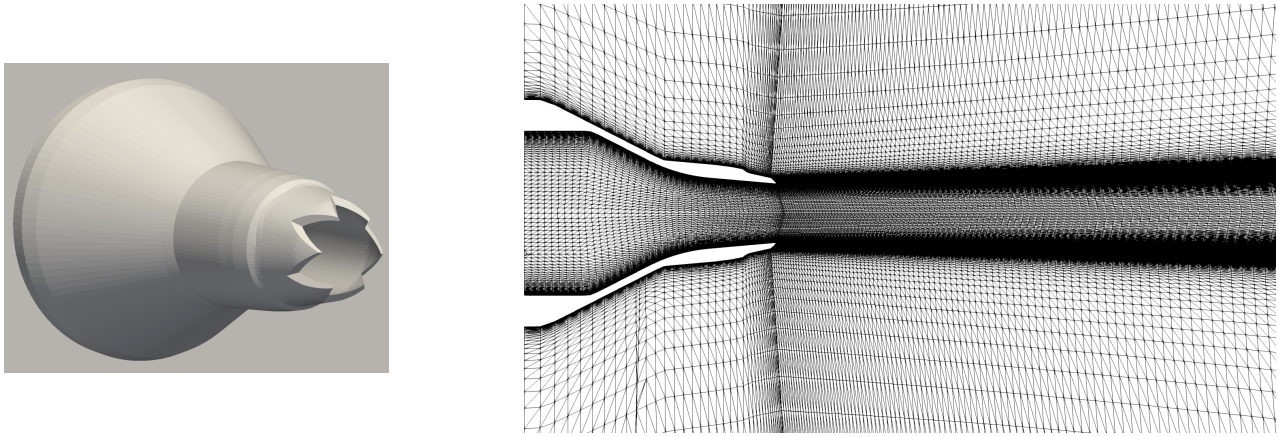

Fig. 4 SMC006 chevron nozzle: (a) geometry, (b) 2.76M point structured hexahedral mesh, zoomed to show boundary layer and shear layer resolution

The mean flow RANS simulation is performed using the open-source *SU*2 code [10]. The finite volume method (FVM) is applied on arbitrary unstructured meshes using a standard edge-based data structure with control volumes constructed using a median-dual, vertex-based scheme. The continuity, momentum and energy equations for a compressible gas are solved together with the ideal gas equation of state. The standard $k-\omega$ model is used, with the two additional equations governing the turbulent quantities solved using the standard coefficient values. The structured computational grid is generated in repeated 1/6th sector blocks corresponding to each chevron. Regions of the computational domain corresponding to the shear layers and boundary layers are suitable refined to capture the

high spatial gradients of velocity and temperature expected in these flow features. The simulation results are compared against experimental data from Bridges and Wernet [7] in Figures 5 and 6. The mean flow axial velocity profile at all three axial locations is captured with reasonably high accuracy. The turbulent kinetic energy profiles maintain a reasonable shape but show a higher discrepancy in magnitude, particularly at distances further downstream of the nozzle exit where the SMC006 mesh becomes significantly coarser. However, it should be noted that volume 'averaged' integral methods such as this one are typically robust to minor inaccuracies in the base flow, and it is possible to obtain a relatively high quality noise prediction even from these approximately correct RANS solutions.

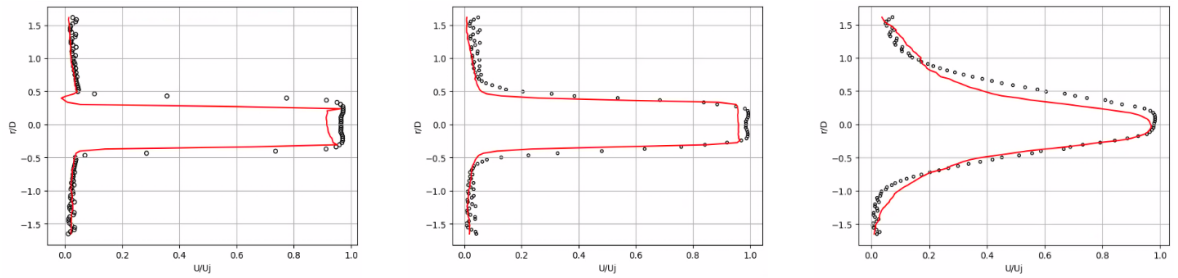

x/D = 0.1 **x/D = 1.0** **x/D = 3.6**

Fig. 5 Comparison of RANS mean axial velocity (black) against experimental data (red).

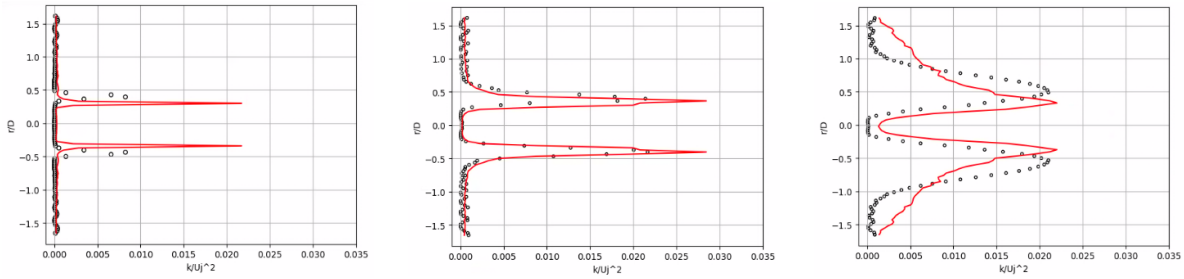

x/D = 0.1 **x/D = 1.0** **x/D = 3.6**

Fig. 6 Comparison of RANS mean turbulent kinetic energy (black) against experimental data (red).

D. Sound-flow interaction effects

The effects of sound refraction by the mean flow can be assessed in isolation from the source model by looking at the distribution of the flow factor Φ. This quantity represents the factor by which the measured amplitude at observer location $\mathbf{x}$ due to a source at $\mathbf{y}$ is altered by refraction effects, as compared to a situation in which the same source were placed in a quiescent medium. Figure 7 shows the distribution of flow factor for observers at two different polar angles. As physically expected, refraction has a negligible effect for an observer at $\theta = 90^o$, as indicated by the flow factor value being close to unity everywhere. At $\theta = 30^o$, the effects of refraction are much more significant. Rays emanating from sources located in the core of the jet undergo total internal reflection upon encountering the shear layer as shown by the

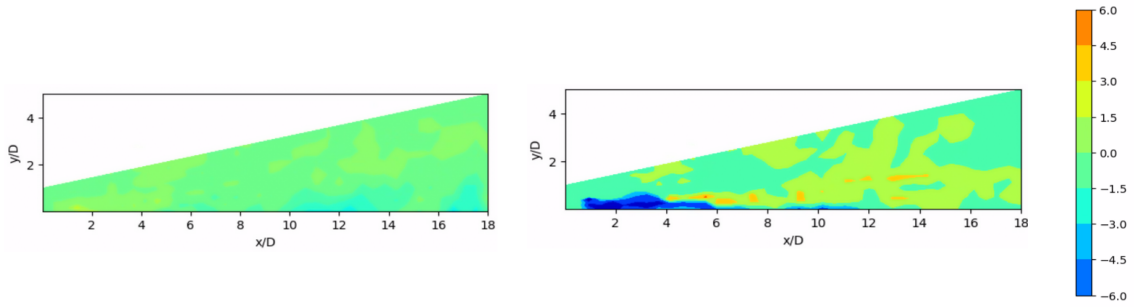

Fig. 7 Flow factor (in dB) for observer angles of (a) $\theta = 90^o$ and (b) $\theta = 30^o$. Observer above plane of figure ($\phi = 90^o$).

ray paths diagram in Figure 2 (where velocity gradients are high in the direction normal to the ray path) - consequently, sound emanating from this portion of the flow field sees a considerable reduction in amplitude reaching the far field. In contrast, rays emanating from source locations further downstream of the nozzle exit, and particularly outside the radial extent of the potential core, are refracted away from the jet axis. This corresponds to the spatial regions of amplification clustered around these source locations.

1. Far field noise predictions

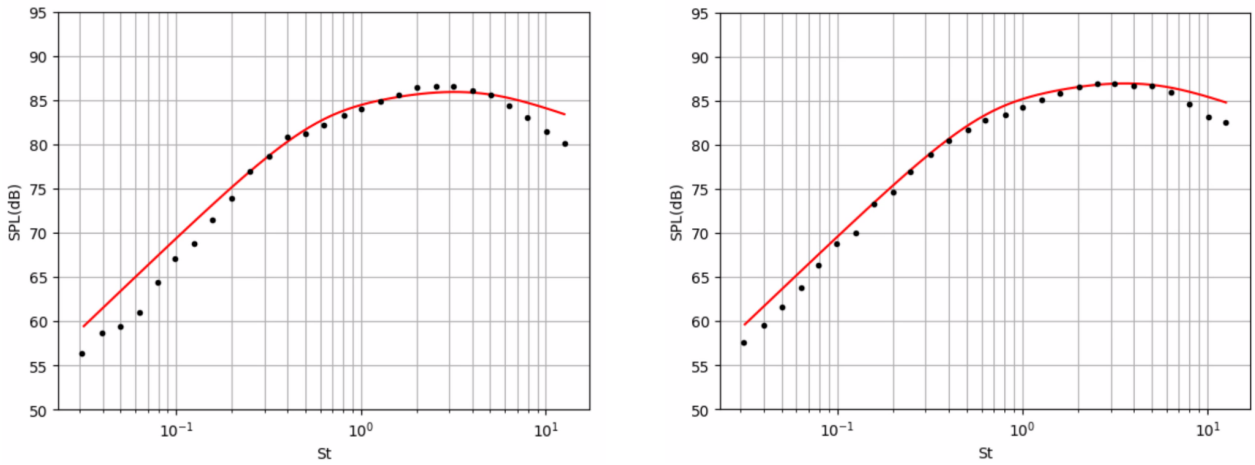

Fig. 8 Far field SPL prediction (red) at (a) $\theta = 50^o$ and (b) $\theta = 70^o$ compared against experimental data (black)

The coupled acoustic prediction capability of the source model with ray tracing is assessed by comparing the far field SPL at different polar observer angles against experimental measurements [8] (figures 8 and 9). It can be seen that with the refraction effects taken into account via incorporation of the flow factor, the predictions compare favorably with experiments. Consistent with the observations of the previous section, at $\theta = 90^o$ the addition of ray tracing makes

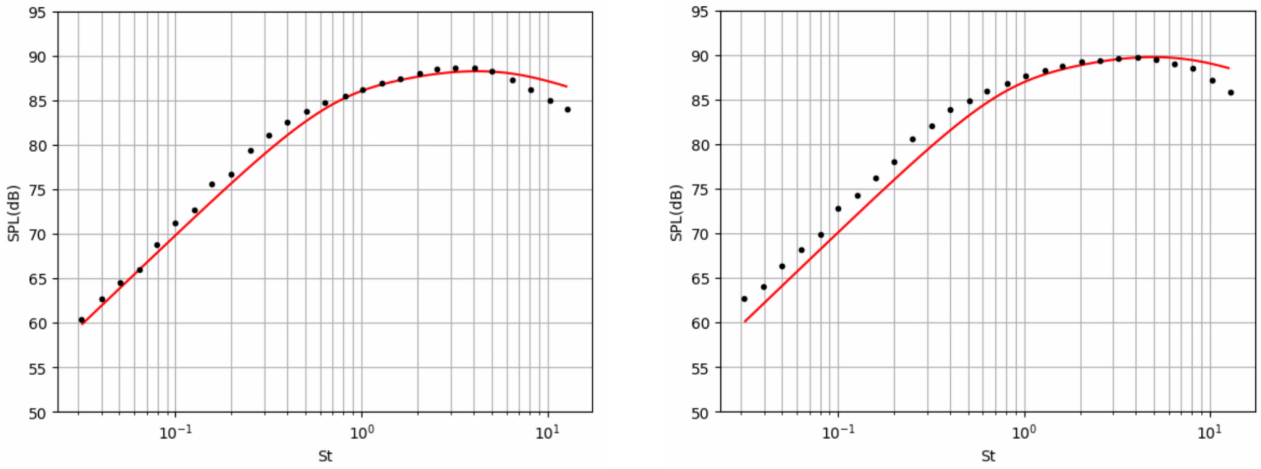

Fig. 9 Far field SPL prediction (red) at (a) $\theta = 90^o$ and (b) $\theta = 110^o$ compared against experimental data (black)

very little difference to the computed spectrum, and very good agreement is obtained. At other polar angles, while the overall spectrum shape, magnitude and peak frequency location are captured, the spectrum agreement shows greater discrepancy. In particular, the fall-off expected at frequencies higher than the spectrum peak is not well captured by this model. Higher frequency broadband noise, particularly peak noise, is related to the flow field close to the end of the potential core. It is expected that an overprediction or underprediction of the potential core by the RANS simulation will have an impact on the predicted noise level in this type of hybrid methodology. It has been observed in the literature that the $k - \epsilon$ turbulence model[4], and in particular the SST model[11], results in an overprediction of the potential core length of approximately 15% when applied to the prediction of turbulent jet flows. The high frequency discrepancies observed in the computed spectra are therefore in part to be expected.

2. Validation of JAX adjoint gradients and coupled shape gradients

In order to validate the automatic gradient computation performed in the Jax code, we perturb the values of the base flow at a large number of randomly sampled points in the mesh. We then compare the resulting finite difference gradients of the far field sound pressure level (SPL) with respect to the base flow variable at that point against the corresponding gradient value obtained from the Jax gradient function. Figure 10 shows one such comparison of the gradients of SPL with respect to speed of sound. There is very good agreement overall. The small degree of discrepancy observed is expected due to the form of the differentiated code - as the adjoint code performs the time marching along each ray in reverse, some errors are accumulated in the reverse RK4 step.

The coupling between the AD-enabled code in Jax with the AD framework in SU2 is designed to work with any Jax-implemented objective function, and additionally with any of the SU2 flow solvers (Euler, Navier-Stokes, SA/SST RANS) in two or three dimensions. To validate this capability, we study two airfoil optimization test problems. The first

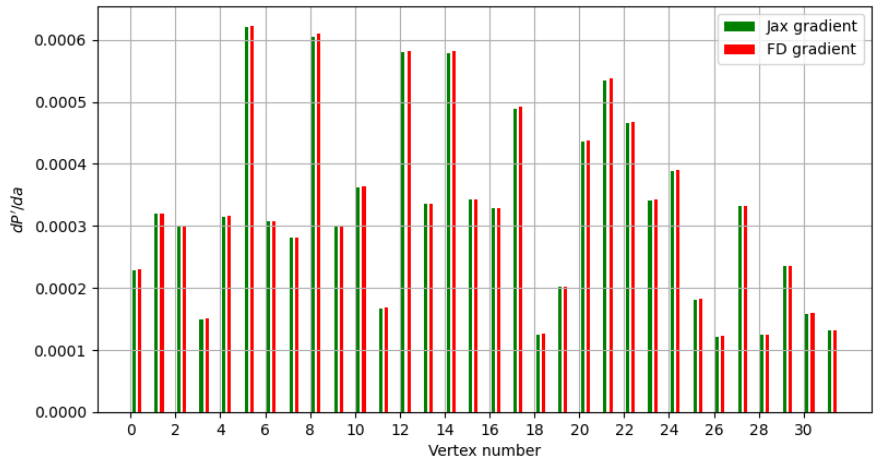

Fig. 10 Comparison of JAX AD and finite difference gradients of integrated SPL with respect to the speed of sound at mesh points

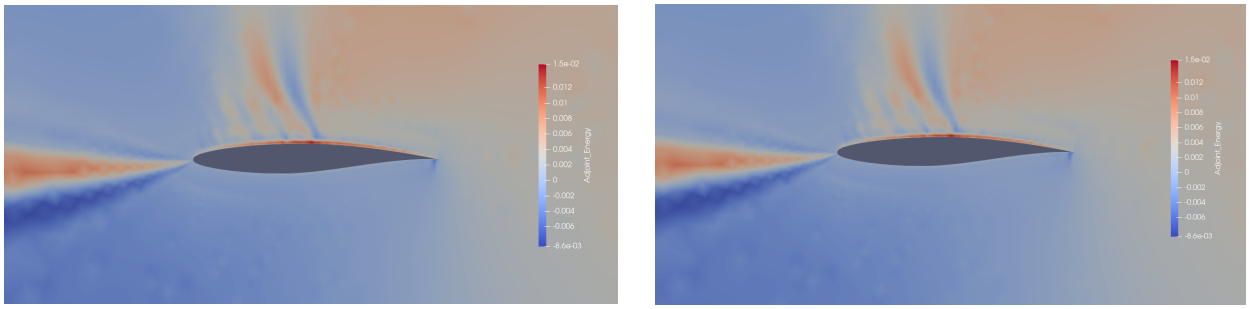

SU2 discrete adjoint **JAX accumulated adjoint**

Fig. 11 RAE2822 SST RANS test problem: adjoint energy distribution

is the NACA 0012 airfoil in inviscid transonic flow, with the drag coefficient as the objective function. The second is the RAE 2822 airfoil in turbulent transonic flow, with the integrated surface pressure as the objective function. In both cases the airfoil surface is parameterized by Hicks-Henne bump functions. We compute the shape optimization gradients for each test problem using our coupled Jax framework, and also using the SU2 DOT capability, as both test problems use a native SU2 objective function. Figure 11 shows the adjoint energy field obtained for the turbulent RAE 2822 problem using each of the two methods. The two fields show good agreement, as do the shape gradients obtained for each test problem using the two methods, shown in Figures 12 and 13.

Finally, we apply the coupled code to the SMC006 nozzle case, with the acoustic source and propagation Jax codes used to compute the objective function and accumulated gradients. The geometry is parameterized using a free form deformation (FFD) box positioned around the chevrons. The resulting normalized gradients with respect to FFD control point positions are shown in Table 1, together with the values obtained using finite differences; a reasonably good

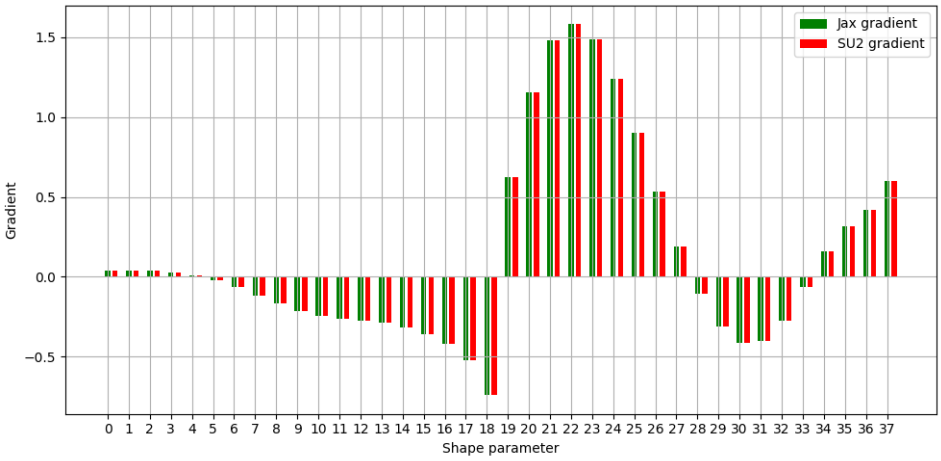

Fig. 12 Comparison of coupled Jax-SU2 and SU2 AD gradients for inviscid NACA0012 test problem.

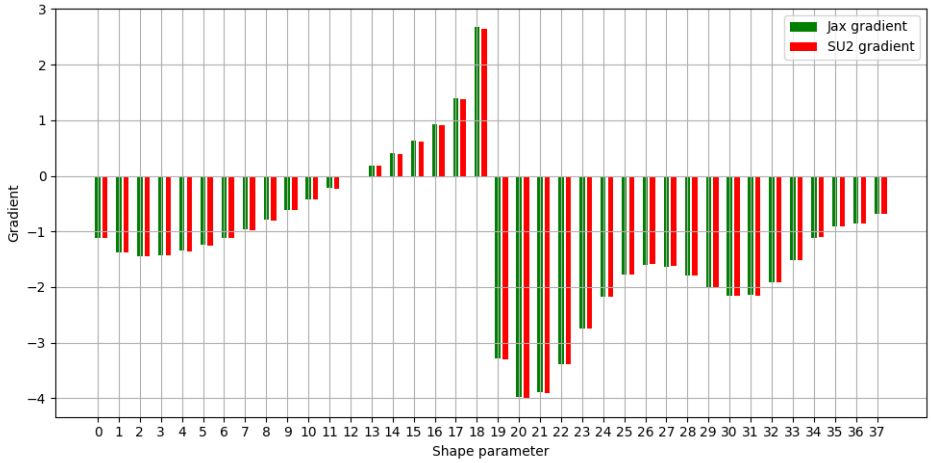

Fig. 13 Comparison of coupled Jax-SU2 and SU2 AD gradients for SST RANS RAE2822 test problem.

agreement is obtained.

Param	AD grad	FD grad	Param	AD grad	FD grad	Param	AD grad	FD grad
1	0.01573	0.01587	4	-0.17381	-0.17428	7	-0.14060	-0.14173
2	0.11644	0.11651	5	-0.17142	-0.17212	8	-0.11842	-0.11975
3	0.15966	0.15990	6	-0.15907	-0.15999	9	-0.09415	-0.09567

Table 1 Comparison of AD and finite difference gradients for SMC006 optimization problem.

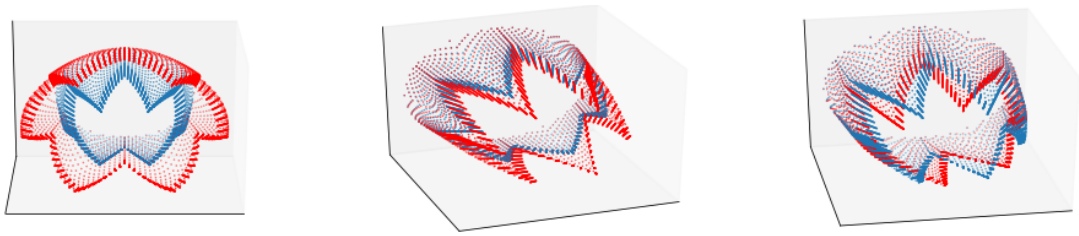

Expansion **Penetration** **Twist**

Fig. 14 Examples of parametric chevron deformations applied to the SMC006 nozzle.

3. Parametric deformation and outlook to further work

It has been widely discussed in the literature[9][13] that the geometric parameter with the greatest influence on the acoustic field is the chevron penetration. The degree of penetration may be measured by the difference in nozzle diameter from the base of the chevron to the tip. The influence of this design parameter may be explained by considering the shear layer. A higher degree of chevron penetration increases the axial vorticity generated; the resulting enhanced shear layer mixing shortens the effective jet plume length, reducing the extent of the region over which large scale flow structures (i.e. low frequency acoustic sources) are distributed. However, more aggressive turbulent mixing results in an increase in fine scale mixing noise, observed in the higher frequency range. The overall acoustic impact of chevrons is therefore observed as crossover, where the low frequency noise is attenuated and the higher frequencies amplified compared to a baseline geometry.

As we continue with this work, one aspect we will continue to explore is the effect of the choice of parameterization on the final optimized nozzle design. Integration of our geometrical acoustic method with the SU2 platform has allowed us to leverage existing tools for automated design optimization, such as mesh deformation routines and automated parameterization using FFD boxes. While this description of the geometry is highly expressive, it is difficult to correspond the resulting deformations to intuitive geometric transformations, or to maintain realistic constraints such as internal thickness or rotational symmetry. We have therefore extended the existing FFD deformations and gradient computation routines to include a limited parameter set more physically relevant to nozzle shape design, three examples of which are shown in Figure 14.

E. Summary

In this work, we have implemented a hybrid RANS-based acoustic prediction tool, consisting of an acoustic source model based on Ribner's formulation of Lighthill's acoustic analogy, coupled with a far field propagation model based on a geometrical acoustics method. We use an SST RANS simulation performed using the SU2 code as input to the prediction tool to compute the far field SPL at different polar observer angles. The resulting far field spectra compare favorably with experimental data, demonstrating that this type of hybrid prediction methodology provides a reliable and

computationally affordable alternative to acoustic prediction methods requiring expensive unsteady simulations such as LES or DNS. Our implementation of the source and propagation models as separate modules allows us to study their effects in isolation. Computation of the spatial distribution of the flow factor allows us to capture the effects of mean flow sound refraction. Furthermore, we have integrated our AD-enabled implementation of this acoustic prediction tool with the existing discrete adjoint framework in SU2. This overall coupled framework allows us to efficiently compute the gradient of acoustic objective functions with respect to design parameters chosen to describe the nozzle configuration. We have validated this coupled workflow, both in the context of SU2 native objective function test problems, and in the context of far field noise reduction of the SMC006 chevron nozzle widely used in aeroacoustic design and benchmarking studies.

In our intended further work, we will perform automated shape optimization of the SMC006 alongside other nozzle geometries. An aspect we are particularly interested in exploring is the effect of parameterization upon the final design - specifically, the differences achieved by using FFD vs an explicit parameterization (chevron twist, penetration depth, nozzle length etc.) or a constrained free form design, for example applying FFD to only a single sector of the chevron nozzle while enforcing the rotational symmetry of the nozzle design overall. We also intend to explore the effects upon the optimized geometry of optimizing with respect to multiple objectives - for example, minimizing noise at multiple observer angles and frequencies, or enforcing constraints such as constant thrust upon the nozzle flow.

References

[1] A.D. Pierce. *Acoustics – An Introduction to its physical principles and applications*. Acoustical Society of America, 1991.

[2] M. Azarpeyvand and R. H. Self. "Improved jet noise modeling using a new time-scale". In: *The Journal of the Acoustical Society of America* 126.3 (2009), pp. 1015–1025. DOI: 10.1121/1.3192221. eprint: https://doi.org/10.1121/1.3192221. URL: https://doi.org/10.1121/1.3192221.

[3] Thomas F. Balsa and Philip R. Gliebe. "Aerodynamics and Noise of Coaxial Jets". In: *AIAA Journal* 15.11 (1977), pp. 1550–1558. DOI: 10.2514/3.60822. eprint: https://doi.org/10.2514/3.60822. URL: https://doi.org/10.2514/3.60822.

[4] Stanley Birch et al. "A RANS based Jet Noise Prediction Procedure". In: *13th AIAA/CEAS Aeroacoustics Conference (28th AIAA Aeroacoustics Conference)*. DOI: 10.2514/6.2007-3727. eprint: https://arc.aiaa.org/doi/pdf/10.2514/6.2007-3727. URL: https://arc.aiaa.org/doi/abs/10.2514/6.2007-3727.

[5] D. Blokhintsev. "The propagation of sound in an inhomogeneous and moving medium". In: *Journal of the Acoustical Society of America* 18.2 (1946), pp. 322–328.

[6] James Bradbury et al. *JAX: composable transformations of Python+NumPy programs*. Version 0.2.5. 2018. URL: http://github.com/google/jax.

[7] J. Bridges and M. Wernet. *Establishing consensus turbulence statistics for hot subsonic jets*. AIAA-2010-3751. 2010.

[8] James Bridges and Clifford Brown. "Parametric Testing of Chevrons on Single Flow Hot Jets". In: *10th AIAA/CEAS Aeroacoustics Conference*. DOI: 10.2514/6.2004-2824. eprint: https://arc.aiaa.org/doi/pdf/10.2514/6.2004-2824. URL: https://arc.aiaa.org/doi/abs/10.2514/6.2004-2824.

[9] B. Callender, E. Gutmark, and S. Martens. "Far-Field Acoustic Investigation into Chevron Nozzle Mechanisms and Trends". In: *AIAA Journal* 43.1 (2005), pp. 87–95. DOI: 10.2514/1.6150. eprint: https://doi.org/10.2514/1.6150. URL: https://doi.org/10.2514/1.6150.

[10] Thomas D. Economon et al. "SU2: An Open-Source Suite for Multiphysics Simulation and Design". In: *AIAA Journal* 54.3 (2015), pp. 828–846. DOI: 10.2514/1.J053813. URL: http://dx.doi.org/10.2514/1.J053813.

[11] William Engblom, Abbas Khavaran, and James Bridges. "Numerical Prediction of Chevron Nozzle Noise Reduction Using Wind-MGBK Methodology". In: *10th AIAA/CEAS Aeroacoustics Conference*. DOI: 10.2514/6.2004-2979. eprint: https://arc.aiaa.org/doi/pdf/10.2514/6.2004-2979. URL: https://arc.aiaa.org/doi/abs/10.2514/6.2004-2979.

[12] Rafael C. Engel, Carlos R.I. Silva, and Cesar J. Deschamps. "Application of RANS-based method to predict acoustic noise of chevron nozzles". In: *Applied Acoustics* 79 (2014), pp. 153–163. ISSN: 0003-682X. DOI: https://doi.org/10.1016/j.apacoust.2013.12.019. URL: https://www.sciencedirect.com/science/article/pii/S0003682X13003009.

[13] Enrico Fabiano et al. "Towards Adjoint-based Sensitivity Analysis for Supersonic Jet Noise". In: *AIAA AVIATION 2020 FORUM* (2020). DOI: 10.2514/6.2020-3131. eprint: https://arc.aiaa.org/doi/pdf/10.2514/6.2020-3131. URL: https://arc.aiaa.org/doi/abs/10.2514/6.2020-3131.

[14] Carlos R. S. Ilário et al. "Prediction of jet mixing noise with Lighthill's Acoustic Analogy and geometrical acoustics". In: *The Journal of the Acoustical Society of America* 141.2 (2017), pp. 1203–1213. DOI: 10.1121/1.4976076. eprint: https://doi.org/10.1121/1.4976076. URL: https://doi.org/10.1121/1.4976076.

[15] Abbas Khavaran, Eugene A. Krejsa, and Chan M. Kim. "Computation of supersonic jet mixing noise for an axisymmetric CD nozzle using k-epsilon turbulence model". In: 1992.

[16] Michael James Lighthill and Maxwell Herman Alexander Newman. "On sound generated aerodynamically I. General theory". In: *Proceedings of the Royal Society of London. Series A. Mathematical and Physical Sciences* 211.1107 (1952), pp. 564–587. DOI: 10.1098/rspa.1952.0060. eprint: https://royalsocietypublishing.org/doi/pdf/10.1098/rspa.1952.0060. URL: https://royalsocietypublishing.org/doi/abs/10.1098/rspa.1952.0060.

[17] Philip J. Morris and F. Farassat. "Acoustic Analogy and Alternative Theories for Jet Noise Prediction". In: *AIAA Journal* 40.4 (2002), pp. 671–680. DOI: 10.2514/2.1699. eprint: https://doi.org/10.2514/2.1699. URL: https://doi.org/10.2514/2.1699.

[18] H. S. Ribner. "Quadrupole correlations governing the pattern of jet noise". In: *Journal of Fluid Mechanics* 38.1 (1969), pp. 1–24. DOI: 10.1017/S0022112069000012.

[19] Rod H. Self and Mahdi Azarpeyvand. "Jet noise prediction using different turbulent scales". In: *Acoustical Physics* 55.3 (May 2009), pp. 433–440. DOI: 10.1134/S106377100903021X.

[20] C. Tam and Laurent Auriault. “Jet Mixing Noise from Fine-Scale Turbulence”. In: 1998.

III. Performance Evaluation of a Graph Neural Network-Augmented Multi-Fidelity Workflow for Predicting Aerodynamic Coefficients on Delta Wings at Low Speed

Conceptual design of a stable and efficient supersonic transport (SST) aircraft during takeoff and landing, where higher angle-of-attack (AOA) induces complex aerodynamic phenomena such as vortex lift and flow separation, can be challenging. Existing analysis methods face a fidelity-cost trade-off: high-fidelity (HF) methods, such as computational fluid dynamics (CFD), offer prediction accuracy but are computationally expensive for solver-in-the-loop analyses, while low-fidelity (LF) methods, such as vortex lattice method (VLM), lack the ability to capture nonlinear flow physics. To address this gap, this paper proposes a multi-fidelity conceptual design analysis workflow that integrates a graph neural network (GNN)-based surrogate model into VLM to augment the analysis fidelity of LF tools. The surrogate model learns the discrepancies between LF and HF pressure fields, enabling accurate and efficient aerodynamic analyses on arbitrary quantities of interest. When evaluated on a dataset with various Delta wing geometries, the proposed workflow achieves an approximately fivefold reduction in the normalized root mean square error (NRMSE) for the predicted lift, drag, and pitching moment coefficients compared to using VLM alone. The results also highlight the proposed workflow's generalizability across new flow conditions and wing geometries, while identifying its limitations in prediction accuracy variance across the test dataset. Overall, the proposed workflow provides an efficient and effective framework for aerodynamic assessment in conceptual design with improved fidelity.

Nomenclature

α	=	angle of attack [degree]
C_D	=	drag coefficient
$C_{D,i}$	=	induced drag coefficient
C_L	=	lift coefficient
$C_{L,\max}$	=	maximum lift coefficient
C_M	=	pitching moment coefficient
C_p	=	pressure coefficient
ΔC_p	=	local loading coefficient
ΔC_p^{HF}	=	high-fidelity (HF) ΔC_p
ΔC_p^{LF}	=	low-fidelity (LF) ΔC_p

ΔC_p^{pred}	=	surrogate model predicted ΔC_p
$\partial C_M / \partial \alpha$	=	pitch stiffness
Γ	=	vortex strength [m^2/s]
Ma	=	free-stream Mach number
Re	=	Reynolds number
$\bar{v} = [u, v, w]^T$	=	velocity vector [m/s]
$\bar{V}_\infty = [U_\infty, V_\infty, W_\infty]^T$	=	free-stream velocity vector [m/s]
x, y, z	=	Cartesian coordinate
y^+	=	dimensionless grid-to-wall spacing

A. Introduction

The development of supersonic transport (SST) aircraft dates back to the 1960s, with the groundbreaking Concorde first taking flight in 1969. During its operation, shortcomings in operational costs, range, and noise lead to its decommissioning [25]. Since then, significant efforts on SST configuration research focus on sonic boom mitigation, optimization techniques, and testing [25, 31, 29], yet few publicly available examples exist of the low-speed characteristics of potential configuration features of the next-generation SST [29]. To answer this call, the National Aeronautics and Space Administration (NASA)-funded Supersonic Configurations at Low Speeds (SCALOS) project establishes a joint effort among the University of Washington, the University of Michigan, Stanford University, and Boeing Research and Technology to provide insights regarding the performance, handling qualities, noise impact, and stability and control (S&C) low-speed behavior associated with aircraft takeoff and landing of emerging SST configurations [29].

Over recent years, significant understanding has been gained for SCALOS configurations. Researchers have conducted parametric design space surveys to identify configurations that meet efficiency and controllability requirements, and developed wind tunnel model design and testing techniques [30, 41, 43, 17, 28]. Other advances include the quantification of static and dynamic stability characteristics [42, 21, 20]. Efforts in control design focus on early-stage vehicle and control co-design and disturbance rejection [5, 10, 3, 1]. Additionally, studies have focused on the validation of computational fluid dynamics (CFD) tools for high-fidelity simulation, data correction, stability assessment, and jet noise analysis [22, 33, 20, 35]. Finally, significant development has been made for multidisciplinary design optimization (MDO) framework for aeroelastic effects on flight dynamics, dynamic stability derivatives, and handling quality [11, 9], as well as for vehicle design [33, 12].

Among these advances, a core focus of the SCALOS project is vehicle design under stability constraints at both the platform level and the controller level. The stability constraints are crucial because the SCALOS project focuses on SST vehicles during takeoff and landing phases, where the vehicle operates at high angle-of-attacks (AOAs). At such

conditions, nonlinear aerodynamics including vortex breakdown, vortex lift, and separations may exacerbate instability [8], and the vehicle is also subject to gust disturbances [3]. Additionally, co-design of SST optimized for high-speed cruise and low-speed stability is challenging as these objectives are often conflicting [33]. Imposing stability constraints early in the design process thus helps mitigate the need and risk for retrofits and redesign in later stages, and ensures a sufficient control authority in controller design [33, 1].

To incorporate stability constraints in a MDO environment, moment derivatives need to be quantified. Data sources with different fidelities exist. At the highest fidelity, the moment derivatives can be obtained from flight tests. However, in conceptual design, this level of fidelity is often unattainable due to safety concerns and high costs. At a lower fidelity, these coefficients can be obtained from experiments, either wind tunnel or water tunnel [20, 21, 40]. However, in the early conceptual design phase, these types of studies are often considered too "expensive", as designers are required to survey a vast design space under limited time. To accelerate the assessment, designers rely on even lower fidelity tools during the conceptual design phase for faster evaluations.

These tools are mainly computational methods at various fidelities. On the higher end, methods such as Detached-eddy Simulation (DES) have demonstrated the ability to accurately model the vortical flow field and predict the location of vortex breakdown [24], thereby leading to more accurate moment derivatives estimation. However, such methods are often considered too expensive to carry out in conceptual design. On the lower end, potential flow solvers such as vortex lattice method (VLM) are used. These methods provide fast aerodynamic quantification, but cannot model nonlinear flow physics, leading to inaccurate assessments in flight phases that feature vortex lift, vortex breakdown, and separations [14]. In the past, theoretical and semi-empirical models, such as the Polhamus suction analogy, have been used to add vortex lift corrections to the VLM solutions [32, 15, 12]; however, these corrections are usually domain-specific, such that proper correction for one configuration at one flight condition may not be applicable to another. For SCALOS-like configurations aerodynamics prediction across a wide range of AOAs, the authors observed that relying only on Polhamus correction [32] is inadequate to capture the moment derivatives trends. Finally, Reynolds-averaged Navier-Stokes (RANS)-based CFD methods are widely used in moment derivatives estimation. The fidelity and computational cost of RANS lies between DES and VLM, and Seraj and Martins showed the accuracy of RANS-based pitching moment coefficient (C_M) evaluation for SCALOS-like configuration up to an AOA of 15° [33]. However, having a RANS solver in the aerodynamic shape optimization loop, especially in the conceptual design phase where the design space is large and the base geometry is subject to large shape morphing, is still often considered too expensive to carry out.

The aforementioned fidelity-cost trade-off exits ubiquitously in every aerodynamic shape optimization problem. To reduce the evaluation cost in an optimization loop, surrogate modeling techniques are often used. A surrogate model approximates the behavior of high-fidelity (HF) data using a simplified mathematical model, thereby allowing faster evaluations. Some common surrogate models utilized in conceptual aircraft design include polynomial chaos expansions

[12], hierarchical kriging [27], and machine learning models [44]. These methods demonstrate accurate prediction capability and integrate well with the current MDO evaluation cycles. Despite the wide application and utility, most of these methods are limited to predicting a fixed subset of scalar-valued Quantities of interests (QOIs). Two major issues arise from this limitation: firstly, the set of QOIs needs to be defined *a priori*. If new QOIs need to be assessed during the design optimization cycle, new surrogate models often need to be trained as the knowledge transfer among surrogate models is challenging. Secondly, designers rely not only on QOIs from HF data to gain engineering insights into the design problem, but also on flow field data, which provides rich information about the strengths and weaknesses of a design point. Thus, a surrogate model that exhibits field data prediction capability is preferable. For the SCALOS stability-constrained aerodynamic design optimization case, a preferable surrogate model thus should have a cheap online evaluation cost, show acceptable prediction accuracy in force and moment coefficients, and integrate well with the current MDO frameworks.

Recently, there has been a surge of surrogate modeling techniques that satisfy the above-mentioned criteria. One popular methodology is proper orthogonal decomposition (POD)-kriging, where a Gaussian Process Regression model is built for reduced-order modal coefficients [26]. Another popular approach is to use deep neural network (DNN) to predict high-fidelity (HF) field data from a given low-fidelity (LF) input [37]. Among DNN methods, graph neural network (GNN)-based surrogate modeling techniques have shown promising performance in reconstructing HF CFD flow fields [16, 4, 7]. Encouraged by these studies, the authors developed a GNN-based surrogate model (`VortexNet`) that augments VLM local loading coefficients (ΔC_p) using RANS CFD pressure fields tailored for conceptual design [36]. This model integrates geometric and aerodynamic features, offering a generalizable and data-driven solution for enhancing LF assessment in conceptual design MDO frameworks. While the model demonstrates strong capability in capturing nonlinear flow features such as vortex lift and flow separation, the predictive quality of force and moment coefficients integrated from the predicted local loading coefficients ΔC_p^{pred} by this surrogate model has not been thoroughly evaluated. This study, therefore, discusses approaches to integrate the `VortexNet` surrogate model into an MDO framework and quantitatively assesses the quality of aerodynamic coefficients integrated from the surrogate model's field predictions.

B. Methodology

The proposed multi-fidelity workflow utilizes two flow solvers: the low-fidelity vortex lattice method (VLM) solver shipped with `SUAVE` [18], a conceptual-level aircraft design environment, and the high-fidelity computational fluid dynamics (CFD) Reynolds-averaged Navier-Stokes (RANS) solver available in `SU2` [6], a CFD suite for the solution of partial differential equations (PDE) and PDE-constrained optimization problems. To establish a foundation for the subsequent discussions, we present a brief summary of the governing equations solved by each method. The VLM theory is covered in Section III.B.1, while the CFD theory is detailed in Section IV.B.2. In Section IV.B.4, we provide a

short discussion on the graph neural network (GNN)-based multi-fidelity surrogate model (`VortexNet`). For more technical details of the `VortexNet` surrogate model, readers are referred to Shen, Needels, and Alonso [36]. Finally, these tools are integrated into a multi-fidelity workflow, as discussed in Section III.B.4.

1. Low-fidelity Method: Vortex Lattice Method (VLM)

`SUAVE`'s VLM features a Python-based implementation of the `VORLAX` code [23]. It models "compressibility-corrected," inviscid, attached flows for both subsonic and supersonic conditions by using a panel method that represents the base geometry with infinitesimally thin, cambered or uncambered panels. Each panel consists of a horseshoe vortex with trailing vortices extending to infinity and a bound vortex at the quarter-chord location. The control point $[x_c, y_c, z_c]$ is located at the three-quarter-chord point of each panel. The `VORLAX` implementation of VLM differs from typical textbook VLM [2] as multiple application-specific correction terms are introduced. To assist the discussion in later sections, we include a short summary of VLM. One should refer to Miranda, Elliott, and Baker's original manuscript for the exact algorithm used in `VORLAX` [23].

According to the Biot-Savart Law, the induced velocity from a vortex filament can be described as:

$$\mathbf{v} = \frac{\Gamma_n}{4\pi} \int_c \frac{d\mathbf{l} \times \mathbf{r}}{r^3}, \tag{33}$$

where Γ_n is the vortex filament strength, $d\mathbf{l}$ is an infinitesimal segment of the vortex filament, $\mathbf{r}$ is a vector pointing from the vortex filament to a point in space, and c is the length of the vortex filament. For a horseshoe vortex with known endpoints A and B in space, the induced velocity vector $\mathbf{v}$ at any point C in space can be expressed as:

$$\mathbf{v}_{AB} = \frac{\Gamma_n}{4\pi} \left(\frac{\mathbf{r}_0}{|\mathbf{r}_1 \times \mathbf{r}_2|} \left(\frac{\mathbf{r}_0 \mathbf{r}_1}{|\mathbf{r}_0 \mathbf{r}_1|} - \frac{\mathbf{r}_0 \mathbf{r}_2}{|\mathbf{r}_0 \mathbf{r}_2|} \right) \right), \tag{34}$$

where $\mathbf{r}_0$ is the vector from point A to B, $\mathbf{r}_1$ is the vector from point A to C, and $\mathbf{r}_2$ is the vector from point B to C. In Equation 34, all vectors can be computed if the control point and vortex filament locations are known, thereby establishing a function between Γ_n and $\mathbf{v}$. In a system with multiple vortex filaments, the resultant induced velocity at any point in space is the linear superposition of all vortex filament contributions. For a system with N horseshoe vortices (panels), at the control point m, the induced velocity is then

$$\mathbf{v}_m = \sum_{n=1}^{N} C_{m,n} \Gamma_n, \tag{35}$$

where $C_{m,n}$ is the influence matrix computed from Equation 34.

Applying the tangency boundary condition $\mathbf{n} \cdot \mathbf{v} = 0$ on both the body surface and the wake uniquely defines the system. These boundary conditions, together with the spatial correlations, can be conveniently summarized into a

right-hand side vector (RHS), resulting in the final linear system for $\mathbf{\Gamma}$, the vector all vortex strengths at all filaments as:

$$AIC\,\mathbf{\Gamma} = RHS, \tag{36}$$

where AIC is the aerodynamic influence coefficient matrix representing the induced velocity contributions from each vortex filaments to each panel's control points, and RHS represents the free-stream flow contributions to the boundary conditions. The linear system can thus be solved for individual lattice vortex strengths.

Once the vortex filament strengths are solved, the pressure coefficient distribution is computed by

$$C_p = -\frac{2}{q_\infty^2}(U_\infty u + V_\infty v), \tag{37}$$

where U_∞ and V_∞ are the components of the free-stream velocity vector of magnitude q_∞, and u and v are the induced velocity components. C_p is the field pressure coefficient ($C_p = (P - P_\infty)/q_\infty$). In our study, an infinitesimally thin panel is used, such that the local loading coefficients between the lower and upper wing surfaces, ΔC_p, is the C_p computed from the previous equation.

Finally, the aerodynamic coefficients are computed by summing the resultant panel-normal forces obtained from the local loading coefficients ΔC_p applied on each panel. The panel-normal forces are then decomposed into components that are normal to the free-stream direction (lift) and parallel to the free-stream direction (drag), subject to sideslip angle and leading-edge suction [32] corrections. It is worth noting that the drag coefficient C_D computed is the induced drag coefficient $C_{D,i}$. However, as the following sections compare C_D generated from various-fidelity sources, we will not differentiate between C_D and $C_{D,i}$ in this study.

In this study, lattice panels are created in `SUAVE` on an infinitesimally thin mean camber plane of a wing using a 30×30 discretization on both span-wise and chord-wise directions. The result ΔC_p computed by VLM, due to its low-fidelity nature, is denoted by ΔC_p^{LF}.

2. High-fidelity Method: Computational Fluid Dynamics (CFD)

`SU2` solves the Navier-Stokes equations expressed in differential form as

$$\mathcal{R}(U) = \frac{\partial U}{\partial t} + \nabla \cdot \bar{F}^c(U) - \nabla \cdot \bar{F}^v(U, \nabla U) = 0, \tag{38}$$

where the conservative variables are

$$U = [\rho, \rho\bar{v}, \rho E]^T. \tag{39}$$

The convective and viscous fluxes are given by

$$\bar{F}^c = \begin{bmatrix} \rho\bar{v} \\ \rho\bar{v} \otimes \bar{v} + \bar{\bar{I}}p \\ \rho E\bar{v} + p\bar{v} \end{bmatrix} \tag{40}$$

and

$$\bar{F}^v = \begin{bmatrix} . \\ \bar{\bar{\tau}} \\ \bar{\bar{\tau}} \cdot \bar{v} + \kappa\nabla T \end{bmatrix} \tag{41}$$

respectively, where ρ is the fluid density, $\bar{v} = [u, v, w]^T \in \mathbb{R}^3$ is the flow speed in Cartesian coordinate, E is the total energy per unit mass, p is the static pressure, $\bar{\bar{\tau}}$ is the viscous stress tensor, T is the temperature, κ is the thermal conductivity, and μ is the viscosity. The static pressure p is solved by using ideal gas equation of state such that for a perfect gas with gas constant R and specific heat ratio γ, the pressure is:

$$p = (\gamma - 1)\rho \left(E - 0.5(\bar{v} \cdot \bar{v})\right). \tag{42}$$

The viscous stress tensor can be expressed in vector notation as

$$\bar{\bar{\tau}} = \mu\left(\nabla\bar{v} + \nabla\bar{v}^T\right) - \mu\frac{2}{3}\bar{\bar{I}}\left(\nabla \cdot \bar{v}\right), \tag{43}$$

where laminar viscosity, μ, is calculated using Sutherland's law and thermal conductivity is computed as $\kappa = \mu c_p/Pr$, where c_p is the specific heat capacity at constant pressure and Pr is the Prandtl number.

We utilize the RANS solver within `SU2` to simulate steady, turbulent flow conditions. Following the Boussinesq hypothesis, the effective viscosity is calculated by summing the laminar (dynamic) viscosity μ_d and the turbulent viscosity μ_t, which requires modeling. To model the turbulent viscosity, we use the one-equation Spalart-Allmaras (SA) turbulence model with rotation and curvature corrections [39, 38]. Prior research by Seraj and Martins has demonstrated that the SA turbulence model is sufficient for predicting vortex effects in steady regimes while keeping computational costs manageable [34]. All simulations are conducted using the Jameson-Schmidt-Turkel scheme for convective discretization, coupled with implicit time integration utilizing an adaptive Courant–Friedrichs–Lewy number to enhance numerical stability and convergence. A Cauchy convergence criterion for C_D is applied, where the solution is converged if the change in C_D for the wing over the previous 100 iterations is less than 1×10^{-4}.

For each geometry analyzed, a fluid domain extending approximately 46 root chord lengths upstream and downstream of the wing is used. The computational mesh is generated using `Pointwise`, with a maximum deviation between the surface mesh and the actual geometry of less than 1×10^{-5} [m]. To maintain consistency in global mesh properties and boundary conditions across all geometries, a `Pointwise` script is employed to create meshes with identical mesh property definitions. The resulting mesh achieves a $y^+ < 1$ for most areas of the wing, except regions near the wing tips at the trailing edge, thereby satisfying the resolution requirements of the turbulence model for accurate boundary layer modeling. The wing surface boundary condition is a no-slip adiabatic wall boundary condition, and the free-stream boundaries use a characteristic-based far-field boundary condition.

Once the CFD is converged, the wing surface pressure coefficient C_p is used as the HF training labels for the surrogate model. However, it is worth notice that these CFD surface pressure coefficient fields have a much finer surface discretization than the lattice panels used in VLM. To assist a more efficient surrogate model training and to reduce the graph neural network (GNN) graph size, the HF pressure fields are standardized using projection. Under this standardization, the CFD surface pressure coefficients are projected onto the lattice panels defined in the Low-fidelity Method: Vortex Lattice Method (VLM) section using the same definition as how VLM computes the local loading coefficient ΔC_p, which generates the training label ΔC_p^{HF} for the surrogate model. This process is described by the following equations:

$$\Delta C_p^{HF} = C_{p,\text{lower}}^{HF} - C_{p,\text{upper}}^{HF}, \tag{44}$$

where C_p^{HF} is a vector in $\mathbb{R}^{30x30}$, which is the dimension of the number of panels used in VLM. The pressure coefficient for each side can be calculated by:

$$C_{p,\text{side}}^{HF} = \frac{1}{q_\text{ref}} \left[\frac{\sum_{i \in \mathcal{I}} \delta_\text{side}(i) P_i A_i}{\sum_{i \in \mathcal{I}} \delta_\text{side}(i) A_i} \right]_{\mathcal{I}=1}^{N}, \tag{45}$$

where i index a specific HF surface mesh cell, P_i is the local pressure, A_i is the cell area, $\mathcal{I}$ is the set of all surface nodes whose (x_i, y_i) coordinates lie within the boundary of a LF lattice panel, indexed from 1 to N, under vertical projection, and q_ref is the reference pressure computed from free-stream conditions. $\delta_\text{side}(i)$ is a surface sides selection mask such that, for example, for the lower surface:

$$\delta_\text{lower}(i) = \begin{cases} 1 & \text{if } z_i < 0, \\ 0 & \text{otherwise.} \end{cases} \tag{46}$$

3. Surrogate Modeling

To enable multi-fidelity aerodynamic analyses that bridge the fidelity gap between VLM and CFD and address the fidelity-cost trade-off, we use a surrogate model to augment the LF analyses. The surrogate model used in the current study is a graph neural network (GNN)-based field data prediction tool designed specifically for conceptual design data structures. Specifically, the surrogate model takes a graph representation of an aircraft geometry from VLM lattice panel grids and augments the LF ΔC_p^{LF} to a surrogate predicted quasi-HF field prediction ΔC_p^{pred} using the learned mapping between the differences between LF ΔC_p^{LF} and HF ΔC_p^{HF} [36]. Previous study shows that such a surrogate model demonstrates strong prediction capability in capturing nonlinear flow features, such as vortex lift and flow separation. The computation cost of ΔC_p^{pred} prediction is comparable to that of VLM. Additionally, it has moderate generalization capability for unseen geometries and flow conditions. This makes it a strong candidate for multi-fidelity surrogate-based aerodynamic analysis of SCALOS-like configurations.

The inputs to this surrogate model are the aircraft geometry and flow conditions. For the aircraft geometry, the lattice panels used in VLM analyses are transformed into a graph. Each node in the graph corresponds to the physical location of the control point of a panel and edges are defined based on a neighborhood 4-node connectivity pattern.

In a graph context, a graph has node and edge features and both nodes and edges are assigned with a feature vector. The Euclidean distances between one node to its neighboring nodes are included in the edge features vector. The node features vector has two components: geometry conditions and flow conditions. For geometry conditions, physical x_c and y_c coordinates [m] of the panel control points, local wing thickness [m], local upper and lower surface curvatures [m^{-1}] and local slopes are included in node feature vector. All the "local" features are evaluated at the control points; for example, the local wing thickness is the vertical distance between the upper and lower wing surfaces at each control point. For flow conditions, the angle-of-attack (AOA) [rad], Mach number (Ma), Reynolds number (Re), and the panel's corresponding LF local loading coefficient ΔC_p^{LF} are added to node feature vectors. The output of the surrogate model is the predicted local loading coefficient ΔC_p^{pred} at each panel.

To assess the impact of integrating this surrogate model into a multi-fidelity workflow for conceptual design, we study the aerodynamic Quantities of interests (QOIs) prediction accuracy obtained using this surrogate model. Because the surrogate model is still under development, directly studying a full aircraft configuration, such as one of the SCALOS configurations, may introduce additional complexities and errors due to the geometry's complexity. Therefore, to simplify the problem while maintaining relevance, we focus on isolated Delta wings, as many of the SCALOS configurations feature highly swept wing platforms. Thus, the dataset used to train the surrogate model features a family of Delta wing geometries.

We use two major design parameters to parameterize the geometry: root airfoil shape (NACA 4-digit series) and leading-edge sweep angle. In the surrogate model training, we build 15 Delta wings using root airfoils from NACA 0010, NACA 0016, NACA 0024, NACA 2416, and NACA 4416, and leading-edge sweep angles of 55°, 65°, and 75°.

Across all geometries, the root chord length is kept constant at 0.65 meters, and the span is allowed to vary to match the leading-edge sweep angle. These geometries are then evaluated using both LF and HF simulations under 40 different free-stream conditions using Latin Hypercube Sampling (LHS). The bounds for free-stream conditions are: AOA from 0° to 20°, Ma from 0.35 to 0.5, and Re from 6.5×10^6 to 1×10^7. In total, 600 LF and HF samples are simulated to train the surrogate model. These samples are then randomly partitioned into model training set and test set in a 70% to 30% ratio. During the model training, the surrogate model is only exposed to the training set, and the test set is used to evaluate the model's performance.

4. Multi-Fidelity Workflow

The aforementioned analyses are integrated to augment the fidelity of aerodynamic coefficients estimation in a coherent multi-fidelity workflow, as illustrated in Figure 15. In this chart, intermediate stages of data are presented in rounded boxes. Two types of data exist: data obtained in the online phase for MDO, that is, data obtained within the `SUAVE` environment, is colored in light gold, and data obtained in the offline phase, that is, the data generated for surrogate model training, is colored in light blue. Arrows connecting blocks represent the workflow steps, and annotations beside the arrows indicate the relevant tools that are used for each step.

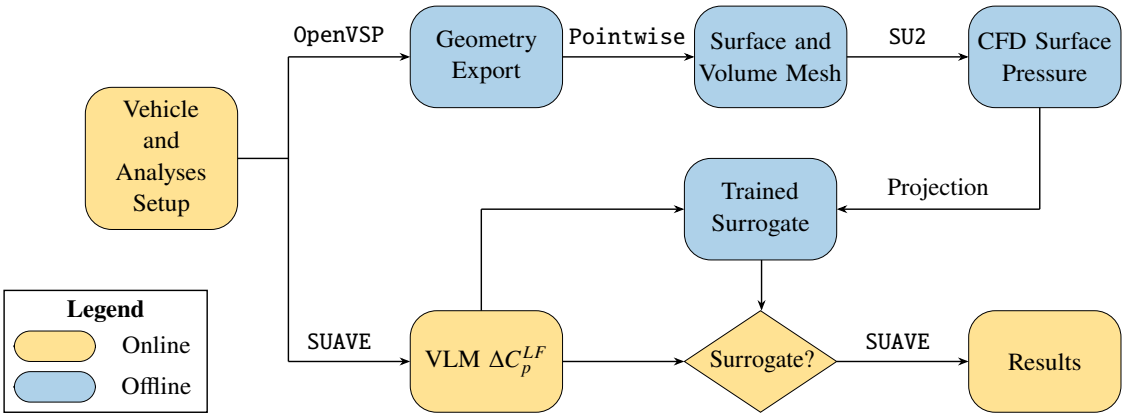

Fig. 15 Block diagram of the augmented aerodynamic coefficients estimation workflow integrated into the `SUAVE` environment. Each block represents an intermediate stage in the design workflow, with "online" stages colored gold and "offline" stages colored blue.

The workflow starts with defining vehicle geometry and analyses. `SUAVE` features a data structure for vehicle definition that is particularly suitable for both conventional and unconventional conceptual vehicle design, thus allowing most aircraft configurations to be parametrically defined [19]. In the current study, the authors find that most of the previous SCALOS configurations [43] can be constructed within `SUAVE` using existing geometry classes. Once the vehicle is defined, the corresponding analyses need to be defined. In `SUAVE`, various analysis fidelities exist, and in the current study we rely on the `Vortex_Lattice` aerodynamics analysis module. Analysis parameters, such as lattice

panel shape parameters including the number of panels in chordwise and spanwise directions, spacing parameters, and the Polhamus suction analogy flag, need to be defined. In the current study, we use 30 panels in both the chordwise and spanwise directions. The spanwise panel spacing uses a cosine spacing, while the chordwise panel spacing uses even spacing. The Polhamus suction analogy is active for leading-edge panels.

Once the vehicle geometry and analyses setup are completed, the workflow diverges into two branches. In the online phase, a VLM analysis is carried out to obtain ΔC_p^{LF} and lattice panel geometry using algorithms defined in Section III.B.1. Beyond standard `SUAVE` VLM output fields, the AIC matrix and RHS vectors in Equation 49 are also recorded for surrogate model training [36]. In the offline phase, the `SUAVE` vehicle is exported to an `OpenVSP` vehicle using `SUAVE`'s `OpenVSP` application programming interface (API) for geometry export. Creating an `OpenVSP` geometry allows a user to create surface and volume meshes in a meshing software of one's choice. In the current study, we selected `Pointwise` to create CFD surface and volume meshes. `Pointwise` is selected due to the authors' familiarity with the software and its capability in scripting and generating high-quality RANS meshes using its `T-Rex` anisotropic boundary layer mesh capability. For all geometries in this study, a `Pointwise` script is used to control the mesh properties, including average nodal spacing, growth rate, and `T-Rex` growth parameters, to maintain a relatively consistent mesh quality.

Following the creation of the volume mesh, the `Pointwise` volume mesh is exported in `SU2` format for CFD computation. Details of the `SU2` CFD configuration can be found in the High-Fidelity Solver: Computational Fluid Dynamics section (Section IV.B.2. Once the CFD computation converges, a surface projection as described in Section IV.B.2 is used to project the surface pressure C_p onto the lattice panels to obtain the HF local loading coefficient ΔC_p^{HF}. This ΔC_p^{HF} serves as the reference HF data for training the surrogate model.

It is worth noting that alternative projection methods can be used without altering the overall workflow. The offline phase concludes with surrogate model training, where a dataset generated from various geometries and flow conditions, as described in Surrogate Modeling, is provided as input. Once training is complete, the surrogate model is ready to be used in online assessment.

In online assessment, for example, when one needs to evaluate the aerodynamics of new geometries or at new flow conditions, the vehicle definitions and analyses setup follow the same process as previously discussed in this section. However, in the `Vortex_Lattice` setting, one can choose whether a surrogate model should be used to augment the VLM ΔC_p^{LF}, as marked by a diamond-shaped decision point in the block diagram in Figure 15. If a surrogate model is used, it takes in ΔC_p^{LF} and generates ΔC_p^{pred} to replace the original ΔC_p^{LF}. Such replacement does not affect the existing functionalities in `SUAVE`'s `Vortex_Lattice`, and thus all aerodynamic coefficients that are already defined in `SUAVE` can be evaluated. This also means that the existing design optimization methods defined in `SUAVE` can be used when a first-order optimizer is used.

C. Results

The main objective of this study is to evaluate the performance of aerodynamic coefficients, our quantities of interest (QOIs), integrated from ΔC_p^{pred} field data predicted by the surrogate model `VortexNet`. Specifically, we aim to assess the accuracy of these QOIs obtained from the surrogate model and discuss relevant trends with respect to free-stream conditions and geometry variations, thereby establishing preliminary error bounds for the workflow.

In multi-fidelity workflows, it is common to take data from the highest level of fidelity as a reference. In our proposed workflow, we consider CFD-predicted surface pressure coefficients and aerodynamic coefficients as the "ground-truth" reference. When a surrogate model is used to replace the CFD evaluation, an accurate surrogate should thus produce QOIs similar to those from CFD. We define errors as the differences between QOIs computed with and without using the surrogate model. In the current study, two sources of errors exist. The first is an epistemic discretization error introduced during the surrogate model training database preparation. Instead of using CFD surface pressures (C_p), the surrogate model is trained on projected CFD surface pressures ΔC_p^{HF}. This projection process introduces discretization errors that cannot be reduced during model training and will lead to differences in computed QOIs, even if the surrogate perfectly reconstructs ΔC_p^{HF}. This projection error can be reduced by using a finer lattice panel spacing or by optimally defining the projection methods. The second error is the surrogate model's modeling error due to its imprecise representation of ΔC_p^{HF}. This error can be reduced through model training and hyper-parameter optimization. In this study, the surrogate model's modeling error is minimized by using optimal surrogate model hyper-parameters, while we have not extensively explored error reduction techniques for the epistemic discretization error.

We assess the workflow's performance from three distinct perspectives. First, to evaluate the minimal QOIs prediction error, we analyze the relative errors in C_L, C_D, and C_M between QOIs integrated from the surrogate model predictions ΔC_p^{pred} and those integrated from projected CFD surface pressures ΔC_p^{HF}. This test is conducted on the test set discussed in Surrogate Modeling, where `VortexNet` is expected to perform optimally, thereby establishing the best-case performance characteristics. The relevant results are presented in Evaluation of Workflow Performance on Training Data. Second, we study the QOIs performance of the workflow on geometries seen during training but at unseen free-stream conditions. We compare the QOIs accuracy obtained from VLM, the `VortexNet` surrogate model, and projected CFD against the CFD ground truth. These results are presented in Generalization to Unseen Free-stream Conditions on Known Geometries. Third, we examine the QOIs prediction characteristics of the proposed workflow on geometries not seen during surrogate model training, to demonstrate its performance in interpolating within the design space. This generalization assessment is presented in Generalization to Unseen Free-stream Conditions and Geometries. The following sections discuss these three assessments.

1. Evaluation of Workflow Performance on Training Data

Our first effort to quantify the proposed workflow's QOIs prediction accuracy compares QOIs integrated from the surrogate model predictions ΔC_p^{pred} with those integrated from the projected CFD surface pressures ΔC_p^{HF}. The difference thus quantifies the modeling error introduced by the surrogate model. We then compare the QOIs predictions with those obtained using only the VLM solver without surrogate model augmentation, to showcase the improvement in QOIs fidelity, especially for wings at higher AOAs.

The dataset used for this test is the test set described in Surrogate Modeling. It is worth noting that, although the selection of the best neural network parameters is based on the test set loss, the surrogate model was not exposed to these samples during network training. Thus, the corresponding QOIs presented here are well-suited for surrogate modeling error quantification. A total of 15 Delta wing geometries are tested under various AOAs in $[0, 20]^\circ$, Ma in $[0.35, 0.5]$, and Re in $[6.5, 10] \times 10^6$. In total, the test dataset contains 180 samples.

For the benefit of future discussion, it is necessary to define two error indices. The first error index is the normalized root mean square error (NRMSE), which will be introduced latter. The second error index is the relative error, which describes the percentage difference between the surrogate model inferred QOI and the reference QOI. As the surrogate model predicts ΔC_p^{pred}, the local loading coefficient, an integration across panels needs to be carried out. The resultant relative error between ΔC_p^{pred} and ΔC_p^{HF} is thus defined as:

$$\text{Relative Error} = \frac{\int_S \Delta C_p^{\text{pred}} dS}{\int_S \Delta C_p^{HF} dS} - 1, \tag{47}$$

where $\int_S$ represents a surface integration over the lattice panels' surface S.

The relative errors for C_L, C_D, and C_M are presented in Figure 16 from top to bottom, and plotted against AOA, Ma, Re from left to right. The maximum relative error for C_L is 96.3%, with an average error of 8.62%. The maximum relative error for C_D is 96.3%, with an average error of 8.93%. The maximum relative error for C_M is 99.3%, with an average error of 7.94%. These maxima correspond to a free-stream condition at AOA of 0.07°, Ma of 0.45 and Re of 7.72×10^6. The relative error is large because the flow is at low AOA, resulting in small reference QOIs values.

Based on the relative errors across flow conditions, it is observed that the surrogate model's performance is not correlated with Ma and Re, as minimal correlations can be identified across the Ma and Re ranges. The prediction errors for all QOIs are mainly correlated with AOA; at small AOA the prediction errors are large due to small reference values. Towards higher AOA, we observe that the model prediction error decreases. This variation is most likely due to the increase in reference values. By visually examining the scatter of relative errors across AOAs, especially for C_L, it seems that the variance increases with increasing AOA. This might be due to an increase of the complexity of flow physics at higher AOA; as the database encompasses 15 wing geometries at various free-stream conditions, different

flow patterns may arise at certain higher AOA. However, a statistical test indicates no significant correlation between AOA and the spread of the scatter in C_L. Overall, when neglecting the outliers at small AOAs, the relative error is bounded by $[-17.83\%, 13.74\%]$ for C_L, $[-26.22\%, 13.74\%]$ for C_D, and $[-19.95\%, 10.22\%]$ for C_M.

To further compare the errors obtained from this surrogate model augmented workflow against the traditional workflow of using only VLM, we compare the QOIs computed using these two methods. As the relative error describes the error for individual samples, using it for this comparison across all free-stream conditions will result in a cumbersome error representation. Instead, we rely on the normalized root mean square error (NRMSE) to describe the error, defined as:

$$\text{NRMSE}(f^{\text{method}}) = \frac{1}{\overline{f^{\text{HF}}}} \sqrt{\frac{1}{N} \sum_{i=1}^{N} (f_i^{\text{method}} - f_i^{\text{HF}})^2}, \tag{48}$$

where f_i^{method} is a QOI evaluated by a specific method, f_i^{HF} is the reference HF QOI and under the current test is computed from ΔC_p^{HF}, $\overline{f^{\text{HF}}}$ is the mean of the reference QOI values, and N is the total number of samples in the set. The NRMSE thus represents the deviation of the predicted QOI from the reference value, normalized by the average reference value, allowing for comparison across QOIs.

The results are shown in Figure 17, with the QOIs C_L, C_D, and C_M listed from left to right. The NRMSE for each individual wing geometry are plotted by color at a scale of 2.2% to 63.4%, with the VLM-only errors displayed in the top row and the `VortexNet` surrogate-augmented errors in the bottom row.

Under the given dataset, it is observed that the VLM-only prediction error increases with airfoil thickness, a trend that can be expected since, during the VLM setup, no thickness information is utilized by the potential flow solver as the wing is modeled with an infinitesimally thin panel. It is also observed that the VLM error decreases with increasing leading-edge sweep angle. This is most likely because, at similar free-stream conditions, wings with higher sweep angles are less affected by the leading-edge vortices. Both the leading edge vortex strength, as discussed by Hemsch and Luckring, and the wing's afterbody vortex-affected area are reduced [13]. As a result, the lower aspect ratio wing has less nonlinear aerodynamic forces, and hence the VLM predictions tend to perform better.

When comparing the `VortexNet` surrogate-augmented QOIs predictions with those from VLM, it is clear that the surrogate-augmented predictions are more accurate compared to the projected CFD reference values. While the maximum NRMSEs are 47.1%, 60.8%, and 63.4% for VLM predictions of C_L, C_D, and C_M, respectively, the maximum NRMSEs for surrogate-augmented predictions are 11.8%, 13.6%, and 13.7%, respectively. On average, the VLM predictions yield errors of 29.1%, 35.3%, and 32.0%, while the surrogate-augmented predictions have NRMSEs of 7.2%, 7.6%, and 6.8% for C_L, C_D, and C_M, respectively, resulting in an approximately fivefold reduction in QOIs estimation error. We also noticed that the surrogate model performs especially well for wings with a root airfoil of 16% thickness-to-chord ratio. The exact nature of this pattern is not clear; it may be due to the fact that a large portion of the training dataset design space has a root airfoil with 16% thickness-to-chord ratio, and worth future investigation.

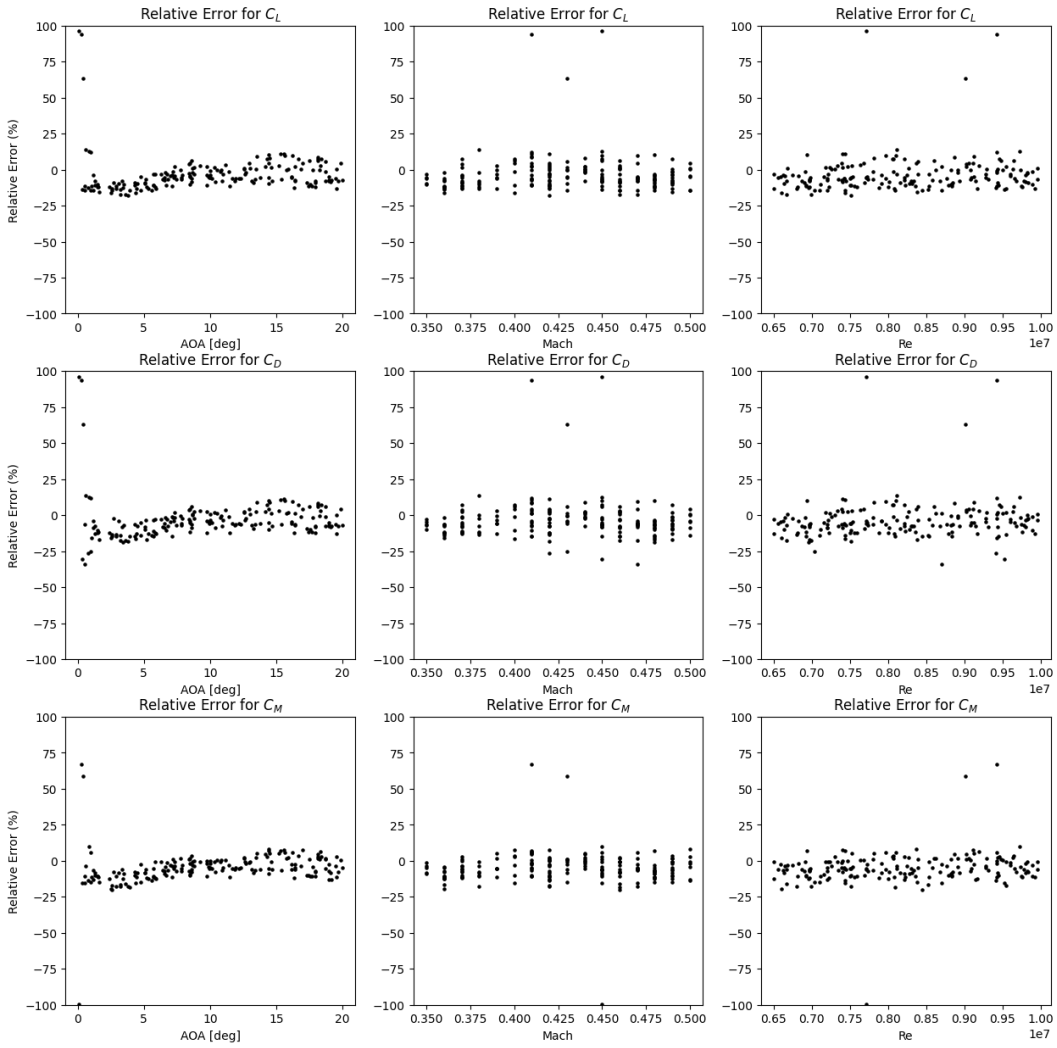

Fig. 16 Relative error for all samples in the test set, plotted with aerodynamic coefficients C_L, C_D, and C_M from top to bottom rows and against free-stream condition variables AOA [deg], Ma, and Re from left to right columns.

2. Generalization to Unseen Free-stream Conditions on Known Geometries

As a second test, we examine the QOIs prediction accuracy for geometries seen during surrogate model training but at unseen flow conditions. In this test, we extend the error quantification beyond the surrogate model's modeling error. We quantify both the epistemic discretization error and the surrogate model's modeling error. We compare the QOIs obtained directly from CFD, serving as our reference values; the QOIs computed using projected CFD surface pressures ΔC_p^{HF}, which highlight the epistemic discretization error; the integrated QOIs derived from the surrogate model's predictions ΔC_p^{pred}, which contains both epistemic discretization error and the surrogate model's modeling error; and those QOIs computed directly by VLM, which serves as the LF benchmark. We examine the C_L, C_D, and C_M polars over an AOA range from 5° to 25°, at intervals of two degrees. The free-stream Mach number is held constant at 0.4,

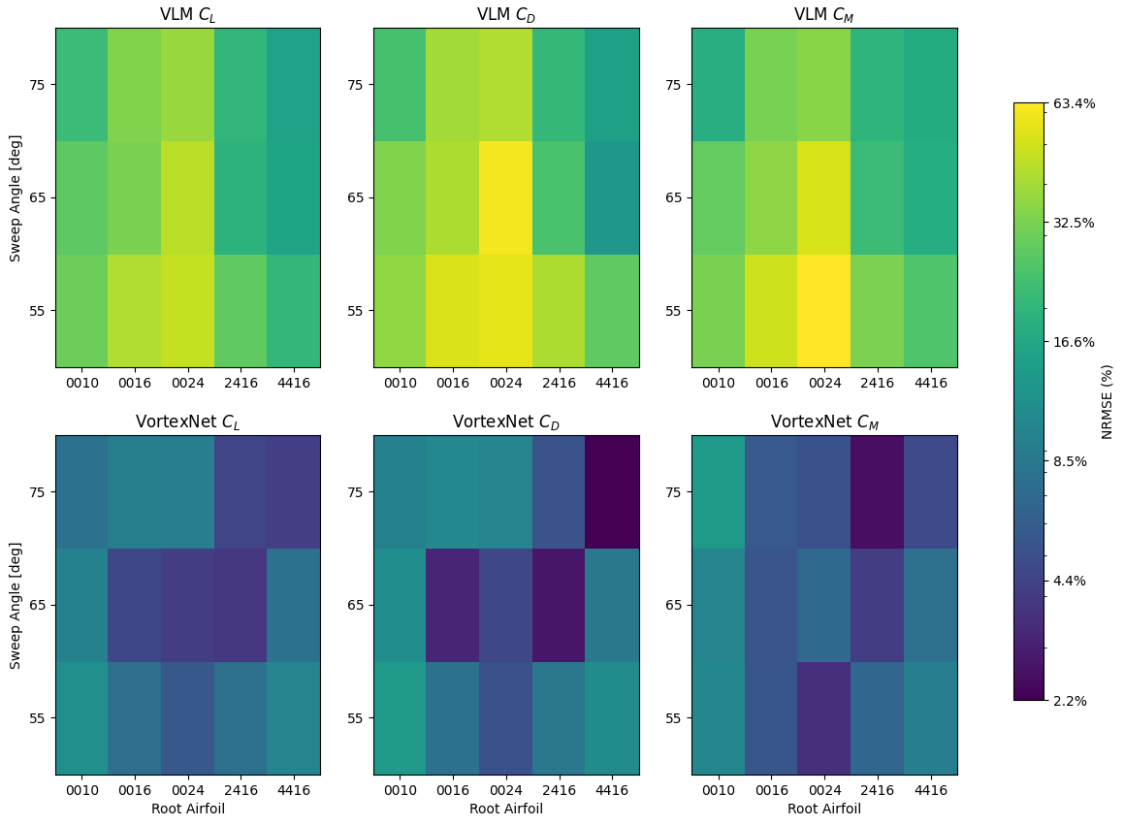

Fig. 17 Normalized error (NRMSE) for C_L, C_D, and C_M (from left to right column-wise) for aerodynamics prediction from VLM (top row) and integrated QOIs from surrogate model's ΔC_p^{pred} (bottom row) against the reference QOIs integrated from ΔC_p^{HF}. NRMSE shown by color and grouped by geometries.

and the Reynolds number at 7.0×10^6.

The changes of C_L, C_D, and C_M with AOA for each individual Delta wing geometry are presented in Appendix: Aerodynamic Coefficients Comparison for Delta Wing Geometries , from Figure 22 to Figure 36. For each figure, the VLM-estimated QOIs are plotted with hollow blue circles, the QOIs integrated from projected CFD ΔC_p^{HF} are plotted with red diamonds, the QOIs integrated from the `VortexNet` surrogate model ΔC_p^{pred} are plotted with green circles, and the CFD reference values from `SU2` are plotted with orange crosses. The dashed black line indicates an AOA of 20°, which is the upper bound of the AOA in the surrogate model's training dataset. Therefore, the QOIs predictions from `VortexNet` beyond 20° represent extrapolations by the surrogate model.

It is worth noting that RANS CFD QOIs estimations at higher AOAs can deviate significantly from quantification made by higher-fidelity methods, such as wind tunnel testing or DES simulations, as highlighted by Seraj and Martins [34]. Nevertheless, since the proposed workflow can incorporate HF field data from any CFD fidelity, and given that RANS is considered a higher-fidelity method compared to VLM, we use the RANS CFD QOIs results as the reference to demonstrate the effectiveness of the proposed multi-fidelity workflow.

Across all geometries, the QOIs computed using the proposed surrogate model workflow consistently perform better

than those computed using only the VLM, except for the geometry with a 75° leading-edge sweep and NACA 0010 root airfoil (Figure 32). For most geometries, the surrogate model yields reasonably good predictions in the extrapolation region as well, except for wing geometries with a 65° leading-edge sweep and NACA 0010 root airfoil (Figure 27), NACA 2416 root airfoil (Figure 30), and NACA 4416 root airfoil (Figure 31), and the 75° leading-edge sweep with NACA 0010 root airfoil (Figure 32) and NACA 4416 root airfoil (Figure 36). For these geometries at AOA beyond 20°, the surrogate model predicts an afterbody separation that can be identified through examining the corresponding ΔC_p^{pred}, thus artificially reducing the C_L at high AOA while increasing its C_M.

For wings with a 55° leading-edge sweep, the CFD-predicted QOIs show stronger nonlinear flow physics effects than those with higher leading-edge sweeps. This is evidenced by the existence of a maximum lift coefficient $C_{L,\max}$ for the 55° leading-edge sweep with NACA 0010 root airfoil (Figure 22) at an AOA around 21°, with NACA 0016 root airfoil (Figure 23) at around 23°, and for the 55° leading-edge sweep with NACA 2416 root airfoil (Figure 25) at around 19°. For the wing with a 55° leading-edge sweep and NACA 4416 root airfoil (Figure 26), the slope of the lift curve $\partial C_L/\partial\alpha$ significantly reduces after an AOA of 17°.

When comparing the QOIs predictions from the surrogate model to the CFD reference for 55° leading-edge sweep wings (Figure 22 to Figure 26), the surrogate model demonstrates strong agreement with the CFD references and provides significantly better predictions than those from VLM. These improvements, evident in both the trend-wise capturing and the alignment of absolute values for the QOIs polars, are particularly notable as the aerodynamics of these wings are governed by nonlinear flow physics, which LF methods cannot model accurately. Consequently, the proposed multi-fidelity workflow significantly enhances the fidelity of aerodynamic analyses for these platforms.

To summarize and compare the QOIs prediction errors from various methods, we evaluate the NRMSE values for QOIs computed using the projected CFD, the `VortexNet` surrogate model predictions, and the VLM, all compared against the CFD reference values. The NRMSEs are grouped by geometries and workflow methods so that, for each wing geometry under a given method, the NRMSE represents an average deviation of predictions across all AOAs, including the extrapolation region, against CFD references. The results are shown in Figure 18, with the QOIs C_L, C_D, and C_M listed from left to right. The VLM-only errors are displayed in the top row, the `VortexNet` surrogate-augmented errors in the middle row, and the projected CFD errors are shown in the bottom row.

On average, the epistemic discretization error induced by calculating QOIs using projected surface pressures is 16.2%. An examination of the ΔC_p^{HF} field reveals that the majority of this discretization error originates near the wing apex at the central body. This region exhibits large errors due to the use of span-wise cosine spacing, which results in larger panel sizes and excessive averaging of pressure fields with high gradients. The largest average NRMSE occurs in the C_D prediction, with an error of 41.1% observed. In addition, the average NRMSEs for C_L and C_M are 4.6% and 3.0%, respectively. The C_D prediction error is much larger than the others because the C_D are computed using VLM solver from the projected local loading coefficient ΔC_p^{HF}, which reports $C_{D,i}$ and will not match to that of CFD

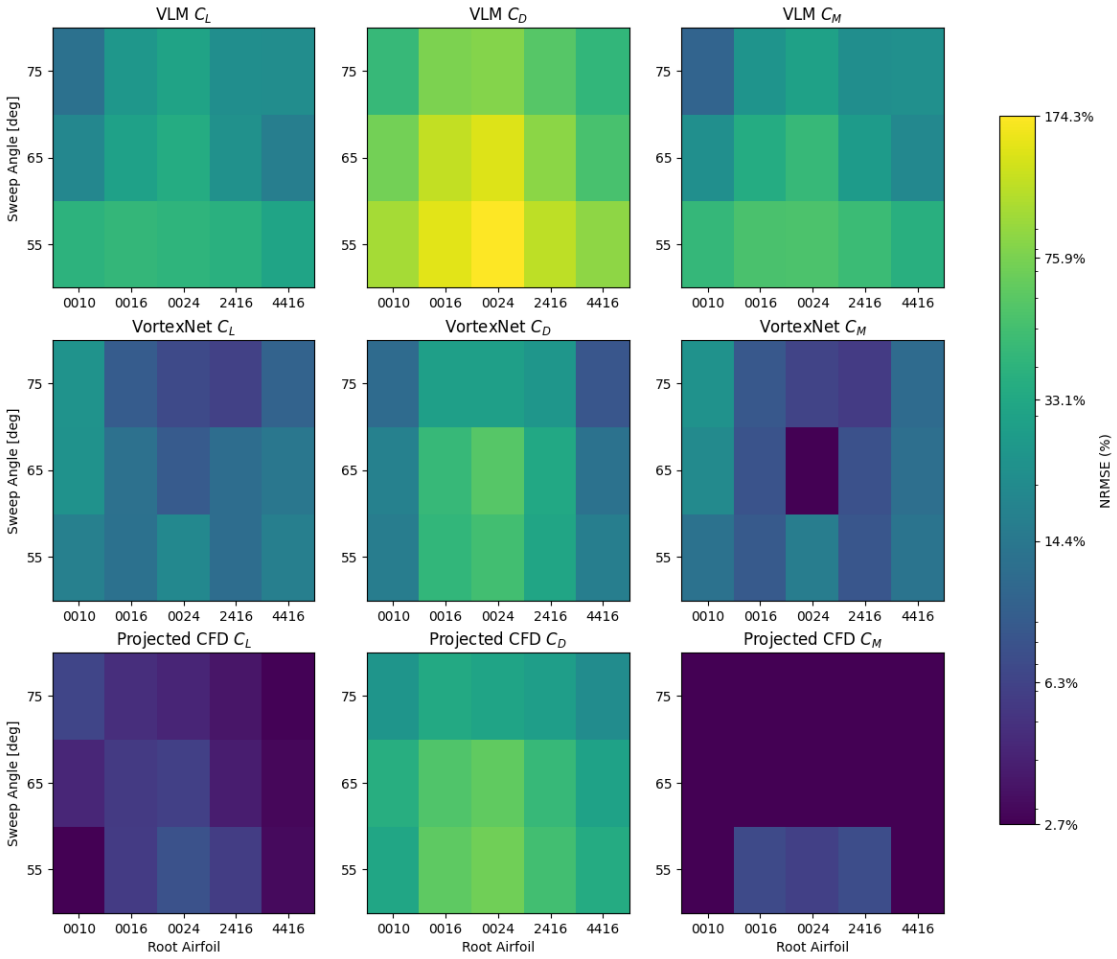

Fig. 18 Normalized error (NRMSE) for C_L, C_D, and C_M (from left to right, column-wise) comparing QOIs from VLM, integrated QOIs from the surrogate model (ΔC_p^{pred}), and projected CFD (ΔC_p^{HF}) against the CFD reference. The results are grouped by geometries, with NRMSE values represented by color.

reference as discussed in Low-fidelity Method: Vortex Lattice Method (VLM).

Additionally, the QOIs computed using the surrogate model have an error of 17.5% on average. Considering that the minimum QOIs prediction error using the surrogate model is the epistemic discretization error discussed earlier (since the projected CFD ΔC_p^{HF} are considered as "ground truth" for the surrogate model during training), the fact that this test returns an error close to the epistemic discretization error indicates that the surrogate model's modeling error is low. The average errors for C_L, C_D, and C_M are 13.4%, 28.0%, and 10.9%, respectively. In comparison, the VLM method has an average NRMSE of 51.1%. Specifically, the errors for C_L, C_D, and C_M are 28.1%, 92.8%, and 32.3%, respectively. Although the database in this test contains extrapolation samples for the surrogate model, the QOIs' average NRMSE from the proposed mixed-fidelity workflow is still smaller than that of VLM by almost three-fold. These results show that the prediction accuracy of the proposed surrogate model integrated workflow significantly increases the fidelity of the aerodynamic database predictions compared to using the VLM alone.

In static stability quantification, one of the important parameters is the pitch stiffness $\partial C_M/\partial\alpha$. In conceptual design, the pitch stiffness, or the static margin computed from it, is often included in a MDO problem as a constraint term. For a full aircraft, the pitching moment is computed about the aircraft's center of gravity. In the current test case of an isolated wing, the location of the center of gravity is somewhat arbitrary, as its exact location depends on other components such as the engine placement, fuselage, and tail. Therefore, we selected a hypothetical moment reference location at the wing apex and computed the pitch stiffness about this reference point to represent the pitch stiffness of the whole aircraft.

The pitch stiffness computation uses moment coefficients presented in the C_M plots from Figure 22 to Figure 36. It is worth noting that the sample spacing, which is at 2° intervals, is not sufficient to compute $\partial C_M/\partial\alpha$ using a finite-difference method due to the introduction of significant truncation errors. Instead, we interpolated all data points using univariate splines, specifically third-order continuously differentiable piecewise polynomials, to interpolate between the scatter points. The $\partial C_M/\partial\alpha$ can then be computed analytically by differentiating these piecewise polynomials. The results are presented in Figure 19, with results obtained from VLM shown in blue, from CFD shown in orange, from projected CFD shown in red, and from the `VortexNet` surrogate model shown in green. The dashed black line indicates a extrapolation region for the surrogate model with AOA larger than 20°.

From Figure 19, it can be first noticed that the pitch stiffness computed using the projected CFD ΔC_p^{HF} does not deviate significantly from the CFD references, indicating minimal discretization error introduced in pitch stiffness quantification. Additionally, for wings with significant vortex lift influence (leading-edge sweep of 55° across all root airfoils), the pitch stiffness computed from the surrogate model ΔC_p^{pred} aligns relatively well with the CFD reference values, even within the extrapolation region. Although the surrogate model does not capture the full variance of the CFD references, it represents the change of reference pitch stiffness with respect to AOA in a trend-wise manner. Compared to the VLM reference, which does not capture the trend evolution of pitch stiffness with respect to AOA and deviates by more than twofold at high AOA, the pitch stiffness computed using the proposed surrogate model significantly enhances the analysis fidelity.

However, the pitch stiffness estimation accuracy from the surrogate model degrades for certain geometries. For wing geometries with leading-edge sweeps of 65° and 75° and a root airfoil of NACA 0010, the pitch stiffness computed from surrogate model ΔC_p^{pred} is overestimated, and the prediction accuracy is worse than that obtained directly using VLM. This is most likely because, for wings with high sweep and thin airfoils, fewer nonlinear flow dynamics affect the wing lift. As a result, the existing VLM method with leading-edge suction correction is sufficient to quantify the pitch stiffness, while the trained surrogate model is biased towards adding nonlinear effects due to its training samples. For other geometries, such as wings with leading-edge sweeps of 65° and root airfoils of NACA 2416 and NACA 4416, and the wing with a leading-edge sweep of 75° and a root airfoil of NACA 0016 and 2416, the pitch stiffness computed from the surrogate model deviates from reference values in the extrapolation region but aligns well with the references

within the training dataset's AOA range. In all these cases, the surrogate model tends to overestimated the pitch stiffness, corresponding to an underestimation of C_L and early prediction of maximum lift coefficient $C_{L,\max}$ occurrence.

The exact reason why the surrogate model prediction degrades in certain extrapolation tasks requires further investigation. However, using a regression model like the `VortexNet` surrogate model for extrapolation is generally not recommended. The extrapolated pitch stiffness results presented in this section are primarily for examining the model's robustness rather than for applications in conceptual design. In practical conceptual design cases, the best way to avoid such prediction quality degradation and performance variation across geometries in the extrapolation region is to expand the training set to include all AOAs under investigation, as the surrogate model performs relatively well within the database's AOA range.

3. Generalization to Unseen Free-stream Conditions and Geometries

Our final test case focuses on the proposed workflow's generalizability to geometries not seen during model training. When integrating the proposed surrogate model into a conceptual design workflow that involves design space exploration, a common approach is to first conduct a coarse sampling of the design space and generate both high- and low-fidelity databases. These databases are then used to train the surrogate model. Once the surrogate model is trained with adequate prediction accuracy, we can use it in design space exploration to achieve higher design fidelity while relying only on low-fidelity methods such as VLM and the surrogate model augmentation. Therefore, it is important for the surrogate model to demonstrate acceptable generalizability for geometry interpolation within the design space spanned by samples in the coarse database. The tests in this section aim to provide a preliminary assessment of the proposed workflow's generalizability to unseen geometries, while a quantitative assessment of the model's robustness remains a topic for future research.

To study generalizability, we select four new Delta wing geometries within the design space spanned by the training sample geometries. Specifically, we choose two sweep angles, 60° and 70°, and two root airfoils, NACA 0013 and NACA 3416. These combinations can be interpreted as interpolated geometries from the database presented in Evaluation of Workflow Performance on Training Data (Section III.C.1). The resulting four geometries are: 60° NACA 0013, 60° NACA 3416, 70° NACA 0013, and 70° NACA 3416. Each geometry is simulated under 11 different far-field conditions, varying the angle of attack (AOA) from 5° to 25° in increments of two degrees. The free-stream Mach number is held constant at 0.4, and the Reynolds number at 7.0×10^6, matching the conditions reported in Generalization to Unseen Free-stream Conditions on Known Geometries (Section III.C.2).

The changes of C_L, C_D, and C_M with AOA for each individual delta wing geometry are presented in Appendix: Aerodynamic Coefficients Comparison for Delta Wing Geometries , from Figure 37 to Figure 40, using the same formatting as discussed in Section III.C.2. For all unseen geometries, we observe prediction quality and trend-wise characteristics similar to those in Section III.C.2. Specifically, the C_L obtained from the proposed surrogate-augmented

workflow tends to predict an earlier occurrence of $C_{L,\max}$. The prediction error, when referenced against the CFD reference C_L, increases with greater deviation from the database range in the extrapolation region. However, overall, the QOIs obtained from integrating the surrogate model's ΔC_p^{pred} predictions closely follow the CFD references and can be interpreted as a fidelity improvement over VLM results.

Similar to the previous pitch stiffness comparison in Section III.C.2, the $\partial C_M/\partial\alpha$ about the wing apex is computed using C_M from VLM, projected CFD, the `VortexNet` surrogate model, and CFD reference values, following an identical approach. The results are presented in Figure 20. In these figures, the columns represent Delta wings with leading-edge sweep angles of 60° and 70° from left to right, and the rows represent root airfoil shapes of NACA 0013 and NACA 3416 from top to bottom. From the pitch stiffness comparison, we find similar performance assessment conclusions as in the previous section: the $\partial C_M/\partial\alpha$ computed using the surrogate-augmented workflow captures key high-fidelity reference trends. The prediction error also increases within the extrapolation region.

Finally, we compared the NRMSE for QOIs obtained from the VLM, the `VortexNet` surrogate model, and projected CFD against the CFD references. The results are presented in Figure 21. On average, the epistemic discretization error induced by calculating QOIs using projected surface pressures is 15.3%, which does not deviate much from the error quantification in Section III.C.2. The largest average NRMSE occurs in the C_D prediction, where an error of 40.1% is observed. The average NRMSEs for C_L and C_M are 4.1% and 1.9%, respectively. The average NRMSE for the surrogate model predicted QOIs is 16.9%. Although this error is lower than the corresponding average error in Section III.C.2, the reduction is most likely due to the fact that the current test involves a database that contains fewer design space variations. The average NRMSEs for C_L, C_D, and C_M are 13.9%, 25.3%, and 11.3%, respectively. The difference between the surrogate model predicted NRMSE and the projected CFD NRMSE is also comparable to that in the previous test in Section III.C.2. We conclude that the workflow does not present significant deviations in QOIs prediction accuracy when applied to unseen geometries. Finally, for comparison, the average NRMSE for QOIs predicted from VLM is 43.1%, which corresponds to a 2.6 times larger average NRMSE than that from the surrogate model.

Across all assessments, the proposed surrogate model outperforms the VLM-based approach in QOIs prediction accuracy. Additionally, a significant performance degradation is not observed for this dataset after introducing new geometries. This observation supports the proposed workflow's generalizability potential for accommodating geometry variation within the design space. However, a more detailed sensitivity study, with a richer design space inclusion, is needed for future research to demonstrate the proposed workflow's effectiveness in SCALOS-like vehicles' conceptual design.

D. Conclusions and Future Work

In this work, we propose a novel multi-fidelity aerodynamic analysis workflow by integrating a pre-trained graph neural network (GNN)-based surrogate model named `VortexNet` into the vortex lattice method (VLM) module of the `SUAVE` conceptual design suite. The surrogate model maps the low-fidelity VLM local loading coefficient (ΔC_p^{LF}) field data to a projected computational fluid dynamics (CFD) local loading coefficient on the VLM lattice panels (ΔC_p^{HF}). This approach incorporates higher-fidelity information, such as pressure fields impacted by nonlinear flow dynamics, into the low-fidelity design environment. The online evaluation cost of using the surrogate model is comparable to that of running the VLM alone. Overall, the proposed workflow achieves notable aerodynamic coefficients prediction accuracy gains while addressing the fidelity-cost trade-off challenge in the conceptual design environment.

The workflow's prediction accuracy is assessed through three tests. First, we evaluated the prediction accuracy of C_L, C_D, and C_M (QOIs) on the test set of surrogate model's training set. We found that the proposed workflow achieves a fivefold reduction in prediction average normalized root mean square error (NRMSE) compared to the VLM's QOIs estimation. Second, we evaluated the workflow's QOIs prediction quality on a dataset with unseen flow conditions, including extrapolated flow conditions at angle-of-attacks (AOAs) beyond the surrogate model's training set. We estimate that the proposed workflow achieves a threefold average NRMSE reduction compared to traditional VLM-based analysis. Finally, we tested the workflow's prediction quality on unseen geometries not included during surrogate model training. The results indicate that the proposed multi-fidelity workflow achieves a 2.6-fold reduction in NRMSE compared to VLM's. Furthermore, no significant deviation in prediction accuracy is observed when the workflow is applied to unseen geometries, highlighting its potential for applications in design space exploration.

Overall, the workflow shows strong generalizability across unseen geometries and flow conditions, with consistent performance improvements over the VLM method. However, this performance is case-dependent; for some geometries with high leading-edge sweep and thin wing thickness, the multi-fidelity workflow's QOI estimations may be worse than relying on the VLM alone. This inconsistency in prediction capability highlights the need for future research involving a more extensive analysis of the proposed workflow's performance across a broader design space. Such research would help identify trust regions and quantify error bounds, providing clarity on the flow conditions and geometries under which applying the multi-fidelity augmentation is beneficial.

These results highlight the potential of using the `VortexNet` surrogate model in a multi-fidelity aerodynamic analysis workflow for conceptual design applications, achieving quasi-high-fidelity prediction quality under limited computational cost. Future work will focus on extending the current study to a broader design space, including SCALOS-like platforms, and applying the proposed workflow for design space exploration and aerodynamic shape optimization applications under stability constraints.

E. Acknowledgment

This work is supported by NASA, Award 80NSSC19K1661, under the Commercial Supersonics Technology (CST) program, Supersonic Configurations at Low Speeds, with Sarah Langston as the NASA technical grant monitor. The authors extend their gratitude to Eli Livne, Kuang-Ying Ting, Chester Nelson, and Kenneth Wiersema for their valuable discussion on supersonic aircraft configurations. The first author also wants to thank Jacob Needels for his assistance with the manuscript preparation and Emilio Botero for his discussion of the `SUAVE` software environment. Additionally, the authors would like to thank the Stanford Research Computing Center (SRCC) for providing computational resources on the Sherlock cluster and the Google Cloud Research Credit Program for granting access to GPU resources on the Google Cloud Platform.

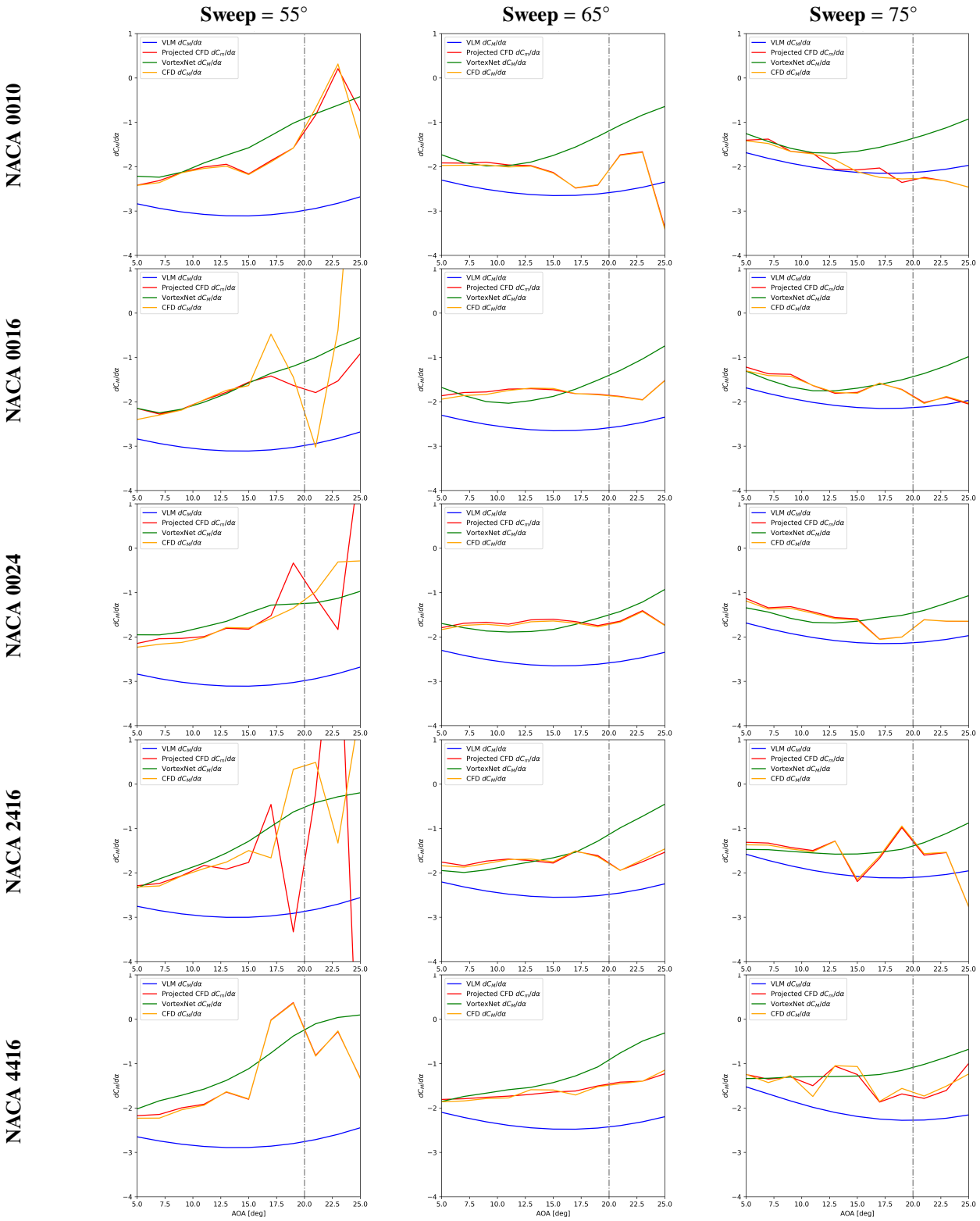

Fig. 19 Plots of pitch stiffness ($dC_M/d\alpha$) for various delta wing geometries, grouped by leading-edge sweep angles ($55°$, $65°$, and $75°$ from left column to right) and root airfoil shapes (from NACA 0010 to NACA 4416 from top to bottom). The C_M values obtained from VLM, projected CFD ΔC_p^{HF}, surrogate model predicted ΔC_p^{pred}, and the CFD reference values are plotted in blue, red, green, and orange, respectively. The dashed black line indicates an angle of attack (AOA) of $20°$; AOAs beyond $20°$ represent extrapolations for the surrogate model.

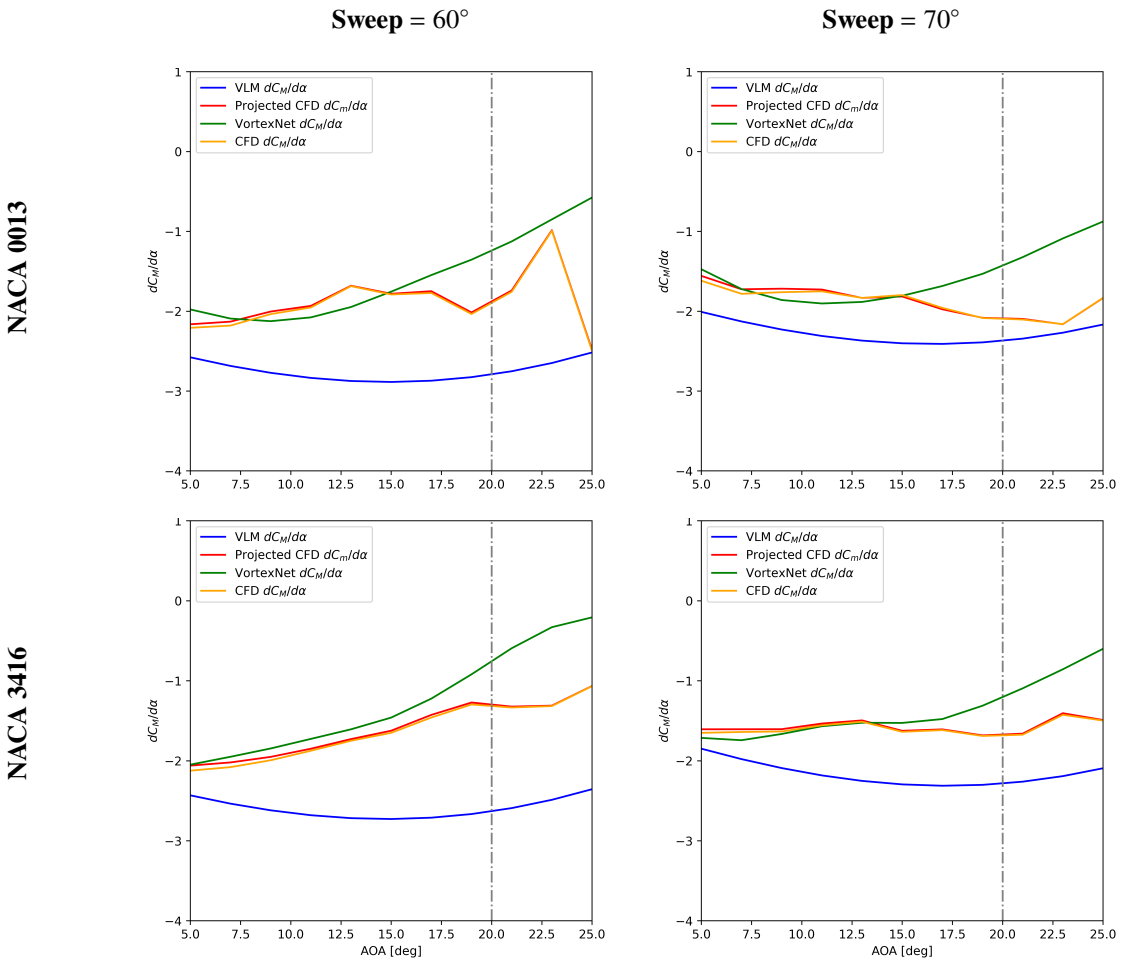

Fig. 20 Plots of pitch stiffness ($dC_M/d\alpha$) for four new geometries under the generalization test, grouped by leading-edge sweep angles (60° and 70° left column to right) and root airfoil shapes (from NACA 0013 to NACA 3416 from top to bottom). The C_M values obtained from VLM, projected CFD ΔC_p^{HF}, surrogate model predicted ΔC_p^{pred}, and the CFD reference values are plotted in blue, red, green, and orange, respectively. The dashed black line indicates an angle of attack (AOA) of 20°; AOAs beyond 20° represent extrapolations for the surrogate model.

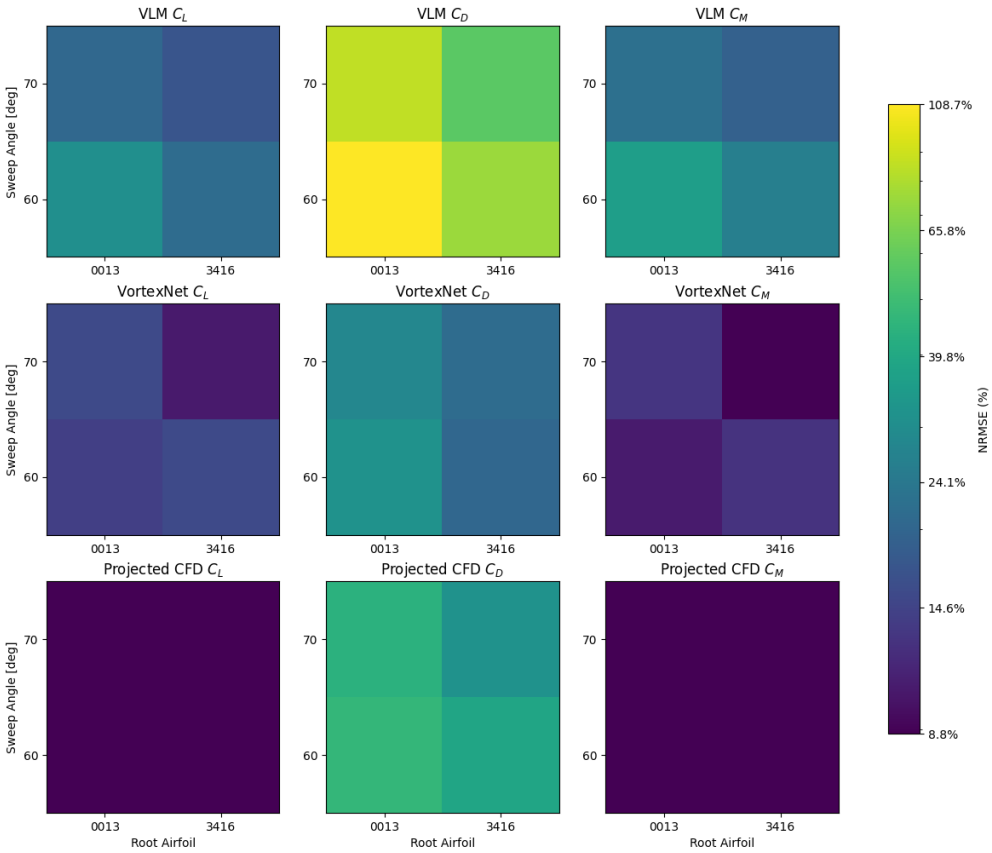

Fig. 21 Normalized error (NRMSE) for C_L, C_D, and C_M (from left to right, column-wise) comparing QOIs from VLM, integrated QOIs from the surrogate model (ΔC_p^{pred}), and projected CFD (ΔC_p^{HF}) against the CFD reference. The results correspond to the unseen geometries prediction test and are grouped by geometries, with NRMSE values represented by color.

F. Appendix: Aerodynamic Coefficients Comparison for Delta Wing Geometries

The C_L, C_D, and C_M for various Delta wing geometries at constant $M_\infty = 0.4$ and $Re = 7.0 \times 10^6$ are summarized in Figures 22 to 36. Aerodynamic coefficients at various angles of attack (AOA) are plotted as scatter points, with results obtained from VLM shown as blue hollow circles and CFD results as orange crosses. The results obtained by integrating ΔC_p^{HF} from projected CFD C_p are denoted as "Projected CFD" and are marked by red diamonds. Results obtained by integrating ΔC_p^{pred} from the `VortexNet` prediction are denoted as "VortexNet" and are marked by green dots. For C_M, a third-order spline is used to interpolate between the scatter points and is plotted with solid lines matching the corresponding color of the data series. A black dash-dotted line indicates an AOA of 20°, which is the largest AOA in the training set for `VortexNet`. Thus, the `VortexNet` aerodynamic coefficients for AOA larger than 20° are extrapolations by the surrogate model.

The following aerodynamic coefficients are the results of the proposed workflow's predictions for unseen free-stream conditions, as discussed in Generalization to Unseen Free-stream Conditions on Known Geometries.

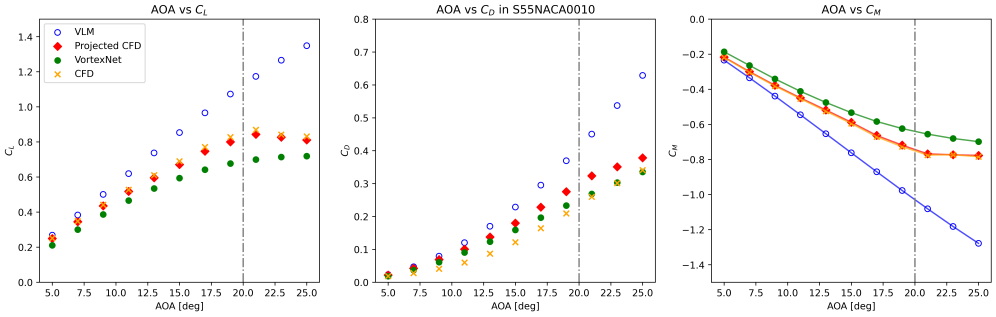

Fig. 22 Comparison of aerodynamic coefficients (C_L, C_D, C_M) obtained from various sources for a Delta wing with a root airfoil of NACA 0010 and a leading-edge sweep angle of 55°.

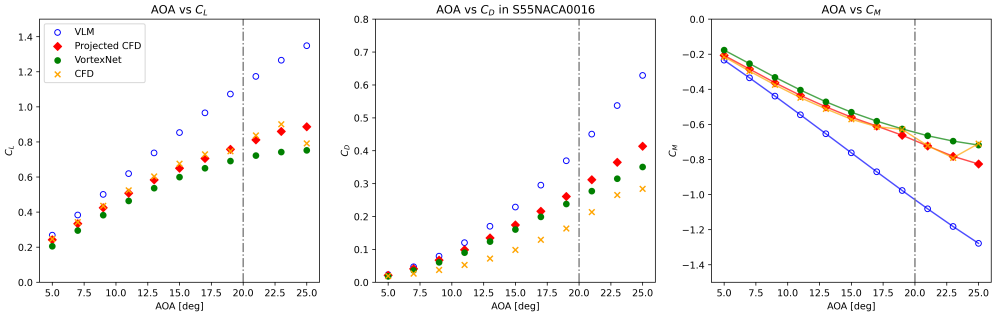

Fig. 23 Comparison of aerodynamic coefficients (C_L, C_D, C_M) obtained from various sources for a delta wing with a root airfoil of NACA 0016 and a leading-edge sweep angle of 55°.

The following aerodynamic coefficients are the results of the proposed workflow's predictions for unseen geometries, as discussed in Generalization to Unseen Free-stream Conditions and Geometries.

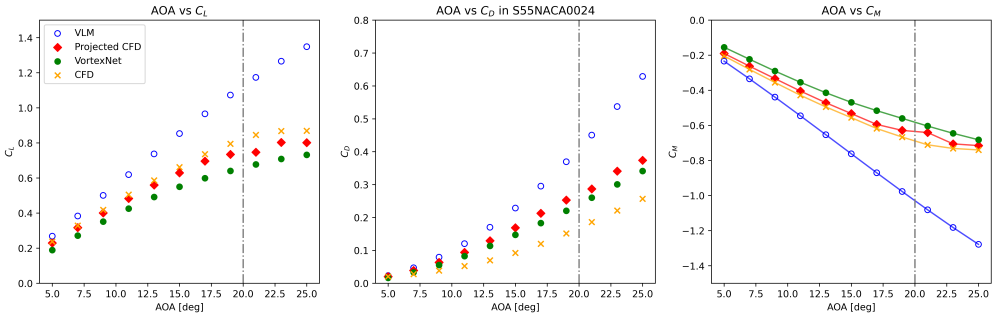

Fig. 24 Comparison of aerodynamic coefficients (C_L, C_D, C_M) obtained from various sources for a delta wing with a root airfoil of NACA 0024 and a leading-edge sweep angle of 55°.

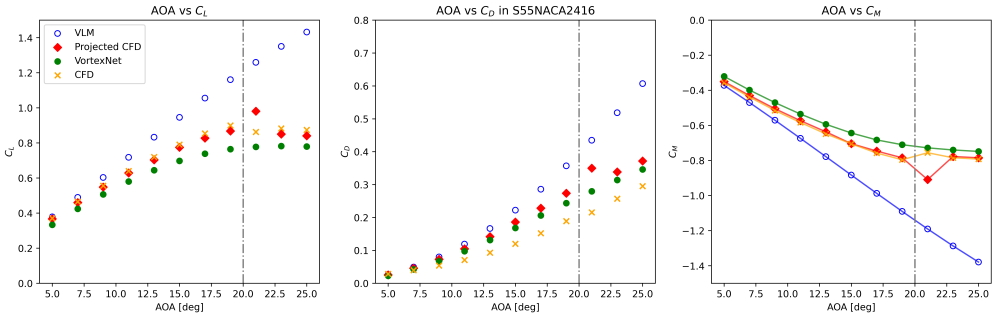

Fig. 25 Comparison of aerodynamic coefficients (C_L, C_D, C_M) obtained from various sources for a delta wing with a root airfoil of NACA 2416 and a leading-edge sweep angle of 55°.

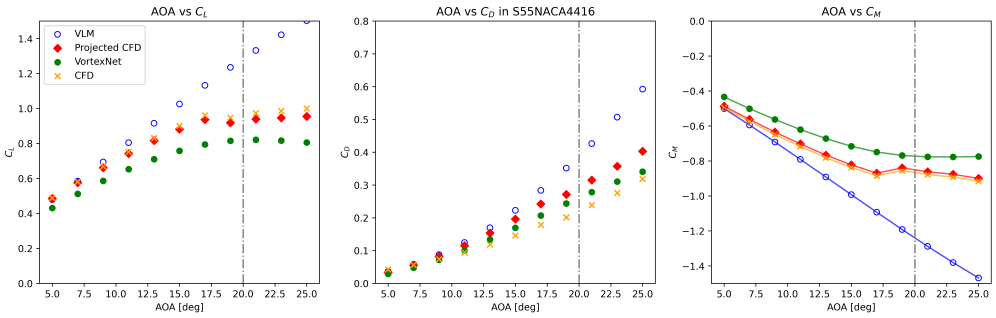

Fig. 26 Comparison of aerodynamic coefficients (C_L, C_D, C_M) obtained from various sources for a delta wing with a root airfoil of NACA 4416 and a leading-edge sweep angle of 55°.

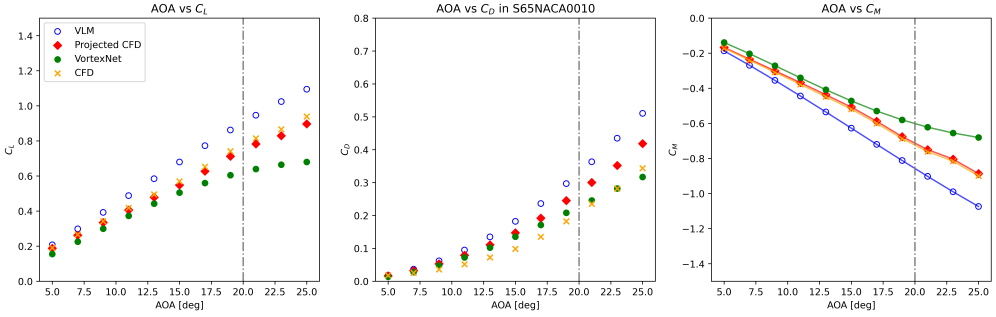

Fig. 27 Comparison of aerodynamic coefficients (C_L, C_D, C_M) obtained from various sources for a delta wing with a root airfoil of NACA 0010 and a leading-edge sweep angle of 65°.

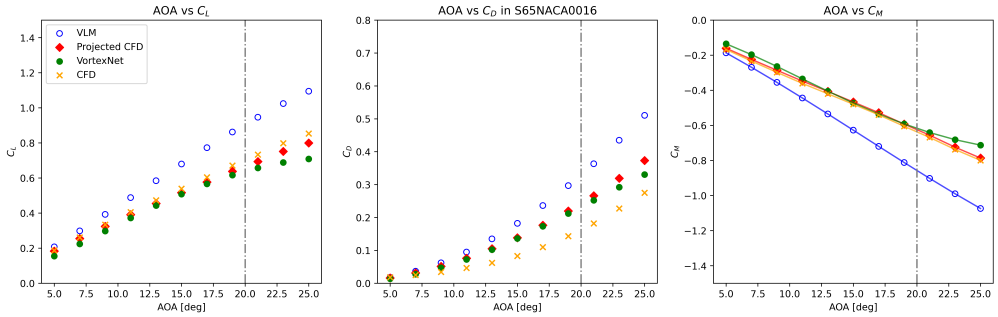

Fig. 28 Comparison of aerodynamic coefficients (C_L, C_D, C_M) obtained from various sources for a delta wing with a root airfoil of NACA 0016 and a leading-edge sweep angle of 65°.

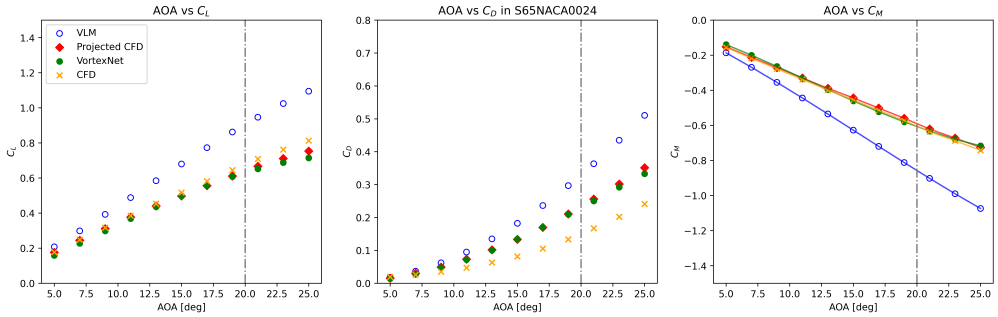

Fig. 29 Comparison of aerodynamic coefficients (C_L, C_D, C_M) obtained from various sources for a delta wing with a root airfoil of NACA 0024 and a leading-edge sweep angle of 65°.

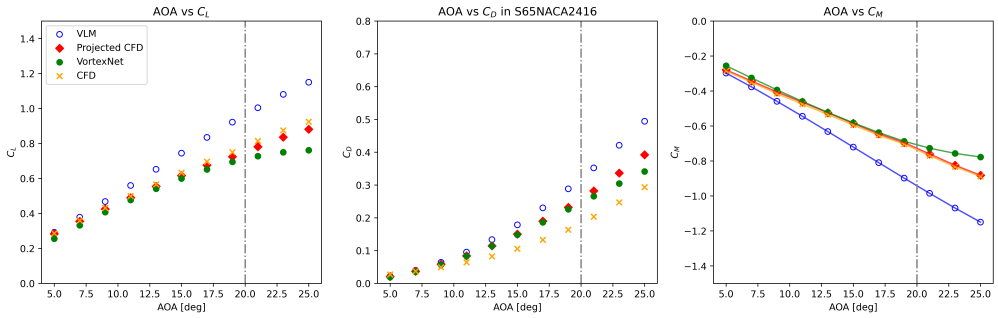

Fig. 30 Comparison of aerodynamic coefficients (C_L, C_D, C_M) obtained from various sources for a delta wing with a root airfoil of NACA 2416 and a leading-edge sweep angle of 65°.

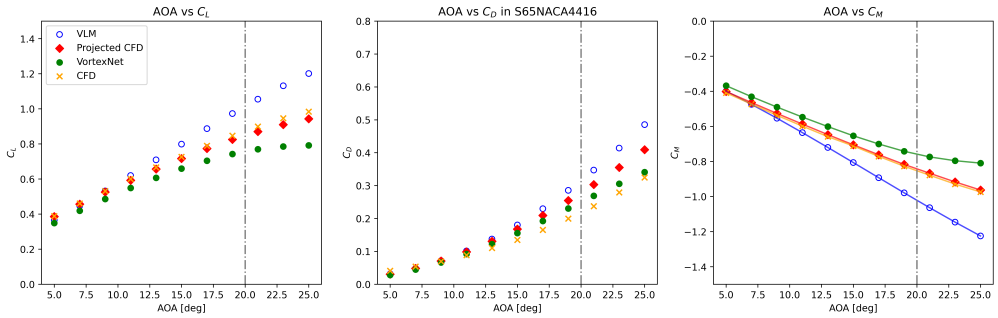

Fig. 31 Comparison of aerodynamic coefficients (C_L, C_D, C_M) obtained from various sources for a delta wing with a root airfoil of NACA 4416 and a leading-edge sweep angle of 65°.

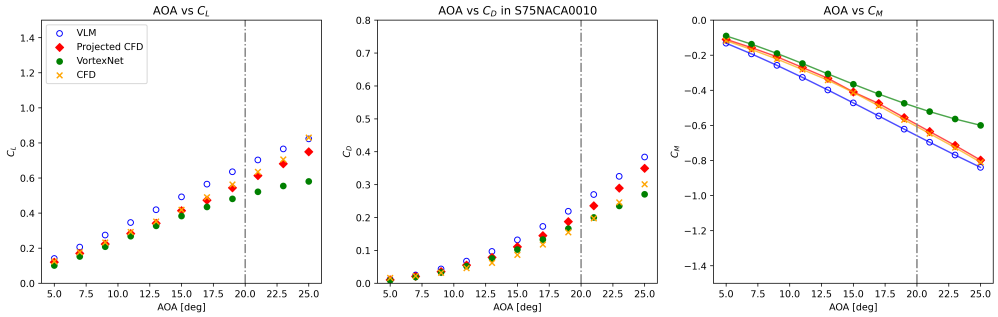

Fig. 32 Comparison of aerodynamic coefficients (C_L, C_D, C_M) obtained from various sources for a delta wing with a root airfoil of NACA 0010 and a leading-edge sweep angle of 75°.

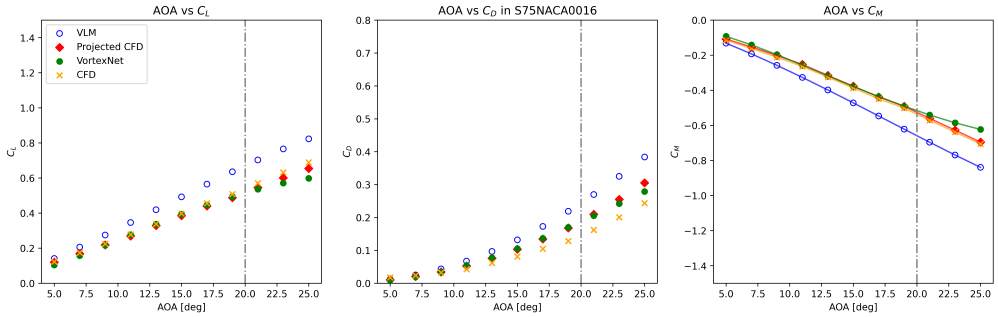

Fig. 33 Comparison of aerodynamic coefficients (C_L, C_D, C_M) obtained from various sources for a delta wing with a root airfoil of NACA 0016 and a leading-edge sweep angle of 75°.

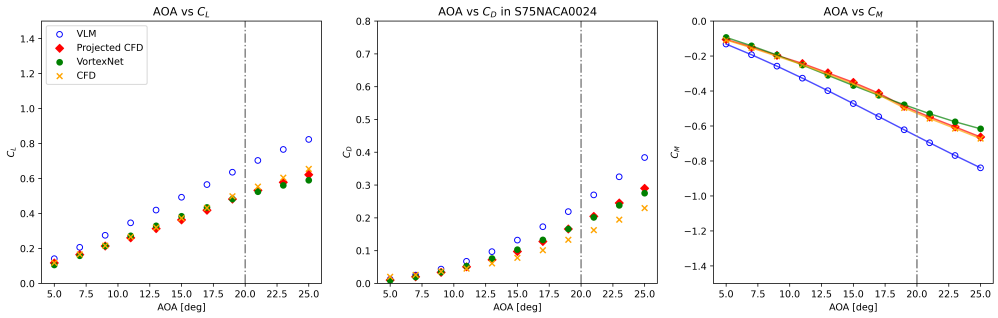

Fig. 34 Comparison of aerodynamic coefficients (C_L, C_D, C_M) obtained from various sources for a delta wing with a root airfoil of NACA 0024 and a leading-edge sweep angle of 75°.

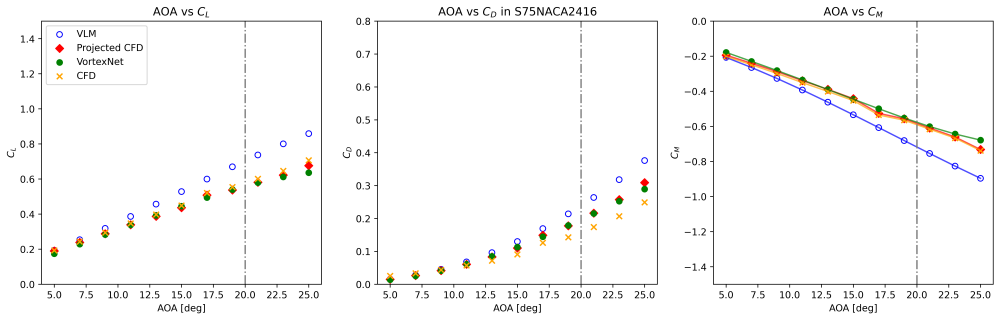

Fig. 35 Comparison of aerodynamic coefficients (C_L, C_D, C_M) obtained from various sources for a delta wing with a root airfoil of NACA 2416 and a leading-edge sweep angle of 75°.

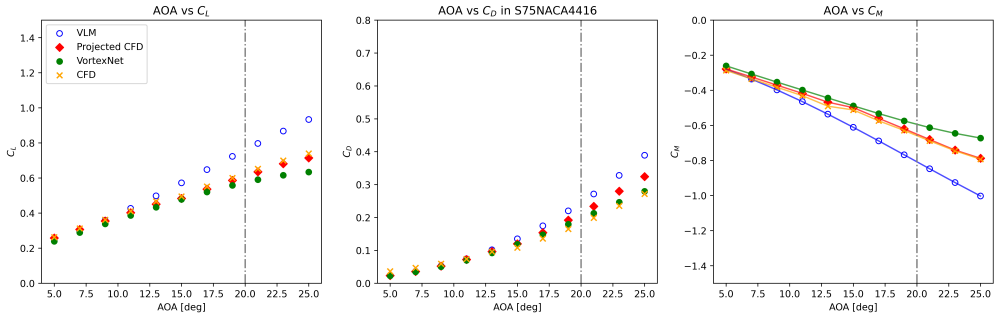

Fig. 36 Comparison of aerodynamic coefficients (C_L, C_D, C_M) obtained from various sources for a delta wing with a root airfoil of NACA 4416 and a leading-edge sweep angle of $75°$.

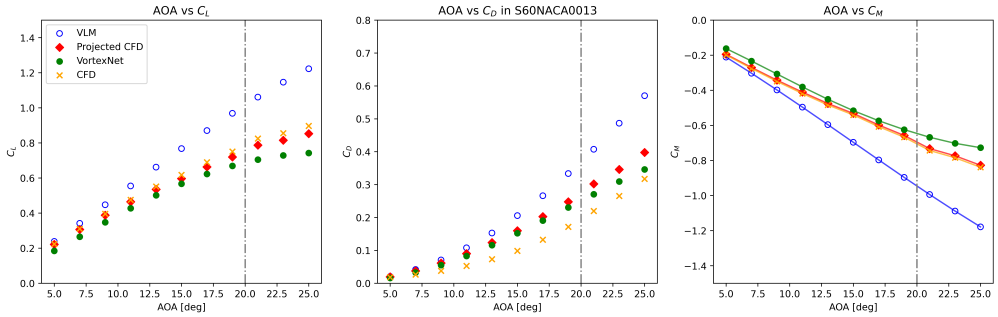

Fig. 37 Comparison of aerodynamic coefficients (C_L, C_D, C_M) obtained from various sources for a delta wing with a root airfoil of NACA 0013 and a leading-edge sweep angle of $60°$.

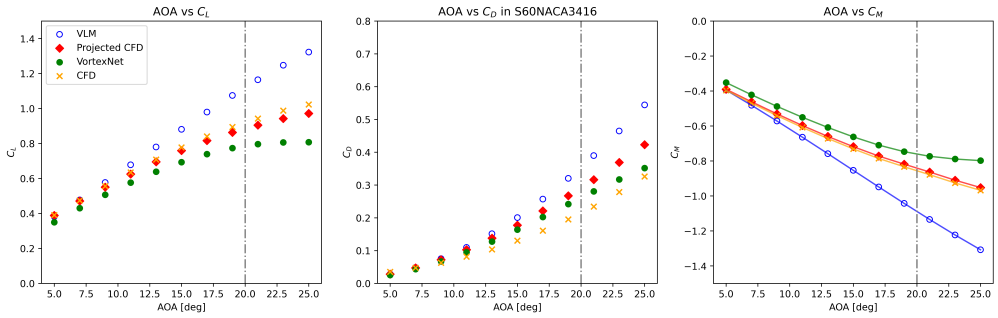

Fig. 38 Comparison of aerodynamic coefficients (C_L, C_D, C_M) obtained from various sources for a delta wing with a root airfoil of NACA 3416 and a leading-edge sweep angle of $60°$.

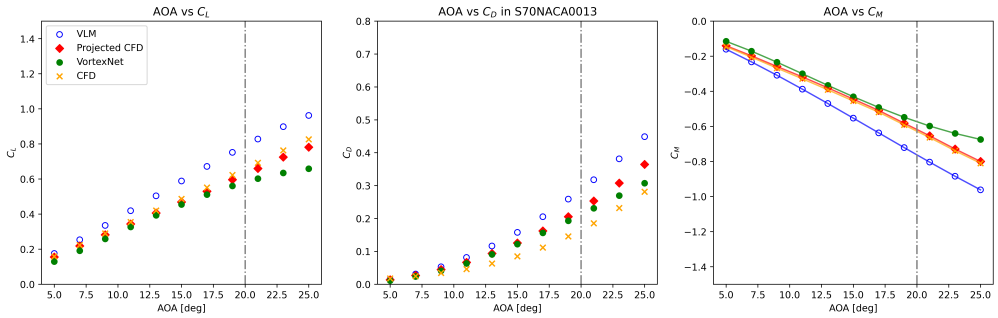

Fig. 39 Comparison of aerodynamic coefficients (C_L, C_D, C_M) obtained from various sources for a delta wing with a root airfoil of NACA 0013 and a leading-edge sweep angle of $70°$.

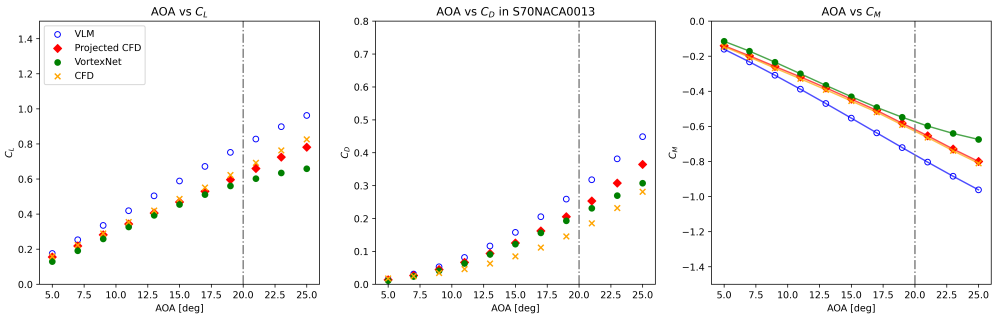

Fig. 40 Comparison of aerodynamic coefficients (C_L, C_D, C_M) obtained from various sources for a delta wing with a root airfoil of NACA 3416 and a leading-edge sweep angle of $70°$.

References

[1] Bernardo Bahia Monteiro, Ilya Kolmanovsky, and Carlos E. S. Cesnik. "Controller Agnostic Design Metrics for Stochastic Disturbance Rejection". In: *AIAA SCITECH 2024 Forum*. 2024. DOI: https://doi.org/10.2514/6.2024-0901.

[2] John J Bertin and Russell M Cummings. *Aerodynamics for engineers*. en. 6th ed. Cambridge, England: Cambridge University Press, Aug. 2021, pp. 354–362.

[3] Rafael Bertolin et al. "Gust Rejection of a Supersonic Aircraft During Final Approach". In: *AIAA SCITECH 2022 Forum*. 2022. DOI: 10.2514/6.2022-2174. eprint: https://arc.aiaa.org/doi/pdf/10.2514/6.2022-2174.

[4] J. Chen, E. Hachem, and J. Viquerat. "Graph neural networks for laminar flow prediction around random two-dimensional shapes". In: *Physics of Fluids* 33.12 (2021). ISSN: 10897666. DOI: 10.1063/5.0064108.

[5] Torbjørn Cunis, Ilya V. Kolmanovsky, and Carlos E. Cesnik. "Control Co-Design Optimization: Integrating nonlinear controllability into a multidisciplinary design process". In: *AIAA SCITECH 2022 Forum*. 2022. DOI: 10.2514/6.2022-2176. eprint: https://arc.aiaa.org/doi/pdf/10.2514/6.2022-2176.

[6] Thomas D. Economon et al. "SU2: An Open-Source Suite for Multiphysics Simulation and Design". In: *AIAA Journal* 54.3 (2016), pp. 828–846. DOI: 10.2514/1.J053813. eprint: https://doi.org/10.2514/1.J053813.

[7] Mohamed Elrefaie, Faez Ahmed, and Angela Dai. "DrivAerNet: A Parametric Car Dataset for Data-Driven Aerodynamic Design and Graph-Based Drag Prediction". In: *Volume 3A: 50th Design Automation Conference (DAC)*. IDETC-CIE2024. American Society of Mechanical Engineers, Aug. 2024. DOI: 10.1115/detc2024-143593.

[8] Thiago A. Guimarães and Carlos E. Cesnik. "The Impact of Vortex Breakdown on the Longitudinal Flight Behavior of the Scalos Aircraft". In: *AIAA SCITECH 2024 Forum*. 2024. DOI: 10.2514/6.2024-0902. eprint: https://arc.aiaa.org/doi/pdf/10.2514/6.2024-0902.

[9] Thiago A. Guimarães, Carlos E. Cesnik, and Ilya Kolmanovsky. "Flexibility Assessment of the Aeroelastic-flight-dynamic Behavior for Supersonic Aircraft". In: *AIAA SCITECH 2023 Forum*. 2023. DOI: 10.2514/6.2023-0417. eprint: https://arc.aiaa.org/doi/pdf/10.2514/6.2023-0417.

[10] Thiago A. Guimarães, Carlos E. Cesnik, and Ilya Kolmanovsky. "Unsteady Vortex Lattice Linearization and Sensitivity Analyses for Control Models in Supersonic Aircraft Design". In: *AIAA SCITECH 2023 Forum*. 2023. DOI: 10.2514/6.2023-0416. eprint: https://arc.aiaa.org/doi/pdf/10.2514/6.2023-0416.

[11] Thiago A. Guimarães, Carlos E. Cesnik, and Ilya V. Kolmanovsky. "An Integrated Low-Speed Aeroelastic-Flight-Dynamics Framework for Modeling Supersonic Aircraft". In: *AIAA SCITECH 2022 Forum*. 2022. DOI: 10.2514/6.2022-2175. eprint: https://arc.aiaa.org/doi/pdf/10.2514/6.2022-2175.

[12] Thiago A.M. Guimarães, Carlos E.S. Cesnik, and Ilya Kolmanovsky. "Low Speed Aerodynamic Modeling for Control-related Considerations in Supersonic Aircraft Design". In: *AIAA AVIATION 2021 Forum* (2021), pp. 1–18. DOI: 10.2514/6.2021-2531.

[13] Michael J. Hemsch and James M. Luckring. “Connection between leading-edge sweep, vortex lift, and vortex strength for delta wings”. In: *Journal of Aircraft* 27.5 (1990), pp. 473–475. DOI: 10.2514/3.25305.

[14] Hemant Joshi and Peter Thomas. “Review of vortex lattice method for supersonic aircraft design”. In: *The Aeronautical Journal* (2023), pp. 1–35.

[15] C. Lan and C.-H. Hsu. “Effects of vortex breakdown on longitudinal and lateral-directional aerodynamics of slender wings by the suction analogy”. In: *9th Atmospheric Flight Mechanics Conference*. 1982. DOI: 10.2514/6.1982-1385. eprint: https://arc.aiaa.org/doi/pdf/10.2514/6.1982-1385.

[16] Jinxing Li et al. “Multi-fidelity graph neural network for flow field data fusion of turbomachinery”. In: *Energy* 285.July (2023), p. 129405. ISSN: 03605442. DOI: 10.1016/j.energy.2023.129405.

[17] Eli Livne, Chester P. Nelson, and Kuang-Ying Ting. “Supersonic Configurations at Low Speeds (SCALOS): Progress at the University of Washington”. In: *AIAA SCITECH 2024 Forum*. 2024. DOI: 10.2514/6.2024-0898. eprint: https://arc.aiaa.org/doi/pdf/10.2514/6.2024-0898.

[18] Timothy MacDonald et al. “SUAVE: An Open-Source Environment Enabling Multi-Fidelity Vehicle Optimization”. In: *18th AIAA/ISSMO Multidisciplinary Analysis and Optimization Conference*. 2017. DOI: 10.2514/6.2017-4437. eprint: https://arc.aiaa.org/doi/pdf/10.2514/6.2017-4437. URL: https://arc.aiaa.org/doi/abs/10.2514/6.2017-4437.

[19] Timothy MacDonald et al. “SUAVE: an open-source environment enabling multi-fidelity vehicle optimization”. In: *18th AIAA/ISSMO Multidisciplinary Analysis and Optimization Conference*. 2017, p. 4437. DOI: https://doi.org/10.2514/6.2017-4437.

[20] Todd E. Magee, Patrick J. Hayes, and Abdollah Khodadoust. “Dynamic Stability Characteristics for Commercial Supersonic Configurations at Low-Speed Flight Conditions – Part II”. In: *AIAA SCITECH 2024 Forum*. 2024. DOI: 10.2514/6.2024-0900. eprint: https://arc.aiaa.org/doi/pdf/10.2514/6.2024-0900.

[21] Todd E. Magee et al. “Dynamic Stability Characteristics for Commercial Supersonic Configurations at Low-Speed Flight Conditions”. In: *AIAA SCITECH 2022 Forum*. 2022. DOI: 10.2514/6.2022-1802. eprint: https://arc.aiaa.org/doi/pdf/10.2514/6.2022-1802.

[22] Nicolas Mavriplis et al. “Supersonic Configurations at Low Speeds (SCALOS): CFD Aided Wind Tunnel Data Corrections”. In: *AIAA SCITECH 2023 Forum*. 2023. DOI: 10.2514/6.2023-0231. eprint: https://arc.aiaa.org/doi/pdf/10.2514/6.2023-0231.

[23] Luis R. Miranda, Robert D. Elliott, and William M. Baker. “A generalized vortex lattice method for subsonic and supersonic flow applications”. In: *NASA. Langley Res. Center Vortex-Lattice Utilization* (1977). URL: https://ntrs.nasa.gov/citations/19780008059.

[24] Anthony M Mitchell et al. “Analysis of delta-wing vortical substructures using detached-eddy simulation”. In: *AIAA journal* 44.5 (2006), pp. 964–972. DOI: https://doi.org/10.2514/1.755.

[25] John Morgenstern et al. *Advanced concept studies for supersonic commercial transports entering service in the 2018-2020 period phase 2*. Tech. rep. June. NASA Glenn Research Center, 2015. URL: https://ntrs.nasa.gov/citations/20150015837.

[26] Markus Mrosek, Carsten Othmer, and Rolf Radespiel. "Reduced-Order Modeling of Vehicle Aerodynamics via Proper Orthogonal Decomposition". In: *SAE Int. J. Passeng. Cars - Mech. Syst.* 12 (3 2019), pp. 225–236. DOI: 10.4271/06-12-03-0016.

[27] Jayant Mukhopadhaya et al. "Multi-fidelity modeling of probabilistic aerodynamic databases for use in aerospace engineering". In: *International Journal for Uncertainty Quantification* 10.5 (2020), pp. 425–447. ISSN: 21525099. DOI: 10.1615/Int.J.UncertaintyQuantification.2020032841. arXiv: 1911.05036.

[28] Chester P. Nelson et al. "Supersonic Configurations at Low Speeds (SCALOS): Configuration Comparison of SCALOS to Existing Designs". In: *AIAA SCITECH 2023 Forum*. 2023. DOI: 10.2514/6.2023-0228. eprint: https://arc.aiaa.org/doi/pdf/10.2514/6.2023-0228.

[29] Chester P. Nelson et al. "Supersonic Configurations at Low Speeds (SCALOS): Project Background and Progress at University of Washington". In: *AIAA SCITECH 2022 Forum* (2022). DOI: 10.2514/6.2022-1803.

[30] Chester P. Nelson et al. "Supersonic Configurations at Low Speeds (SCALOS): Project Background and Progress at University of Washington". In: *AIAA SCITECH 2022 Forum*. 2022. DOI: 10.2514/6.2022-1803. eprint: https://arc.aiaa.org/doi/pdf/10.2514/6.2022-1803.

[31] Michel Nöding et al. "Simulation of landing and take-off noise for supersonic transport aircraft at a conceptual design fidelity level". In: *Aerospace* 9.1 (2022), pp. 1–23. ISSN: 22264310. DOI: 10.3390/aerospace9010009.

[32] Edward Charles Polhamus. "A concept of the vortex lift of sharp-edge delta wings based on a leading-edge-suction analogy". In: *NASA. Langley Res. Center* (1966). URL: https://ntrs.nasa.gov/citations/19670003842.

[33] Sabet Seraj and Joaquim R. Martins. "Aerodynamic Shape Optimization of a Supersonic Transport Considering Low-Speed Stability". In: *AIAA SCITECH 2022 Forum*. 2022. DOI: 10.2514/6.2022-2177. eprint: https://arc.aiaa.org/doi/pdf/10.2514/6.2022-2177.

[34] Sabet Seraj and Joaquim R. R. A. Martins. "Predicting the High-Angle-of-Attack Characteristics of a Delta Wing at Low Speed". In: *Journal of Aircraft* 59.4 (2022), pp. 1071–1081. DOI: 10.2514/1.C036618. eprint: https://doi.org/10.2514/1.C036618.

[35] Tejal K Shanbhag et al. "A comparison of jet acoustic analysis methods". In: *AIAA AVIATION 2021 Forum*. 2021, p. 2102. DOI: https://doi.org/10.2514/6.2021-2102.

[36] Yiren Shen, Jacob T. Needels, and Juan J. Alonso. "VortexNet: A Graph Neural Network-Based Multi-Fidelity Surrogate Model for Field Predictions". In: *AIAA SCITECH 2025 Forum*. January. 2025.

[37] Yiren Shen et al. "Application of Multi-Fidelity Transfer Learning with Autoencoders for Efficient Construction of Surrogate Models". In: *AIAA SCITECH 2024 Forum*. January. 2024, pp. 1–19. ISBN: 9781624107115. DOI: 10.2514/6.2024-0013.

[38] Michael L. Shur et al. “Turbulence Modeling in Rotating and Curved Channels: Assessing the Spalart-Shur Correction”. In: *AIAA Journal* 38.5 (2000), pp. 784–792. DOI: 10.2514/2.1058. eprint: https://doi.org/10.2514/2.1058.

[39] P. Spalart and S. Allmaras. “A one-equation turbulence model for aerodynamic flows”. In: *30th Aerospace Sciences Meeting and Exhibit*. 1992. DOI: 10.2514/6.1992-439. eprint: https://arc.aiaa.org/doi/pdf/10.2514/6.1992-439.

[40] Kuang-Ying Ting et al. “Supersonic Configurations at Low Speeds (SCALOS) Longitudinal Aerodynamics: Configuration Variations and Control Surfaces Effects”. In: *AIAA SCITECH 2023 Forum*. 2023. DOI: 10.2514/6.2023-0230. eprint: https://arc.aiaa.org/doi/pdf/10.2514/6.2023-0230.

[41] Kuang-Ying Ting et al. “Supersonic Configurations at Low Speeds (SCALOS): Model Geometry and Aerodynamic Results”. In: *AIAA SCITECH 2022 Forum*. 2022. DOI: 10.2514/6.2022-1800. eprint: https://arc.aiaa.org/doi/pdf/10.2514/6.2022-1800.

[42] Kuang-Ying Ting et al. “Supersonic Configurations at Low Speeds (SCALOS): The Aerodynamic Effects of Control Surfaces”. In: *AIAA SCITECH 2023 Forum*. 2023. DOI: 10.2514/6.2023-0229. eprint: https://arc.aiaa.org/doi/pdf/10.2514/6.2023-0229.

[43] Kuang-Ying Ting et al. “Supersonic Configurations at Low Speeds (SCALOS): The Incremental Effects of Configuration Variations and Model Regression Studies”. In: *AIAA SCITECH 2023 Forum*. 2023. DOI: 10.2514/6.2023-0230. eprint: https://arc.aiaa.org/doi/pdf/10.2514/6.2023-0230.

[44] Andrew M. Wissink and Nathan S. Hariharan. “An Overview of the CREATE™ Applied Surrogates Institute”. In: *AIAA SCITECH 2024 Forum*. 2024. DOI: 10.2514/6.2024-0011. eprint: https://arc.aiaa.org/doi/pdf/10.2514/6.2024-0011.

IV. VortexNet: A Graph Neural Network-Based Multi-Fidelity Surrogate Model for Field Predictions

Aircraft design relies on accurate aerodynamic predictions. High-fidelity (HF) methods, such as computational fluid dynamics (CFD), provide accurate aerodynamic analyses but are computationally expensive for early-stage design. Conversely, low-fidelity (LF) methods, such as the vortex lattice method (VLM), offer cost-effective solutions but struggle to capture complex flow phenomena, limiting their predictive accuracy. The conceptual design process thus presents a fidelity-cost trade-off, requiring a balance between HF and LF data in early design phases. This study introduces `VortexNet`, a graph neural network (GNN)-based surrogate model designed to bridge the fidelity gap between LF and HF aerodynamic predictions. `VortexNet` learns corrections to LF panel-wise local loading coefficient field data using data-driven insights from HF CFD simulations, enabling pressure coefficient field predictions across a range of Delta wing geometries and free-stream conditions. The model demonstrates strong prediction accuracy and generalizability across configurations, effectively capturing nonlinear flow features under geometric variations. A hyper-parameter sensitivity study and a preliminary prediction mechanism explanation, leveraging the latent space ablation technique, are conducted to rationalize the model's predictive capabilities and provide guidance for future improvements in `VortexNet`-like surrogate modeling. These results indicate that `VortexNet` has potential as a valuable tool for conceptual design in multidisciplinary design optimization (MDO), while emphasizing the need for further validation and refinement.

Nomenclature

AOA	=	Angle of Attack [degree]
b	=	span length [m]
c	=	chord length [m]
C_p	=	pressure coefficient
ΔC_p	=	local loading coefficient
ΔC_p^{HF}	=	high-fidelity (HF) ΔC_p
ΔC_p^{LF}	=	low-fidelity (LF) ΔC_p
ΔC_p^{pred}	=	surrogate model predicted ΔC_p

$\mathcal{F}$	=	a generic mapping function
Γ	=	vortex strength [m^2/s]
$G(V, E)$	=	a graph with nodes V and edges E
$\mathbf{h}$	=	a generic feature array in surrogate modeling
$\mathcal{L}$	=	a generic loss term
Ma	=	free-stream Mach number
p	=	pressure [Pa]
q_{ref}	=	reference pressure [Pa]
q^{LF}	=	low-fidelity (LF) field vector
q^{HF}	=	high-fidelity (HF) field vector
Re	=	Reynolds number
R^2	=	coefficient of determination
$\bar{v} = [u, v, w]^\mathsf{T}$	=	velocity vector [m/s]
x, y, z	=	Cartesian coordinate
y^+	=	dimensionless grid-to-wall spacing

A. Introduction

Aircraft design involves computational modeling to predict and optimize vehicle aerodynamic performance. Accurate simulation can be accomplished using high-fidelity (HF) computational fluid dynamics (CFD) codes to solve the Navier-Stokes equations, a set of coupled nonlinear partial differential equations (PDE), which govern viscous, compressible flow. Despite significant progress in CFD techniques and high-performance computing hardware, CFD remains computationally expensive [6, 42], and this computational cost is exacerbated in many-query applications, such as design optimization, where a large number of flow-field evaluations across a wide range of flight conditions and vehicle configurations are required. Such costs generally prohibit relying exclusively on CFD for the conceptual design phase of an aircraft. During this phase, engineers and researchers frequently utilize low-fidelity (LF) methods, subject matter expert knowledge, and historical data to explore the design space and draft an initial design [29, 38]. As the aircraft configuration matures, the candidate designs are assessed and revised with higher fidelity tools, including CFD and wind tunnel testing. This process carries the risk that inaccuracies introduced by lower fidelity tools will result in a non-optimal configuration, requiring significant revision in later stages and adversely impacting development cost and schedule. Improved accuracy in conceptual level design tools has the potential to improve prediction quality of, and confidence in, configuration performance, and motivates the introduction of HF design tools earlier in the design cycle.

However, constraints on computational cost necessitate the development of strategies which can accurately augment LF model predictions across the joint design-mission space while minimizing required computational cost.

1. Motivation

Recent interest in multidisciplinary design optimization (MDO) [24, 49] calls for a more closely integrated design-assessment cycle. Many conceptual aircraft design suites have been developed to address this need, such as `SUAVE` [51, 22]. These software suites provide aircraft design analysis and optimization frameworks that incorporate hierarchical multi-fidelity (MF) analyses across multiple disciplines. At the lowest fidelity, pressure distribution and force and moment coefficients are typically computed using a vortex lattice method (VLM) code [30, 7, 26, 48] due to its relative simplicity and low computational cost. The VLM models the pressure distribution on the aircraft based on potential flow theory, neglecting compressibility, viscous effects, and aspects of geometry such as wing thickness. Despite limitations on accuracy, vehicle configurations, and free-stream condition trust region, the VLM has been demonstrated to be an accurate LF model for preliminary design configuration changes [17].

Despite the relative popularity of the VLM, its underlying assumptions make it incapable to model certain physical phenomena. For example, the VLM prediction of the pitching moment of a Delta wing at high AOA can be unreliable because nonlinear effects, such as vortex lift, vortex-boundary layer interactions, and flow separation, are not captured by the VLM model. Under such flow conditions, the force and moment predictions from VLM are largely inaccurate. Relying on VLM for conceptual vehicle design may lead to a non-optimal or infeasible design for this phase of flights. An option to improve VLM prediction accuracy is to incorporate theoretical or semi-empirical models, such as the Polhamus correction [35], into VLM solvers. However, this approach has drawbacks regarding the accuracy and platform applicability: correction parameters need to be tuned for specific wing platforms and flow mechanism to produce accurate predictions [15, 25]. When a large design space is explored in a conceptual design task, validating the correction parameters themselves across the design space can be a complicated task. Alternatively, rather than adding additional correction terms to LF models, a MF, data-driven surrogate model can be used to correct correct LF predictions. Such frameworks are attractive for being extensible to different problems with accuracy comparable to the highest fidelity analysis tool, given sufficient samples and training.

2. Background

One common surrogate modeling approach is to learn corrections to scalar-valued aerodynamic force and moment coefficients through Bayesian frameworks, such as through MF Gaussian processes regression (GPR), to synthesize multiple data sources, allowing lower-fidelity solver results to be calibrated by higher-fidelity solver predictions with lower uncertainty [18]. Mukhopadhaya et al. demonstrated such approach to generate multi-fidelity probabilistic aerodynamic databases for simulation of commercial aircraft, employing data from panel codes, CFD, and wind tunnel

experiments. SUAVE has a built-in module to accommodate MF data sources and build surrogate models for design optimization purposes, demonstrating a good balance between computational efficiency and accuracy [22]. However, standard GPR is limited to scalar-valued quantities of interest, making it challenging to apply to high-dimensional data like flow fields or surface pressures. In many applications, accurate prediction of field data is necessary, such as to location dependent phenomena, such as turbulent transition and flow separation, or to allow the integration of arbitrary Quantities of interest (QOI) unknown *a priori*. The ability of the surrogate to produce field data predictions also aids in the interpretability of results, improving understanding and confidence in predictions.

Popular techniques for surrogate modeling of aerodynamic field data frequently utilize proper orthogonal decomposition (POD) [3]. By decomposing the flow-field into a set of spatial modes, POD permits a parameterized model of field variables based on the selection of modal frequencies for a truncated expansion. One popular methodology is POD-kriging, where modal coefficients are selected using GPR. This method has been previously applied to aerodynamic design optimization of passenger cars [27]. However, challenges remain for POD-based methods. A large number of modes are required to capture nonlinear phenomena, including moving coherent structures in the flow-field. Incorporation of MF data is also challenging, particularly when HF data is limited and contains distinct features not present at lower fidelities. While Mrosek, Othmer, and Radespiel demonstrates the application of POD-kriging to design optimization, generalizability between configurations is a concern. This is particularly the case when the design space is large and geometric variations between designs are significant, which may limit the capability of POD-kriging to provide accurate predictions across geometries.

Rather than relying on linear projection for dimensionality reduction, other approaches utilize machine learning (ML) techniques for surrogate modeling. One popular approach is the use of deep neural network (DNN) to model aerodynamic QOIs based on MF data sources. This method has been applied to airfoil and wing sections design optimization and outperformed GPR-based approaches [55], but is limited to scalar-valued prediction. Flow-field prediction capability is also demonstrated by using a DNN to learn the discrepancy between LF Euler and HF RANS flow fields [42], but for a fixed geometry.

To adequately extend VLM predictions for the case of interest, analysis and optimization of Delta wing configurations at high AOA, both a field prediction capability and strong geometric generalizability are required. To overcome limitations of previous methods, we explored approaches involving a lattice-wise vortex strength modification based on CFD results. Instead of relying on semi-empirical models, we propose using GNN to learn a mapping that calibrates LF predictions using HF CFD results. Recent studies show that GNN has strong potential for this type of mapping, offering superior performance compared to traditional methods [4, 20, 8, 33, 40, 53, 21]. Due to their graph nature, GNN are highly effective at integrating and learning mappings between different fidelity data sources, including field data sampled at different spatial locations [20, 13, 50]. Additionally, complex geometries and physical constraints can be efficiently represented in graph, even with underlying geometries variations, and thus GNN demonstrates superior

generalizability to geometry changes, scalability, and efficiency [8, 20, 9]. These characteristics will be critical for MDO applications as the vehicle configuration, mesh discretization, free-stream conditions, and the QOIs may change during the design-assessment cycle.

3. Overview

Motivated by these research advancements, this study aims to enhance the accuracy of VLM in conceptual aircraft design by proposing a GNN-based mapping function to correct lattice vortex strength using HF CFD data. The proposed network will be tested with a benchmark case of a Delta wing at various AOAs. In Section IV.B, an overview of the MF analysis tools to generate a training dataset are given, as well as the GNN architecture and training procedure used in this work. Section IV.C presents network prediction quality for aerodynamic loading across a range of vehicle geometries. A comprehensive study of how input graph features are propagated through latent layers is conducted, to better understand the relation between network architecture and prediction quality. The paper concludes with an overview of results and directions for future work.

B. Methodology

To construct the proposed GNN-based MF surrogate model, pressure distribution data is used from two models of different fidelity. LF data is generated using the panel-wise pressure distribution computed by a vortex lattice method (VLM) solver integrated in the `SUAVE` software package. For HF data, we use the surface pressure coefficient computed by a computational fluid dynamics (CFD) Reynolds-averaged Navier-Stokes (RANS) solver available in `SU2`. A brief summary of the physical and numerical models for each mehod is presented in Section IV.B.1 for VLM and Section IV.B.2 for CFD. A detailed description of the dataset used to train the surrogate model, along with the dataset preparation procedure and the graph definition, is covered in Section IV.B.3. Finally, the graph neural network (GNN) surrogate model's network architecture and associated training procedure is explained in Section IV.B.4.

1. Low-Fidelity Solver: Vortex Lattice Method

The vortex lattice method models flow over an aircraft as a lattice of bound vortices to solve for the local loading on each panel by computing the vortex strengths that satisfy the boundary condition of zero normal flow on panels. In this study, a Python-based implementation of the `VORLAX` code [26], shipped with the `SUAVE` package [22, 51], is utilized. This VLM uses infinitesimally thin, cambered or uncambered panels to represent the base geometry, and is applicable to "compressibility-corrected," inviscid, attached flows for both subsonic and supersonic conditions.

The computation of the local loading coefficient (ΔC_p), which is a normalized pressure difference between the lower and upper surfaces of a wing, begins with solving the linear system of filament vortex strength (Γ_i), geometric relationship among the lattice, and the boundary conditions of an oncoming flow:

$$AIC\,\mathbf{\Gamma} = RHS, \tag{49}$$

where Γ a vector of the vortex filament strength, AIC is the aerodynamic influence coefficient matrix representing the induced velocity contributions from each vortex filaments to each panel's control points, and RHS represents the free-stream flow contributions to the boundary conditions.

Once Γ is solved, the local induced velocities u and v can be solved using the Biot-Savart Law. The local loading coefficient is thus:

$$C_p = -\frac{2}{q_\infty^2}(U_\infty u + V_\infty v), \tag{50}$$

where U_∞ and V_∞ are the components of the free-stream velocity vector of magnitude q_∞, and u and v are the induced velocity components. C_p is the field pressure coefficient ($C_p = (P - P_\infty)/q_\infty$). In our study, we use infinitesimally thin panels, such that the pressure difference between the lower and upper wing surfaces, ΔC_p, is the C_p computed from Equation 50. In the current study, we take this ΔC_p as the pressure field predicted by LF method.

Total lift and induced drag can then be calculated by summing up all panels' contribution. The details of the VLM implementation, along with leading edge suction correction methods for Delta wing aircraft, can be found in the original `VORLAX` technical report [26].

2. High-Fidelity Solver: Computational Fluid Dynamics

`SU2` is a computational fluid dynamics (CFD) software used for the solution of partial differential equations (PDEs) and PDE-constrained optimization problems on unstructured numerical grids [31, 32, 10]. To simulate compressible flows, `SU2` solves the Navier-Stokes equations expressed in differential form as

$$\mathcal{R}(U) = \frac{\partial U}{\partial t} + \nabla \cdot \bar{F}^c(U) - \nabla \cdot \bar{F}^v(U, \nabla U) - S = 0. \tag{51}$$

The vector of conserved variables, U, can be expressed as

$$U = [\rho, \rho\bar{v}, \rho E]^\mathsf{T} \tag{52}$$

,

where ρ is the fluid density, $\bar{v} = [u, v, w]^\mathsf{T}$ is the flow speed in Cartesian system of reference, E is total energy per unit mass, and S is a generic source term (zero in the absence of external body forces). The convective and viscous fluxes are given by

$$\bar{F}^c = \begin{bmatrix} \rho\bar{v} \\ \rho\bar{v} \otimes \bar{v} + \bar{\bar{I}}p \\ \rho E\bar{v} + p\bar{v} \end{bmatrix} \tag{53}$$

and

$$\bar{F}^v = \begin{bmatrix} . \\ \bar{\bar{\tau}} \\ \bar{\bar{\tau}} \cdot \bar{v} + \kappa\nabla T \end{bmatrix} \tag{54}$$

respectively, where p is the static pressure, $\bar{\bar{\tau}}$ is the viscous stress tensor, T is the temperature, κ is the thermal conductivity, and μ is the viscosity. The viscous stress tensor can be expressed in vector notation as

$$\bar{\bar{\tau}} = \mu\left(\nabla\bar{v} + \nabla\bar{v}^T\right) - \mu\frac{2}{3}\bar{\bar{I}}\left(\nabla \cdot \bar{v}\right). \tag{55}$$

For a perfect gas with gas constant R and constant specific heat ratio γ, the ideal gas equation of state can be used to determine the pressure and temperature as $p = (\gamma - 1)\rho\left[E - 0.5(\bar{v} \cdot \bar{v})\right]$ and $T = p/(\rho R)$, respectively. Laminar viscosity, μ, is calculated using Sutherland's law and thermal conductivity can be computed as $\kappa = \mu c_p/Pr$, where c_p is the specific heat capacity at constant pressure and Pr is the Prandtl number, or set to a constant value. Steady, turbulent flows can be simulated in `SU2` by solving the Reynolds-averaged Navier-Stokes (RANS) equations. In accordance with the Boussinesq hypothesis, the effective viscosity can be computed as the sum of the laminar (dynamic) viscosity and turbulent viscosity as

$$\mu = \mu_d + \mu_t, \tag{56}$$

where the prediction of μ_t is dependent on the particular choice of turbulence model used. In this work, the one-equation Spalart-Allmaras turbulence model with Rotation/Curvature correction is used to solve for the value of the turbulent viscosity [45, 43]. The turbulence model is selected to achieve a balance between the computational cost and adequate vortex effects quantification accuracy, as discussed in a previous study by Seraj and Martins [39]. All simulations employ the Jameson-Schmidt-Turkel scheme for convective discretization [16] and implicit time integration with an adaptive Courant–Friedrichs–Lewy number to converge the steady-state solution. The vehicle boundary condition is specified by a no-slip, adiabatic wall, and a characteristic-based free-stream is used for the far-field boundary. A Cauchy convergence criteria is used, such that the solver stops when the change in C_D for the wing over the previous

100 iterations becomes less than 1×10^{-4}.

3. Dataset

Dataset Overview

The dataset for surrogate model training and testing consists of 15 3-D Delta wing geometries at two levels of fidelity. The HF surface pressure field data is generated using the `SU2` CFD solver to simulate the steady-state aerodynamics with a RANS solver as described in Section IV.B.2. The flow domain is discretized using `Pointwise`'s automatic unstructured volume mesh capability [34]. The outer mold line of each underlying geometry is accurately captured by enforcing a maximum surface mesh-to-geometry deviation of less than 1×10^{-5} [m]. Across all geometries, identical mesh property definitions are used to ensure consistency in global mesh properties and boundary conditions, including the T-Rex boundary layer mesh growth profile, leveraging `Pointwise`'s scripting capability. Due to variations in surface body geometry, the total number of elements in the fluid domain ranges from 4.89 to 19.47 million. The resultant mesh achieves $y^+ < 1$ for most parts of each wing, except near the wing tips at the trailing edge, satisfying the turbulence model's y^+ requirements.

The LF data is generated using the VLM implementation in `SUAVE`. For all geometries, a 30×30 lattice discretization is applied in the chord-wise and span-wise directions. The lattice is evenly distributed in the chord-wise direction and follows a cosine distribution in the span-wise direction.

The 15 Delta wing geometries are parameterized using two design variables: leading edge sweep angle and root airfoil shape. The leading edge sweep angles used in this study are 55°, 65°, and 75°. Across all geometries, the root chord length is kept constant at 0.65 [m], resulting in variations in span and reference area of the Delta wing. The root airfoil shapes are taken from NACA 4-digit airfoils, and in this study, NACA0010, NACA0016, NACA0024, NACA2416, and NACA4416 are used. All 15 combinations of the root airfoil shape and leading edge sweep angle are generated using `SUAVE`.

Each geometry is then simulated under 40 different free-stream conditions, varying AOA, Mach number (Ma), and Reynolds number (Re). The AOA is sampled from 0° to 20°, the Ma from 0.35 to 0.5, and the Re from 6.5×10^6 to 1×10^7. A LHS technique is used to generate samples across the three free-stream variables. It is worth noting that the LF VLM simulation does not utilize the Reynolds number in its simulation. In total, 600 test samples are generated across the geometry design space and the free-stream variable space.

The dataset is generated on the Sherlock Cluster at the Stanford Research Computing Center (SRCC), utilizing a 64-core 2.4 GHz partition.

Dataset Preparation

The HF and LF datasets differ significantly in their dimensions. While the LF data resides in $\mathbb{R}^{30\times30}$, the HF data dimension is defined by the number of surface mesh nodes, which varies based on the geometry. Although GNN-based

architectures can accommodate mapping between these different graph structures, training such surrogate models can be computationally expensive and is not the focus of this work.

In this study, the goal is to demonstrate the capability of utilizing such architectures to build surrogate models that enhance conceptual vehicle design at a relatively low computational cost. To achieve this, the authors decided to standardize the HF and LF graphs. One approach is to project the HF surface pressure field onto the lattice panels defined in the VLM. As VLM computes the local loading coefficient $\Delta C_p^{LF} = C_{p,\text{lower}} - C_{p,\text{upper}}$, it was decided that the standardization step for the HF data should project the surface pressure onto the lattice panels to generate the HF local loading coefficient, ΔC_p^{HF}. This process is described by the following equations:

$$\Delta C_p^{HF} = C_{p,\text{lower}}^{HF} - C_{p,\text{upper}}^{HF}, \tag{57}$$

where C_p^{HF} is a vector in $\mathbb{R}^{30x30}$. The pressure coefficient for each side can be calculated by:

$$C_{p,\text{side}}^{HF} = \frac{1}{q_\text{ref}} \left[\frac{\sum_{i \in \mathcal{I}} \delta_\text{side}(i) P_i A_i}{\sum_{i \in \mathcal{I}} \delta_\text{side}(i) A_i} \right]_{\mathcal{I}=1}^{N}, \tag{58}$$

where P_i is the pressure, A_i is the cell area at HF node i, $\mathcal{I}$ is the set of all surface nodes whose (x_i, y_i) coordinates lie within the boundary of a lattice panel, indexed from 1 to N, under vertical projection, and q_ref is the reference pressure computed from free-stream conditions. $\delta_\text{side}(i)$ is an upper or lower surface selection mask that identifies whether a node belongs to the lower or upper surface based on its z_i coordinate (applicable for the root airfoils used in the current study). For example, the $\delta_\text{lower}(i)$ mask can be defined as:

$$\delta_\text{lower}(i) = \begin{cases} 1 & \text{if } z_i < 0, \\ 0 & \text{otherwise.} \end{cases} \tag{59}$$

Node and Edge Features

As discussed in Section IV.B.3, the VLM simulation is Reynolds number agnostic. To enrich the aerodynamic features used in the surrogate model, free-stream conditions, including free-stream AOA, Ma, and Re are incorporated alongside the local loading coefficient ΔC_p^{LF}. Because the proposed surrogate model is intended to augment aerodynamic prediction for design space exploration in conceptual design, it is essential to include geometric properties that influence aerodynamics in the surrogate model input. These geometric properties include wing thickness, surface curvatures, lattice panel control point coordinates, and surface slopes. All geometric features are defined and evaluated at the nodal level.

At the edge level, the Euclidean distance between nodes is used to represent nodal connectivity patterns and spatial relationships among nodes. For each node, the Euclidean distances to its four direct neighboring nodes are included in

the edge feature. The combination of nodal and edge features allows the `VortexNet` surrogate model to capture the spatial and aerodynamical information for aerodynamic characterization.

The nodal and edge features used by the `VortexNet` surrogate model, along with their intended purposes, are summarized in Table 4.

Feature Name	Dimension	Purpose
ΔC_p^{LF}	$[N_{\text{nodes}} \times 1]$	VLM local loading coefficient
AOA $[rad]$	$[N_{\text{nodes}} \times 1]$	free-stream AOA
Ma_∞	$[N_{\text{nodes}} \times 1]$	free-stream Mach number
Re_∞	$[N_{\text{nodes}} \times 1]$	free-stream Reynolds number
Thickness $[m]$	$[N_{\text{nodes}} \times 1]$	wing thickness at lattice panel control points
Upper Surface Curvature $[m^{-1}]$	$[N_{\text{nodes}} \times 1]$	wing upper surface curvature at lattice panel control points
Lower Surface Curvature $[m^{-1}]$	$[N_{\text{nodes}} \times 1]$	wing lower surface curvature at lattice panel control points
Upper surface slope	$[N_{\text{nodes}} \times 1]$	wing upper surface chord-wise slope at lattice panel control points
Lower surface slope	$[N_{\text{nodes}} \times 1]$	wing lower surface chord-wise slope at lattice panel control points
x_c $[m]$	$[N_{\text{nodes}} \times 1]$	lattice panel control points x-coordinates
y_c $[m]$	$[N_{\text{nodes}} \times 1]$	lattice panel control points y-coordinates
Euclidean distance $[m]$	$[4N_{\text{nodes}} \times 1]$	Euclidean distances from one lattice panel control points to its four direct neighbors'

Table 4 List of the nodal and edge features used by the `VortexNet`, along with their dimension and intended purposes.

Once these node and edge features are assembled, a Hyperbolic Tangent (Tanh) standardization [36] is performed for each feature to scale and normalize all feature values to a range between -1 and 1. After these dataset preparation steps, the LF graph and HF training label can be feed into the surrogate for training.

4. Surrogate Modeling

A MF surrogate model is used to establish a mapping function, $\mathcal{F}$, between the LF field variables q^{LF} into their HF counter part q^{HF}. In general, such a mapping can be expressed as

$$q^{HF} \sim \mathcal{F}\left(q^{LF}, \omega_{\mathcal{L}}\right), \tag{60}$$

where $\omega_{\mathcal{L}}$ represent the weights and biases of the network under a specific loss function $\mathcal{L}$. Such a mapping exists if the LF field variables q^{LF} exhibit a one-to-one correspondence with the HF field variables q^{HF}, a hypothesis that has not been tested in this study. To construct such a surrogate model, a GNN based U-net like ML autoencoder is used. The network architecture and the training pipeline are presented in detail in the following sections.

Machine Learning Architecture

A graph consists of a set of nodes and edges $G = (V, E)$, where $V = \{1, ..., n\}$ is a set of nodes and E is a set of edges between nodes $i, j \in V$. A GNN is thus a model that performs machine learning on graphs to incorporate information about the structure of the graph to understand the relationship among nodes and edges [14]. This capability is classified into three prediction tasks: node, edge, and graph predictions. The node prediction capability is of particular interest to the authors, as this type of prediction uses graph information to generate predictions on nodal values through message passing rounds. In each message passing round, each node updates its nodal embedding using information aggregated from its neighbors' embeddings. This type of prediction integrates well with mesh-based simulations, such as VLM or RANS solvers used in this study, as the simulation results' data structure can be easily represented by a graph G [56, 52].

Recently, multiple studies have leveraged GNN architectures to predict physical fields, including across varying fidelities. Pfaff et al. proposed `MeshGraphNets`, which use message-passing mechanisms to learn mesh-based simulation with noticeable efficiency and accuracy for both static and dynamic systems [33]. Their paper also highlighted the capability of `MeshGraphNets` to be discretization independent by training on highly irregular grids. This feature is desirable for the surrogate modeling task in this paper, as the surrogate model must not be sensitive to spatial discretization changes, such as mesh morphing and mesh topology changes, caused by geometry variation in the MDO cycle. Shao et al. proposed an auto-encoder GNN surrogate called `PIGNN-CFD` for rapid prediction of urban wind fields based on irregular unstructured mesh data from CFD simulations [40]. In their work, they added the Reynolds stress tensor residual to the loss function, thereby implicitly building physical constraints into the surrogate model. When applied to multi-scale and multi-fidelity applications, U-net [13] types of architectures are commonly used. Deshpande, Bordas, and Lengiewicz, Yang, Vinuesa, and Kang, and Wei and Freris demonstrated the effectiveness of U-net type GNNs in physical simulations, particularly in the domains of finite element method (FEM)-based structural simulations and smooth particle hydrodynamics (SPH)-based fluid simulations [9, 53, 50]. Their work highlighted the superior performance of graph U-Nets in multi-scale representation learning, accommodating unstructured mesh data, modeling long-range interactions, and being mesh topology-agnostic. Finally, Liu et al. used a graph attention network [47]-based surrogate for fluid simulations and found that the attention mechanism helps describing physical relationships among graph nodes. This mechanism enables the network to learn from different representation subspaces, significantly enhancing its aggregation capability compared to traditional GNNs and allowing it to capture more complex fluid patterns [21].

The `VortexNet` network proposed in this paper has an architecture inspired by the aforementioned works. Specifically, it utilizes a multi-head message aggregation and passing layer using Graph Attention Network v2 (`GATv2`) [5] and incorporates U-net type skip connections between encoders and decoders [13]. The use of multi-head attention enables the network to attend to richer feature subspaces by concurrently building multiple regression models between certain node to its neighbors, thereby enhancing its feature-capturing capability. Additionally, as the network may require multiple layers of message aggregation and passing, U-net type skip connections are employed to short-circuit deep

encoders, improving the network's efficiency in capturing low-frequency features. Overall, the network is designed to handle graph sizes typically used in VLM simulations, which contain hundreds to thousands of nodes. It aims to capture nonlinear flow patterns in RANS simulations and augment VLM results, providing a tool to increase design fidelity during the conceptual design phase.

Figure 41 provides a high-level schematic illustration of the proposed `VortexNet` network. In this figure, the computational graph before and after each major block is shown in black boxes. The graph consists of 4 nodes, arranged in a Delta wing layout, and 5 black solid lines connecting them represent edges in the graph. The authors want to emphasize that the edges and nodes shown here are just for illustration purposes and do not represent the actual graph topology of the input data. The purple vectors (represented by purple boxes) beside each node are the corresponding nodal feature arrays, and the yellow vectors (represented by yellow boxes) beside each edge are the edge feature arrays. As the graph passes through the network, the nodal feature array and edge array may change sizes, which is indicated by the lengthening or shortening of the boxes representing the array. Hence, each individual graph in the boxes represents a snapshot of the graph's status. In this chart, a black arrow indicates a direct connection among stages, and a blue arrow represents a U-net type skip connection that will be explained in the following sections.

The input graph first goes through an Input Encoder, which maps the input features to a latent dimension. The encoded graph then goes through a series of Convolutional Blocks. These blocks use multi-head attention mechanisms, and hence the feature array size may be multiplied by the number of heads. In this network, the first half of the Convolutional Blocks serves as the encoder, and the second half of the Convolutional Blocks serves as the decoder. The decoder blocks receive information from both their previous blocks and the graph information passed on by skip connections. Finally, an Output Decoder, which utilizes an architecture similar to the Convolutional Block but with optional fully connected layers to adjust the output dimension, is used to produce nodal predictions for a field value of interest, such as pressure or velocity fields. The following sections describe the key components of `VortexNet`.

Input Encoders

The Input Encoder comprises two components: a node encoder and an edge encoder. The objective of including this input encoder is to enrich the input nodal features and edge features. Such enrichment is needed because the nodal feature array usually has limited dimension. For example, in the current work, an 11-dimensional nodal feature array is used. Similarly, the edge feature array only contains the distance between connected nodes. Hence, a feature encoding to expand the input feature array to higher dimensional space is beneficial for the latter stage of the Convolutional Blocks, where latent relationship will be identified. A linear transformation is used for both the node encoder and the edge encoder, such that

$$\mathbf{h}_i^{'} = \mathbf{W}_n \mathbf{h}_i + \mathbf{b}_n, \tag{61}$$

where $\mathbf{h}_i^{'}$ is the encoded feature, $\mathbf{h}_i$ is the input feature, $\mathbf{W}_n$ are the learnable weights and $\mathbf{b}_n$ are the learnable

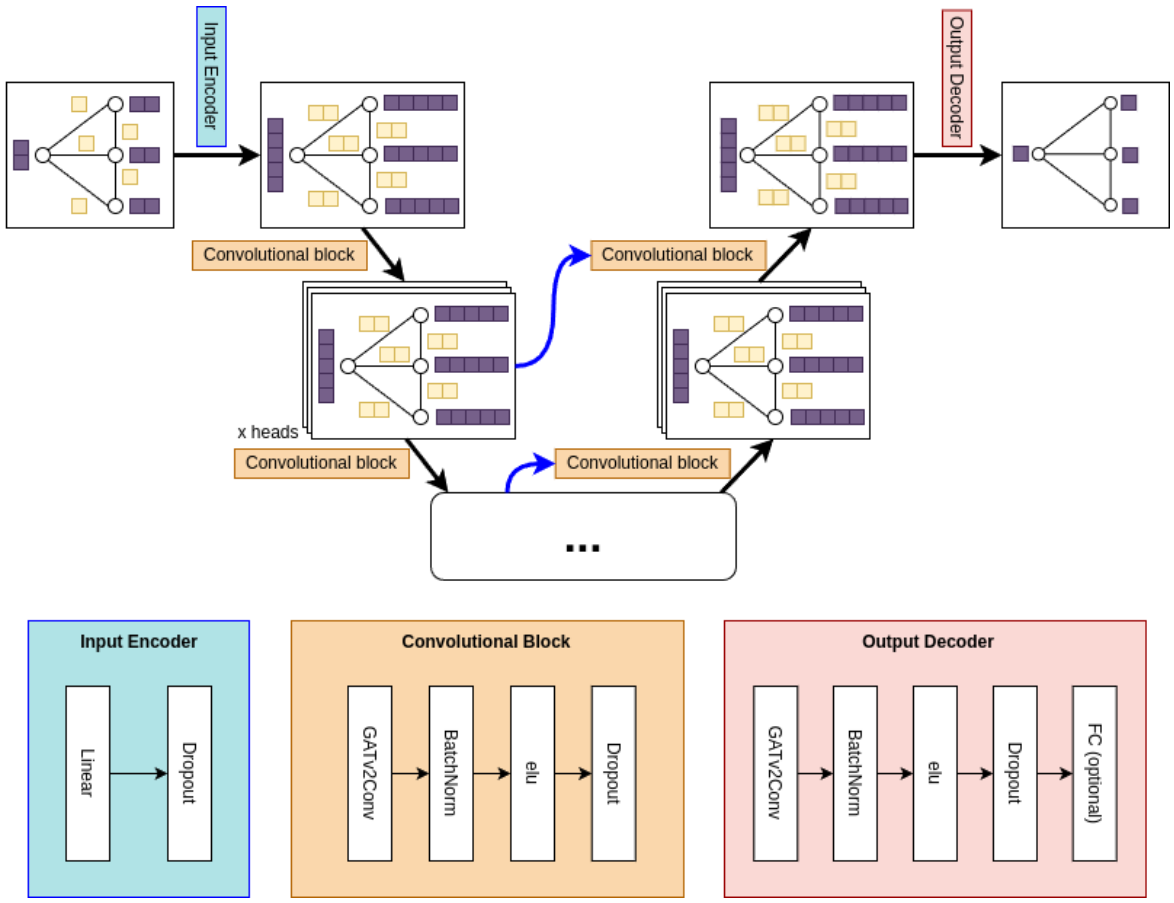

Fig. 41 Schematic of the proposed `VortexNet` graph neural network (GNN) architecture. Colors indicate different network blocks. A black arrow indicates represents direct message passing between blocks, and a blue arrow denotes a skip connection to the receiving block. The figure also presents snapshots of the graph at each computational step, showing nodes, edges, and their associated feature arrays.

bias. The node encoder encodes nodal feature to a dimension of [`hidden_feature` × `hidden_feature`], with `hidden_feature` being a hyper-parameter used by `VortexNet`, and the edge encoder encodes edge feature to a dimension of `hidden_feature`. After the linear layer, a dropout layer is used for the node feature array.

Convolutional Block

In each Convolutional Block, the primary mechanism for updating node features based on graph structure is by using `GATv2Conv` layers [5]. Specifically, the `GATv2Conv` computes a weighted average of the transformed featured of the neighborhood nodes for each nodes, expressed as,

$$\mathbf{h}_i^{'} = \sigma\left(\sum_{j \in \mathcal{N}_i} \alpha_{ij} \mathbf{W}\mathbf{h}_j\right), \tag{62}$$

where $\mathbf{h}_i^{'}$ is the new feature representation at node i, $\mathcal{N}_i$ is the set of neighboring nodes connected to node i by direct edges, α_{ij} and $\mathbf{W}$ are the learned weights, $\mathbf{h}_j$ is the input feature array at node j, and σ is an activation function. The

attention weights α_{ij} indicate the importance of node j's features to node i and allow every node to attend to every other node connected by the graph, thereby effectively disregarding the structural information of the graph [47]. This property can help the convolution block to behave in a mesh-discretization-independent manner when the node and edge features are designed properly. The actual attention function is defined as:

$$\alpha_{ij} = \text{softmax}_j\left(e(\mathbf{h}_i, \mathbf{h}_j)\right) = \text{softmax}_j\left(\mathbf{a}^T \text{LeakyReLU}(W \cdot [\mathbf{h}_i][\mathbf{h}_j])\right), \tag{63}$$

where $e(\mathbf{h}_i, \mathbf{h}_j)$ is the feature importance score of neighbor j to node i, $\mathbf{a}$ is a learned weights.

The `PyTorch` `GATv2Conv` layer employs multiple attention heads that allow the model to attend to information from different representation subspaces. In the multi-head attention scenario, multiple independent attention mechanisms execute the transformation of Equation 62, and then the resulting feature array $\mathbf{h}_i^{'}$ is concatenated.

Utilizing this `GATv2Conv` layer, the Convolution Block consists of one `GATv2Conv` layer that maps the input graph with a nodal feature array in $\mathbb{R}^{\mathbb{F}}$, where $\mathbb{F}$ is defined by the hyper-parameter `hidden_feature`, to a nodal feature array in $\mathbb{R}^{\mathbb{F}\times\texttt{heads}}$ after concatenation. Additionally, `heads` is a hyper-parameter specifying the number of heads. The input-output dimension is consistent across all layers except for the first Convolution Block after the Input Encoder, where the input feature dimension is $\mathbb{R}^{\mathbb{F}\times\mathbb{F}}$. After the `GATv2Conv` layer, the feature passes through batch normalization, an exponential linear unit (elu) activation function, and a dropout regularization layer. The dropout layer includes a tunable hyper-parameter named `dropout_rate`.

In the `VortexNet` architecture, the Convolutional Block is repeated (`hops` $-$ 1) times, where `[hops]` is a tunable hyper-parameter. It is worth noting that in many previous graph U-net-like architectures, pooling layers are used to successively reduce the computational graph size in deeper encoder layers [9, 53, 50]. However, such pooling layers are not used in the current network because the implications of using these methods remain uncertain to the authors during this work. Moreover, the removal of pooling layers reduces the size of the network architecture's hyper-parameter search space. A discussion on the implication of including pooling layers to the `VortexNet` architecture is presented in the Results section IV.C.

Output Decoder

The Output Decoder's major role is to map latent space features to the desired output dimension. This block contains layers identical to those used in a Convolution Block, except that the `GATv2Conv` layer now maps the feature array from $\mathbb{R}^{\mathbb{F}\times\texttt{heads}}$ to $\mathbb{R}^1$. An optional fully connected (FC) layer is appended at the end of this block to enable graph size adjustment for the final output. In the context of this work, since the input graph and training labels have identical graph sizes, this fully connected layer is not used.

Although edge features can be extracted after the Output Decoder block, they are discarded. Consequently, the Output Decoder provides scalar value predictions for each node, which represent the field value predictions that mimic

the HF training labels.

Skip Connections

The skip connection is marked by the blue curvy arrow in Figure 41. For the i^{th} Convolutional Block, its output is connected to the $(\texttt{hops} - i - 1)^{th}$ block's input. Thus, the first encoder block's output is skip-connected to the Output Decoder, the second encoder block's output is connected to the last decoder block, and so on. As the latent space dimension remains consistent across all these encoder-decoder blocks, these skip connections do not require dimension adjustments.

A skip connection weight hyper-parameter, denoted as `Alpha`, is used to control the amount of skip connection information that the subsequent decoder utilizes, such that the feature array $\mathbf{h}_i$ seen by the decoder is

$$\mathbf{h}_i = \mathrm{A}\mathbf{h}_{i,\text{skip connection}} + (1 - \mathrm{A})\mathbf{h}_{i,\text{previous block}}. \tag{64}$$

5. Training

The prediction accuracy of `VortexNet` relies heavily on the training scheme. Throughout experiments, it has been observed that a training scheme with a combination of learning rate scheduling, regularization techniques, and physical loss terms helps `VortexNet` to achieve higher prediction accuracy. The following sections discuss the training scheme used in this work.

K-fold Cross Validation

The entire dataset, as described in Section IV.B.3, is randomly partitioned into a 30% − 70% test-training split. For network training, only the training set is exposed to the `VortexNet`, while the test set is reserved for performance characterization. The training set is further randomly partitioned into four batches. In each fold of the k-fold training, one batch of the training set serves as the cross-validation set, such that the model prediction loss on this set drives the optimization of the model weights, while the remaining subsets serve as the training data. This technique exposes the model to diverse data distributions and prevents overfitting to specific cross-validation subsets [2].

In standard k-fold cross-validation training, the models trained in each fold are independent. After completing training across all k folds, a voting algorithm is typically employed to select the best-performing model among the folds, or a weighting algorithm is used to combine the trained models across folds.

In the current study, we applied the k-fold cross-validation training but made minor adjustments to the model voting mechanism. Instead of training mutually independent models in each fold, our training script recycles the best model weights identified so far from all previous folds' training. Specifically, a register actively stores the best-performing model, as evaluated by the cross-validation loss, and in each fold training resumes from the current best model.

In using this training scheme, the cross-validation set in the later folds may overlap with the training data of previous folds, potentially inflating the model performance in later folds. However, this strategy was chosen for two reasons.

First, the size of the total training set is limited compared to the number of trainable weights in the `VortexNet`. Using standard k-fold training prohibits making a full use of the training set. Second, the way physical loss terms are used in training necessitates such model recycling, as discussed in the next section.

Loss Function

The loss function used in this study for both training and cross-validation is a compound loss defined as:

$$\mathcal{L} = \text{SmoothL1Loss}\left(q^{HF}, q^{\text{pred}}\right) + \Lambda \text{PhysicalLoss}\left(q^{\text{pred}}\right) + \Omega \text{SignLoss}\left(q^{HF}, q^{\text{pred}}\right), \tag{65}$$

where "SmoothL1Loss," "PhysicalLoss," and "SignLoss" are the three loss terms; q^{HF} is the high-fidelity data provided as training labels; $q^{\text{pred}} = \mathcal{F}\left(q^{\text{LF}}, w_{\mathcal{L}}\right)$ is the `VortexNet` predicted field output; Λ is the weight of the physical loss which is controlled by two hyper-parameters as described in Equation 69; and Ω is a hyper-parameter controlling the weight of the sign loss (`penalty_weight`). The "SmoothL1Loss" is well-documented in the `PyTorch` manual and will not be repeated here [37].

The "SignLoss" term penalizes sign mismatches between the predicted fields and the training labels. Specifically, it is defined as:

$$\text{SignLoss}(q, \hat{q}) = \frac{1}{N} \sum_{i=1}^{N} \left(\mathbf{1}\left(\text{sign}(q_i) \neq \text{sign}(\hat{q}_i)\right)\right), \tag{66}$$

where q and $\hat{q}$ are two arbitrary vectors with the same dimensions, N is the length of array q, and $\mathbf{1}$ is an indicator function that returns 1 if the statement is true and 0 otherwise. This loss term is introduced to address a limitation of the "SmoothL1Loss," which cannot differentiate between positively and negatively biased predictions. By incorporating the "SignLoss," the total loss equation can be adjusted to better handle sign errors, with its contribution controlled by the `[penalty_weight]` hyper-parameter.

Finally, the "PhysicalLoss" term is introduced to further improve the model's prediction capability. In designing surrogate models, two typical approaches are commonly employed: physics-driven and data-driven. In the physics-driven approach, the governing equations can either be embedded in the aggregation function or incorporated into the loss term. For surrogate models aimed at HF flow field prediction, the residuals of the Navier-Stokes equations at selected points are often used to drive the network convergence [11]. While accurate, such networks are computationally expensive to train. Alternatively, in the data-driven approach, the physical loss is omitted, making the network comparatively cheaper to train. However, this approach often suffers from high variance in prediction errors.

Considering that the proposed surrogate model is intended for conceptual design purposes, where trend-wise accuracy and delta values of QOIs are more critical than the absolute prediction accuracy, we aim to employ a lightweight physical constraint. This constraint helps calibrate the surrogate model predictions for trend-wise quality without adding significant complexity to the network architecture. In this study, we propose a physical loss term based on LF VLM

simulation to improve the network's trend-wise prediction quality. For non-linear flow features, such as flow separation, vortex breakdown, and vortex attachment phenomena in subsonic wings, the data-driven approach is used.

To compute the physical loss, recall that VLM solves the following linear equation:

$$AIC \cdot \Gamma = RHS, \tag{67}$$

where AIC is the aerodynamic influence coefficient matrix, Γ is the vortex strength, and RHS is the Neumann boundary condition for normal flow. The resolved vortex strength can then be used to calculate the total pressure coefficient difference, ΔC_p. When a surrogate model is used to predict $q^{\text{pred}} = \Delta C_p^{\text{pred}}$, this field can be passed backward through the stored lattice geometry information to compute the predicted vortex strength distribution, Γ^{pred}. The physical loss term can thus be expressed as a 2-norm of the residual:

$$\text{PhysicalLoss}(q^{\text{pred}}) = ||AIC \cdot \Gamma^{\text{pred}}(q^{\text{pred}}) - RHS||. \tag{68}$$

In the above physical loss computation, no real-time computation of the AIC and RHS matrices is required, as this information can be stored during the dataset assembly phase, thereby creating minimal overhead for network training.

When the physical loss weight Λ is large, the surrogate-predicted ΔC_p^{pred} will closely resemble the VLM results. However, this undermines the intent of using the surrogate model to map LF field data to HF field data. To address this, an exponential decay of the physical loss weight Λ is applied during the k-fold training. Initially, the model is trained to closely match the VLM solver. While the model kept the learned mapping, the physical constraint is gradually relaxed. Towards the final folds, the surrogate model's training convergence is primarily driven by data to capture the non-linear flow patterns present in HF simulations. The following equation is used to decay the physical loss weight across folds:

$$\Lambda_i = \Lambda^{\max} \exp\left(\frac{\Lambda^{\min}/\Lambda^{\max}}{k-1}(i-1)\right), \text{for } i \in \{1, ..., k\}, \tag{69}$$

where $\Lambda^{\max}$ is a hyper-parameter (`max_phys_loss`) representing the initial physical loss weight, $\Lambda^{\min}$ is a hyper-parameter (`min_phys_loss`) representing the final physical loss weight, and k is the number of folds in k-fold training.

Optimizer and Training Scheme

Optimization is carried out using the ADAM optimizer with an initial learning rate controlled by the hyper-parameter `learning_rate` and a decay rate specified by `decay_rate` [19]. A dynamic learning rate adjuster is implemented to halve the learning rate when the validation loss stops improving across training epochs. An early stopping scheduler is set such that if the model performance does not improve over the last 500 epochs, training for the current fold is terminated, and the best model trained so far is returned to reduce the risk of overfitting. For all nodal features, 2% random noise

is added to enhance the model's robustness. Throughout all training and model configurations, as determined by hyper-parameters, a batch size of 32 is used. Training is conducted on a NVIDIA A100 graphics processing unit (GPU).

C. Results

The results are organized as follows: First, the hyper-parameter optimization results are presented in Section IV.C.1, including insights into optimal network parameters identified during the study, as well as results on hyper-parameter sensitivities. Second, `VortexNet`'s prediction accuracy is evaluated using two tests. The first test reports the local loading coefficients (ΔC_p) prediction accuracy for test set, while the second test evaluates the surrogate model's generalizability on unseen geometries. These results are presented in Section IV.C.2. Third, we present a latent space ablation study to understand how the graph features are utilized across latent layers in Section IV.C.5.

1. Network Training and Hyper-Parameter Optimization

The surrogate model (`VortexNet`) described in Surrogate Modeling is trained using the dataset detailed in Dataset. Since the proposed surrogate model involves several training hyper-parameters, a hyper-parameter sensitivity study is conducted to provide inductive insights into the relationship between model performance and these hyper-parameters, as well as to offer guidance for optimizing surrogate models similar to the `VortexNet` in future studies. These hyper-parameters are defined in Surrogate Modeling, but for the convenience of readers, Table 5 summarizes the hyper-parameters included in this study.

Hyper-parameter Name	Value Range	Definitions
`hops`	int$[3, 20]$	total layers of Convolutional Block
`hidden_feature`	int$[3, 64]$	hidden layers feature width
`heads`	int$[2, 8]$	number of heads for multi-heads attention
`dropout_rate`	$[0.1, 0.5]$	dropout regularization weight
`Alpha`	$[0.0, 1.0]$	skip connection bandwidth
`penalty_weight`	$[1, 10] \times 10^{-2}$	sign loss weight
`max_phys_loss`	$[0, 0.5]$	maximum physical loss weight in Equation 69
`min_phys_loss`	$[1, 1000] \times 10^{-5}$	minimum physical loss weight in Equation 69
`learning_rate`	$[1, 100] \times 10^{-2}$	initial learning rate to the ADAM optimizer
`decay_rate`	$[1, 1000] \times 10^{-5}$	decay rate to the ADAM optimizer

Table 5 List of the hyper-parameters studied, along with their value range and definitions.

The hyper-parameter optimization study is conducted using `Optuna`, an open-source hyper-parameter optimization framework that automates hyper-parameter search using advanced sampling schemes and efficient pruning algorithms [1]. The hyper-parameters, along with their bounds listed in Table 5, define the search space, and `Optuna` automatically identifies the optimal hyper-parameter settings that minimize the model test loss on the test set. The model test loss is defined as the mean-square error (MSE) between the predicted ΔC_p^{pred} and the corresponding HF ΔC_p^{HF} across the

entire test set.

A total of 100 hyper-parameter configurations are generated in this study. The training time varies across configurations, but on average, each configuration takes 2.36 hours to train.

The average test loss across all hyper-parameter configurations is 9.55×10^{-2}, with a standard deviation of 4.85×10^{-2}. The average hyper-parameters across the 100 configurations are listed in Table 6 to provide a baseline for understanding the typical settings explored during the study. As the `Optuna` search spans a large hyper-parameter space, the test loss ranges from 3.99×10^{-2} to 0.246. This indicates that some combinations of hyper-parameters are sub-optimal for the prediction task.

Hyper-parameter Name	Average Value
`hops`	6.95
`hidden_feature`	42.88
`heads`	5.72
`dropout_rate`	1.82×10^{-1}
`Alpha`	2.58×10^{-1}
`penalty_weight`	2.23×10^{-2}
`max_phys_loss`	2.89×10^{-1}
`min_phys_loss`	1.99×10^{-3}
`learning_rate`	6.35×10^{-2}
`decay_rate`	3.56×10^{-4}

Table 6 Average hyper-parameter values from all hyper-parameter configurations under the optimization study.

Performing sensitivity analysis directly on the entire set of hyper-parameter samples is not ideal, as these sub-optimal parameter combinations would skew the sensitivity results. Instead, we use the K-means algorithm to cluster the 10-dimensional hyper-parameter space and perform the sensitivity study only on the subset of configurations that show consistently low test loss. Based on trial-and-error testing, the hyper-parameter configurations are clustered into five groups. To simplify the visualization of these clusters, principal component analysis (PCA) is employed to reduce the 10-dimensional parameter space to three dimensions. Figure 42(a) illustrates the clustering pattern with respect to the first two PCA axes. From these results, it is evident that cluster 3 outperforms the other clusters in terms of the test loss. This cluster is thus selected for the sensitivity study, and it is marked in green in Figure 42(b).

The selected best-performing cluster consists of 24 configurations, with an average test loss of 0.059. The average hyper-parameter values in this cluster are listed in Table 7. Comparing with the average values across the entire 100 test configurations in Table 6, the best-performing cluster uses a shallower network (less `hops`) with smaller latent feature size (less `hidden_feature`). The best-performing cluster also utilizes a more stringent enforcement on physical loss during the early epochs of training (higher `max_phys_loss`), but relaxed the physical loss constraint more towards the end of training (lower `min_phys_loss`).

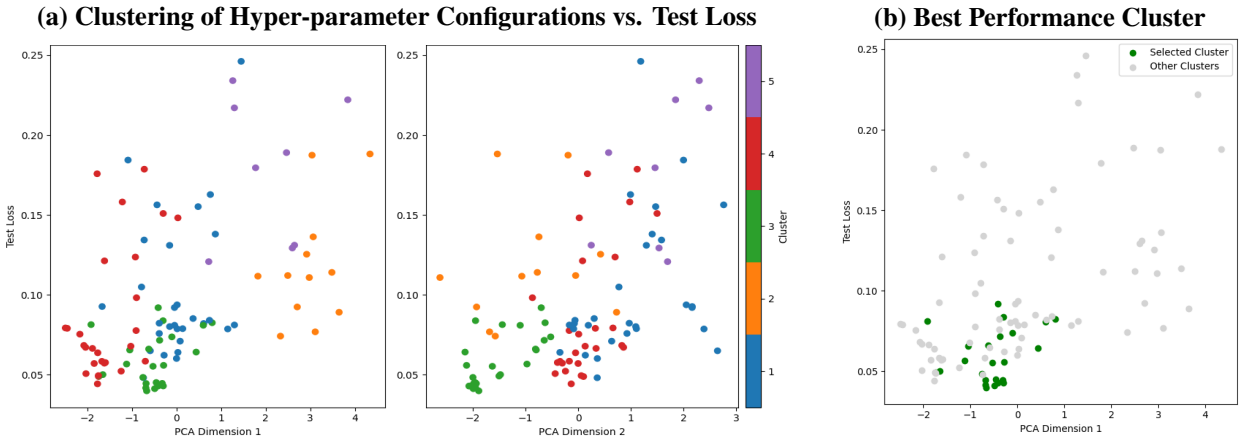

Fig. 42 Clustering results of hyper-parameter configurations based on test loss. (a) Hyper-parameter configurations K-means clusters visualized along the first two PCA axes. (b) The best-performing cluster (Cluster 3), identified based on consistently low test loss, is highlighted in green.

Hyper-parameter Name	Average Value
`hops`	4.83
`hidden_feature`	38.6
`heads`	6.86
`dropout_rate`	1.58×10^{-1}
`Alpha`	1.05×10^{-1}
`penalty_weight`	1.29×10^{-2}
`max_phys_loss`	4.25×10^{-1}
`min_phys_loss`	9.81×10^{-4}
`learning_rate`	1.73×10^{-2}
`decay_rate`	1.50×10^{-4}

Table 7 Average hyper-parameter values from the best-performing cluster.

A box chart summarizing the hyper-parameter configurations in this cluster is presented in Figure 43. As illustrated in the figure, most runs have a hidden feature size in the range of $[28, 46]$, use a 7-head attention mechanism, employ 4-hop convolutions, and have a skip connection bandwidth in the range of $[0.00761, 0.109]$. In this cluster, the spread of hyper-parameters such as `heads`, `hops`, `decay_rate`, `penalty_weight`, and `min_phys_loss` is relatively small, indicating that these hyper-parameters have converged toward optimal values in the best-performing cluster.

The model with the best performance across all 100 runs is also part of this cluster. The model has a test loss MSE of 0.0399, with hyper-parameters listed in Table 8. Comparing with the best performance cluster's average hyper-parameters, this specific model utilized a similar network but with much smaller skip connection bandwidth (smaller `Alpha`). This indicates that the best performance model's Convolutional Blocks mainly accept information from their preceding Convolutional Blocks, instead of receiving shallower features similar to that of a U-net architecture. This also indicates that although the `VortexNet` architecture is setup to be an autoencoder that has both the encoder

and the decoder components, the best performance model functions like an encoder only network. More details of the `VortexNet` explainability is provided in Prediction Explanations Section IV.C.5.

Hyper-parameter Name	Average Value
`hops`	4
`hidden_feature`	33
`heads`	7
`dropout_rate`	1.36×10^{-1}
`Alpha`	8.02×10^{-3}
`penalty_weight`	1.31×10^{-2}
`max_phys_loss`	4.64×10^{-1}
`min_phys_loss`	8.07×10^{-4}
`learning_rate`	1.91×10^{-2}
`decay_rate`	1.11×10^{-4}

Table 8 `VortexNet` hyper-parameters that lead to the lowest test loss.

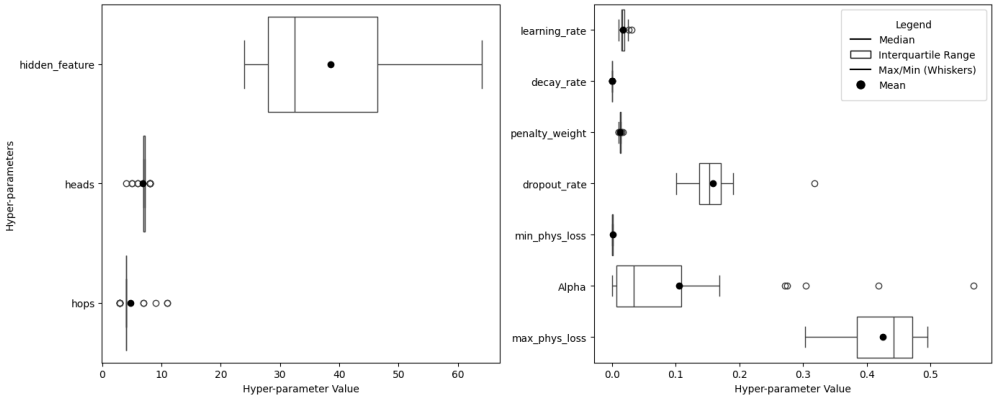

Fig. 43 Hyper-parameter statistics of the best-performing cluster.

For sensitivity analysis, one way to quantify the significance of input variables on a function's output value, such as the test loss in this study, is through variance-based methods like first-order Sobol' indices [44]. Such analysis is particularly suitable for non-linear functions such as the surrogate model in the present study, as the response of surrogate test loss to input hyper-parameters is inherently non-linear. However, this type of analysis is prohibitively expensive for the current study. One approach to reduce the computational cost of computing Sobol' indices is to use a surrogate model. This method, however, is also not applicable here because the size of the sample in the best-performing cluster is too small to train a surrogate model with adequate variance-capturing capability, as evaluated by the R^2 score.

As a result, the authors rely on linear sensitivity analysis to gain insights into the model's sensitivity to hyper-parameters. In linear sensitivity analysis, a linear regression model is applied to each hyper-parameter array after

standardizing it to a standard distribution. Consequently, the test loss can be modeled as a linear summation:

$$\mathcal{L}(X) = \sum_{i=0}^{N} \beta_i X_i, \tag{70}$$

where X_i represents a hyper-parameter array, $X_0 = 1$, N is the total number of hyper-parameters, and β_i is the corresponding linear coefficient [12]. The sensitivity of each hyper-parameter is then defined as:

$$\text{Sensitivity}(X_i) = \frac{|\beta_i|}{\sum_{j=0}^{N} |\beta_j|}. \tag{71}$$

Although this sensitivity definition does not capture the total variance, it provides an ad-hoc capability to explain the relative importance of one hyper-parameter compared to the others. The resultant sensitivities, along with the linear correlation coefficients, are presented in Figure 44.

(a) Hyper-parameters Sensitivity Index **(b) Hyper-parameters Linear Correlation**

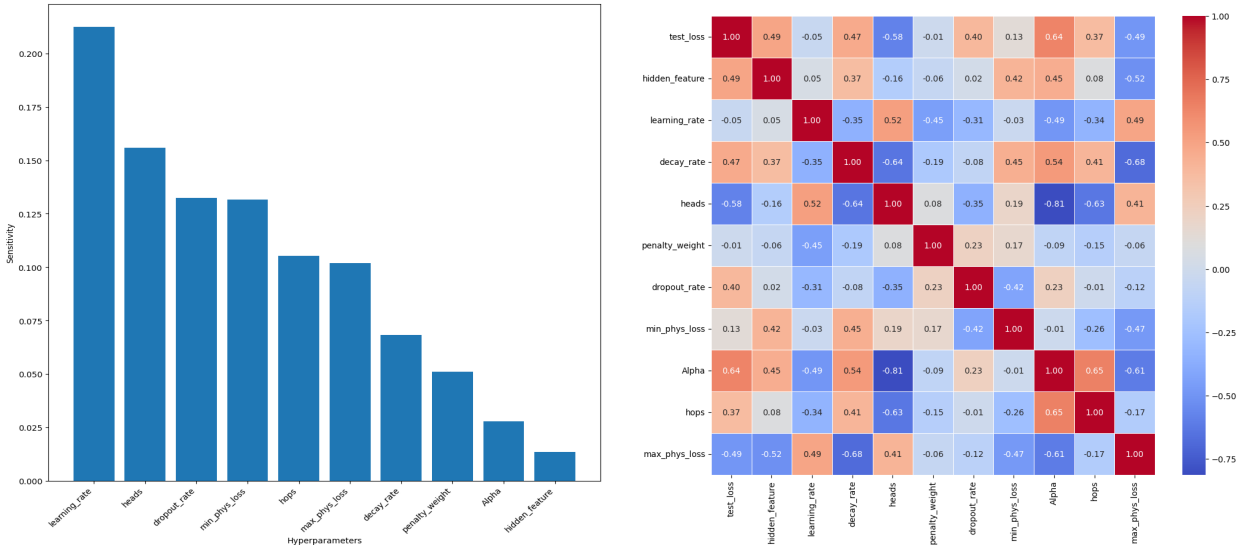

Fig. 44 Sensitivity index and correlation coefficients for hyper-parameters versus model performance in the best-performance cluster. (a) hyper-parameters sensitivity, and (b) hyper-parameters linear correlation.

For architecture hyper-parameters, it is identified that `heads`, `dropout_rate`, and `hops` have a significant impact on model prediction accuracy, while `hidden_feature` size and skip-connection weight `Alpha` have a minor impact. Among these, increasing `heads` leads to worse model performance, likely due to limitations in dataset size and allocated training resources, causing the model to become prone to high-variance errors. Conversely, increasing `hops` and `dropout_rate` improves model's performance. Considering the high sensitivity of these hyper-parameters, future studies should consider extending their ranges to include higher values. For `hidden_feature` and `Alpha`, although linear correlation studies indicate a positive correlation, their effects remain unclear due to their relatively low sensitivity

indices. A more extensive hyper-parameter search should be conducted for these parameters.

For training hyper-parameters, it is identified that `learning_rate`, `min_phys_loss`, and `max_phys_loss` have a significant impact on model performance, while `decay_rate` and `penalty_weight` do not. However, correlation studies reveal no linear relationship between `learning_rate` and test loss, likely because `learning_rate` is dependent on other training and model configuration parameters. Thus, fine-tuning of `learning_rate` should be conducted for future model training. It is also observed that a `max_phys_loss` value that is too large may negatively affect model performance. For `min_phys_loss`, in the best-performing model, the average physical loss on the validation set during the last folds of training is on the order of 40. A data loss-to-physical loss contribution ratio of $2.24 : 1$ is observed when the average physical loss is multiplied by its weight `min_phys_loss`. Finally, for `penalty_weight`, no significant impact is identified. This is likely because this loss component contributes minimally to the total loss, as the model becomes robust in predictions without violating sign constraints toward the end of training.

2. Aerodynamics Predictions

The main objective of this study is to develop a surrogate modeling technique that maps field data across different fidelities, thereby increasing fidelity in vehicle conceptual design without significantly raising costs. In this work, we focus on predicting local loading coefficients (ΔC_p). Aerodynamic coefficients can be obtained by integrating ΔC_p over panels, and we refer readers to Shen and Alonso for the aerodynamic coefficient results [41].

To evaluate the model's performance, we consider two distinct aspects. First, to gauge its prediction accuracy, we examine the root-mean-square error (RMSE) of the local loading coefficient (ΔC_p) field predictions ΔC_p^{pred} against the projected CFD references ΔC_p^{HF}, as outlined in Dataset. Second, to assess the model's generalizability and its potential for assisting in design space exploration, we evaluate its ΔC_p^{pred} RMSE against ΔC_p^{HF} using new geometries that were not exposed to the surrogate model during training. The following sections discuss these two assessments.

3. Local Loading Coefficients (ΔC_p) Prediction

The RMSEs for the training set, test set, and the entire dataset are 0.194 with an R^2 value of 0.838, 0.192 with an R^2 value of 0.841, and 0.193 with an R^2 value of 0.839, respectively. No significant difference between the test and training sets is observed and most variance in the dataset is captured by the trained model, indicating that the resultant model is well-trained.

To visualize the ΔC_p from the VLM, `VortexNet` predictions, and CFD references, a geometry configuration at high AOA was randomly selected. The selected Delta wing configuration features a leading edge sweep angle of 55° and a root airfoil of NACA2416. The free-stream conditions are AOA at 16.4°, Ma at 0.47, and a Re of 9.78×10^6. The corresponding CFD pressure coefficients (C_p) on the upper and lower wing surfaces are presented in Figure 45. The surface C_p exhibiting a "vortex lift" pattern: on the upper surface toward the wing outboard near the trailing edge,

suction effects induced by the separated vortex are evident.

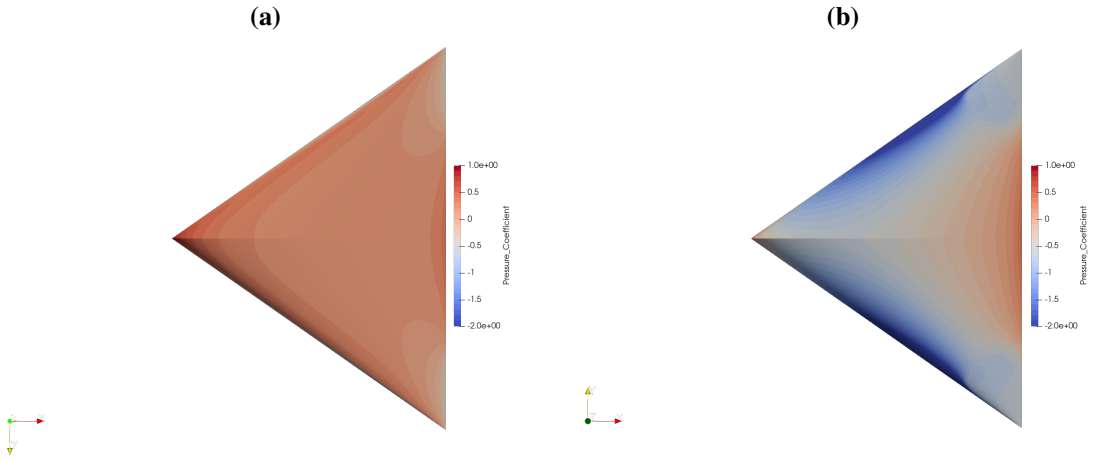

Fig. 45 The HF surface pressure coefficient obtained from CFD for a wing with 55° **leading edge sweep and root airfoil profile of NACA2416 at AOA**$= 16.4^\circ$**,** $M_a = 0.47$**, and** $R_e = 9.78 \times 10^6$**.**

The aforementioned C_p is then projected onto lattice panels. Figure 46(c) shows the projected ΔC_p^{HF}, which serves as the "ground-truth" reference. The projected pressure field preserves flow features from the CFD, including faint traces of vortex lift at the wing outboards. In Figure 46(a), the ΔC_p^{LF} computed from VLM is shown. This pressure field follows potential flow theory, and no vortex lift or flow separations are observed. The VLM pressure field serves as input to `VortexNet` as part of the nodal features.

Figure 46(b) shows the ΔC_p^{pred} predicted by `VortexNet`. Comparing these pressure fields, it is evident that the predicted pressure field exhibits strong visual similarity to the projected CFD pressure field, both in the predicted ΔC_p values and the overall pressure distribution. However, artifacts of spiky, high-frequency reconstruction error are noticeable near the wing apex and wing tips. These errors can arise from the network's inability to fully resolve the fine-scale features, a common challenge in surrogate modeling. Additionally, in the mid-chord central body, the ΔC_p^{pred} prediction does not fully align with the reference field ΔC_p^{HF}. Despite these discrepancies, the authors believe that the surrogate model's predictions provide higher fidelity than those of VLM, as it captures nonlinear flow features.

Although not shown, ΔC_p^{pred} predictions for other geometries and free-stream conditions follow a similar pattern, with `VortexNet`'s predictions appearing visually closer to the projected CFD fields (ΔC_p^{HF}) than to those of VLM (ΔC_p^{LF}).

To provide a more quantitative analysis of the ΔC_p prediction error, we compared the RMSE across all geometries in the test set. The corresponding values are presented in Table 9. The RMSE ranges from 0.117 to 0.275 in the observed dataset. On average, the RMSE is 0.189 with a standard deviation of 0.0442 across all geometries. Although geometries with a leading-edge sweep angle of 75° exhibit the largest average error, an analysis of variance (ANOVA) test reveals no significant statistical bias between sweep angle and the error, or between root airfoil shape and the error. However, it

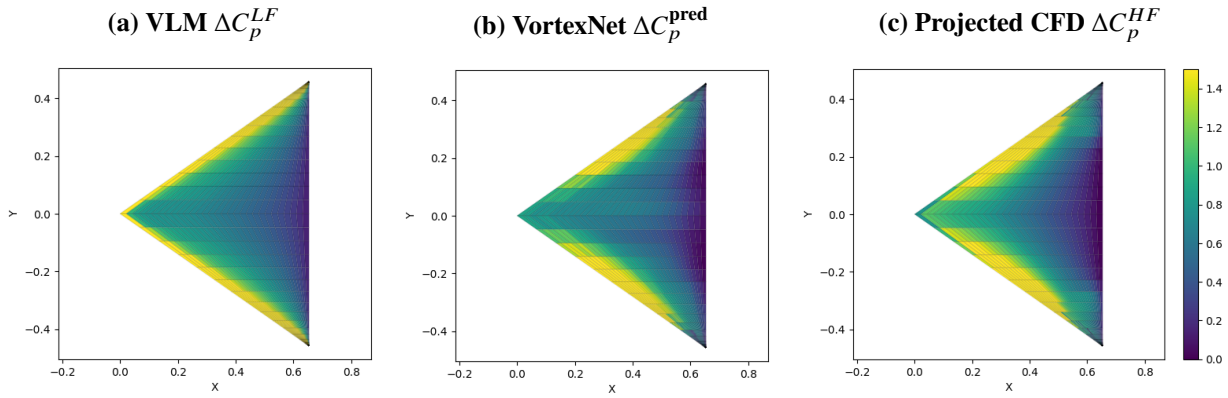

Fig. 46 Lattice panels and local loading coefficients ΔC_p are visualized using color maps ranging from $\Delta C_p = 0$ to $\Delta C_p = 1.5$, with (a) VLM ΔC_p^{LF}, also serving as the LF input, (b) `VortexNet` ΔC_p^{pred}, and (c) the reference HF ΔC_p^{HF} obtained by projecting the CFD surface pressure onto the lattice panels.

can be concluded that `VortexNet`'s prediction accuracy depends on the input geometries. For some geometries, the prediction quality is better than the others.

Sweep Angle [degrees]	**Root Airfoil (NACA 4-digits)**				
	0010	**0016**	**0024**	**2416**	**4416**
55	0.140	0.200	0.164	0.156	0.186
65	0.164	0.253	0.117	0.170	0.201
75	0.223	0.168	0.176	0.275	0.248

Table 9 Test set RMSE between ΔC_p^{pred} and ΔC_p^{HF}, grouped by wing geometries.

4. Aerodynamic Prediction for Unseen Geometries

One potential use case of the proposed `VortexNet` is to assist in design space exploration during conceptual design. In such applications, a design space is first defined by specifying a set of geometric parameters and their respective bounds. A coarse sampling of geometries across this design space is then generated for both HF and LF data querying, which is used to train the surrogate model. Subsequent design space exploration can rely on the surrogate model to provide quasi-high-fidelity aerodynamic evaluations. Consequently, it is essential to evaluate the proposed surrogate model's generalizability to geometries not included in the training dataset.

To study generalizability, we tested geometries and feature arrays not encountered by the network during training and evaluation. Four design points within the geometric parameter ranges of the training set's design space were selected. Specifically, we chose two leading-edge sweep angles (60° and 70°) and two root airfoils (NACA 0013 and NACA 3416). The 60° and 70° sweep angles can be viewed as intermediate values between the 55°, 65°, and 75° sweeps in the training set. The NACA 0013 airfoil is intermediate in thickness between NACA 0010 and NACA 0016, inducing a variation in

wing thickness, while the NACA 3416 airfoil lies between NACA 2416 and NACA 4416, inducing a camber variation. A combination of these design variables yields four new wing geometries: 60° NACA 0013, 60° NACA 3416, 70° NACA 0013, and 70° NACA 3416. Each geometry is then simulated under 11 different far-field conditions, with AOA, Mach number, and Reynolds number sampled using LHS. The sampling bounds for AOA, Ma, and Re are $[0°, 20°]$, $[0.35, 0.5]$, and $[6.5, 10] \times 10^6$, respectively, matching those used to construct the training set as discussed in Dataset.

The resulting RMSE are listed in Table 10. The maximum RMSE observed is 0.389 for the 70° Delta wing with the NACA 3416 airfoil, and the minimum RMSE is 0.185 for the 60° Delta wing with the NACA 0013 airfoil. On average, the RMSE is 0.288, representing a 52.3% (or 2.2 standard deviation) increase from the average RMSE reported in Table 9. Under this limited new-geometry dataset, by examining the RMSE correlation to the nature of geometry interpolation, we speculate that a camber variation in underlying geometry leads to greater prediction errors for `VortexNet` than those that originate from a thickness variation.

One way to interpret the individual RMSE values presented in Table 10 is to compare the error of a specific geometry against its neighboring design points from Table 9. For instance, the wing with a 60° leading-edge sweep and a NACA 0013 airfoil has four neighbors in Table 9: 55° NACA 0010, 65° NACA 0010, 55° NACA 0016, and 65° NACA 0016. The average RMSE for these four neighbors is 0.189 with a standard deviation of 0.0491. A comparison of the RMSE of 60° NACA 0013 with its neighbors reveals no significant RMSE variation induced by interpolating among these geometries as the RMSE for new geometry (0.185) is within plus-minus two standard deviations to its neighbors' average RMSE (0.189 ± 0.0983).

Applying a similar argument to the 70° NACA 0013, 60° NACA 3416, and 70° NACA 3416 wings, we find that the RMSE for the 70° NACA 0013 configuration does not significantly differ from reference values in the test set reported in Table 9. However, for the two wings with the NACA 3416 airfoil, both deviate significantly in RMSE relative to their neighboring design points. Within this limited geometry variation test, we also do not observe a strong dependence of RMSE on sweep angle variations. These results support our speculation that a camber variation may introduce larger prediction errors, while overall `VortexNet` maintains moderate generalizability when presented with unseen geometries, as evidenced by the consistent prediction accuracy for the 60° and 70° NACA 0013 wings.

The exact nature of the prediction accuracy variation across the design space is a topic for future investigation. First, a larger unseen geometry test set is needed to examine the model's prediction accuracy more thoroughly and confirm whether these deviations are persistent. Second, the discrepancy could be due to insufficient training samples provided with camber variations. Expanding the design space coverage to include more camber shapes in the `VortexNet` training set may help reduce prediction errors. Finally, panel distribution used in VLM may need improvements. Currently, even chord-wise spacing is used, and this spacing scheme may be inadequate for capturing surface curvature variations, particularly near the leading and trailing edges.

A qualitative study was also conducted by visually examining the resulting ΔC_p^{pred} fields with reference to VLM and

Sweep Angle [degrees]	Root Airfoil (NACA 4-digits)	
	0013	**3416**
60	0.185	0.323
70	0.257	0.389

Table 10 `VortexNet` prediction RMSE for each new geometries.

CFD ΔC_p results. For comparison across geometries, we present the ΔC_p for all geometries at AOA of 18°, Ma of 0.4 and Re of 7×10^6. The results are presented in Figure 47.

When comparing `VortexNet`'s prediction accuracy to the results shown in Figure 46, we observe that for previously unseen geometries, the surrogate model introduces more artifacts in its predictions. For the 70° NACA 0013 configuration, the surrogate model fails to accurately capture the highest ΔC_p values. Small wavelength artifacts of high- and low-pressure variation can be seen for 70° geometries along the chord at half span y-location ($y/b = 0.5$). Nevertheless, when considered alongside other fidelity methods, `VortexNet` still demonstrates intermediate capability between VLM and CFD in capturing flow features. The authors believe that by refining the surrogate model architecture, discussed in Section Prediction Explanations, and improving the training data sampling scheme, the model's generalizability can be further enhanced.

5. Prediction Explanations

While the proposed `VortexNet` demonstrates strong prediction accuracy and generalizability, the underlying mechanism by which the GNN leverages and aggregates input graph features remains unclear. The complexity of GNNs makes extracting human-intelligible explanations from trained networks challenging [54]. Nevertheless, the authors have conducted a preliminary analysis of the `VortexNet`'s latent space. This section aims to understand how input graph features are utilized across latent layers and provide guidance for refining future `VortexNet`-like GNN architectures.

Among various methods for latent space analysis, we performed an ablation study on latent space features to investigate the resultant ΔC_p predictions. The best-performing model, as discussed in Section IV.C.1, was used. For the data sample, we selected a run with a 55-degree sweep, NACA2416 root airfoil, $M_a = 0.47$, and $Re = 9.78 \times 10^6$ (the same case shown in Figure 46). The study begins with the latent space after the first Convolutional Block in Figure 41. At this stage, the nodal feature array was recorded, and clustering was performed on the feature array. Since the node features exist in a high-dimensional space ($\mathbb{R}^{\mathbb{F} \times \texttt{heads}}$), the t-SNE dimensionality reduction technique was applied to project the feature space to two dimensions [46]. K-means clustering was then used to classify nodes into four clusters [23], and their corresponding nodal indices were recorded.

The ablation study involves recursively isolating the contribution of each cluster by zeroing out nodal feature arrays belonging to other clusters at the current layer. This operation is repeated across all Convolutional Block layers.

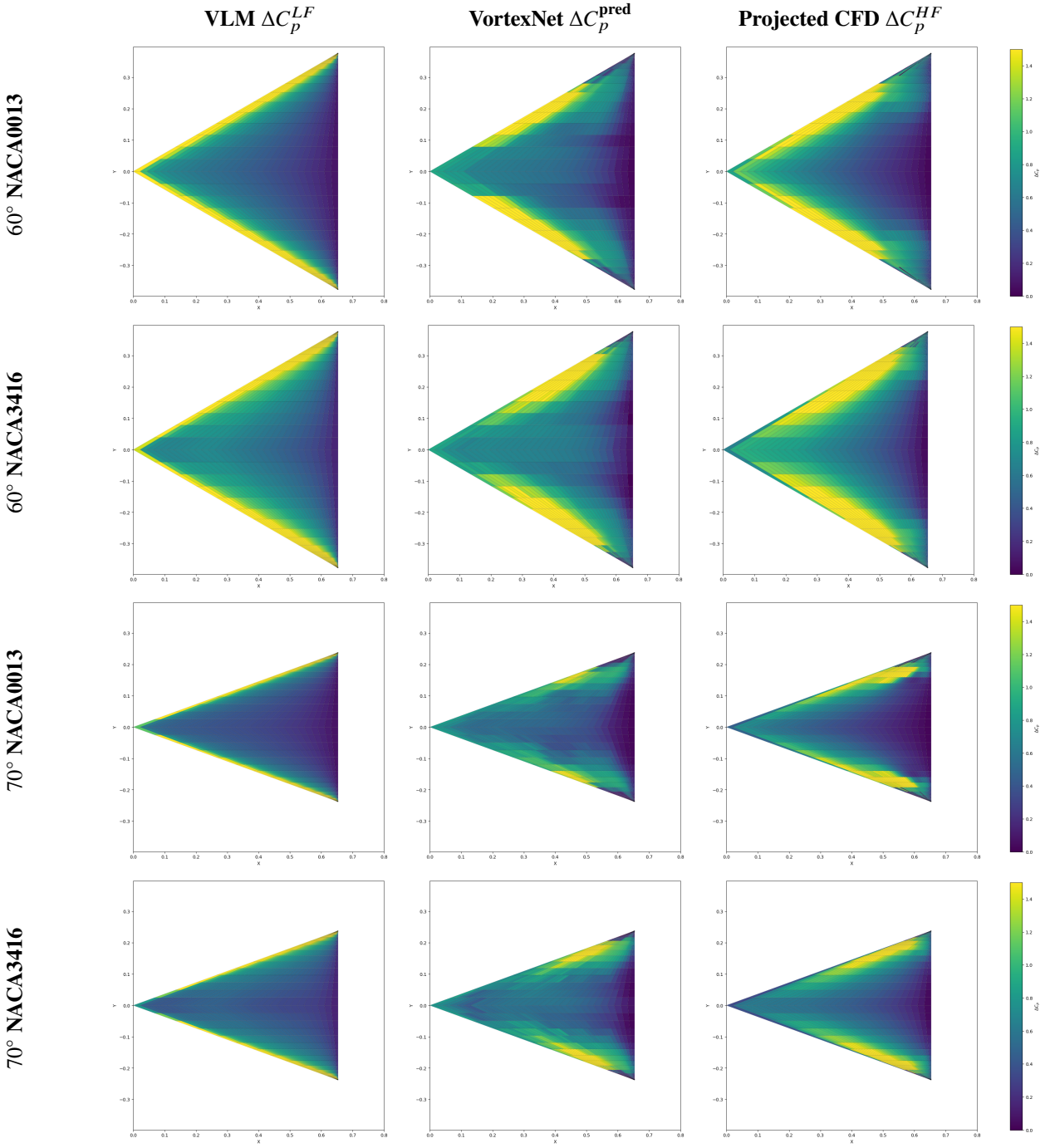

Fig. 47 Lattice panels and local loading coefficients ΔC_p are visualized using color maps ranging from $\Delta C_p = 0$ to $\Delta C_p = 1.5$ for four new geometries. From top to bottom: 60° NACA 0013, 60° NACA 3416, 70° NACA 0013, and 70° NACA 3416. From left to right: ΔC_p^{LF} obtained from VLM, `VortexNet` ΔC_p^{pred} predictions, and projected CFD ΔC_p^{HF}.

For instance, when analyzing the contribution of cluster one after the first Convolutional Block (layer 0), the nodal feature arrays of all other clusters at the current layer were manually set to zero. The modified feature array was then propagated through subsequent Convolutional Blocks to the final ΔC_p prediction. This approach isolates the local loading coefficient contributions from each cluster.

For deeper layers beyond the first Convolutional Block, the clustering definition obtained after the first Convolutional Block was reused by keeping track of the associativity between the nodal index and the cluster bins. At a specific layer, nodal feature arrays corresponding to a specific cluster were retained, while others were set to zero, and the resultant feature arrays were propagated to the Output Block. By analyzing ΔC_p predictions of a single cluster across multiple layers, the effects of multi-hop convolution can be studied. This controlled modification allows for an analysis of how individual layers influence the final output.

The results of the ablation study are presented in Figure 48. Each column corresponds to ΔC_p predictions using the nodal features of a specific cluster, while each row represents the effects of conducting the ablation study at a particular layer. The final row (layer 3) corresponds to the model's final output ΔC_p for each clusters. When the pressure fields of all clusters are superposed, the result recovers the `VortexNet`'s prediction on ΔC_p^{pred} shown in Figure 46.

Two trend-wise insights can be identified from this figure. Firstly, different clusters correspond to distinct regions of the wing. For example, "Cluster 0" corresponds to the leading edge of the wing, while "Cluster 3" focuses more on the afterbody. "Cluster 1" and "Cluster 2" primarily correspond to the left and right outboard sections of the wing, as evident from the ΔC_p prediction differences at "Layer 0." However, this distinction becomes less apparent across deeper layers.

Secondly, across layers, field features become increasingly "localized." In the earlier layers, most field features exhibit large wavelengths, corresponding to global aerodynamic characteristics. In the later layers, the features shift to smaller wavelengths, and sharp discontinuities sometimes appear. This observation aligns with the expected behavior of such U-net like deep networks: deeper layers distill more localized features while shallower layers attention on more global features.

To assist in relating these clusters to specific regions of the wing, Figure 49 is provided. This figure shows by color coding of the clusters in Figure 48 and their corresponding position on the wing. Certain selected nodal indices are also presented along with their nodes to help assist future discussion.

To quantitatively visualize the ΔC_p prediction from this study, we compared the relative error (ϵ) between the prediction from one isolated cluster ($\Delta C_p^{\text{isolated}}$) at a specific layer and the unmodified ΔC_{pred} prediction. The relative error is defined as:

$$\epsilon(\Delta C_p^{\text{isolated}}) = \frac{\Delta C_p^{\text{isolated}} - \Delta C_p^{\text{pred}}}{\Delta C_p^{\text{pred}}}. \tag{72}$$

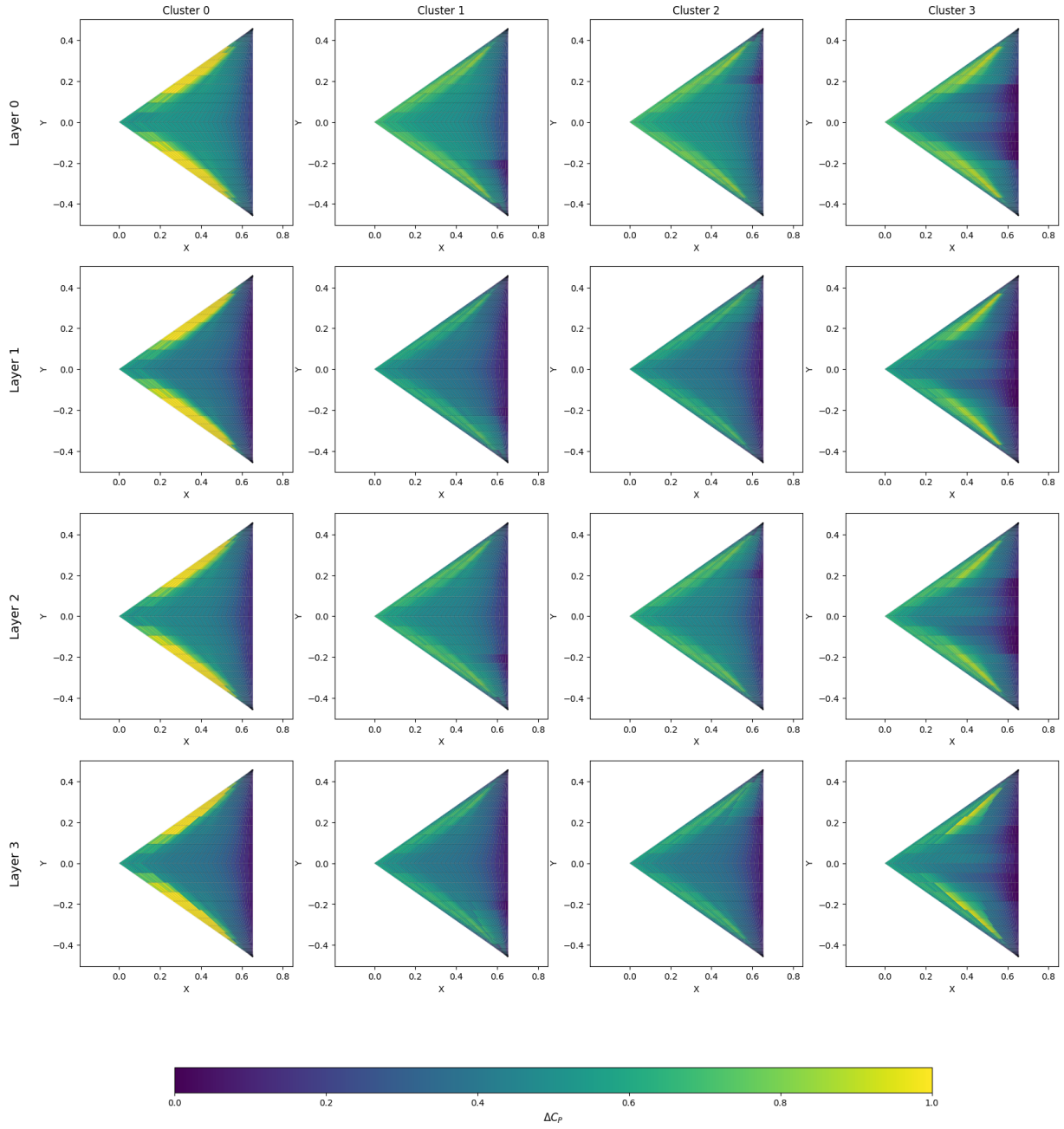

Fig. 48 Ablation study results illustrating ΔC_p predictions for node features within each cluster (columns). The rows represent the effects of the ablation study conducted at specific layers.

This relative error is a vector with a length equal to the number of nodes. In Figure 50, this vector is plotted along the y-axis and ordered by nodal index. The nodal index of 0 corresponds to the wing apex, while indices 495 and 900 correspond to the right tip and left tip of the wing, respectively, as illustrated in Figure 49. Along the x-axis, each column represents a specific "layer-cluster" combination. For instance, the x-tick labeled “01” corresponds to the relative error $\Delta C_p^{\text{isolated}}$ obtained by isolating cluster 1 at layer 0.

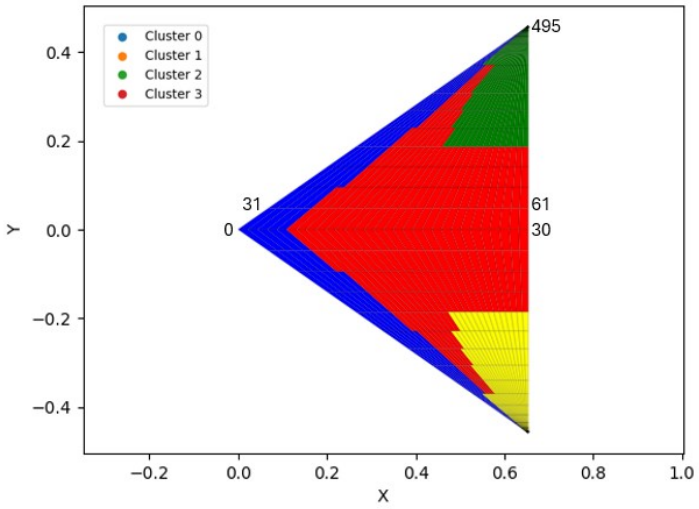

Fig. 49 Identified cluster locations on the wing, with several nodal indices marked along the nodes for reference.

From Figure 50, comparing the locations of high-error nodes (marked in yellow) across layers confirms that different clusters attend to distinct regions of the wing, as high error appears in different areas for each cluster. For instance, in "Layer 0", high-error nodes are primarily located along the leading and trailing edges of the wing. For example, when analyzing the relative error of Layer 0 Cluster 3 (marked by x-label "03"), where the cluster mainly focuses on the afterbody, the leading-edge prediction exhibits high error. Thus a periodic high-error pattern can be observed in nodal indices that are multiples of 30.

When comparing error patterns across layers, a more intriguing trend emerges. Globally, there are oblique "corridors" of high-error nodes that shift to higher nodal indices as layers become deeper. After correlating the high error nodal index to physical geometry, it is identified that these corridors represent high-error regions moving from the outer edges of the wing toward the inner regions. This observation aligns with the message-passing mechanism of the GNN, where nodal features are aggregated from neighboring nodes at each hop. The slope of these corridors indicates the speed at which information propagates through the graph. From the results in Figure 50, it is evident that information propagation occurs at a relatively low speed. By the final Convolution Block, much of the information has not reached the chord-wise center of the wing (e.g., nodal indices that are multiples of 15). This performance is suboptimal because, for information to traverse the wing geometry, a significantly deeper network would be required. However, deeper networks are more challenging to train and prone to high-variance error.

To address this limitation, improved edge definitions that connect nodes beyond direct neighbors could be implemented. Alternatively, using a fully connected graph may help mitigate this issue, though the implications of adopting such a graph remain unclear as the addition of trainable parameters may decrease the prediction accuracy under limited HF samples. Additionally, since pooling layers are not utilized in this network, we believe that incorporating a properly designed pooling mechanism could assist information propagation by reducing the computational graph

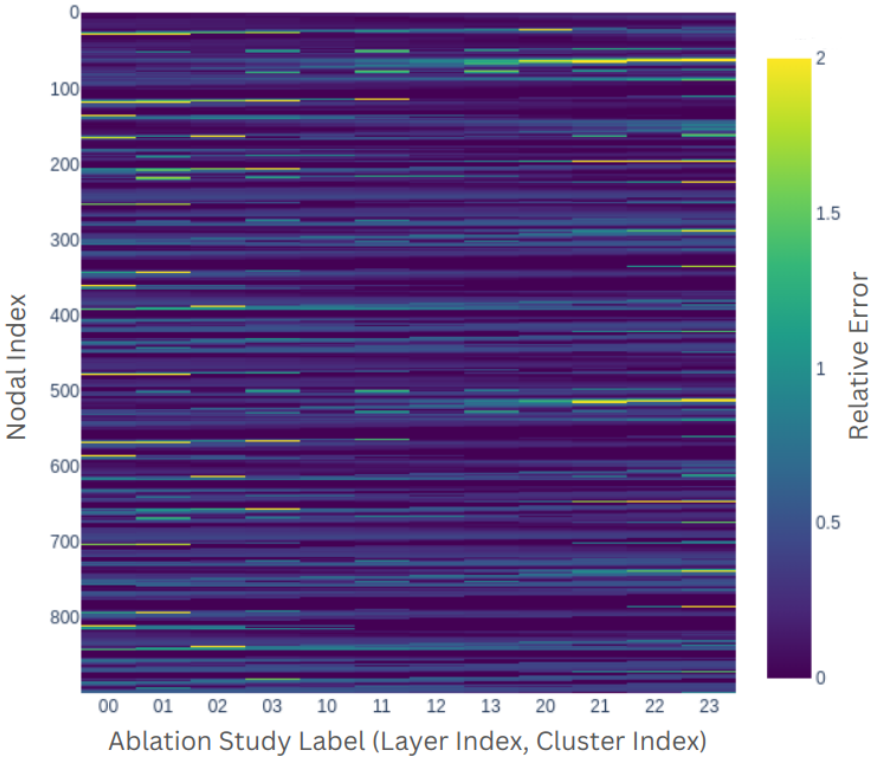

Fig. 50 Relative error (ϵ) for ΔC_p predictions under the ablation study, plotted by graph nodal index (VLM control points) along the y-axis and "layer-cluster" combinations along the x-axis.

size toward deeper layers. This highlights the need for future research on optimizing graph definitions and model architectures in `VortexNet`-like surrogate modeling techniques.

Finally, the latent spaces after t-SNE projection at layer 0 to 2 are visualized in Figure 51. At shallower layers, as shown in Figure 51(a), the distribution of nodal feature clusters loosely follows the geographical distribution of the corresponding nodes in physical space. For instance, one can still identify the relative positions of the leading edges, afterbody, left outboard wing, and right outboard sections from the t-SNE axes. However, in deeper layers, this grouping by physical space separation diminishes. In Figure 51(b), the clusters corresponding to the left and right outboard sections merge. This phenomenon suggests that, at this layer, information related to flow conditions becomes more dominant. Since the flow conditions for the left and right outboard sections are symmetric due to the free-stream conditions in the training dataset, the geographical distinctions in physical space become irrelevant.

At even deeper layers, as shown in Figure 51(c), the physical space separation becomes nearly indistinguishable, and the clustering instead reflects how different geographical components share similar flow conditions. Examining the distribution of features across the space, one may argue that the latent layers exhibit some level of coherent manifold structure. However, as pooling layers are not utilized in the current architecture, the resultant visualization appears too noisy, and the presence and significance of such manifolds remain unclear. Further research is needed to incorporate pooling mechanisms into the graph definition and investigate whether the latent space presents a coherent manifold structure.

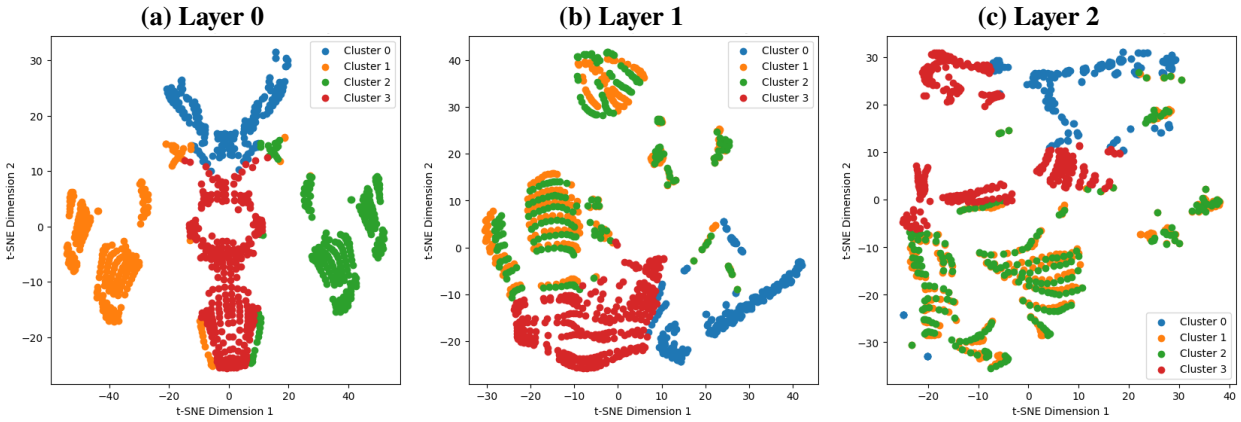

Fig. 51 Projected latent space nodal features plotted against the t-SNE axes, with scatter dot colors indicating the corresponding clusters of the nodes.

D. Conclusions and Future Work

In this work, we propose a novel graph neural network (GNN)-based surrogate model named `VortexNet` for aircraft conceptual design. The surrogate model integrates high-fidelity (HF) computational fluid dynamics (CFD) data into field data predictions generated by low-fidelity (LF) prediction tools, such as vortex lattice method (VLM). Compared

to traditional surrogate modeling techniques, which primarily focus on specific scalar variables, the field data prediction capability allows for arbitrary Quantities of interests (QOIs) to be evaluated within conceptual design environments. By leveraging GNN, the surrogate model learns a mapping of field data differences between HF and LF predictions. Once trained, the surrogate model can generate quasi-HF field data predictions that capture the pressure field impacted by nonlinear flow physics at a cost comparable to that of running a VLM, thereby addressing the fidelity-cost trade-off challenge in the conceptual design phase.

The `VortexNet` architecture utilizes U-net-style skip connections for global feature capturing and employs graph attention network (GAT) convolutional blocks for local flow feature capturing, such as vortex lift and flow separation. Data assembly methods, implicit physical constraint enforcement, and training schemes tailored to `VortexNet` are also explored and presented. To optimize model prediction accuracy, a hyper-parameter optimization study was conducted, identifying specific hyper-parameters that need closer attention in future `VortexNet`-like surrogate model training.

The model's prediction accuracy is evaluated both qualitatively and quantitatively. When provided with an input graph seen during training, the surrogate model demonstrates strong performance in reconstructing qualitative flow features and achieves low prediction RMSE, establishing significant fidelity improvements over LF-based aerodynamic prediction methods. The model's generalizability is also assessed, showing moderate capability in predicting pressure fields for unseen geometries. However, performance declines are observed when wing camber is varied, highlighting areas for further refinement. Despite these limitations, the model demonstrates potential as a mesh-agnostic surrogate. Such capability is critical for conceptual aircraft design under design space exploration. Finally, a latent space ablation study is conducted to preliminarily explain the prediction mechanism of the proposed network. The study reveals that `VortexNet` achieves its prediction capability by effectively blending geometrical information and flow features in the latent space. It also indicates a need for future improvements in graph topology and model architecture, as the current information-passing mechanism among graph nodes operates inefficiently.

Future work will focus on enhancing the model's generalizability and improving feature-capturing efficiency for more complex geometries, graphs, and broader aerodynamic conditions. We believe that the model's prediction capability can be further enhanced through the introduction of pooling mechanisms, refinement of edge connectivity graphs, and the use of more representative training datasets. The application of the proposed surrogate model for interpolating between fidelity levels beyond VLM and RANS CFD also presents an intriguing avenue for further studies. Future work may also include comparison with other surrogate modeling methodologies for field data prediction in order to characterize training data requirements, prediction accuracy, and computational cost for design space exploration tasks, relative to comparable methods.

E. Acknowledgment

This work was supported by the Air Force Office of Scientific Research under Grant FA9550-22-1-0004 and NASA, Award 80NSSC19K1661, under the Commercial Supersonics Technology (CST) program, Supersonic Configurations at Low Speeds (SCALOS), with Sarah Langston as the NASA technical grant monitor. The authors extend their gratitude to Eli Livne, Kuang-Ying Ting, Chester Nelson, and Kenneth Wiersema for their valuable discussions on supersonic aircraft configurations. The first author also wishes to thank Emilio Botero for his discussion of the `SUAVE` software environment and Ran Jiang for her assistance with the schematic drawing. Additionally, the authors would like to thank the Stanford Research Computing Center (SRCC) for providing computational resources on the Sherlock cluster and the Google Cloud Research Credit Program for granting access to GPU resources on the Google Cloud Platform.

References

[1] Takuya Akiba et al. “Optuna: A Next-generation Hyperparameter Optimization Framework”. In: *Proceedings of the 25th ACM SIGKDD International Conference on Knowledge Discovery & Data Mining*. KDD ’19. Anchorage, AK, USA: Association for Computing Machinery, 2019, pp. 2623–2631. ISBN: 9781450362016. DOI: 10.1145/3292500.3330701. URL: https://doi.org/10.1145/3292500.3330701.

[2] Davide Anguita et al. “The’K’in K-fold Cross Validation.” In: *ESANN*. Vol. 102. 2012, pp. 441–446. URL: https://www.esann.org/sites/default/files/proceedings/legacy/es2012-62.pdf.

[3] Gal Berkooz, Philip Holmes, and John L. Lumley. “The Proper Orthogonal Decomposition in the Analysis of Turbulent Flows”. In: *Annual Review of Fluid Mechanics* 25 (1993), pp. 539–575. DOI: https://doi.org/10.1146/ANNUREV.FL.25.010193.002543.

[4] Nolan Black and Ahmad R. Najafi. “Learning finite element convergence with the Multi-fidelity Graph Neural Network”. In: *Computer Methods in Applied Mechanics and Engineering* 397 (2022), p. 115120. ISSN: 00457825. DOI: 10.1016/j.cma.2022.115120.

[5] Shaked Brody, Uri Alon, and Eran Yahav. *How Attentive are Graph Attention Networks?* 2022. arXiv: 2105.14491 [cs.LG]. URL: https://arxiv.org/abs/2105.14491.

[6] Steven L. Brunton, Bernd R. Noack, and Petros Koumoutsakos. “Machine Learning for Fluid Mechanics”. In: *Annual Review of Fluid Mechanics* 52 (2020), pp. 477–508. ISSN: 00664189. DOI: 10.1146/annurev-fluid-010719-060214. arXiv: 1905.11075.

[7] Kinga Budziak. *Aerodynamic Analysis with Athena Vortex Lattice (AVL)*. Hamburg: Aircraft Design, Systems Group (AERO), Department of Automotive, and Aeronautical Engineering, 2015. URL: https://www.fzt.haw-hamburg.de/pers/Scholz/arbeiten/TextBudziak.pdf.

[8] J. Chen, E. Hachem, and J. Viquerat. “Graph neural networks for laminar flow prediction around random two-dimensional shapes”. In: *Physics of Fluids* 33.12 (2021). ISSN: 10897666. DOI: 10.1063/5.0064108.

[9] Saurabh Deshpande, Stéphane P.A. Bordas, and Jakub Lengiewicz. “MAgNET: A graph U-Net architecture for mesh-based simulations”. In: *Engineering Applications of Artificial Intelligence* 133 (July 2024), p. 108055. ISSN: 0952-1976. DOI: 10.1016/j.engappai.2024.108055.

[10] Thomas D. Economon et al. “SU2: An Open-Source Suite for Multiphysics Simulation and Design”. In: *AIAA Journal* 54.3 (2016). DOI: 10.2514/1.J053813.

[11] Hamidreza Eivazi et al. “Physics-informed neural networks for solving Reynolds-averaged Navier–Stokes equations”. In: *Physics of Fluids* 34.7 (July 2022), p. 075117. ISSN: 1070-6631. DOI: 10.1063/5.0095270. eprint: https://pubs.aip.org/aip/pof/article-pdf/doi/10.1063/5.0095270/19816179/075117_1_online.pdf.

[12] H Christopher Frey and Sumeet R Patil. “Identification and review of sensitivity analysis methods”. en. In: *Risk Anal* 22.3 (June 2002), pp. 553–578. DOI: 10.1111/0272-4332.00039.

[13] Hongyang Gao and Shuiwang Ji. “Graph U-Nets”. In: *Proceedings of the 36th International Conference on Machine Learning, ICML 2019, 9-15 June 2019, Long Beach, California, USA*. Ed. by Kamalika Chaudhuri and Ruslan Salakhutdinov. Vol. 97. Proceedings of Machine Learning Research. PMLR, 2019, pp. 2083–2092. URL: http://proceedings.mlr.press/v97/gao19a.html.

[14] William L. Hamilton, Rex Ying, and Jure Leskovec. “Representation Learning on Graphs: Methods and Applications”. In: *CoRR* abs/1709.05584 (2017). arXiv: 1709.05584. URL: http://arxiv.org/abs/1709.05584.

[15] Daniel Huynh et al. “Application of a Semi-Empirical Method to Model Subsonic Vortex Lift over Sharp Leading-Edge Delta Wings”. In: *AIAA SCITECH 2023 Forum*. 2023. DOI: 10.2514/6.2023-2457. eprint: https://arc.aiaa.org/doi/pdf/10.2514/6.2023-2457.

[16] A. Jameson, Wolfgang Schmidt, and Eli Turkel. “Numerical solution of the Euler equations by finite volume methods using Runge Kutta time stepping schemes”. In: *14th Fluid and Plasma Dynamics Conference*. 1981. DOI: 10.2514/6.1981-1259. eprint: https://arc.aiaa.org/doi/pdf/10.2514/6.1981-1259.

[17] Hemant Joshi and Peter Thomas. “Review of vortex lattice method for supersonic aircraft design”. In: *The Aeronautical Journal* (2023), pp. 1–35.

[18] Marc C. Kennedy and Anthony O’Hagan. “Bayesian calibration of computer models”. In: *Journal of the Royal Statistical Society: Series B (Statistical Methodology)* 63.3 (2001), pp. 425–464. DOI: https://doi.org/10.1111/1467-9868.00294. eprint: https://rss.onlinelibrary.wiley.com/doi/pdf/10.1111/1467-9868.00294.

[19] Diederik P. Kingma and Jimmy Ba. “Adam: A Method for Stochastic Optimization”. In: *3rd International Conference on Learning Representations, ICLR 2015, San Diego, CA, USA, May 7-9, 2015, Conference Track Proceedings*. Ed. by Yoshua Bengio and Yann LeCun. 2015. URL: http://arxiv.org/abs/1412.6980.

[20] Jinxing Li et al. “Multi-fidelity graph neural network for flow field data fusion of turbomachinery”. In: *Energy* 285.July (2023), p. 129405. ISSN: 03605442. DOI: 10.1016/j.energy.2023.129405.

[21] Qiang Liu et al. *Fluid Simulation System Based on Graph Neural Network*. 2022. arXiv: 2202.12619 [physics.flu-dyn]. URL: https://arxiv.org/abs/2202.12619.

[22] Timothy MacDonald et al. “SUAVE: An Open-Source Environment Enabling Multi-Fidelity Vehicle Optimization”. In: *18th AIAA/ISSMO Multidisciplinary Analysis and Optimization Conference*. 2017. DOI: 10.2514/6.2017-4437. eprint: https://arc.aiaa.org/doi/pdf/10.2514/6.2017-4437. URL: https://arc.aiaa.org/doi/abs/10.2514/6.2017-4437.

[23] J MacQueen. “Some methods for classification and analysis of multivariate observations”. In: *Proceedings of 5-th Berkeley Symposium on Mathematical Statistics and Probability/University of California Press*. 1967. URL: https://projecteuclid.org/ebooks/berkeley-symposium-on-mathematical-statistics-and-probability/Some-methods-for-classification-and-analysis-of-multivariate-observations/chapter/Some-methods-for-classification-and-analysis-of-multivariate-observations/bsmsp/1200512992.

[24] Joaquim R.R.A. Martins. “A Coupled-Adjoint Method for High-fidelity Aero-structural Optimization”. PhD thesis. Stanford University, 2002.

[25] David S. Miller and Richard M. Wood. “Leeside flows over delta wings at supersonic speeds”. In: *Journal of Aircraft* 21.9 (1984), pp. 680–686. DOI: 10.2514/3.45014. eprint: https://doi.org/10.2514/3.45014.

[26] Luis R. Miranda, Robert D. Elliott, and William M. Baker. “A generalized vortex lattice method for subsonic and supersonic flow applications”. In: *NASA. Langley Res. Center Vortex-Lattice Utilization* (1977). URL: https://ntrs.nasa.gov/citations/19780008059.

[27] Markus Mrosek, Carsten Othmer, and Rolf Radespiel. “Reduced-Order Modeling of Vehicle Aerodynamics via Proper Orthogonal Decomposition”. In: *SAE Int. J. Passeng. Cars - Mech. Syst.* 12 (3 2019), pp. 225–236. DOI: 10.4271/06-12-03-0016.

[28] Jayant Mukhopadhaya et al. “Multi-fidelity modeling of probabilistic aerodynamic databases for use in aerospace engineering”. In: *International Journal for Uncertainty Quantification* 10.5 (2020), pp. 425–447. ISSN: 21525099. DOI: 10.1615/Int.J.UncertaintyQuantification.2020032841. arXiv: 1911.05036.

[29] Daniel Neufeld, Joon Chung, and Kamran Behdinian. “Aircraft Conceptual Design Optimization Considering Fidelity Uncertainties”. In: *Journal of Aircraft* 48.5 (2011), pp. 1602–1612. DOI: 10.2514/1.C031312. eprint: https://doi.org/10.2514/1.C031312.

[30] D. Owens. “Weissinger’s model of the nonlinear lifting-line method for aircraft design”. In: *36th AIAA Aerospace Sciences Meeting and Exhibit*. 1998. DOI: 10.2514/6.1998-597. eprint: https://arc.aiaa.org/doi/pdf/10.2514/6.1998-597.

[31] Francisco Palacios et al. “Stanford University Unstructured (SU2): an Open-source Integrated Computational Environment for Multi-physics Simulation and Design”. In: *51st AIAA Aerospace Sciences Meeting including the New Horizons Forum and Aerospace Exposition*. 2013, p. 287. DOI: https://doi.org/10.2514/6.2013-287.

[32] Francisco Palacios et al. “Stanford University Unstructured (SU2): Analysis and Design Technology for Turbulent Flows”. In: *52nd Aerospace Sciences Meeting*. 2014, p. 0243. DOI: https://doi.org/10.2514/6.2014-0243.

[33] Tobias Pfaff et al. *Learning Mesh-Based Simulation with Graph Networks*. 2021. arXiv: 2010.03409 [cs.LG]. URL: https://arxiv.org/abs/2010.03409.

[34] Pointwise. *Pointwise, Cadence Design Systems*. retrived 26 April 2023. URL: http://www.pointwise.com/.

[35] Edward Charles Polhamus. “A concept of the vortex lift of sharp-edge delta wings based on a leading-edge-suction analogy”. In: *NASA. Langley Res. Center* (1966). URL: https://ntrs.nasa.gov/citations/19670003842.

[36] PyTorch. *Tanh Standardization*. retrived 30 November 2024. URL: https://pytorch.org/docs/stable/generated/torch.nn.Tanh.html.

[37] Contributors PyTorch. *Smoothl1loss*. retrived 30 November 2024. URL: https://pytorch.org/docs/stable/generated/torch.nn.SmoothL1Loss.html.

[38] Daniel P Raymer. *Aircraft design: A conceptual approach*. 4. ed. AIAA education series. Reston, Va.: American Institute of Aeronautics and Astronautics, 2006. ISBN: 1563478293. URL: http://www.loc.gov/catdir/toc/ecip068/2006004706.html.

[39] Sabet Seraj and Joaquim R. R. A. Martins. "Predicting the High-Angle-of-Attack Characteristics of a Delta Wing at Low Speed". In: *Journal of Aircraft* 59.4 (2022), pp. 1071–1081. DOI: 10.2514/1.C036618. eprint: https://doi.org/10.2514/1.C036618.

[40] Xuqiang Shao et al. "PIGNN-CFD: A physics-informed graph neural network for rapid predicting urban wind field defined on unstructured mesh". In: *Building and Environment* 232 (2023), p. 110056. ISSN: 0360-1323. DOI: https://doi.org/10.1016/j.buildenv.2023.110056.

[41] Yiren Shen and Juan J. Alonso. "Performance Evaluation of a Graph Neural Network-Augmented Multi-Fidelity Workflow for Predicting Aerodynamic Coefficients on Delta Wings at Low Speed". In: *AIAA SCITECH 2025 Forum*. January. 2025.

[42] Yiren Shen et al. "Application of Multi-Fidelity Transfer Learning with Autoencoders for Efficient Construction of Surrogate Models". In: *AIAA SCITECH 2024 Forum*. January. 2024, pp. 1–19. ISBN: 9781624107115. DOI: 10.2514/6.2024-0013.

[43] Michael L. Shur et al. "Turbulence Modeling in Rotating and Curved Channels: Assessing the Spalart-Shur Correction". In: *AIAA Journal* 38.5 (2000), pp. 784–792. DOI: 10.2514/2.1058. eprint: https://doi.org/10.2514/2.1058.

[44] Ralph C Smith. "Uncertainty quantification: Theory, implementation, and applications". en. In: SIAM, Dec. 2013, pp. 321–344.

[45] P. Spalart and S. Allmaras. "A one-equation turbulence model for aerodynamic flows". In: *30th Aerospace Sciences Meeting and Exhibit*. 1992. DOI: 10.2514/6.1992-439. eprint: https://arc.aiaa.org/doi/pdf/10.2514/6.1992-439.

[46] Laurens Van der Maaten and Geoffrey Hinton. "Visualizing data using t-SNE." In: *Journal of machine learning research* 9.86 (2008), pp. 2579–2605. URL: http://jmlr.org/papers/v9/vandermaaten08a.html.

[47] Petar Veličković et al. "Graph Attention Networks". In: *International Conference on Learning Representations* (2018). URL: https://openreview.net/forum?id=rJXMpikCZ.

[48] *Vortex-Lattice Utilization*. National Aeronautics and Space Administration. 1976. URL: https://ntrs.nasa.gov/api/citations/19760021075/downloads/19760021075.pdf.

[49] Li Wang et al. "High-Fidelity Multidisciplinary Sensitivity Analysis and Design Optimization for Rotorcraft Applications". In: *AIAA Journal* 57.8 (2019), pp. 3117–3131. DOI: 10.2514/1.J056587.

[50] Lan Wei and Nikolaos M. Freris. "Multi-scale graph neural network for physics-informed fluid simulation". In: *The Visual Computer* (May 2024). ISSN: 1432-2315. DOI: 10.1007/s00371-024-03402-6.

[51] A. Wendorff et al. *SUAVE: An Aerospace Vehicle Environment for Designing Future Aircraft*. Version 2.1. 2020. URL: https://github.com/suavecode/SUAVE.

[52] Zonghan Wu et al. "A Comprehensive Survey on Graph Neural Networks". In: *IEEE Transactions on Neural Networks and Learning Systems* 32.1 (Jan. 2021), pp. 4–24. ISSN: 2162-2388. DOI: 10.1109/tnnls.2020.2978386.

[53] Sunwoong Yang, Ricardo Vinuesa, and Namwoo Kang. *Enhancing Graph U-Nets for Mesh-Agnostic Spatio-Temporal Flow Prediction*. 2024. arXiv: 2406.03789 [cs.LG]. URL: https://arxiv.org/abs/2406.03789.

[54] Rex Ying et al. *GNNExplainer: Generating Explanations for Graph Neural Networks*. 2019. arXiv: 1903.03894 [cs.LG]. URL: https://arxiv.org/abs/1903.03894.

[55] Xinshuai Zhang et al. "Multi-fidelity deep neural network surrogate model for aerodynamic shape optimization". In: *Computer Methods in Applied Mechanics and Engineering* 373 (2021), p. 113485. ISSN: 00457825. DOI: 10.1016/j.cma.2020.113485.

[56] Yingxue Zhao et al. "A review of graph neural network applications in mechanics-related domains". In: *Artificial Intelligence Review* 57.11 (Oct. 2024), p. 315. ISSN: 1573-7462. DOI: 10.1007/s10462-024-10931-y.

Supersonic Configurations at Low Speeds (SCALOS)

Final Report

December 15, 2024

Appendix C

Boeing R&T

Water Tunnel Tests at the Boeing Flow Visualization Water Tunnel

This document fulfills the Final Report deliverable for NASA Contract Number 80NSSC19K1661,
University of Washington Purchase Order BPO45534

SCALOS Final Report
Boeing Activities

December 9, 2024

Points of Contact

Technical
Todd Magee, Principal Investigator
14441 Astronautics Lane, Huntington Beach, CA 92647
Phone: 714-642-4053
E-mail: todd.magee@boeing.com

Contracts
Kurt Braaten, Contracts Specialist
14441 Astronautics Lane, Huntington Beach, CA 92647
Phone: 714-658-4451
E-mail: kurt.h.braaten@boeing.com

The Boeing Company
14441 Astronautics Lane, Huntington Beach, CA 92647

SCALOS Final Report

By

Todd Magee, Pat Hayes and Abdi Khodadoust
Boeing Research and Technology

The Boeing SCALOS effort is comprised of a series of dynamic stability water tunnel tests at the Boeing Flow Visualization Water Tunnel of the University of Washington 2020, 2017 and 2015 supersonic configurations. There was also commensurate vortex lattice and CFD conducted to compare with the FVWT results. This work was conducted over a 5-year period from 2019 through 2024. All this work is documented in three American Institute for Aeronautics and Astronautics (AIAA) conference papers. These papers are contained below and serve as the Boeing SCALOS Final Report.

Dynamic Stability Characteristics for Commercial Supersonic Configurations at Low-Speed Flight Conditions – Presented at the SciTech 2022 Conference

Dynamic Stability Characteristics for Commercial Supersonic Configurations at Low-Speed Flight Conditions

Todd Magee[1], Patrick Hayes[2], and Abdollah Khodadoust[3]
Boeing Research and Technology, Huntington Beach, CA, 92647

and

Andrew Dorgan[4]
Boeing Research and Technology, Hazelwood, MO, 63031

Low-speed dynamic stability is critical to the safe operation of low-boom supersonic aircraft. Determination of dynamic stability derivative data at low-speed takeoff and landing conditions using both experimental and computational methods are shown for supersonic configuration features that are common on low sonic boom aircraft. These include trades on nose length, wing planform, nacelle location, horizontal tail location and canard on/off. Experimental methods use the Boeing Flow Visualization Water Tunnel (FVWT) with a 6-component, submersible balance, together with a state-of-the-art data acquisition and motion control system. Dynamic stability derivative coefficients are determined from forced oscillation testing using the Single-point Method. Comparisons between numerical methods and the experimental data are shown, using both Boeing Computational Fluid Dynamics (BCFD) Reynolds Averaged Navier-Stokes (RANS) and Unsteady Reynolds Averaged Navier-Stokes (URANS). Experimental results are also compared with vortex lattice methods. Results show the accuracy and effectiveness of forced oscillation testing of a small-scale model in a low-cost water tunnel. Reynolds number insensitivity is observed in the water tunnel and computational results due to the vortex dominated features of the water tunnel and supersonic configuration.

Nomenclature

A = amplitude of oscillation
AFLR3 = Advancing-Front/Local-Reconnection unstructured grid generator
b = span length, ft
BCFD = Boeing Computational Fluid Dynamics
CFD = Computational Fluid Dynamics
$\bar{c}$ = mean aerodynamic chord, ft
CD = drag force coefficient
CD_q = drag force - pitch damping coefficient, $\frac{\partial C_D}{\partial q}$
$CD_{\dot{\alpha}}$ = pitching moment coefficient due to instantaneous change in angle-of-attack, $\frac{\partial CD}{\partial(\dot{\alpha}\bar{c}/(2*Vinf))}$
CZ = lift force coefficient
CL_q = lift force – pitch damping coefficient, $\frac{\partial C_L}{\partial q}$
$CL_{\dot{\alpha}}$ = pitching moment coefficient due to instantaneous change in angle-of-attack, $\frac{\partial CL}{\partial(\dot{\alpha}\bar{c}/(2*Vinf))}$
Cl = rolling moment coefficient
Cl_p = rolling moment – roll damping coefficient, $\frac{\partial C_l}{\partial p}$

[1]Chief Engineer Supersonics, Advanced Aerodynamic Design, 14441 Astronautics Lane / H022-F368, AIAA Associate Fellow.
[2]NAART Lab Manager, Advanced Aerodynamic Design, 14441 Astronautics Lane / H022-F368.
[3]Manager, Advanced Aerodynamic Design, 14441 Astronautics Lane / H022-F368, AIAA Associate Fellow.
[4]Associate Technical Fellow, Aerodynamic Analysis & Testing, 325 James S. McDonnell Blvd / S306-4030, AIAA Senior Member

Dynamic Stability Characteristics for Commercial Supersonic Configurations at Low-Speed Flight Conditions – Part II – Presented at the SciTech 2024 Conference

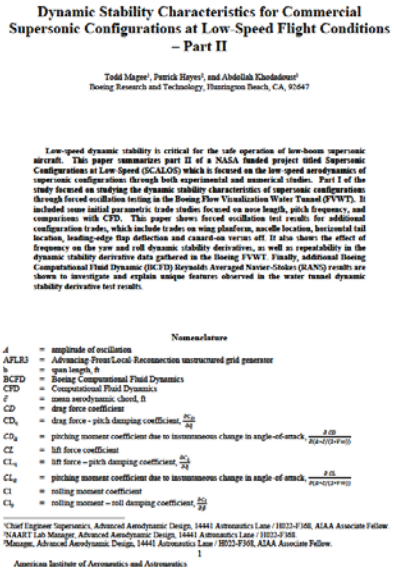

Dynamic Stability Characteristics for Commercial Supersonic Configurations at Low-Speed Flight Conditions – Part II

Todd Magee[1], Patrick Hayes[2], and Abdollah Khodadoust[3]
Boeing Research and Technology, Huntington Beach, CA, 92647

Low-speed dynamic stability is critical for the safe operation of low-boom supersonic aircraft. This paper summarizes part II of a NASA funded project titled Supersonic Configurations at Low-Speed (SCALOS) which is focused on the low speed aerodynamics of supersonic configurations through both experimental and numerical studies. Part I of the study focused on studying the dynamic stability characteristics of supersonic configurations through forced oscillation testing in the Boeing Flow Visualization Water Tunnel (FVWT). It included some initial parametric trade studies focused on nose length, pitch frequency, and comparisons with CFD. This paper shows forced oscillation test results for additional configuration trades, which include trades on wing planform, nacelle location, horizontal tail location, leading-edge flap deflection and canard-on versus off. It also shows the effect of frequency on the yaw and roll dynamic stability derivatives, as well as repeatability in the dynamic stability derivative data gathered in the Boeing FVWT. Finally, additional Boeing Computational Fluid Dynamic (BCFD) Reynolds Averaged Navier-Stokes (RANS) results are shown to investigate and explain unique features observed in the water tunnel dynamic stability derivative test results.

Nomenclature

A = amplitude of oscillation
AFLR3 = Advancing Front/Local-Reconnection unstructured grid generator
b = span length, ft
BCFD = Boeing Computational Fluid Dynamics
CFD = Computational Fluid Dynamics
$\bar{c}$ = mean aerodynamic chord, ft
CD = drag force coefficient
CD_q = drag force - pitch damping coefficient, $\frac{\partial C_D}{\partial q}$
CD_α = pitching moment coefficient due to instantaneous change in angle-of-attack, $\frac{\partial CD}{\partial(\alpha\bar{c}/(2\cdot V_\infty))}$
CL = lift force coefficient
CL_q = lift force – pitch damping coefficient, $\frac{\partial C_L}{\partial q}$
CL_α = pitching moment coefficient due to instantaneous change in angle-of-attack, $\frac{\partial CL}{\partial(\alpha\bar{c}/(2\cdot V_\infty))}$
Cl = rolling moment coefficient
Cl_p = rolling moment – roll damping coefficient, $\frac{\partial C_l}{\partial p}$

[1]Chief Engineer Supersonics, Advanced Aerodynamic Design, 14441 Astronautics Lane / H022-F368, AIAA Associate Fellow
[2]NAART Lab Manager, Advanced Aerodynamic Design, 14441 Astronautics Lane / H022-F368
[3]Manager, Advanced Aerodynamic Design, 14441 Astronautics Lane / H022-F368, AIAA Associate Fellow.

Dynamic Stability Characteristics for Commercial Supersonic Configurations at Low-Speed Flight Conditions – Part III – To be presented at the SciTech 2025 Conference

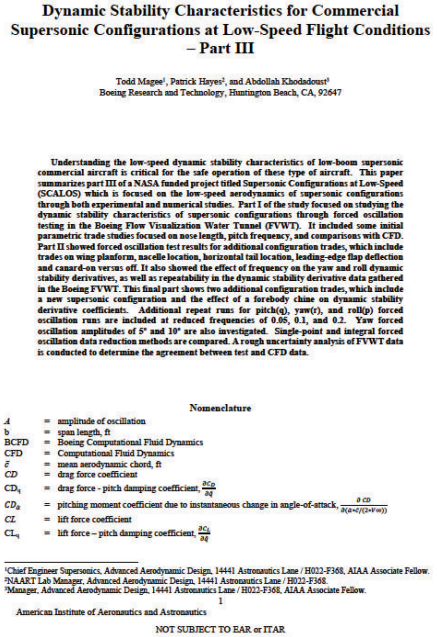

Dynamic Stability Characteristics for Commercial Supersonic Configurations at Low-Speed Flight Conditions – Part III

Todd Magee[1], Patrick Hayes[2], and Abdollah Khodadoust[3]
Boeing Research and Technology, Huntington Beach, CA, 92647

Understanding the low-speed dynamic stability characteristics of low-boom supersonic commercial aircraft is critical for the safe operation of these type of aircraft. This paper summarizes part III of a NASA funded project titled Supersonic Configurations at Low-Speed (SCALOS) which is focused on the low-speed aerodynamics of supersonic configurations through both experimental and numerical studies. Part I of the study focused on studying the dynamic stability characteristics of supersonic configurations through forced oscillation testing in the Boeing Flow Visualization Water Tunnel (FVWT). It included some initial parametric trade studies focused on nose length, pitch frequency, and comparisons with CFD. Part II showed forced oscillation test results for additional configuration trades, which include trades on wing planform, nacelle location, horizontal tail location, leading-edge flap deflection and canard-on versus off. It also showed the effect of frequency on the yaw and roll dynamic stability derivatives, as well as repeatability in the dynamic stability derivative data gathered in the Boeing FVWT. This final part shows two additional configuration trades, which include a new supersonic configuration and the effect of a forebody chine on dynamic stability derivative coefficients. Additional repeat runs for pitch(q), yaw(r), and roll(p) forced oscillation runs are included at reduced frequencies of 0.05, 0.1, and 0.2. Yaw forced oscillation amplitudes of 5° and 10° are also investigated. Single-point and integral forced oscillation data reduction methods are compared. A rough uncertainty analysis of FVWT data is conducted to determine the agreement between test and CFD data.

Nomenclature

A = amplitude of oscillation
b = span length, ft
BCFD = Boeing Computational Fluid Dynamics
CFD = Computational Fluid Dynamics
$\bar{c}$ = mean aerodynamic chord, ft
CD = drag force coefficient
CD_q = drag force - pitch damping coefficient, $\frac{\partial C_D}{\partial q}$
CD_α = pitching moment coefficient due to instantaneous change in angle-of-attack, $\frac{\partial CD}{\partial(\alpha\bar{c}/(2\cdot V_\infty))}$
CL = lift force coefficient
CL_q = lift force – pitch damping coefficient, $\frac{\partial C_L}{\partial q}$

[1]Chief Engineer Supersonics, Advanced Aerodynamic Design, 14441 Astronautics Lane / H022-F368, AIAA Associate Fellow.
[2]NAART Lab Manager, Advanced Aerodynamic Design, 14441 Astronautics Lane / H022-F368.
[3]Manager, Advanced Aerodynamic Design, 14441 Astronautics Lane / H022-F368, AIAA Associate Fellow.

Supersonic Configurations at Low Speeds (SCALOS)

Final Report

December 15, 2024

Appendix D

University of Washington

Kirsten Wind Tunnel Tests – an Overview

Supersonic Configurations at Low Speeds (SCALOS): Wind Tunnel Tests at the University of Washington - an Overview and Some Key Insights

Kuang-Ying Ting*, Chester P. Nelson†, Kenneth Wiersema‡, and Eli Livne§
University of Washington, Seattle, WA 98195

A substantial effort was dedicated, as a part of the NASA funded SCALOS project, to low-speed wind tunnel testing of multiple configurations at the University of Washington's Kirsten Wind Tunnel. A large number of runs were completed between the years 2020 and 2024. They add to a substantial number of runs carried out earlier years. The wind tunnel model development and testing was integrated into the University of Washington's capstone airplane design program. The overall goal was to "map the configuration design space" by testing configurations that capture, in their many shape variations, key elements of potential geometries of efficient future supersonic long-range aircraft, including wing planforms, tail geometries, fuselage and canard geometries, engine locations, high lift devices, and more. Overviews of the progress of SCALOS testing in the Kirsten Wind Tunnel were presented in the years 2021 to 2024. The present paper, building on those earlier overviews, is a final summary of the Kirsten Wind Tunnel work done to date. The hope is that the wind tunnel data that was generated for the project will help identify key configuration shape parameters that significantly influence the performance and stability characteristics of similar supersonic configurations at low speeds and, thus, guide designers and provide representative, realistic, test cases for CFD analysts to use.

Nomenclature

Abbreviations

BMC	Balance Moment Center
BR&T	Boeing Research & Technology
CFD	Computational Fluid Dynamic
CG	Center of Gravity
CST	Commercial Supersonic Technology
FVWT	Flow Visualization Water Tunnel
HSCT	High Speed Civil Transport
KWT	Kirsten Wind Tunnel
LOD	Lift-over-drag ratio
LTO	Landing and Take-Off
MFTF	Mixed Flow Turbofan engines
MMC	Model Moment Center
RSAC	Research Supersonic Airliner Concept
S&C	Stability and Control
SA	Stability Axis
SCALOS	Supersonic Configurations at Low Speeds
T&I	Tare and Interference
TOL	Take-off and Landing
UAV	Unmanned Aerial Vehicle
UWAL	University of Washington Aeronautical Laboratory

SCALOS Designation

A	Aft-body fuselage
AD	Aft-deck
ALT	Alternative concept leading edge
AS	Aileron Spoiler
BR	Bottom rear
CF	Canard Fairings
CS	Clam-shell spoilers
D	Downward/lower
DF	Dorsal Fin
E	Nacelle Electric ducted fans
F	Forebody fuselage
FD	Flight deck/cockpit
FP	Flex-Panel leading edge
FS	Mid-chord Flap spoilers
FTD	Forbody trip dots
FTDEX	Forebody Trip Dots Extended
FTDEX2	Forebody Trip Dots Extended from nose ring
H	Horizontal tail
HTD	Horizontal stabilizer Trip Dots
IB	Inboard
ICE	Icing on wing leading edges
L	Long/extended
LE	Leading Edge
LEIB	Leading Edge Inboard

*Ph.D. student, William E. Boeing Dept. of Aeronautics and Astronautics, and AIAA Student Member, kyting@uw.edu
†Affiliate Assoc. Professor and Retired Boeing Technical Fellow, William E. Boeing Dept. of Aeronautics and Astronautics, cpnelson@uw.edu
‡Graduate Research Assistant, William E. Boeing Dept. of Aeronautics and Astronautics, and AIAA Student Member, kennew4@uw.edu
§Boeing Endowed Professor, William E. Boeing Dept. of Aeronautics and Astronautics, and AIAA Fellow, eli@aa.washington.edu

LEOB	Leading Edge Outboard
LG	Landing Gears
MS	Metal spine
MVR	Morphing-variable-radius leading edge
N	Nacelles
NB	Fuselage Nose Boom
NC	Nose Chine
NM	Nose Modification
NRTD	Nose Ring Trip Dots
NSRD	Nacelle Shock Reflected Deck
OB	Outboard
OG	Ogive
P	Nacelle Paddles
RT	Raked Wingtip
S	Sharp leading edge
SF	Splitter Flap
SM	Sheet Metal
SS	Sealed-Slate leading edge
SSD	Spoiler-Slot Deflector
TE	Trailing Edge
TEAD	Trailing Edge Aft-Deck
TEIB	Trailing Edge Inboard ≡ Flaps
TEOB	Trailing Edge Outboard ≡ Ailerons
TR	Top rear
U	Upper
V	Vertical tail
VF	Ventral Fin
W	Wing
WF	Wing fence
WR	Wingtip Rudders
WRD	Wingtip Rudders Deflection
WTD	Wing leading edge Trip Dots

Variables

α	Angle of attack
$\bar{c}$	Mean aerodynamic chord
β	Sideslip angle
Γ	Dihedral angle
Λ_{LE}	Wing outboard leading edge sweep angle
$\partial C_M/\partial C_L$	static margin
b	Span
C_D	Drag force coefficient
C_L	Lift force coefficient
C_L vs. C_D	Drag polar
C_L/C_D	Lift-over-drag ratio
C_M	Pitching moment coefficient
C_N	Yawing moment coefficient
C_R	Rolling moment coefficient
C_Y	Side force coefficient
C_{D_0}	Zero-lift drag coefficient
C_{L_α}	Lift coefficient derivatives
$C_{L_{\text{max}}}$	Maximum lift coefficient
C_{M_0}	Zero-pitch moment coefficient
C_{M_α}	Pitching moment coefficient derivatives
$C_{M_{\alpha=0}}$	Zero-alpha pitching moment coefficient
d	Diameter of body
l	Length of body
Re	Reynolds number
S_{ref}	Wing reference area
t/c	Thickness to chord ratio
AR	Aspect ratio

I. Introduction

The NASA funded SCALOS project (Supersonic Configurations at Low Speeds) was launched as an effort to contribute to the development of commercial supersonic technology by focusing on the low-speed characteristics of "modern" supersonic configurations: those that evolved after the conclusion of the High Speed Civil Transport (HSCT) project of the 1990s and a few smaller projects that followed and that incorporate low-boom and better supersonic cruise performance shaping made possible by advanced CFD shape optimization technology of the last 30 years. The project was a collaboration between the University of Washington (in the lead), the University of Michigan, Stanford University, and Boeing Research and Technology. Descriptions of the work by the project teams 2020-2024 can be found in References: [1–18] by the University of Michigan, References [19–30] by the University of Washington, [31–33] by Stanford University, and [34–36] by Boeing Research & technology.

One of the thrusts of the University of Washington's (UW) work was low-speed wind tunnel testing in the 12 ft x 8 ft UW's Kirsten Wind Tunnel. It was driven by the recognition that most work on commercial supersonic design in recent years was focused on low boom and supersonic performance and that more data and more understanding that would guide the low-speed aspects of the design of resulting supersonic vehicle shapes were needed. As stated in earlier papers on the SCALOS project, "a viable, certifiable, supersonic airliner must also be efficient subsonically and meet all performance, handling qualities, and stability and control (S&C) requirements at low speeds." The desire in the SCALOS project (and earlier projects on this challenge at the University of Washington") was to "map the configuration design space" by testing as many configuration features and general arrangements as possible in order to identify trends and gain insights, as well as obtain reference data, that would help researchers and designers in the future.

It was not possible, of course, to carry out an exhaustive mapping of the entire configuration design space with its many geometric design variables and all their combinations. The selection of configurations to be tested, therefore,

was guided by studying the host of configurations that were investigated and reported by research organizations and companies over the last 20 years or so, augmented by engineering experience regarding shape and arrangement elements of major importance. References [37, 38] served as important guides. Years of earlier senior-year capstone airplane design at the UW, with many alternative supersonic configurations that were designed, wing-tunnel tested, and flown to study their low-speed characteristics ([39]) added wind tunnel test information to the new information that was gathered during the years of the SCALOS project, also with deep involvement of UW senior capstone airplane design teams. The focus on commercial supersonic airplane design at the University of Washington, with its emphasis on low-speed characteristics, substantial commercial quality wind tunnel tests, and exploratory flight tests of scaled research UAVs (RUAVs) benefited hundreds of students who graduated the UW's William E. Boeing Department of Aeronautics and Astronautics.

Previous overviews of UW low-speed wind tunnel testing scope and key results can be found in [19, 20, 23, 28]. Those overviews describe progress, year by year, of the SCALOS project-driven Kirsten Wind Tunnel tests and include presentations of key insights regarding the effects of various configuration features on the stability and control as well as lift and drag characteristics. This paper presents the overall scope of the UW's KWT effort and a few key insights at the conclusion of the SCALOS project. The full test results database has been delivered to NASA.

In parallel to the UW KWT's work, tests were carried out at the Boeing Huntington Beach Flow Visualization Water Tunnel (FVWT) aimed at providing dynamic derivative data for selected SCALOS configurations including flow visualization tests that made it possible to better understand the unsteady flow-field dynamics involved. The Boeing FVWT effort has been described in References [34, 35]. An up to date paper on the Boeing work is to be presented at the SciTech2025 conference (Ref. [36])

II. The KWT Wind Tunnel Tests

A. Test Model Geometry

The aerodynamic data obtained for the SCALOS effort should be generically applicable to similar aircraft geometries of any size, from a 5-foot UAV to a 300-foot HSCT design. The particular wind tunnel model component sizes of wings, tails, nacelles and fuselages, were selected based on 1/22 scale representations of 75-100 passenger Mach 1.8 airliner concepts with twin mixed-flow turbofans (MFTF). The test model has an inboard wing section and support interface that can serve as a "backbone", allowing the creation of various configurations based on the same model core for configuration variation studies. The particular modular nature of the wind tunnel model made it possible to test wing-only configurations as well as wing plus aft deck configurations before proceeding to add a fuselage, tail surfaces, canard surfaces, engine nacelles, and landing gear. Different outboard wings were tested as well as a selection of high-lift and roll control devices. The thin nature of the wing-only models led to the selection of the KWT's fork mount as the mount on top of which models would be installed ([40]. Figure 1 shows the cases of the Wing 15 (W15) core of the model on the fork, without and with an aft deck - cases that neither a sting mount nor the single strut support of the KWT (which is much thicker than the prongs of the fork mount) would be able to support without significant geometric changes to the wing.).

Note: Double numerals attached to model parts identifiers (W for wing, F for fuselage, etc.) refer to the year in which the parts were developed. SCALOS wind tunnel work began in 2020. In earlier years, as mentioned above, various supersonic configurations were developed and studied by capstone airplane design teams at the senior level at the University of Washington, assisted by graduate students and faculty advisors, and parts as well as results from this earlier work were added to the SCALOS test results database. W15, is, therefore, the 2015 project wing. Figure 2 shows some of the research UAVs (RUAVs) that were developed by the UW before the beginning of the SCALOS project. All of them were thoroughly tested in the Kirsten Wind Tunnel. Note the 2015 University of Washington's RUAV at the bottom of the figure ((which served as the initial configuration of the SCALOS modular KWT model).

Figure 3a shows the wing planforms that were tested from 2015 and through 2024. Planforms of canard, vertical tails, and horizontal tails are shown in Figure 3.

The key geometric information about the configurations tested (Fig. 3a) is provided in Table 1. Note that the span (b), mean aerodynamic chord ($\bar{c}$), wing reference area S_{ref}, and aspect ratio (AR) of the canard, horizontal, and vertical tails in Table 1 are based on their exposed area outside of the fuselage body.

The Appendix (in Table 4) presents the designations of the modular components of the SCALOS project tested, not including the control and high-lift devices. Inboard and outboard leading edge geometries are shown in Figure 3.

Fig. 1 Wing 15 (from the 2015 UW model) alone and with an aft deck on the KWT fork

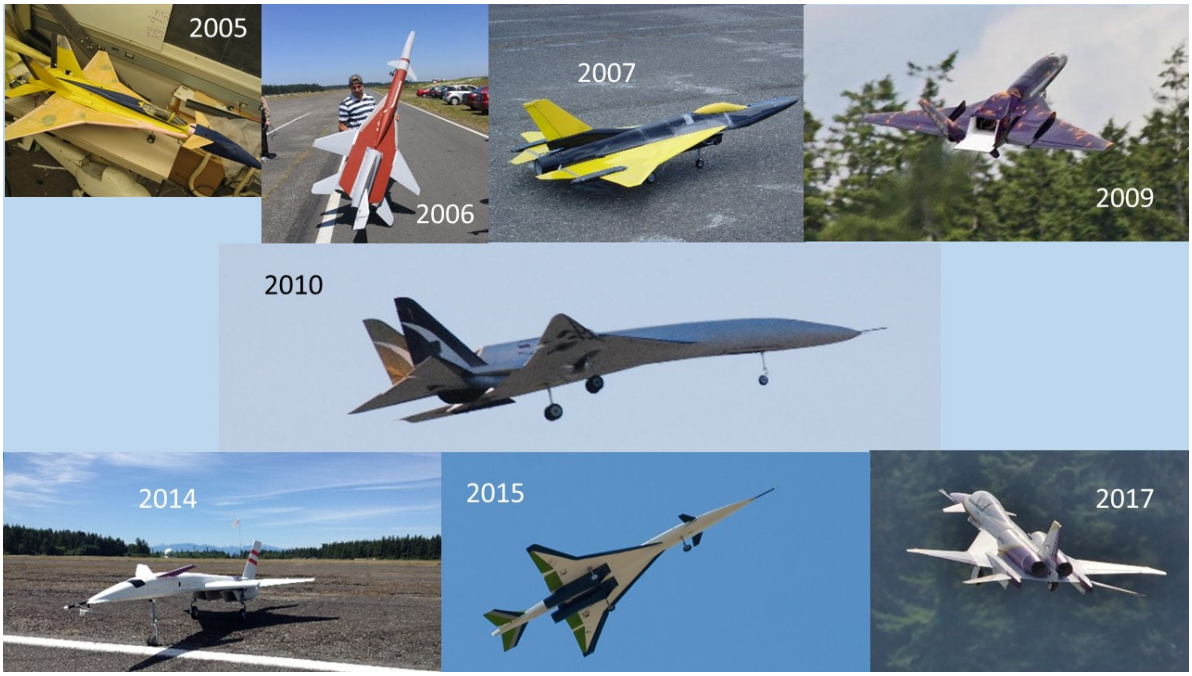

Fig. 2 Pre-SCALOS Capstone Airplane Design Research UAVs developed at the University of Washington

Trailing edge surfaces (clam shell drag devices, etc.), spoilers, ventral fins, were built using stiff sheet metal. Ailerons were 3D printed.

Several roll control devices were studied, including conventional ailrons, speed brakes/aileron spoilers (A.U), spoiler-slot deflectors (SSD) ([41–43]), mid-chord spoilers (FS), and clamshell speed brakes (CS). The SSDs are shown conceptually in Figure 4. The detailed part designation and deflection angles are tabulated in Tables 4 and 5 in the Appendix §(Section V).

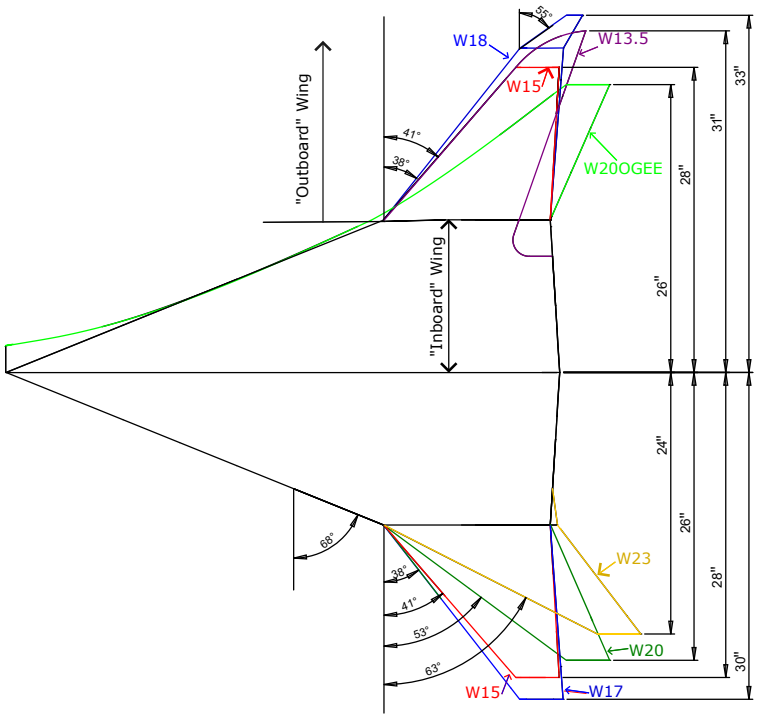

(a) Wing

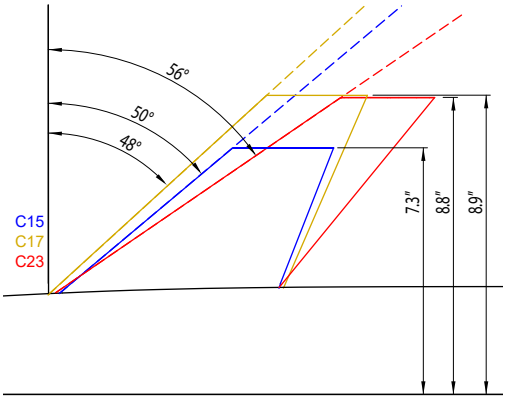

(b) Canards

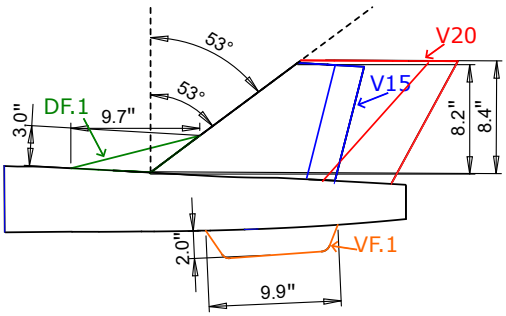

(d) Vertical tails

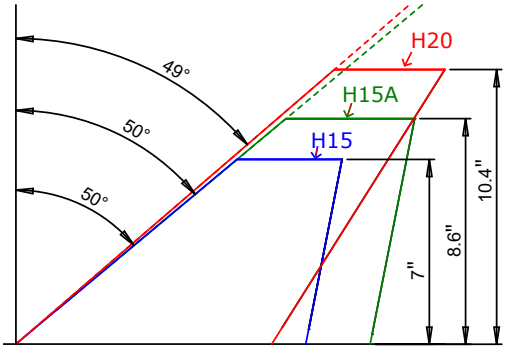

(c) Horizontal tails

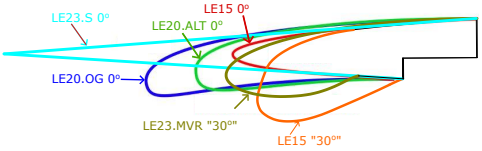

(e) Inboard leading edges

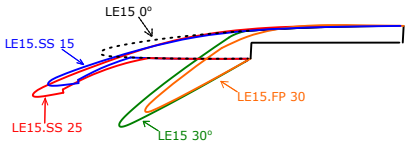

(f) Outboard leading edges

Fig. 3 Wing and tail geometry variations

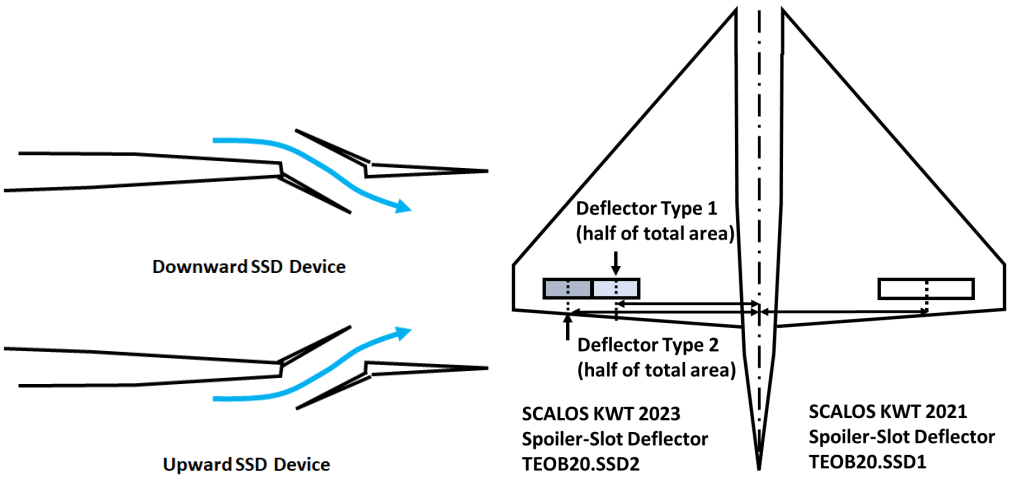

(a) Side view **(b) Top view**

Fig. 4 Exploratory spoiler-slot deflector (not to scale)

Nacelles geometry is shown in Figure 5

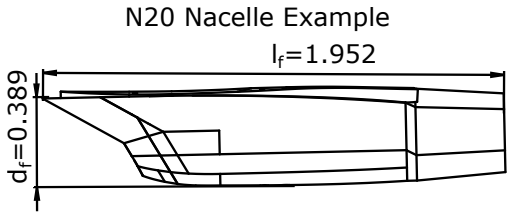

Fig. 5 Dimensional reference for bottom mounted nacelle

Additional geometric variations that were tested included an area-ruled fuselage, longer, higher fineness fuselages and nacelle shock reflection decks (for low-boom), upper and lower-weighted fore-body super-ellipse cross-sections, multiple nacelle locations, large aft-decks, twin verticals, a V-tail arrangement, and a landing gear.

Out of the many configurations that were tested, of particular interest is a configuration that was selected for conceptual design pursuits, named RSAC (Reference Supersonic Airplane Configuration). The conceptual design of the RSAC configuration is described in the final SCALOS project report. The associated wind tunnel model (denoted UW-S-24A) is based on the general configuration of the Boeing 765-070A from the N+2 studies. It evolved from UW configuration UW-S-21 (Figure 6) and is shown in Figure 7 in the take-off and landing configuration.

Note the area-ruled fuselage, no aft deck and larger horizontal tail surfaces, and slight differences in longitudinal arrangement in order to make the area distribution closer to that of a Sears-Haack body.

The Appendix (Section V) presents detailed tables of model parts and their designations (Table 4) and control surfaces and their designations (Table 5. The configuration variations that were tested in the pre-SCALOS-project years 2015, 2016, 2017, and 2018 are shown in Tables, 6, 7, 8, and 9, respectively, in the Appendix (see 3 for test years and test entry numbers).

Additional tables of tested configuration variations show configurations that were tested from 2020 to 2023 (Table 10), 2017 low-tail configurations (Table 11), the 2020 low-tail configurations (Table 12) , the 2020 T-Tail configurations (Table 13), the 2021 low-tail configurations (Table 14. Also 2023 configurations (Table 15) and the 2024 tests 16.

Fig. 6 The UW-S-21 Model in the KWT test section

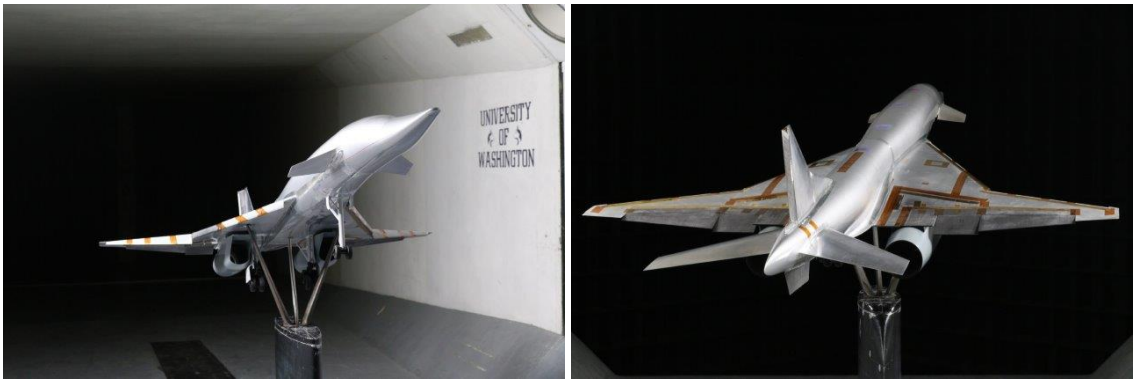

Fig. 7 UW-S-24A in the Takeoff and Landing Configuration

Table 1 SCALOS wind tunnel model components specification

	Designation	$\Lambda_{LE}(^\circ)$	$\Gamma(^\circ)$	b (ft)	$\bar{c}$ (ft)	$S_{ref}(ft^2)$	t/c_{max}	AR
Canard	C15	50	0	1.22	0.400	0.277	0.04	5.37
	C17	47.6	0	1.48	0.535	0.380	0.04	5.76
	C23	55.6	0	1.42	0.399	0.350	0.04	5.76
Outboard Wing	W13.5	41.0	4.67	5.22	1.73	8.17	0.05	3.34
	W15	41.0	4.67	4.67	2.01	8.30	0.05	2.63
	W17	38.1	4.17	5.00	1.92	8.58	0.05	2.91
	W18	38.2	10.2	5.46	1.86	8.66	0.05	3.39
	W20	53.5	4.74	4.40	2.09	8.09	0.05	2.39
	W23	63.0	4.45	4.00	2.28	7.83	0.05	2.04
Horizontal Tail	H15	50.1	0	1.17	0.623	0.594	0.04	2.30
	H15A	50.2	0	1.43	0.777	0.939	0.04	2.18
	H18	50.2	10	1.97	0.828	1.54	0.05	2.51
	H20	49.2	0	1.74	0.585	0.882	0.08	3.43
	V23.H	37.6	50.3	1.41	0.617	0.804	0.05	2.47
	H24	49.25	0	1.81	0.581	0.865	0.08	3.78
Vertical Tail	V15	50.1	0	0.74	1.07	0.579	0.05	0.946
	V16T.2	51.1	0	0.610	0.706	0.409	0.05	0.910
	V20	53.3	0	0.777	1.36	0.934	0.05	0.646
	V23.V	37.6	50.3	1.77	0.659	1.00	0.025	3.13
Ventral Fin	VF.1	29.9	0	0.167	0.7334	0.0033	0.1	0.228
	VF.2	30.2	0	0.1775	0.7540	0.1329	0.0033	0.2370
	VF24T	16	30	0.1567	0.3501	0.1087	0.00714	0.4518
Dorsal Fin	DF.1	73.8	0	0.17	0.75	0.16	0.04	0.181
	Designation	d (ft)	l (ft)	$S_{wet,\,ext}$ (ft^2)	S_f (ft^2)	$S_{wet,\,int}$ (ft^2)		
Fuselage	F15	0.542	9.55	10.603	0.221			
	F15.L	0.542	11.57	12.927	0.211			
	F24	0.57	9.82	12.483	0.283			
	AD16	2.81	2.33	9.234	0.280			
Nacelle	N15	0.375	2.165	2.094	0.133	2.199		
	N16	0.398	1.990	1.623	0.082	1.822		
	N18	0.469	2.788	3.119	0.152	2.733		
	N20	0.389	1.952	2.284	0.138	1.708		
	N23	0.389	2.633	2.327	0.144	2.369		

B. The Kirsten Wind Tunnel (KWT)

All wind tunnel tests were carried out in the Kirsten Wind Tunnel (KWT) at the University of Washington. The tunnel has a filleted rectangular test section of 12 ft in width by 8 ft in height and by 10 ft in length. It is a low-speed, closed-circuit, atmospheric, dual-return wind tunnel as shown in Fig. 8. The tunnel has two sets of 14' 9" -diameter seven-bladed propellers that can drive the air up to 200 miles per hour through the test section for a maximum dynamic pressure of 100 psf. The raw data from the external balance requires correction to obtain final force and moment values. The mechanical interaction of forces and moments in the balance system are corrected using standard correction protocols of the tunnel. Corrections of weight tare and strut tare are applied. Moments are transferred from the balance moment center (BMC) to model moment center (MMC). Corrections for blockage, flow angularity, and wall effects are computed and added to the initial coefficients. The final coefficients are transferred from the wind axes to the stability axes. Additional CFD and test work was carried out to develop dedicated wind tunnel corrections for the kind of configurations tested for this project, as described in [21, 26] and [27].

The majority of tests were conducted at 40 psf and this was later lowered to 32 psf to prevent model adverse dynamics (severe buffeting of the large models at high angles of attack). Data between these two different dynamic pressures was shown to be fully repeatable, other than a slight Reynolds number related skin friction drag effect in $C_{D_{\min}}$ seen at low angles of attack.

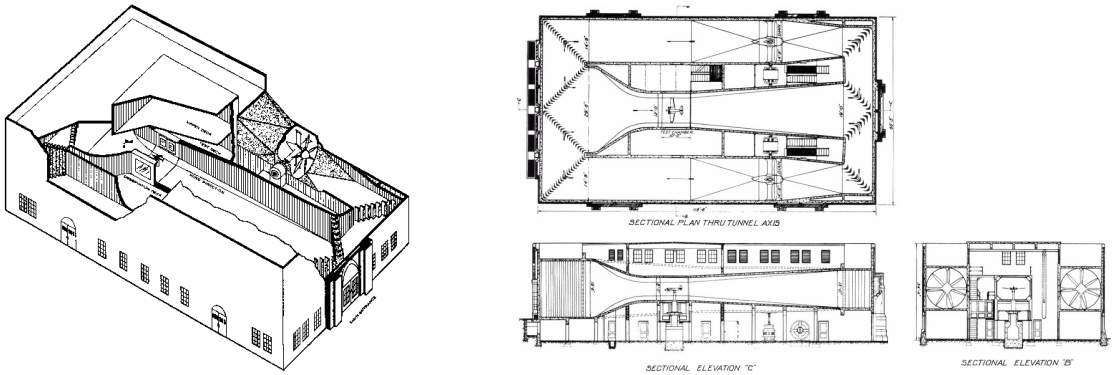

Fig. 8 Kirsten Wind Tunnel at the University of Washington [44]

C. Test Conditions and Entries

Wind tunnel tests were conducted at several tunnel dynamic pressures. For each dynamic pressure, tests were carried out over a range of sideslip angles, β, and angles of attack, α, from -10 up to 30 degrees. Table 2 presents the dynamic pressures in psf with corresponding Reynolds numbers based on baseline-wing's (W15) mean aerodynamic chord length (see Table 1). Table 3 summarizes all test entries completed from 2015 to 2024, with the SCALOS tests carried out between 2020 and 2024. The table also shows 2015-2018 tests which are beyond SCALOS period of performance. These were partly funded by support for senior design capstone by Boeing, and earlier by AFOSR.

The highly slender commercial supersonic configurations required for low-boom and solid supersonic cruise performance are subject to significant nonlinear aerodynamic mechanisms due to vortex dominated high-lift and vortex breakdown on the thin cranked-delta wings, the long slender fuselage ahead of the wing and its canard surfaces and any front fuselage and tail nonlinear effects magnified by the large moment arms involved.

Although actual angles of attack in flight and sideslip angles (especially during takeoff, approach, and landing conditions with LE flaps deflected) are expected to be kept in the linear range, protected by warnings and automatic AOA limiter systems, SCALOS wind tunnel tests were pursued at angles of attack and sideslip angles well into the nonlinear range to allow developers to address, early in the design process, nonlinear flight mechanics stability and control constraints beyond the flight envelope to tackle overshoot conditions and the loss of control dangers that they present (Ref. [45].

Table 2 Dynamics pressure and Reynolds number at standard sea level

q (psf)	3.5	6.25	10	14	20	30	32	40	60
Re	6.90×10^5	0.93×10^6	1.17×10^6	1.39×10^6	1.66×10^6	2.03×10^6	2.10×10^6	2.35×10^6	2.87×10^6

Table 3 Kirsten Wind Tunnel test entries

Entry number	Year	Month	Test period (days)	Total Runs (#)	Data collection
UW2128	2015	April	6	249	Force & moments and flow visualization
UW2166	2016	April	6	256	Force & moments and flow visualization
UW2200	2017	April	6	216	Force & moments and flow visualization
UW2237	2018	April	6	287	Force & moments and flow visualization
UW2295	2020	August	3	23	Force & moments
UW2298	2020	September	6	133	Force & moments
UW2320	2021	June	7.5	148	Force & moments
UW2324	2021	August	4	54	Flow visualization
UW2326	2021	September	6	225	Force & moments
UW2331	2021	November	5	150	Force & moments and flow visualization
UW2354	2023	May	20	456	Force & moments and tare & interference
UW2367	2024	Feb	10	226	Force & moments
12			85.5	2400	

III. Insights

The substantial amount of wind tunnel data collected by the SCALOS project and the 5 years of senior capstone design testing and model development before it at the University of Washington makes its possible to study the effects of configuration shape and arrangement on the aerodynamic characteristics of the configurations studied. Actual values of the various aerodynamic derivatives of the different configurations are, of course, important and allow estimating the aerodynamic characteristics of a large number of configurations that fall, in shape and arrangement, into the configuration design space that the tests cover. The results also allow fine-tuning and validation of CFD math models for the resulting CFD technology for this technology to then be used in parametric design studies of new configurations.

In this paper we choose to focus on general trends and selected insights. In what follows we study and present the effects of wing planform, tail configurations, canards, aft-decks, and the location of engine nacelles - that is, the overall configuration without detailed "local" variations in the form of control and high-lift device motions. The plan is to present, in a separate publication, insights based on the parametric testing of various control and high-lift devices. Trends that are presented in the following discussion were generated using partially corrected KWT data. As will be shown in this paper, the final fully-corrected data shows essentially equal trends and very similar levels as the pre-final data.. The final corrected data is available in the test results database for the replication of the studies shared here and for other studies of the effect of the many configuration variations that were tested on the overall aerodynamic characteristics. It should be noted that unless noted otherwise, all SCALOS data has been reduced using the MAC and reference area of wing W15 (gross projected area and its equivalent trapezoid MAC).

A. Longitudinal characteristics

Figures 9 and 10 show the effects of wing planform shape on the pitching moment coefficient CM versus α and CM vs. CL curves. The configurations covered by the figures include Wings + Fuselage + VT15 + VentralFin1 + DorsalFin1 components (see tables of components and their designation in the paper and Appendix). There are no canards, nacelles, or horizontal tails. All wing flaps are at zero. Data is presented in stability-axis orientation with the CG (moment center) at 25% MAC.

The configurations are statically stable up to about 7 degrees angle of attack. The W17 wing becomes statically unstable at about 8 degrees. Note the tendency of W17 to regain static stability at 12 degrees to lose it again at 16 degrees AOA. Around AOA-0 degrees the most statically stable are Wings 13.5 and Wing 17 (See also Ref. [46] for an HSCT-era exploration of wing planforms.

Deflecting leading edge flaps generally improves the stability and drag polar shape of all the planforms by delaying

the alpha for leading edge vortex separation (although at some loss in CL at alpha). As this is fundamentally favorable for landing and takeoff conditions, it is assumed the LTO regime will involve some combination of LE and TE flap settings optimized for trimmed L/D at the operating CL's. However, planform selection is likely constrained by "flaps-up" characteristics at higher subsonic speeds and certification conditions with various failure scenarios for the flaps and flight controls. In particular, it is desirable for pitch-up to be delayed, the CM change to be less abrupt, and for the difference in static stability before and after the pitching moment break to be minimized.

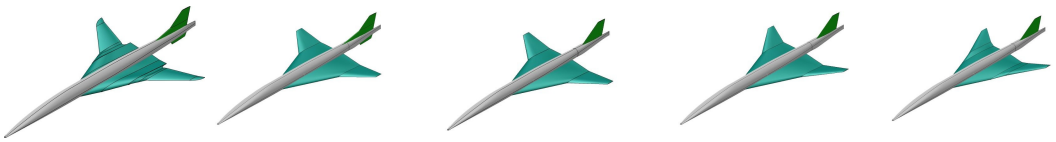

(a) W13.5 **(b) W15** **(c) W17** **(d) W20** **(e) W23**

Fig. 9 Key wing planforms

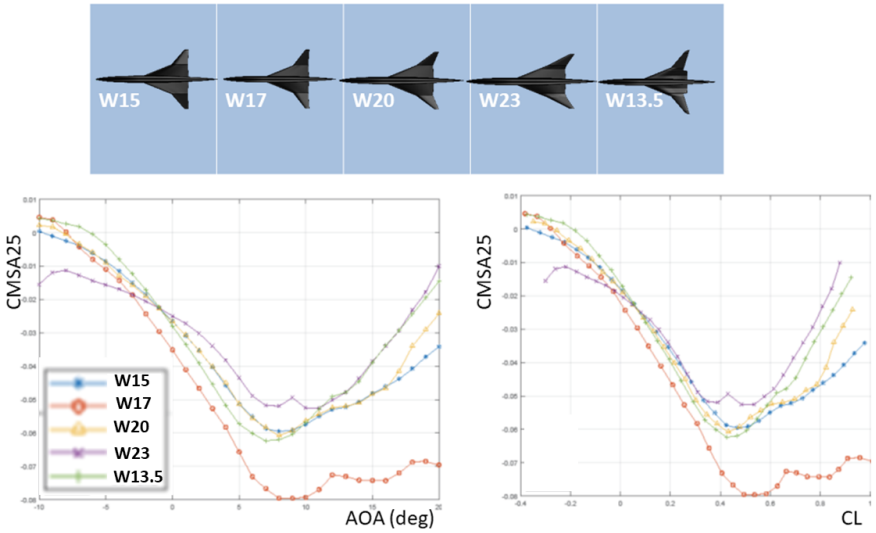

Fig. 10 Wing planform effects

A study of longitudinal control options is presented in Figure 11. Shown are CM (at 0.25 MAC) vs. AOA curves for full configurations with nacelles on, common fuselages, common main wing (W15), no TE/LE flap deflections, based on a common reference area and a common MAC. Note the delay in the start of pitchup, the more moderate pitchup, and the higher static stability at small AOAs of the low-mounted aft-tail case. That case, however, also shows a region of deep stall from about 20 degrees AOA and higher. The canard, not surprisingly, degrades low AOA static stability without the presence of a horizontal tail and leads to more severe longitudinal instability compared to the other longitudinal control tail options, indicating that a farther forward CG would be needed to retain stability if a canard is employed for pitch trim/control, whether in conjunction with elevons or an aft-tail.

However, it should be noted that the basic planform-dominated shape of the pitching moment curve is relatively unchanged - the lift generated by the canard versus alpha acts to rotate the entire moment curve as though the aircraft was being flown at a farther aft CG. This indicates that equivalent static stability can potentially be recovered by flying at a farther forward CG while retaining the canard's control authority advantage of having a longer "tail arm" from the CG, relative to an aft-tailed configuration. For a given required pitch control / trim authority the canard arrangement may therefore get away with a smaller surface than an equivalent aft tail. It should also be noted that canard configurations have repeatedly shown that the lift generated by canard for trimming at forward CG in the linear alpha region does not increase overall lift because the canard down-wash decreases the wing lift by roughly the same amount. Trim with the canard acts essentially a "couple" in CM.

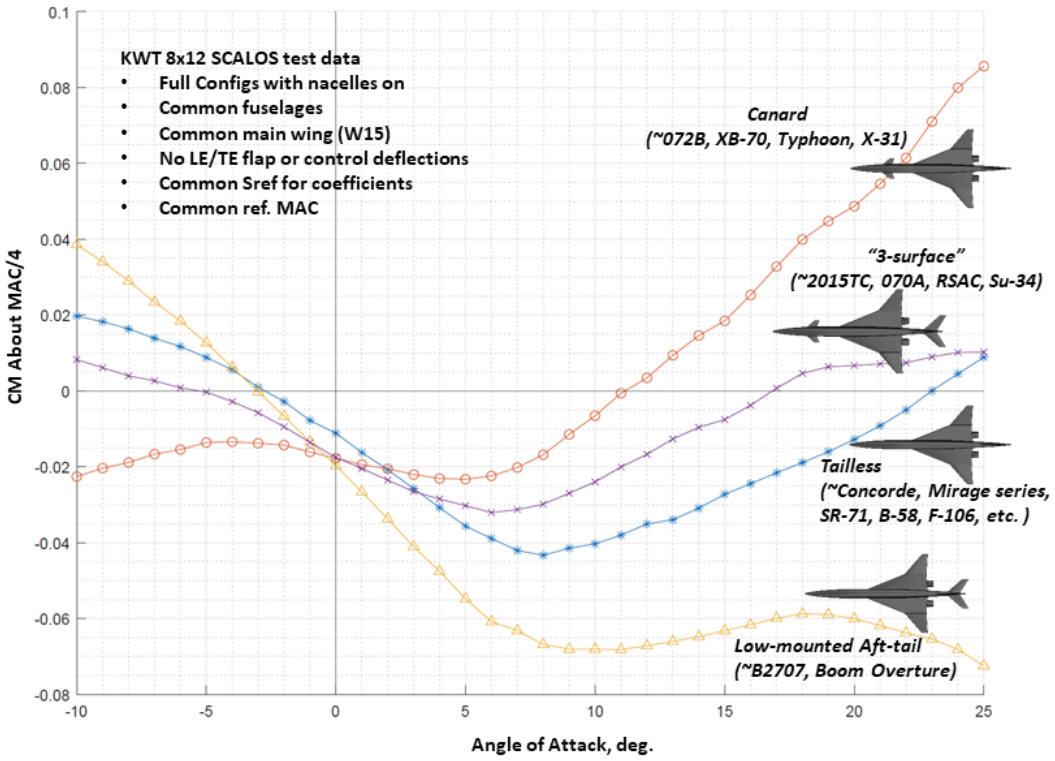

Fig. 11 Longitudinal control options

The effect of adding an aft-deck is shown in Figure 12. Again, as in the case of the previous figure, a common fuselage and a common main wing (W15) were used, with no LE/TE flap deflections, and with common reference area and reference MAC. The stabilizing effect of the aft deck is obvious. In both the aft-deck and aft tail case as well as the three-surface plus aft deck case, there is practically no loss of longitudinal static stability (except for a small range of AOA between 25 and 27 degrees, where the 3-surface plus aft-deck configuration is marginally stable.

It is likely that this small transitory region of instability could be easily smoothed with fly-by-wire control laws or possibly eliminated during aero detail design. It should be noted that the aft-deck and tailed-aft deck arrangements show excessive static pitch stability about the wing quarter MAC CG location, which could cause high trim drag and larger pitch-control-induced loads on the airframe. This indicates that taking advantage of the aft-deck arrangements requires that the CG be located farther aft. This may be a net-favorable trade-off for some aircraft as the linearity of the pitch stability means that stability at aft CG will not be a limiting factor when operating at higher CL's. The inherently more linear pitch curve shape of the aft-deck arrangements comes with a penalty in wetted area (CDo), but increased potential for reducing sonic boom and transonic drag rise, and for integrating upper-surface nacelles for LTO noise shielding. The area-rule characteristics of the aft-deck arrangement can also lead to a somewhat larger cabin cross-section in the forward portion, possibly making this arrangement more attractive for business jet sized applications.

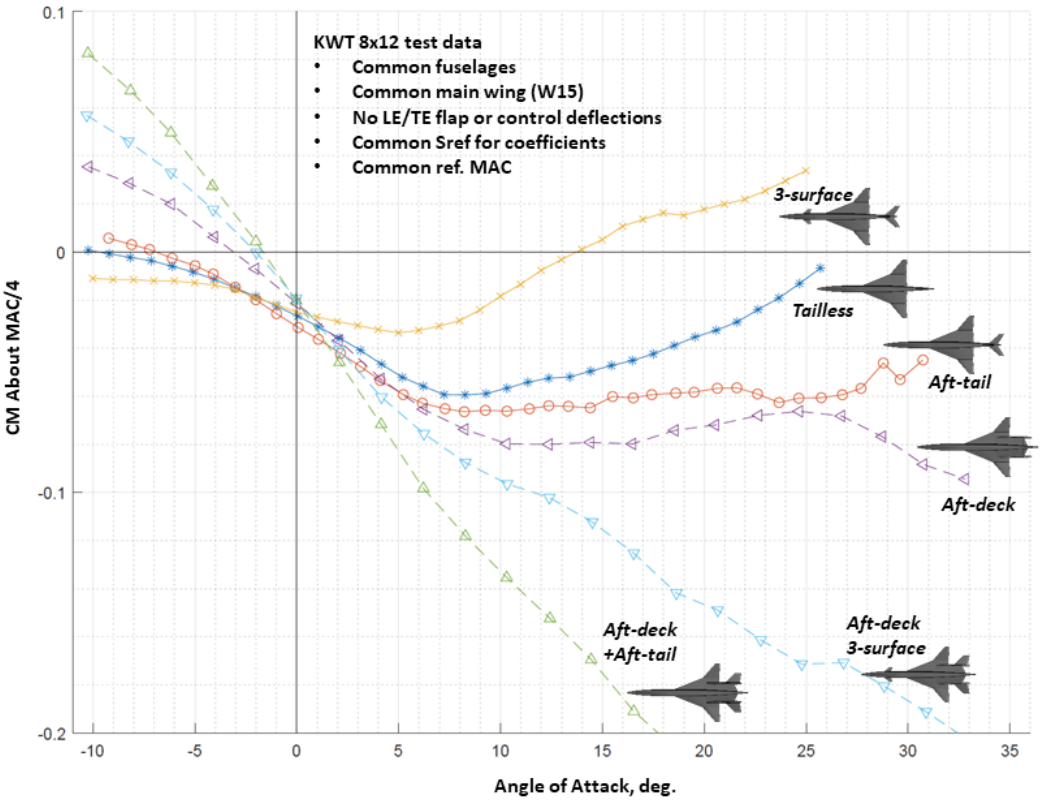

Fig. 12 Longitudinal control with an aft deck: Cm.25 vs angle of attack

The effect of adding an aft-deck on CM vs. CL curves is shown in Figure 13. The aft-deck has a strong stabilizing effect on the low-speed longitudinal static stability. It adds drag, of course. From the aeroelastic perspective it leads to the stiffening of the aft empennage and, therefore, has the potential to alleviate, passively, empennage flutter.

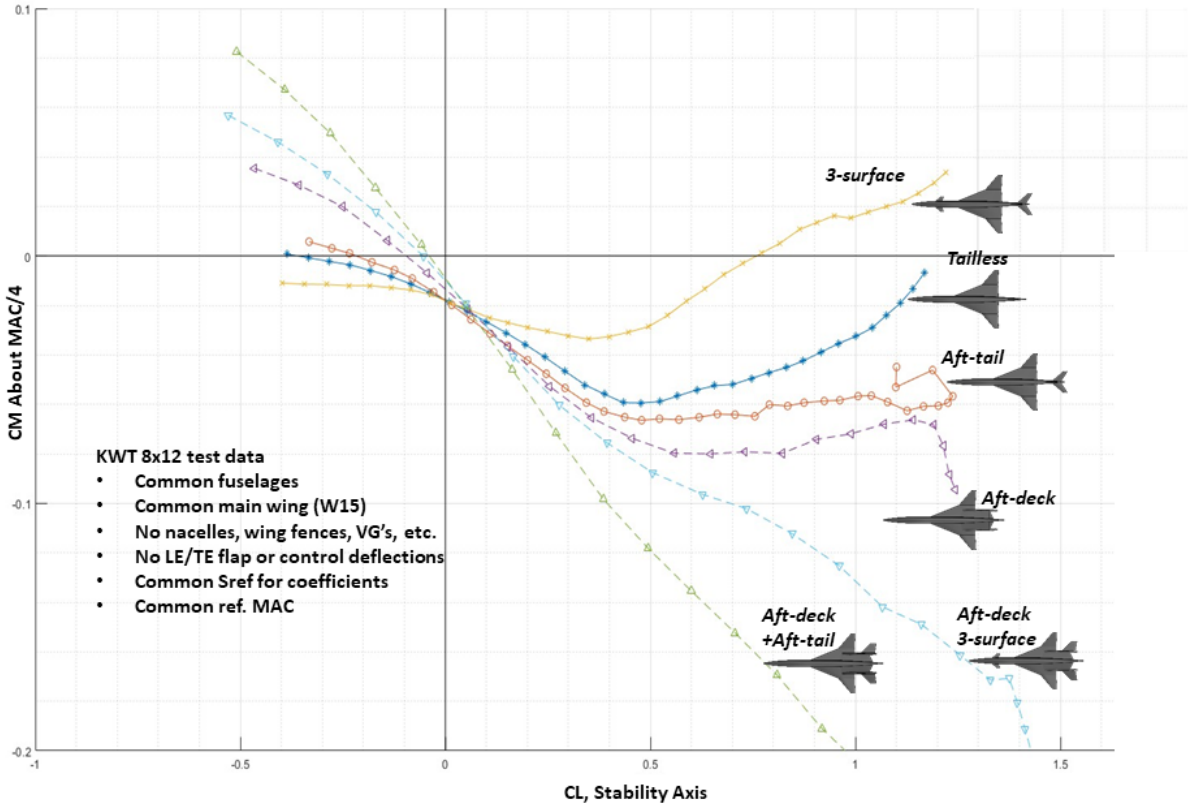

Fig. 13 Longitudinal control with an aft deck: Cm.25 vs CL

An effort is made in Figure 14 to bring alternative longitudinal configuration arrangements to a common basis. All cases shown in the figure were "balasted" to a reference 5% static margin. They were all trimmed to zero CM0, with no constraint on CG location and trim drag.

The figure shows that the Aft-deck + stabilator configurations, with or without canard, have nearly linear CM (at a wetted-area penalty) and no pitchup. Canard lift vs. AOA degrades static margin by 4-8% at fixed CG. The 3-surface 'tube & wing' general arrangement (similar to RSAC) looks the most unstable in this comparison, has the earliest and most abrupt pitch-up, but has min. trim drag over a greater CG & TE flap deflection range. What's "best" here depends on performance trade-offs and configuration integration/CG constraints

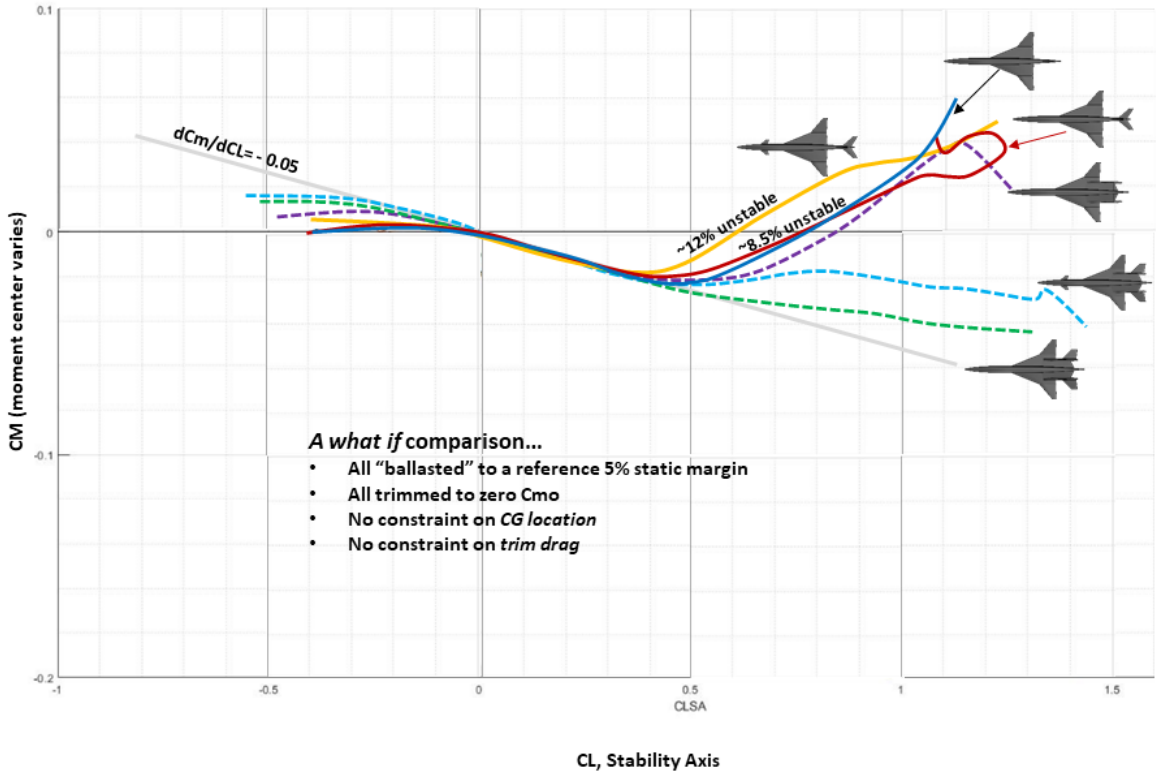

Fig. 14 Longitudinal control: CM vs. CL differences on a common basis

Figure 15 shows the contribution of the horizontal stabilizer to longitudinal static stability with and without an aft-deck. As the figure shows, the aft-deck "sponson mounted" stabilizers are very effective while the aft-body-mounted stabilizers help post pitch-up but contribute almost nothing below about 7 degrees AOA.

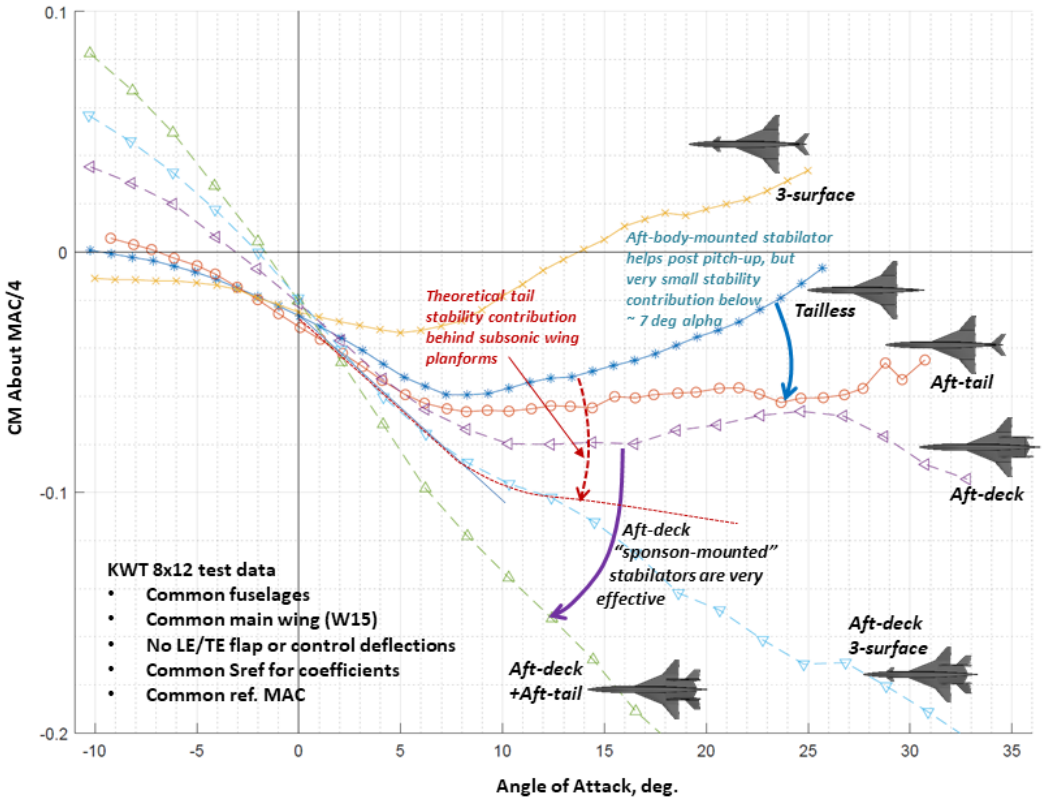

Fig. 15 Longitudinal control: Conventional horizontal tail vs. aft deck

The effect of horizontal stabilizer area on pitch control authority is studied in Fig. 16. It is interesting to note that there is very little change in CMalpha static stability for a 50% stabilizer area increase. It seems that the large inboard wing is acting as a strong "flow straightener" (which is similar to the HSCT experience, $d\epsilon/d\alpha$ close to 1). As a result you cannot fix pitch instability by increasing the tail volume Vbar ($\bar{V}_H$). The increase in pitch authority for adding stabilator area is a ratio of only 4:5, rather than 1:1, which would also have an impact on tail sizing criteria for this class of aircraft.

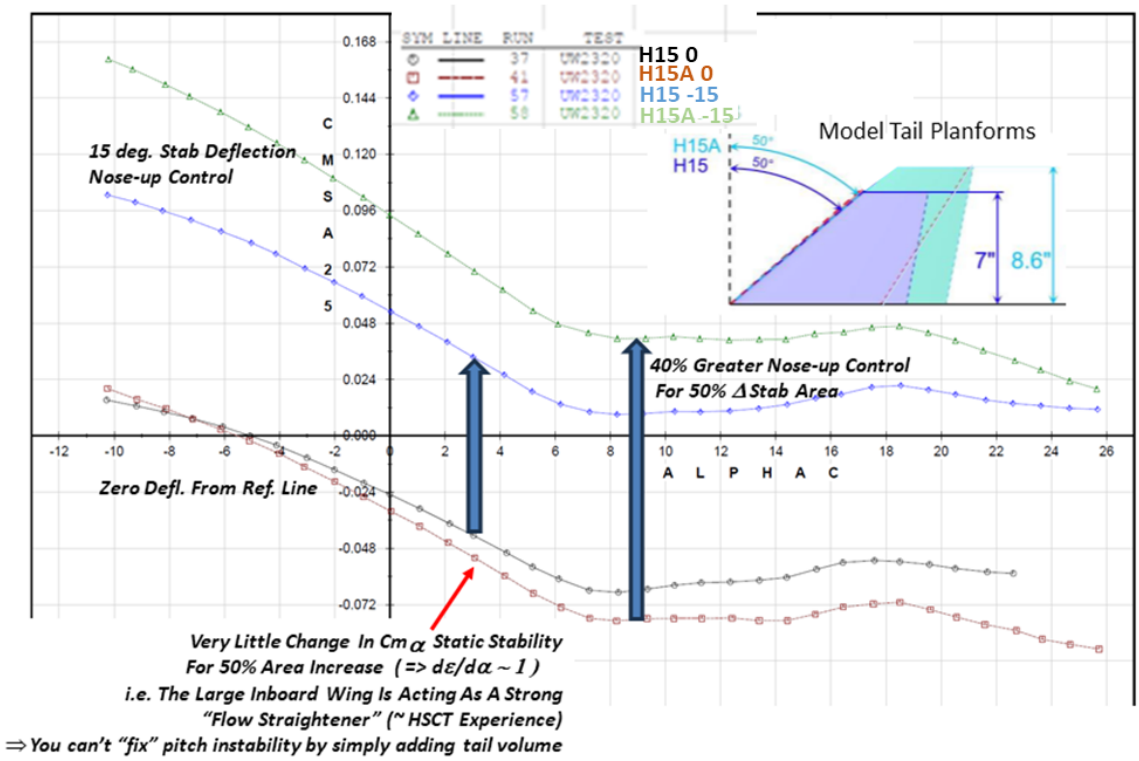

Fig. 16 Longitudinal control: Effect of horizontal tail area

Figure 17 shows an example of canard contributions. This is based on 2017 data with an aft-deck. As can be seen, above a CL of about 0.8 the canard is not effective due to canard stall. This indicates that a pure-canard (aft-tailless) configuration would also need pitch control from wing elevons to provide adequate pitch authority at high alpha conditions.

Some aft-body + tail configurations show very nonlinear results at larger canard deflections (the broken red line on the figure). Testing at UW prior to SCALOS, with various canard planforms and locations, indicated that: (1) this non-linearity can be mitigated to a certain extent by further configuration development, and (2) that selection of the canard planform can impact the canard's own stall behavior (hence pitch-down tendency at large combinations of alpha and canard deflection).

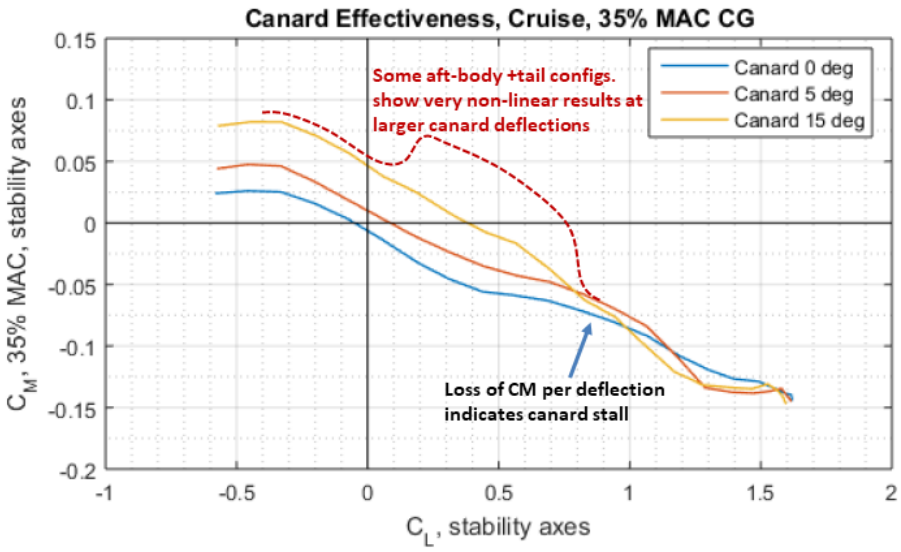

Fig. 17 Longitudinal control: Canard effectiveness

Shifting attention to the effect of vertical location of the horizontal tail, Figure 18 shows CM vs AOA curves for T-Tail, Mid-tail, low-tail, and no-tail configurations based on the common fuselage and W15 with with no LE/TE flap deflections. The T-Tail provides much more stability at low AOAs and becomes highly unstable above pitch-up. Note the beginning of a turn of the CM vs AOA curve around 25 degrees AOA which may lead to deep stall, as is common in the case of T-Tail configurations (as the T-Tail begins to emerge below the wake of the wing).

The low-tail configuration shows deep stall after about 23 degree AOA. It is unstable above 6 degrees AOA and below -6 degrees AOA. The low stability of the tailless configuration relative to the tailed ones is obvious and expected.

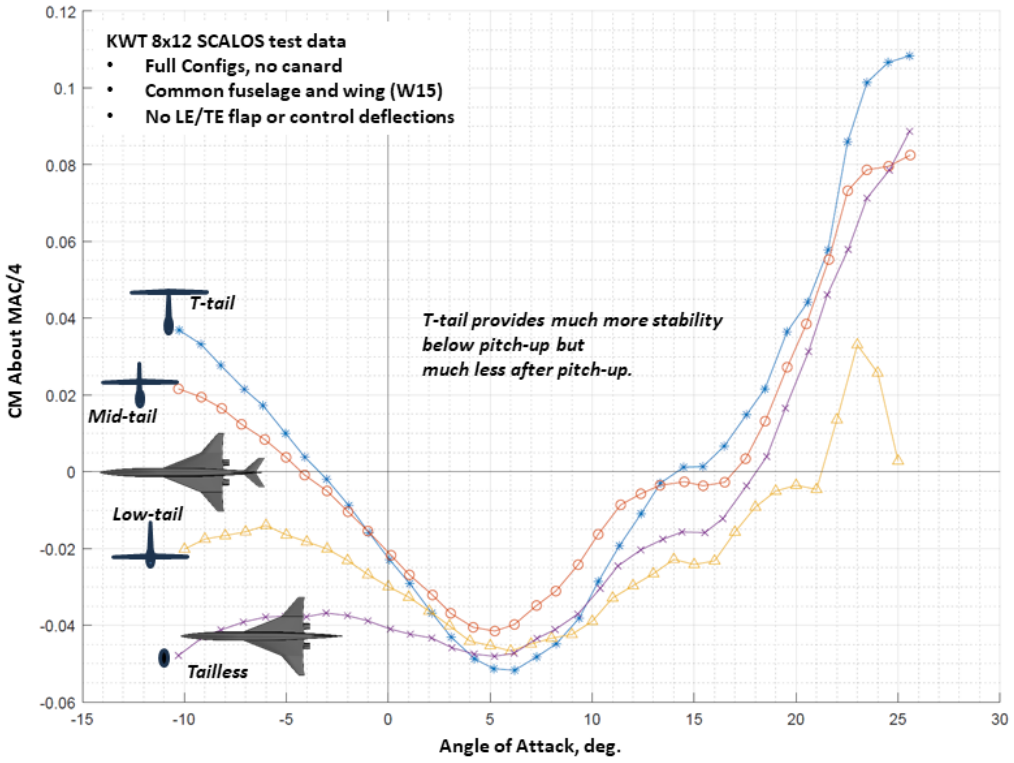

Fig. 18 Longitudinal control: Effect of vertical location of the horizontal tail

The following figure (Fig. 19) shows CM vs. CL curves for the various vertical positions of the horizontal stabilizer for the same configurations as in the previous figure. Data shifted ("pseudo-trimmed") to a common CM_0 of zero shows the the T-Tail provides much more negative dCM/dCL (static margin) at fixed CG location but is the most unstable post pitch-up.

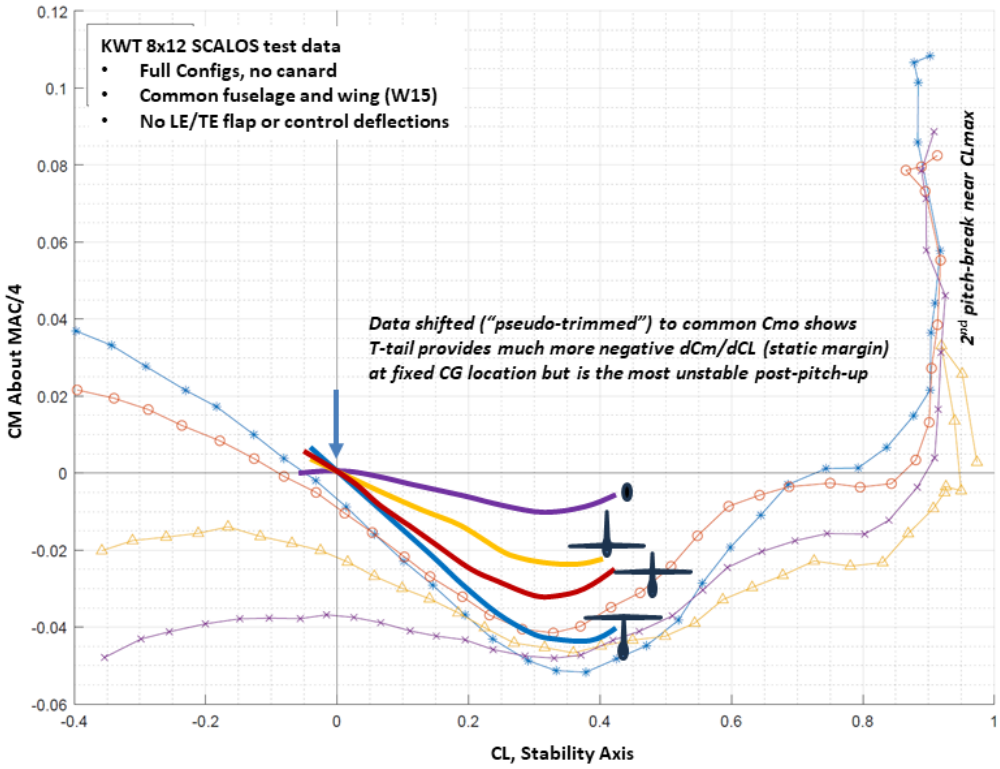

Fig. 19 Longitudinal control: Effect of vertical location of the horizontal tail - CM vs. CL

As mentioned earlier, the results presented here so far to study configuration shape and arrangement effect trends are those that were corrected partially before the final set of wind tunnel corrections for the SCALOS tests was ready. The following two figures (20 and 21) show comparisons between partially-corrected and fully-corrected KWT results for one of the cases that seems to be most sensitive to the type of corrections used: the case of the vertical location of the horizontal tail, which at high negative and positive angles of attack brings the tail, relatively far behind the wing, close to the floor and ceiling of the test section and behind the fork support and the pylon that covers the connection of the fork support to the below-the-floor external balance.

As both figures show, the differences in corrected results are minor and the trends are practically the same.

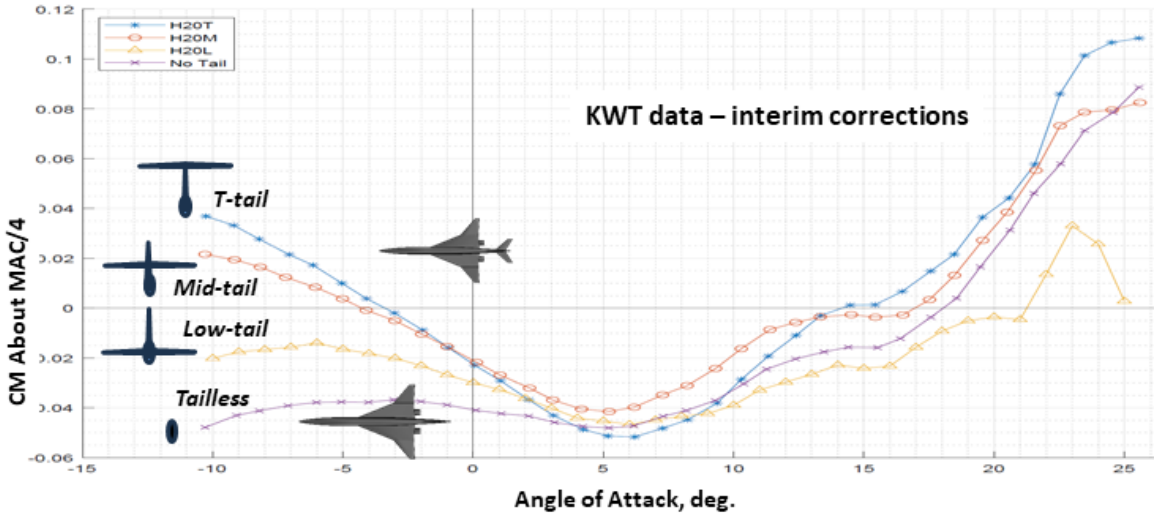

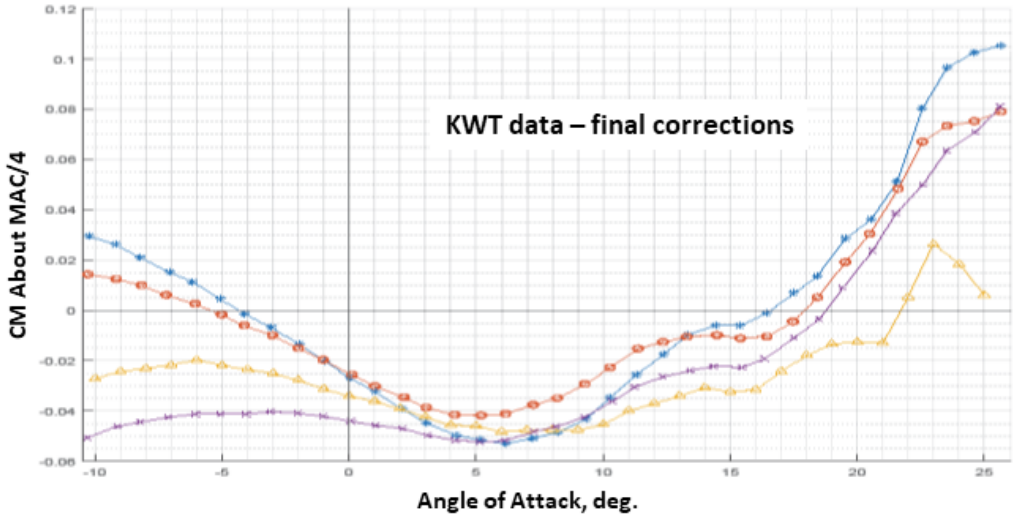

Fig. 20 Longitudinal control: Effect of vertical location of the horizontal tail - CM vs. AOA: KWT final corrected data versus KWT data corrected partially

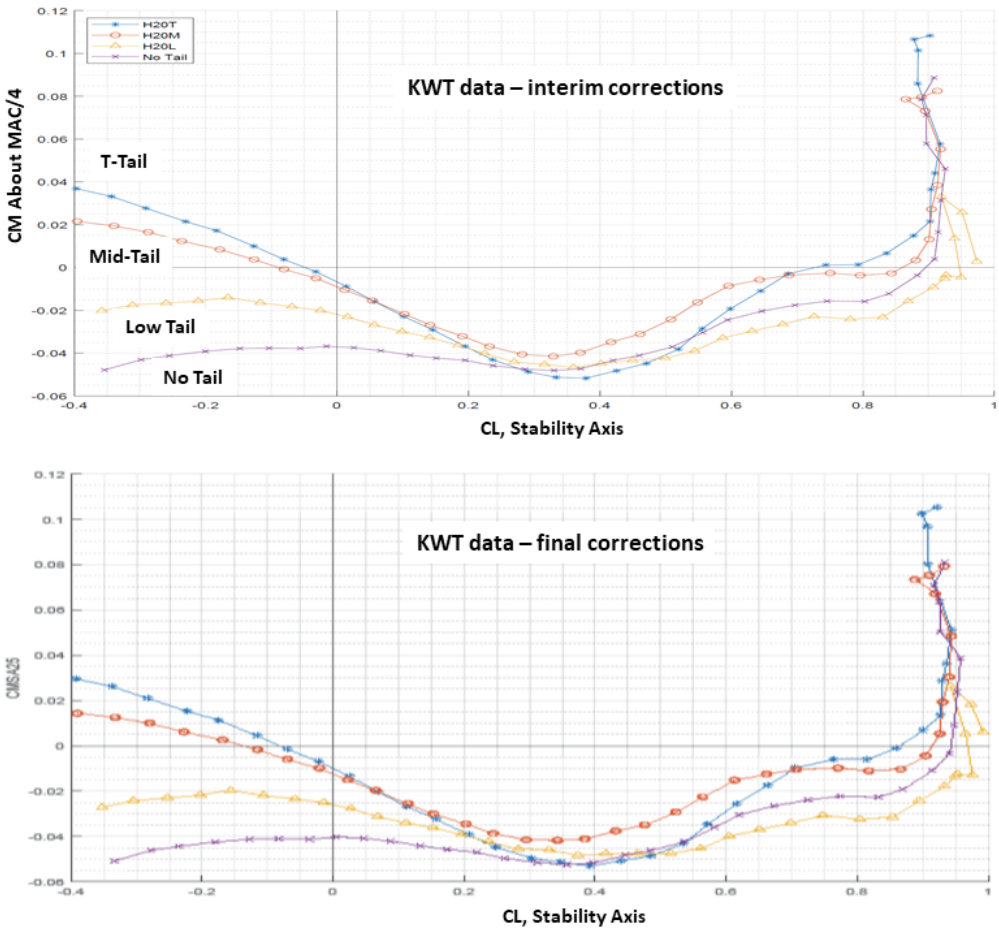

Fig. 21 Longitudinal control: Effect of vertical location of the horizontal tail - CM vs. CL: KWT final corrected data versus KWT data corrected partially

In Figure 22 we can see the effect of using LE/TE flap deflections to improve pitch-up. The "clean" configuration in this case includes a W17 wing plus F15+A15+N20.B+V15+C15.F+H20.L+VF1+DF1 (See the table of names of components to identify all components). Plotting CM about 0.25MAC versus CL for various sideslip angles, the figure links various parts of the CM vs CL curves to important maneuvers. The "approach configuration" includes full-span TEs at 10 deg down, canards at +5 degrees, full span LE flaps at 30 degrees and a stabilizer at zero degrees rotation. The configurations is, thus untrimmed.

It is interesting to note that with flaps down there is about a 70% increase in pitch-up CL. "Approach" LE/TE CM in this example looks like that of subsonic aircraft but the pitchup still occurs before CLmax. 45 deg bank puts CL past the local pitch-up instability. That may mean "special conditions for certification. This example looks favorable, but 25 % CG may not be attainable with the full scale airframe (unless the limited region of instability can be smoothed out with fences or other aerodynamic "fixes" during detailed configuration development) and any allowable negative static margin depends on short period dynamics, Iyy rotational inertia, and aerodynamic damping coefficients, CMq. It should be noted that W17 has what appear to be the most "low-speed-friendly" aero characteristics of all the tested planforms.

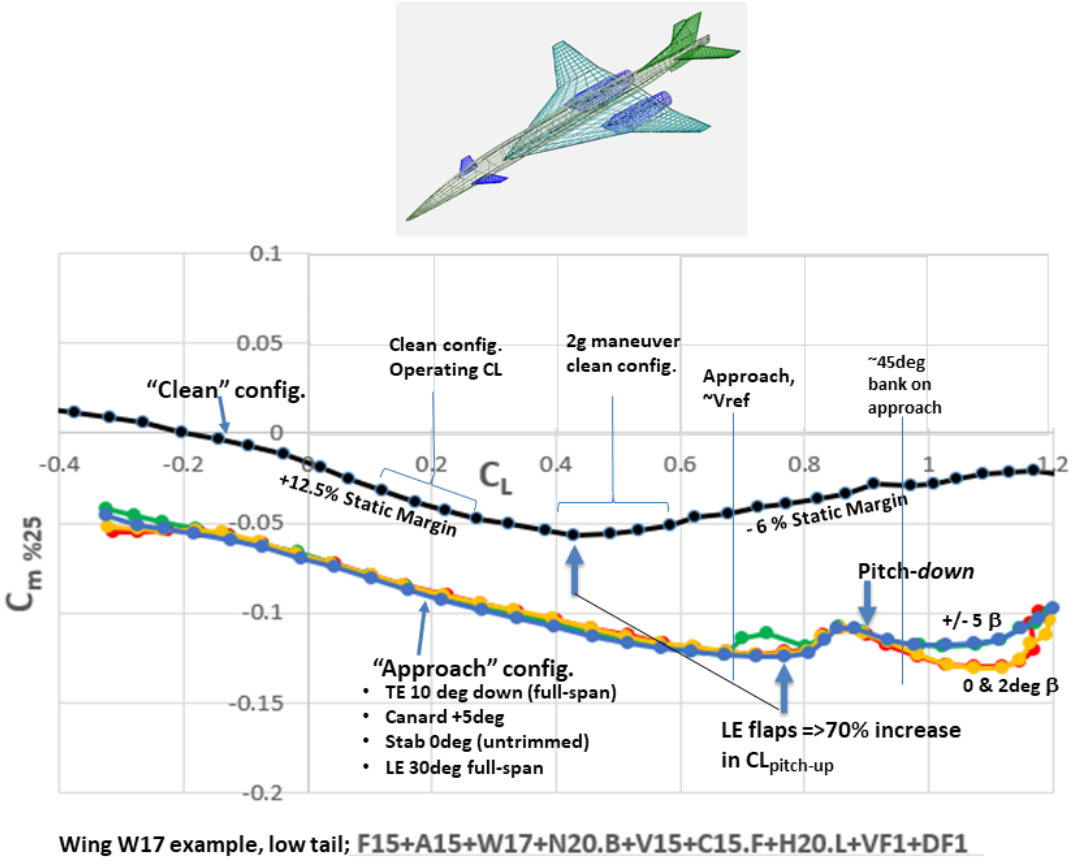

Fig. 22 Longitudinal control: Clean vs. approach configurations. CM vs. CL

Shifting attention from pitch stability to lift and drag, Figure 23 compares the lift and the Lift/Drag of an RSAC like configuration (UW-S-24) to two low boom concepts.

The figure shows KWT test results at wind tunnel Reynolds numbers for configurations without wing fences, vortex generators, etc. and with no LE/TE flap deflections. Common Ref. area and MAC are used. The "Icon-2" Arrangement is a Boeing-NASA N+3 configuration from the N+3 study ([38]) (based on the general arrangement of the 795-107B) and the SCALOS "Low-Boom" is a UW ogee wing configuration with a longer fuselage, top-mounted nacelles, and a T-Tail. Note the better lift and lift over drag characteristics of the RSAC configuration.

The L/D levels at wind tunnel Reynolds numbers are considerably lower for all of the SCALOS configurations than

they would be for a Concorde or HSCT sized aircraft even if only accounting for skin friction differences. However, the comparisons shown here give some idea of the likely penalties incurred at low subsonic conditions when constraining the general arrangement for minimum sonic boom. Although the Icon-2 clean configuration shows less L/D penalty at 0.45-0.65 CL for LTO/low-noise conditions, the higher wing sweep would tend to make the leading and trailing edge flap deflections relatively less effective, so the L/D gap between it and RSAC would be expected to widen when both are optimized for takeoff and approach field performance and noise.

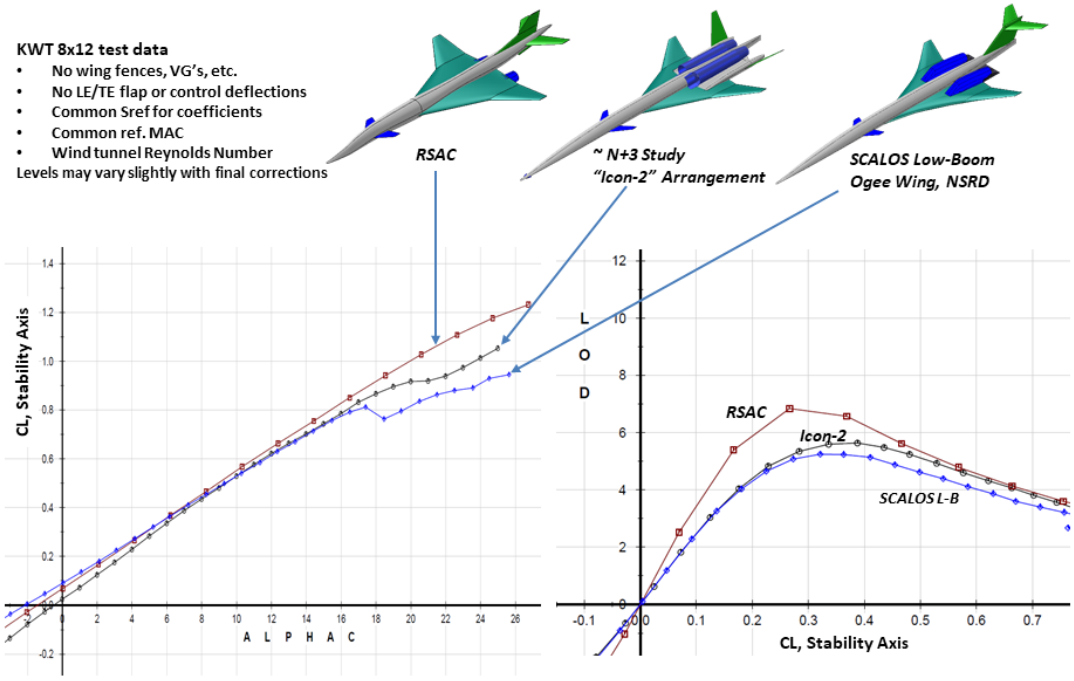

Fig. 23 Lift & Drag Performance Comparison Of RSAC Type With Low-Boom Concepts

The longitudinal (Pitch) Stability Comparison of the RSAC Type configuration is compared to the Low-Boom configurations of the previous figure in Figure 24. Note that much milder nature of the CM vs. CL curve of the RSAC but its somewhat earlier pitch-up.

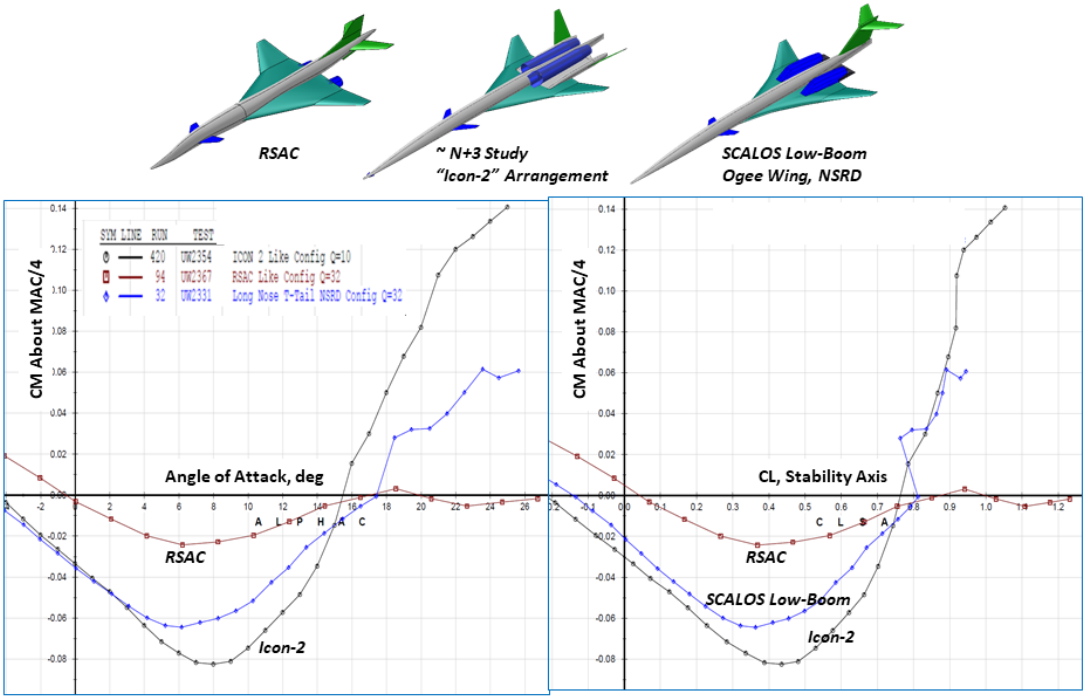

Fig. 24 Longitudinal (Pitch) Stability Comparison Of RSAC Type With Low-Boom Configurations

A few observations regarding the directional (yaw) stability differences between RSAC type configurations and Low-Boom concepts are made possible by Figure 25. The ICON2 and the SCALOS Low-Boom configurations are used again to represent low-boom concepts . The SCALOS L-B has a Nacelle Shock Reflection Deck (NSRD) - a short aft-deck that is the minimum aft deck required on a low-boom configuration (it is similar to the "drool tray" seen under the X-59's engine nozzle). It is important to note that the general arrangement used here was based on Icon-2 but that there is no public geometry for that aircraft, only some basic views and an artist rendering.

The figure shows that relative to the two "low-boom" concepts, the RSAC configuration has nearly 2X yaw stability "stiffness" at AOA=0 (but does not increase with AOA). The RSAC configuration does not show "nose slice" instability with AOA at beta=0.

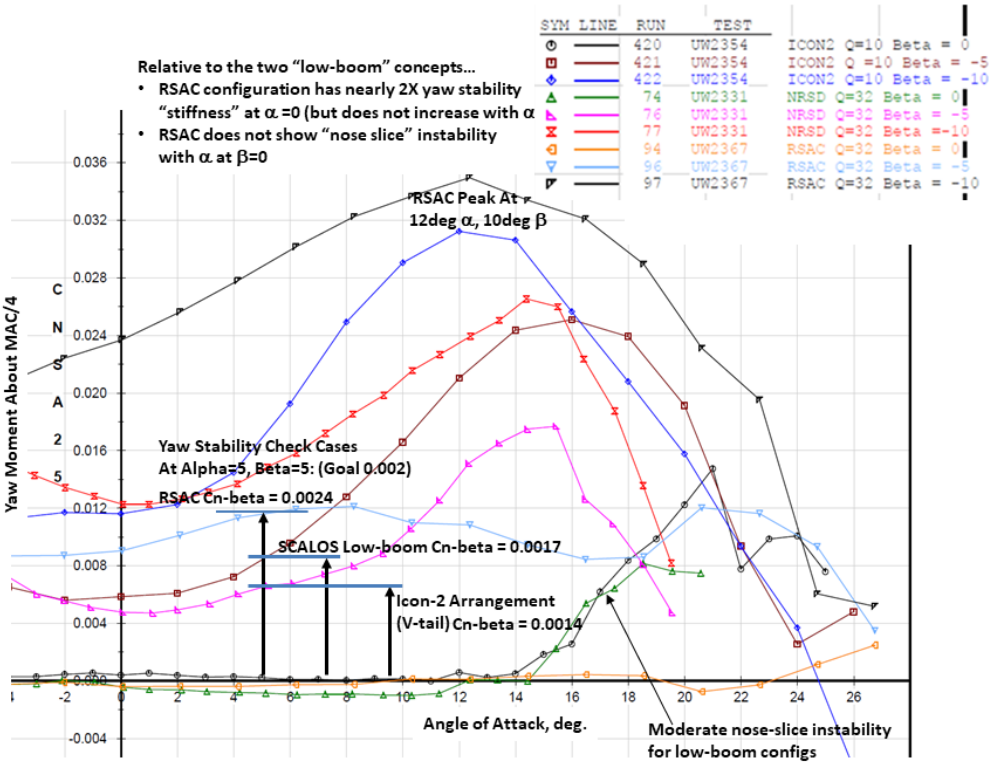

Fig. 25 Directional (Yaw) Stability Comparison Of RSAC Type With Low-Boom Concepts

Moving from static yaw stability to roll stability, comparison of lateral (roll) behavior for RSAC and the two low-boom concepts is shown in Figure 26. The figure allows us to find roll moment coefficient derivatives with respect to beta (the dihedral effect) at different AOAs. The cl_β (roll due to yaw) cases at AOA=5 degrees and Beta=5 degrees are -0.002 for the RSAC, -.0015 for the low-boom SCALOS, and -.0028 for the V-tail ICON-2 (with a goal of -0.002, but that's only for early design purposes, given that the final value is affected by a combination of flight conditions). The SCALOS low-boom has static roll reversal at about 15 deg. AOA and roll-off at about 18 deg. AOA at zero sideslip. Note: All of the KWT datasets use the designation CR or Crm for rolling moment coefficient rather than the commonly used Cl.

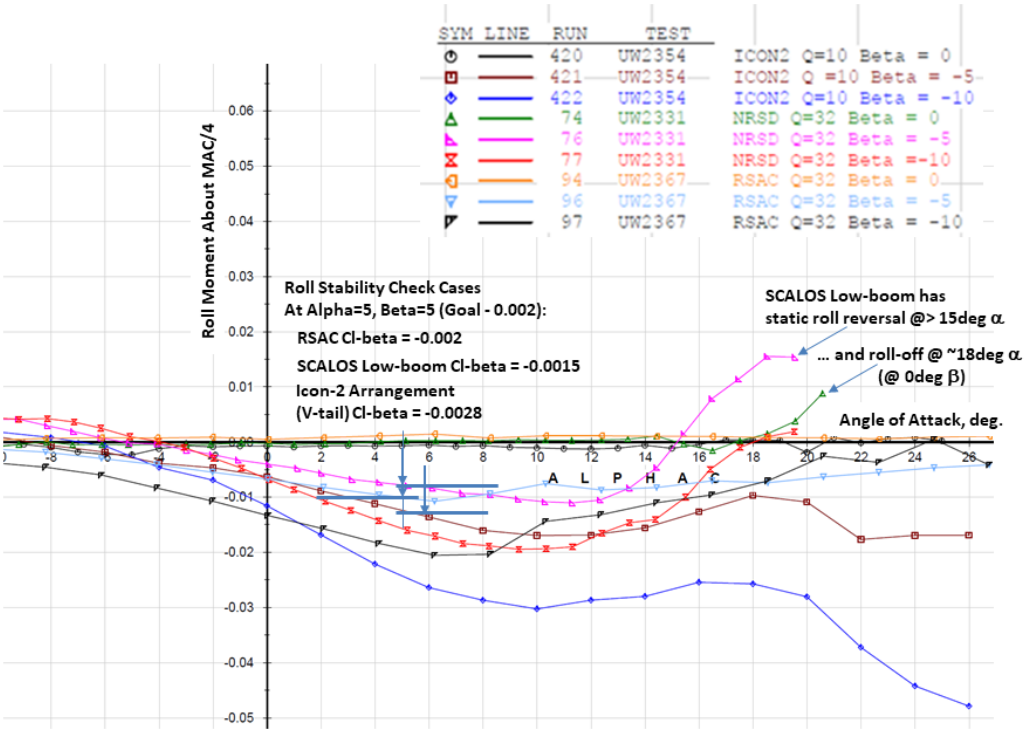

Fig. 26 Lateral (Roll) Stability Comparison Of RSAC Type With Low-Boom Concepts

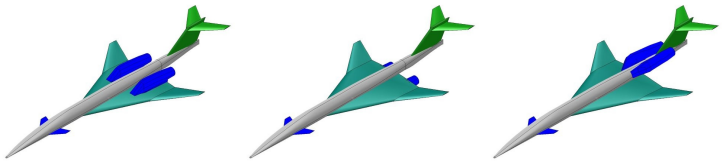

(a) top mounted **(b) bottom mounted** **(c) top rear mounted**

Fig. 27 UW-S-20 configuration with nacelle location variations

Much effort during the development of SCALOS configurations for the configuration design space mapping was dedicated to the effect of engine nacelles and their location. Figure 28 shows the effect of nacelles location on lift. The bottom-mounted nacelles show a slight lift-curve-slope reduction by a higher CL range. The mounting of nacelles at the rear fuselage has a favorable lift curve slope and the highest CL at AOA = 25 degrees.

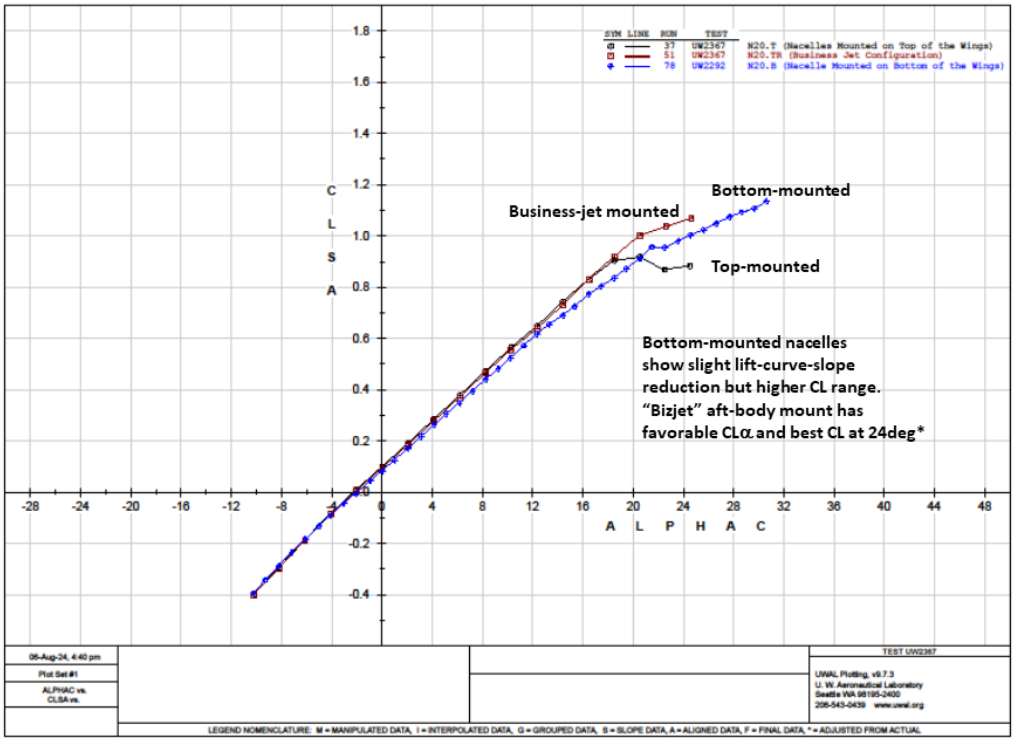

Fig. 28 Effect Of Nacelle Location on Lift

The effect Of nacelle location on L/D is shown in Figure 29. The data used for the figure is untrimmed. The bottom mounted nacelles show some L/D advantage. However test Reynolds number effects may play a role here. There is practically no difference between the top-mounted and aft-body mounted nacelle cases.

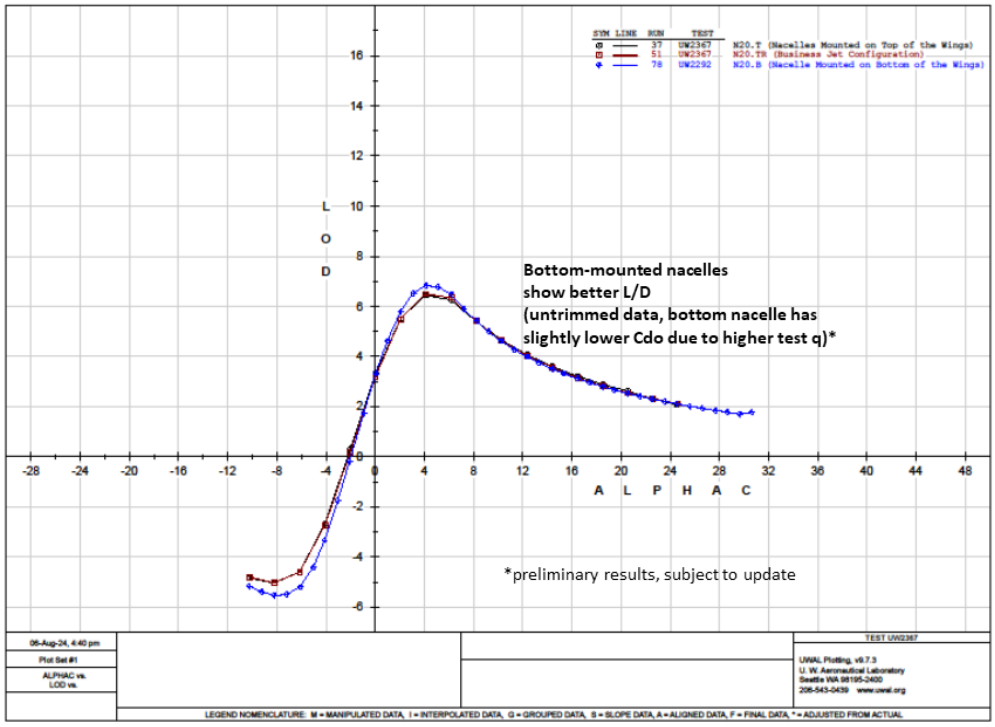

Fig. 29 Effect Of Nacelle Location on Lift/Drag

The effect of nacelle locations on static pitch stability is shown in Figures 30 (CM versus AOA) and 31 (CM vs. CL). The bottom-mounted nacelles show a more positive CM_0. But the pre- and post pitch-up break and the stability levels are similar for all cases. The issue of flow quality into the inlets at high AOAs in the top mounted and aft-fuselage mounted cases is mot discussed here. Experience at the University of Washington with top mounted engine nacelles on supersonic configurations in the years 2009 and 2010 (see Figure 2) showed that good to acceptable inlet flow quality could be obtained throughout the flight envelope by placing the nacelles properly longitudinally and laterally). It is important to remember that engines' distance from each other together with the structure that would guarantee that an explosive failure of one engine would not impair the other must be determined simultaneously in an optimal multidisciplinary manner.

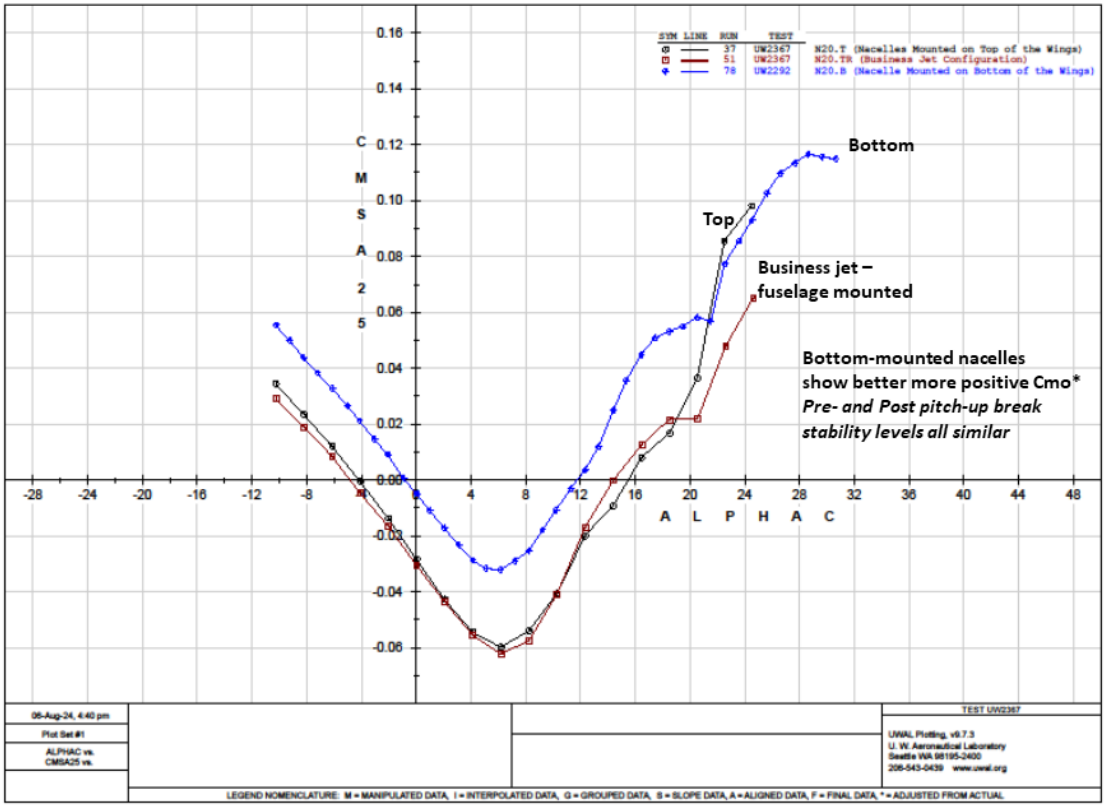

Fig. 30 NacelleLocation: Effect on CM

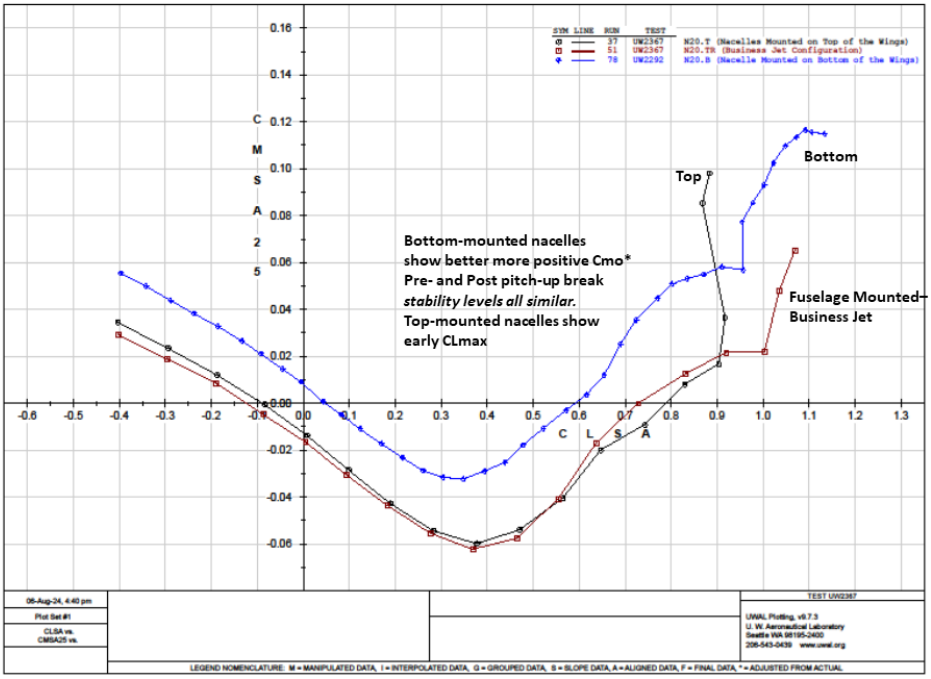

Fig. 31 Nacelle Location: Effect on CM vs. CL

The Nacelle location impacts on the lat-dir stability characteristics of the configurations tested is shown in Fig. 32 for the configurations shown in Figure 27. The top-mounted nacelles appear to have a more non-linear behavior at high AOAs.

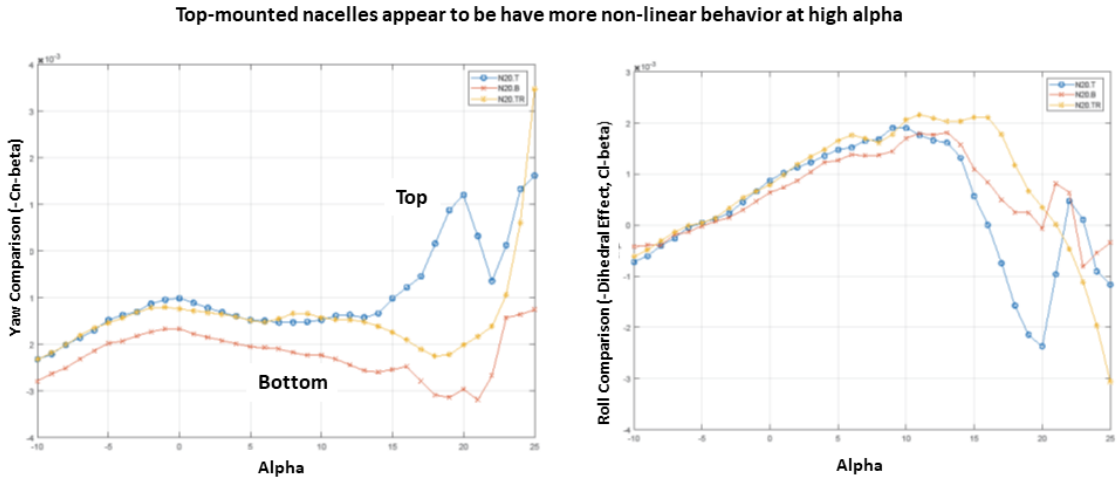

Fig. 32 Nacelle Location: Effect Lateral-Directional Stability

IV. Conclusion

A substantial subsonic experimental study of slender supersonic airplane configurations has been conducted to investigate the effects of various configuration shape parameters and control devices on the subsonic aerodynamic characteristics of a 1/22 scaled wind tunnel model of a 75-100 seat Mach 1.8 conceptual design airliner. All tests were conducted at the Kirsten Wind Tunnel at the University of Washington.

The paper focused on the effects of overall configuration shapes and arrangements on the low-speed static stability and control as well as lift and drag characteristics. The effects of wing planforms, tail surface sizes and locations, aft-deck, canard, fuselage slenderness (low-boom vs. less low-boom features), and engine nacelle locations were studied. The effects of various control device options and the effects of configuration shapes and arrangements will be discussed in other publications.

Subject to the limitations of the Kirsten Wind Tunnel test program, selected key lessons are:

1) The wing-only wing+fuselage configurations studied (which also included a vertical tail as well as ventral and dorsal fins) are all longitudinally stable about the reference quarter-MAC to about 7 degrees AOA. W17 seems to be the most statically stable with pitchup at around 9 degrees AOA. Its post pitchup behavior is more benign compared to the other wing planforms that were studied.
2) A horizontal tail improved longitudinal static stability, as expected. A combination of an aft-deck and horizontal stabilizers improves longitudinal static stability and can eliminate pitchup in the range of 0 to about 30 degrees AOA. The aft deck is favorable also from the low-boom perspective as it allows distribution of lift forces more

gradually and smoothly lengthwise. It also adds stiffness to the empennage area. But it adds wetted area.

3) Regarding the vertical location of the horizontal tail, the T-Tail provides much more negative dCM/dCL but delays the pitchup by only about 1 degree AOA compared to the low-tail and mid-tail arrangements. The tailless configuration is the least longitudinally stable. Tests at AOAs up to 25 degrees show a deep stall for the low-tail case at about 23 degrees AOA and tendencies towards deep-stall of the T-Tail and mid-tail configurations at 25 degrees AOA. The change in static stability level between pre- and post pitch-up is largest for the T-tail arrangement, potentially making CG management and pitch augmentation more difficult. This concern may be somewhat mitigated by the fact that the Cmq pitch damping proved greater in dynamic tests at Boeing's FVWT facility (i.e. unstable static margin but more stable "maneuver margin").
4) The "tension" between the shaping of configurations for high supersonic efficiency and low boom and the needs, at low speeds, for high lift over drag, acceptable handling qualities, and noise minimization is captured quite well by the results of the KWT tests. The slender supersonic configurations studied display pitch up and, often, deep stall at relatively low angles of attack. Canards tend to destabilize and horizontal tails tend to stabilize the configurations in pitch, but any flow separation on these surfaces would have substantial impact on the longitudinal static stability because of the long moment arms involved. The more swept back main outer wings suffer from earlier pitch up problems due to earlier breakdown of their LE vortices. An aft deck, which functions as an "area behind" for more lifting surface "action" behind the CG leads to delayed pitch up and a milder pitch nonlinearity compared to configurations without aft deck. But this comes with drag penalties because of the additional surface area.
5) The large-chord inner section of the wing acts as a flow "straightener", forcing the flow to follow the plane of the wing, and therefore reducing the effectiveness of the horizontal tail's contributions to static pitch stability. This effect is expected to weaken the further away from the wing the horizontal tail would be. Increasing horizontal tail area does provide some increase in static stability, mainly at the higher angles of attack. However, increasing the tail arm by lengthening the aft body would also introduce body bending aeroelastics, potentially reducing the horizontal tail's pitch control effectiveness (another complex trade-off).
6) Adding LE and TE flaps down for an approach configuration leads to major improvements in longitudinal stability. With increases in wing sweep (for supersonic efficient and low boom) LE flap contributions may suffer and much attention will be required to the optimal design of flap systems in such cases.
7) The RSAC 3-surface configurations, selected for conceptual design work on a reference supersonic commercial airplane, has lift and lift/drag characteristics the are superior to two representative low-boom configurations that were also studied and it had a milder Cm vs. CL curve.
8) Out of the three nacelle mounting options that were studied (wing bottom and wing top mounted nacelles as well as rear-fuselage mounted nacelles) the bottom mounted nacelles had the better max L/D and the rear-fuselage mounted nacelles had the better lift vs. AOA behavior. The L/D results should be approached cautiously because of the Reynolds number differences between wind tunnel tests and the full size airplane. Regarding lateral-directional static stability, the top-mounted nacelles display more nonlinear rolling and yawing moment behavior at high angles of attack. The final locations of engine nacelles must take into account flow quality into the inlets and safety requirements regarding the distance between engines and the weight of the structure that would be required to prevent a failure in one engine to degrade the performance of the other. However, top-mounted engines, especially with the Nozzle Shock Reflection Deck (NSRD) fairings below the nozzle, offer the best opportunity for minimizing the sonic boom effects of the propulsion system, as well as providing opportunities for partially shielding takeoff and landing noise at the inlet and jet-exhaust ends of the engine.
9) Finally, Presentations in earlier papers, 2022-2024, that focused on the KWT tests presented test results and test result trends that were based on partially-corrected test data, available before the final test corrections were established in late 2024. Examining partially-corrected and fully-corrected test results for some key cases before the completion of the present paper showed that the trends regarding the way that configuration shape and arrangement affect the overall aerodynamic behavior are essentially the same. For results and trends based on the fully-corrected data a fully-corrected set of test results is now available and was delivered to NASA.

Flow visualization and CFD simulations will add insight and will be reported in later publications.

A major goal of the SCALOS project was to build a public low-speed aero database for designers and to contribute a better understanding of the effects of various shapes on the performance and S&C characteristics that would drive the design of future supersonic configurations.

Open questions in need of addressing include: the effects of aeroelastic deformations on the stability and control

of the slender SCALOS configurations studied at the KWT; the integration of static aerodynamic information with dynamic aerodynamic information (in the form of dynamic stability derivatives and integrated dynamic aeroservoelastic models); full 6dof and multi-dof simulations and control system designs; tradeoffs between performance, airframe noise, stability, and handling qualities demands; and the certification criteria and allowances required to ensure safety of operation. More development of CFD modeling that would capture with sufficient accuracy the aerodynamic behavior of the SCALOS configurations and any of their derivatives is also required plus CFD technology that would help with the development of wind tunnel corrections for the new generation of supersonic commercial configurations guided those studied by the SCALOS project.

Testing to validate the predicted effects of wing twist, supersonic airfoil shape variations, and optimized leading/trailing edge flap configurations was beyond the scope of the SCALOS effort.

There is much more to do. It is hoped that the contributions described in this paper and the associated SCALOS project papers will be useful to the developers of commercial supersonic flight technology in the future.

Acknowledgments

Support by NASA, Award/Contract #80NSSC19K1661, under the Commercial Supersonic Technology (CST) program, Supersonic Configurations at Low Speeds, with Sarah Langston as the NASA technical grant monitor is gratefully acknowledged. The authors would like to thank Lori Ozoroski, Sriram Rallabhandi, Melissa Carter, Sarah Langston, and Peter Coen from NASA for the opportunity to conduct this needed research for supersonic aircraft. The authors would also like to thank the 2020-2024 UW senior capstone airplane design project teams for their assistance and contributions.

References

[1] Seraj, S., and Martins, J. R. R. A., "Predicting the High Angle of Attack Characteristics of a Delta Wing at Low Speed," *AIAA Aviation Forum*, 2021. https://doi.org/10.2514/6.2021-2612.

[2] Seraj, S., and Martins, J. R. R. A., "Aerodynamic Shape Optimization of a Supersonic Transport Considering Low-Speed Stability," *AIAA SciTech Forum*, 2022. https://doi.org/10.2514/6.2022-2177.

[3] Seraj, S., and Martins, J. R. R. A., "Predicting the High-Angle-of-Attack Characteristics of a Delta Wing at Low Speed," *Journal of Aircraft*, Vol. 59, No. 4, 2022, pp. 1071–1081. https://doi.org/10.2514/1.C036618.

[4] Seraj, S., Yildirim, A., Anibal, J. L., and Martins, J. R. R. A., "Improving the Performance of a Compressible RANS Solver for Low and High Mach Number Flows," *Eleventh International Conference on Computational Fluid Dynamics*, 2022.

[5] Seraj, S., and Martins, J. R. R. A., "Minimum Trim Drag for a Three-Surface Supersonic Transport Aircraft," *AIAA Aviation Forum*, 2023. https://doi.org/10.2514/6.2023-3472.

[6] Seraj, S., Yildirim, A., Anibal, J. L., and Martins, J. R. R. A., "Dissipation and time step scaling strategies for low and high Mach number flows," *Journal of Computational Physics*, Vol. 491, 2023, p. 112358. https://doi.org/10.1016/j.jcp.2023.112358.

[7] Anibal, J. L., Seraj, S., Yildirim, A., and Martins, J. R. R. A., "Mixed continuation methods for robust CFD Newton solvers," *AIAA SciTech Forum*, 2023. https://doi.org/10.2514/6.2023-2296.

[8] Hajdik, H. M., Yildirim, A., Wu, N., Brelje, B. J., Seraj, S., Mangano, M., Anibal, J. L., Jonsson, E., Adler, E. J., Mader, C. A., Kenway, G. K. W., and Martins, J. R. R. A., "pyGeo: A geometry package for multidisciplinary design optimization," *Journal of Open Source Software*, Vol. 8, No. 87, 2023, p. 5319. https://doi.org/10.21105/joss.05319.

[9] Seraj, S., "Aerodynamic Design Optimization of a Supersonic Transport Aircraft Considering Low-Speed Stability," Ph.D. thesis, University of Michigan, 2024. https://doi.org/10.7302/22987.

[10] Guimarães, T. A., Cesnik, C. E., and Kolmanovsky, I., "Low Speed Aerodynamic Modeling for Control-related Considerations in Supersonic Aircraft Design," *AIAA Aviation 2021 Forum*, AIAA Paper 2021-2531, 2021. https://doi.org/10.2514/6.2021-2531.

[11] Guimarães, T. A., Cesnik, C. E., and Kolmanovsky, I. V., "An Integrated Low-Speed Aeroelastic-Flight-Dynamics Framework for Modeling Supersonic Aircraft," *AIAA SciTech 2022 Forum*, AIAA Paper 2022-2175, 2022. https://doi.org/10.2514/6.2022-2175.

[12] Guimarães, T. A., Cesnik, C. E., and Kolmanovsky, I., "Unsteady Vortex Lattice Linearization and Sensitivity Analyses for Control Models in Supersonic Aircraft Design," *AIAA SciTech 2023 Forum*, AIAA Paper 2023-0416, 2023. https://doi.org/10.2514/6.2023-0416.

[13] Guimarães, T. A., Cesnik, C. E., and Kolmanovsky, I., "Flexibility Assessment of the Aeroelastic-flight-dynamic Behavior for Supersonic Aircraft," *AIAA SciTech 2023 Forum*, AIAA Paper 2023-0417, 2023. https://doi.org/10.2514/6.2023-0417.

[14] Guimarães, T. A., and Cesnik, C. E., "The Impact of Vortex Breakdown on the Longitudinal Flight Behavior of the SCALOS Aircraft," *AIAA SciTech 2024 Forum*, 2024.

[15] Cunis, T., Kolmanovsky, I. V., and Cesnik, C. E., "Control Co-Design Optimization: Integrating nonlinear controllability into a multidisciplinary design process," *AIAA SciTech 2022 Forum*, AIAA Paper 2022-2176, 2022. https://doi.org/10.2514/6.2022-2176.

[16] Bertolin, R., Chaves Barbosa, G., Cunis, T., Kolmanovsky, I. V., and Cesnik, C. E., "Gust Rejection of a Supersonic Aircraft During Final Approach," *AIAA SciTech 2022 Forum*, AIAA Paper 2022-2174, 2022. https://doi.org/10.2514/6.2022-2174.

[17] Monteiro, B. B., Kolmanovsky, I., and Cesnik, C. E., "Controller Agnostic Design Metrics for Stochastic Disturbance Rejection," *AIAA SciTech 2024 Forum*, 2024. https://doi.org/10.2514/6.2024-0901.

[18] Monteiro, B. B., "Control Related Metrics for Multidisciplinary Design Optimization," Ph.D. thesis, University of Michigan, 2024. https://doi.org/10.7302/23748.

[19] Nelson, C. P., Ting, K.-Y., Mavriplis, N., Soltani, R., and Livne, E., "Supersonic Configurations at Low Speeds (SCALOS): Project Background and Progress at University of Washington," *AIAA SciTech 2022 Forum*, AIAA Paper 2022-1803, 2022. https://doi.org/10.2514/6.2022-1803.

[20] Ting, K.-Y., Mavriplis, N., Soltani, R. M., Nelson, C. P., and Livne, E., "Supersonic Configurations at Low Speeds (SCALOS): Model Geometry and Aerodynamic Results," *AIAA SciTech 2022 Forum*, AIAA Paper 2022-1800, 2022. https://doi.org/10.2514/6.2022-1800.

[21] Mavriplis, N., Ting, K.-Y., Moustafa, A., Hill, C., Soltani, R. M., Nelson, C. P., and Livne, E., "Supersonic Configurations at Low Speeds (SCALOS): Test / Simulation Correlation Studies," *AIAA SciTech 2022 Forum*, AIAA Paper 2022-1801, 2022. https://doi.org/10.2514/6.2022-1801.

[22] Mavriplis, N., "RANS-CFD Based Assessment of Corrections Applied to the Measured Characteristics of Supersonic Configurations in a Low Speed Wind Tunnel," Master's thesis, University of Washington, 2022. URL http://hdl.handle.net/1773/49591.

[23] Nelson, C. P., Ting, K.-Y., Ignacio, J., Mavriplis, N., Soltani, R., and Livne, E., "Supersonic Configurations at Low Speeds (SCALOS): Configuration Comparison of SCALOS to Existing Designs," *AIAA SciTech 2023 Forum*, AIAA Paper 2023-0228, 2023. https://doi.org/10.2514/6.2023-0228.

[24] Ting, K.-Y., Mavriplis, N., Soltani, R. M., Nelson, C. P., and Livne, E., "Supersonic Configurations at Low Speeds (SCALOS): The Aerodynamic Effects of Control Surfaces," *AIAA SciTech 2023 Forum*, AIAA Paper 2023-0229, 2023. https://doi.org/10.2514/6.2023-0229.

[25] Ting, K.-Y., Mavriplis, N., Soltani, R. M., Nelson, C. P., and Livne, E., "Supersonic Configurations at Low Speeds (SCALOS) Longitudinal Aerodynamics: Configuration Variations and Control Surfaces Effects," *AIAA SciTech 2023 Forum*, AIAA Paper 2023-0230, 2023. https://doi.org/10.2514/6.2023-0230.

[26] Mavriplis, N., Ting, K.-Y., Soltani, R. M., Nelson, C. P., and Livne, E., "Supersonic Configurations at Low Speeds (SCALOS): CFD Aided Wind Tunnel Data Corrections," *AIAA SciTech 2023 Forum*, AIAA Paper 2023-0231, 2023. https://doi.org/https://doi.org/10.2514/6.2023-0231.

[27] Ting, K.-Y., Nelson, C. P., and Livne, E., "Supersonic Configurations at Low Speeds (SCALOS): Tare & Interference Corrections for SCALOS Configurations Tested at the University of Washington's Kirsten Wind Tunnel," *AIAA SciTech 2024 Forum*, 2024. https://doi.org/10.2514/6.2024-0899, AIAA Paper 2024-0899.

[28] Ting, K.-Y., Nelson, C. P., Wiersema, K., and Livne, E., "Supersonic Configurations at Low Speeds (SCALOS): Progress at the University of Washington," *AIAA SciTech 2024 Forum*, 2024. https://doi.org/10.2514/6.2024-0898, AIAA Paper 2024-0898.

[29] Ting, K.-Y., Soltani, R. M., Wiersema, K., Nelson, C. P., and Livne, E., "Lateral-directional Aerodynamics: Configuration Variations and Control Surface Effects," *AIAA SciTech 2025 Forum*, AIAA Paper, 2025. Abstract Accepted.

[30] Wiersema, K., Ting, K.-Y., Nelson, C. P., and Livne, E., "Supersonic Configurations at Low Speeds(SCALOS): Correlation of CFD / Wind Tunnel Test Results," *AIAA SciTech 2025 Forum*, AIAA Paper, 2025. Abstract Accepted.

[31] Shanbhag, T. K., Zhou, B. Y., Molina, E., and Alonso, J., "A Comparison of Jet Acoustic Analysis Methods," *AIAA Aviation 2021 Forum*, AIAA Paper 2021-2102, 2021. https://doi.org/10.2514/6.2021-2102.

[32] Shen, Y., and J., A. J., "Performance Evaluation of a Graph Neural Network-Augmented Multi-Fidelity Workflow for Predicting Aerodynamic Coefficients on Delta Wings at Low Speed," *AIAA SciTech 2025 Forum*, 2025. Session APA-82/SPSN-04, Supersonic Aerodynamics I.

[33] Shen, Y., Needels, J. T., and Alonso, J. J., "VortexNet: A Graph Neural Network-Based Multi-Fidelity Surrogate Model for Field Predictions," *AIAA SciTech 2025 Forum*, 2025. Session APA-22, Special Session: Applied Surrogate Modeling III.

[34] Magee, T. E., Hayes, P. J., Dorgan, A. J., and Khodadoust, A., "Dynamic Stability Characteristics for Commercial Supersonic Configurations at Low-Speed Flight Conditions," *AIAA SciTech 2022 Forum*, AIAA Paper 2022-1802, 2022. https://doi.org/10.2514/6.2022-1802.

[35] Magee, T. E., Hayes, P. J., Dorgan, A. J., and Khodadoust, A., "Dynamic Stability Characteristics for Commercial Supersonic Configurations at Low-Speed Flight Conditions – Part II," *AIAA SciTech 2024 Forum*, 2024. https://doi.org/10.2514/6.2024-0900.

[36] Magee, T. E., Hayes, P. J., and Khodadoust, A., "Dynamic Stability Characteristics for Commercial Supersonic Configurations at Low-Speed Flight Conditions – Part III," *AIAA SciTech 2025 Forum*, 2025.

[37] Welge, H., Bonet, J., Magree, T., Chen, D., Hollowell, S., Kutzmann, A., Mortlock, A., Stengle, J., Nelson., C., Adamson, E., Baughcum, S., Britt, R., Miller, G., and Tai, J., "N+2 Supersonic Concept Development and Systems Integration," Tech. Rep. CR-2010-216842, NASA, 2010.

[38] Welge, H.R, Bonet, J., Magee, T., Tompkins, D., Britt, T.R., Nelson, C., Miller, G., Stenson, D., Staubach, J.B., Bala, N., Duge, R., O'Brien, M., Cedoz, R., Barlow, A., Martins, S., Viars, P., Rasheed, A., Kirby, M., Raczynski, C., Roughen, K., Doyle, S., Alston, K., Page, J., and Plotkin, K.J., "N+3 Advanced Concept Studies for Supersonic Commercial Transport Aircraft Entering Service in the 2030-2035 Period," Tech. Rep. CR-2011-217084, NASA, April 2011. URL https://ntrs.nasa.gov/api/citations/20110010973/downloads/20110010973.pdf.

[39] Livne, E., and Nelson, C., "From Blank Slate to Flight Ready New Small Research UAVs in Twenty Weeks-Undergraduate Airplane Design at the University of Washington," *AIAA Paper 2012-845*, 2012. https://doi.org/10.2514/6.2012-845, 50th AIAA Aerospace Sciences Meeting including the New Horizons Forum and Aerospace Exposition.

[40] Barlow, J., Rae, J. W. H., and Pope, A., *Low Speed Wind Tunnel Testing - 3rd edition*, John Wiley & Sons, Inc., 1999. Pages 278 and 281, Figures 730 and 734, ISBN 0-471-55774-9.

[41] Watson, J. M., "Low-Speed Lateral-Control Investigation of a Flap-Type Spoiler Aileron With and Without a Deflector and Slot on a 6-Percent-Thick, Tapered, 45 degrees Sweptback Wing of Aspect Ratio 4," Tech. Rep. NACA RM L52GIO, NACA, 1952.

[42] Vogler, R., "Wind-Tunnel Investigation at High Subsonic Speeds of a Spoiler-Slot-Deflector Combination on an NACA 65A006 Wing With Quarter-Chord Line Swept Back 32.6," Tech. Rep. NACA RM L53D17, NACA, 1953.

[43] Hammond, A., "Low-Speed Investigation of the Lateral-Directional Characteristics of a Flap-Type Spoiler and a Spoiler-Slot Deflector on a 30 degrees Sweptback Wing-Fuselage Model Having an ASpect Ratio of 3, a Taper Ratio of 0.5, and NACA 65A004 Airfoil Section," Tech. Rep. NACA RM L56F18, NACA, August 1956. URL https://ntrs.nasa.gov/api/citations/19930089324/downloads/19930089324.pdf.

[44] "The University of Washington's Kirsten Wind Tunnel," , 1936-present. URL https://www.aa.washington.edu/AERL/KWT, accessed: December 1str, 2023.

[45] Foster, J., Cunningham, K., Fremaux, C., Shah, G., Stewart, E., Rivers, R., Wilborn, J., , and Gato, W., "Dynamics Modeling and Simulation of Large Transport Airplanes in Upset Conditions," 2005. https://doi.org/10.2514/6.2005-5933, *AIAA* Guidance, Navigation, and Control Conference, Session: GNC-12: Aviation Safety I: Control Upset Prevention and Recovery, also available at: https://ntrs.nasa.gov/api/citations/20050214373/downloads/20050214373.pdf.

[46] Nelson, C., "Effects of wing planform on HSCT off-design aerodynamics," , June 1992. URL https://doi.org/10.2514/6.1992-2629, *AIAA* Paper 1992-2629.

V. Appendix

A. Model Part Designation

Table 4 SCALOS model component designations

	Fab. Year	Designation	Description
Fuselage	2015	F15	2015 symmetric "eggshell" cross-section forebody fuselage
	2015	F15.U	2015 upper "eggshell" cross-section forebody fuselage without canard capability
	2015	F15.D	2015 downward "eggshell" cross-section forebody fuselage without canard capability
	2021	F15.L	2015 symmetric "eggshell" cross-section forebody fuselage extended version
	2023	F23	2015 symmetric "eggshell" cross-section forebody fuselage with inverted mount capability
	2023	F24	2024 area-ruled forebody fuselage
	2015	A15	2015 aft-body fuselage with horizontal tail low-mount only capability
	2016	A16	2016 aft-body fuselage on aft-deck
	2020	A20	2015 aft-body fuselage with horizontal tail mid- and T-mount capability
	2023	A23	2015 aft-body fuselage with all tail-mount and inverted model mount capability
	2024	A24	2024 area-ruled aft-body fuselage with low tail-mount only capability
Wing	2013	W IB	SCALOS inboard core wing
	2015	W15	2015 outboard wing
	2017	W17	2017 outboard wing
	2018	W18	2018 outboard wing
	2020	W20	2020 outboard wing
	2023	W23	2023 outboard wing
	2023	W13.5	2015 outboard wing modified to represent 2013 outboard wing
Aft-deck	2016	AD16	2016 wing aft-deck
	2020	NSRD	2020 nozzle shock-reflected deck (top-mount nacelle only)
Nacelle	2015	N15	2015 low-mounted nacelles
	2016	N16	2016 aft-body fuselage integrated 2016 nacelles
	2017	N17	2017 nacelles cuff, sheet metal and 3D printed inlets on N16
	2017	N17.1	2017 nacelles cuff, sheet metal and 3D printed modified inlets on N16
	2018	N18	2016 aft-body fuselage integrated 2018 nacelles
	2020	N20(.T/.B/.TR)	2020 nacelles
	2023	N23.BR	2023 aft-deck bottom mount nacelles
Canard	2015	C15(.F/.M/.A)	2015 all-moving canard
	2015	C15(F/M/A).2	2015 alternative all-moving canard metal sleeves on C15
	2017	C17(.F/.M/.A)	2017 all-moving canards metal sleeves on C15 (C18 ≡ C17)
	2017	C17(F/M/A).D1	2017 dogtooth all-moving canards metal sleeves on C15
	2021	C17(F/M/A).1	2017 alternative all-moving canards metal sleeves on C15 (remake)
	2021	C15(F/M/A).1	2015 alternative all-moving canards (remake symmetric)
	2023	C23(.F/.M/.A)	2023 all-moving canard (3D printed)
	2024	C23(F/M/A).1	2023 all-moving canards
Vertical tail	2015	V15	2015 single vertical tail
	2016	V16(.F/.A)	2016 single vertical tail
	2016	V16(.F/A).1	2016 enlarged single vertical tail metal sleeves on V16
	2016	V16T.2	2016 twin vertical tail without deflection (3D printed)
	2016	V16T.3	2016 enlarged twin vertical tail metal sleeves on V16T.2 without deflection
	2017	V17(.F/.A)	2017 single vertical tail
	2017	V17(.F/A).1	2017 enlarged single vertical tail metal sleeves on V17 (extended span and)
	2018	V18(.F/.A)	2018 single vertical tail (10% increase from V17)
	2018	V18(F/A).1	2018 enlarged single vertical tail metal sleeves on V18 (4.5" extended span and)
	2018	V18(F/A).2	2018 enlarged single vertical tail metal sleeves on V18 (4.5" extended span and 787 like esque tip sweep,)
	2020	V20	2020 single vertical tail with Mid- and T-tail mount capability
	2021	V15.1	2015 single vertical tail with rudder deflection capability
	2023	V23	2023 V-tail
Horizontal tail	2015	H15	2015 all-moving horizontal tail with $\Gamma = 0°$
	2015	H15A	2015 RUAV all-moving horizontal stabilizer with $\Gamma = 0°$
	2016	H16	2016 all-moving horizontal stabilizer with $\Gamma = -10°$
	2017	H17	2017 all-moving horizontal stabilizer larger metal sleeves on H16 with $\Gamma = -10°$
	2017	H17.2	2017 all-moving horizontal stabilizer smaller metal sleeves on H16 with $\Gamma = -10°$
	2018	H18	2018 all-moving horizontal stabilizer with $\Gamma = 0°$ (3D printed)
	2020	H20(.M/.T)	2020 all-moving horizontal stabilizer with $\Gamma = 0°$

Continued on next page

Table 4 –continued from previous page

	Fab. Year	Designation	Description
	2020	H20.L	2020 all-moving horizontal stabilizer metal sleeve on H15 with $\Gamma = 0°$
	2021	H20L.1	2020 all-moving horizontal stabilizer metal sleeves on H15 with $\Gamma = 0°$ (remake)
	2021	H15A.1	2015 RUAV all-moving horizontal stabilizer metal sleeves on H15 with $\Gamma = 0°$ (remake)
	2023	H20L.2	2020 all-moving horizontal stabilizer on H15 with $\Gamma = 0°$ (machined)
	2023	H15A.2	2015 RUAV all-moving horizontal stabilizer on H15 with $\Gamma = 0°$ (machined)
	2024	H24	2024 all-moving horizontal stabilizer with $\Gamma = 0°$
Additional	2015	WTD	2015 outboard wing leading edge trip dots
	2015	WR15	2015 wingtip rudders
	2015	WRD15	2015 wingtip rudders with deflections
	2015	P15	2015 nacelle exit paddles
	2015	E15	2015 nacelle electric ducted fans
	2016	VF16T	2016 twin ventral fin sheet metal with swept LE and rounded TE
	2016	VF16T.2	2016 twin ventral fin sheet metal with swept LE and TE
	2016	SF16	2016 splitter flap under wing aft-deck
	2016	WF16	2016 wing fence
	2016	NB16	2016 fuselage nose boom
	2017	FD17	2017 flight deck/ cockpit
	2017	RT17	2017 outboard wing with raked wingtip extension
	2018	NRTD.18	Fuselage nose ring trip dots (9-inch behind the nose)
	2018	RT18	2018 outboard wing with raked wingtip extension
	2018	LG18	2018 nose and main landing gears (3D printed)
	2018	ICE18	2018 icing on wing leading edge with aluminum tape
	2020	NRTD.20	Fuselage nose ring trip dots (0.5-inch behind the nose)
	2020	FTD	Forward trip dots (below canard, 10-inch forward)
	2020	FTDXD	Forward trip dots (below canard, 15-inch forward)
	2020	DF.1	2015 vertical tail dorsal fin
	2020	VF.1	2015 aft-body fuselage ventral fin
	2021	NC21	2021 nose chine (wood)
	2021	FS21	mid-chord spoilers
	2021	CS21	clam shell speed brakes
	2023	NC23	2023 nose chine (sheet metal)
	2024	NC24	2024 nose chine (sheet metal) forward: leveled with canard, approx 4-inch ahead of canard body: aligned with wing leading edge, approx 3-inch above
	2024	CF15	2015 forebody fuselage canard fairing
	2024	CF24	2024 area-ruled forebody fuselage canard fairing
	2024	LG24	2024 nose and main landing gears (3D printed)
	2024	DF.2	2015 vertical tail dorsal fin (3D printed)
	2024	VF.2	2024 aft-body fuselage ventral fin (sheet metal)
	2024	VF.3	2024 aft-body fuselage ventral fin (3D printed)
	2024	VF24T	2024 aft-body fuselage twin ventral fin (sheet metal)
	2024	NM24	2024 forebody fuselage extended flat nose modification
	2024	NM24.P	2024 forebody fuselage extended pointy nose modification (3D printed)
	2024	WF24	2024 wing fence
	2024	FTDXD2	Forward trip dots (below canard, extend to nose ring)
	2024	HTD	Horizontal stabilizer trip dots (0.5 inches behind leading edge)
Control surfaces			
LEIB	2015	LEIB15	2015 inboard wing baseline leading edges
	2017	LEIB17	2017 inboard wing baseline leading edges
	2017	LEIB17.ALT	2017 inboard wing alternated cruise leading edges
	2017	LEIB17.MVR	2017 inboard wing morphing variable radius leading edge
	2018	LEIB18	2018 inboard wing baseline leading edges
	2020	LEIB15.1	2015 inboard wing baseline leading edges (remake)
	2020	LEIB20.ALT	2020 inboard wing alternated cruise leading edges
	2020	LEIB20.OG+strake	2020 inboard wing ogive leading edges with strakes
	2023	LEIB23.S	2023 inboard wing sharp cruise leading edges
	2023	LEIB23.MVR	2023 inboard wing morphing variable radius leading edge
	2024	LEIB24.MVR	2024 inboard wing morphing variable radius leading edge
	2024	LEIB20.ALT	2020 inboard wing alternated cruise leading edges geometry with deflections
LEOB	2015	LEOB15	2015 outboard wing baseline leading edges
	2017	LEOB17	2017 outboard wing drooped leading edges
	2018	LEOB18	2018 outboard wing baseline leading edges
	2018	LEOB18.SM	2018 outboard wing leading edges with deflection (sheet metal)
	2020	LEOB20	2020 outboard wing baseline leading edges

Continued on next page

Table 4 –continued from previous page

	Fab. Year	Designation	Description
	2020	LEOB20.OG	2020 outboard wing alternated cruise leading edges
	2023	LEOB15.SS	2015 outboard wing sealed slat panel leading edges
	2023	LEOB15.FP	2015 outboard wing flex panel leading edges
	2023	LEOB23	2023 outboard wing baseline leading edges
TEIB	2015	TEIB15.SM	2015 inboard wing trailing edges with deflection (sheet metal)
	2020	TEIB15	2015 inboard wing baseline trailing edges
	2023	TEIB13.5	2015 wing modification to shorter chord constraint to same area
	2024	TEAD24	2016 aft-deck trailing edge elevator flap (sheet metal)
TEOB	2015	TEOB15	2015 outboard wing baseline trail edges
	2015	TEOB15.SM	2015 outboard wing trail edges with deflection (sheet metal)
	2017	TEOB17	2017 outboard wing baseline trail edges
	2020	TEOB20	2020 outboard wing baseline trail edges
	2021	TEOB15.R	2015 outboard wing baseline trail edges (1/3 area reduction, delta crank preserved)
	2021	TEOB20.R	2020 outboard wing baseline trail edges (1/3 area reduction, delta crank preserved)
	2021	TEOB20.AS21	2020 outboard wing aileron spoilers (roll-control speed brakes)
	2021	TEOB20.SSD21	2020 outboard wing spoiler-slot deflector (roll-control speed brakes)
	2023	TEOB20.SSD23	2020 outboard wing spoiler-slot deflector (roll-control speed brakes)
	2023	TEOB13.5	2015 wing modification to shorter chord constraint to same area
	2023	TEOB23	2023 outboard wing baseline trail edges

Table 5 SCALOS control surfaces and deflections

	Designation	Deflections	Description
Wing inboard leading edge	LEIB15	0°, +15°, +30°	2015 inboard wing baseline leading edges
(LEIB)	LEIB15.1	0°, +15°, +30°	2015 inboard wing baseline leading edges
	LEIB17	30°	2017 inboard wing baseline leading edges
	LEIB17.ALT	0°	2017 inboard wing alternated cruise leading edges
	LEIB17.MVR	30°	2017 inboard wing morphing variable radius leading edges
	LEIB18	0°, +30°	2018 inboard wing baseline leading edges
	LEIB20.ALT	0°, +12°, +57°	2020 inboard wing alternated cruise leading edges
	LEIB20.OG + Strake	0°	2020 inboard wing ogive leading edges with strakes
	LEIB23.S	0°	2023 inboard wing sharp cruise leading edges
	LEIB23.MVR	30°	2023 inboard wing morphing variable radius leading edges
	LEIB24.MVR	30°	2024 inboard wing morphing variable radius leading edges
Wing inboard trailing edge	TEIB15.SM	0°, +32°	2013 custom inboard wing trailing edges (2015 wing modification)
(flap ≡ TEIB)	TEIB15	0°, +15°, +30°	commutative inboard wing baseline trailing edges
	TEIB13.5	0°	2015 wing modification to shorter chord constraint to the same area
	TEAD24	0°, ±15°	2024 aft-deck trailing edge elevator flap (sheet metal)
Wing outboard leading edge	LEOB15	0°, +15°, +30°	2015 outboard wing baseline leading edges
(LEOB)	LEOB15.SS	+15°, +25°	2015 outboard wing sealed slat panel leading edges
	LEOB15.FP	+30°	2015 outboard wing flex panel leading edges
	LEOB17	0°, +30°	2017 outboard wing baseline drooped leading edges
	LEOB18	0°	2018 outboard wing baseline leading edges
	LEOB18.SM	+30°	2018 outboard wing leading edges with deflection (sheet metal)
	LEOB20	0°, +15°, +30°	2020 outboard wing baseline leading edges
	LEOB20.OG	0°	2020 outboard wing ogive leading edges
	LEOB23	0°, +15°, +30°	2023 outboard wing baseline leading edges
Wing outboard trailing edge	TEOB15.SM	±10°, +20°	2015 outboard wing baseline trailing edges
(aileron ≡ TEOB)	TEOB15	0°, ±10°, ±25°	2015 outboard wing baseline trailing edges
	TEOB15.R	±10°, ±25°	2015 outboard wing reduced area trailing edges (1/3 area reduction)
	TEOB13.5	0°	2015 wing modification to shorter chord constraint to the same area
	TEOB17	0°, ±10°, ±20°	2017 outboard wing baseline trailing edges
	TEOB20	0°, ±10°, ±25°	2020 outboard wing baseline trailing edges
	TEOB20.R	±10°, ±25°	2020 outboard wing reduced area trailing edges (1/3 area reduction)
	TEOB20.AS21	−45°	2020 outboard wing aileron spoilers (1/3 area of baseline aileron)
	TEOB20.SSD21	±45°	2020 outboard wing spoiler-slot deflector (1/3 area of baseline aileron)
	TEOB20.SSD23	±67°	2020 outboard wing spoiler-slot deflector (1/6 area of baseline aileron)
	TEOB23	0°, ±10°, ±20°	2023 outboard wing baseline trailing edges
Vertical tail (rudder)	V15	0°	2015 single vertical tail without rudder deflections
	V15.1	0°, +10°, +25°	2015 single vertical tail with rudder deflections
	V16/V16.1	0°, +20°, +30°	2016 single vertical tail with rudder deflections

Continued on next page

Table 5 – continued from previous page

	Designation	Deflections	Description
	V17/V17.1	0°, +10°, +20°	2017 single vertical tail with rudder deflections
	V18/V18.1/V18.2	0°, +10°, +20°	2018 single vertical tail with rudder deflections
	V20	0°, +10°, +20°	2020 vertical tail with rudder deflections
	V16T.2/V16T.3	0°	2016 twin vertical tails without rudder deflection
	V23	0°, ±10°, −20° , −30°	2023 V-tail with rudder deflections
Horizontal tail (all-moving)	H15/H15A/H20.L H15A.1/H20L.1	0°, ±5°, ±10°, ±15°, ±20°, ±25°, ±30° (+2.0°)	2015 horizontal stabilizer at Γ = 0° with commutative incident blocks. H15A, H20.L, H15A.1, and H20L.1 are metal sleeves over H15. All (H15, H15A, H20.L, H15A.1, and H20L.1) have +2.0° bias.
	H15A.2	0°, ±5°, ±10°, ±15°, ±20°, ±25°, ±30° (+2.0°)	2015 RUAV horizontal stabilizer at Γ = 0° with commutative incident blocks with+2.0° bias
	H20L.2	0°, ±5°, ±10°, ±15°, ±20°, ±25°, ±30° (+0.4°)	2020 horizontal stabilizer at Γ = 0° with commutative incident blocks with +0.4° bias
	H16/H17.1/H17.2	0°, −2.5°, ±5°, −10°, ±15°, −30°	Wing aft-deck incident blocks with horizontal stabilizer deflections at Γ = −10°
	H18	0°, −5°, ±10°, ±20°, −30° 0°, +10°, −20°, −30°	Wing aft-deck incident blocks with horizontal stabilizer deflections at Γ = 0° and Γ = −10°
	H20.M, H20.T	0, ±5, ±10, ±15 (+0.4°)	2020 all-moving stabilizer at mid- and T-tail mounts deflections with +0.4° bias
	H24	0 (+0.4°)	2024 horizontal stabilizer deflections with +0.4° bias
Canard (all-moving)	C15/C15.2/C15.1 C17/C17D.1/C17D.2 C23/C23.1	0°, ±5°, ±10°, ±15°, ±20°, ±25°, ±30°	Commutative forebody fuselage incident blocks with canard deflections at Γ = 0°
Additional	FS21	±45°	mid-chord spoiler on top and bottom of the wing
	CS21	−45°	clam shell speed brakes at the rear fuselage

B. Model Designation

Table 6 2015 (UW2128) configuration build-up and variants

Figure	Designation	Forebody	Aft-body	Wing	Aft-deck	Nacelle	Vertical tail	Horizontal tail	Canard	Additional
				W15						
		F15	A15	W15						
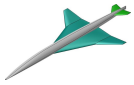		F15	A15	W15				H15		
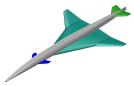		F15	A15	W15				H15	C15.M	
		F15	A15	W15.2		N15	V15			
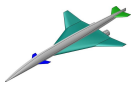		F15	A15	W15		N15		H15	C15.M	
		F15	A15	W15		N15	V15	H15A		
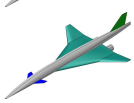		F15	A15	W15.2		N15	V15		C15.F	
		F15	A15	W15.2		N15	V15	H15A		

Continued on next page

Table 6 – continued from previous page

Figure	Designation	Forebody	Aft-body	Wing	Aft-deck	Nacelle	Vertical tail	Horizontal tail	Canard	Additional
		F15U	A15	W15		N15	V15	H15A		
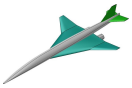		F15D	A15	W15		N15	V15	H15A		
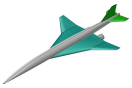		F15	A15	W15			V15	H15	C15.M	
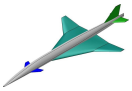		F15	A15	W15			V15	H15	C15.F	
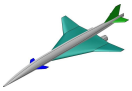	UW-S-15A	F15	A15	W15		N15	V15	H15	C15.M	
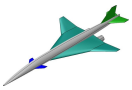	UW-S-15B	F15	A15	W15		N15	V15	H15A	C15.M	
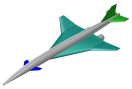	UW-S-15C	F15	A15	W15		N15	V15	H15A	C15.F	
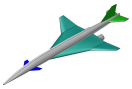	UW-S-15D	F15	A15	W15		N15	V15	H15A	C15F.2	
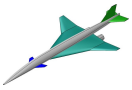	UW-S-15F	F15	A15	W15		N15	V15	H15A	C15M.2	
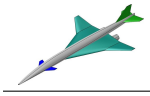	UW-S-15G	F15	A15	W15.2		N15	V15	H15A	C15F.2	

Table 7 2016 (UW2166) configuration build-up and variants

Figure	Designation	Forebody	Aft-body	Wing	Aft-deck	Nacelle	Vertical tail	Horizontal tail	Canard	Additional
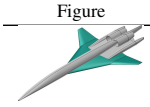		F15	A16	W15	AD16	N16				
		F15	A16	W15	AD16	N16		H16		
		F15	A16	W15	AD16	N16	V16T.2	H16		
		F15	A16	W15	AD16	N16	V16.F	H16		VF16.T
		F15	A16	W15	AD16	N16	V16.A	H16		VF16.T
		F15	A16	W15	AD16	N16	V16.F	H16		VF16T.2
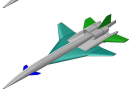		F15	A16	W15	AD16	N16	V16F.1	H16		VF16T.2

Continued on next page

Table 7 – continued from previous page

Figure	Designation	Forebody	Aft-body	Wing	Aft-deck	Nacelle	Vertical tail	Horizontal tail	Canard	Additional
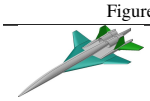		F15	A16	W15	AD16	N16	V16T.2	H16		VF16.T
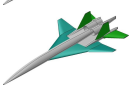		F15	A16	W15	AD16	N16	V16T.3	H16		VF16.T
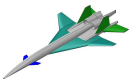		F15	A16	W15	AD16	N16	V16T.3	H16	C15.F	VF16.T
		F15	A16	W15	AD16	N16	V16T.3	H16	C15.M	VF16.T
		F15	A16	W15	AD16	N16	V16T.3	H16	C15F.2	VF16.T
		F15	A16	W15	AD16	N16	V16T.3	H16	C15M.2	VF16.T
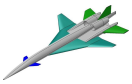		F15	A16	W15	AD16	N16	V16F.1	H16	C15.F	VF16T.2

Table 8 2017 (UW2200) configuration build-up and variants

Figure	Designation	Forebody	Aft-body	Wing	Aft-deck	Nacelle	Vertical tail	Horizontal tail	Canard	Additional
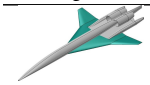		F15	A16	W15	AD16	N16				
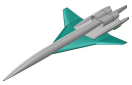		F15	A16	W15	AD16	N16				VF16T.2
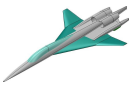		F15	A16	W15	AD16	N16				VF16T.2 + FD17
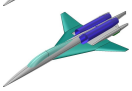		F15	A16	W17	AD16	N17.1				VF16T.2 + FD17
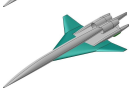		F15	A16	W17+RT17	AD16	N17.1				VF16T.2 + FD17
		F15	A16	W15	AD16	N16	V16.F	H16	C15.F	VF16T.2
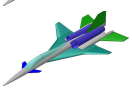		F15	A16	W17+RT17	AD16	N17.1	V17F.1	H17	C17.F	FD17
		F15	A16	W15	AD16	N16	V16.F	H16	C15.F	VF16T.2 + FD17
		F15	A16	W15	AD16	N16	V16.F	H16	C17.F	VF16T.2 + FD17
		F15	A16	W15	AD16	N16	V16.F	H17	C17.F	VF16T.2 + FD17
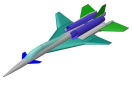		F15	A16	W15	AD16	N17	V16.F	H17	C17.F	VF16T.2 + FD17

Continued on next page

Table 8 – continued from previous page

Figure	Designation	Forebody	Aft-body	Wing	Aft-deck	Nacelle	Vertical tail	Horizontal tail	Canard	Additional
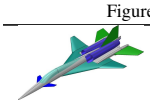		F15	A16	W15	AD16	N17	V17.F	H17	C17.F	VF16T.2 + FD17
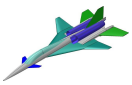		F15	A16	W15	AD16	N17.1	V17.F	H17	C17.F	VF16T.2 + FD17
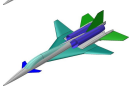		F15	A16	W17	AD16	N17.1	V17.F	H17	C17.F	VF16T.2 + FD17
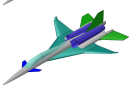		F15	A16	W17+RT17	AD16	N17.1	V17.F	H17	C17.F	VF16T.2 + FD17
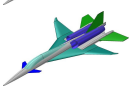		F15	A16	W17+RT17	AD16	N17.1	V17.F	H17	C17F.D	VF16T.2 + FD17
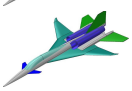		F15	A16	W17+RT17	AD16	N17.1	V17F.1	H17	C17.F	VF16T.2 + FD17

Table 9 2018 (UW2237) configuration build-up and variants

Figure	Designation	Forebody	Aft-body	Wing	Aft-deck	Nacelle	Vertical tail	Horizontal tail	Canard	Additional
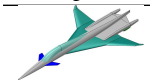		F15	A16	W17+RT17	AD16					VF16T.2 + FD17
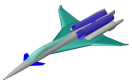		F15	A16	W17+RT17	AD16	N18				VF16T.2 + FD17
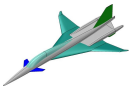		F15	A16	W17+RT17	AD16		V17.F			VF16T.2 + FD17
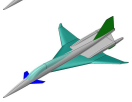		F15	A16	W17+RT17	AD16		V18.F			VF16T.2 + FD17
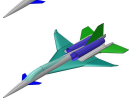		F15	A16	W17+RT17	AD16	N18	V17.F			VF16T.2 + FD17
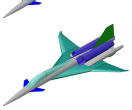		F15	A16	W17+RT17	AD16	N18	V18.F			VF16T.2 + FD17
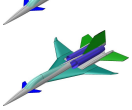		F15	A16	W17+RT17	AD16	N18	V18F.2	H17	C17.F	FD17
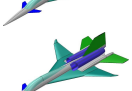		F15	A16	W17+RT18	AD16	N18	V18F.2	H17	C17.F	FD17
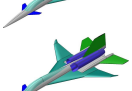		F15	A16	W18	AD16	N18	V18F.2	H17	C17.F	FD17
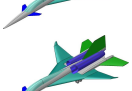		F15	A16	W18	AD16	N18	V18F.2	H17	C17.F	FD17 + LG18
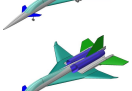		F15	A16	W17+RT17	AD16	N18	V17.F	H17	C17.F	VF16T.2 + FD17

Continued on next page

Table 9 – continued from previous page

Figure	Designation	Forebody	Aft-body	Wing	Aft-deck	Nacelle	Vertical tail	Horizontal tail	Canard	Additional
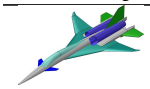		F15	A16	W17+RT17	AD16	N18	V17.F	H18	C17.F	VF16T.2 + FD17
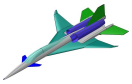		F15	A16	W18	AD16	N18	V18.F	H17	C17.F	VF16T.2 + FD17
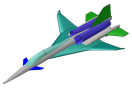		F15	A16	W18	AD16	N18	V18.F	H18	C17.F	VF16T.2 + FD17
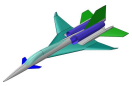		F15	A16	W18	AD16	N18	V18F.1	H17	C17.F	VF16T.2 + FD17
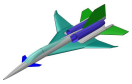		F15	A16	W18	AD16	N18	V18F.2	H17	C17.F	VF16T.2 + FD17
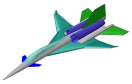		F15	A16	W18+RT18	AD16	N18	V18F.2	H17	C17.F	VF16T.2 + FD17

Table 10 SCALOS table of model configuration variations tested (2020-24)

Figure	Designation	Forebody	Aft-body	Wing	Aft-deck	Nacelle	Vertical tail	Horizontal tail	Canard	Additional
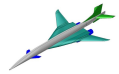	UW-S-13A	F15	A15	W13.5		N20.B	V15	H20.L	C15.F	DF.1 + VF.1
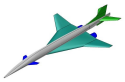	UW-S-17A	F15	A15	W18		N20.B	V15	H20.L	C15.F	DF.1 + VF.1
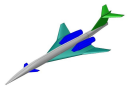	UW-S-20A	F15	A20	W20		N20.T	V20	H20.T	C15.F	
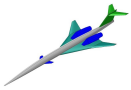	UW-S-20AL	F15L	A20	W20		N20.T	V20	H20.T	C15.F	
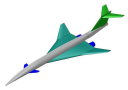	UW-S-20B	F15	A20	W20		N20.B	V20	H20.T	C15.F	
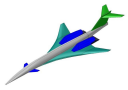	UW-S-20C	F15	A20	W20	NSRD	N20.T	V20	H20.T	C15.F	OG + strake
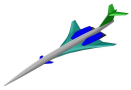	UW-S-20CL	F15.L	A20	W20	NSRD	N20.T	V20	H20.T	C15.F	OG + strake
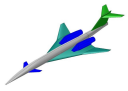	UW-S-20D	F15	A20	W20		N20.T	V20	H20.T	C17.F	
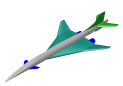	UW-S-20E	F15	A15	W20		N20.B	V15	H20.L	C15.F	DF.1 + VF.1
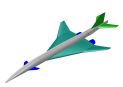	UW-S-20F	F15	A15	W20		N20.B	V15	H20.L	C15.F	

Continued on next page

Table 10 – continued from previous page

Figure	Designation	Forebody	Aft-body	Wing	Aft-deck	Nacelle	Vertical tail	Horizontal tail	Canard	Additional
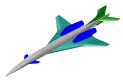	UW-S-20G	F15	A15	W20		N20.T	V15	H20.L	C15.F	DF.1 + VF.1
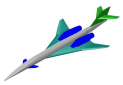	UW-S-20H	F15	A20	W20		N20.T	V20	H20.M	C15.F	
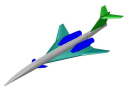	UW-S-20I	F15	A20	W20		N20.T	V20	H20.T	C15.A	
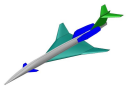	UW-S-20J	F15	A20	W20		N20.TR	V20	H20.T	C15.F	
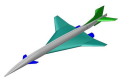	UW-S-21A	F15	A15	W15		N20.B	V15	H20.L	C15.F	DF.1 + VF.1
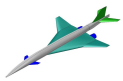	UW-S-21B	F15	A15	W15		N20.B	V15	H20.L	C15.F	
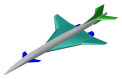	UW-S-21C	F15	A15	W15		N20.B	V15	H20.L	C17.F	DF.1 + VF.1
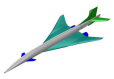	UW-S-23A	F23	A23	W23		N20.B	V15	H20.L	C15.F	DF.1 + VF.1
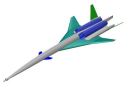	UW-S-23E	F15.L	A18	W20	AD16	N18	V23		C15.F	OG + strake
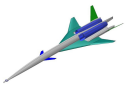	UW-S-23F	F15.L	A18	W20	AD16	N18	V23		C23	OG + strake
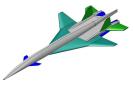	UW-S-23G	F15	A16	W15	AD16	N23.BR	V16T.2	H18	C15.F	
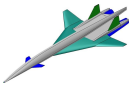	UW-S-23H	F15	A16	W15	AD16	N23.BA	V16T.2		C15.F	
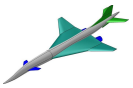	UW-S-24A	F24	A24	W15		N20.B	V15	H24.L	C15.F	DF.1 + VF.1
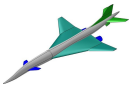	UW-S-24B	F24	A24	W15		N20.B	V15	H24.L	C15.F	DF.1 + VF.24

Table 11 2017 low-tail configuration build-up and variants

Figure	Designation	Forebody	Aft-body	Wing	Aft-deck	Nacelle	Vertical tail	Horizontal tail	Canard	Additional
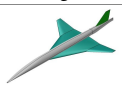		F15	A15	W17			V15			

Continued on next page

Table 11 – continued from previous page

Figure	Designation	Forebody	Aft-body	Wing	Aft-deck	Nacelle	Vertical tail	Horizontal tail	Canard	Additional
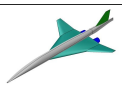		F15	A15	W17		N20.B	V15			
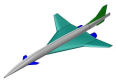		F15	A15	W17		N20.B	V15		C15.F	DF.1 + VF.1
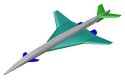		F15	A15	W17		N20.B		H20.L	C15.F	VF.1
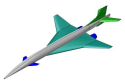	UW-S-17A	F15	A15	W17		N20.B	V15	H20.L	C15.F	DF.1 + VF.1

Table 12 2020 low-tail configuration build-up and variants

Figure	Designation	Forebody	Aft-body	Wing	Aft-deck	Nacelle	Vertical tail	Horizontal tail	Canard	Additional
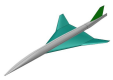		F15	A15	W20			V15			
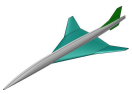		F15	A15	W20			V15			DF.1 + VF.1
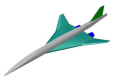		F15	A15	W20		N20.B	V15			
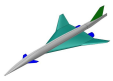		F15	A15	W20		N20.B	V15		C15.F	
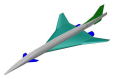		F15	A15	W20		N20.B	V15		C15.F	DF.1 + VF.1
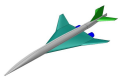		F15	A15	W20		N20.B	V15	H20.L		
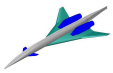		F15	A15	W20		N20.B			C15.F	
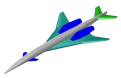		F15	A15	W20		N20.T		H20.L	C15.F	
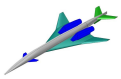		F15	A15	W20		N20.T		H20.L	C15.F	VF.1
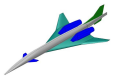		F15	A15	W20		N20.T	V15		C15.F	DF.1 + VF.1
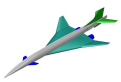	UW-S-20E	F15	A15	W20		N20.B	V15	H20.L	C15.F	DF.1 + VF.1

Continued on next page

Table 12 – continued from previous page

Figure	Designation	Forebody	Aft-body	Wing	Aft-deck	Nacelle	Vertical tail	Horizontal tail	Canard	Additional
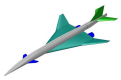	UW-S-20F	F15	A15	W20		N20.B	V15	H20.L	C15.F	
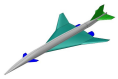	UW-S-20F-2	F15	A15	W20		N20.B	V15	H15.A	C15.F	
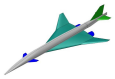	UW-S-20F-3	F15	A15	W20		N20.B	V15	H15	C15.F	
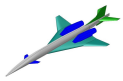	UW-S-20G	F15	A15	W20		N20.T	V15	H20.L	C15.F	DF.1 + VF.1
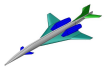	UW-S-20G-2	F15	A15	W20		N20.T	V15	H20.L	C15.F	DF.1

Table 13 2020 T-tail configuration build-up and variants

Figure	Designation	Forebody	Aft-body	Wing	Aft-deck	Nacelle	Vertical tail	Horizontal tail	Canard	Additional
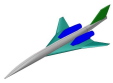		F15	A20	W20		N20.T	V20			
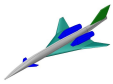		F15	A20	W20		N20.T	V20		C15.F	
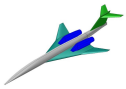		F15	A15	W20		N20.B	V20	H20.T		
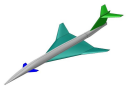		F15	A20	W20			V20	H20.T	C15.F	
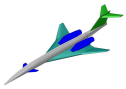	UW-S-20A	F15	A20	W20		N20.T	V20	H20.T	C15.F	
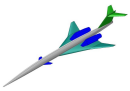	UW-S-20AL	F15.L	A20	W20		N20.T	V20	H20.T	C15.F	
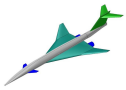	UW-S-20B	F15	A20	W20		N20.B	V20	H20.T	C15.F	
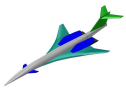	UW-S-20C	F15	A20	W20	NSRD	N20.T	V20	H20.T	C15.F	OG + strake
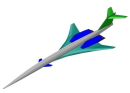	UW-S-20CL	F15.L	A20	W20	NSRD	N20.T	V20	H20.T	C15.F	OG + strake
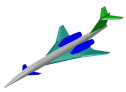	UW-S-20D	F15	A20	W20		N20.T	V20	H20.T	C17.F	

Continued on next page

Table 13 – continued from previous page

Figure	Designation	Forebody	Aft-body	Wing	Aft-deck	Nacelle	Vertical tail	Horizontal tail	Canard	Additional
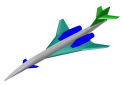	UW-S-20H	F15	A20	W20		N20.T	V20	H20.M	C15.F	
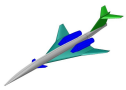	UW-S-20I	F15	A20	W20		N20.T	V20	H20.T	C15.A	
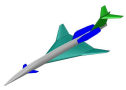	UW-S-20J	F15	A20	W20		N20.TR	V20	H20.T	C15.F	

Table 14 2021 low-tail configuration build-up and variants

Figure	Designation	Forebody	Aft-body	Wing	Aft-deck	Nacelle	Vertical tail	Horizontal tail	Canard	Additional
				W15						
		F15	A15	W15						
		F15	A15	W15			V15			DF.1+VF.1
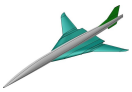		F15	A15	W13.5			V15			DF.1 + VF.1
		F15	A15	W15			V15	H15		DF.1+VF.1
		F15	A15	W15			V15	H15A		DF.1+VF.1
		F15	A15	W15			V15	H20.L		DF.1+VF.1
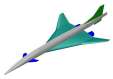		F15	A15	W15		N20.B	V15		C15.F	DF.1 + VF.1
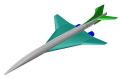		F15	A15	W15		N20.B	V15	H20.L		DF.1 + VF.1
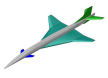		F15	A15	W15			V15	H20.L	C15.F	DF.1 + VF.1
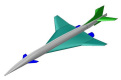	UW-S-21A	F15	A15	W15		N20.B	V15	H20.L	C15.F	DF.1 + VF.1
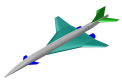	UW-S-21B	F15	A15	W15		N20.B	V15	H20.L	C15.F	

Continued on next page

Table 14 – continued from previous page

Figure	Designation	Forebody	Aft-body	Wing	Aft-deck	Nacelle	Vertical tail	Horizontal tail	Canard	Additional
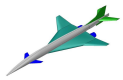	UW-S-21C	F15	A15	W15		N20.B	V15	H20.L	C17.F	DF.1 + VF.1
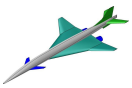	UW-S-21D	F15	A15	W15		N20.B	V15	H20L	C23.F	DF.1 + VF.1
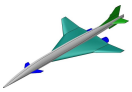	UW-S-21E	F15	A15	W15		N20.B	V15	H15	C15.F	DF.1 + VF.1
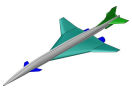	UW-S-21F	F15	A15	W15		N20.B	V15	H15A	C15.F	DF.1 + VF.1
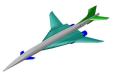	UW-S-13A	F15	A15	W13.5		N20.B	V15	H20.L	C15.F	DF.1 + VF.1

Table 15 2023 configuration build-up and variants

Figure	Designation	Forebody	Aft-body	Wing	Aft-deck	Nacelle	Vertical tail	Horizontal tail	Canard	Additional
				W (IB)						
				W15	AD16					
				W23						
		F15	A15	W23						
		F15	A15	W23			V15			
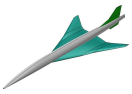		F15	A15	W23			V15			DF.1 + VF.1
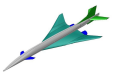	UW-S-23A	F15	A15	W23		N20.B	V15	H20.L	C15.F	DF.1+VF.1
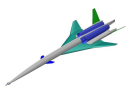	UW-S-23E	F15.L	A18	W20	AD16	N18	V23		C15.F	NC + OG + strake
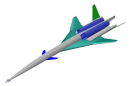	UW-S-23F	F15.L	A18	W20	AD16	N18	V23		C23	NC + OG + strake

Table 16 2024 configuration build-up and variants

Figure	Designation	Forebody	Aft-body	Wing	Aft-deck	Nacelle	Vertical tail	Horizontal tail	Canard	Additional
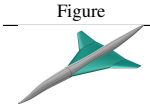		F24	A24	W15						
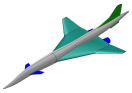		F24	A24	W15		N20.B	V15		C15.F	DF.1 + VF.1
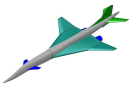	UW-S-24A	F24	A24	W15		N20.B	V15	H24.L	C15.F	DF.1 + VF.1
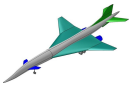		F24	A24	W15		N20.B	V15	H24.L	C15.F	DF.1 + VF.1 + LG24
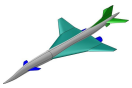	UW-S-24B	F24	A24	W15		N20.B	V15	H24.L	C15.F	DF.1 + VF.24
		F15	A16	W15	AD16		V16T.2		C15.F	
	UW-S-23G	F15	A16	W15	AD16	N23.BA	V16T.2	H18	C15.F	
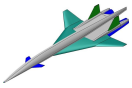	UW-S-23H	F15	A16	W15	AD16	N23.BA	V16T.2		C15.F	

Supersonic Configurations at Low Speeds (SCALOS)

Final Report

December 15, 2024

Appendix E

University of Washington

Selected Lateral-Directional Kirsten Wind Tunnel Results

Supersonic Configurations at Low Speeds (SCALOS) Lateral-directional Aerodynamics: Configuration Variations and Control Surface Effects

Kuang-Ying Ting*, Kenneth Wiersema† Reza M. Soltani‡, Chester P. Nelson§, and Eli Livne¶
University of Washington, Seattle, WA 98195

The NASA-funded SCALOS project has been focusing on the low-speed characteristics of advanced long-range supersonic configurations. A substantial configuration design space survey was conducted to guide the selection of sample configurations for testing. All wind tunnel experiments were carried out at the University of Washington's Kirsten Wind Tunnel. A few tests were conducted at the Flow Visualization Water Tunnel (FVWT) at Boeing Research & Technology (BR&T) mainly for dynamic stability derivatives but also for static derivatives. The test matrix featured realistic model parts and geometries for the future supersonic aircraft, including the effects of lifting planform variations, control surface features, high-lift devices, engine locations, etc. All experimental data were gathered to build the desired SCALOS aerodynamic database at subsonic speeds essential for analysis and simulation of the landing and take-off phases of flight. In past publications the SCALOS project presented aerodynamic test results with a focus on the longitudinal aerodynamic characteristics. This paper presents selected test results with a focus on the lateral-directional aerodynamics of SCALOS, including comparative effects of configuration differences with notes on configuration parameters that have significant impacts on performance and stability characteristics at low-speed flight conditions. It is hoped that this information will fill the existing gap of the subsonic low speed data for supersonic passenger aircraft and will provide realistic test cases for both designers and CFD developers for this part of the flight envelope.

*Ph.D. student, William E. Boeing Dept. of Aeronautics and Astronautics, and AIAA Student Member, kyting@uw.edu
†Graduate Research Assistant, William E. Boeing Dept. of Aeronautics and Astronautics, and AIAA Student Member, kennew4@uw.edu
‡Senior Research Scientist, William E. Boeing Dept. of Aeronautics and Astronautics, reza2@uw.edu
§Senior Research Scientist, Professor and Retired Boeing Technical Fellow, William E. Boeing Dept. of Aeronautics and Astronautics, cpnelson@uw.edu
¶Boeing Endowed Professor, William E. Boeing Dept. of Aeronautics and Astronautics, and AIAA Fellow, eli@aa.washington.edu

Nomenclature

Abbreviations

BMC	Balance Moment Center
BR&T	Boeing Research & Technology
CFD	Computational Fluid Dynamic
CG	Center of Gravity
CST	Commercial Supersonic Technology
FVWT	Flow Visualization Water Tunnel
HSCT	High Speed Civil Transport
IB	Inboard
KWT	Kirsten Wind Tunnel
LE	Leading Edge
LOD	Lift-over-drag ratio
MFTF	Mixed Flow Turbofan engines
MAC	Mean Aerodynamic Center
MMC	Model Moment Center
NSRD	Nozzle Shock-Reflecting Deck
OB	Outboard
RSAC	Research Supersonic Airliner Concept
SA	Stability Axis
SCALOS	Supersonic Configurations at Low Speeds
TE	Trailing Edge
TOL	Take-off and Landing
UAV	Unmanned Aerial Vehicle
UWAL	University of Washington Aeronautical Labo ratory
TEOB	Trailing Edge Outboard ≡ Ailerons

Variables

α	Angle of attack
β	Sideslip angle
Γ	Dihedral angle
Λ_{LE}	Wing outboard leading-edge sweep angle
$\frac{\partial C_M}{\partial C_L}$	Static margin
$\bar{c}$	Mean aerodynamic center
b	Wing span
C_D	Drag force coefficient
C_L	Lift force coefficient
C_L vs. C_D	Drag polar
$\frac{C_L}{C_D}$	Lift-over-drag ratio
C_M	Pitching moment coefficient
C_n	Yawing moment coefficient
C_R	Rolling moment coefficient
C_Y	Side force coefficient
C_{D_0}	Zero-lift drag coefficient
C_{L_α}	Lift coefficient derivatives
$C_{L_{max}}$	Maximum lift coefficient
C_{M_0}	Zero-pitch moment coefficient
C_{M_α}	Pitching moment coefficient derivatives
$C_{M_{\alpha=0}}$	Zero-alpha pitching moment coefficient
d_f	Diameter of fuselage
l_f	Length of fuselage
Re	Reynolds number
S_{ref}	Wing reference area
$\frac{t}{c}$	Thickness to chord ratio

Introduction

Building on the introduction to Ref. [1]: "The emergence of new concepts for civilian supersonic cruise aircraft in the Post-High Speed Civil Transport (HSCT) era, including low-boom "quiet" supersonic configuration concepts over the last 10-20 years, calls for re-examination of the design trade-offs for long-range supersonic transport category aircraft. While most of the works in recent years dedicated to supersonic aircraft aerodynamics have been focused on the supersonic characteristics of the new configurations, a viable, certifiable, supersonic airliner must also be efficient in its subsonic phases of their flights and meet all performance, handling qualities, and stability and control (S&C) requirements at these speeds. There is already a significant knowledge base on aircraft configuration applied aerodynamics, including supersonic fighter jets and large aircraft, commercial airliners, and bombers (see selected references [2–29]," and a more comprehensive review in [30] which the present SCALOS effort is augmenting with new data in the public domain).

More from [1]: "New generation supersonic airliner and corporate jet designs employ different wing planforms, propulsion and control arrangements and are often much more slender (overall length to wingspan ratios as high as 3.5). The subsonic characteristics of most of these features have not been covered well by public-domain research thus far [31–49]. A major goal of the NASA-funded Commercial Supersonic Technology (CST) Supersonic Configurations at Low Speeds (SCALOS) project is therefore to study representative supersonic configurations and their variations from the applied aerodynamics perspective, covering flow field physics, performance, S&C, propulsion integration options, and impacts on landing and take-off (LTO) noise.

An overview of the SCALOS project's 2020-2025 effort in the applied aerodynamics area is presented in [50] and [51], covering years of low-speed testing in the Kirsten Wind Tunnel (KWT) at the University of Washington Aeronautical Laboratory (UWAL). Of particular interest regarding the present paper and its focus on lateral-directional characteristics is Ref [52] which studies control effector effects in the longitudinal case. Tests at the Flow Visualization Water Tunnel (FVWT) at Boeing Research & Technology (BR&T) ([53]-[55] provided dynamic stability derivatives.

This paper presents selected experimental results of the lateral-directional aerodynamic characteristics of the SCALOS models tested to date at the University of Washington. It focuses on the configuration parameters that have major impact on the lateral-directional aerodynamics from the past wind tunnel reports and efforts [50-51]. In this paper low-speed results from Kirsten Wind Tunnel for various SCALOS configurations are presented. All data are corrected using the standard KWT corrections such as test section blockage, the effects of the test section wall, test section flow angularity, buoyancy, and various corrections that are specific to the balance and its mechanics of converting loads on the model to balance measurements. In addition to these corrections tare and interference effects due to the model support system were obtained experimentally specifically for the SCALOS via several experiments conducted at the KWT [56] and the results are implemented in the corrected data. The KWT database presented in this paper is, therefore, the final corrected data. **The term "corrected" data is used to denote data that represent free-flight characteristics of the tested models based on measured in-tunnel test results**. Results and discussion are presented the next section. Concluding remarks are provided at the end of the paper.

Experimental Setup

A. Test Model Geometry

In the presentation of the wind tunnel models and wind tunnel capabilities and procedures we borrow heavily from earlier papers on the SCALOS KWT tests to make the paper more self-contained.

The model is designed with an inboard wing section and support interface that can serve as a "backbone", allowing the creation of various configurations based on the same core model for semi-parametric studies. Figure 1 illustrates the major planform variations that were tested from 2015 and through 2024 with overlays of various shapes, e.g., different outboard wing shapes, different leading-edge shapes, canard shapes, nacelles and their locations, etc. In addition, the effects of various high lift and roll control devices such as conventional ailerons, speed brakes/aileron spoilers, spoiler-slot deflectors, mid-chord spoilers were studied too. Additional geometric variations such as area-ruled fuselage and landing gear effects were investigated too. The key geometric information about the configurations tested in Fig. 1 are tabulated in Tab. 1. Note that the span (b), mean aerodynamic chord ($\bar{c}$), wing reference area S_{ref}, and aspect ratio (AR) of the canard, horizontal, and vertical tails in Table 1 all are based on their exposed area outside of the fuselage body. Interested readers are refer to [50]-[51] for various built-up models with their respective component parts designations in the Appendix covering the designations of the modular components with corresponding control surfaces and deflection, the various model built-up, and model variations.

B. Kirsten Wind Tunnel

All wind tunnel tests were carried out in the Kirsten Wind Tunnel (KWT) at the University of Washington. The tunnel has a filleted rectangular test section of 12 ft in width by 8 ft in height and by 10 ft in length. It is a low-speed, closed-circuit, atmospheric, dual-return wind tunnel as shown in Fig. 3. The tunnel has two sets of 14’ 9" -diameter seven-bladed propellers that can move the air up to 200 miles per hour through the test section corresponding to a maximum dynamic pressure of 100 psf. The raw data from the external balance requires correction to obtain final force and moment values. The mechanical interaction of forces and moments in the balance system are corrected using standard correction protocols of the tunnel. Corrections of weight tare and strut tare are applied. Moments are transferred from the balance moment center (BMC) to the model moment center (MMC). Corrections for blockage, flow angularity, and wall effects are computed and added to the initial coefficients. The final coefficients are transferred from the wind axes to the stability axes. Additional CFD and test work was carried out to improve the wind tunnel corrections for the kind of configurations tested for this project, as described in [50] and [55, 56] on the establishment of high-fidelity, SCALOS-specific, corrections. Most tests were conducted at a dynamic pressure of 40 psf and later lowered to 32 psf to prevent model dynamics (severe buffeting of the model at high angles of attack). Data between these two different dynamic pressures was shown to be fully repeatable, other than a slight Reynolds number related to the skin friction drag effect in $C_{D\text{min}}$ seen at low angles of attack. More information about the wind tunnel and the testing procedure can be found in [50,51,57]

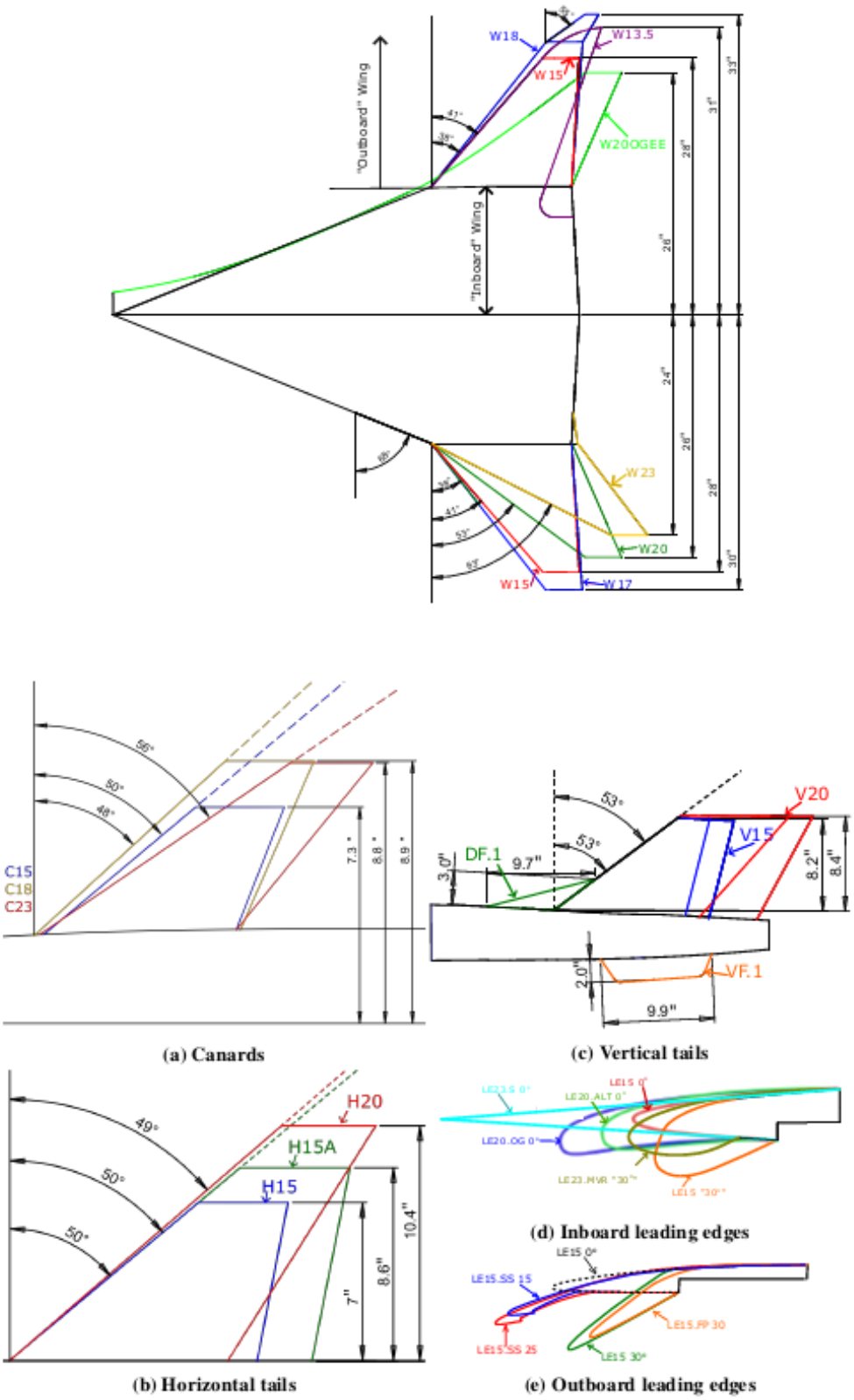

Figure 1: Planform Shapes

Table 1 SCALOS wind tunnel model components specification

	Designation	Λ_{LE} (°)	Γ(°)	b (ft)	$\bar{c}$ (ft)	S_{ref} (ft^2)	t/c_{max}	AR
Canard	C15	50	0	1.22	0.400	0.277	0.04	5.37
	C18	47.6	0	1.48	0.535	0.380	0.04	5.76
	C23	55.6	0	1.42	0.399	0.350	0.04	5.76
Outboard Wing	W13.5	41.0	4.67	5.22	1.73	8.17	0.05	3.34
	W15	41.0	4.67	4.67	2.01	8.30	0.05	2.63
	W17	38.1	4.17	5.00	1.92	8.58	0.05	2.91
	W18	38.2	10.2	5.46	1.86	8.66	0.05	3.39
	W20	53.5	4.74	4.40	2.09	8.09	0.05	2.39
	W23	63.0	4.45	4.00	2.28	7.83	0.05	2.04
Horizontal Tail	H15	50.1	0	1.17	0.623	0.594	0.04	2.30
	H15A	50.2	0	1.43	0.777	0.939	0.04	2.18
	H18	50.2	10	1.97	0.828	1.54	0.05	2.51
	H20	49.2	0	1.74	0.585	0.882	0.08	3.43
	V23.H	37.6	50.3	1.41	0.617	0.804	0.05	2.47
	H24	49.25	0	1.81	0.581	0.865	0.08	3.78
Vertical Tail	V15	50.1	0	0.74	1.07	0.579	0.05	0.946
	V16T.2	51.1	0	0.610	0.706	0.409	0.05	0.910
	V20	53.3	0	0.777	1.36	0.934	0.05	0.646
	V23.V	37.6	50.3	1.77	0.659	1.00	0.025	3.13
Ventral Fin	VF.1	29.9	0	0.167	0.7334	0.0033	0.1	0.228
	VF.2	30.2	0	0.1775	0.7540	0.1329	0.0033	0.2370
	VF24T	16	30	0.1567	0.3501	0.1087	0.00714	0.4518
Dorsal Fin	DF.1	73.8	0	0.17	0.75	0.16	0.04	0.181
	Designation	d_f (ft)	l_f (ft)					
Fuselage	F15	0.542	9.55					
	F15.L	0.542	11.57					
	F24	0.57	9.82					
	AD16	2.81	2.33					
Nacelle	N15	0.375	2.165					
	N18	0.469	2.788					
	N20	0.389	1.952					
	N23	0.389	2.633					

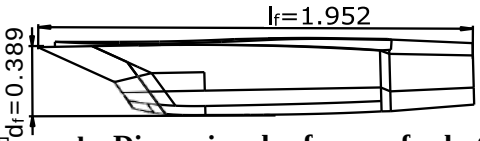

Fig. 2 N20 Nacelle Example: Dimensional reference for bottom mounted nacelle

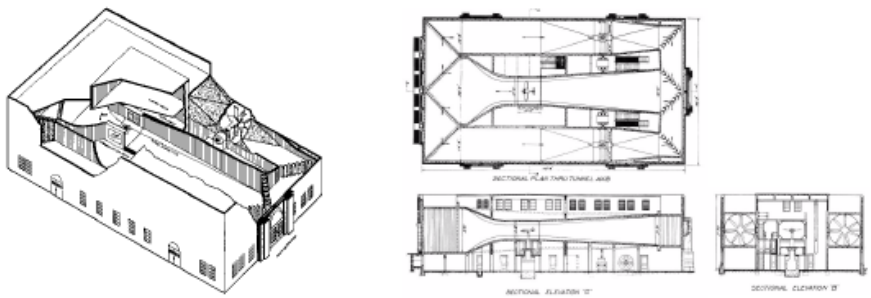

Fig. 3: The Kirsten Wind Tunnel at the University of Washington

C. Test Conditions

Wind tunnel tests were conducted at several tunnel dynamic pressures. For each dynamic pressure, tests were carried out over a range of sideslip angles, β, and angles of attack, α, from -10 up to 30 degrees. The high angles of attack and sideslip tests were pursued to allow developers to address nonlinear flight mechanics stability and control constraints beyond flight envelope. Moreover, for these angles of attack variations effects of formation, interaction, separation and burst of various vortices that from over different parts of the model such as canard, wing, slender fuselage, etc. will be studied. Table 2 presents the dynamic pressures in psf with the corresponding Reynolds numbers based on the baseline wing's (W15) mean aerodynamic chord length, Fig. 1, as shown in Table 1. In this paper, all data presented are for a nominal dynamic pressure of $32\ psf$, with the corresponding Reynolds number, $Re = 2.10 \times 10^6$ based on the mean aerodynamic chord.

Table 2 Dynamics pressure and Reynolds number at standard sea level

$q\ (psf)$	3.5	6.25	10	14	20	30	32	40	60
Re	6.90×10^5	0.93×10^6	1.17×10^6	1.39×10^6	1.66×10^6	2.03×10^6	2.10×10^6	2.35×10^6	2.87×10^6

Results and Discussion

Wind tunnel tests were conducted for several tunnel dynamic pressures, the effects of various model configuration variations on the aerodynamic lift force coefficient (C_L), drag force coefficient (C_D), side force coefficient (C_Y), pitching moment coefficient (C_M), rolling moment coefficient (C_R), and yawing moment coefficient (C_n) of the UW-SCALOS model will be presented and discussed here for a nominal dynamic pressure of $32\ psf$, corresponding to the $Re = 2.10 \times 10^6$. There are small physical areas and MAC variations among different wing planforms. In this paper all data are non-dimensionalized with respect to the reference area of the W15 model in S_{ref}, its MAC, and MMC for comparison purposes.

All aerodynamic data presented in this paper are corrected using the standard KWT corrections such as test section blockage, the effects of the test section wall, test section flow angularity, buoyancy, and various corrections that are specific to the balance and its mechanics of converting loads on the model to balance measurements. In addition to these corrections tare and interference effects because of the model support system were obtained experimentally specifically for the SCALOS via several experiments and are implemented in the corrected data. Therefore, the data presented in this paper is final corrected data. All aerodynamic coefficients are presented in the stability axes, *SA*. The numbers in the labels and legends of all figures are the center of gravity (CG) locations in percentages with respect to the W15 reference 25% MAC. For each case, the configurations were tested over a range of angles of attack and sideslip angles. All aerodynamic forces and moments were collected and non-dimensionalized to coefficients form based on the W15 reference quantities, Fig. 1 and Table 1.

Table 3 SCALOS table of model configuration variations tested (2020-23)

Figure	Designation	Forebody	Aft-body	Wing	Aft-deck	Nacelle	Vertical tail	Horizontal tail	Canard	Additional
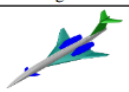	UW-S-20A	F15	A20	W20		N20.T	V20	H20.T	C15.F	
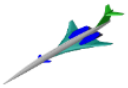	UW-S-20CL	F15.L	A20	W20	NSRD	N20.T	V20	H20.T	C15.F	OG + strake
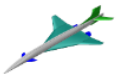	UW-S-21A	F15	A15	W15		N20.B	V15	H20.L	C15.F	DF.1 + VF.1
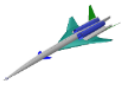	UW-S-23E	F15.L	A18	W20	AD16	N18	V23		C15.F	NC + OG + strake
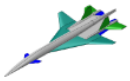	UW-S-23G	F15	A16	W15	AD16	N23.BR	V16T.2	H18	C15.F	
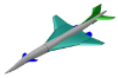	UW-S-24A	F24	A24	W15		N20.B	VF.1	H24	C15.F	

Configuration Lateral-directional Characteristics

As mentioned previously, several models of the SCALOS having different wings, horizontal, vertical, and canard planforms, as shown in Fig. 1, as well as nacelles and their locations, fuselage, forebody, aft-body, aft-deck, etc. were tested for various sideslip angles and angles of attacks. In addition to these configurations, models were tested with various leading and trailing edges flap rotations, flap/flaperon effects, horizontal tail locations and rotations, canard's location, shapes and deflection angles. Models were tested with various rudders (directional control authority), and aileron (roll control authority) too. Interested readers are referred to Ref. [58] for different variations of the SCALOS that have been tested up to now. In the present paper, however, the lateral-directional data for a few models of SCALOS, the configuration variations of which are shown in table 3 along with their photos shown in Fig. 4, will be discussed. All data are corrected for the wind tunnel blockage walls, wake, etc. effects, as well as the model support tare and interference effects [56]. In this section of the paper, the lateral directional data for four SCALOS models, UW-S-20A, UW-S-20CL, UW-S-21A, and UW-S-23G , Fig. 4, are presented and discussed.

Figure 5 shows effects of SCALOS configurations on the lift and moment at various angles of attacks. The data are also shown for the sideslip angles of $\beta = 0, 5, and\ 10$ degrees. All models were tested at a dynamic pressure of $32\ psf$ corresponding to the Reynolds number of $Re = 2.1x10^6$. However, the UW-S-23E SCALOS model was tested at a dynamic pressure of $6\ psf$. From Fig. 5a it is seen that for $\beta = 0$ degree case, all models generate the same lift values for angles of attack of $4^o \leq \alpha \leq 12^o$, however, for higher angles of attacks, different models show different lift variations for both positive and negative alphas.

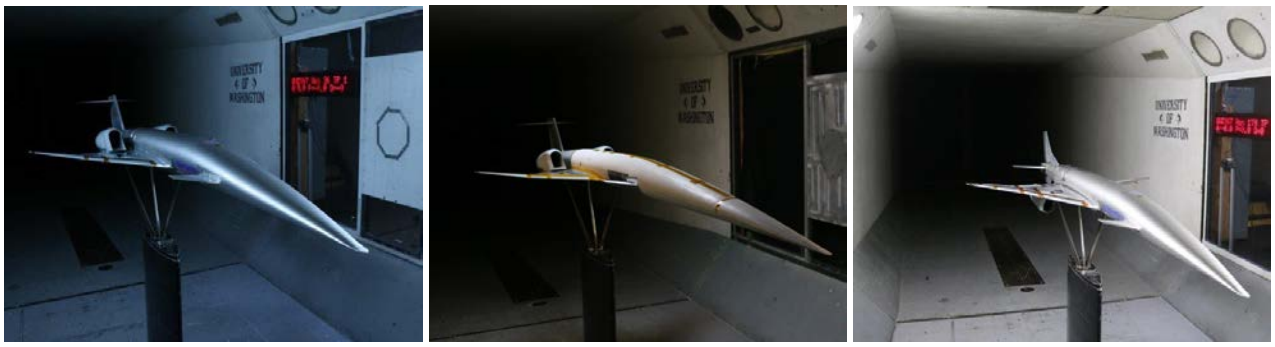

(a) UW-S-20A **(b) UW-S-20CL** **(c) UW-S-21A**

(d) UW-S-23E **(e) UW-S-23G** **(f) UW-S-24A**

Fig. 4: UW-S configurations

The SCALOS models UW-S-21A, UW-S-23G, and UW-S-24A do not show signs of stall at the highest angles of attacks tested, $\alpha \cong 24^o$, while other models are seen to stall near $\alpha \cong 20^o$. These variations are clearly seen in the pitching moment variations specially on the C_{M_0} , and C_{M_α} values, pitching moment break angles, which are most likely caused by addition of different parts, nacelle shape and locations, ventral and dorsal fins, etc. as shown in table 3. Similar effects are seen when the models are tested at sideslip angles of $\beta = 5, and$ 10 degrees (Fig. 5b, c). Figure 5 further shows that the pitch moment behavior of the UW-S-23G that has twin vertical tails and N23.BR nacelle along with AD16 after deck is much different than other SCALOS models. This model does not show any pitch-up, pitch breakdown, for all sideslips and angles of attack tested here, while the other models all show pitch breakdown, statically unstable behavior, near $\alpha \cong 10^o$ for all cases shown in Fig. 5d-f. The pitching moment derivative, C_{M_α} for the UW-S-23G model is seen to be negative and constant for angles of attack of up to about $\alpha \cong 20^o$ for all cases, while for other models, C_{M_α} is negative and relatively constant up to $\alpha \cong 8^o - 9^o$ and create nose up pitch moment, positive C_{M_α}, for higher angles of attack, statically unstable. All models are seen to be stable around zero degrees angle of attack, $C_{M_0} > 0$ with the UW-S-23G model being the most stable one having a relatively large C_{M_0} and negative C_{M_α} for all angles of attack tested. It seems that both UW-S-20A and UW-S-21A tend to regain their static stability around $\alpha \geq 20^o$ for all sideslip angles tested.

Figure 6 shows effects of sideslip angles, $\beta = 0, 5, and$ 10 degrees, on the variations of the lateral-directional force and moments coefficients of different SCALOS models shown in Fig. 4. At zero degrees sideslip angles (Fig. 6 a-c) all coefficients are zero for all angles of attack tested. The slight deviation from zero values at high angles of attack could be attributed to the model sensitivity to

flow separation and unsteady effects. It is seen that UW-S-23E, UW-S-20CL, and UW-S-20A show this type of sensitivity more than other models at high angles of attack. However, the non-zero variations of the lateral-directional force and moment coefficients of UW-S-23E at high angles of attack may be due to the low dynamic pressure, $q = 6\ psf$, in which it was tested.

Effects of sideslip angles, $\beta = 5, and\ 10$ degrees on the lateral-directional force and moments coefficients of the SCALOS models are shown in Figs. 6, d-i. From these figures it is seen that for all models both $C_Y\ and\ C_N$ have relatively constant non-zero values for angles of attacks of $-10^o \leq \alpha \leq 10^o$ for both sideslip angles. However, for $\beta = 10$ degrees, variations of $C_N\ vs\ \alpha$ is seen to be nonlinear for $\alpha \geq \pm 5^o$ which is attributed to the vortex formation over the windward wing. For higher angles of attack, this non-linear variation increases with different models showing different values. These nonlinearities are caused by the asymmetrical flow fields as well as the asymmetrical flow separations over different lifting surfaces of the models. All models, except UW-S-23G, are seen to lose their directional control authority when tested at $\beta = 10$ degrees for angles of attack of $\alpha \cong 10^o - 23^o$. For the UW-S-23E that was tested at $= 6\ psf$, the loss of directional control authority occurs between $\alpha \cong 10^o - 19^o$ (Fig. 6i). Beyond these angles of attack, all models regain their directional control authority as seen in Fig. 6h, i. The UW-S-23G model does not show loss of directional control authority at all angles of attack and at $\beta = 10$ degrees.

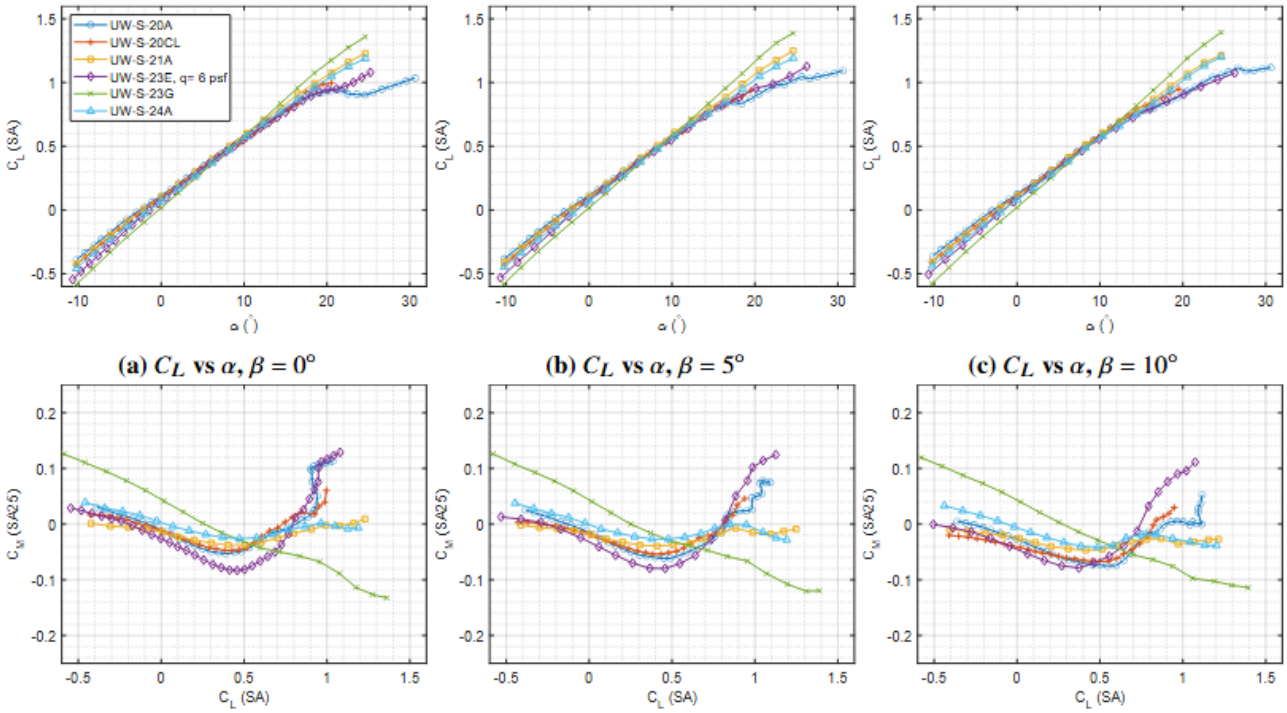

(a) C_L vs $\alpha, \beta = 0°$ (b) C_L vs $\alpha, \beta = 5°$ (c) C_L vs $\alpha, \beta = 10°$

(d) C_M vs. $C_L, \beta = 0°$ (e) C_M vs. $C_L, \beta = 5°$ (f) C_M vs. $C_L, \beta = 10°$

Fig. 5 Configuration variation longitudinal forces and moments vs. α

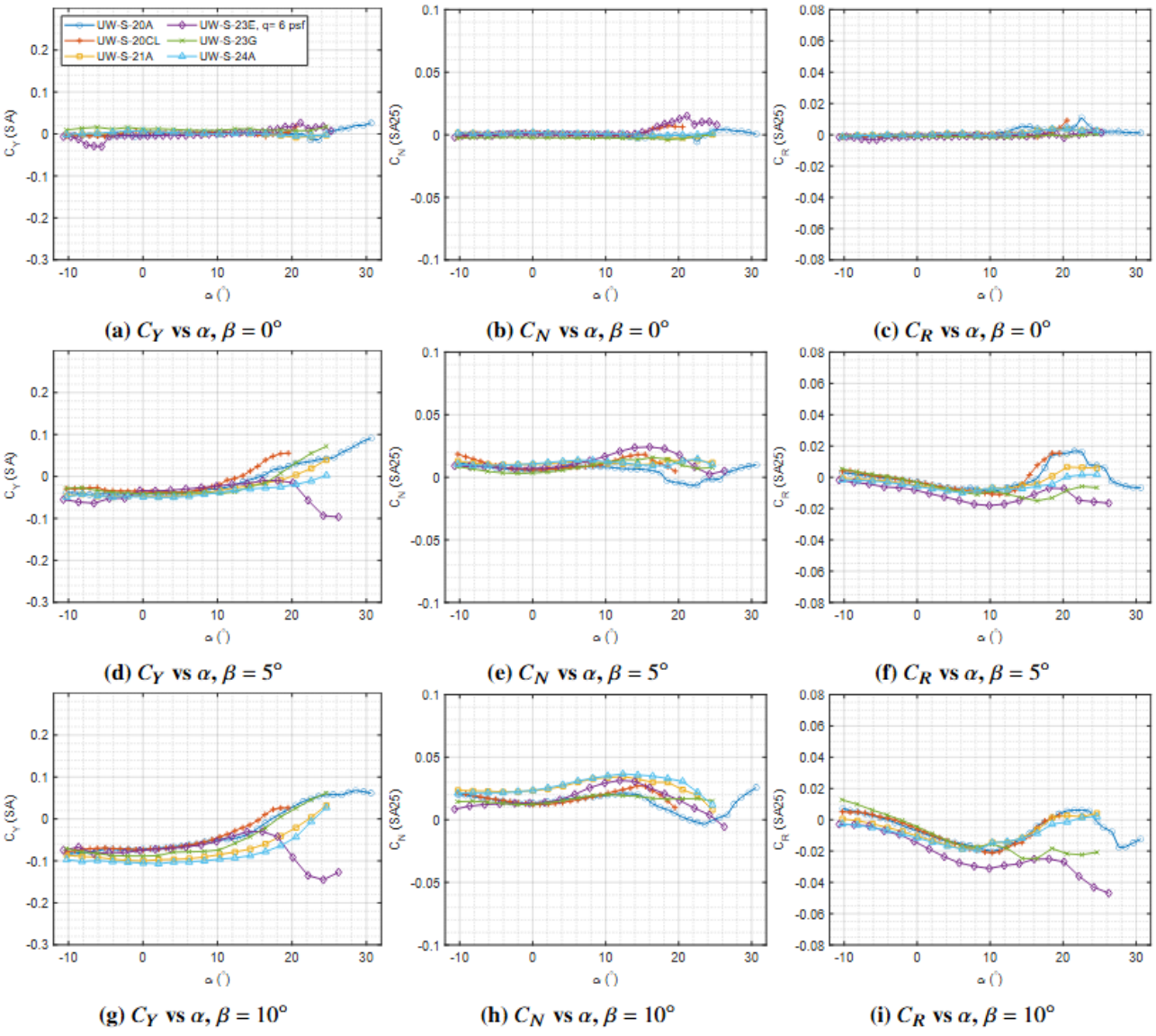

Fig. 6 Configuration variations lateral directional forces and moments vs α

Variations of the lateral-directional force and moment coefficients with sideslip angles for angles of attack of, $\boldsymbol{\alpha = 0, 10, \text{and } 20}$ degrees are shown in Fig. 7. As the angle of attack is increased from zero to 10 degrees, $\boldsymbol{C_{Y_\beta}}$ remains negative, however, its absolute value for all 4 models decreases. The UW-S-23G model shows an almost linear variation of $\boldsymbol{C_Y \; vs \; \beta}$ for all sideslip angles, while the other three models show slight nonlinearity in their side force variations with side slip angle and the non-linearity increases as alpha increases from zero to 10 degrees.

For the largest angles of attack, $\boldsymbol{\alpha = 20^o}$, Fig. 7g shows that $\boldsymbol{C_Y}$ for all four SCALOS models varies nonlinearly with sideslip angles. From this figure it is clearly seen that near zero sideslip angle the side force slope becomes very large for the UW-S-20CL model and has positive slopes for other three models, yaw reversal (directional divergence). For $\boldsymbol{\beta \geq 3^o}$ all models tend to regain their negative side force slope, $\boldsymbol{C_{Y_\beta} < 0}$.

The yawing moment coefficient variations for all models show positive C_{N_β} and its value decreases with increasing angles of attack (Fig. 7b, e, n). Similar to the side force coefficient variations near $\beta = 0^o$, the UW-S-20A model shows yaw divergence (weathercock instability) but regains its stability for $\beta \geq 2^o$ (Fig. 7h). The UW-S-23G model is seen to have very close to linear variations of C_N *vs* β for all angles of attack tested while the other three models show nonlinearity as alpha increases from zero to 20 degrees. The roll stability of the models for various sideslip angles and for three angles of attack are shown in Fig7 c, f, i. All four models have stable dihedral derivative, $C_{R_\beta} < 0$, for angles of attack of 0 and 10 degrees with almost constant C_{R_β} . The absolute values of C_{R_β} for all models increase as alpha increases from zero to 10 degrees. Note that the notation C_{R_β} is used here (following the notation used by the KWT) and not the more common C_{l_β} notation for a rolling moment derivative. Both the UW-S-21A, and UW-S-20A models show very large positive C_{R_β} for $-2^o \leq \beta \leq 3^o$ for $\alpha = 20^o$, large roll reversal, like the side force and yaw moment coefficients (Fig. 7 g, h) with a loss of directional authority, while C_{R_β} for the UW-S-23G model remains stable. This instability will affect the roll and spiral modes as well as the Dutch roll behavior. Both the UW-S-21A, and UW-S-20A models regain their directional control authority, however, for $\beta \geq 3^o$. Table 3 shows that the UW-S-23G model is equipped with an aft-deck and a twin vertical tail, both of which may have a significant influence on the lateral directional stability of the SCALOS configurations. At 20 degrees angle of attack, the leading-edge vortex of the windward wing is reduced by break downs, and vortex bursts cover a large portion of the wing surface, hence reducing the lift force of the windward wing while that of the leeward one might still be only mildly affected. This imbalance of the lift of the windward and leeward wings lift forces creates rolling and yawing moments. Apparently, both aft-deck and twin vertical tails of the UW-S-23G model significantly reduce these nonlinearities. The aft deck produces an extra lift which would counteract the loss of the lift due to vortex bursting and flow separation on the wing surface. In any effort to understand the aerodynamics of SCALOS configurations at sideslip and at high angles of attack it is important to examine the effects of the front fuselage and the vortex action it creates – by itself and with its canards and chines.

Flow Visualization Studies

Figures 8-10 show the effects of sideslip angles on the oil flow visualization as well as longitudinal and lateral directional force and moment coefficients of the UW-S-21A SCALOS model at various sideslips and angles of attack. The UW-S-21A model is a three-surface configuration with canards and a conventional empennage system with a single vertical tail and low horizontal tails. Effects of angles of attack on the longitudinal aerodynamic coefficients of this model have been discussed in detail in previous publications (Refs. [51, 53, 54]). As the model is yawed, the effective sweep angle of the windward wing decreases while that of the leeward one increases, resulting in asymmetric vortex formation, location, and breakdown. The asymmetries of the vortices result in differences in the lift on each side of the wing with respect to angles of attack. As the angle of attack increases, the windward wing vortex will form and burst sooner at more upstream locations than that of the leeward vortex. These differences are responsible for typical longitudinal, lateral, and directional instabilities, such as a pitch-up, a roll reversal, and directional divergence, respectively.

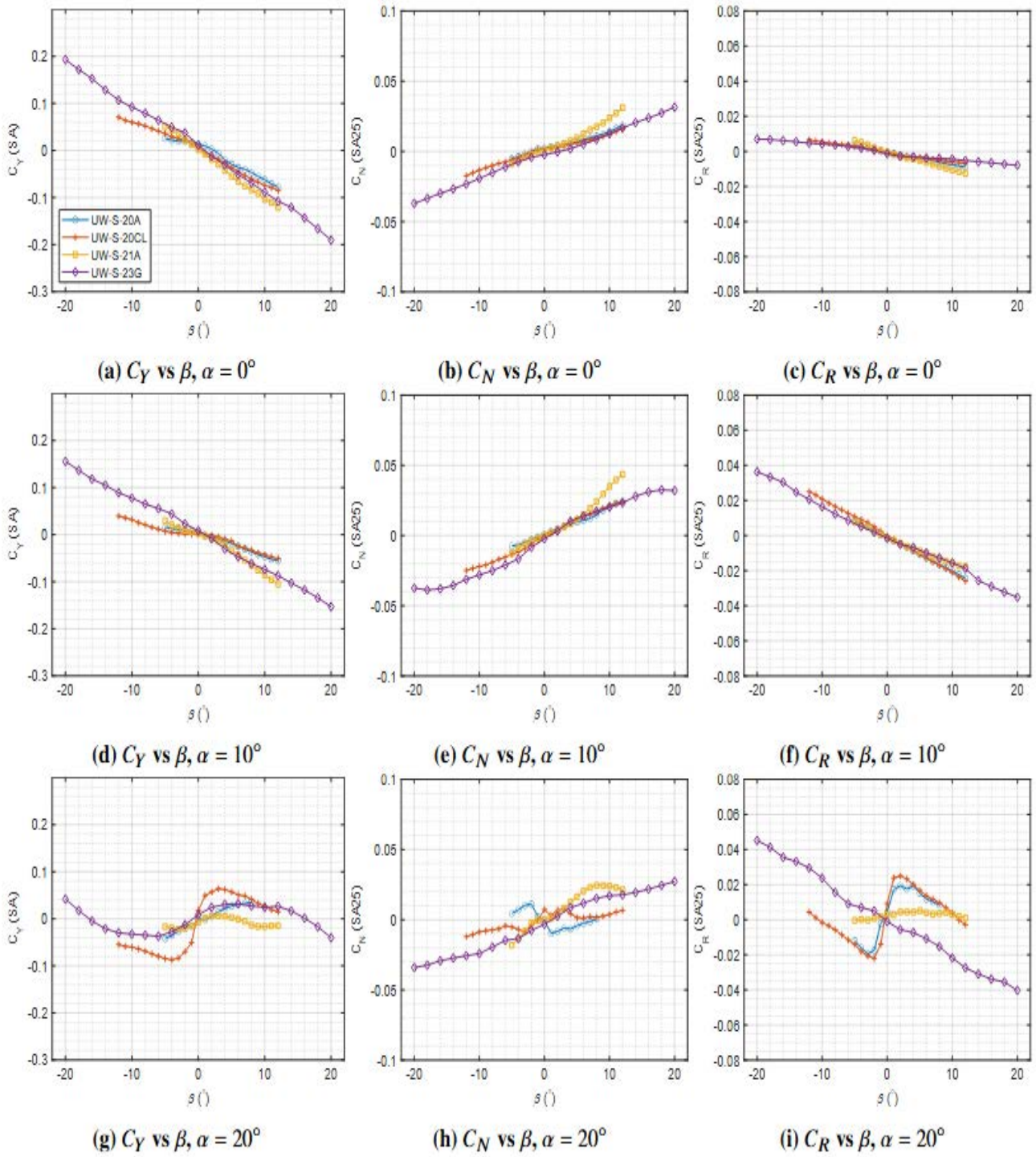

(a) C_Y vs β, $\alpha = 0°$ (b) C_N vs β, $\alpha = 0°$ (c) C_R vs β, $\alpha = 0°$

(d) C_Y vs β, $\alpha = 10°$ (e) C_N vs β, $\alpha = 10°$ (f) C_R vs β, $\alpha = 10°$

(g) C_Y vs β, $\alpha = 20°$ (h) C_N vs β, $\alpha = 20°$ (i) C_R vs β, $\alpha = 20°$

Fig. 7 Configuration variations lateral directional forces and moments vs. β

Minimal differences are shown in the oil flow visualization between β = 0° and β = 5° up to α < 15°, Fig. 8. However, distinct differences between the two sideslip angles are shown at $\alpha \geq$ 15°. For β = 0°, the inboard vortex breakdown moves onto the wing surface at $\alpha \approx$ 15° for both left- and right-wing surfaces. For β = 5°, the windward wing vortex bursts over the wing surface at lower angles of attack than that of the leeward one. The breakdown of both vortices over the wing surface decreases the lift at the wing's trailing edge, resulting in a pitch-up tendency. For $\alpha \geq$ 20°, both burst vortices for β = 0° and β = 5° move upstream toward the wing apex, resulting in another strong pitch-up tendency seen in Fig. 9.

Figures 9a-c show effects of sideslip angles on the longitudinal forces and moments of the model. Up to $\alpha \approx 12°$ angle of attack, C_{L_α} does not vary with sideslip angle. Beyond 12 degrees angle of attack, C_{L_α} decreases slightly with increasing sideslip angle.

The maximum lift to drag ratio, $\left.\frac{C_L}{C_D}\right| max$, is significantly affected by the sideslip angle too (Fig. 9c). Figures 9d-f show variations of the lateral directional force and moments coefficients with angles of attack for sideslip angles of $\beta = 0, 2, 5, and\ 10$ degrees. As the sideslip angle is increased absolute values of all three coefficient at zero degrees angle of attack increase and their variations with angles of attack are seen to be constant for $\beta = 0,\ and\ 2$ degrees. For $\beta = 5$ degrees, both $C_Y\ and\ C_N$ do not vary significantly with angle of attack, while C_R decreases linearly with alpha up to about 10 degrees angles of attack. With further increase of alpha, C_R increases and becomes almost zero for alpha larger than 18 degrees. A similar trend is seen for the C_R variations with angles of attack for $\beta = 10^o$ (Fig. 9f). The slope of the rolling moment coefficient with alpha for the five degrees sideslip angle is much smaller than that of the ten degrees one. These differences are due to differences in the strength of the leeward and windward vortices. For all sideslip angles tested, Fig. 9f shows that the rolling moment coefficient becomes almost zero for angles of attack of $\alpha \geq 19°$ which indicate that both windward and leeward vortices are burst over a large portion of the wing surfaces.

Figure 10 shows the effects of angle of attack on the variations of the lateral-directional force and moments with sideslip angles. At low angles of attack, $-5^o \leq \alpha \leq 5^o$, all three coefficients vary almost linearly with sideslip angles. For larger angles of attack, $\alpha > 5^o$, the variations become non-linear, and the non-linearity increases as alpha is increased. As explained before, these non-linear variations are due to the asymmetrical vortices forming over the windward and leeward wing surfaces which create asymmetric lift on the wing surfaces, resulting in the rolling and yawing moment variations.

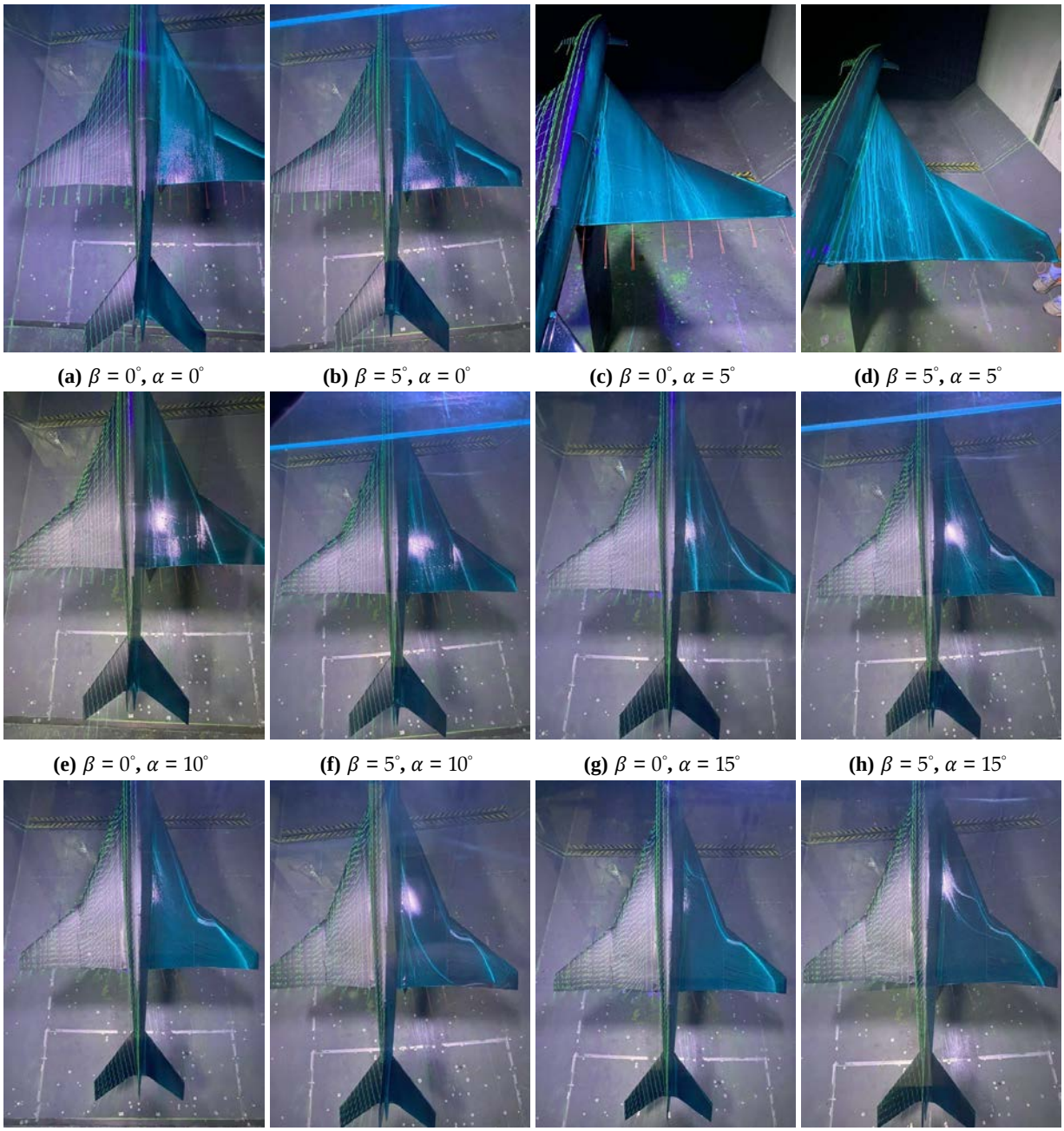

(a) $\beta = 0^{\circ}$, $\alpha = 0^{\circ}$ **(b)** $\beta = 5^{\circ}$, $\alpha = 0^{\circ}$ **(c)** $\beta = 0^{\circ}$, $\alpha = 5^{\circ}$ **(d)** $\beta = 5^{\circ}$, $\alpha = 5^{\circ}$

(e) $\beta = 0^{\circ}$, $\alpha = 10^{\circ}$ **(f)** $\beta = 5^{\circ}$, $\alpha = 10^{\circ}$ **(g)** $\beta = 0^{\circ}$, $\alpha = 15^{\circ}$ **(h)** $\beta = 5^{\circ}$, $\alpha = 15^{\circ}$

(i) $\beta = 0^{\circ}$, $\alpha = 20^{\circ}$ **(j)** $\beta = 5^{\circ}$, $\alpha = 20^{\circ}$ **(k)** $\beta = 0^{\circ}$, $\alpha = 25^{\circ}$ **(l)** $\beta = 5^{\circ}$, $\alpha = 25^{\circ}$

Fig. 8 UW-S-21A without nacelle Flow Visualization at $\beta = 0^{\circ}$ and $\beta = 5^{\circ}$

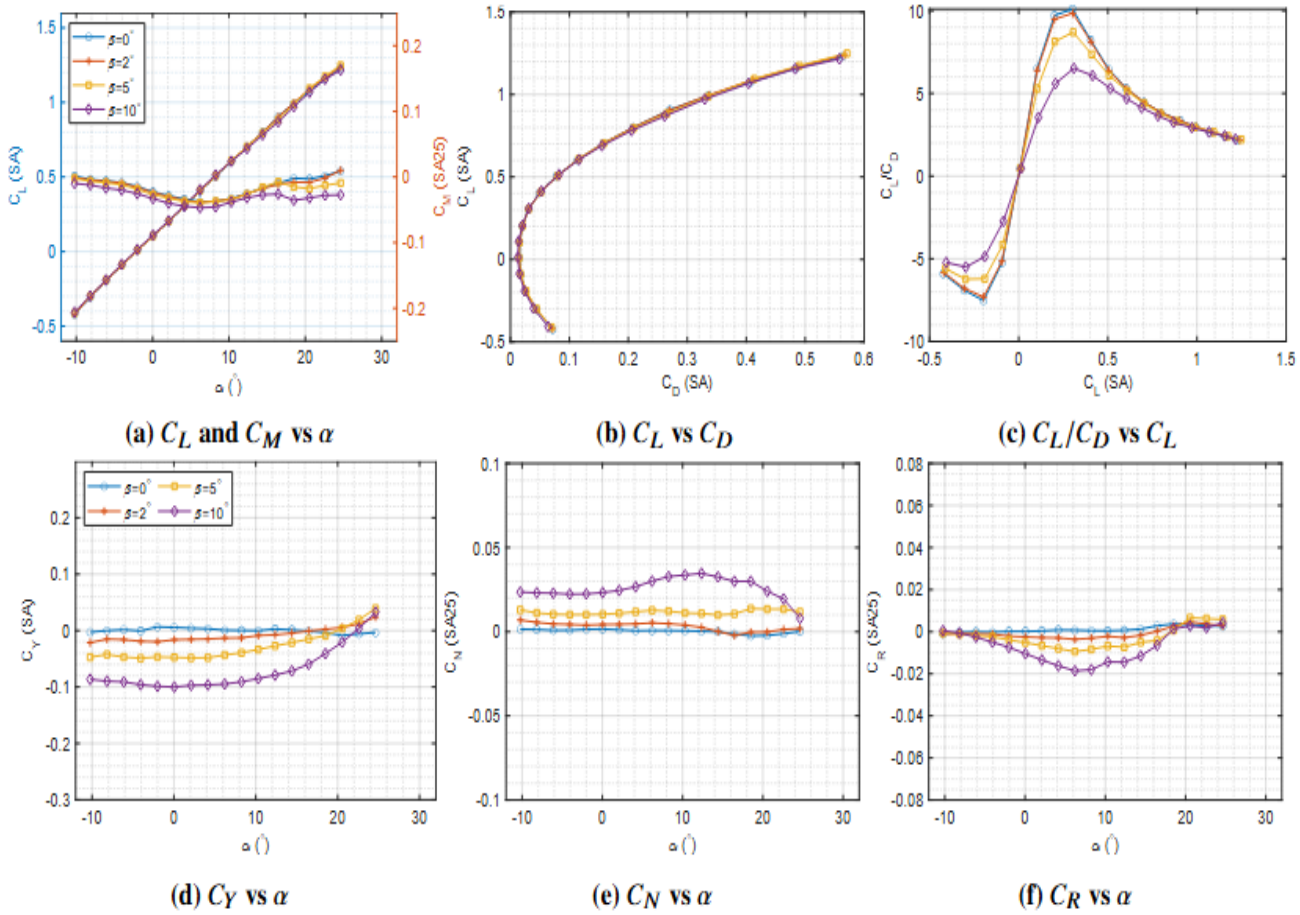

Fig. 9 UW-S-21A forces and moments vs. α

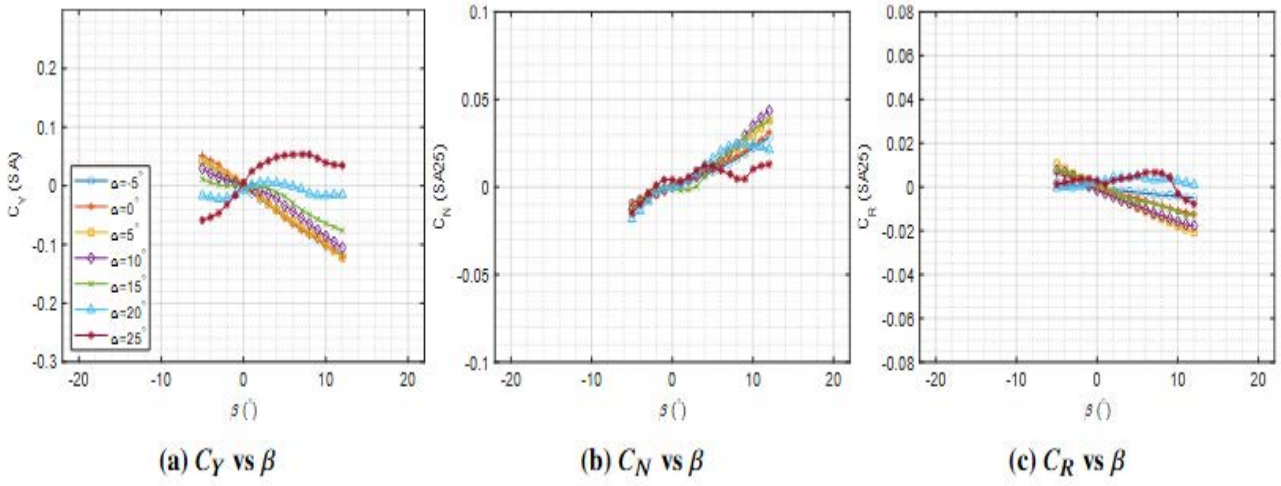

Fig. 10 UW-S-21A forces and moments vs. β

Canard Contributions

The UW-S-20A model, shown in Fig. 11 and Table 3, is a three-surface configuration with canards, top-mounted nacelles, and a T-tail empennage system. The canard rotations range from $\delta_C = -30°$ to $+30°$. Figure 12 shows the lift and pitching moment coefficients of this model for different canard rotations at angles of attack at sideslip angles of $\beta = 0°$, 5°, and 10°. For all sideslip angles tested, the model shows a pitch-up tendency at about $\alpha \cong 8^o - 10^o$ as seen from Figs. 12 d-f. This pitch-up tendency is caused by the flow separation over the outboard section of the wing surfaces which also reduces C_{L_α}. At $\beta = 0°$, the canard rotations do not change the lift values prior to $\alpha \approx 15°$, which is the angle of attack when both inboard and outboard vortices start to merge over the wing surface (Fig. 8). Beyond $\alpha \approx 15°$, the vortex burst decreases the local lift at the trailing-edge section of the wing, resulting in further pitch-up tendency of the model. The inboard vortex at the inboard section of the wing increases in strength near $\alpha > 15°$ resulting in an increase in the lift for $\delta_C = -15°$ to 30° up to $\alpha \approx 22°$. For $\delta_C = -30°$, the maximum lift, $C_{L_{max}}$, occurs at $\alpha \approx 18°$ as seen from Fig. 12a. For $\delta_C = -15°$ and $-30°$, the reductions of $C_{L_{max}}$ and α_{C_L} are due to the massive flow separation over the lower surface of the canard and the corresponding wake it generates, affecting the flow field over the wing surface and reducing the inboard vortex strength.

Overall Fig. 12a shows that canard rotation reduces both $C_{L_{max}}$ and stall angle of attack. The pitching moment variations with angles of attack with canard rotations show that C_{M_0} is proportional to canard rotations but C_{M_α} remain almost constant except for $\delta_C = \pm 30°$. The values of $C_{M_0} > 0$ for all canard rotation angles indicate static longitudinal stability with respect to the chosen moment reference point. For $\beta = 10^o, C_{M_0} < 0$ for $\delta_C = -5^o$, $-15°$, and -30^o (Fig.12f), which indicates that for these canard rotation angles the model cannot be trimmed at positive angles of attack if yawed at 10 degrees. Positive canard rotations increases C_{M_0} while negative rotations have the reverse effects (Fig. 12 d-f).

The pitch up angle (the transition to longitudinal instability) does not vary with canard angles of attack for $\alpha \cong 8^o - 10^o$, but $|C_{M_\alpha}|$ beyond the pitch up angle is reduced significantly, especially for $\beta = 10^o$ (Fig. 12f). Figure 12d shows that this T-tail configuration gets into deep stall around $\alpha \approx 22^o$ for the zero-sideslip angle case, caused probably by the wake of the wing affecting the tail.

For the low tail configuration, Fig. 5d shows that the deep stall for the no canard models occurs at lower angles of attack. The lift force coefficients do not vary significantly with sideslip angles of 5 and 10 degrees. A kink in the C_L variation is observed for $\beta = 5°$ and 10°. The kink happens at $\alpha \approx 18°$ for $\beta = 5°$ while for $\beta = 10°$, it occurs at $\alpha \cong 15^o$. Of course, its location varies slightly with canard rotation angle too. Beyond the kinks the lift increases for both sideslip angles with respect to increasing the angle of attack. The present kinks in the lift variation

for $\beta \neq 0^{\circ}$ are due to the asymmetric vortex formation, vortex merging, and vortex burst reaching the windward and leeward portions of the wing surfaces and moving toward the wing apex as the angles of attack are increased. For both sideslip angles shown here, no sign of stalls is seen from Figs. 12 b and c while for the zero-sideslip case, a clear stall for all canard rotations is noticed (Fig. 12a). Figures 12e-f show that the pitch up break angle of attack has been affected by the sideslip angle too. For the zero-sideslip angle, the pitch up break angle for all canard rotations occurs at about $\alpha \approx 8^{o} - 9^{o}$ angles of attack, while for $\beta = 10^{\circ}$, this happens at $\alpha > 10^{o}$. In comparison with the previous case, Fig. 5d, for models with no canard, it seems that canard improves the nose-up pitching behavior of the model.

Effects of canard rotations on the variations of the lateral-directional force and moment coefficients of the UW-S-20A model with angles of attack for three different sideslip angles of $\beta = 0, 5, and\ 10$ degrees are shown in Figs. 13 and 14. For all cases examined, this figure shows that canard does not have significant effects on the directional control behavior of this SCALOS model.

For the 10^{o}sideslip angle it is seen that the value of C_R (rolling moment coefficient) at zero degrees angles of attack is affected by the canard rotation angel while its slope C_{R_β} has not been influenced notably (Fig. 13i). For all canard settings, Figs. 13h and i show that this model loses directional roll as well as side weathercock control stability when set to $\beta = 5, 10$ degrees for angles of attack of $10^{o} < \alpha \leq 20^{o}$. This is most likely caused by the asymmetrical vortex burst moving onto the wing surface toward the wing apex. For higher angles of attack, it seems that the model regains its roll control authority, but C_Y remains positive. Figure 14 shows that for $-10^{o} \leq \beta \leq 10^{o}$ and for $\alpha = 0^{o}, 10^{o}$ this model has directional control force derivatives, $C_{Y_\beta} < 0$, $C_{N_\beta} > 0$, $C_{R_\beta} < 0$, and canard rotation does not have a significant influence on their variations.

(a) $\delta_C = 30^{\circ}$ **(b)** $\delta_C = 15^{\circ}$ **(c)** $\delta_C = 5^{\circ}$

Figure 11 a-c: UW-S-20A with canard rotations

(d) $\delta C = -5^{\circ}$ **(e)** $\delta C = -15^{\circ}$ **(f)** $\delta C = -30^{\circ}$

Fig. 11 d-f:: UW-S-20A with canard rotations

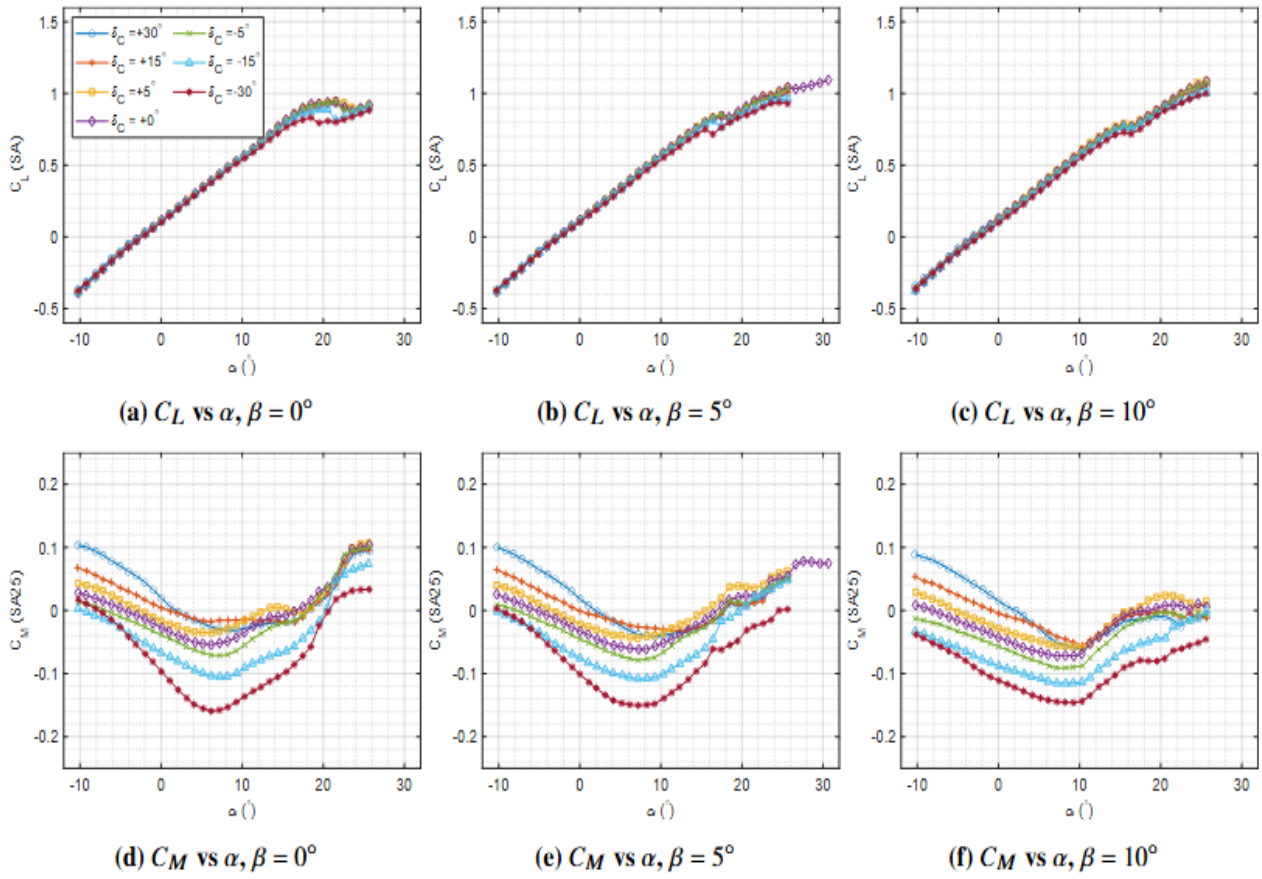

(a) C_L vs $\alpha, \beta = 0^{\circ}$ (b) C_L vs $\alpha, \beta = 5^{\circ}$ (c) C_L vs $\alpha, \beta = 10^{\circ}$

(d) C_M vs $\alpha, \beta = 0^{\circ}$ (e) C_M vs $\alpha, \beta = 5^{\circ}$ (f) C_M vs $\alpha, \beta = 10^{\circ}$

Fig. 12 UW-S-20A with canard rotations longitudinal forces and moments vs. α

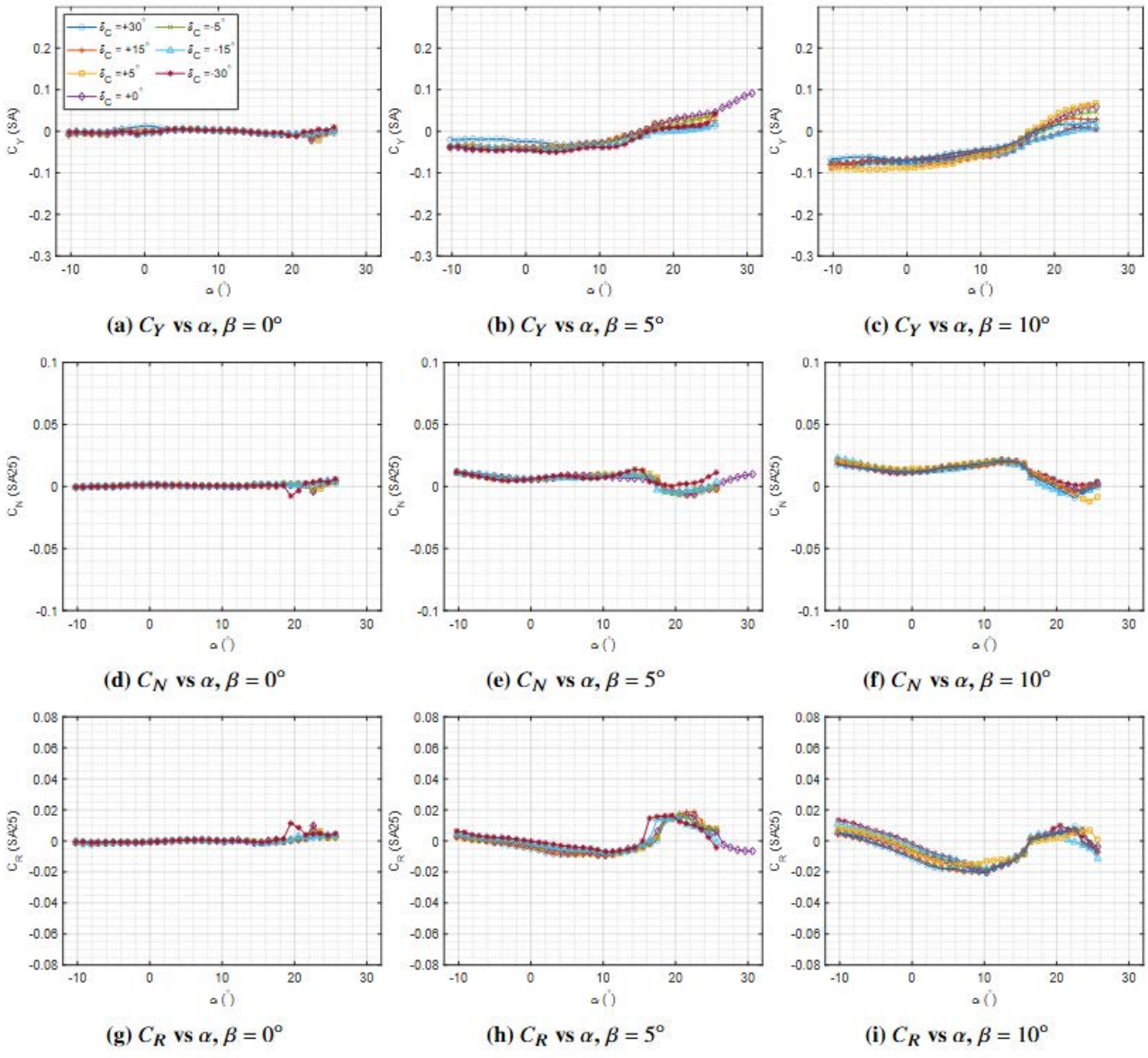

(a) C_Y vs α, $\beta = 0°$ (b) C_Y vs α, $\beta = 5°$ (c) C_Y vs α, $\beta = 10°$

(d) C_N vs α, $\beta = 0°$ (e) C_N vs α, $\beta = 5°$ (f) C_N vs α, $\beta = 10°$

(g) C_R vs α, $\beta = 0°$ (h) C_R vs α, $\beta = 5°$ (i) C_R vs α, $\beta = 10°$

Fig. 13 UW-S-20A with canard rotations lateral directional forces and moments vs. α

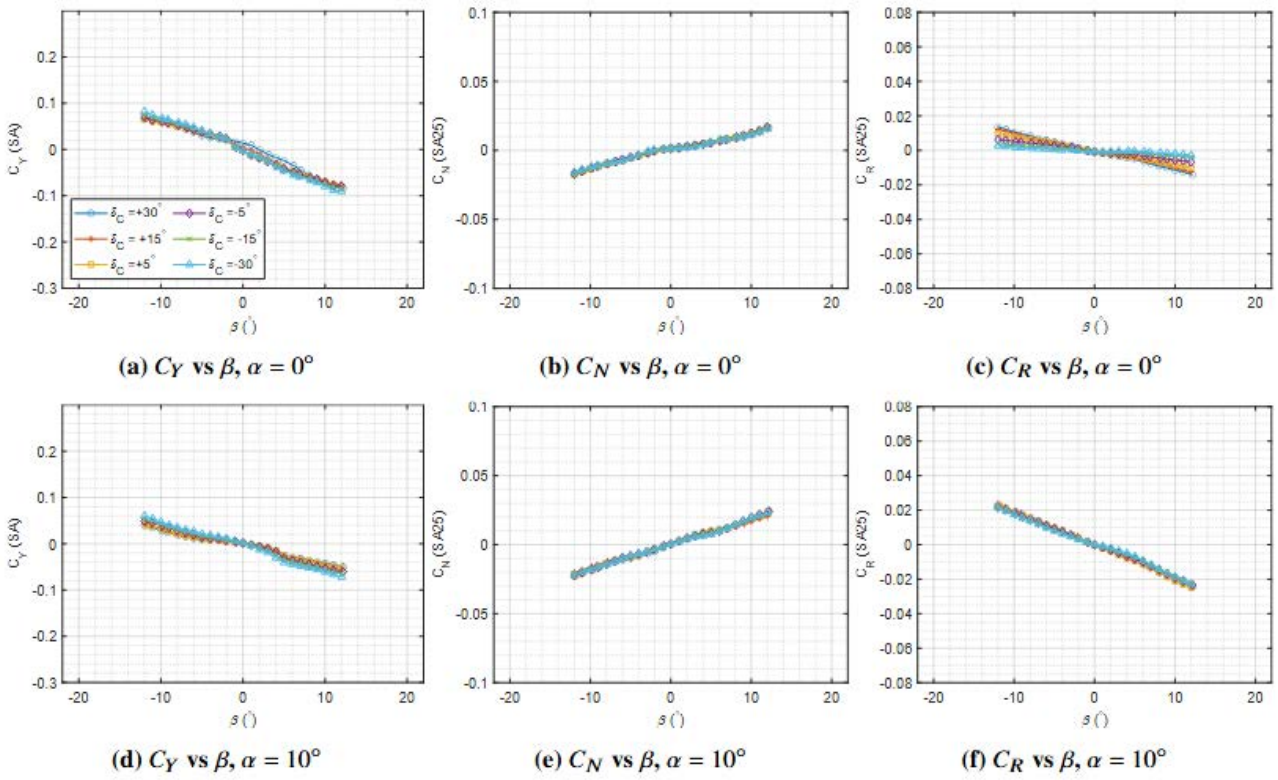

Fig. 14 UW-S-20A with canard rotations forces and moments vs. β

Directional Control Authority

1. UW-S-20A

Figure 15 shows the UW-S-20A model where its vertical fin is equipped with a rudder that is rotated by δ_{Rud} = 0°, +10°, +20°. The model has a T-tail configuration and is equipped with both canard and top-mounted nacelles. The effects of angles of attack on the lateral and directional characteristics of this SCALOS configuration at several sideslip angles, $\beta = 0, 2, 5\ and\ 10$ degrees, for the three different rudder rotations mentioned above are shown in Fig. 16. Positive rolling and yawing moments indicate a right wing down rotation and a right nose rotation of the aircraft respectively. For an aircraft to be both laterally and directionally stable, $C_{N_\beta} > 0$, and $C_{R_\beta} < 0$. If the sign of these stability derivatives changes, static instability will appear.

Figure 16 shows that at, -10° $\leq \alpha \leq$ 10° , the model has both lateral and directional stability for all side slip angles tested. As mentioned before, for these angles of attack, both windward and leeward vortices are stable. Their strength varies due to the larger and smaller wing surface that they cover i.e. the leeward vortices cover a smaller effective wing surface while those of the windward ones cover a larger wing surface. As a result, the lift of the windward side of the wing is larger than that of the leeward one, creating a rolling moment to the right and a nose-right rotation of the aircraft. It should be noted that the windward vortex over a portion of the wing might be burst, but the remaining unburst portion of the vortex may be still strong enough to create enough lift which is larger than that of the right wing, leeward wing.

The rudder rotations seem to not have significant effects on the slope of the lateral and directional characteristics of the model for these angles of attack., As δ_{Rud} is varied the curves shift. Note that C_Y, C_N , and C_R are zero at β = 0° and δ_{Rud} = 0°, but when the $\delta_{Rud} \neq 0°$, the values of these coefficients at β = 0° change. At β = 5° and β = 10°, Fig.16 shows that rudder rotations did not significantly change the rolling moment variation of the model with angles of attack.

At α = 20°, Fig. 16 shows that both lateral and directional stability derivatives change sign due to the asymmetric vortex breakdown over the windward and leeward wing sections. The burst leading-edge vortex moves upstream at the windward, reducing the lift of the windward side, which is responsible for the roll reversal. Figure 17 shows that for all three rudder rotations lateral directional force and moments vary linearly with sideslip angle variations of $-10^o \leq \beta \leq 10^o$ for angles of attack of $\alpha = 0, 5, 10, and$ 15 degrees with stable values, $C_{Y_\beta} < 0$, $C_{N_\beta} > 0$, $C_{R_\beta} < 0$. When alpha is increased to 20^o, both C_N , and C_R show yaw and roll reversals around $\boldsymbol{-2^o \leq \beta \leq 3^o}$, (Figs. 17n, 17o) as seen before. For larger sideslip angles, the model regains its lateral-directional stability.

(a) δ_{rud} = 0° **(b)** δ_{rud} = +10° **(c)** δ_{rud} = +20°

Fig. 15 UW-S-20A with rudder rotations

2. UW-S-21A

Figure 18 shows three photos of the UW-S-21A SCALOS model (Table 3), which is equipped with bottom nacelles, low-tail empennage system. The rudder is rotated at δ_{Rud} = 0°, +10°, +20°. There are some differences between the UW-S-21A and UW-S-20A models (see Fig. 1 and table 1 for more information). Similar to the UW-S-20A model, the UW-S-21A SCALOS model was tested at various sideslip angles, $\beta = 0, 2, 5\ and$ 10 degrees and a range of angles of attack. Figures 19 and 20 show effects of rudder rotations on the variations of the lateral-directional force and moments with angles of attack for different sideslip angles and with angles of attack of $\alpha = 0, 5, 10, 15, and$ 20 degrees. The variations of aerodynamic characteristics are very similar to those of the UW-S-20A model shown in Figs. 16 and 17. It seems that rudder rotations have larger effects on directional stability derivatives. It is noted that the loss of directional control authority seen at 20 degrees angle of attack for a certain range of sideslip angles for the UW-S-20A model (Figs. 17n, 17o) does not exist for this model at similar test conditions (Figs. 20n, 20o).

At 20 degrees angle of attack, $C_{R_\beta} \cong 0$ for all three rudder rotation angles (Fig. 20o) while $C_{N_\beta} > 0$. There exists a plateau in the $C_N vs\ \beta$ curves near $\beta = 0$ (Figs. 20 k, 20n) where C_N remains constant as β is increased for $\alpha = 15, and$ 20 degrees.

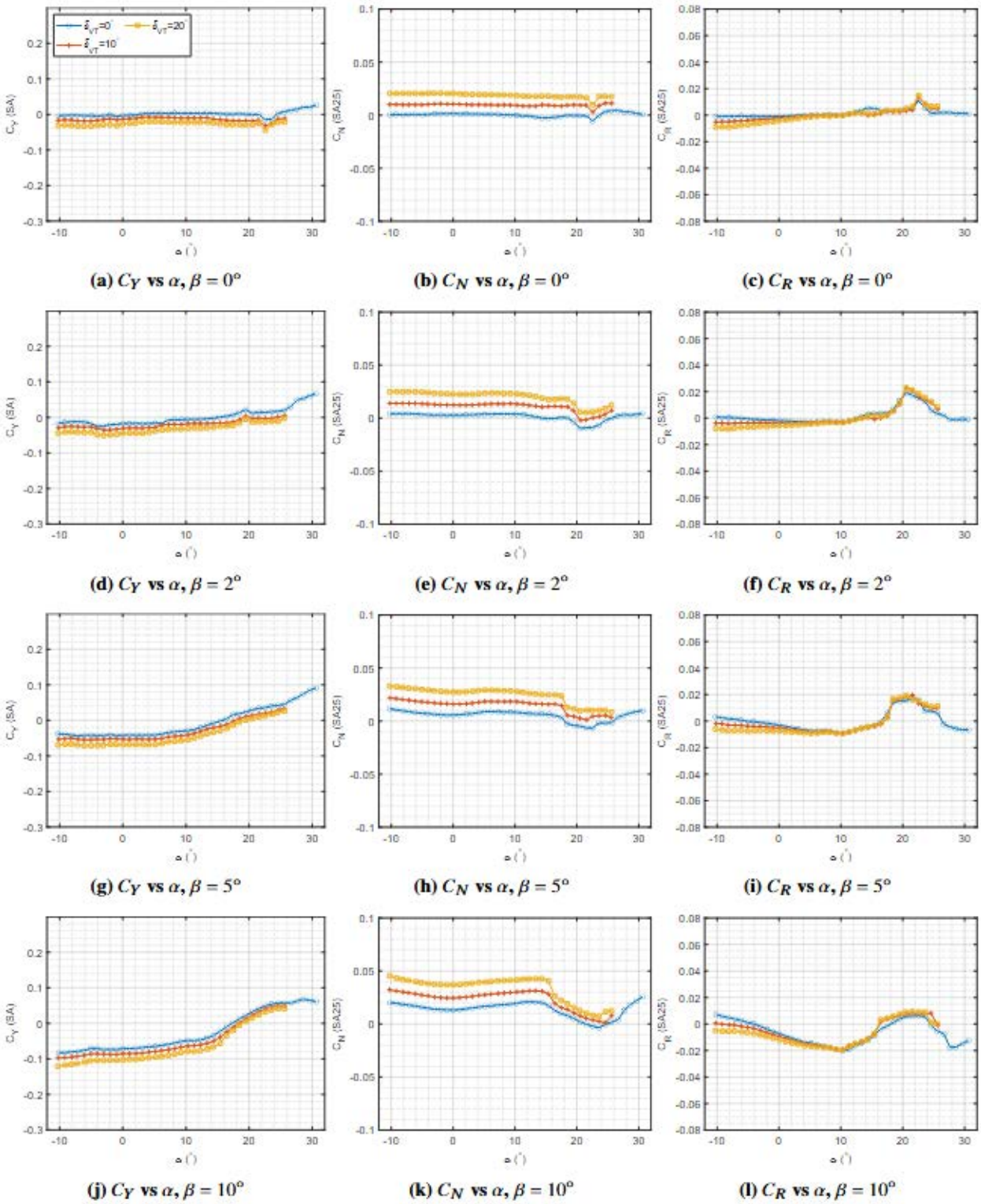

(a) C_Y vs $\alpha, \beta = 0°$ (b) C_N vs $\alpha, \beta = 0°$ (c) C_R vs $\alpha, \beta = 0°$

(d) C_Y vs $\alpha, \beta = 2°$ (e) C_N vs $\alpha, \beta = 2°$ (f) C_R vs $\alpha, \beta = 2°$

(g) C_Y vs $\alpha, \beta = 5°$ (h) C_N vs $\alpha, \beta = 5°$ (i) C_R vs $\alpha, \beta = 5°$

(j) C_Y vs $\alpha, \beta = 10°$ (k) C_N vs $\alpha, \beta = 10°$ (l) C_R vs $\alpha, \beta = 10°$

Fig. 16 UW-S-20A with rudder rotations: forces and moments vs. α

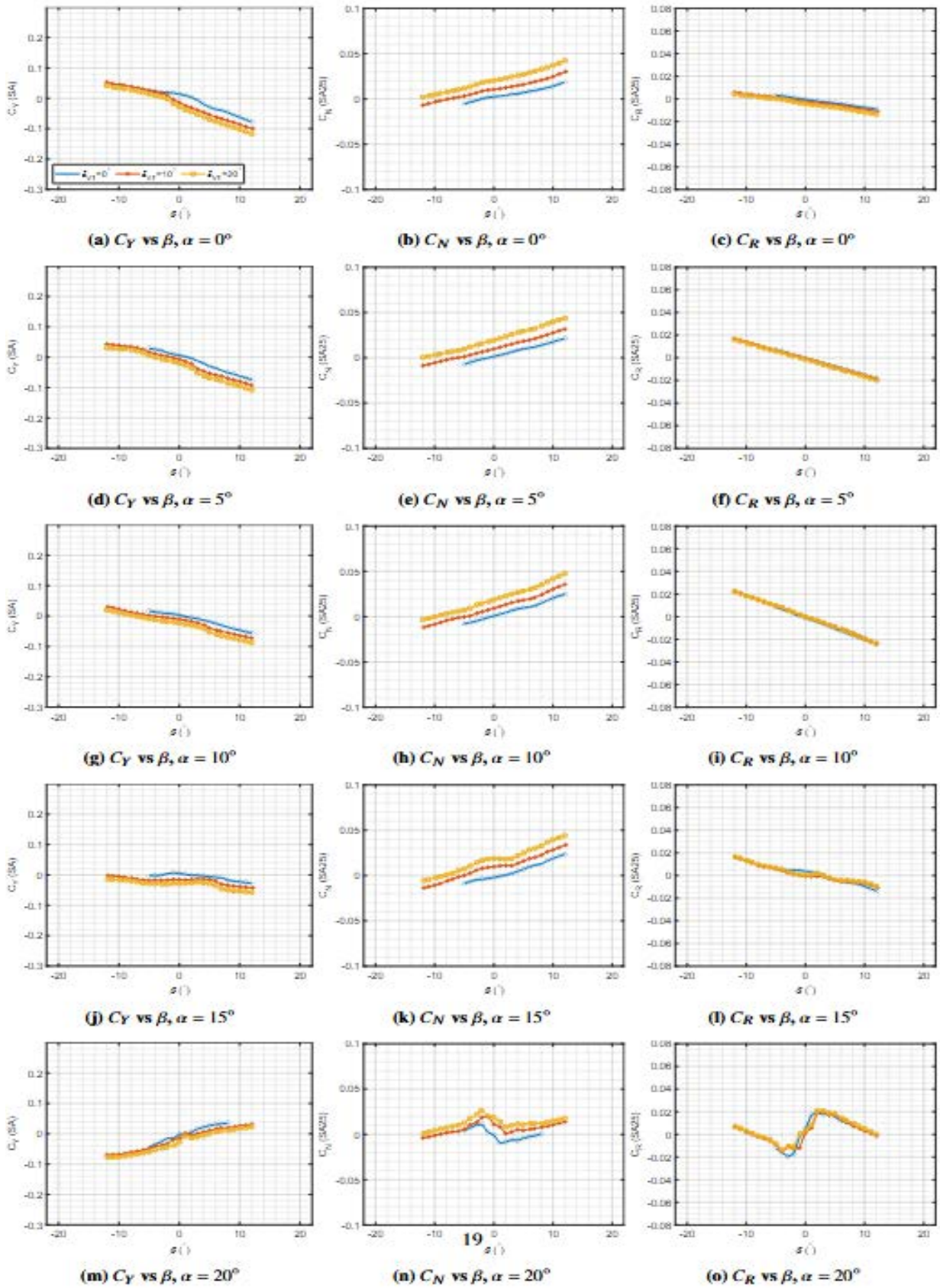

(a) C_Y vs β, $\alpha = 0°$ (b) C_N vs β, $\alpha = 0°$ (c) C_R vs β, $\alpha = 0°$

(d) C_Y vs β, $\alpha = 5°$ (e) C_N vs β, $\alpha = 5°$ (f) C_R vs β, $\alpha = 5°$

(g) C_Y vs β, $\alpha = 10°$ (h) C_N vs β, $\alpha = 10°$ (i) C_R vs β, $\alpha = 10°$

(j) C_Y vs β, $\alpha = 15°$ (k) C_N vs β, $\alpha = 15°$ (l) C_R vs β, $\alpha = 15°$

(m) C_Y vs β, $\alpha = 20°$ (n) C_N vs β, $\alpha = 20°$ (o) C_R vs β, $\alpha = 20°$

Fig. 17 UW-S-20A with rudder rotations: forces and moments vs. β

In contrast to the dihedral stability derivative, both side force and yaw moment coefficients vary nonlinearly with sideslip angles for angles of attack of $\alpha \geq 10^o$ as shown in Fig. 20. For the 20 degrees angle of attack case, Fig. 20n shows that for sideslip angles $\beta \geq 8^o$, $C_{N_\beta} \approx 0$, loss of rudder effectiveness, i.e. as the sideslip angle is increased, these rudder rotations, δ_{Rud} =+10°, +20°, are not capable of producing further yaw moment. Apparently for this large angle of attack the entire empennage system is immersed in the separated flow of the canard, wing and fuselage.

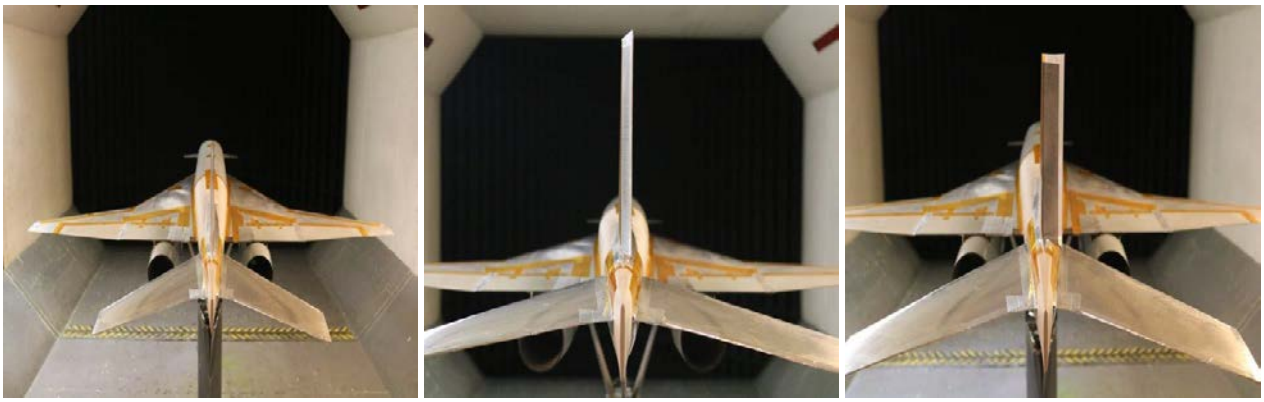

(a) δ_{Rud} = 0° **(b)** δ_{Rud} = 10° **(c)** δ_{Rud} = 25°

Fig. 18 UW-S-21A with rudder rotations

Nacelle locations and Engine-out conditions

1. Nacelle locations

In this part of the paper the effects of nacelle locations on the aerodynamic forces and moments of the UW-S-20 models are investigated. Four photos of the UW-S-20A SCALOS models with /without nacelles are shown in Fig. 21. The nacelles are located on the bottom and top of the wing and on the sides of the fuselage as shown in Figs. 21b, c, e, respectively. Details of the models are given in table 1 and ref [51]. All experimental force and moments are obtained at a dynamic pressure of $q = 32\ psf$, corresponding to the Reynolds no. of $Re = 2.1x10^6$.

Figure 22 shows variations of the lift and moment of the model with different nacelle locations with angles of attack for sideslip angles of $\beta = 0, 5, and\ 10$ degrees. The figure shows that nacelle locations do not have significant effects on the lift variations of the model, except for the top mounted nacelle model, N20.T, which stalls at about 20^o angles of attack for the zero-sideslip angle case (Fig. 22a). For other nacelle location cases the lift coefficient slope is seen to be reduced slightly around 20^o angles of attack, but it does not seem that the models are stalled.

For other sideslip angles, variations of the lift coefficient with angles of attack are similar and only C_{L_α}'s are affected by the sideslip angles. As β increases, C_{L_α} for all four cases are seen to be reduced. Nacelle locations have effects on the C_{M_0}, where the model with N20.B has largest C_{M_0} and N20.TR has the smallest C_{M_0}. Nacelle locations do not have significant effects on the slope of the pitching moment curve, C_{M_α}, prior to the pitch up longitudinal instability initiation angle of attack. The pitch-up occurrence angle of attack for all cases is seen to be at about $\alpha \cong 8^o$ and it increases slightly with sideslip angle (Fig. 22a-c). Sideslip angle reduces C_{M_0} for all models,

leaving only the N20.B model trimmable at positive angles of attack, $C_{M_0} > 0$, when yawed at 10 degrees. Therefore, for the other models to be trimmable at positive angles of attack when yawed, other means of control, canard deflection, for example, should be employed.

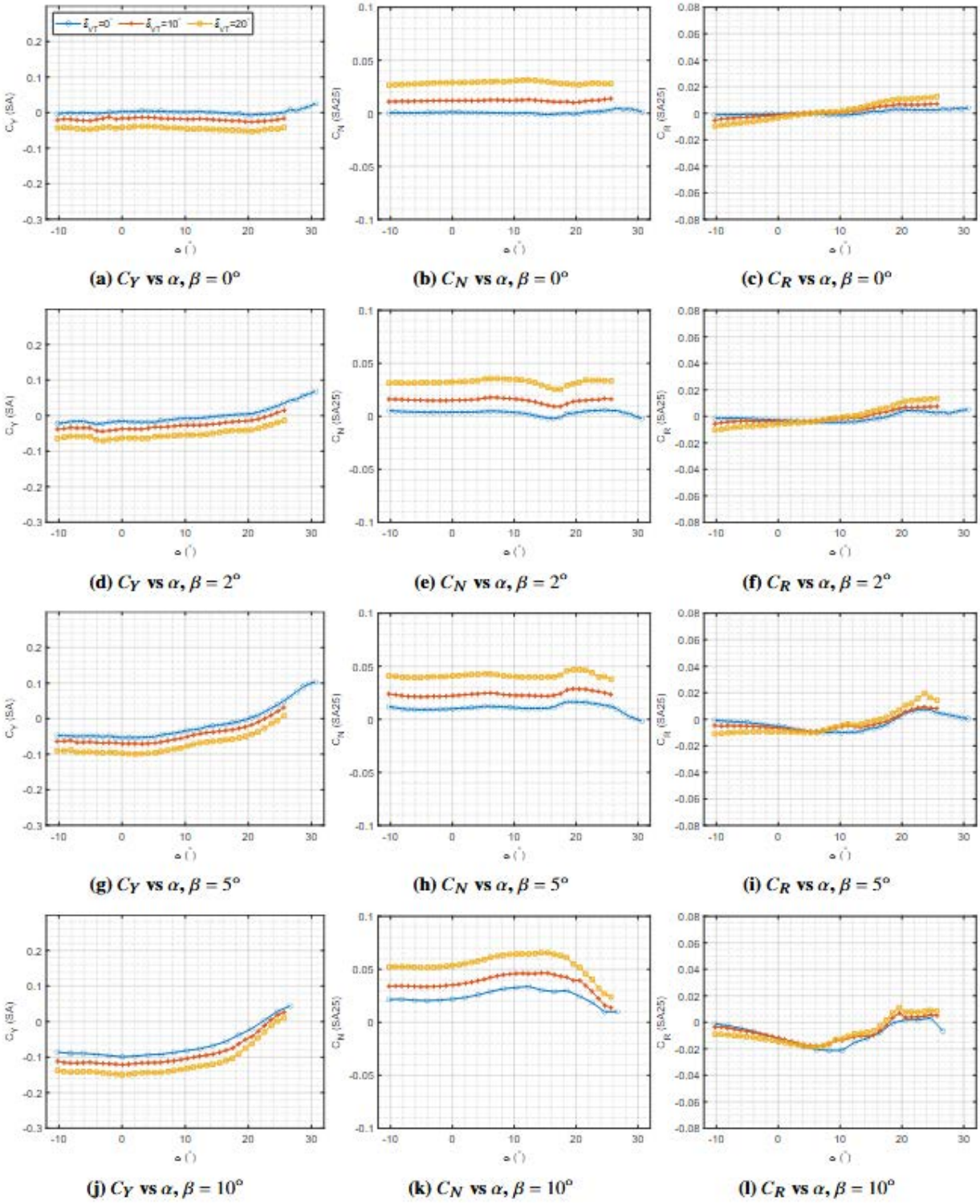

(a) C_Y vs $\alpha, \beta = 0°$ (b) C_N vs $\alpha, \beta = 0°$ (c) C_R vs $\alpha, \beta = 0°$

(d) C_Y vs $\alpha, \beta = 2°$ (e) C_N vs $\alpha, \beta = 2°$ (f) C_R vs $\alpha, \beta = 2°$

(g) C_Y vs $\alpha, \beta = 5°$ (h) C_N vs $\alpha, \beta = 5°$ (i) C_R vs $\alpha, \beta = 5°$

(j) C_Y vs $\alpha, \beta = 10°$ (k) C_N vs $\alpha, \beta = 10°$ (l) C_R vs $\alpha, \beta = 10°$

Fig. 19 UW-S-21A with rudder rotations forces and moments vs. α

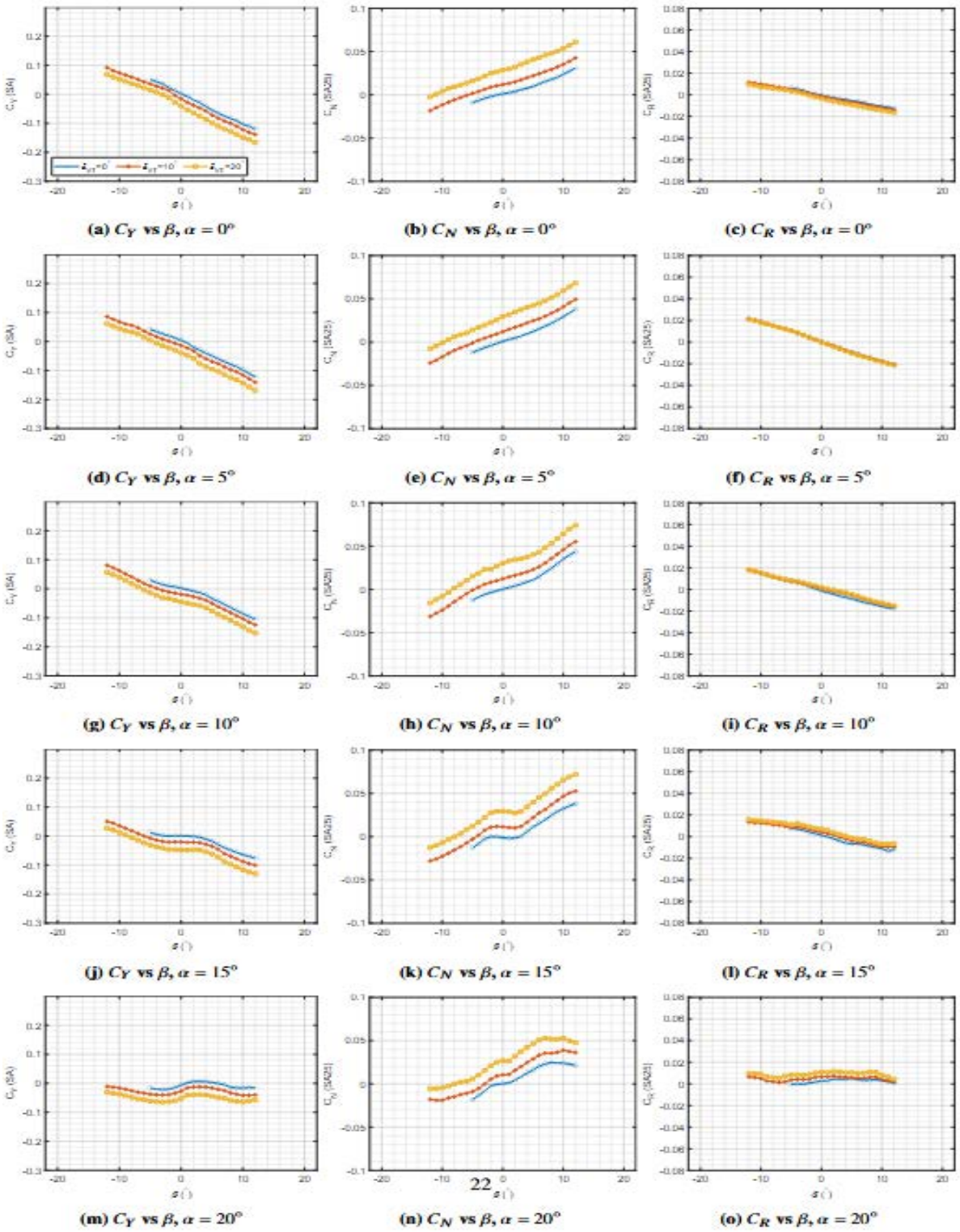

Fig. 20 UW-S-21A with rudder rotations forces and moments vs. β

Figure 23 shows variations of the lateral-directional force and moment coefficients with angles of attack for side slip angles of $\beta = 0, 5, and\ 10$ degrees for all different nacelle locations. For the zero-degree sideslip angle case all coefficients for all cases are zero for all angles of attack. The slight nonzero values of the coefficients at high angles of attack are caused by massive separated and unsteady flow. As the sideslip angle is increased to 5 degrees (Fig. 23d-f) the side force coefficient, which has an initial constant negative value up to about 8 degrees angle of attack, varies nonlinearly for higher alphas with a positive slope. The yawing moment coefficient C_N stays constant up to about 20 degrees angle of attack for all models, except for the N20.T model where C_N becomes negative for $18^o \leq \alpha \leq 24^o$, reflecting a loss of weathercock stability. For $\alpha \geq 23^o$ the N20.T model regains its weathercock stability. All models show roll stability for $\beta = 5, and\ 10$ degrees up to about 10 degrees angles of attack, $C_R < 0$, Fig. 23 f, i. For higher angles of attack, $\alpha > 10^o$, $C_R$becomes positive.

All lateral directional stability derivatives show relatively linear variation with sideslip angles, in the range of $\beta = \pm 10^o$ for $\alpha = 0, and\ 10$, for top and bottom nacelle locations (Fig. 24). The data are shown with the no nacelle model for comparison. It is seen that nacelle addition, whether top or bottom wing mounted, increases lateral directional stability derivatives, making the model more stable. All models are seen to have stable lateral directional behavior for the mentioned sideslips and angles of attack ranges, $C_{Y_\beta} < 0,\ C_{N_\beta} > 0,\ C_{R_\beta} < 0$.

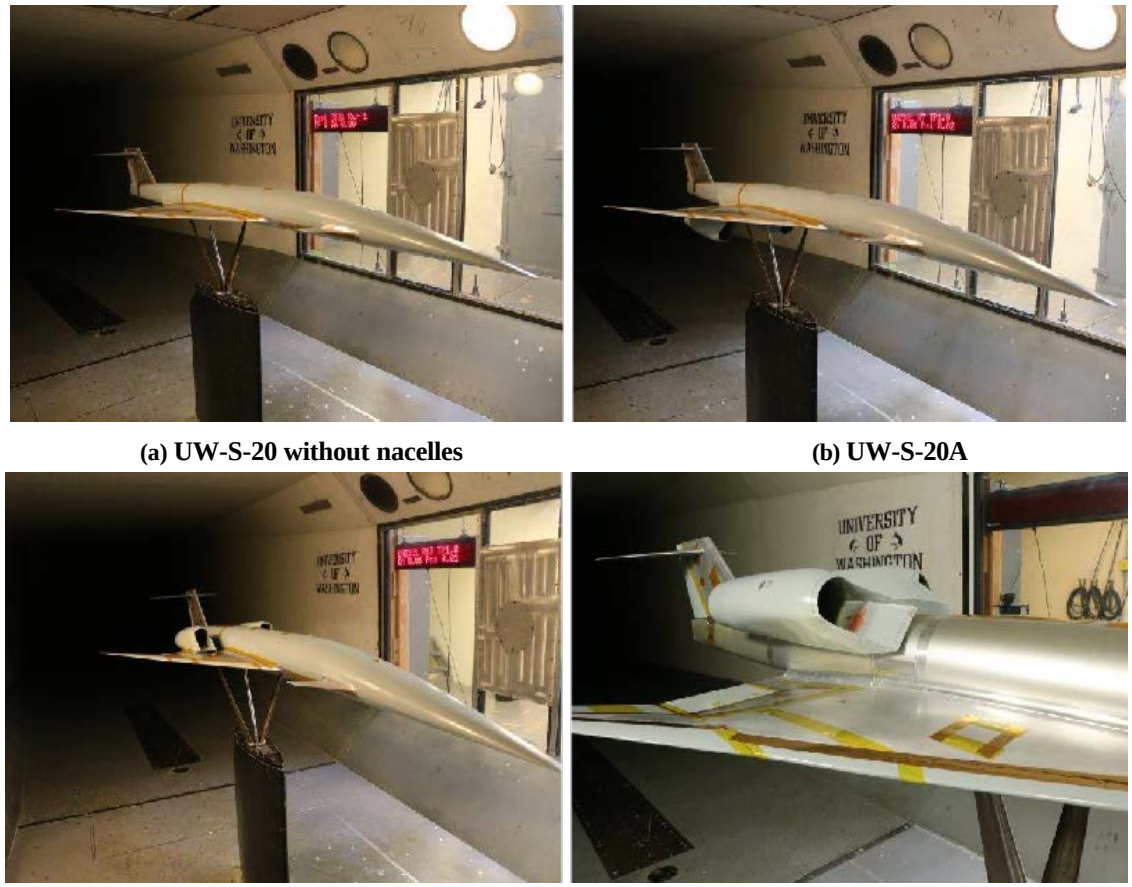

(a) UW-S-20 without nacelles **(b) UW-S-20A**

(c) UW-S-20B **(d) UW-S-20J**

Fig. 21 UW-S-20 configurations [51]

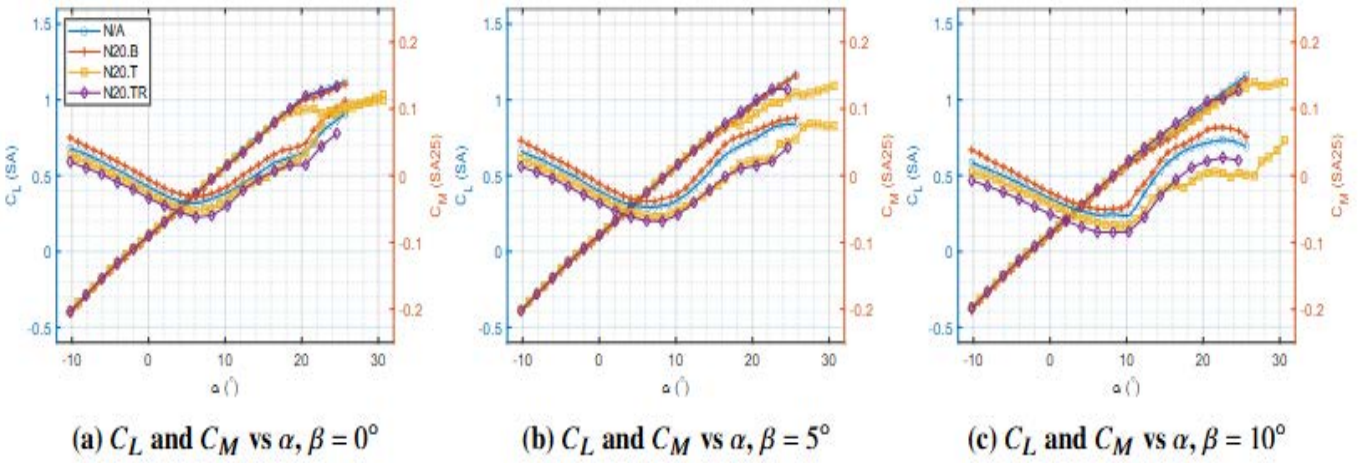

Fig. 22 UW-S-20 with nacelle location variation: longitudinal forces and moments vs. α

2. Engine out simulations

The engine out case study was investigated by partially or fully closing both or one nacelle exits. Figures 25a-e show photos of the UW-S-20A model with fully open nacelles, left nacelle open while right nacelle exit area is reduced by 50%, both right and left nacelle exit areas are reduced by 50%, left nacelle open while right nacelle exit area is fully closed, both left and right nacelle exit areas are fully closed, respectively. All experimental aerodynamic forces and moments were obtained for the same conditions mentioned before.

Figures 26a-e show variations of the lift and pitching moment coefficients with angles of attack for sideslip angles of $\beta = 0, \pm 5, and \pm 10$ degrees for all cases of the reduced nozzle exit areas mentioned above. The reduced exit nacelle areas do not seem to have significant effects on both lift and pitching moment variations with angles of attack for zero and positive sideslip angles (Figs. 26a-c). Fig. 26a shows that the model with fully open exit area nacelles stalls at slightly higher angles of attack, The pitch moment variations are the same for all cases. C_{M_0}, C_{M_α}, and pitch up angles of attack, longitudinal instability, for all cases examined are the same (Figs. 26a-c). As mentioned before, the deep stall for all cases seems to occur around 22 degrees angles of attack (Fig. 26a). For the negative sideslip angles Figs. 26 d, e show that C_{M_0} slightly varies with the reduced nacelle exit area. The pitch up for all cases occurs at the same angles of attack, about 8-10 degrees.

Figure 27 shows the effects of nacelle reduced exit areas on the lateral-directional force and moment coefficients. For all sideslip angles tested lateral-directional force and moment coefficients do not show significant changes due to the nacelle reduced exit areas and the variations with angles of attack are the same for all cases.

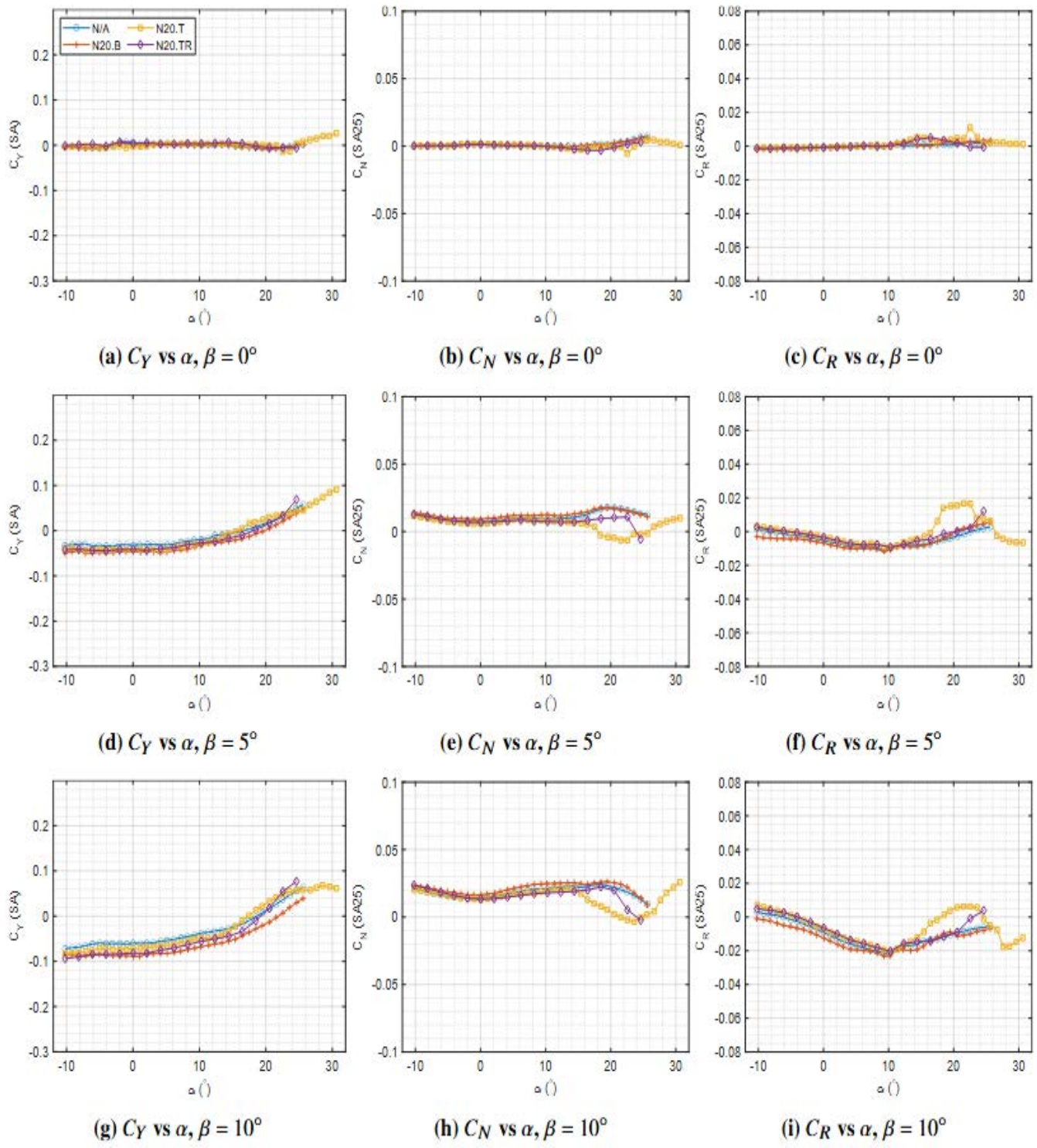

(a) C_Y vs α, $\beta = 0°$ (b) C_N vs α, $\beta = 0°$ (c) C_R vs α, $\beta = 0°$

(d) C_Y vs α, $\beta = 5°$ (e) C_N vs α, $\beta = 5°$ (f) C_R vs α, $\beta = 5°$

(g) C_Y vs α, $\beta = 10°$ (h) C_N vs α, $\beta = 10°$ (i) C_R vs α, $\beta = 10°$

Fig. 23 UW-S-20 with nacelle location variation: lateral directional forces and moments vs. α

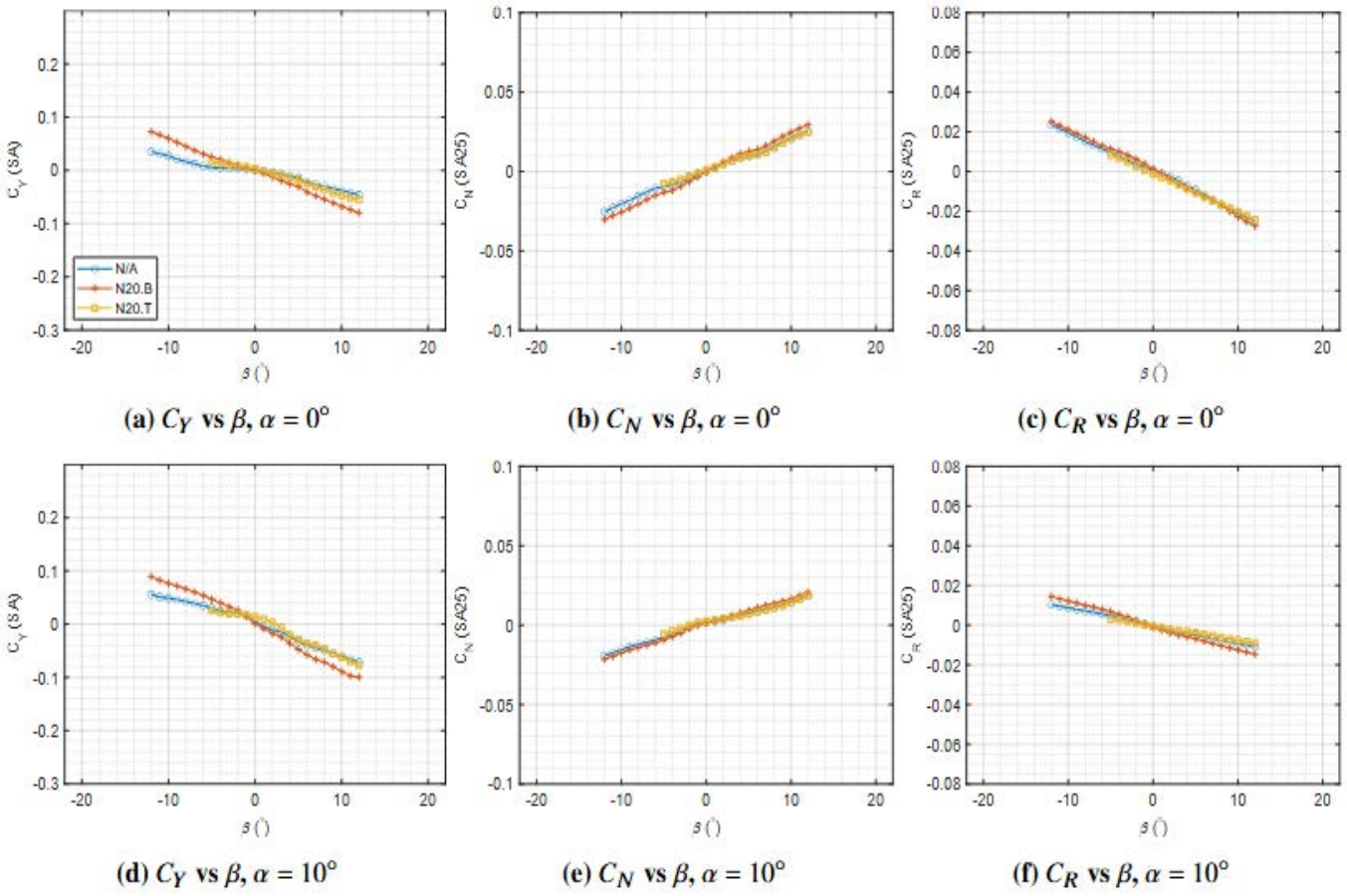

(a) C_Y vs β, $\alpha = 0°$ (b) C_N vs β, $\alpha = 0°$ (c) C_R vs β, $\alpha = 0°$

(d) C_Y vs β, $\alpha = 10°$ (e) C_N vs β, $\alpha = 10°$ (f) C_R vs β, $\alpha = 10°$

Fig. 24 UW-S-20A configuration: effect of nacelle locations on lateral-directional force and moment coefficients

Ailerons Rotations

The effects of the trailing-edge outboard aileron (TEOB) rotations on both longitudinal and lateral-directional forces and moment coefficients of the UW-S-20A and UW-S-21A are presented in this section of the paper. For both models tests were conducted with full and reduced chord ailerons. The ratio of chords of the reduced chord and full chord ailerons was 2/3. Figures 28a-c and 32a-c show photos of the UW-S-20A and UW-S-21A SCALOS models with full and reduced chord aileron, respectively. Tests were conducted for both positive and negative aileron rotations. Figures 29 and 33 show the effects of full and reduced chord aileron rotations on the lift and pitch moment variations of the UW-S-20A and UW-S-21A models with angles of attack for several sideslip angles respectively. For both zero and 2-degrees sideslip angles, aileron rotations do not have significant effects on the lift and pitch moment variations of the UW-S-20A model which has a T-tail empennage system and bottom nacelle location (Fig. 29a, b). For the $\beta = 5^o$case, Fig. 29c shows that the pitching moment coefficients for both reduced aileron rotations of $\delta_{ail} = \pm 10^o, \pm 20^o$, have been slightly shifted, C_{M_0} is slightly increased, while C_{M_α}remains the same for the zero and non-zero aileron rotations.

.

(a) Blockages L/R 0%/ 0% **(b) Blockages L/R 0%/ 50%** **(c) Blockages L/R 50%/ 50%**

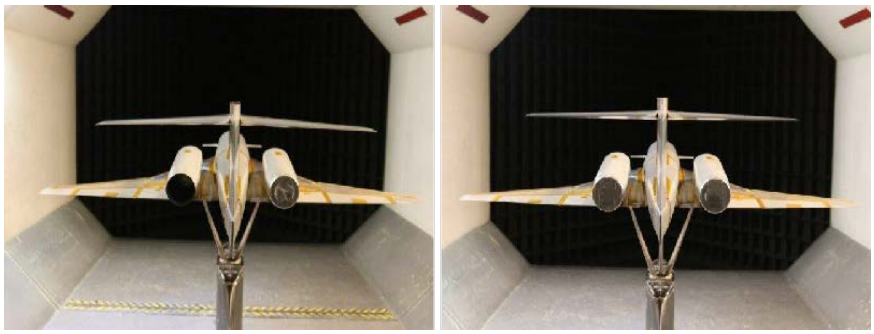

(d) Blockages L/R 0%/ 100% **(e) Blockages L/R 100%/ 100%**

Fig. 25 UW-S-20A with reduced nozzle exit areas

Similarly, the UW-S-21A model with a low horizontal tail and with top wing mounted nacelles, does not show any significant variations in its lift and pitching moment developments with full or reduced aileron rotations (Figs. 33a-c). Figs.33 a-c show that aileron rotation significantly reduces C_{M_α} both prior to the pitch-up initiation, $\alpha \approx 10^o$, and post pitch up initiation, $10^o \leq \alpha \leq 20^o$, and the nose-up behavior is smooth and gradual in comparison with the previous case (UW-S-20A model, Fig. 29a). Beyond 20 degrees angles of attack, $C_{M_\alpha} \approx 0$ – a neutrally stable longitudinal behavior (Fig. 33 a-c).

The trailing-edge aileron rotation has significant effects on the rolling moment variations of both models with angles of attack and sideslip angles. As the aileron is rotated, the value of C_R at zero degrees angle of attack for all sideslip angles tested increases, creating more rolling moment. The roll dihedral stability derivative, C_{R_β} , at zero degrees angle of attack is not affected by the aileron deflection (Fig. 31c). At $\alpha = 10^o$, Fig. 31f shows that $\left|C_{R_\beta}\right|$ increases with aileron rotation. Figure 31f shows that $\left|C_{R_\beta}\right|$ does not vary when δ_{ail} is increased from $\pm 10^o \; to \; \pm 20^o$. It appears that for this angle of attack, ailerons lose their effectiveness when rotated by more than $\pm 10^o$. Similar effects are observed for the UW-S-21A model with both full and reduced aileron chords. The shifts in the C_R values at zero degrees angles of attack for all sideslip angles are more for the full aileron chord. Variations of the C_R with angles of attack are the same for both full and reduced aileron chord (Figs. 34f, 34i).

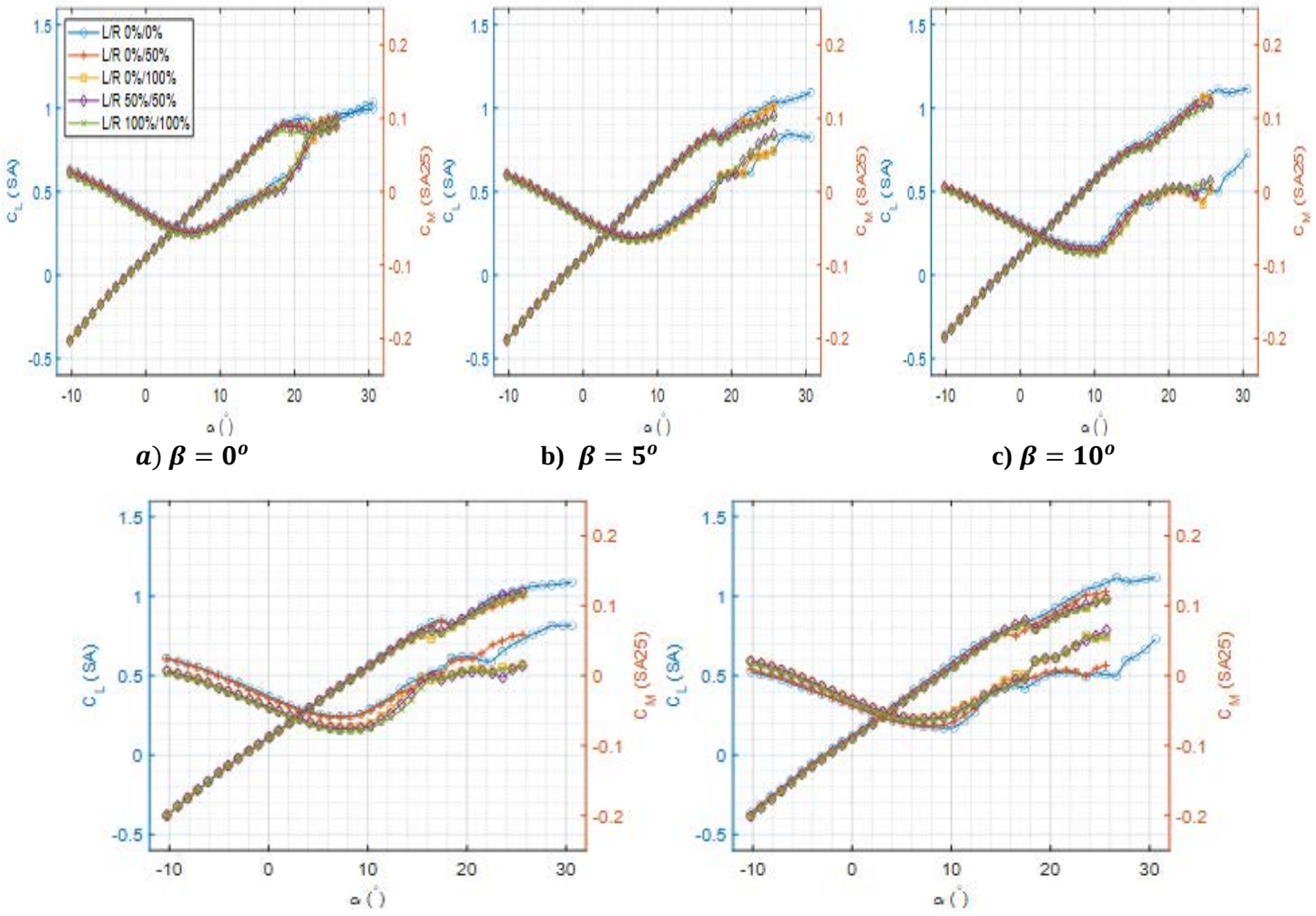

$\boldsymbol{a}$) $\boldsymbol{\beta = 0^o}$ b) $\boldsymbol{\beta = 5^o}$ c) $\boldsymbol{\beta = 10^o}$

$\boldsymbol{d}$) $\boldsymbol{\beta = -5^o}$ e) $\boldsymbol{\beta = -10^o}$

Fig. 26: Effect of reduced nacelle exit areas on the longitudinal forces and moments

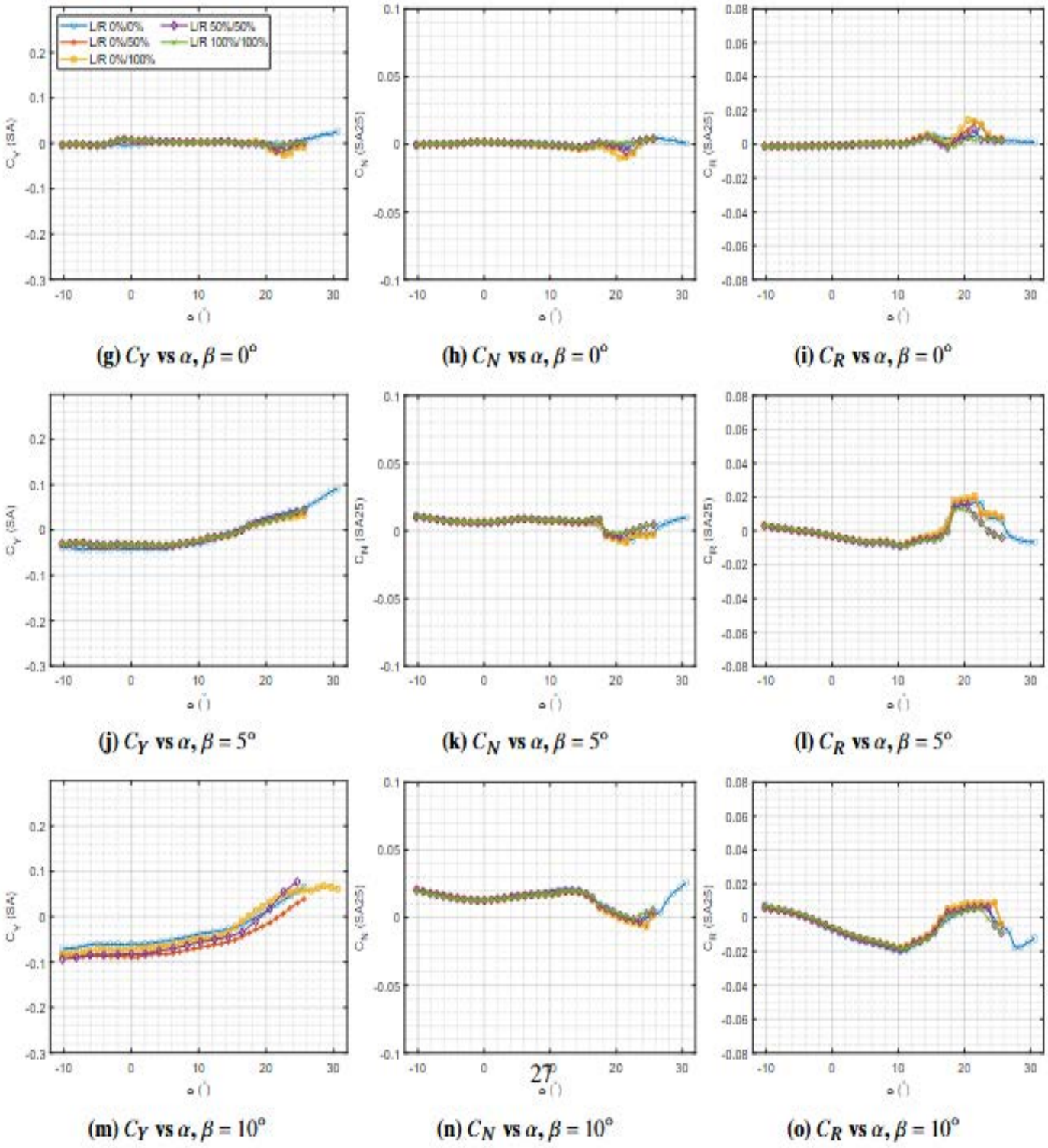

(g) C_Y vs $\alpha, \beta = 0^o$ **(h) C_N vs $\alpha, \beta = 0^o$** **(i) C_R vs $\alpha, \beta = 0^o$**

(j) C_Y vs $\alpha, \beta = 5^o$ **(k) C_N vs $\alpha, \beta = 5^o$** **(l) C_R vs $\alpha, \beta = 5^o$**

(m) C_Y vs $\alpha, \beta = 10^o$ **(n) C_N vs $\alpha, \beta = 10^o$** **(o) C_R vs $\alpha, \beta = 10^o$**

Fig. 27: Effects of reduced nozzle exit areas on the lateral directional forces and moments

(a) TEOB20 0°, UW2326-0111 **(b) TEOB20.R ±10°, UW2326-0124** **(c) TEOB20.R ±25°, UW2326-0116**

Fig. 28 UW-S-20A with ailerons rotations (TEOB – Trailing Edge Outboard)

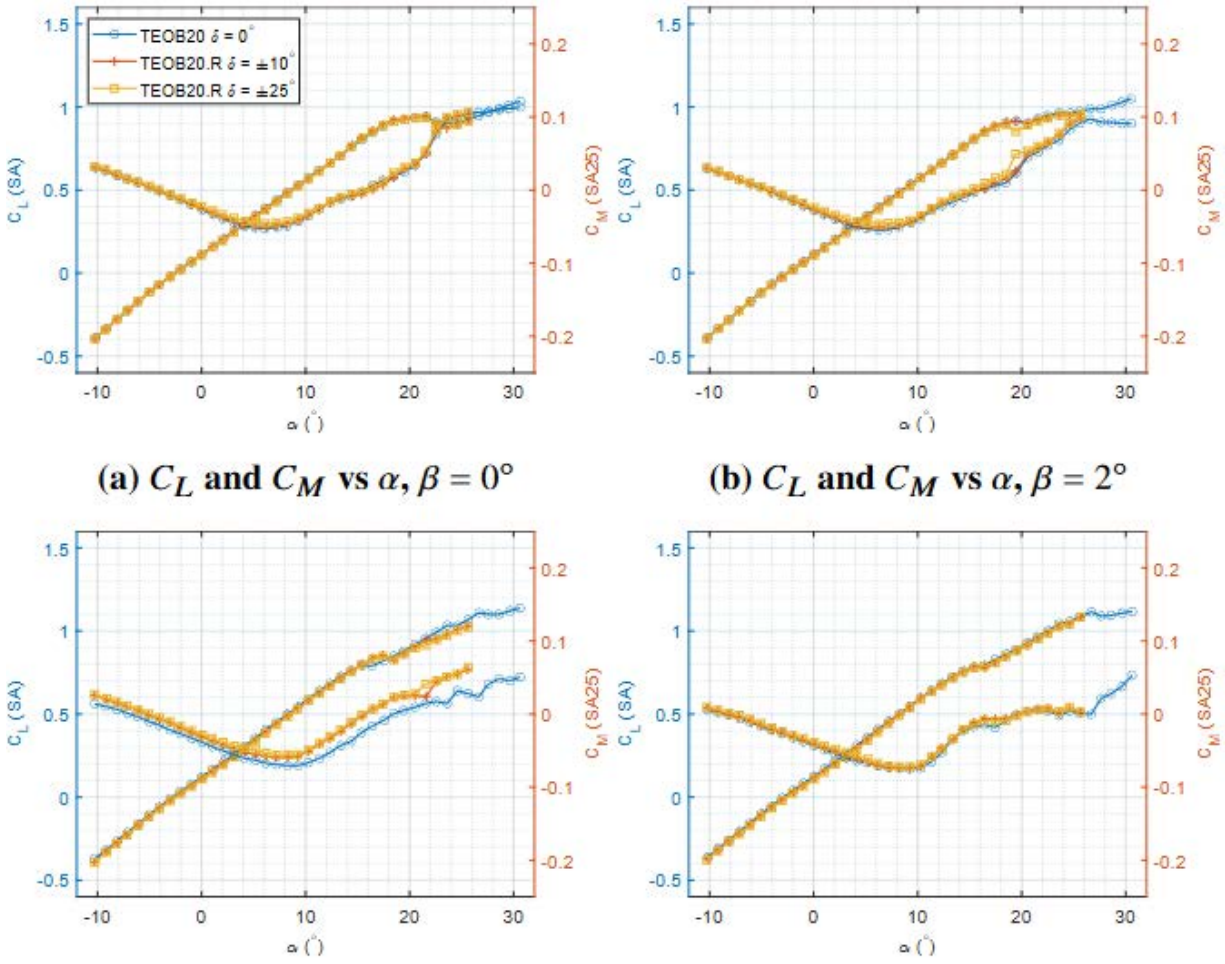

(a) C_L and C_M vs $\alpha, \beta = 0°$ **(b) C_L and C_M vs $\alpha, \beta = 2°$**

(c) C_L and C_M vs $\alpha, \beta = 5°$ **(d) C_L and C_M vs $\alpha, \beta = 10°$**

Fig. 29 Effects of reduced chord ailerons on the longitudinal forces and moments

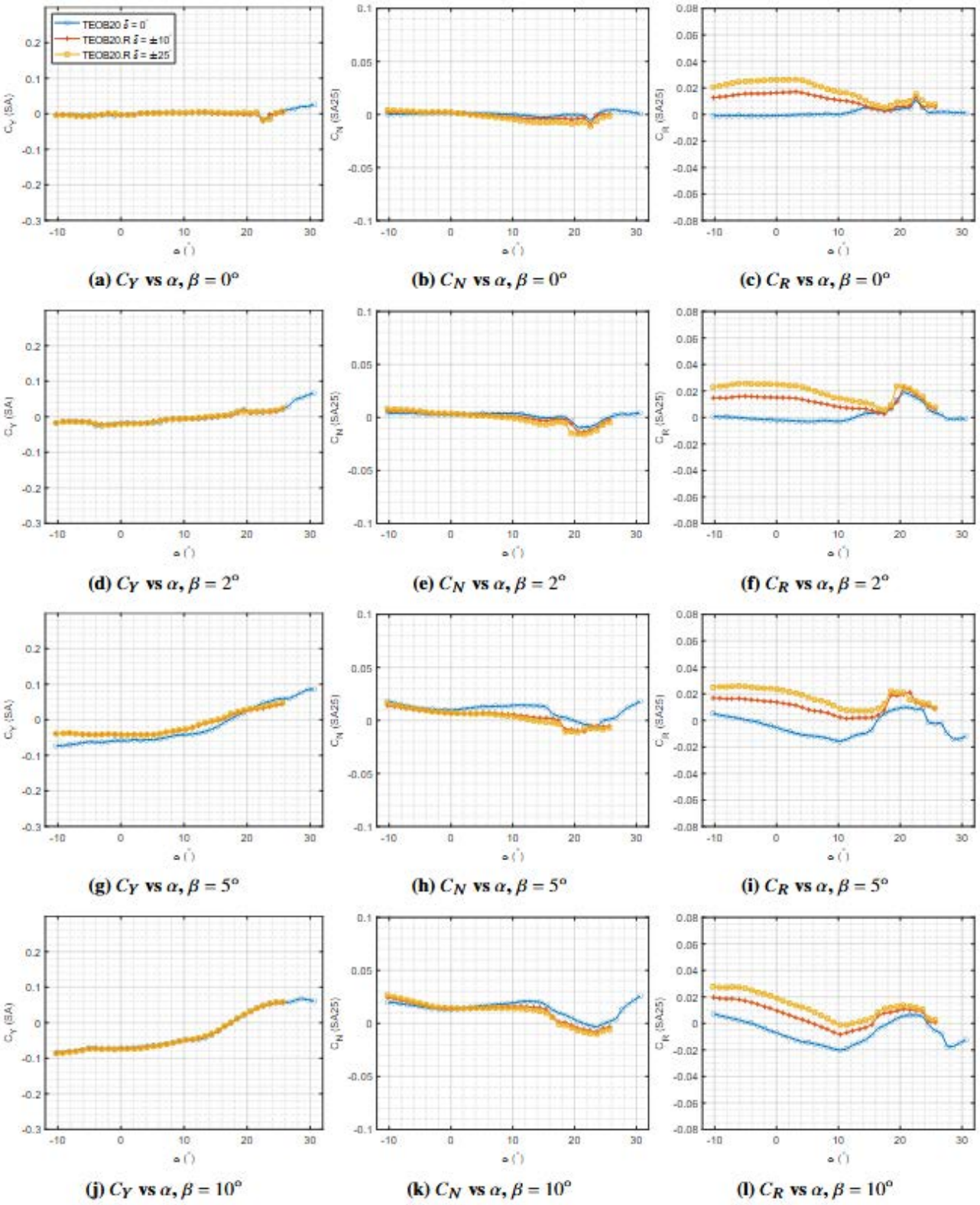

(a) C_Y **vs** $\alpha, \beta = 0°$ **(b)** C_N **vs** $\alpha, \beta = 0°$ **(c)** C_R **vs** $\alpha, \beta = 0°$

(d) C_Y **vs** $\alpha, \beta = 2°$ **(e)** C_N **vs** $\alpha, \beta = 2°$ **(f)** C_R **vs** $\alpha, \beta = 2°$

(g) C_Y **vs** $\alpha, \beta = 5°$ **(h)** C_N **vs** $\alpha, \beta = 5°$ **(i)** C_R **vs** $\alpha, \beta = 5°$

(j) C_Y **vs** $\alpha, \beta = 10°$ **(k)** C_N **vs** $\alpha, \beta = 10°$ **(l)** C_R **vs** $\alpha, \beta = 10°$

Fig. 30 Effects of reduced chord ailerons on the lateral directional forces and moments

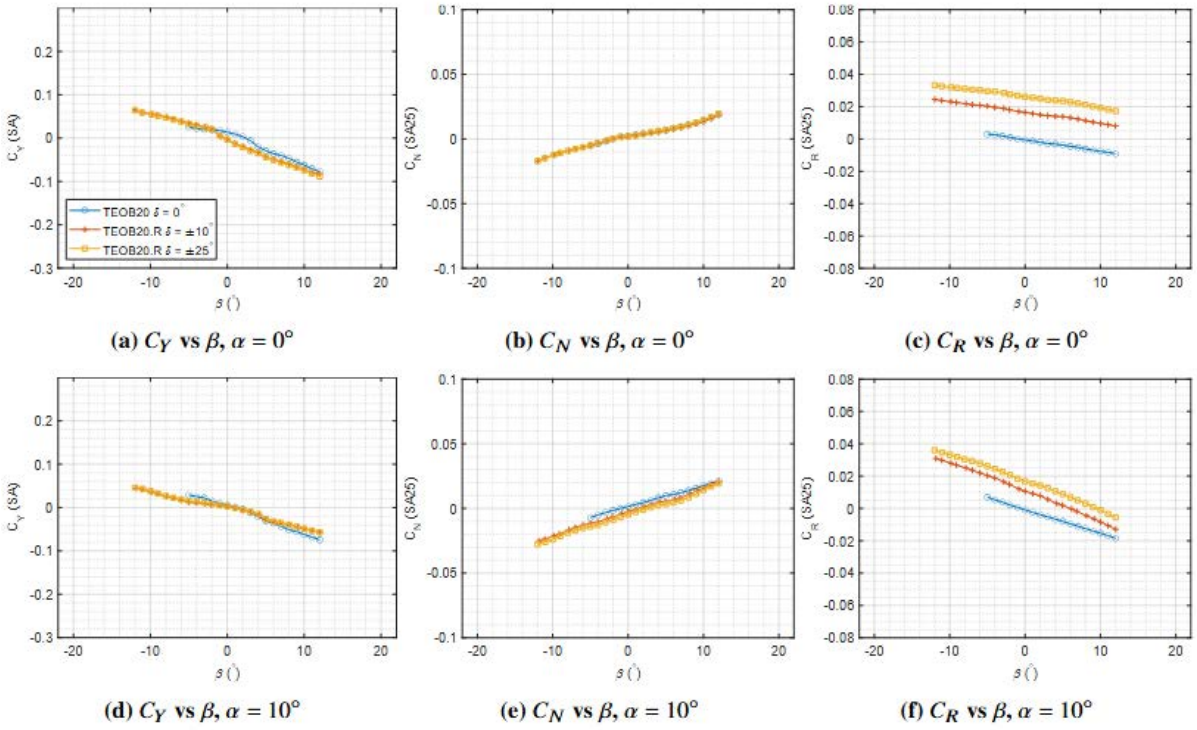

(a) C_Y vs β, $\alpha = 0°$ **(b) C_N vs β, $\alpha = 0°$** **(c) C_R vs β, $\alpha = 0°$**

(d) C_Y vs β, $\alpha = 10°$ **(e) C_N vs β, $\alpha = 10°$** **(f) C_R vs β, $\alpha = 10°$**

Fig. 31: UW-S-20A with reduced chord ailerons - lateral directional forces and moments

(a) TEOB15 0° **(b) TEOB15** ±10° **(c) TEOB15** ±25°

(d)TEOB15.R ±10° **(e) TEOB15.R** ±25°

Fig. 32: UW-S-21A with full / reduced chord ailerons rotations

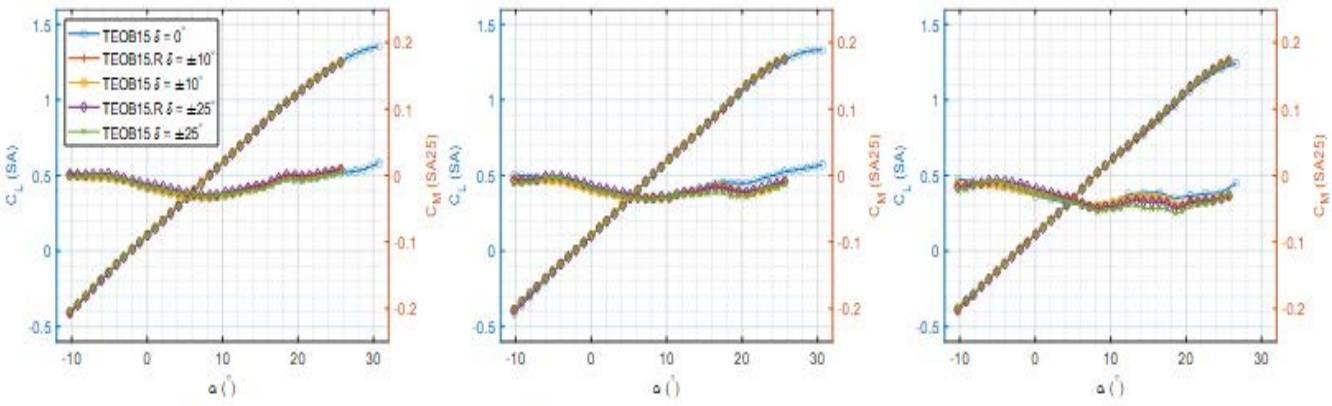

(a) C_L and C_M vs $\alpha, \beta = 0°$ (b) C_L and C_M vs $\alpha, \beta = 5°$ (c) C_L and C_M vs $\alpha, \beta = 10°$

Fig. 33 Effects of full / reduced chord ailerons on the longitudinal forces and moments

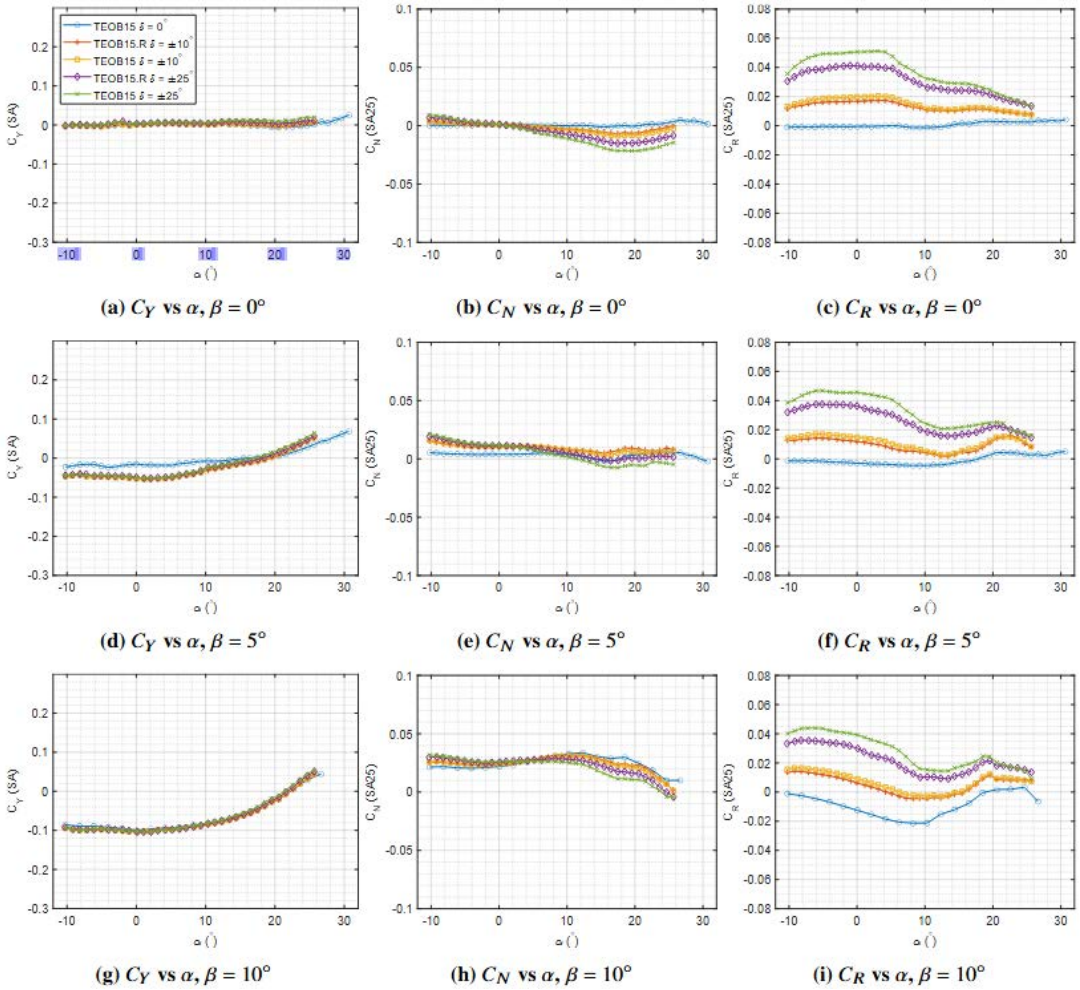

(a) C_Y vs $\alpha, \beta = 0°$ (b) C_N vs $\alpha, \beta = 0°$ (c) C_R vs $\alpha, \beta = 0°$

(d) C_Y vs $\alpha, \beta = 5°$ (e) C_N vs $\alpha, \beta = 5°$ (f) C_R vs $\alpha, \beta = 5°$

(g) C_Y vs $\alpha, \beta = 10°$ (h) C_N vs $\alpha, \beta = 10°$ (i) C_R vs $\alpha, \beta = 10°$

Fig.34 Effects of full / reduced ailerons rotations on lateral directional forces and moments

B. Take-off and Landing Conditions

Additional wind tunnel tests were carried out to investigate aerodynamic forces and moments of the SCALOS models during take-off and landing. The UW-S-24A model was used for these tests and its photos for different conditions are shown in Figs. 35 a-d. Variations of the lift and pitching moment with angles of attack for several sideslip angles are shown in Figs. 36a-d. The data are for cruise; rotated canards; canard and wing leading and trailing-edge flaps rotated; and canards, wing leading and trailing-edge flaps and landing gears deployed cases. For all sideslip angles tested, Figs. 35a-d show that canard rotation does not have significant effects on the lift developments of this SCALOS.

For the other two cases tested, C_{L_0} is seen to be shifted as expected. Note that flap deflection increases effective wing camber and effective angle of attack, and, as a result, C_{L_0} increases. For angles of attack greater than 10 degrees, C_{L_α} of the models with rotated $\delta_C + \delta_{L.E.} + \delta_{T.E.}$ and with $\delta_C + \delta_{L.E.} + \delta_{T.E.} + LG24$ for all sideslip angles decreases. Beyond 20 degrees angles of attack these configurations develop slightly less lift than that of the cruise configuration.

No signs of stalls are present in all cases. Canard rotation is seen to increase $|C_{M_0}|$, for all sideslip angles. The $|C_{M_0}|$ of models equipped with $\delta_C + \delta_{L.E.} + \delta_{T.E.}$ and $\delta_C + \delta_{L.E.} + \delta_{T.E.} + LG24$ reduce $C_{M_0} < 0$, making the configurations not trimmable at positive angle of attack. For the sideslip angles of zero and 2 degrees, the models with $\delta_C + \delta_{L.E.} + \delta_{T.E.}$ and $\delta_C + \delta_{L.E.} + \delta_{T.E.} + LG24$ produce a slight nose up pitching moment around zero degrees angle of attack, $C_{M_\alpha} > 0$. For $\alpha \geq 5^o$ nose down moment is generated (Figs. 36 a, b). For $\alpha \geq 14^o$ the models with $\delta_C + \delta_{L.E.} + \delta_{T.E.}$ and $\delta_C + \delta_{L.E.} + \delta_{T.E.} + LG24$ produce slight nose up pitching moments. The C_{M_α} derivative for the cruise and rotated-canard cases are near zero - a neutral longitudinal stability condition. For larger sideslip angles, $\beta = 5$ and 10 degrees, Figs. 36 c, and 36d show that $C_{M_\alpha} < 0$ for tests with $\delta_C + \delta_{L.E.} + \delta_{T.E.}$ and $\delta_C + \delta_{L.E.} + \delta_{T.E.} + LG24$ on, up to about 10 degrees angles of attack and C_{M_α} become nearly zero for $\alpha \geq 10^o$.

For the cases of cruise, rotated canards; canards and wing leading and trailing flaps; and canards, wing leading and trailing flaps and landing gears deployed cases, variations of the lateral-directional force and moment coefficient with angles of attack for sideslip angles of $\beta = 0, 2, 5,$ and 10 degrees are shown in Fig. 37. The only noticeable effects are observed for $\alpha \geq 10^o$ and with $\beta =$ $5,$ and 10 degrees (Figs. 37 h, i, k, l). The side force coefficient does not vary significantly with the above rotations. In combination with the rudder rotations photos that are shown in Fig. 38 and Fig. 39 show that all lateral directional coefficients are affected while the effects on the rolling moment are seen to be minimal.

As the rudder is rotated, the vertical tail develops more or less lift (side force), depending on the direction of rudder rotation, and via the moment arm yawing moments change. The resulting small rolling moments are created by the vertical distance from the vertical tail aerodynamic center to the model moment center. Figure 39 shows that rudder rotation shifts the side force coefficient at zero degrees sideslip, but the slope of the curve does not vary significantly. Similar effects are seen for the yawing moment variations with sideslip angles for all angles of attack shown in Fig. 39, with C_N shifted due to rudder rotation at zero sideslip angle. Variations of the yawing moment coefficient with sideslip angles for all configurations are highly nonlinear for angles of 10 and 20 degrees (Fig. 39 e, h) which is most likely due to the asymmetrical flow field over the windward and leeward wing surfaces, and the low tail immersed in the canard, wing, and fuselage wake. For the $\alpha = 20^o$case, Figs.39g, and 39h show that $C_{Y_\beta} > 0$ while $C_{N_\beta} \approx 0$ - a plateau in the C_N vs β curve, for sideslip angles of $-2^o \leq \beta \leq 2^o$.

(a) Cruise condition **(b) Canard deflected**

© Wing L.E/T.E. deflected **(d) Wing L.E./T.E. deflected &landing gear deployed**

Fig. 35 UW-S-24A take-off and landing configuration wind tunnel model build-up

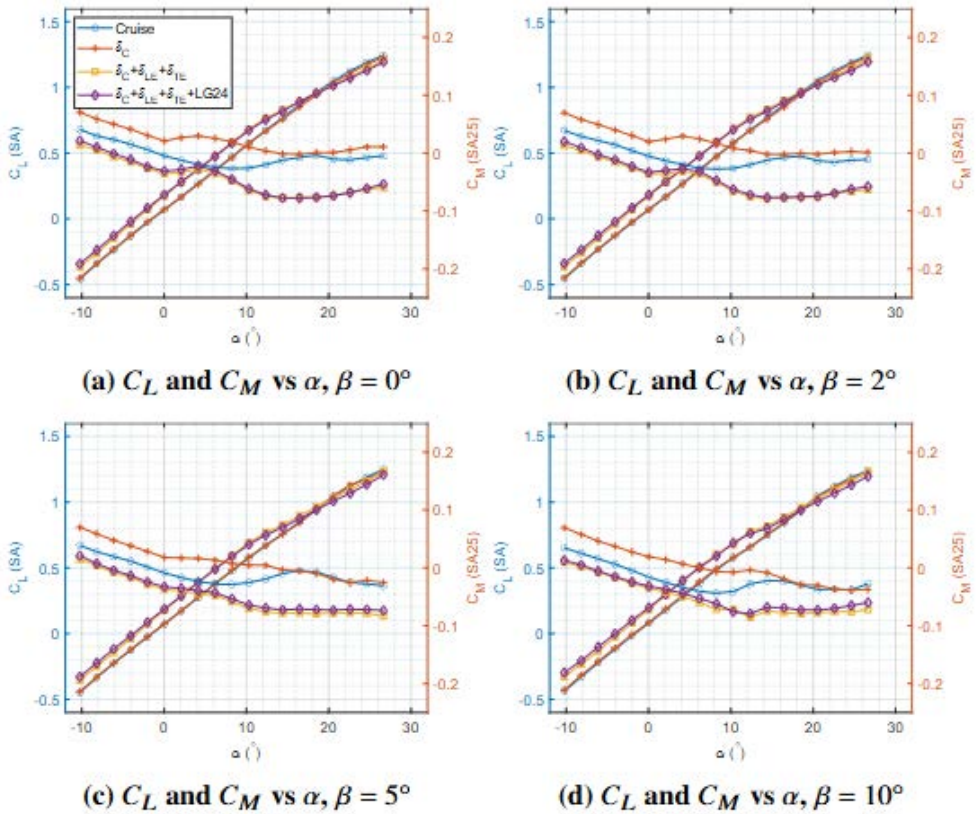

(a) C_L and C_M vs α, $\beta = 0°$ **(b) C_L and C_M vs α, $\beta = 2°$**

(c) C_L and C_M vs α, $\beta = 5°$ **(d) C_L and C_M vs α, $\beta = 10°$**

Fig. 36 UW-S-24A take-off / landing configuration cases: longitudinal forces and moments

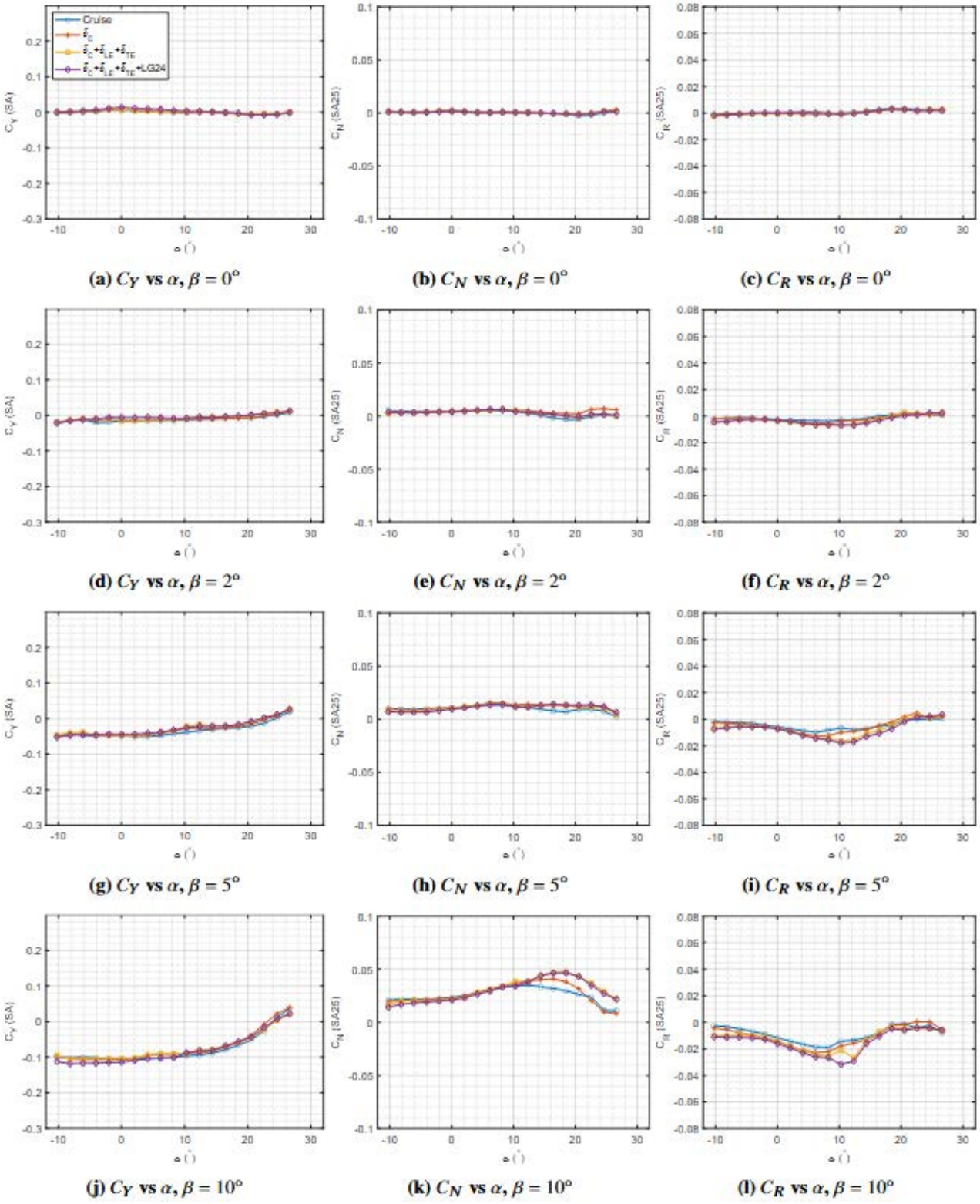

(a) C_Y **vs** $\alpha, \beta = 0°$ **(b)** C_N **vs** $\alpha, \beta = 0°$ **(c)** C_R **vs** $\alpha, \beta = 0°$

(d) C_Y **vs** $\alpha, \beta = 2°$ **(e)** C_N **vs** $\alpha, \beta = 2°$ **(f)** C_R **vs** $\alpha, \beta = 2°$

(g) C_Y **vs** $\alpha, \beta = 5°$ **(h)** C_N **vs** $\alpha, \beta = 5°$ **(i)** C_R **vs** $\alpha, \beta = 5°$

(j) C_Y **vs** $\alpha, \beta = 10°$ **(k)** C_N **vs** $\alpha, \beta = 10°$ **(l)** C_R **vs** $\alpha, \beta = 10°$

Fig. 37: UW-S-24A take-off /landing configurations: lateral directional forces and moments

(a) UW-S-24A **(b)** $\delta_{\text{Rud}} = 0^{\circ}$ **(c)** $\delta_{\text{Rud}} = 25^{\circ}$

Fig. 38: UW-S-24A LTO configuration with rudder rotations

Conclusion

An intensive low-speed wind tunnel study was conducted to investigate the effects of various configuration changes on the performance as well as stability and control characteristics of slender supersonic airplane configurations in their low-speed flight envelope. All tests were conducted at the Kirsten Wind Tunnel at the University of Washington. The configurations included different canard positions and shapes, horizontal and vertical tails positions and shapes, dorsal and ventral fin effects, nacelle locations, rudder and aileron rotations, nacelle exit area blockage, landing and takeoff simulation, and additional effects on both longitudinal and lateral-directional characteristics of the models. It is hoped that the database that was created will fill some of the existing gaps of information regarding low-speed performance and stability of future commercial supersonic passenger aircraft. Wind tunnel "corrections" were applied to the in-tunnel measured raw test data to produce forces and moments on the models in free-flight following standard wind tunnel correction techniques ([57],[58]) plus model support test and interference (T&I) corrections based on dedicated tests ([56]).

The paper discusses the lateral-directional characteristics and longitudinal characteristics at sideslip in detail. A few general notes can be made:

1. Model configuration variations have significant effects on both longitudinal and lateral-directional stability and control of the different SCALOS models studied, with the UW-S-23G model being the most stable one longitudinally. In general, the pitch-up , longitudinal instability and the angle of attack at which it occurs become more severe with increased sideslip angles.
2. Canard rotation affects stall characteristics, $C_{L_{max}}, \alpha_{C_{L_{max}}}$, pitch-up tendency of the SCALOS configurations, C_{M_α}beyond nose up angle of attack, deep stall appearance, and rolling moment at zero angle of attack. The canard seems to improve the pitch-up behavior of the models.

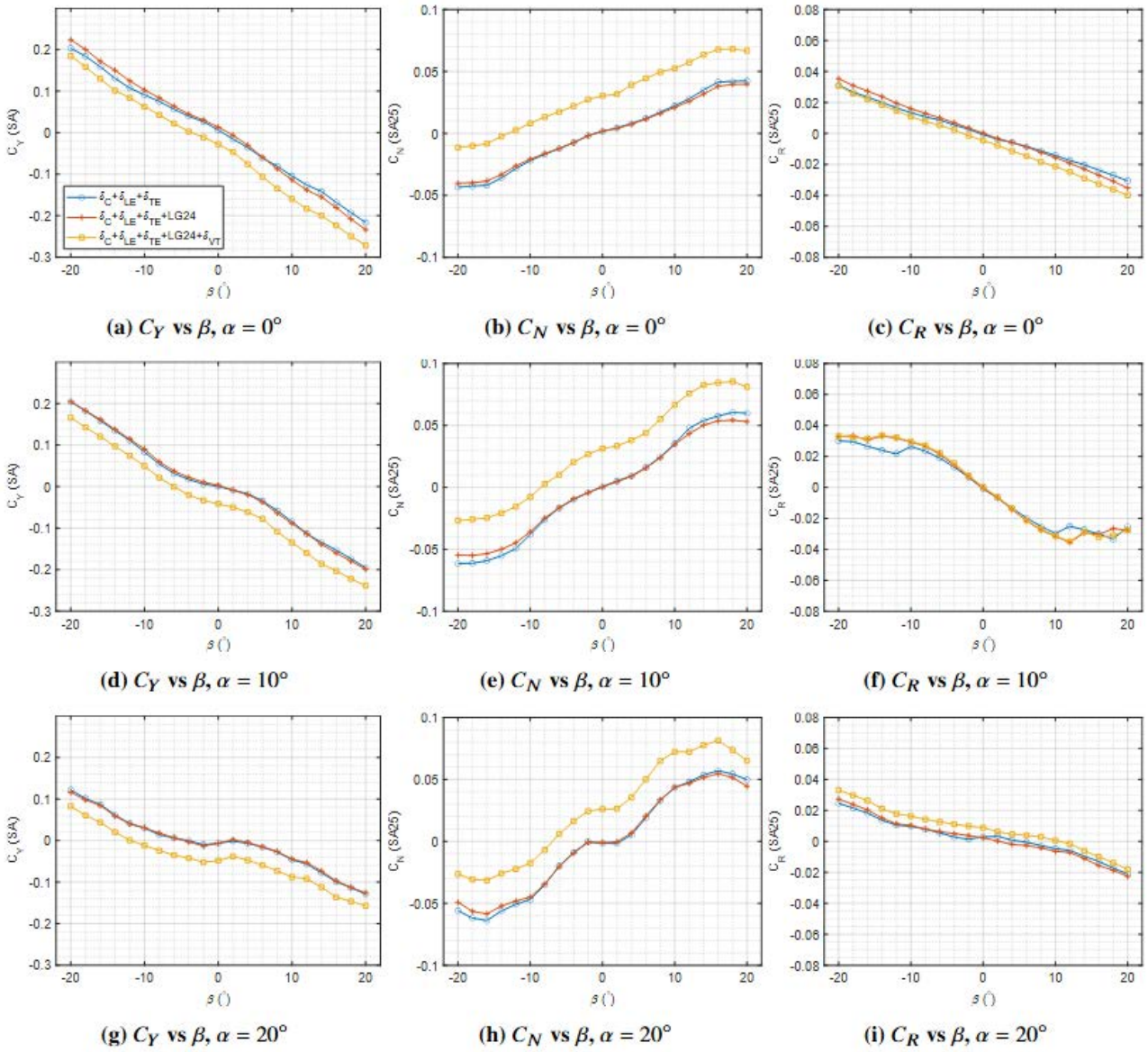

(a) C_Y vs β, $\alpha = 0°$ **(b) C_N vs β, $\alpha = 0°$** **(c) C_R vs β, $\alpha = 0°$**

(d) C_Y vs β, $\alpha = 10°$ **(e) C_N vs β, $\alpha = 10°$** **(f) C_R vs β, $\alpha = 10°$**

(g) C_Y vs β, $\alpha = 20°$ **(h) C_N vs β, $\alpha = 20°$** **(i) C_R vs β, $\alpha = 20°$**

Fig. 39: UW-S-24A take-off /landing configuration with different δ_{Rud} rotations: the effect on lateral directional forces and moments

Conclusion (continued):

3. The SCALOS model with the T-tail empennage has a better rolling moment variation at all angles of attack for all rudder rotation angles tested. Rudder rotation shifts both side force and yaw moment coefficient at zero degrees angle of attack but does not change C_{Y_β} and C_{N_β} at low to moderate angles of attack.
4. Nacelle location affects C_{M_0}, but not C_{M_α}. The model with the wing bottom mounted nacelles stalls at lower angles of attack than the top mounted nacelles case. Nacelle

addition, whether top or bottom mounted, increases lateral directional stability derivatives, making the model more stable.

5. The engine out simulation done by fully or partially blocking nacelles exit area leads to no significant changes in the longitudinal and lateral-directional stability derivatives in all cases. A slight shift in the $C_{M_0}, C_Y, and\ C_N$ values at zero degrees angle of attack for the negative sideslip angles are noticed, however. For the rolling moment case, the slope of $C_R\ vs\ \alpha$ curves for $\alpha > 0^o$ at negative sideslip angles changes.
6. Aileron and reduced chord aileron rotations have significant effects on the longitudinal stability of the UW-S-21A model. The trailing-edge aileron rotation affects the rolling moment variations of both models with angles of attack and sideslip angles and shifts the $C_R\ vs\ \alpha$ curves but does not change the slope. Reduced chord ailerons have minimal effect on the rolling moment variations of both models.
7. Take-off and landing configuration changes affect the values of lift at zero degrees angle of attack for a certain range of alphas, and have significant effects on the longitudinal stability prior to and post the pitch up angle of attack. The effects on the lateral-directional stability derivatives are minimal.

Acknowledgments

Support by NASA, Award/Contract #80NSSC19K1661, under the Commercial Supersonic Technology (CST) program, Supersonic Configurations at Low Speeds, with Sarah Langston as the NASA technical grant monitor is gratefully acknowledged. The authors would like to thank Lori Ozoroski, Sriram Rallabhandi, Melissa Carter, Sarah Langston, and Peter Coen from NASA for the opportunity to conduct this needed research for supersonic aircraft. The authors would also like to thank the staff and crew of the University of Washington's Kirsten Wind Tunnel and the 2020-2024 UW senior capstone airplane design project teams for their assistance and contributions.

References

[1] Nelson, C. P., Ting, K.-Y., Ignacio, J., Mavriplis, N., Soltani, R., and Livne, E., "Supersonic Configurations at Low Speeds (SCALOS): Configuration Comparison of SCALOS to Existing Designs," *AIAA SciTech 2023 Forum*, AIAA Paper 2023-0228, 2023. https://doi.org/10.2514/6.2023-0228.

[2] Finck, R. D., Ellison, D. E., and Malthan, L. V. P. I..-., "USAF (United States Air Force) Stability and Control DATCOM (Data Compendium)," Tech. Rep. TR-83-3048, Air Force Wright Aeronautical Laboratories, 1978. AD B072483.

[3] "ESDU (Engineering Sciences Data Unit) Aerodynamics,", 1964-present. URL https://esdu.com/cgi-bin/ps.pl?sess=unlicensed_ 1210526230324pwb&t=ser&p=ser_aero, accessed: December 1str, 2023.

[4] Sigalla, A., and Hallstaff, T., "Aerodynamics of Powerplant Installation on Supersonic Aircraft," *Journal of Aircraft*, Vol. 4, No. 4, July 1967, pp. 273–277. https://doi.org/10.2514/3.43834.

[5] Buckner, J., Hill, P., and Benepe, D., "Aerodynamic Design Evolution of the YF-16,", *AIAA Paper 1974-935*, https://doi.org/10.2514/6.1974-935.

[6] Buckner, J., and Webb, J., "Selected Results from the YF-16 Wind Tunnel Test Program," *8th Aerodynamic Testing Conference*, 1974, p. 619. https://doi.org/10.2514/6.1974-619.

[7] Smetana, F., Summery, D., and Johnson, W., "Riding and Handling Qualities of Flight Aircraft: A Review and Analysis," Tech. Rep. CR-1975, NASA, 1975.

[8] Hoerner, S. F., and Borst, H. V., "Fluid-dynamic Lift: Practical Information on Aerodynamic and Hydrodynamic Lift," *NASA STI/Recon Technical Report A*, Vol. 76, 1975, p. 32167.

[9] Kulfan, R.M., and Sigalla, A., "Real Flow Limitations in Supersonic Airplane Design," *Journal of Aircraft*, Vol. 16, No. 10, 1979, pp. 645–658. https://doi.org/10.2514/3.58585.

[10] Radkey, R., Welge, H., and Roensch, R., "Aerodynamic Design of a Mach 2.2 Supersonic Cruise Aircraft," *Journal of Aircraft*, Vol. 15, No. 6, 1978, pp. 351–357. https://doi.org/10.2514/3.58369.

[11] Leyman, C., "A Review of the Technical Development of Concorde," *Progress in Aerospace Sciences*, Vol. 23, No. 3, 1986, pp. 185–238. https://doi.org/10.1016/0376-0421(86)90007-2.

[12] Wood, R., Niedling, L., Miller, D., Klein, J., and Hahne, D., "Status Review of a Supersonically Biased Fighter Wing Design Study," *Journal of Aircraft*, Vol. 21, No. 10, 1984, pp. 767–775. https://doi.org/doi:10.2514/3.45040.

[13] Nelson, C, "Effects of Wing Planform on HSCT Off-Design Aerodynamics," *AIAA Paper 1992-2629*, 1992. https://doi.org/10. 2514/6.1992-2629.

[14] Antani, D., and Morgenstern, J., "HSCT High-lift Aerodynamic Technology Requirements," *AIAA Paper 1992-4228*, 1992. https://doi.org/10.2514/6.1992-4228, Guidance, Navigation and Control Conference.

[15] Benoliel, A., and Mason, W., "Pitch-up Characteristics for HSCT class Planforms - Survey and Estimation," *AIAA Paper 1994-1819*, 1994. https://doi.org/10.2514/6.1994-1819, 12th Applied Aerodynamics Conference.

[16] Mann, M., and Carlson, H., "Aerodynamic Design of Supersonic Cruise Wings with a Calibrated Linearized Theory," *Journal of aircraft*, Vol. 31, No. 1, 1994, pp. 35–41. https://doi.org/10.2514/3.46452.

[17] Baize, D., "1997 NASA High-Speed Research Program Aerodynamic Performance Workshop," Tech. Rep. CP-1999-209691, NASA, 1997.

[18] Hahne, D., "1999 NASA High-Speed Research Program Aerodynamic Performance Workshop," Tech. Rep. CP-1999-209704, NASA, 1999.

[19] "Critical Propulsion Components," Tech. Rep. CR-2005-213584, NASA, 2005.

[20] Furukawa, T., and Makino, Y., "Conceptual Design and Aerodynamic Optimization of Silent Supersonic Aircraft at JAXA,"
AIAA 2007-4166, 2007. https://doi.org/10.2514/6.2007-4166.

[21] Martin, S., "Publishable Activity Report," Tech. Rep. HISAC-T-6-26-1, Dassault Aviation, 2008.

[22] Welge, H., Bonet, J., Magree, T., Chen, D., Hollowell, S., Kutzmann, A., Mortlock, A., Stengle, J., Nelson., C., Adamson, E., Baughcum, S., Britt, R., Miller, G., and Tai, J., "N+2 Supersonic Concept Development and Systems Integration," Tech. Rep. CR-2010-216842, NASA, 2010.

[23] Bruner, S., Baber, S., Harris, C., Caldwell, N., Keding, P., Rahrig, K., Pho, L., and Wlezian, R., "NASA N+ 3 subsonic fixed wing silent efficient low-emissions commercial transport (SELECT) vehicle study," Tech. Rep. 2010-216798, NASA, 2010.

[24] Welge, H., Nelson, C., and Bonet, J., "Supersonic Vehicle Systems for the 2020 to 2035 Timeframe," *AIAA 2010-4930*, 2010. https://doi.org/10.2514/6.2010-4930, 28th AIAA Applied Aerodynamics Conference.

[25] Benson, L. R., *Quieting the Boom: The Shaped Sonic Boom Demonstrator and the Quest for Quiet Supersonic Flight*, NASA, 2013.

[26] Morgenstern, J., Norstrud, N., Sokhey, J., Martens, S., and Alonso, J. J., "Advanced Concept Studies for Supersonic Commercial Transports Entering Service in the 2018 to 2020 Period, Phase I Final Report," Tech. Rep. CR-2013-217820, PMF-01766, NASA, 2013. URL https://ntrs.nasa.gov/api/citations/20130010174/downloads/20130010174.pdf.

[27] Magee, T., Shaw, S., and Fugal, S., "Experimental Validations of a Low Boom Aircraft Design," *AIAA Paper 2013-646*, 2013. https://doi.org/10.2514/6.2013-646, 51st AIAA Aerospace Sciences Meeting including the New Horizons Forum and Aerospace Exposition.

[28] Trefny, C. J., Hirt, S. M., Anderson, B. H., Fink, L., and Magee, T., "Performance of a Supersonic Over-Wing Inlet with Application to a Low-Sonic-Boom Aircraft," 2014. https://doi.org/10.2514/6.2014-3802, 50th AIAA/ASME/SAE/ASEE Joint Propulsion Conference.

[29] Morgenstern, J., Buonanno, M., Yao, J., Murugappan, M., Paliath, U., Cheung, L., Malcevic, I., Ramakrishnan, K., Pastouchenko, N., Wood, T., Martens, S., Viars, P., Tersmette, T., Lee, J., Simmons, R., Plybon, D., Alonso, J., Palacios, F., Lukaczyk, T., and Carrier, G., "Advanced Concept Studies for Supersonic Commercial Transports Entering Service in the 2018 to 2020 Period Phase 2," Tech. Rep. CR-2015-218719, NASA, 2015. URL https://ntrs.nasa.gov/api/citations/20150015837/downloads/ 20150015837.pdf.

[30] Sun, Y., and Smith, H., "Review and prospect of supersonic business jet design," *Progress in Aerospace Sciences*, Vol. 90, 2017, pp. 12–38. https://doi.org/10.1016/j.paerosci.2016.12.003.

[31] Karling, K., "Aerodynamics of the Viggen 37 aircraft," *NASA Technical Memorandum, NASA TM-88403*, 1975.

[32] Solies, U., "Low speed handling qualities of the High-Speed Civil Transport," 1995. https://doi.org/10.2514/6.1995-3912, Aircraft Engineering, Technology, and Operations Congress.

[33] Herrmann, U., "Supersonic Commercial Transport Low-Speed Performance," *JAXA Special Publication*, 2001, pp. 486 – 497. Proceedings of International Workshops on Numerical Simulation Technology for Design of Next Generation Supersonic Civil Transport (SST-CFD Workshop).

[34] Van Muijden, J., and Elsenaar, B., "Numerical prediction capabilities and analysis of flow development for a supersonic civil transport at low speed," *Proceedings of CEAS Aerospace Aerodynamics Conference, Cambridge*, 2002, pp. 10–12. https://doi.org/10.1.1.156.6598.

[35] Kwak, D-Y., Miyata, K., Noguchi, M., Rinoie, K., and Fujita, T., "Aerodynamic Characteristics of Rolled SST Configuraton with LE and TE Flaps at High Angles of Attack," *21st AIAA Applied Aerodynamics Conference*, 2003. https://doi.org/10.2514/6.2003- 3413.

[36] Brandi, V., "Navier-Stokes Analysis for SCT Low-speed High-lift Flight and Wind Tunnel Configurations," *24th International Congress of the Aeronautical Sciences*, 2004.

[37] Herrmann, U., "Low-speed high-lift performance improvements obtained and validated by the EC-project EPISTLE," *24th International Congress of the Aeronautical Sciences*, 2004.

[38] Van Muijden, J., "Improvement and Verification of Low-speed Aerodynamic Characteristics of a Supersonic Civil Transport Aircraft," *Proceedings of the Institution of Mechanical Engineers, Part G: Journal of Aerospace Engineering*, Vol. 220, No. 6, 2006, pp. 569–580. https://doi.org/10.1243/09544100JAERO87.

[39] Lei, Z., "Flow Simulation of a Supersonic Transport Configuration at Low-Speed and High-Lift Conditions," *Journal of aircraft*, Vol. 45, No. 5, 2008, pp. 1514–1521. https://doi.org/10.2514/1.33856.

[40] Kawazoe, H., Abe, S., Matsuno, T., Yamada, G., and Obayashi, S., "Low-speed aerodynamic characteristics of a busemann-type silent supersonic biplane," *27th Congress of the International Council of the Aeronautical Sciences 2010, ICAS 2010*, 2010, pp. 1491–1450.

[41] Gaffuri, M., and Brezillon, J., "Unstructured Mesh Capabilities for Supersonic Wing Design at Low-Speed Conditions," *CFD and Optimization, An ECCOMAS Thematic Conference*, 2011, p. 048.

[42] Lei, Z., and Kwak, D.-Y., "Numerical Optimization of Leading-Edge Deflection Angles for an SST Configuration at Low Speed," *27th International Congress of the Aeronautical Sciences*, 2011. https://doi.org/10.2514/6.2013-238.

[43] Livne, E., and Nelson, C., "From Blank Slate to Flight Ready New Small Research UAVs in Twenty Weeks-Undergraduate Airplane Design at the University of Washington," *AIAA Paper 2012-845*, 2012. https://doi.org/10.2514/6.2012-845, 50th AIAA Aerospace Sciences Meeting including the New Horizons Forum and Aerospace Exposition.

[44] Kwak, D., Gaffuri, M., Ohira, K., and Brezillon, J., "Numerical Study of the Reynolds Number Effect on Low Aspect Ratio Wings at Low Speed," *28th International Congress of the Aeronautical Sciences*, 2012.

[45] Lei, Z., Kwak, D.-y., and Rinoie, K., "Experimental Optimization of Leading-Edge Deflection Angles for an SST Configuration at Low Speed," *AIAA Paper 2013-238*, 2013. https://doi.org/10.2514/6.2013-238, 51st AIAA Aerospace Sciences Meeting including the New Horizons Forum and Aerospace Exposition.

[46] Ohira, K., and Kwak, D.-Y., "Investigation of Turbulence Models for the Supersonic Transport Configuration at Low-Speed and High Alpha Flight Condition," *AIAA Paper 2014-3098*, 2014.

https://doi.org/10.2514/6.2014-3098, 32nd AIAA Applied Aerodynamics Conference.

[47] Langston, S., Nelson, C. P., and Livne, E., "Low-Speed Stability and Control of a Reduced Scale Long-Range Supersonic Configuration with Reduced-Size or No Vertical Tail," *AIAA Paper 2016-1036*, 2016. https://doi.org/10.2514/6.2016-1036, AIAA Atmospheric Flight Mechanics Conference.

[48] Setoguchi, N., and Kanazaki, M., "Low-Speed and High Angle of Attack Aerodynamic Characteristics of Supersonic Business Jet with Forward Swept Wing," *AIAA Paper 2020-0534*, 2020. https://doi.org/10.2514/6.2020-0534, AIAA SciTech 2020 Forum.

[49] Duong Nguyen, T., Kashitani, M., Kusunose, K., Taguchi, M., and Takita, Y., "Analysis of a Wing–Fuselage Biplane with Trailing- Edge Flaps in Low-Speed Flow," *Journal of Aircraft*, Vol. 59, No. 2, 2022, pp. 350–363. https://doi.org/10.2514/1.C036154.

[50] Ting, K.-Y., Wiersema, K., Nelson, C. P., and Livne, E., "Supersonic Configurations at Low Speeds (SCALOS): Progress at the University of Washington," *AIAA SciTech 2024 Forum*, AIAA Paper 2024-0898, 2024. https://doi.org/https://doi.org/10.2514/6. 2024-0898.

[51] Ting, K.-Y., Nelson, C. P., Wiersema, K., and Livne, E., "Supersonic Configurations at Low Speeds (SCALOS): Wind Tunnel Tests at the University of Washington - an Overview and Some Key Insights," *AIAA SciTech 2025 Forum*, January 2025, Orlando, FL.

[52] Ting, K.-Y., Mavriplis, N., Soltani, R. M., Nelson, C. P., and Livne, E., "Supersonic Configurations at Low Speeds (SCALOS): The Aerodynamic Effects of Control Surfaces," *AIAA SciTech 2023 Forum*, AIAA Paper 2023-0229, 2023. https://doi.org/10.2514/6.2023-0229.

[53] Magee, T. E., Hayes, P. J., Dorgan, A. J., and Khodadoust, A., "Dynamic Stability Characteristics for Commercial Supersonic Configurations at Low-Speed Flight Conditions," AIAA Paper 2022-1802, 2022. https://doi.org/10. 2514/6.2022-1802.

[54] Magee, T. E., Hayes, P. J., Dorgan, A. J., and Khodadoust, A., "Dynamic Stability Characteristics for Commercial Supersonic Configurations at Low-Speed Flight Conditions–Part II," *AIAA SciTech 2024 Forum*, AIAA Paper 2024-0900, 2024. https://doi.org/https://doi.org/10.2514/6.2024-0900.

[55] Magee, T., Hayes, P., and Khodadoust, A., "Dynamic Stability Characteristics for Commercial Supersonic Configurations at Low-Speed Flight Conditions – Part III", AIAA SciTech2025 Forum, Orlando, FL, January 2025.

[56] Ting, K.-Y., Nelson, C. P., and Livne, E., "Supersonic Configurations at Low Speeds (SCALOS): Tare & Interference Corrections for SCALOS Configurations tested at the University of Washington's KirstenWind Tunnel," *AIAA SciTech 2024 Forum*, AIAA Paper 2024-0899, 2024. https://doi.org/https://doi.org/10.2514/6.2024-0899.

[57] "The University of Washington's Kirsten Wind Tunnel," , 1936-present. URL https://www.aa.washington.edu/AERL/KWT, accessed: December 1str, 2023.

[58] Barlow, J.B., Rae, W.H., and Pope, A., "Low-Speed Wind Tunnel Testing", 3rd edition, Wiley-Interscience; 3rd edition (February 22, 1999)

Supersonic Configurations at Low Speeds (SCALOS)

Final Report

December 15, 2024

Appendix F

University of Washington

RSAC – A Reference Supersonic Airliner Concept

Supersonic Configurations at Low Speeds (SCALOS): Reference Supersonic Airliner Concept (RSAC)

Chester P. Nelson, Kenneth Wiersema
University of Washington, Seattle, WA 98195

I. Introduction

One of the objectives of the SCALOS effort at the University of Washington, was to provide opportunities for undergraduate students, as well as the MS and PhD students, to directly contribute to the project. Engaging the students in the development of a realistic supersonic conceptual design has a number of research and educational benefits (Figure 1).

Between 2005 and 2018, UW's Aeronautics and Astronautics department developed a challenging large-team Senior Design "capstone" curriculum in which 20-30 seniors would work together on the conceptual design and wind tunnel testing of some type of advanced future civil aircraft. A focus on future concept aircraft and technologies promoted the inclusion of "discovery" and research practices in the course, rather than simply having the students execute textbook drawing-and-sizing exercises on a traditional design. These projects included the design and testing of wind tunnel models, and exposure to modern engineering tools such as FEM and CFD analysis, and flight simulation. The student teams, guided by one or more industry specialists, faculty, and graduate student teaching assistants, commonly generated bits of new data and insights of scientific interest to the researchers and industry supporters of the program. Prior to 2020, the curriculum also involved "hands-on" opportunities to build large, instrumented radio-controlled scale models of the concept planes ("Research UAV's"), and in most years, use these to conduct sub-scale test flights (see paper AIAA-2012-0845). In multiple years, the design challenge posed delt with supersonic aircraft (airliners, business jets, or research aircraft), as these types facilitated student exposure to transonic and supersonic applied aerodynamics, civil aircraft performance and certification, as well as thin-wing structures and non-linear S&C issues more common to military fighter aircraft.

Some exposure to supersonic and hypersonic aircraft was a common feature of aero engineering curricula in the 1960's and 70's, but in the post-Concorde/post-HSCT years, supersonic aircraft design seems to have largely disappeared from course content, at least at the undergraduate level. Incorporating support of the SCALOS grant effort into 2020-2024 "capstone" projects has a provided an awareness of the unique challenges posed by supersonic cruise aircraft among the roughly 45 participating seniors. Each year's SCALOS capstone project participants initially attended a series of "on-boarding" lectures, reviewing the fundamental differences in supersonic versus subsonic configuration aerodynamics, propulsion, structural arrangements, performance and noise characteristics. Students were additionally charged with studying the operational, environmental and business challenges of supersonic cruise aircraft, along with reasons that past "SST" attempts have failed in various aspects.

Due to evolutionary changes in UW's undergraduate curriculum, today's capstone projects are more diverse, each with reduced class sizes (8-10), and fewer total project hours available per quarter than pre-

2019. The scope of the 2020-2024 undergrad involvement in the SCALOS effort therefore focused on a few key aspects, including;

1) conducting the initial "design space survey" for the SCALOS studies,
2) aero shape (OML) lofting of selected configurations,
3) CAD-based design and 3D printing of selected wind tunnel model components,
4) support of testing in both the 8x12 foot (KWT) and 3x3 foot research tunnels,
5) plotting and analysis of preliminary results, performance predictions, and
6) the conceptual design of an example airliner configuration (RSAC).

The example airliner configuration, dubbed "Reference Supersonic Airliner Concept" (RSAC), was iteratively developed and refined over the 5 years of the SCALOS effort. Each year's capstone group executed an industry style "design cycle", evolving the configuration definition, progressively improving the concept, adding integration details, and increasing the fidelity of performance inputs and basic S&C considerations.

The SCALOS experimental dataset is intended to provide quantitative aerodynamic data to aid in conceptual design trades, calibration of CFD tools, and provide trends with which to anchor MDO models. The range of general arrangements and aerodynamic features which were wind tunnel tested were chosen as a sampling of the many proposed supersonic cruise concepts published by industry, government research agencies, and academia over the preceding 10-20 years (post-Concorde), as presented previously in paper AIAA 2023-0228. Given the breadth of configuration features tested, these data, with appropriate adjustments, should be generally applicable to configurations sized from roughly 5 feet to 300 feet in length, across applications ranging from Research UAVs to large airliners.

Although the SCALOS data applicability is generic, the semi-parametric wind tunnel testing required that the model wings, nacelles, tails and fuselages be consistently proportioned based on a single example application. The 2015 version of a KWT modular wind tunnel model representing a generic supersonic cruise transport was based on the general arrangement of Boeing's "765-070A" airliner concept from the NASA N+2 studies (NASA/CR-2010-216842), so it was logical to use that configuration as a point-of-departure for sizing SCALOS model components (Figure 2). Early in 2020, student efforts focused on the definition of the first sets of new wind tunnel components for the modular model, including nacelles, a T-tail arrangement, and more highly swept outboard wing panels for the modular model.

Past experiences with supersonic research and technology development programs such as NASA's SCR and HSR programs, and the EU's HISAC program, have demonstrated the value of defining a specific, detailed "baseline" configuration--- a conceptual aircraft design that can be used to evaluate the incremental performance, economic, or environmental impacts of improved technologies or alternate design choices. While the SCALOS wind tunnel database was the prime objective of the effort at UW, having the successive capstone classes use public information to "flesh out" a non-proprietary RSAC configuration provided SCALOS with a unique ancillary product; the RSAC definition provides better visibility of vehicle integration "packaging", and geometry constraints for optimization studies, than was able to be publicly released within the scope of the N+2/N+3 studies.

Published Contractor Reports from the NASA-sponsored "N+2/N+3" studies, conducted by Boeing and Lockheed, were an invaluable resource and were heavily relied upon as a point-of-departure for the definition of the RSAC. Numerous technical papers and reports generated for the High-Speed Civil Transport (HSCT), and its NASA-led "HSR" technology development program, were also key resources for studying configuration trends, lessons learned, and design "rules-of-thumb" guidance early in the RSAC's development.

RSAC- Reference Supersonic Airliner Concept Motivations

- An example "concept plane" for defining SCALOS wind tunnel model parts and defining scale sizing of the propulsion system/model nacelles
- A project platform for UW undergraduate Aero "Capstone" students (8-10/yr)
  - Research participation, wind tunnel testing experience
  - Iteration through realistic 1-year configuration design cycles
  - CFD, CAD, lofting and parts fabrication opportunities
  - Detailed introduction to applied aero of supersonic cruise aircraft
- Provide an "airplane level" assessment- i.e. how do the SCALOS results apply to an example production aircraft conceptual design ?
- Non-proprietary baseline for potential follow-on studies
  - Performance trades, trajectory/noise/field length optimization
  - Evaluation of the impact of alternate design features and general arrangements
  - Potential point-of-departure OML for optimization, structures studies, simulations, MDO exercises

Figure 1- RSAC Conceptual Design Motivations

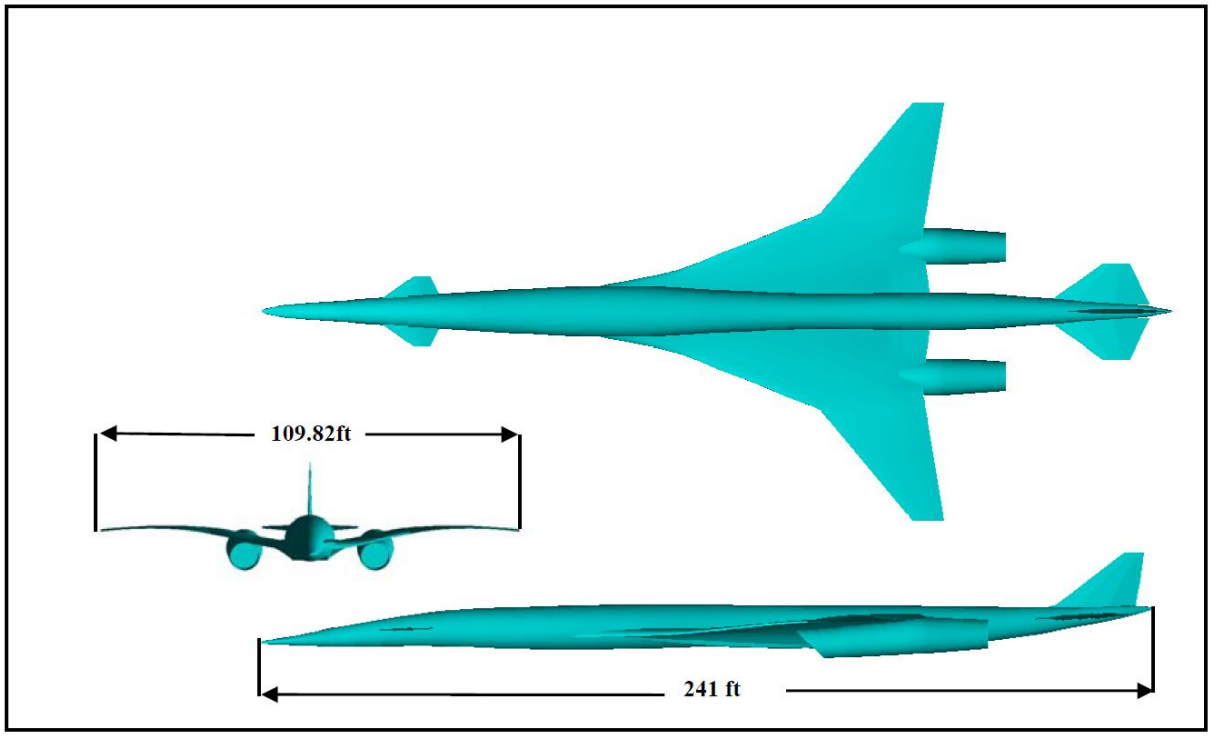

General arrangement of 765-070A.

Figure 2- The Boeing N+2 mid-wing +aft-tail + canard configuration

The resulting RSAC conceptual design definition (Figure 3) is representative of an aircraft that could be viable as a certified production airliner, using technologies that are already at high "TRL", or could be quickly matured. Relative to first generation supersonic transports (Concorde, Tu-144), RSAC is designed to;

a. Substantially reduce fuel burn, emissions, and associated operating costs per passenger-mile,
b. lower the cruising altitude where engine emissions are deposited,
c. have the potential to meet Chapter 14/Stage 5 noise regulations with margin,
d. provide flying qualities and net flight safety equivalent to contemporary subsonic transports under CFR14-FAR25 and equivalent international airworthiness regulations,
e. have more cabin arrangement flexibility and greater passenger seating comfort,
f. have improved transonic/subsonic performance, allowing mixed mission use and reasonable economics during subsonic flight over land,
g. have reduced operating speeds for climb, descent, and approach requiring minimal "special handling" by ATC to mesh with today's more crowded airspace below 39,000ft,
h. have substantially reduced takeoff and landing speeds, for improved safety and arrival/departure sequencing.

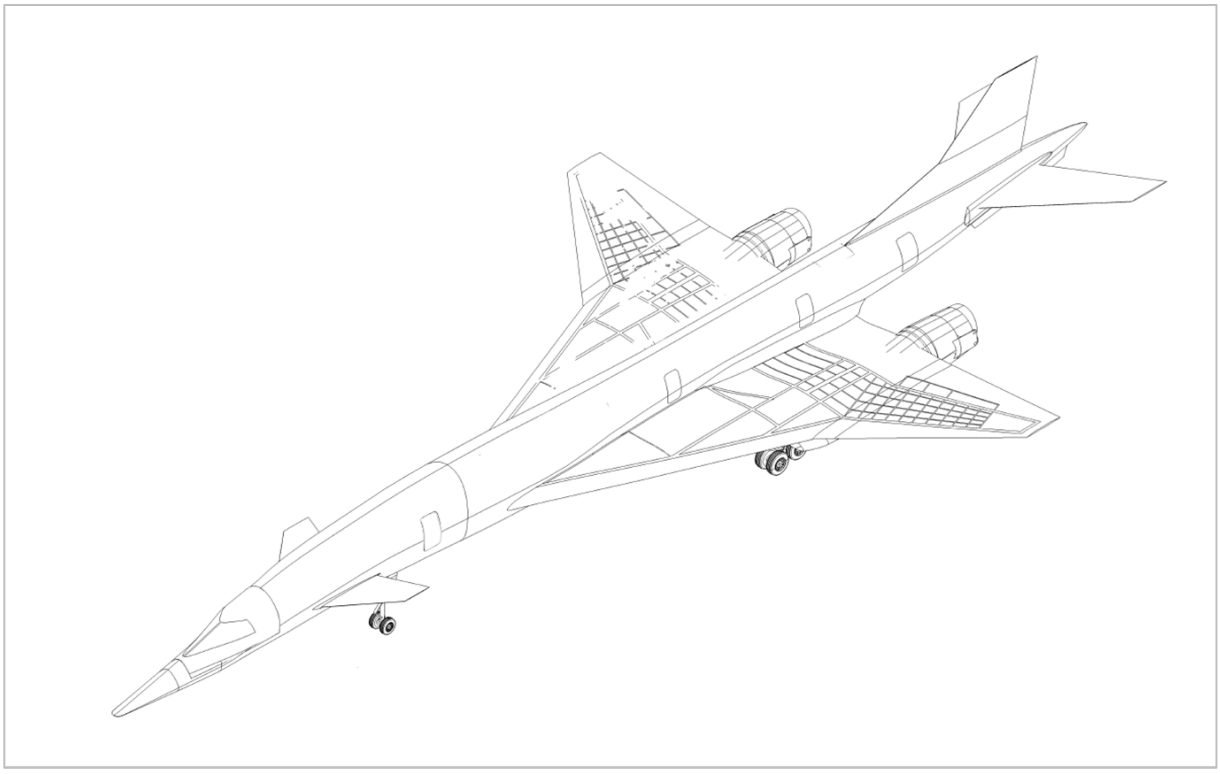

Figure 3- RSAC 4th Major Design Cycle (Model "E") at the End of 2024

II. RSAC Requirements Development

Each year, students supporting the SCALOS capstone project were tasked with a number of reading and documentary video viewing assignments, followed by in-class lectures and discussions of the significant barriers to success which must be overcome for a viable "next generation" supersonic airliner. During the first year (2020) a list of "Tier 1" requirements and objectives was established for the RSAC. This list of requirements was gradually expanded in subsequent design cycles to include detailed guidance on cabin design, structural assumptions, systems, etc. as more integration detail was required.

A. Economic Considerations

All past attempts at civil supersonic aircraft have proven to have unsustainable economics and environmental concerns (Figure 4).

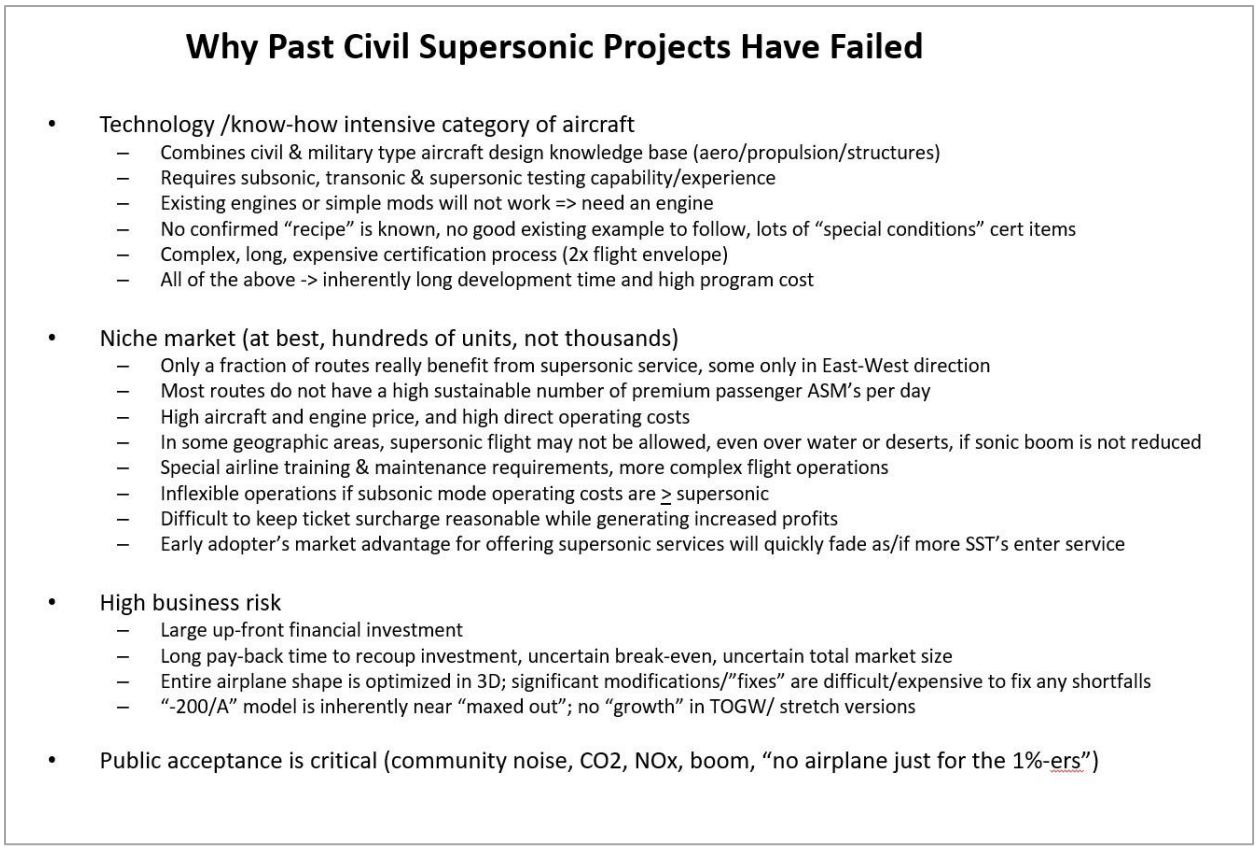

Figure 4- Past Civil Supersonic Aircraft History

Concorde was undoubtedly a great technical achievement. It was operated quite profitably by British Airways (and to a lesser extent Air France) with "flagship" status, for roughly 25 years. In spite of the tragic year 2000 crash which contributed to the end of the airplane's use, the overall safety record of Concorde was comparable to that of many other aircraft designed in the 1960's. However, it has been nearly 25 years since Concorde was retired and it is dangerous to assume that anything regarding Concorde can be used directly as an example of what will work for economic, operational, certification,

configuration, or environmental acceptability in the 21st century. Concorde had fairly unique economic and operating circumstances:

- Concorde operations ended up limited only a few routes with a critical supply of select passengers willing to pay well in excess of "first class" ticket prices
- Concorde passengers were paying for excellent cabin service and significant time savings that included express check-in, security, and baggage handling, not just the flight time
- BA and AF bought their Concordes at or below direct "cost". The French and British governments paid for most of the development in order to re-capture post-WW2 aviation leadership and to cement collaboration on future EEC projects (eventually). With first flight in the same year as Boeing's 747, the Concorde development was reportedly 40% more expensive (~3x the cost in terms of dollars per pound of MTOGW). The Concorde engine was a modification of an existing military engine used in the Avro Vulcan and TSR-2, not a "clean sheet" development.
- For trans-oceanic flights, the coastal arrival/departure airports are usually not the desired travel endpoints. Many passengers make connections to other flights which will take them to their final destinations. Concorde's limited arrival and departure schedule and lack of over-land connecting flights made it less attractive to a segment of potential customers.
- Concorde's higher subsonic cruise speed over land should have been attractive for connecting flights and in-land segments of supersonic flights. However, its poorer subsonic range performance and higher subsonic fuel costs severely limited its use on over-land missions.

A review was made of some of the fundamental changes that have occurred over the past 25 years since Concorde was in service and the NASA HSR program was advancing enabling technologies for the proposed Mach 2.4 High Speed Civil Transport, HSCT (Figure 5).

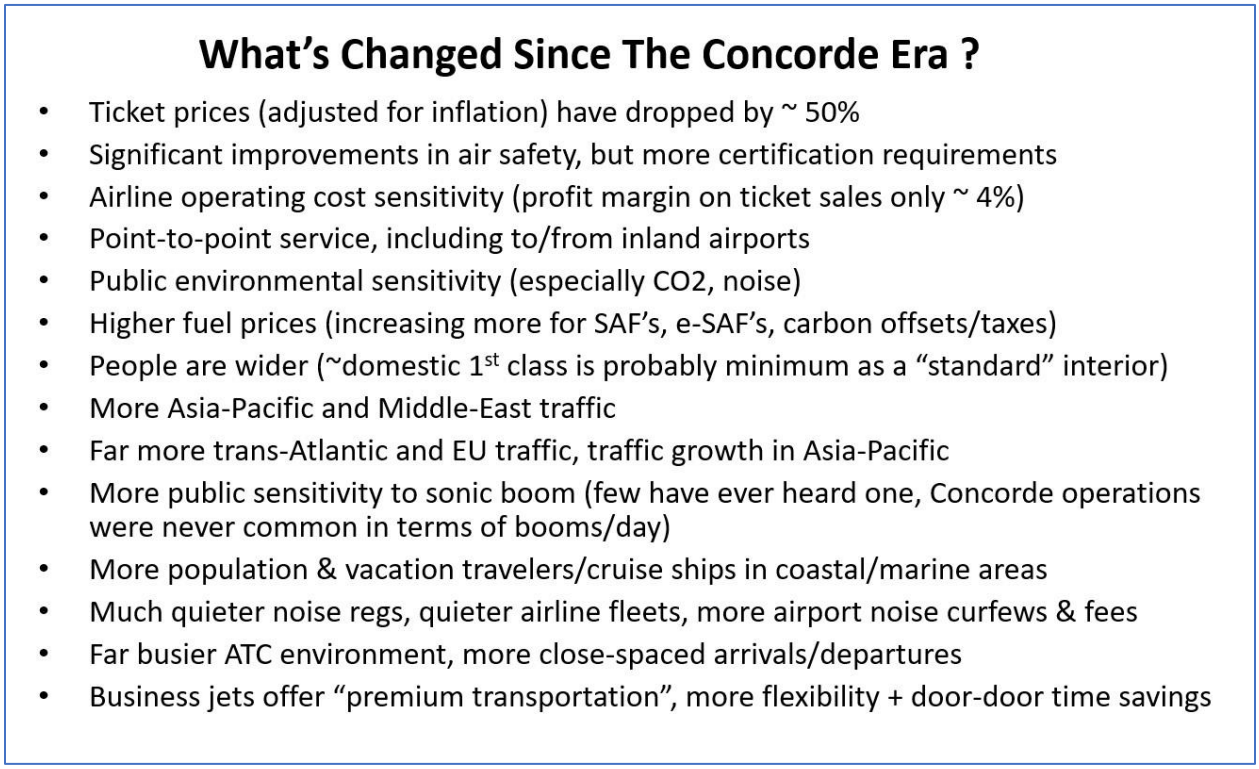

Figure 5- Passenger Air Travel Changes Over the Past 25-30 Years

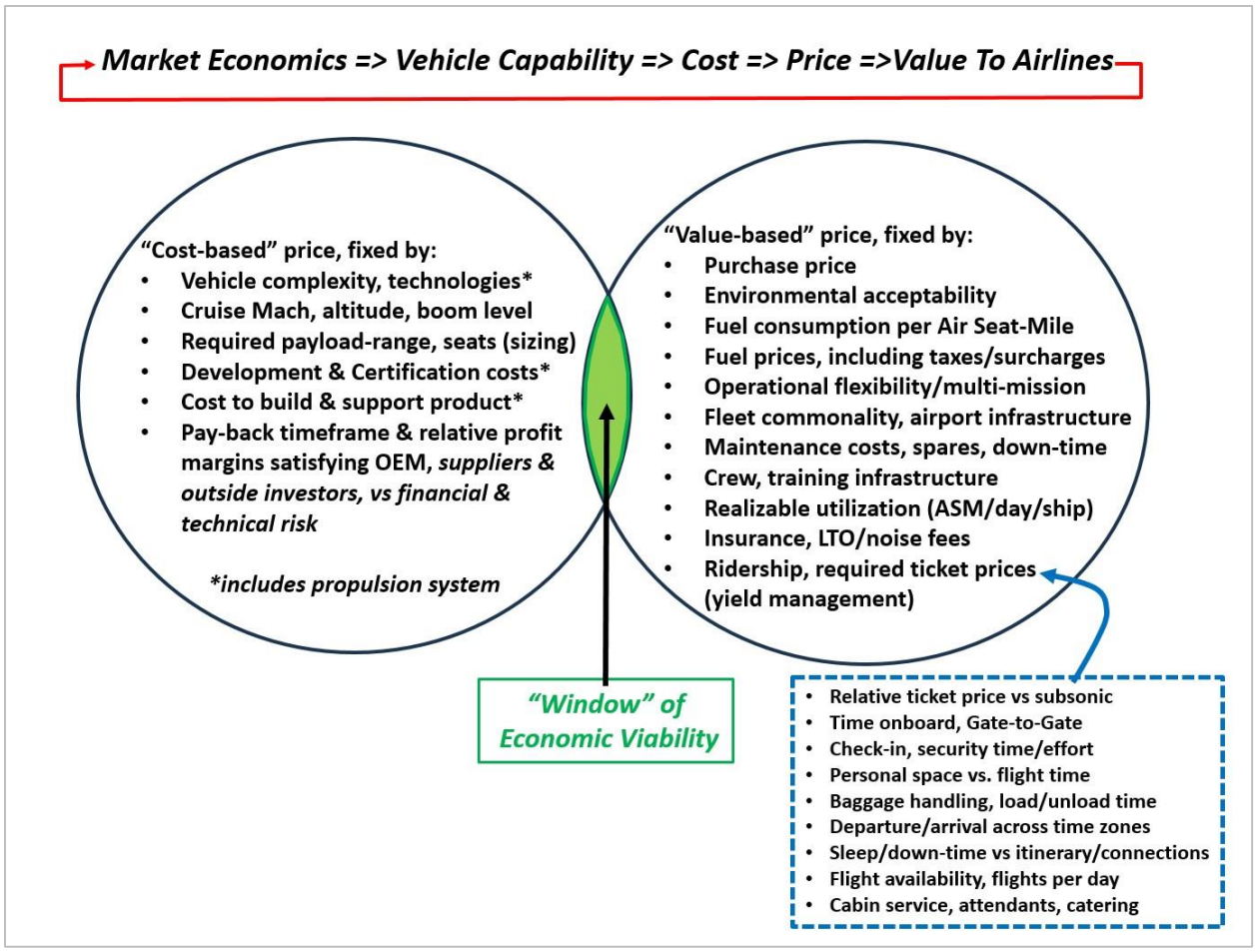

Figure 6- The Cost-Price-Market Feedback Loop

During the 2008-2010 time period, both Boeing and Lockheed conducted supersonic airliner technology needs studies under parallel NASA contracts (NASA/CR-2010-216842, CR–2011-217084 and CR-2015-218719, AIAA-2010-4930). These studies, called N+2 and N+3, proposed a set of commercial supersonic aircraft concepts that could be enabled by technology evolution looking ahead 2 and 3 decades (referenced to the early 2000's). The Boeing N+2 study initially delved extensively into understanding future airline traffic and potential markets for supersonic aircraft, addressed operating economics, likely certification requirements, and configuration concepts to improve fuel efficiency/emissions. The second portion of their N+2 study focused on candidate configurations and technologies for minimizing sonic boom. In both portions, their preferred configurations attempted to provide sufficient wing span and aspect ratio to help meet off-design characteristics as well as landing and takeoff (LTO) noise/performance goals with relatively conventional engine architecture. Boeing's N+3 study extended the N+2 low-boom designs to larger, more advanced concepts, with increased propulsion technology.

The parallel Lockheed studies focused almost exclusively on sonic boom mitigation technologies, conceptualizing aircraft general arrangements and tailored propulsion systems to enable minimum boom levels while still meeting landing and takeoff (LTO) noise goals. The preferred configurations appear to have been allowed to "size out" as required for the low-boom goals, with the airframe largely point-designed for low-boom cruise aerodynamics and most of the burden for LTO noise and operating economics falling primarily on the propulsion system advancements. In both the Lockheed and Boeing studies, the low-boom designs would have carried more developmental risk and longer development time than the "supersonic-over-water" airplanes.

The traffic forecast and markets section of Boeing's N+2 and N+3 contractor reports identified supersonic aircraft like the RSAC to still be "niche" products in the 2030's, compared with programs like the A320 series or 737Max which are selling many thousands of units. Air traffic growth patterns and the categories of potential supersonic flyers appear to have largely followed the trends predicted in the Boeing CR's over the past 15 years, so those are still considered a valid guide for design requirements purposes.

In the end, the economic sustainability will always depend on whether there is a "critical mass" of flyers on each route, several times per day, who will feel they get enough value from supersonic flight to be worth the ticket prices they have to pay. The ticket prices are in turn a fall-out of the revenue an airline needs to pay for the airplane and its operation, plus a small margin of profit. The portion of the airline's cost related to paying the mortgage or lease on the airplane depends on the purchase price, which in turn, depends on the costs and profit margins of the manufacturer (OEM) and suppliers. This chain is called the "cost-price-market loop" (Figure 6). Success of the aircraft program, will depend on finding the right requirements and design compromises that create overlap in the economic viability of both the builders and the owner/operators.

"Success" for the OEM and suppliers, depends on the development and manufacturing costs, the acceptable sales price, and the longevity of production. Small supersonic airliner production runs of 20-50 units are clearly not sustainable, and for many certified aircraft, production runs of at least 150-250 units are required to "break even" with development costs. There are fundamental physics-based reasons for supersonic aircraft to be significantly more costly to develop, certify and build compared to subsonic types of similar payload and range capability (Figure 7).

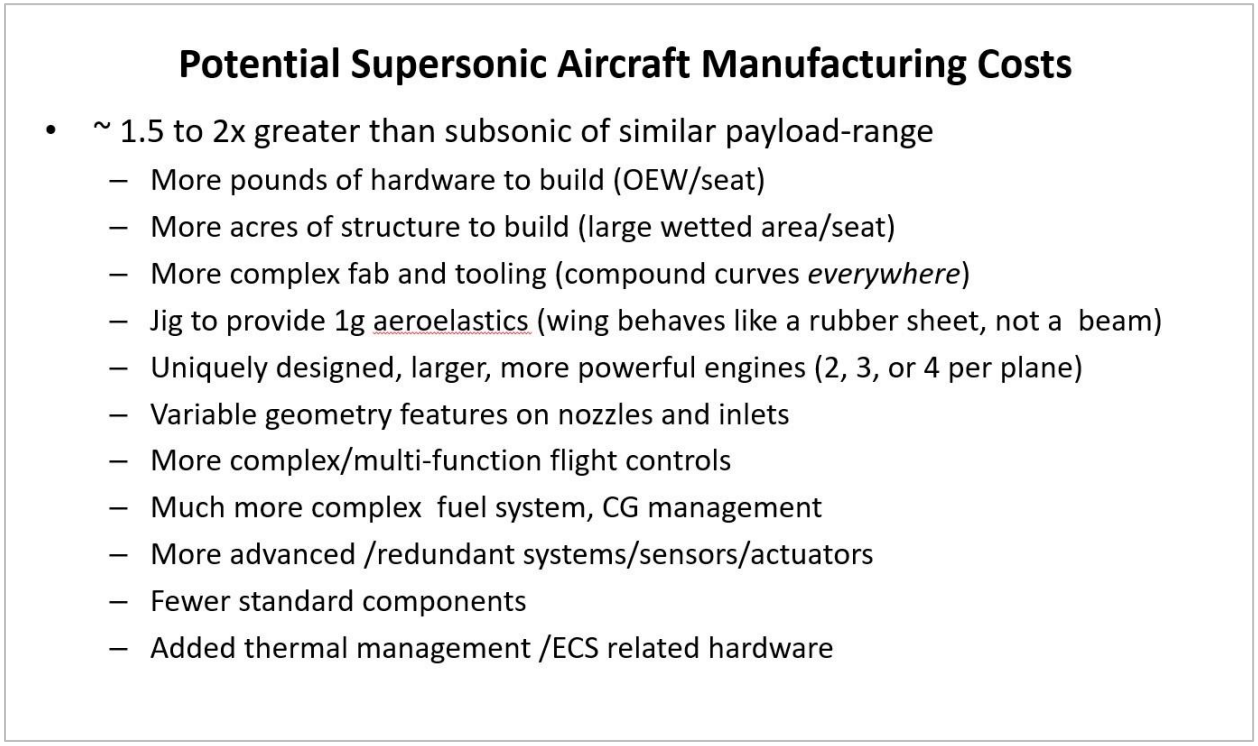

Figure 7- Expect Higher Manufacturing Costs

It can be argued that in order to avoid pitfalls that have killed multiple previous attempts as civilian supersonic products, that conceptual design work and preliminary design phase trade studies should include "gaming" multiple scenarios that could include passenger responses, operator outfitting and uses of the aircraft, future fuel prices, potential regulatory and economic changes, and socio-political pressures that could be expected over the life cycle of the aircraft. Since Concorde's retirement, several aircraft programs offer examples of "clean sheet" designs that needed moderate materials and manufacturing development, selected technology maturation, a number of certification Special Conditions, and a new or significantly-modified engine program (e.g. C-series, A380, 787, 777X, A350). Some recent aircraft have spent longer in the pre-certification flight testing phase, and that is likely to be further increased on a supersonic type due to the 2 to 3 times larger operating envelope that must be demonstrated. Based on such examples, the following timeline assumptions for a non-low-boom RSAC type next generation supersonic airliner are suggested as a reference point:

+ 2 years production airplane concept studies, validate readiness of key technologies & methods

+ 3 years in-depth preliminary design & selected component testing

+ 2.5-3 years detail design and tooling, engine build and cert

+1.5-2 years flight test and certification with pre-production and early production airframes

+ 10 years nominal production run @ 30 airplanes/yr fleet absorption rate (~break-even in 5-6 years)

+ 15 years normal service life per airplane

~ 30+ years minimum total life cycle from conceptual design to retirements if program is successful.

If the above life-cycle sequence is hypothetically started in 2025, the design must remain viable for projected in-service environmental/economic/operational requirements reaching into the 2050-2060 timeframe. Requirements for this, and other all-new aircraft need to consider future scenarios on the order of decades rather than just focusing on requirements for the first customer and initial EIS. That puts it well into the period where significant changes will be taking place in the airline and travel industry under pressure to shift away from fossil fuel use as soon as possible. However, the technical prospects for electric propulsion are not favorable in the foreseeable future for long-range, or large aircraft, so the impact of those changes on RSAC or its competitors will likely be increased operating costs driven by fuel availability, drop-in SAF/SAF blends/e-SAF cost, or the added cost of carbon taxes and offsets. Scenarios of the impact of these costs on ticket prices, curtailed market growth on some routes and the effects of that on and RSAC type or its competitors were beyond the scope of the SCALOS studies.

The challenge of adapting a given design to future market shifts is compounded for supersonic types by the fact that it will have to be very tightly integrated and the aerodynamic outer mold lines (OML) will need to be optimized in 3D as one shape. This makes it very difficult to "stretch" or "shrink", grow the fuel capacity, or change the wing design of any optimized supersonic aircraft to generate follow-on product versions, as is required for subsonic airliner production to remain profitable long-term. It also makes it even more important to maximize up-front testing and quantification of guarantee-able performance because post flight modifications are very difficult and costly. For example, a significant

misprediction of the exact 1-g cruise shape including aeroelastics could require the entire wing to be re-cambered and re-twisted, necessitating a complete re-design and re-fabricating major tooling to prevent a range or fuel-burn miss.

The suggested timeline above assumes a fairly minimal development period using "in-hand" or very near-term technologies. RSAC's requirements assume the use of technologies projected in the 2008-2010 NASA "N+2" supersonic studies which have now progressed to the point they could be matured in just 3-4 years from the start of serious product development efforts. On this basis, the requirement for RSAC's hypothetical entry into service (EIS) date has been specified as the early 2030's. Extreme low-boom technology remains in the research stages (X-59 has not even flown yet) so the RSAC is defined without low-boom features. More advanced, highly variable cycle, multiple flow-path engine technologies considered during the N+2 and N+3 studies, were also not considered as a *requirement* for the RSAC but rather could be the subject of future technology benefits assessments using the RSAC as a baseline.

Anecdotally, a number of past studies have estimated that a supersonic business jet or airliner could have a "sticker price" 2 to 3x higher than a subsonic aircraft of similar payload-range capability. This is understandable given the comparatively limited market and inherently higher manufacturing costs. Based on this rough order of magnitude, an RSAC type might be expected to have a cost-based price of $100 - $200 million. Commercial aircraft programs without ancillary or government support, inherently must have the potential to generate net profits for the OEM, engine company, systems vendors and component sub-contractors. The sum of financial profit potential, and value of such ancillary benefits as facilities expansion and technology leadership, must be more attractive than alternative uses of the available development funds or the project is very unlikely to proceed. It has been argued that privately funded start-ups could have an advantage for launching a new aircraft program because "cannibalization" of existing product lines by a new entry is not a consideration for them. Neither is any concern that problems on a new supersonic program would leak over into other product lines. However, history has proven that even for small general aviation aircraft, successful start-ups in the aviation industry are rare. Due to the very high "barriers to entry" that technical staffing, testing and manufacturing infrastructure, and certification requirements present, there appear to be no historical examples of a start-up ever developing a viable airliner from scratch. To understand the Cost-Price-Market loop's impact on the airline's operating costs, and to facilitate cost versus benefit trade-offs in assessing technology increments, it is desirable to make some rough order of magnitude (ROM) economic assumptions. For instructional purposes, an example is given, without proof, of a plausible scenario for RSAC program economics (Figure 8).

The decision to provide an RSAC definition that relies on near-term technologies for airframe and engines, and uses a familiar "tube-and-wing" general arrangement provides a "least common denominator" baseline for future trades, optimization, and technology infusion. In terms of operating costs, the largest discriminator versus subsonic aircraft will continue to be fuel consumption and its associated costs. Fortunately, the over-arching prerequisite that any future civil supersonic aircraft must be environmentally acceptable to the regulators and in the eyes of the public will inherently promote fuel efficiency.

Example baseline economic scenario for feasibility/design trade metrics:

- $10 Billion airframe development (C-series, adj. for inflation, +50% for supersonic)
- $3 Billion propulsion development program (ROM estimate from past programs)
  ~13 Billion total program cost
- ~$180-200 Million ROM airplane unit cost to build (total, airframe + engines and systems, supplier ROI)
- =>$22 billion for development + 1st 50 units production ("early adopter" customers)
- ~$230-250 Million "sticker" price (~ 767-300ER x 1.15, or 2.7x A220)
- =>Target ~180-240 units to break-even
- Assumed sales target of 300-400 units production run over 12-15 years to saturate the market

- Relative operating costs vs subsonic types;
  - Future "low carbon" fuel prices including SAF mix, taxes/offsets ≥ 2-3x current Jet A
  - Higher crew training and per-hour crew costs (no common type ratings or other aircraft)
  - Higher maintenance & spares costs (proportional to aircraft price)
  - Higher insurance costs (proportional to aircraft price)

Figure 8- A Notional Scenario Basis for Economic Feasibility Trades

B. Environmental Considerations

The enduring design challenge for any civil supersonic aircraft, past or future, is a balancing act reconciling the diametrically opposed aero and propulsion needs of sustained supersonic cruise versus those required for subsonic operations and field performance, all while maintaining compatible flight operations, public safety and environmental acceptability. Along with safety (which must be equivalent to current generation subsonic types, or better), environmental acceptability is an over-arching prerequisite for the success of any future supersonic program. Environment-related concerns have continued to be; noise (sonic boom and landing/takeoff noise), climate impact (persistent contrails, CO2 emissions), ozone layer damage (nitrous oxide emissions), takeoff and landing engine emissions (soot, nitrous oxide, etc., similar to subsonic aircraft), and crew and passenger exposure to high altitude radiation. Supersonic programs must be prepared to fully address not only the regulatory aspects of these challenges, but also public perceptions. The US-SST program and Concorde production were both victims of great underestimation of the development time and cost, and underestimation of public opinion and the birth of environmental activism.

Nearly all aspects of the NASA SCR and HSR supersonic programs in the 1980's and 90's were connected in one way or another to reducing environmental impact. Throughout the 1990s, HSR, and industry's in-house HSCT R&D, made major strides in ejector-suppressor design for jet noise reduction, non-linear CFD-based multi-point full configuration aero shape optimization, CFD for engine turbomachinery design, multi-disciplinary configuration optimization (MDO) and engine cycle optimization, simultaneous optimization of structures for strength/stiffness/flutter, materials and composites manufacturing, and integrated fly-by-wire control of engines and multi-function control surfaces. By the end of the HSR program in 1999, the consensus was that, while a viable HSCT was achievable, the remaining R&D time and cost was prohibitive. A supersonic business jet was seen as a less risky, more achievable, stepping-stone toward supersonics, and several OEM's and research organizations in the U.S. Russian, and the EU continued on that track. Significant progress was made in

the early 2000's on shaping for reduced sonic boom and sonic boom test methods. Lessons learned from that effort carried over to the N+2 studies eight years after HSCT/HSR. One of the key findings was that simply slowing down from Mach 2-2.4 to Mach 1.6-1.8 did not necessarily negate the time benefits on most routes, but lowered the optimum cruise altitude enough to significantly reduce high altitude emissions concerns and make the time-integrated radiation exposure of crews and passengers similar to that of subsonic aircraft. Based on published N+2 concepts, the cruise altitude band for RSAC should begin at 43,000ft and be capped at 55,000ft. This altitude band is still high enough for contrail formation/persistence to not be an issue.

The reduction in altitude and Mach facilitated the use of medium bypass ratio engines, negating the need for the heavy and complex type of ejector-suppressor nozzles needed for HSCT's bypass 0.8 engines. Based on N+2 data and subsequent work, it is assumed that with some optimized combination of engine cycle (BPR/OPR/FPR), a low impact suppressor nozzle, and takeoff thrust reduction controlled by the engine's FADEC system, an RSAC type should be capable of meeting Stage 5/Chapter 14 LTO noise rules, consistent with current subsonic aircraft.

In the case of Concorde, the concerns over LTO noise were a bit overstated at EIS. At the few airports Concorde was approved to operate from regularly, abatement procedures made the Concorde's departure quieter than many older aircraft in service at the time. However, as newer aircraft powered by high bypass ratio turbofans and "hush-kitted" low bypass aircraft arrived and older turbojet aircraft were retired, the Concorde again began to stick out as the "noisy neighbor" of the fleet. By that time however, Concorde had the advantage that it was so few in numbers with so few arrivals and departures per day that few people were seriously annoyed, even by the occasional coastal sonic boom. In fact, the Concorde became a public curiosity and an icon of British and French technology. Even the fact that it burned significantly more fuel than subsonic airliners became not so much serious environmental concern as social annoyance to those who disliked the display of economic privilege. A future next-generation supersonic aircraft will not be successful unless it avoids being seen as the "noisy neighbor" regardless of certification compliance, and can legitimately show that its *net impact on fleet emissions* and CO_2 is insignificant. The latter argument is not out of the question, as will be discussed later.

During the HSCT program, the biggest concerns related to fuel consumption were associated with airline economics, world oil supplies (the end of "cheap oil"), and minimizing nitrous oxide emissions at the high cruise altitudes required for Mach 2.4 flight. A survey of articles and papers from the early 2000's (post HSCT) would indicate that there was still some healthy debate in the scientific and regulatory communities as to the certainty of climate change models and whether the relatively small (~2%) impact of airline CO2 emissions was a worry. By the time of the N+2 studies, the CO_2 footprint of future supersonic aircraft was a primary concern for Boeing, who's study pointed out that; a) some form of low CO_2 sustainable aviation fuel (SAF) would likely be needed, and b) the economic benefits of low-boom supersonic flight over populated areas would have to be weighed against the potentially higher weight, drag, CO_2 footprint, and development cost of minimum boom designs. Each of the proposed low-boom airliner concepts would involve longer-term/higher risk development of flight controls and aero-servo-elastic solutions, and manufacturing methods (especially for larger versions). Today, 15 years later, the airline industry, engine suppliers, and airframers are scrambling to meet agreed-to CO_2 targets and SAF's are still not widely available. Most estimates are that SAF's and SAF blends will cost considerably more than conventional jet fuel---a factor which needs to be accounted for when comparing subsonic and

supersonic operating costs. Today, there is still a lack of in-flight experimental data on the efficacy of designing for minimum sonic boom and Internation standards of boom measurement and acceptable limits have not been established. From this perspective, it was decided that, as it is intended as a base point for future optimization and technology increments, the RSAC definition should not be a "low-boom" design and instead should be focused on representing a design that strikes a balance between fuel-burn-per-seat metrics and acceptable passenger comfort.

In order to cover airline costs, supersonic ticket prices will be at least as expensive as subsonic business class on international flights (though ideally within 20%). Given that supersonic passengers will remain a "premium class" ticketing demographic, their per-seat fuel use and CO2 footprint on a subsonic flight are already 3 to 5 times that of an economy class passenger. Given the shorter flight times (~50-60% of subsonic block times) some percentage of subsonic premium flyers seem likely to switch to supersonic if the ticket surcharge is small. Given the reduced flight times, these supersonic flyers should be willing to "tolerate" a smaller cross-section and somewhat reduced personal space (though probably not as small as Concorde, for which the cabin was about the same as an EMB-175 regional jet). So hypothetically, a sufficiently "efficient" supersonic design would provide an option for some premium travelers to trade subsonic's maximum comfort and multiple meal services for less time spent on the plane, at roughly equal fuel use and CO_2 footprint. It can be estimated that if the transfer of premium passengers from subsonic to supersonic were large enough, it might allow an airline to restructure their fleet mix of aircraft, and passenger class mix, carrying a higher percentage of economy passengers on smaller subsonic aircraft resulting in potential for a net *reduction* in total fleet CO_2 (although effects of the re-mix on ticket prices and profitability are unknown).

People fly in premium classes for many reasons other than simply being "posh". Premium Economy seats, intermediate classes similar to domestic "First Class", and Business class tickets have shown increasing appeal to older travelers who need the leg-room and seat support for health reasons on long flights. People flying long distances with multiple connections across many time zones may seriously need uninterrupted sleep. Business travelers may need working space to prepare presentations. Theses uses indicate that in spite of pressure from some environmental groups, premium travel does have real health and socio-economic benefits for many travelers and is not likely to disappear anytime soon. Picking a potentially achievable target fuel efficiency level that puts the supersonic traveler on par with premium subsonic flyers would go a long way toward explaining the fuel consumption of the supersonic design. For instruction purposes, comparisons were done between Concorde, N+2 configuration examples, and several example air and surface transportation modes (U.S. DOT data). An economy class passenger flying on a current long-haul airliner was shown to have a carbon footprint potentially lower than that of a Toyota Prius passenger. The comparison showed that although Concorde had high fuel-per-seat consumption, it was probably still not as high as the top level of subsonic first-class service offered today by a few airlines.

A reasonable goal for per-seat fuel efficiency of the RSAC would put the RSAC passenger somewhere between the current U.S. average car or light truck, and the average international business class air passenger in terms of CO_2 footprint (Figure 9). This zone of fuel efficiency is similar to that shown to be technically feasible during the original N+2 studies (depending on configuration, range, Mach, and seating configuration). Advances since Concorde for the RSAC should provide fuel burn per seat advantages on a typical trans-Atlantic flight that approach 50% fuel savings relative to Concorde on trans-Atlantic missions (Figure 10).

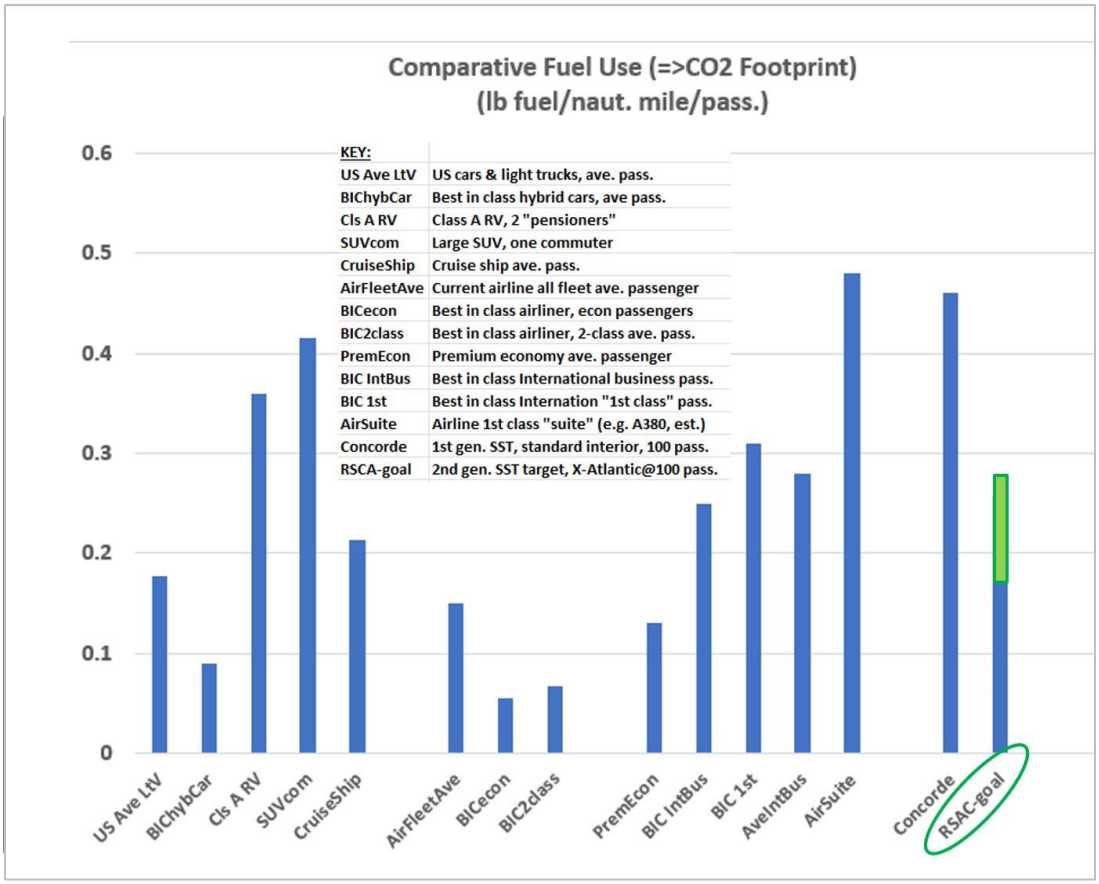

Figure 9- Comparative Fuel Consumption of Various Transportation Modes

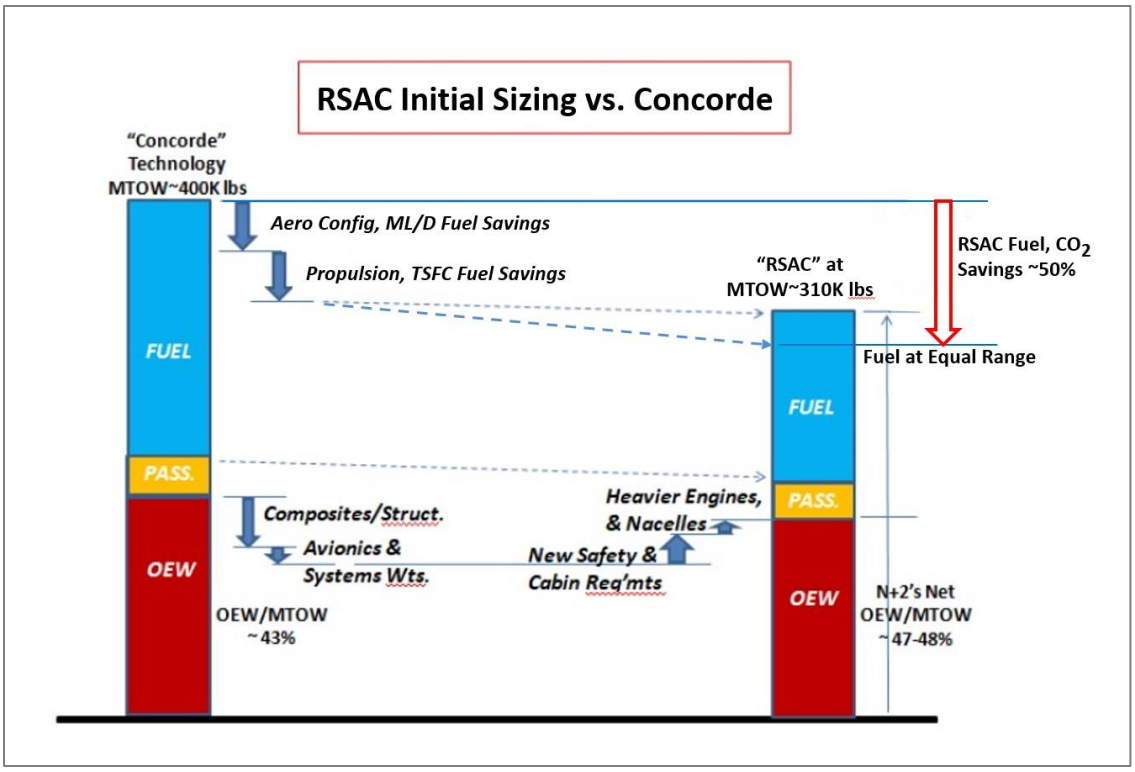

Figure 10: Projected RSAC Technology Fuel Savings Relative to Concorde

C. Range, Mach, and Mission Profile Considerations

Point-to-point routes and city-pairs of future interest dictate that the range capability of the RSCA needs to greater than Concorde (also Tu-144 and the proposed US-SST Boeing 2707). Detailed review of the N+2 speed and range trades confirmed that the N+2 nominal range and Mach assumptions still apply for RSAC, validating the choice of Mach 1.6 as the nominal cruise requirement and Mach 1.8 as the maximum cruise speed (objective).

If the next generation airplane is to capitalize on point-to-point capability for end-to-end time savings rather than a hub-and-spoke model (or at least be able to use non-coastal hubs), then the subsonic over-land flight segments actually need to have lower operating cost and longer range than at supersonic conditions. More supersonic airplanes making more frequent flights over areas of the world with more population than existed in the 1970's-90's, means it is more likely that some jurisdictions will not permit supersonic flight over water in some coastal and island zones. This means that for some flight segments, RSAC will need to be subsonic. While Concord was able to fly over-land at subsonic speeds, it was basically a point-design for Mach 2 over-water missions and suffered a significant fuel burn and range penalty when subsonic. The RSAC configuration needs to be designed to have more operational flexibility.

Today's CFD capability for optimizing the full 3D configuration simultaneously for multiple operating points can give a much shallower trend of range versus Mach. The use of "variable camber" (small cruise leading and trailing edge deflections), and trim optimization with a 3-surface longitudinal control arrangement can further improve fuel use and range at intermediate Mach numbers. Additional operating flexibility can be gained by selecting a supersonic "long-range cruise" speed that is slightly slower than maximum Mach and which can be reliably sustained even on hot days when faster cruise Mach may be temperature limited (engine thrust and airframe/systems temperatures. Totaling the effect of these elements shows the comparative range capability estimated for RSAC versus cruise Mach (Figure 11).

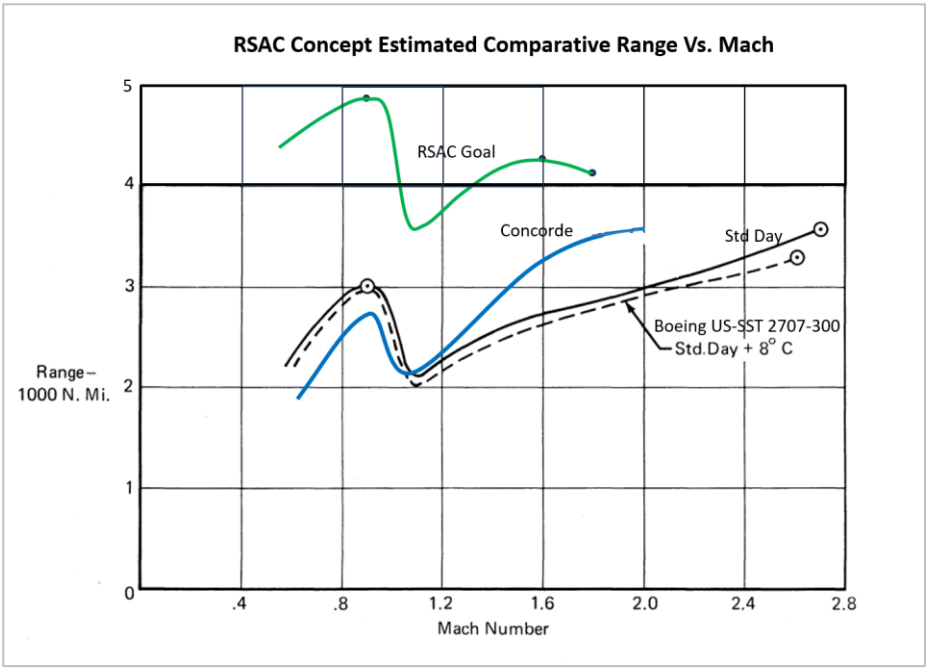

Figure 11- RSAC Projected Range Capability vs. Concorde and US-SST (2707-300)

The Boeing Supersonic Mission Profile (used in the N+2 /N+3 studies) was still deemed appropriate for the RSAC sizing and performance assessments, with the exception that it was updated with a 100nm subsonic cruise leg, added at each end of the supersonic cruise in order to make the profile more representative of actual city-pair over-water missions (Figure 12).

RSAC Performance/Sizing Follows Published Boeing Mission Profile
+ 100nm Subsonic "Cruise" Segment At Each End of The Mission

Boeing Mission Rules (NASA/CR-2010-216842)

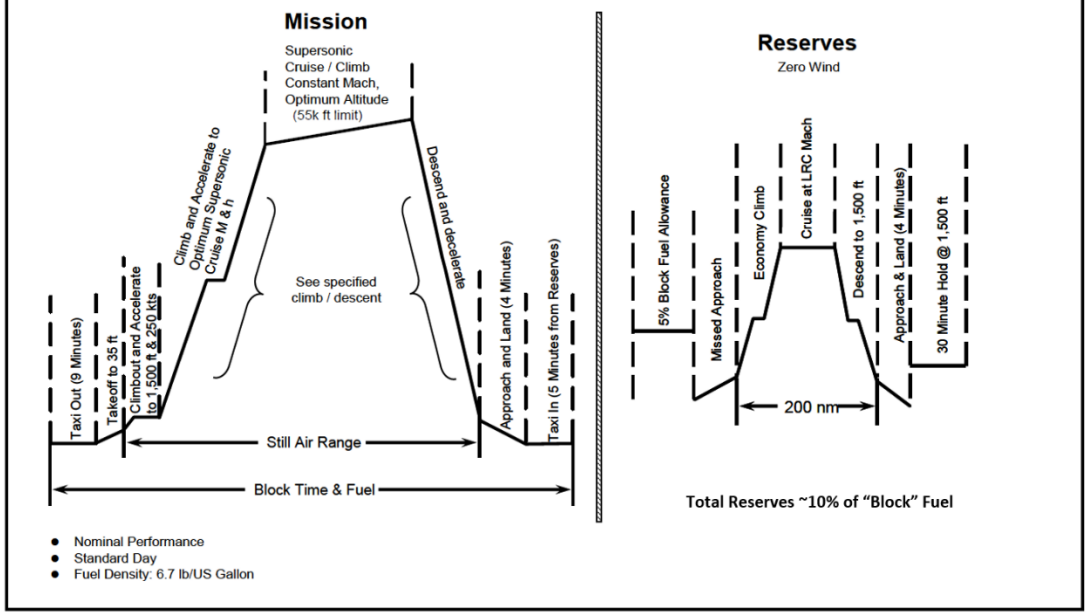

- Nominal Performance
- Standard Day
- Fuel Density: 6.7 lb/US Gallon

Boeing Mission Rules

Climb / Descent Schedule

Mission Profile	ALTITUDE (FT)		MACH		Notes
	Initial	Final	Initial	Final	
CLIMB	1500	10000	0.39	0.45	Climb at 250 KCAS from 1500 ft to 10,000 ft
CLIMB	10000	10300	0.45	0.69	Accelerate to 375 KEAS at roughly constant altitude (10,300 ft)
CLIMB	10300	20774	0.69	0.85	Climb at constant 375 KEAS to Mach 0.85 (~20,800 ft altitude)
CLIMB	20774	35000	0.85	0.85	Climb at constant Mach 0.85 to 35,000 ft
CLIMB	35000	39000	0.85	0.95	Climb and accelerate to Mach 0.95 at 39,000 ft
CLIMB	39000	41000	0.95	M-crz	Climb and accelerate to Supersonic Cruise Mach (1.6 to 2.0) at 41,000 ft
CLIMB	41000	h-opt	M-crz	M-crz	Climb to optimum initial cruise altitude
					Climb/Cruise with 55,000 ft maximum altitude
DESCENT	53000	39000	M-crz	0.95	Descend & decelerate to Mach 0.95 @ 39,000 ft
DESCENT	39000	34960	0.95	0.85	Descend to Mach 0.85 and 273 KEAS (altitude ~ 35,000 ft)
DESCENT	34960	20774	0.85	0.85	Descend at Mach 0.85 and 375 KEAS (altitude ~20,800 ft)
DESCENT	20774	10300	0.85	0.69	Descend at constant 375 KEAS to ~10,300 ft
DESCENT	10300	10000	0.69	0.45	Decelerate to 250 KCAS at roughly constant altitude (10,000 ft)
DESCENT	10000	1500	0.45	0.39	Descend to 1500 ft at constant 250 KCAS

- Nominal Performance
- Standard Day
- Fuel Density: 6.7 lb/US Gallon

Figure 12- Boeing Supersonic Mission Profile

In today's crowded airport environment with high volumes of closely spaced landing approaches, is it unlikely that future supersonic aircraft can be assured of any "special" ATC handling in order to sequence in with subsonic traffic, particularly if the next supersonic product is successful and there are many of them in operation. However, the high approach speeds of supersonic types can be a significant constraint on airplane wing loading sizing and approach attitude. Significantly higher approach speeds have been suggested as certifiable or "manageable" for some proposed supersonic concepts, including those proposed for higher cruise Mach numbers and those with wing planforms constrained by low-boom design. Requirements for landing approach speeds and maximum landing weight were re-examined to see if there was any reason to change the N+2 vintage assumptions. The FAA's online Aircraft Characteristics Database was used to see how the proposed N+2 Vref speed of 155 knots compared with the trend of other aircraft versus size (takeoff gross weight) shown in Figure 13. This comparison confirmed 155 knots is on the high end for all aircraft sizes and 15knots faster than the average aircraft in this TOGW category. The proposed 155 knots target was also evaluated relative to trends versus maximum landing weight (MLW) in Figure 14. On this basis the proposed speed was also within limits but higher than most other aircraft. The proposed MLW of the RSAC was also compared to other aircraft to see if it might be reasonable to lower the approach speed by declaring a lower maximum landing weight. That comparison confirmed that the proposed MLW /MTOW ratio for the RSAC is already at the low end of the trend of all other aircraft (Figure 15). On this basis the MLW requirement for RSAC was held at 220,000lbs and the approach speed Vref at MLW was kept at the original 155 knots. It is assumed that operational approaches would be flown at Vref +7 knots.

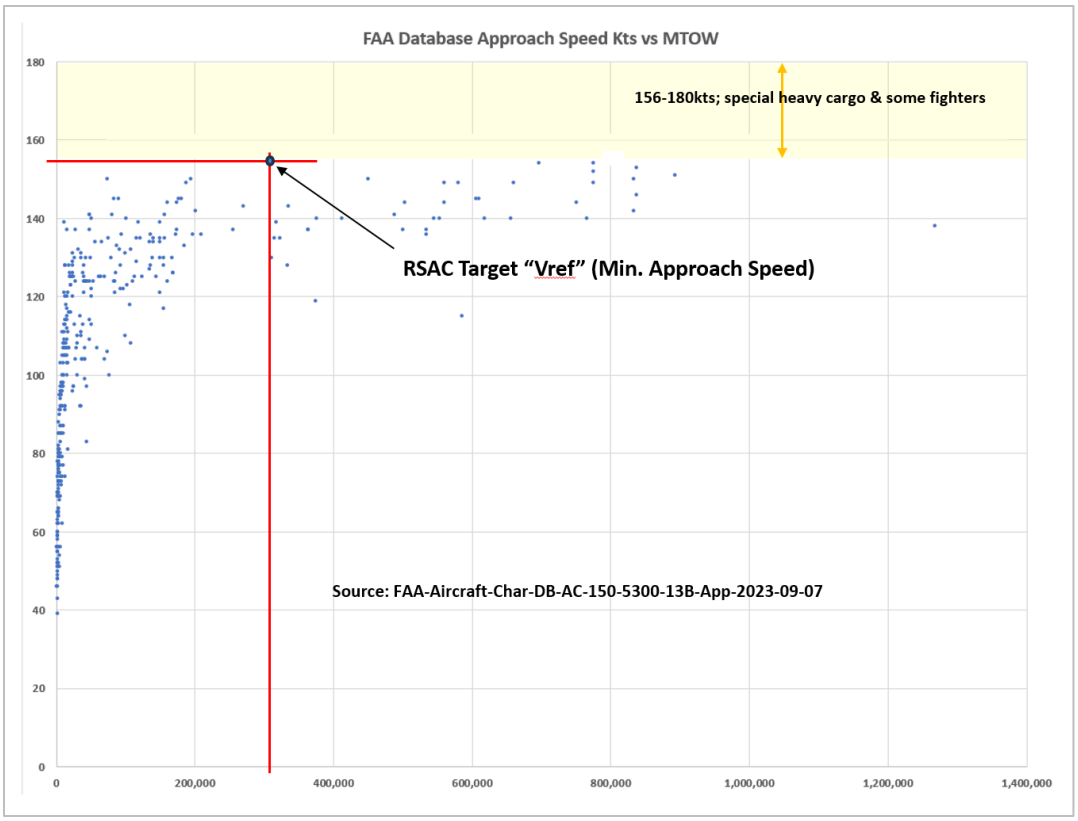

Figure 13- Comparison of Proposed RSAC Vref vs. TOGW

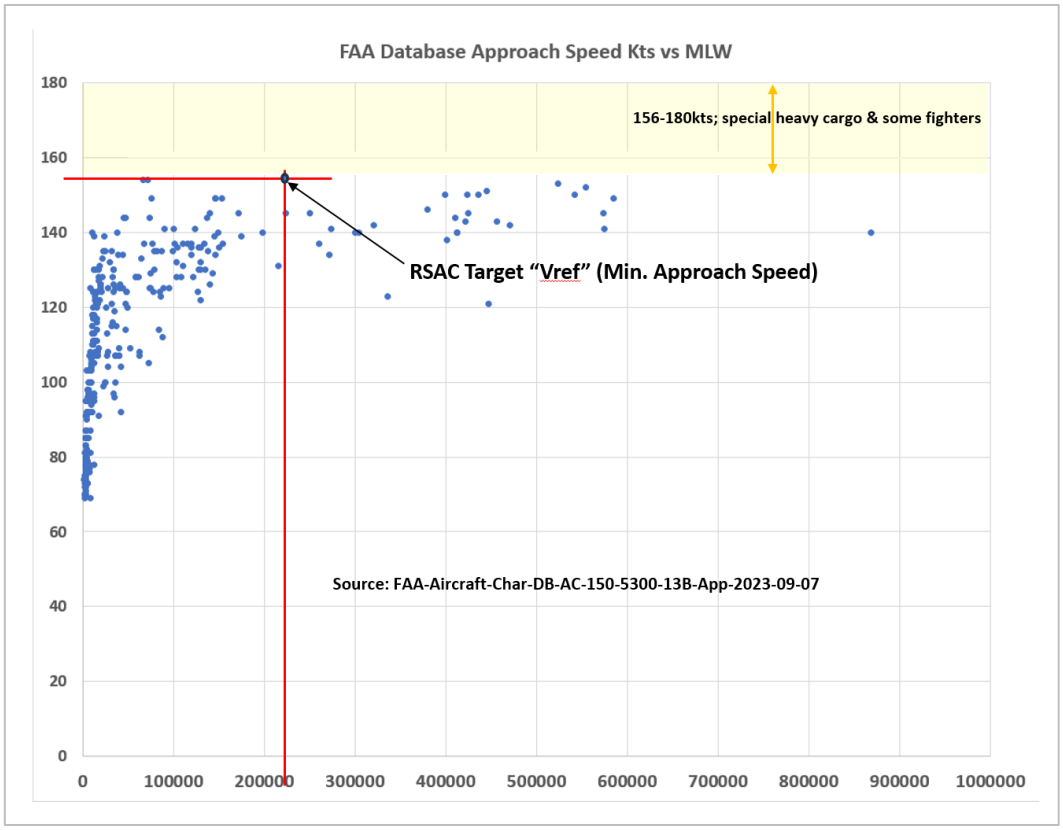

Figure 14- Comparison of Proposed RSAC Vref vs. Max. Landing Weight

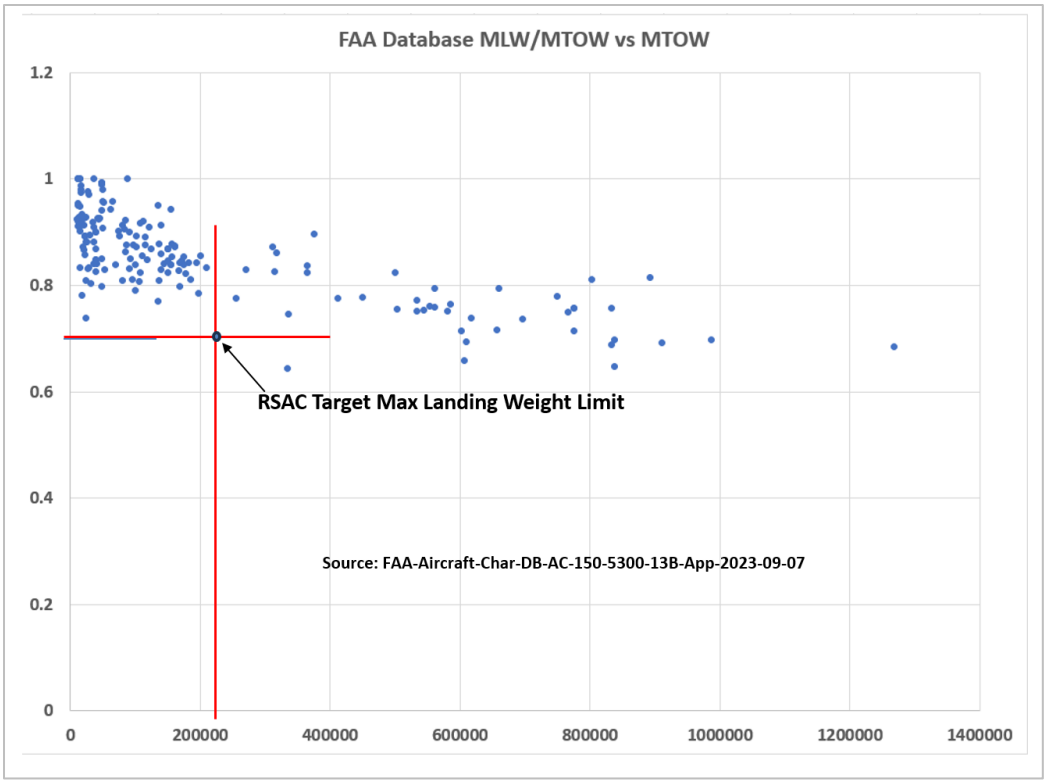

Figure 15- Comparison of Proposed RSAC Landing Weight/TOGW Fraction

D. Combined Requirements Summary

A summary of the combined top level RSAC requirements has been tabulated here for reference:

RSAC Proposed Tier-1 Requirements (Rev. 9, 2023-24)		
Specification	**Requirement (Nominal Perf.)**	**Objective (Stretch Goals)**
Design Range Mission Profile 1	Boeing N+2 Rules+100nm Sub. Ends	Boeing N+2 Rules+100nm Sub. Ends
Supersonic Range @ 90-100 pass.	4000nm	4300nm
Supersonic Cruise Mach	Mach 1.6	Mach 1.8
Subsonic Range/Mach	4450nm, Mach 0.90	4800nm, Mach 0.95
Takeoff/Landing Field Length (SL)	10,000ft / 8500ft	9000ft / 7000ft
Maximum Sized TOGW (lb)	< 320,000lb	< 300,000 lb
Landing Approach Vref @ MLW	155kt	<155kt
Max. Airport Elevation	3000ft	5000-7300ft (Mexico City)
Supersonic Cruise Alt. (Emissions)	43-55,000ft	43-55,000ft
Subsonic Cruise Altitude (ATC)	39,000ft +	39,000ft +
LTO Noise Certification	Stage 5/Chapter 14	Stage 5/Chapter 14 with margins
Cabin seating (exec./spec./econ.)	40/75/120 passengers	60/110/150 passengers
Spec. Interior: Narrow-Body Domest. "1st Class"	80 seats at 38" Pitch, 17-19" min. aisle width	100 seats at 38" Pitch, 17-19" min. aisle width
Baggage/ Bulk Cargo Volume	725 cu ft, 39" crawlspace	< 900 cu ft, belt cargo loader
Fuel burn/seat @3580nm range	0.30 lb/nm/seat	0.28 lb/nm/seat
Sonic boom (over-water operation)	< 2.4 psf N-wave	< 2.0 psf modified N-wave
Flight deck vision	XVS forward vision, side windows	FAR vision polar, +XVS for 3-sec rule
Certification Basis	FAR 25 + Special Conditions	FAR 25 + "Supersonic" Rules
Technology Level Required	Near Term, EIS ~ 2036	Near Term, EIS ~ 2032

III. RSAC Configuration Development

A. Concept Ancestry

The RSAC configuration's "family tree" originated with the UW-S-15 configuration which was one of a series of three exploratory designs supporting a USAF (AFRL) sponsored capstone/graduate student project. This 3-year project, also supported in-part by UWAL and Boeing Commercial Airplanes' Advanced Concepts organization, investigated options for eliminating or significantly reducing the size of vertical tail surfaces on aircraft designed for extended "supercruise". If successful, significant reductions in vertical tail/rudder size could save weight and wetted area drag, improving cruise efficiency (and potentially reducing radar cross-section). A modular wind tunnel model was built for this investigation in 2013 and tested several arrangements including a unique over-under engine arrangement with upper-surface inlets. An alternate concept, featuring differentially moving dihedraled canards and upper-surface wing spoilers, was wind tunnel tested in with a new model in 2014. The 2015 effort tested a "referee" configuration of more conventional layout, intended to compare the relative effectiveness of side-to-side thrust vectoring nozzles as a means of providing the yaw stability augmentation and control authority needed to reduced vertical tail sizes. In all 3 years, students, under the guidance of faculty and industry advisors, and coordinating with external hardware vendors, were directly involved in the process of configuration synthesis and wind tunnel model parts design. In all 3 years, the students also designed and built large instrumented radio-controlled models (Research UAV's, RUAV) of the preferred concepts (Figure 16). Although the novel arrangement of the 2013 team's final "Starfox" concept produced favorable wind tunnel results, complex fabrication challenges and tight schedules forced the R-UAV version to be abandoned before it was flight-ready.

Figure 16- Configuration "UW-S-15" Origins

For the purposes of the AFRL investigation, it was not necessary represent specific full-scale aircraft. The stated objective of the 2015 investigation promoted the selection of a more conventional “tube-and-wing” general arrangement with a conventional aft-tail. New components were defined for the 2013-vintage modular wind tunnel model to represent a generic long-range supersonic cruise aircraft based on the general arrangement of Boeing’s N+2 concept “765-070A” (shown previously in Figure 1). In this configuration, the modular model had provisions for several canards, leading and trailing edge flaps, and two sizes of horizontal tails to be wind tunnel tested (Figure 17).

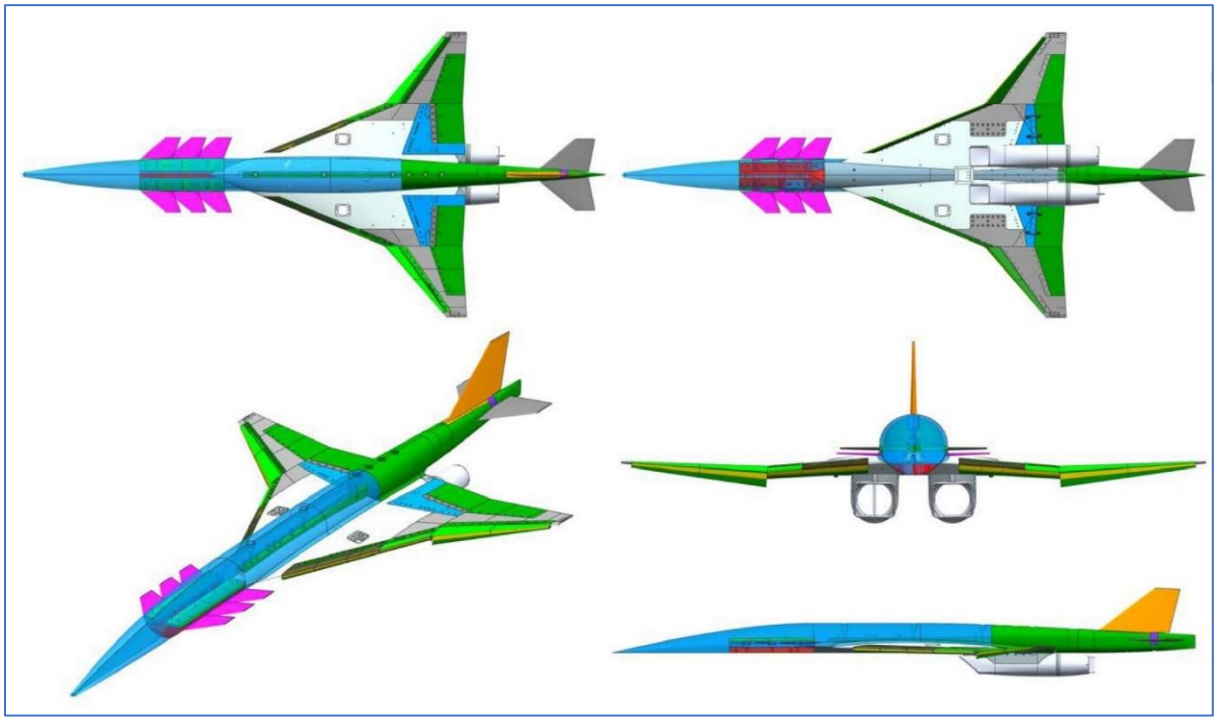

Figure 17- The KWT Modular Model As Configured For 2015 Testing

The configuration chosen for the R-UAV down-selected to a slightly smaller canard option mounted in the forward-most position, and the larger of two horizontal tails tested. This provided a combination of increased static pitch stability and control authority that allowed the R-UAV’s flight-demonstration CG to be slightly farther forward than would be optimal for a full-scale aircraft. In order to meet the goals of eventual vertical tail size reduction, the nacelles were spaced closer together than those of the “070A” concept in order to reduce engine-out yawing moments to a manageable level. This necessitated the main landing gear to be located outboard of the nacelles and would have required them to retract into fairings along-side the nacelles, similar to the Sukhoi Su-27/30/34 series. This feature was not replicated on the R-UAV however because the sub-scale flight demonstration would be done at low maneuver speeds, so the R-UAV was constructed with a fixed landing gear. Given the desire for more manageable pitch stability without augmentation on the R-UAV, the farther forward CG also resulted in a farther forward and taller main landing gear which would have made retractable gear kinematics a bigger challenge at model scale. The nacelles did not attempt to duplicate the type nacelles used on the 017A concept, instead being designed for the R-UAV’s twin electrically-driven ducted fan propulsors (EDF’s) used to simulate the full-scale turbofans, both for the flight test article and in the wind tunnel. The resulting 2015 capstone design configuration UW-S-2015 is shown in Figure 18.

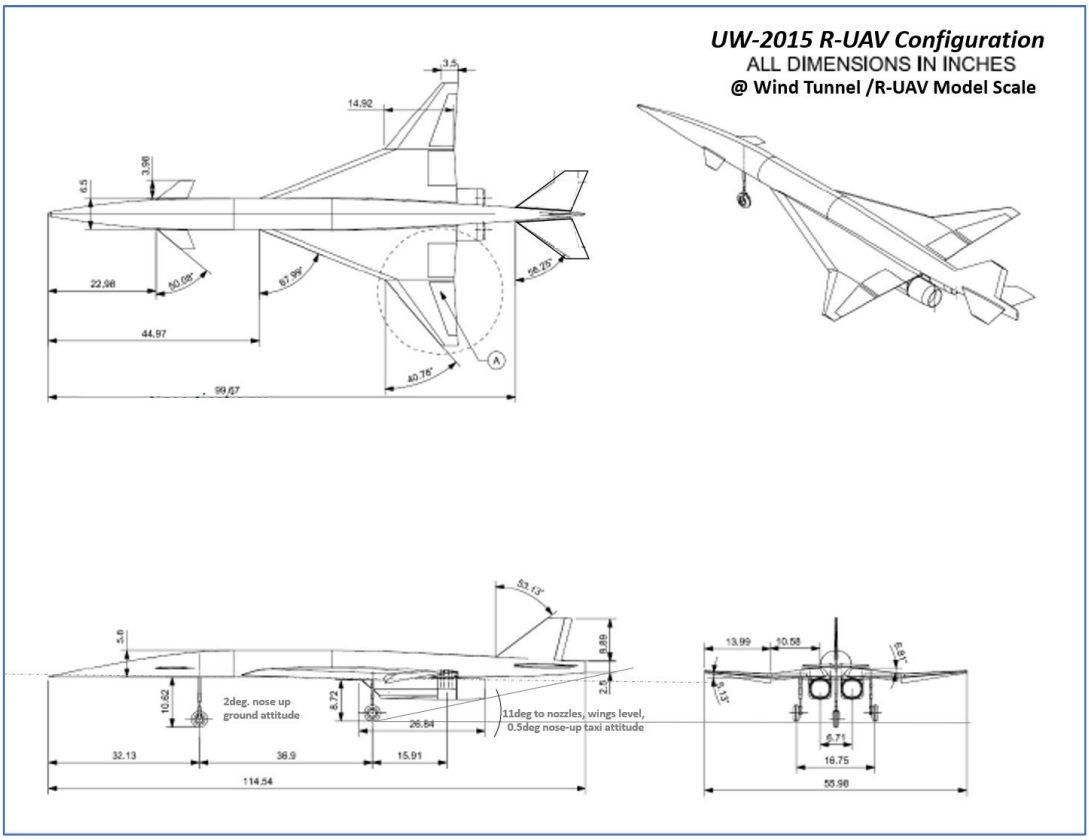

Figure 18- The UW-S-2015 "TVRA/BigBird" R-UAV

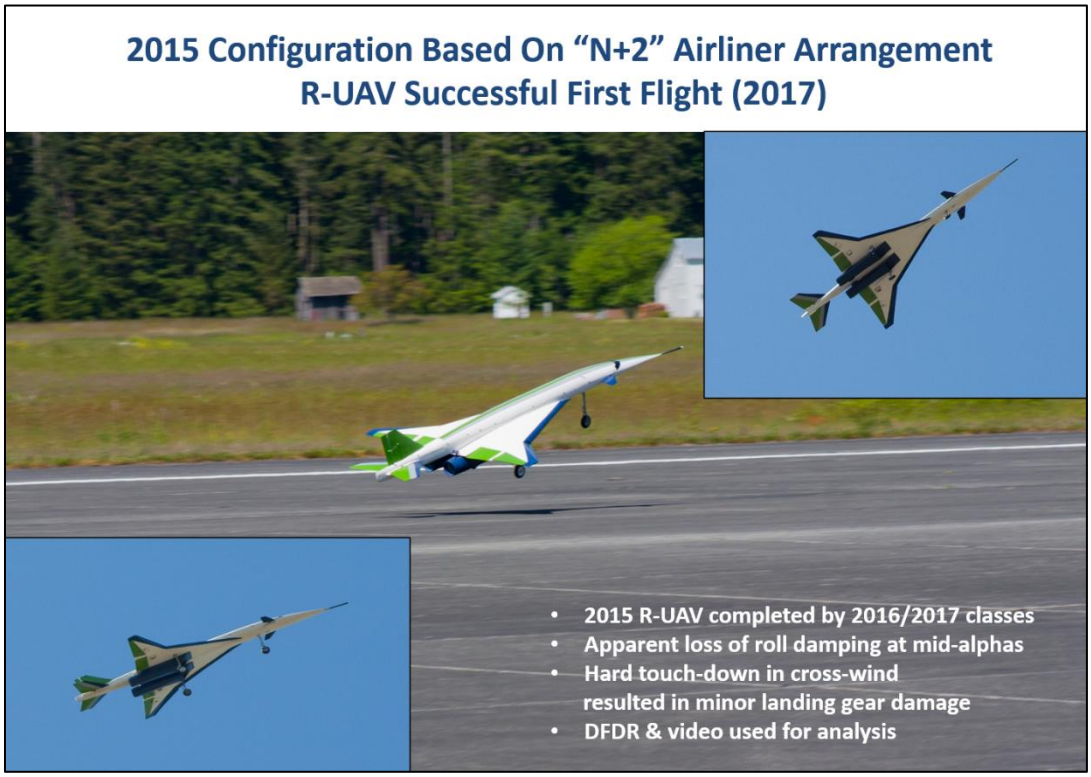

Figure 19- R-UAV Flight Testing of the 2015 Concept Plane

The nine and a half foot-long R-UAV was constructed at 1:1 size ratio relative to the KWT test model. After initial ground checks and taxi tests, the R-UAV required a number of hardware modifications. Modifications and flight testing carried out by the 2017 capstone class (Figure 19) indicated that possible improvements would include increased static yaw stability, the addition of a roll-damper, and reduced horizontal tail trim drag with trailing edge flaps deflected. The R-UAV was "mothballed" for possible future uses.

In early 2020 The SCALOS capstone students worked with advisors to define the first new wind tunnel parts required for testing at KWT, and Boeing BR&T's FVWT facility which would be used for water tunnel flow-visualization and dynamic stability derivative testing. These initial parts included new nacelles more appropriate for representing an "N+2" class full-scale airliner, and new horizontal and vertical tail components. The tail components would allow the first round of SCALOS testing to assess the potential modifications to the 2015 R-UAV configuration, and to compare the effects of the horizontal tail's height location relative to the plane of the wing trailing edge. Other features of interest for initial SCALOS testing included more highly swept outboard wing panels (potentially favorable for vortex lift generation, supersonic L/D and reduced sonic boom), and investigating the effects of mounting the nacelles above the wing (an opportunity for reduced sonic boom and partial noise shielding of inlet and jet exhaust noise at landing and takeoff conditions). The new "N20" nacelles were defined based on a bypass ratio 3.5-3.7 "N+2" study mixed-flow turbofan engine (e.g. see NASA/CR–2013-217797). This choice was partly based on reasoning that the N+2 candidate engines with low jet velocity for low LTO noise would have the largest nacelles, therefore providing test data on the largest likely aerodynamic

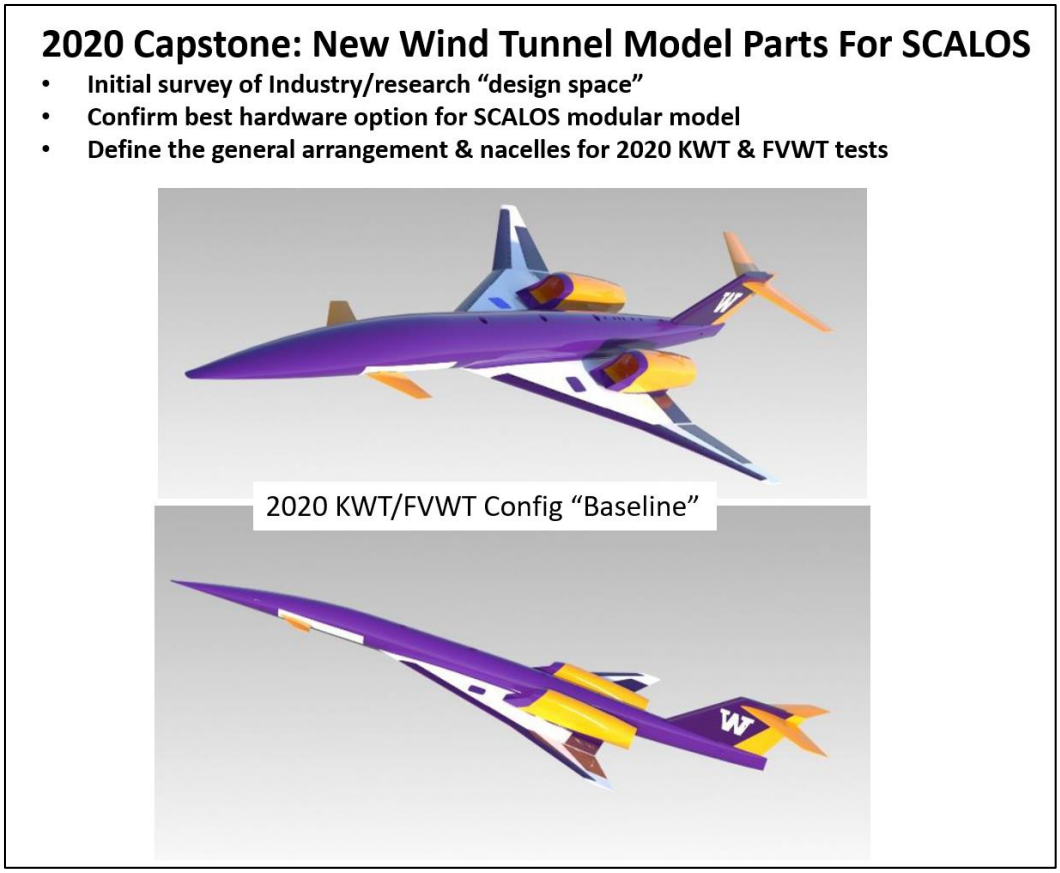

Figure 20- Initial SCALOS Wind Tunnel Configuration "UW-S-20A"

effects for each engine location to be evaluated. The inlets for the new nacelles were chosen to provide external lines representative of Boeing's N+2 "ECRI" type inlet concept (see AIAA-2014-3802). The strut-diverter portion was designed to be a replaceable interface allowing the same nacelle shapes to be installed either inverted above or upright beneath the wing. The wind tunnel model configuration selected for the first SCALOS tests in 2020 combined the T-tail arrangement, over-wing nacelles, and the increased outboard sweep wings. This "UW-S-20A" configuration (Figure 20) was the first configuration released to BR&T for them to begin FVWT model design and fabrication before other geometry had been defined for the KWT testing. It was designated as the interim SCALOS "baseline" for test planning purposes.

In light of the strong interest in it's potential for noise-shielding, the UW-S-20A configuration was initially also considered as the platform to develop into the RSAC. (MD-90 had ~7dB lower cumulative LTO noise than A319 largely due to shielding effects of its aft-body engine location!). However, when the first KWT wind tunnel results became available, the T-tail arrangement (necessary given the over-wing nacelle exhaust location), was shown to have much more non-linear pitching moment behavior and an earlier CLmax (Figure 21) relative to a modified version of the 2015 R-UAV configuration with updated nacelles, and low-mounted horizontal tails.

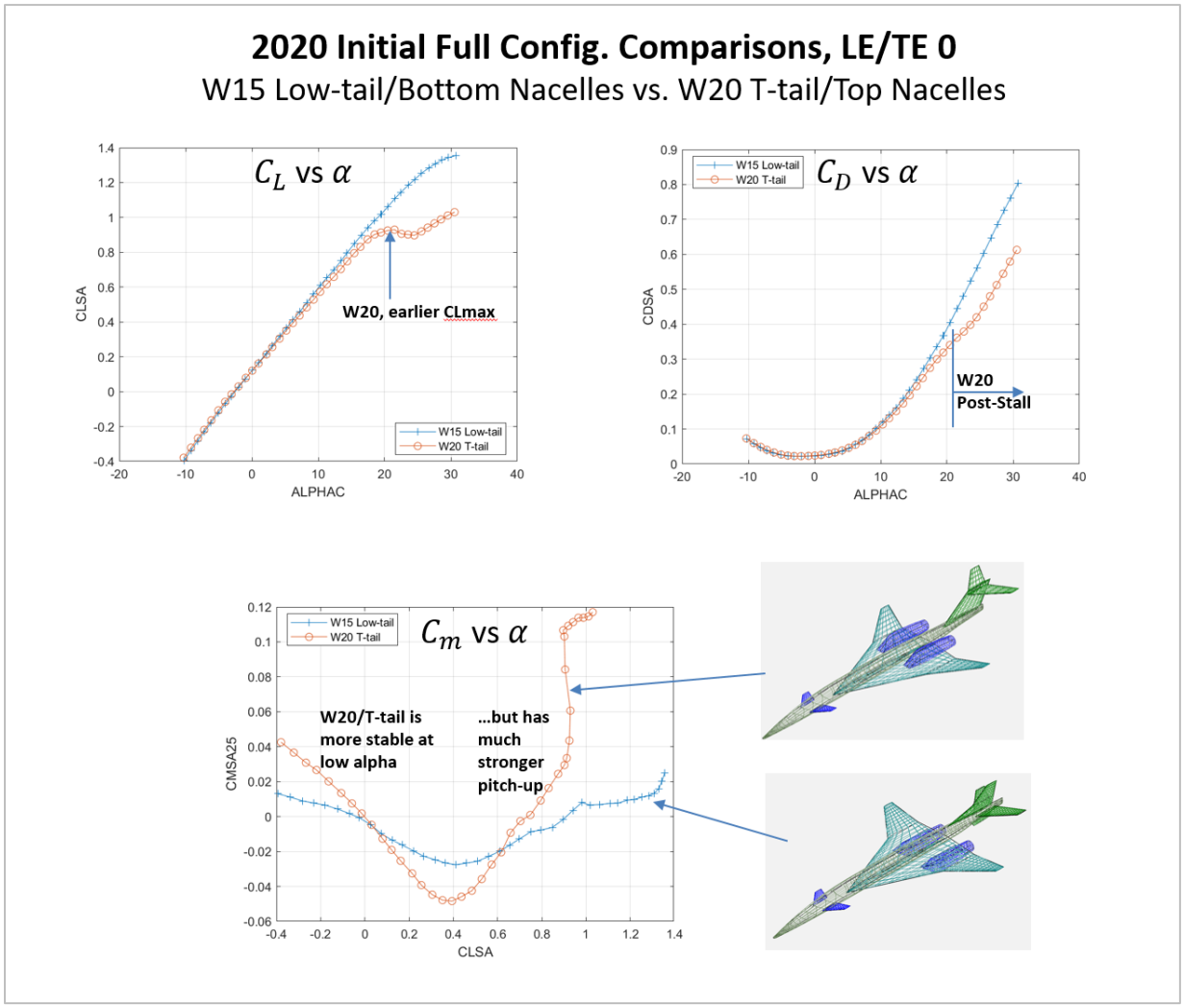

Figure 21- UW-S-20A T-tailed Configuration Longitudinal Test Data vs UW-S-21A

Because the RSAC was intended to serve as a well-behaved “anchor point” against which to trade-off alternate concepts it required a configuration closer to middle of the design space. This removed the T-tail UW-S-20A concept from consideration as the basis for the RSAC. The 2015 R-UAV configuration, updated with the new SCALOS “N20” nacelles moved farther apart, ventral and dorsal fins to improve the yaw stiffness, and a higher aspect ratio horizontal tail (H20) to reduce the tail’s induced/trim drag, became the starting point for development of an RSAC-specific configuration. This SCALOS test configuration, designated UW-S-21A (Figure 22), became a de-facto baseline configuration for the rest of the SCALOS wind tunnel testing program.

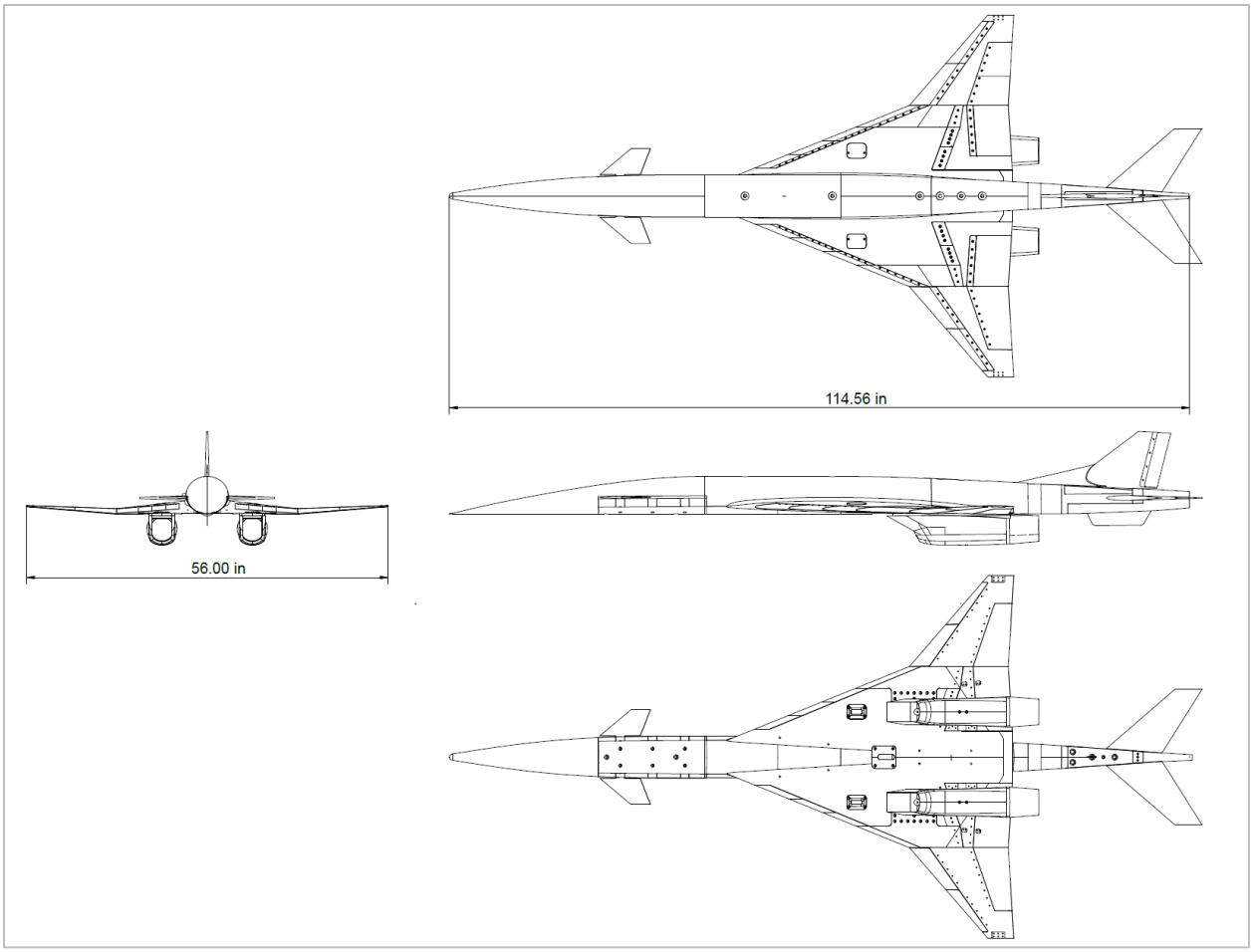

Figure 22- ‘S-21A Wind Tunnel Model, Wing W15, Low-Tail, N20 Nacelles, Ventral & Dorsal Fins

B. Conceptual Design Objectives and RSAC General Arrangement

Given the heavy involvement of students in the SCALOS project, and the study ground-rules allowing only open-source non-proprietary data, the RSAC team had to synthesize a technically reasonable integrated configuration using only data from past UW projects, the current SCALOS aerodynamic findings, and public data sources. The overall design "philosophy" adopted was:

1) Provide a "vision" of what a near-term supersonic airliner could be like,

2) Within conceptual design limitations, the design should be a technically credible, certifiable, "closed"

3) Include reasonable "place-holder" solutions for features or systems that are undefined,

4) Technology levels required should have TRL's high enough to require only "maturation" before production/cert as part of a new airliner development program (e.g. 787, 777X, A380), not major R&D.

The general arrangement and "cranked" wing planform of the modular model wing "W15" are intended to reflect a compromise between high average sweep, short-span wings favored for supersonic cruise point-designs and low-boom, and the lower sweep, lower span-loading planforms that favor subsonic aerodynamics. The 070A N+2 configuration which inspired the UW-S-15 configuration was, in-turn, a scaled-down, lower Mach version of the "2015TC" HSCT, the final "Technology Concept" benchmark aircraft under the HSR program (see NASA CR-2005-213584/VOL1). The W15 wing has a somewhat simplified planform with slightly less outboard panel aspect ratio and sweep, and lacks the higher sweep "strakelet" blending the wing to the side-of-body (needed for HSCT's Mach 2.4 cruise speed).

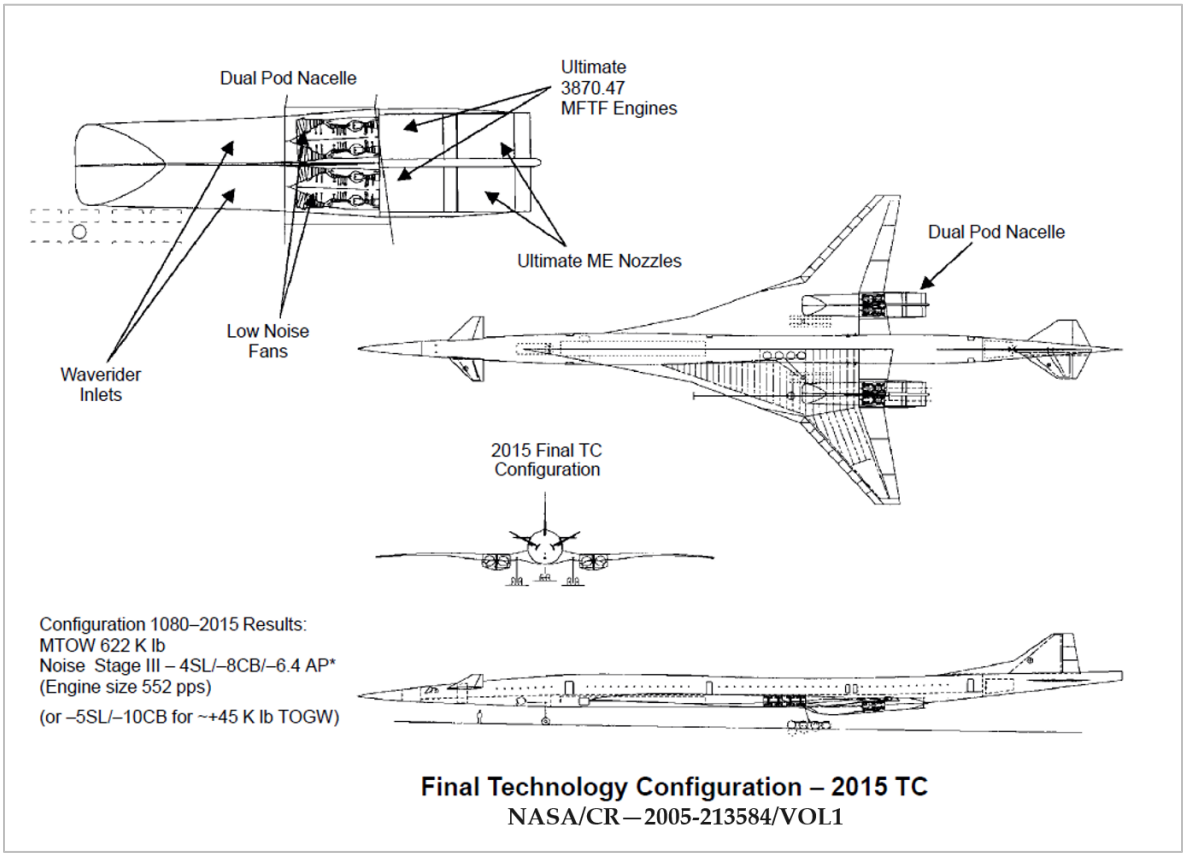

Figure 23- NASA HSR "2015TC" HSCT Technology Concept Benchmark Airplane

The 2015TC was the end-result of several years of aerodynamic, propulsion, acoustics, and structures trades, testing, and Multi-Disciplinary-Optimization (MDO). It's general arrangement and wing planform exemplified an optimal compromise balancing subsonic, transonic, and supersonic performance with structures and LTO noise constraints. The projected mission performance was an impressive 5000nm range at Mach 2.4, carrying 300 mixed-class passengers with a 667,000lb takeoff weight, while limiting LTO cumulative nose to 21.5dB below Stage 3 (i.e. Stage 5/Chapter 14 with 4.5dB margin). Due to economies of scale, the fuel consumption per seat mile would have been even better than the current RSAC goals, and only about 10-15% higher than the current subsonic fleet average.

A number of the constituent technologies, engineering tools, and design/test methods developed under the HSR program have seen application to multiple airplane and engine programs over the past 25 years. Most in-depth additional development in supersonics since the 1990's has been dedicated to further improvements in supersonic cruise optimization and sonic boom prediction/design/testing. Low sonic boom designs clearly favor higher sweep and shorter wingspans, however, the "cranked" wing planforms still seem to provide the best chance of meeting LTO performance and noise requirements in lieu of a major breakthrough in propulsion or integration/materials technology. The SCALOS effort tested 3 wings of higher sweep and/or aspect ratio than the RSAC's W15, and 3 planforms of higher sweep and lesser degrees of "crank" in the leading-edge sweep angles, providing a good database for future trade studies on the LTO performance and noise, and various leading and trailing edge flap configurations.

The SCALOS project was primarily focused on collecting wind tunnel data on a broad range of aerodynamic configurations. The configuration variations in tail location, leading and trailing edges and wing planforms were semi-parametric. Several engine locations and nacelle types were investigated. These variations in the propulsion system integration were done with nacelles defined assuming a constant engine size. The common engine/nacelle size parameters were selected to provide the right proportions between the physical nacelle size and the wing and body sizes, based on thrust and wing area sizing of the 070A, 072B, and 078 concepts from the Boeing N+2 contractor report (NASA CR-216842).

C. Propulsion System Definition

The 2020 capstone class was charged with helping define the common nacelle, "N20", that could be tested on the upper-aft or bottom-aft (N20B) wing surface, or side-mounted on the aft fuselage. It was originally hoped that this nacelle could also be tested on the forward part of the wing, above and below the leading edge (a la B-58 or Aerion AS2), but this proved to be beyond the mechanical and structural capability of the modular model geometry. Published drag data for 070A was simply adjusted by the estimated differences in wetted area and aspect ratio to approximate the drag levels expected for the RSAC using W15. This confirmed the reasonableness of using the same relative nacelle-to-wing proportions on RSAC as being used for the SCALOS wind tunnel models.

Around the time the design of the N20 nacelles began, so did the COVID epidemic. The UW team had initially proposed to use data for a specific N+2 engine cycle, but understandably under the remote-only work situation, they had trouble reconstituting specific ten-year-old engine decks which would have required getting support from Georgia Tech, Boeing, and/or NASA. It was soon realized that for the purposes of both the SCALOS low speed testing and generating reasonable RSAC configuration details, specific optimized engine cycle data was not necessary. What *was* needed was simply performance trends representative of the best-compromise N+2 study engines, representative weights, and corresponding external dimensions of an N+2 technology engine and nozzle with those characteristics. Likewise, any internal details of the inlet or nacelle flow-path were unnecessary so long as the aero OML was representative of an appropriate inlet concept. Students used AEDsys software

package's ONX cycle code, and airplane sizing software to better understand the propulsion system sensitivities (Figure 24). The 2D external compression inlet analysis code was used to better understand axi-symmetric supersonic inlet design sensitivities.

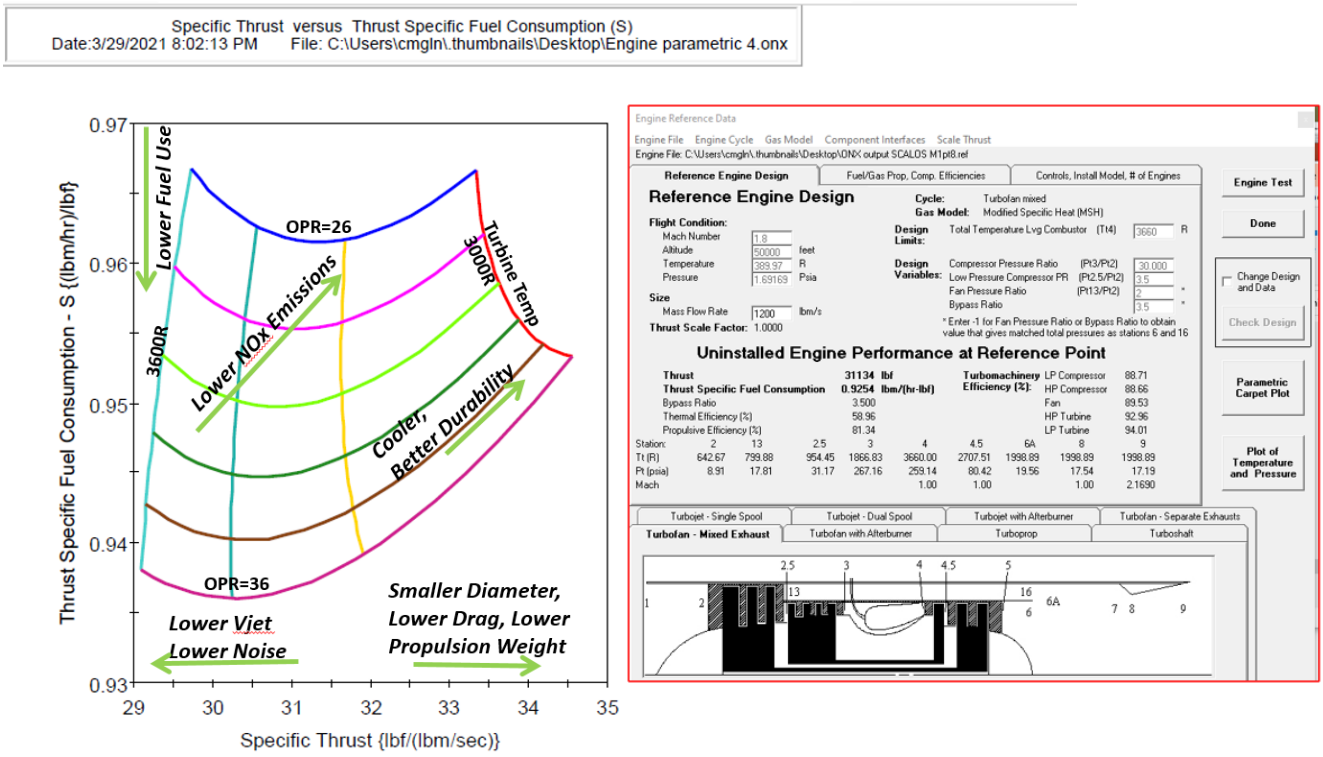

Figure 24- AEDsys Engine Cycle Sensitivity Exercise

Cycle sensitivities investigated with the AEDsys cycle software did not include capability for "variable cycle" modeling. In the Mach 1.6-1.8 cruise regime, fan pressure ratios can be reduced by 1/3 or more relative to the Mach 2.4 HSCT concepts. Some combination of "variable cycle features" would likely benefit the RSAC MFTF engines to allow "fine-tuning" of the TSFC versus Mach at on and off-design operating points. More aggressive variable cycle engines (VCE) with 3 flow streams and more complex nozzles have been investigated for their potential additional benefits (mainly allowing lower cruise bypass ratio, reducing the required engine/nacelle size). However, as of the 2020 start of the SCALOS effort those concepts were assessed at being at too low a TRL (technology readiness level) to meet the objectives of the RSAC as a technology base point. At AIAA SciTech, in 2018 NASA Glenn presented an overview of low-noise supersonic propulsion work (AIAA 2018-0265). Given the resulting trend of noise versus range, the study concluded "VCE's are not significantly better than mixed flow turbofans, given [Chapter 14] noise restrictions" (Figure 25).

Early exploration of Variable Cycle Engines (VCE)
Fan stage count

- Increasing FPR produces smaller engines, more range.
- As FPR further increases, fan losses become prohibitive—add fan stages.
- As fan stages increase past 2, engine weight increases and max range suffers.
- Two-stage VCE significantly better range than two-stage MFTF.
- At FPRs where jet noise is tolerable, the mixed flow turbofan gives comparable or better range.

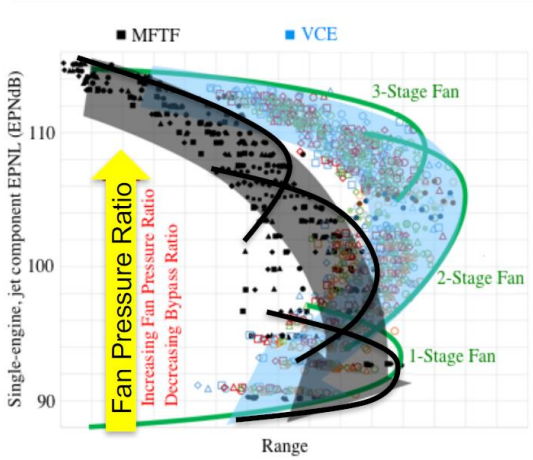

Figure 25- VCE Engine Potential for Low-Noise Supersonics -NASA Glenn 2018

With no proven significant net performance or noise advantage for the more complex VCE options and multi-stream nozzle concepts, the team turned to the engine cycles presented in N+2 study CR's by Boeing, Lockheed, Rolls Royce and NASA. The "representative technology level and cycle" engine down-selected was roughly a scaled version of the Rolls-Royce MFTF engine centerline concept used for Boeing's QEVC concept validation (NASA CR–2013-217797) which was the basis of engine cycle modeling by Georgia Tech (Figure 26).

Basic parameters assumed were;

- Sea Level Static Thrust: 60,000 lbs,
- BPR: ~ 3.5-3.6
- Fan diameter: 84 in
- T41 limit: 3666 deg (engine durability)
- Fan Pressure Ratio ~ 2.1
- OPR ~ 34.5
- Fan diameter: 84 in
- Inlet design altitude 55,000ft

The simple 2D inlet representation from the AEDsys code suite was discarded in favor of one representative of a CFD-optimized inlet shape based on the Boeing "ECRI" inlet (Figure 27) used for the NASA QEVC low-boom concept validation testing (see AIAA 2014-3802).

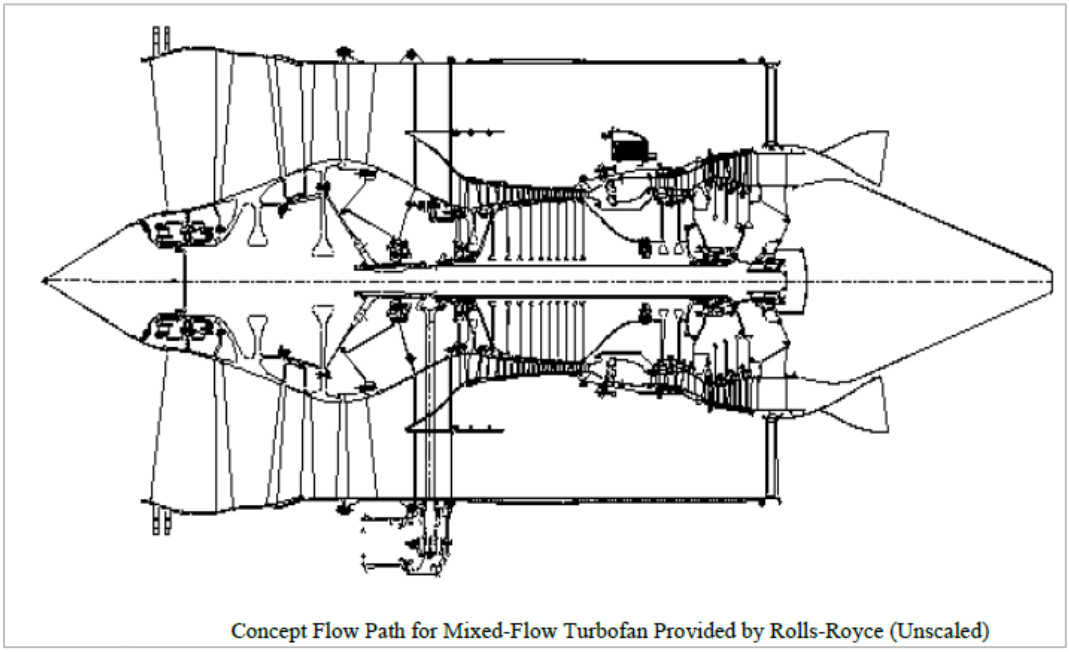

Figure 26- Representative N+2 Engine Concept Selected For RSAC

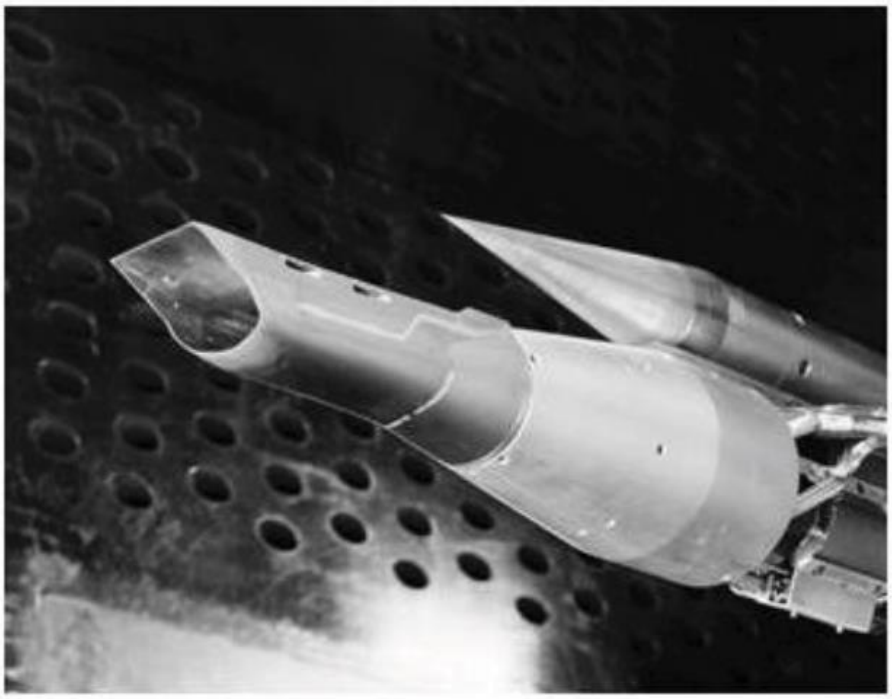

Figure 27- QEVC Isolated Inlet Model NASA Doc./ 20140011175

A generic pressure recovery curve representative of contemporary high-recovery inlets was created, combining data from several sources. This trend was then curve fit to generate an equation that could be used in lieu of tabulated inlet performance, in a performance code.

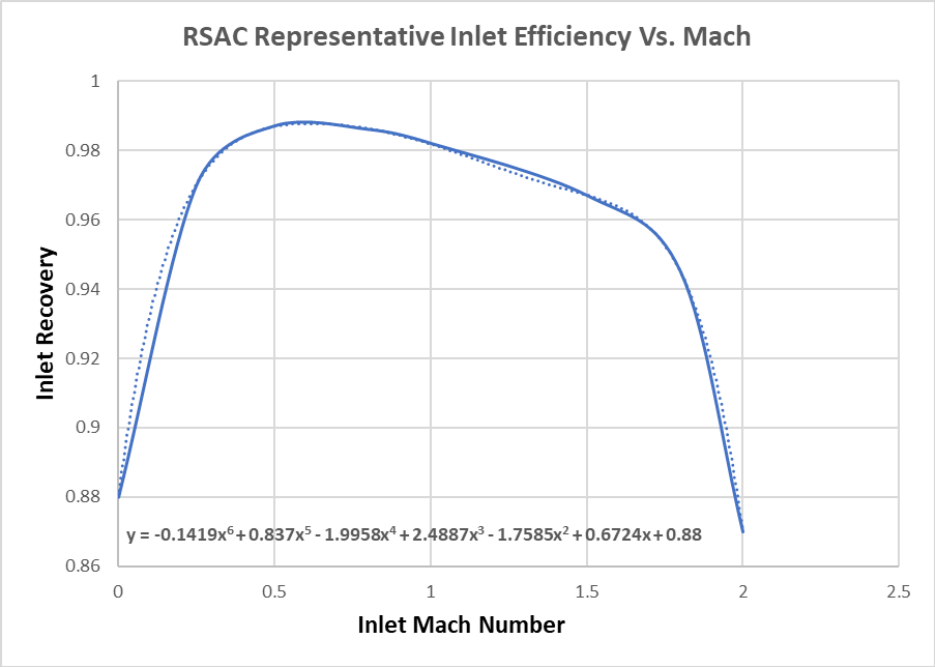

Figure 28- RSAC Representative Inlet Recovery Curve

Thrust lapse and TSFC outputs from the AEDsys software were adjusted with simple algebraic factors to generate a set pf TSFC and net thrust curves that were a good match to the few available published N+2 engine values (Figures 29 and 30).

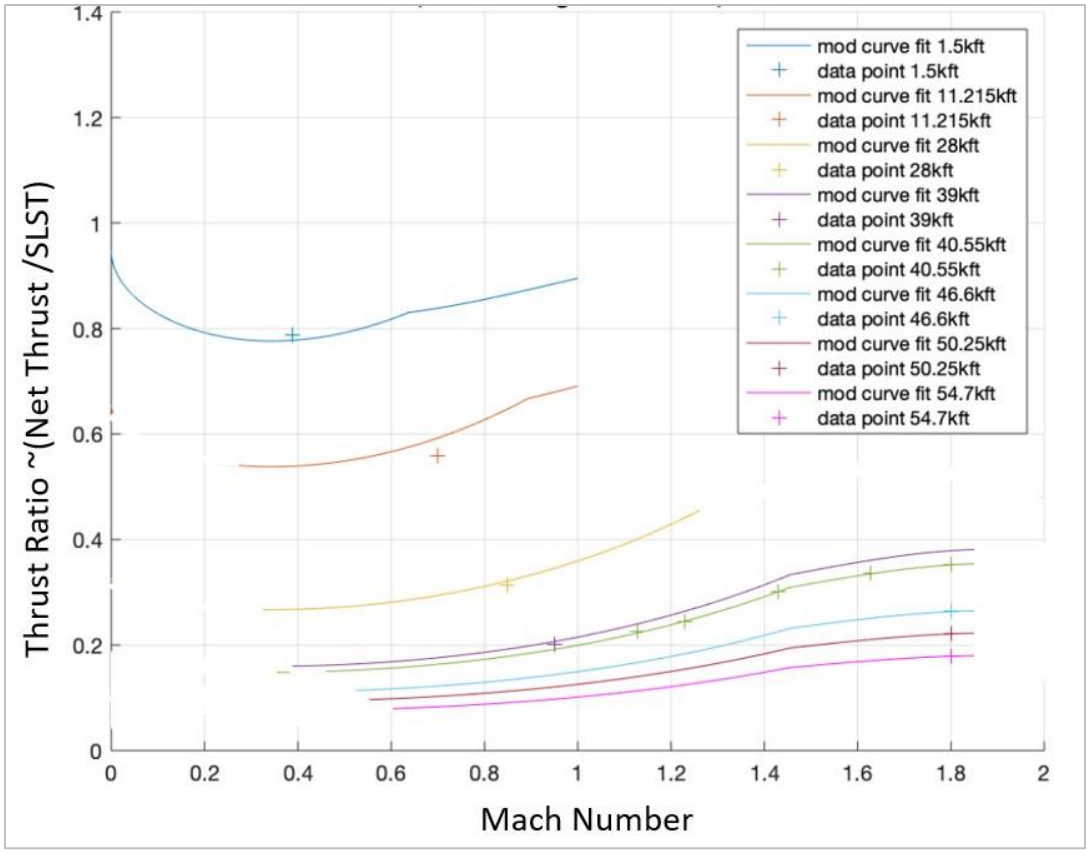

Figure 29- RSAC Representative Engine Net Thrust vs. Mach and Altitude

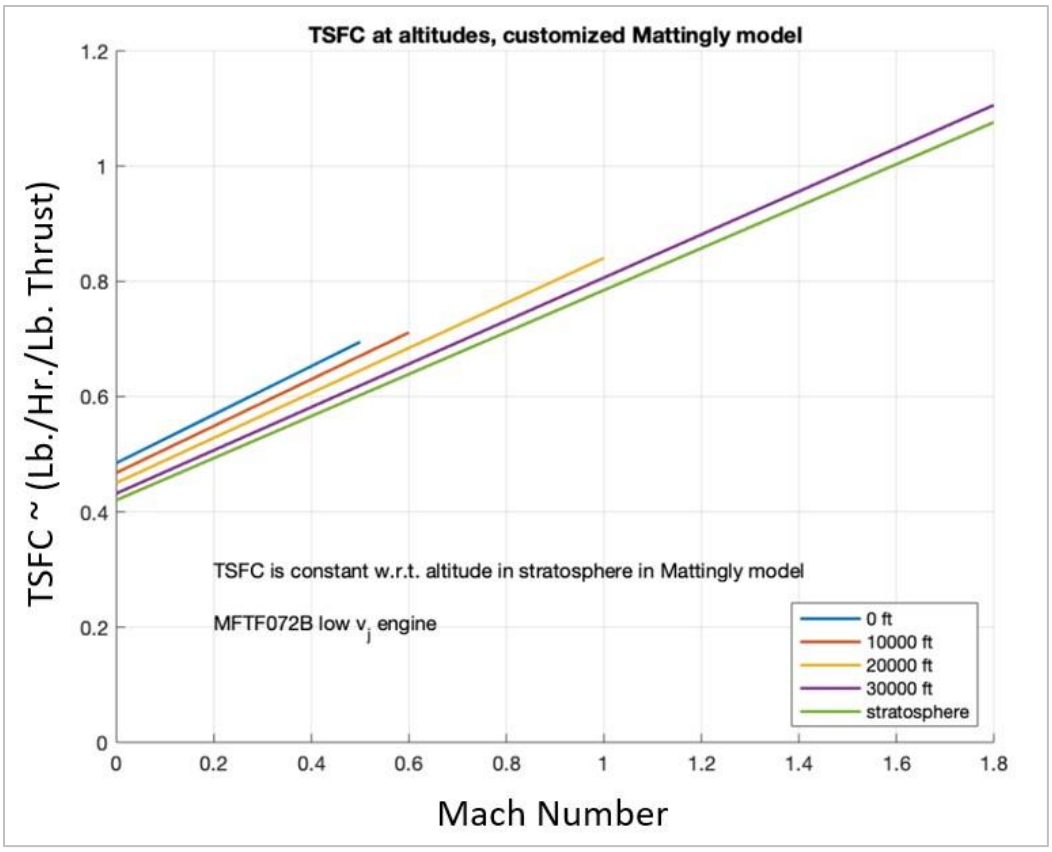

Figure 30- Representative Engine TSFC Relationship for RSAC (Assumes 4% Installation Loss Allowance)

A representative nozzle geometry was also needed for the N20 and RSAC nacelle OML definitions. From the performance standpoint, many con-di variable area nozzle types could be applicable to an RSAC type aircraft. The discriminating requirement for the nozzle concept is that the supersonic cruise aircraft must be certifiable for landing and takeoff (LTO) noise, and that depends primarily on the mixed exhaust jet velocity behind the nozzle. LTO certification compliance is measured at the runway "sideline" where the takeoff noise footprint is widest (typically near the landing gear retracted point), under the immediate climb-out path where communities would be exposed to fly-over noise, and under the approach flight path (Figure 31).

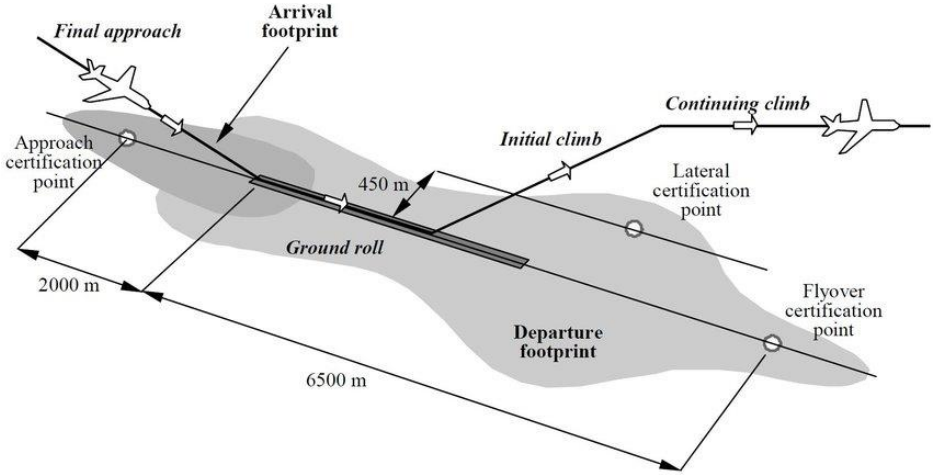

Figure 31- Aircraft Noise Certification Points (ICAO)

As technology has reduced subsonic jet aircraft noise over the years and most of the worldwide fleet shifts to lower noise levels, the certification standards have been significantly tightened. New standards that were introduced after the original "Stage 3" level was defined have been specified as improvements relative to the Stage 3 level. Current regulatory standards are FAA "Stage 5" and the equivalent international standard ICAO Chapter 14 which call for the "cumulative" noise reduction (total at all 3 locations) to be 17dB (Equivalent Perceived Noise Level, EPNL) quieter than the Stage 3 level which HSCT struggled to attain for nearly 10 years. It is also 10dB cumulative below the previous Stage 4. Supersonic cruise requires relatively small engine diameters to minimize propulsion system ram drag, and exhaust velocities in cruise must be slightly higher than the aircraft's speed in order to generate net thrust. This inherently means high "specific thrust" (thrust per engine cross-section). The engine makes its thrust from accelerating a smaller amount of captured air to a higher exhaust jet velocity than for a high bypass engine and therefore generates a lot more exhaust noise on takeoff. This is a particular problem for the "sideline" (lateral) measurement point near gear-up where the aerodynamic drag and lift performance is not as helpful as when the aircraft is up and away. NASA and industry efforts on low noise supersonic propulsion have assumed the current Stage 5, plus a few dB margin, as a valid design/technology target (Figure 32).

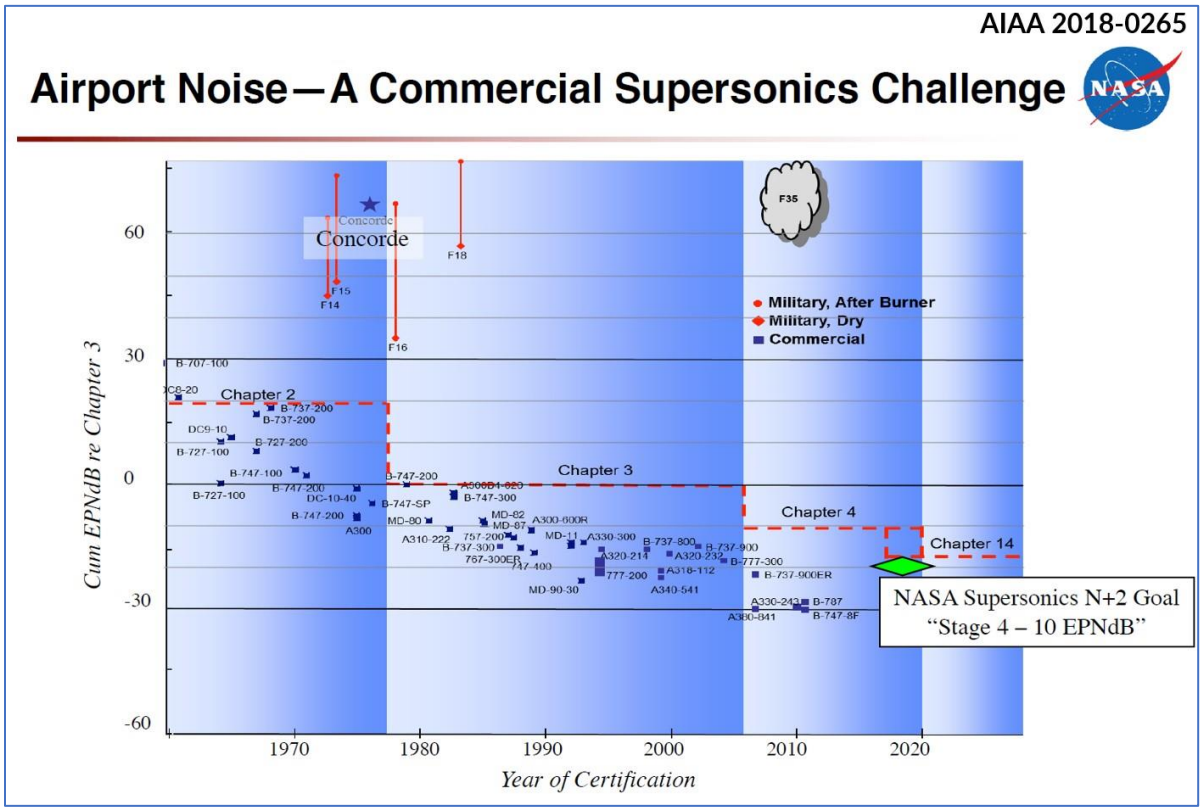

Figure 32- Aircraft Noise Standards History and Assumed Certification Target (NASA)

There has been speculation that a new noise standard will be created for application to supersonic aircraft, but it is unlikely that any leniency will be granted to allow supersonic types to go back to Stage 4 as the certification level. One can imagine that a special "supersonic rule" might exempt near-term supersonics from compliance with a new subsonic "Stage 6" that would continue to ratchet levels down as newer types become compliant with Stage 5. As the current airliner fleet has become quieter as older aircraft are retired, the issue of airport-caused noise has

diminished somewhat and it is conceivable that a future Stage 6 would be introduced as a voluntary goal rather than mandating a phase-out of noisier aircraft. It can be speculated that a new "supersonic" standard might hold to the overall goal of Stage 5 but with some provisions such as allowing noise while on the runway to be higher than at sideline, or allowing some dB of "trading" of noise levels between the three measuring points provided the total noise footprint is reduced by at least as much as the Stage 5 standard.

The RSAC currently assumes that a combination of its aerodynamic configuration, takeoff and landing trajectory optimization, FADEC controlled thrust management on takeoff, the bypass ratio 3.5-3.6 MFTF with some variable cycle features, and a with a high efficiency mixer on a low-impact suppressor nozzle will provide airport noise quieter than the Stage 5 standard, by some [undetermined] margin.

At the NASA Fundamental Aeronautics Program conference in 2008, Rolls-Royce U.S. (Liberty Works) and Perdue University presented advances made in low-impact noise suppressors based on an improved version of Concorde's ejector nozzles. Their concept used a translatable mixer and a variable A8/A9 con-di nozzle integrated with a reverser (similar to Concorde) and ejector-suppressor slot. With the more advanced multi-stream and scarfed type nozzles being at lower TRL, the Rolls-Royce type concept was selected for the representative engine (Figure 33).

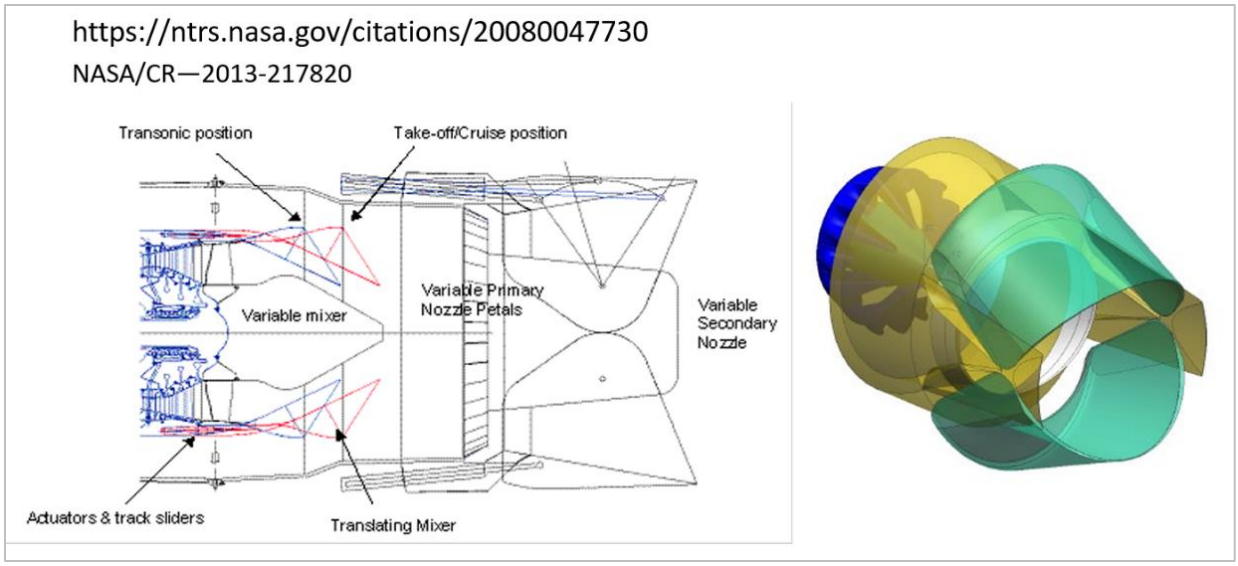

Figure 33- Rolls-Royce Low Weight/Drag Impact Ejector-Suppressor Nozzle Concept

UW graduate and senior capstone students originally planned to do detailed time-integration analysis of multiple landing and takeoff trajectories for RSAC trading-off various thrust-management and speed schedule options using wind tunnel-based performance data for various flap and trim configurations. The resulting trends of thrust versus altitude could be used with future noise-power-distance (NPD) tables of the representative engine (or alternates) to compute noise footprints. Wind tunnel data could also be used to predict engine-out takeoff profiles to compute FAR field length performance for the preferred flap/trim configurations with various control surface usage scenarios. While this study ended up falling outside of the scope of time/staff/funding available for SCALOS, a "place-holder" for full-throttle takeoff thrust lapse rate was declared, based on multiple sources for conceptual design level estimation of medium bypass turbofans.

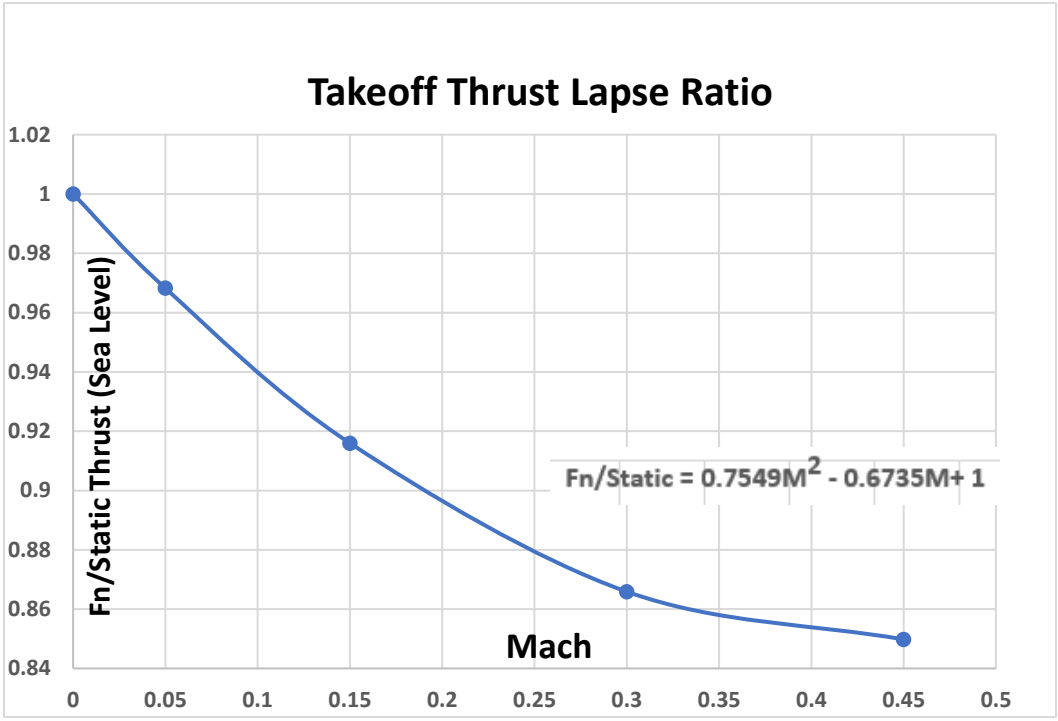

Figure 33- Algebraic Model of Takeoff Thrust Lapse for BPR ~3.5 MFTF Engines

For future trades including FAR takeoff field lengths and engine-out scenarios, a generic engine-out windmill drag curve was also declared, as a composite of several published methods (Figure 34).

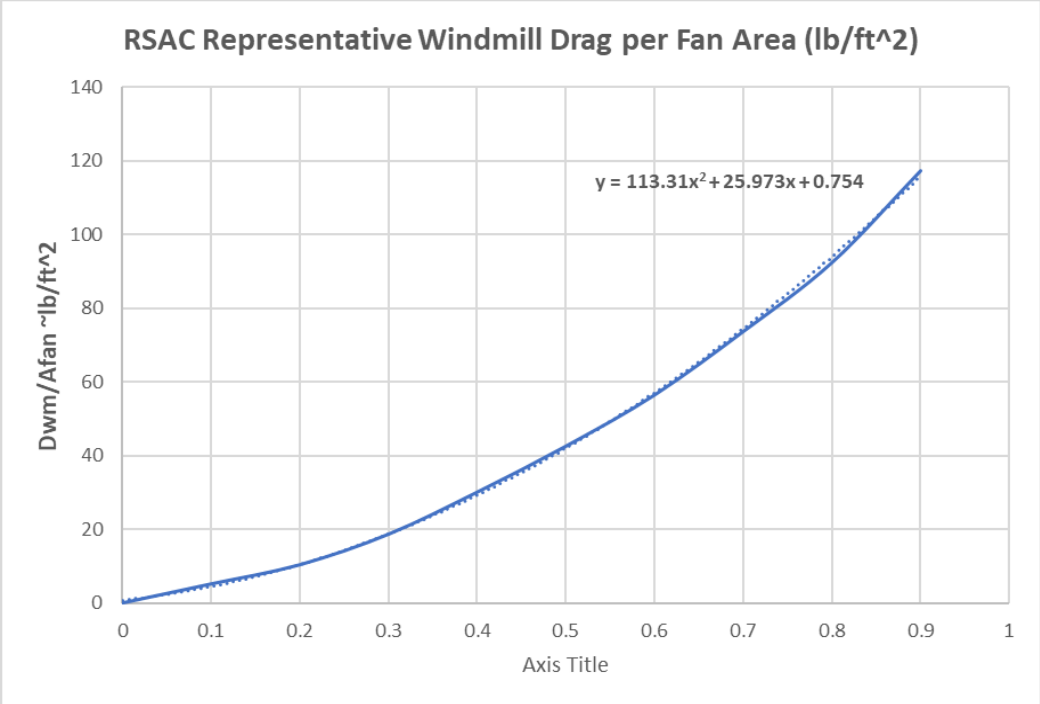

Figure 34- Generic MFTF Engine-Out Windmill Drag Approximation

Special Full Authority Digital Engine Control (FADEC) programming for thrust management to reduce engine noise on takeoff has been a feature of supersonic studies for the past 30+ years. The system baselined for the HSCT during the NASA HSR program in the 1990's, nominally consisted of a 10%

engine “de-rating” to a thrust level less than full thermo-mechanical maximum sea level static thrust, plus the so-called “Programmed Lapse Rate” (PLR) which provided another 10% stepwise reduction in thrust just prior to the sideline noise measurement point. This was followed by a “cut-back” to lower levels yet when over-flying down-range communities, essentially the same as for subsonic aircraft in noise-sensitive areas (e.g. Orange County Airport). The combination of a high-flow ejector-suppressor type nozzle and the 10% derate during ground-roll reduced the exhaust jet velocities of the 0.8 bypass HSCT engines to tolerable levels on the takeoff roll. The PLR step was to be totally automatic (“transparent” operation), but could be over-ridden by the pilot or an automated thrust recovery system in the event of an engine failure or other takeoff emergency. Larger PLR step changes were studied, however, based on simulations it was felt that the pilots and passengers would find the sudden loss of acceleration right after liftoff to be unsettling and introduce the opportunity for confusing the loss of acceleration with the onset of an engine failure. Limiting the step reduction to 10% allowed the PLR thrust reduction to be camouflaged by the nearly simultaneous reduction in drag due to retracting the landing gear. The recovery of up to 10% of lost thrust was also permitted under certification for Automatic Thrust Reserve (ATR) as certified on the 727-200. Today, the automated thrust recovery in the event of an engine failure or thrust asymmetry is covered as an Automatic Takeoff Thrust Control System (ATTCS) under FAR 25.904.

RSAC currently assumes that the bypass ratio 3.5-3.6 MFTF with ejector-suppressor nozzles would have an allowable noise level on the takeoff roll that full-throttle or minimal derate could be used for much of the takeoff roll, especially if regulators allow supersonic types to generate noise levels similar to sideline before the conventional sideline measurement point is reached at gear-up.

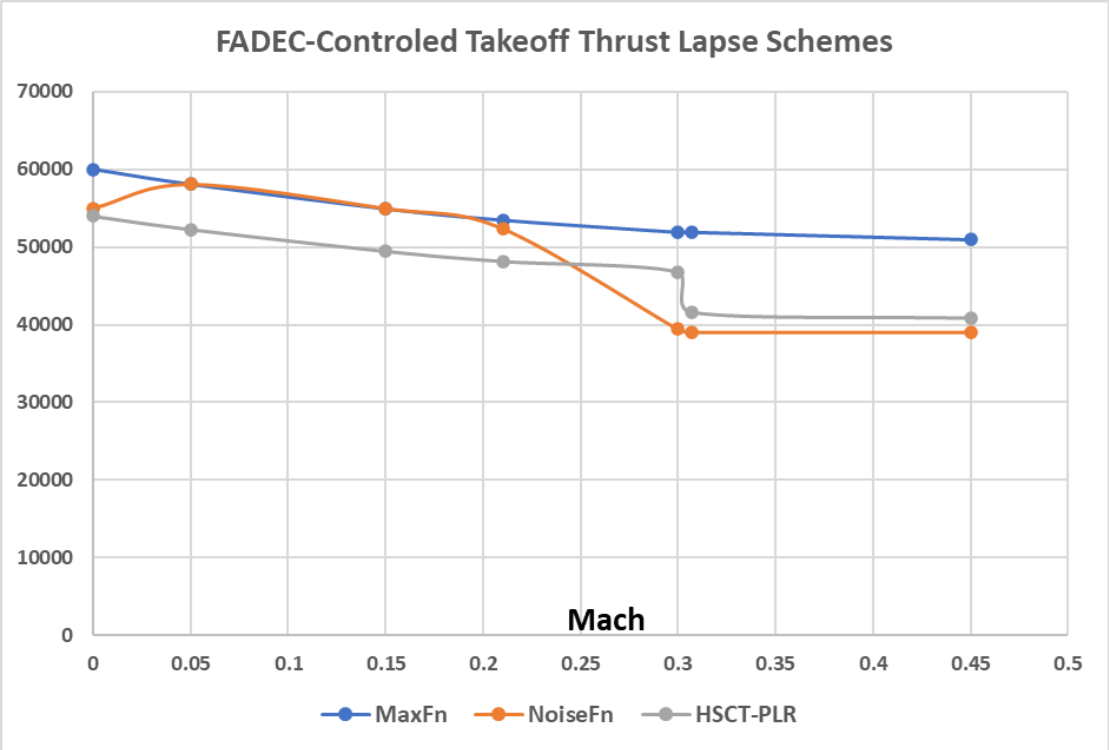

Figure 35- Proposed FADEC-Controlled Thrust Reduction for Noise & Performance

Airframers and engine companies began looking at more tailored types of PLR in the early 2000’s. The the entire thrust reduction that had traditionally been derate + PLR, could be taken as a continuous FADEC action, allowing the largest reduction to take place over 8-10 seconds so the reduced takeoff acceleration would “feel” more like that of a propellor aircraft or jet engine of much higher bypass ratio.

Notionally, a total thrust reduction of greater than 20% may be needed in order to meet Stage 5 with margins, so the RSAC initially assumes a 24% thrust reduction by gear-up. It is preferable that the modulation of thrust would be accomplished without restricting fuel flow to the engine, by adjusting the con-di nozzle. Failure of the nozzle to actuate would simply leave the thrust level and noise higher than intended without interfering with the engine's fuel supply. For purposes of future planned performance/noise trades, Figure 35 illustrates the assumed RSAC thrust levels versus speed during the takeoff roll and initial climb (thrust in pounds, speed in Mach number, orange for RSAC, blue for full thrust, gray showing the HSCT procedure, at sea level standard day conditions). It is likely that less than full thrust would be available at brake release under no headwind conditions to minimize internal flow separation in the inlet.

The chosen inlet concept allows some lip bluntness in the lower third of the inlet highlight, reducing flow separation relative to that of a sharp-lipped axisymmetric circular inlet, but if additional flow is needed for takeoff, options include modifying the inlet to translate the forecowl forward at takeoff to expose a secondary annular intake (as in NASA CR-2010-216842 and X-32), or opening a similar auxiliary flow path by moving a translating sleeve that fits into the OML of the forward inlet. Either of these schemes, with tailored edge shapes on the auxiliary inlet, have the potential to provide flow with limited fan distortion or edge-noise "screech" as was experience with suck-in panels on early 747 nacelles. An advantage of using a 3D inlet type optimized in CFD rather than designing the flow-path using traditional 2D flow representations applied to rectangular, half-conical, or axisymmetric cone inlets, is added flexibility in choosing the inlet capture aperture shape. Logically, an alternate more ovalized inlet aperture could allow the use of a variable A_{cap} using hinged or flex panels, either with moving lower lip segments, similar to Eurofighter Typhoon, or moving side-walls similar to B-1A/B bomber. Propulsion pod weights, based on Boeing N+2 assessments, include a nominal allowance for an auxiliar air system, without specific design or kinematics. The selection of an optimal system would have to trade inlet-related noise, thrust, fan distortion, and protection from landing gear generated FOD. The design of the N20 and RSAC nacelles does not explicitly indicate a preferred solution.

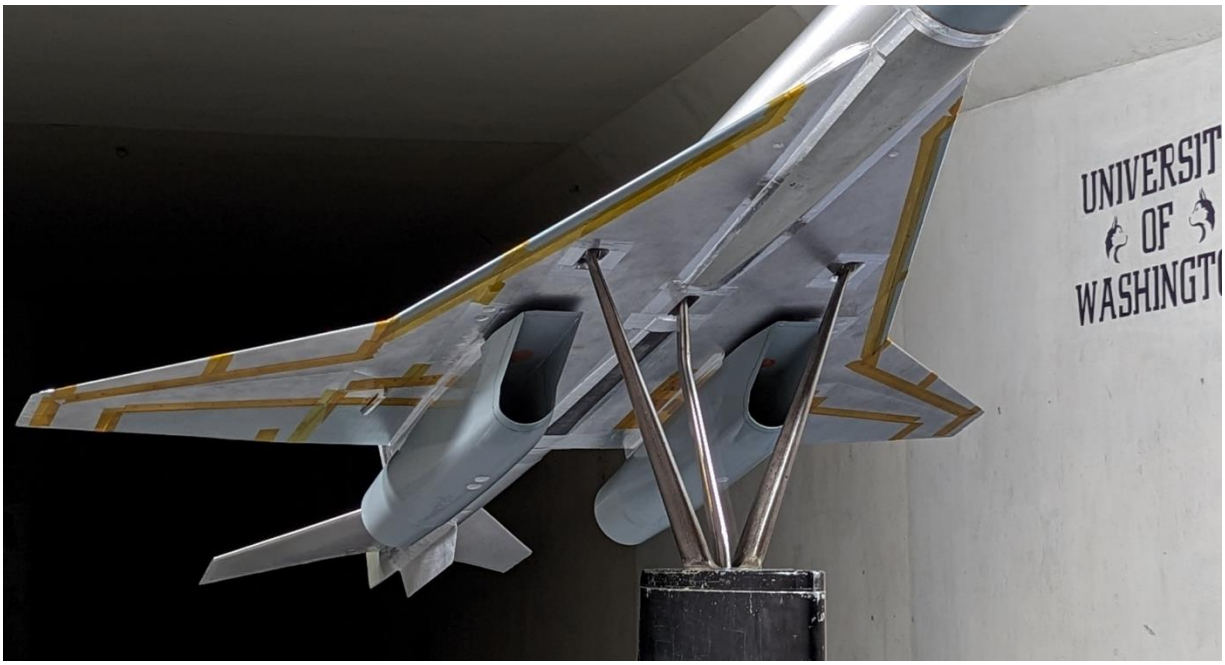

Figure 36- SCALOS N20 Nacelles in Bottom-Mounted (B) Location

The “N20” nacelles were defined for the modular wind tunnel model for SCALOS testing based on the representative MFTF engine and nozzle concepts from Rolls-Royce, and the engine inlet concept based on the Boeing ECRI inlet, consistent with technologies assumed in the previous NASA “N+2” studies. Based on preliminary wing area and thrust sizing estimates for the full-scale RSAC aircraft, the N20B (bottom-mounted) nacelle OML definition translated directly to the initial RSAC configuration. Proportions of the Rolls-Royce engine centerline concept were used to illustrate a notional engine installation within the N20 nacelle shape (Figure 37).

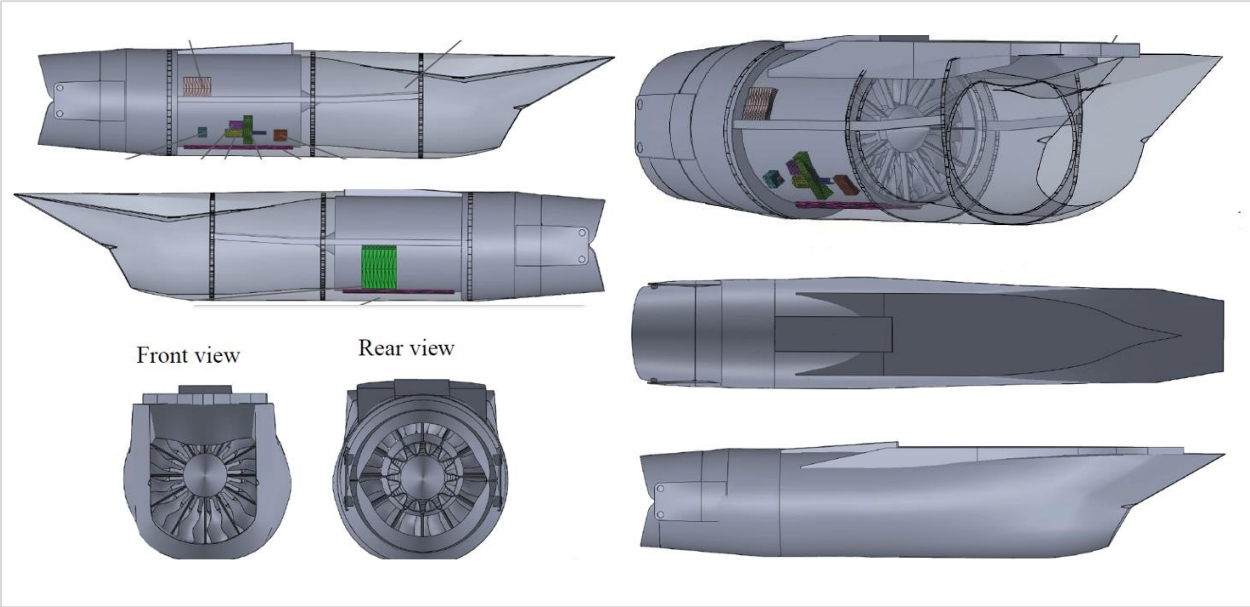

Figure 37- Rolls-Royce Concept Engine and Nozzle With ECRI-Based Inlet

With this definition as a starting point, subsequent design iterations for the full-scale RSAC looked in more detail at notional engine accessory packaging. It was determined that some accessories could likely be contained in a fairing inside the fan duct, but others are better located on the outside of the engine if the nacelle cross-section and keel-line droop are to be minimized. An evolved version of the N20.B nacelle is on the current RSAC (version “E”, December 2024) and includes representative accessory bulges to cover generic accessories arranged on the outside of the fan duct. In the final version, the inlet-engine-nozzle alignment includes a slight S-bend with the engine itself tilted slightly nose-down. This increases the ground clearance margin between the aft portion of the nacelle and the runway.

The nacelles on RSAC have been toed in slightly to approximately align them with the local under-wing flow and to allow less contraction in the flow channel between the engines. RSAC nacelles have also been moved outward five feet (full-scale) relative to the KWT model version in order to provide adequate lateral main landing gear spacing and to simplify gear retraction angles.

The RSAC-E version includes an assumed engine mounting scheme based on HSCT designs. A set of heavy ribs forming a “ramp” on top of the main wing carry-through box provide a reinforced tie-in to the wing box structure and raise the location of a pair of upper lugs for attachment of a box-beam on top of the engine. Lugs on the lower surface of reinforced ribs of the main wing box provide the lower attach locations for the forward end of the nacelle-top box-beam. A V-shaped yoke extends below the sides of the box-beam, attaching to the sides of the engine. Forward and aft engine frames attach to the ends of the over-head box beam (Figure 38). Compressor and turbine sections are kept behind the main wing box.

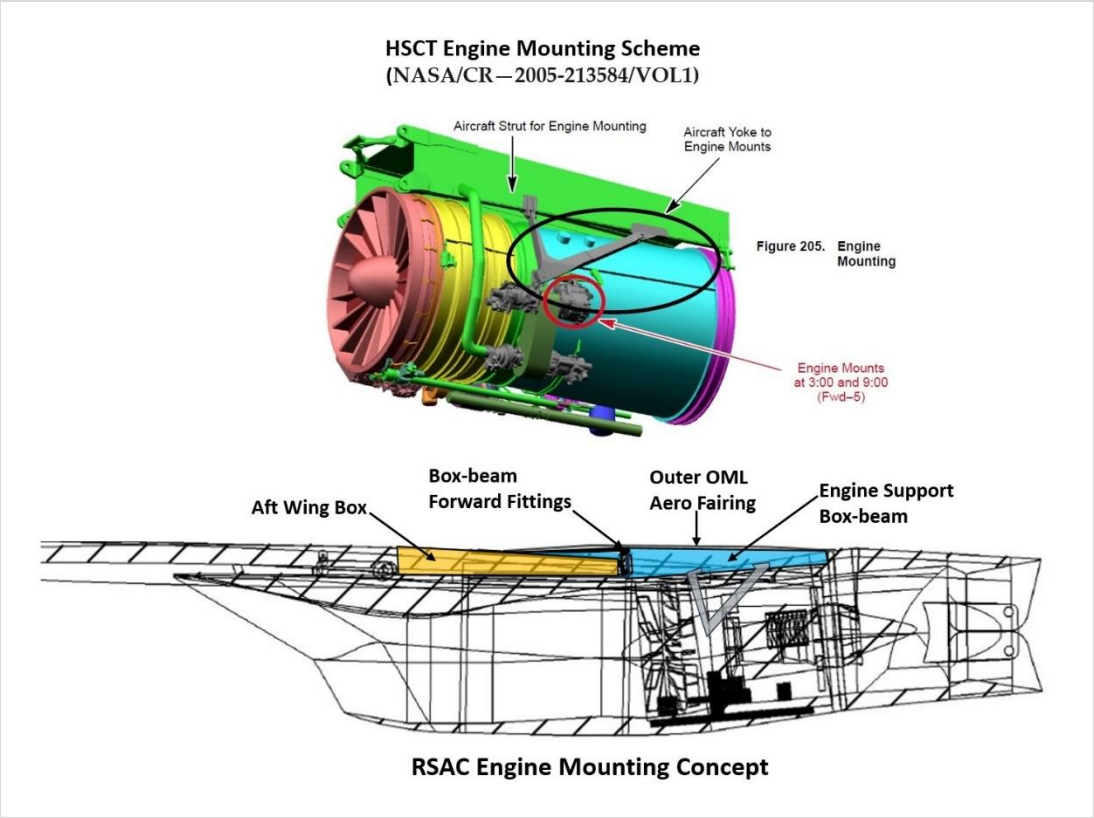

Figure 38- RSAC Proposed Engine Mounting Scheme

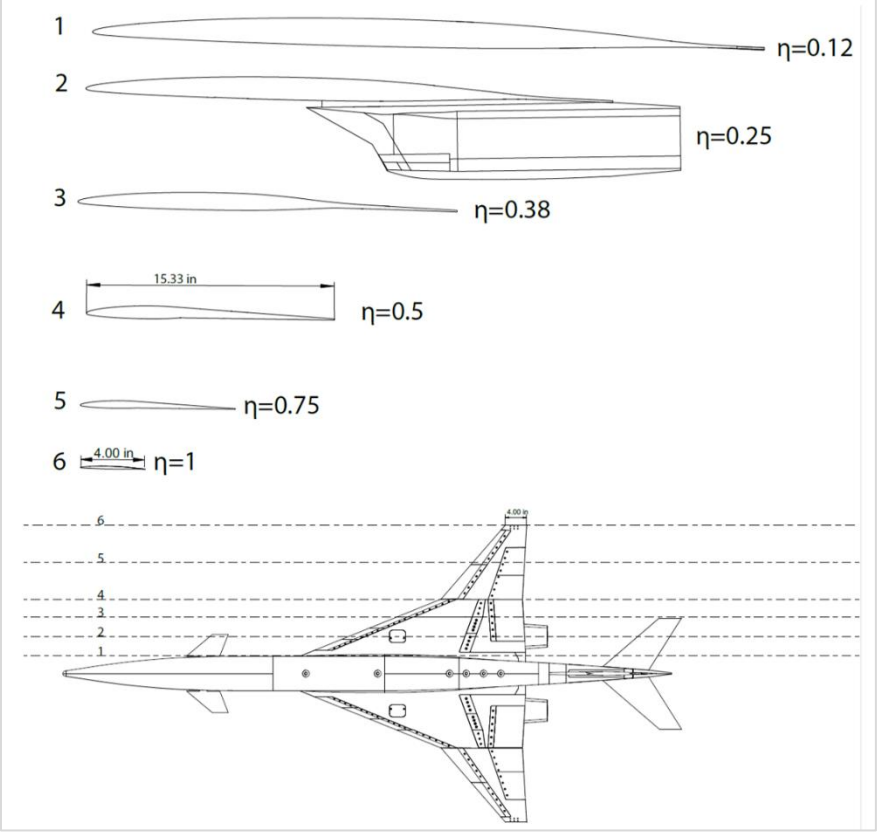

Figure 39- KWT Model Configuration UW-S-21A Wing Loft "Defining Airfoil Sections"

D. RSAC Cruise Aero Outer Mold Lines (OML)

RSAC cruise aero geometry loft lines used the UW-S-21A wind tunnel model definition (Figure 39) as the point-of-departure. Figure 40 shows the principal dimensions of the 1/22 scale model.

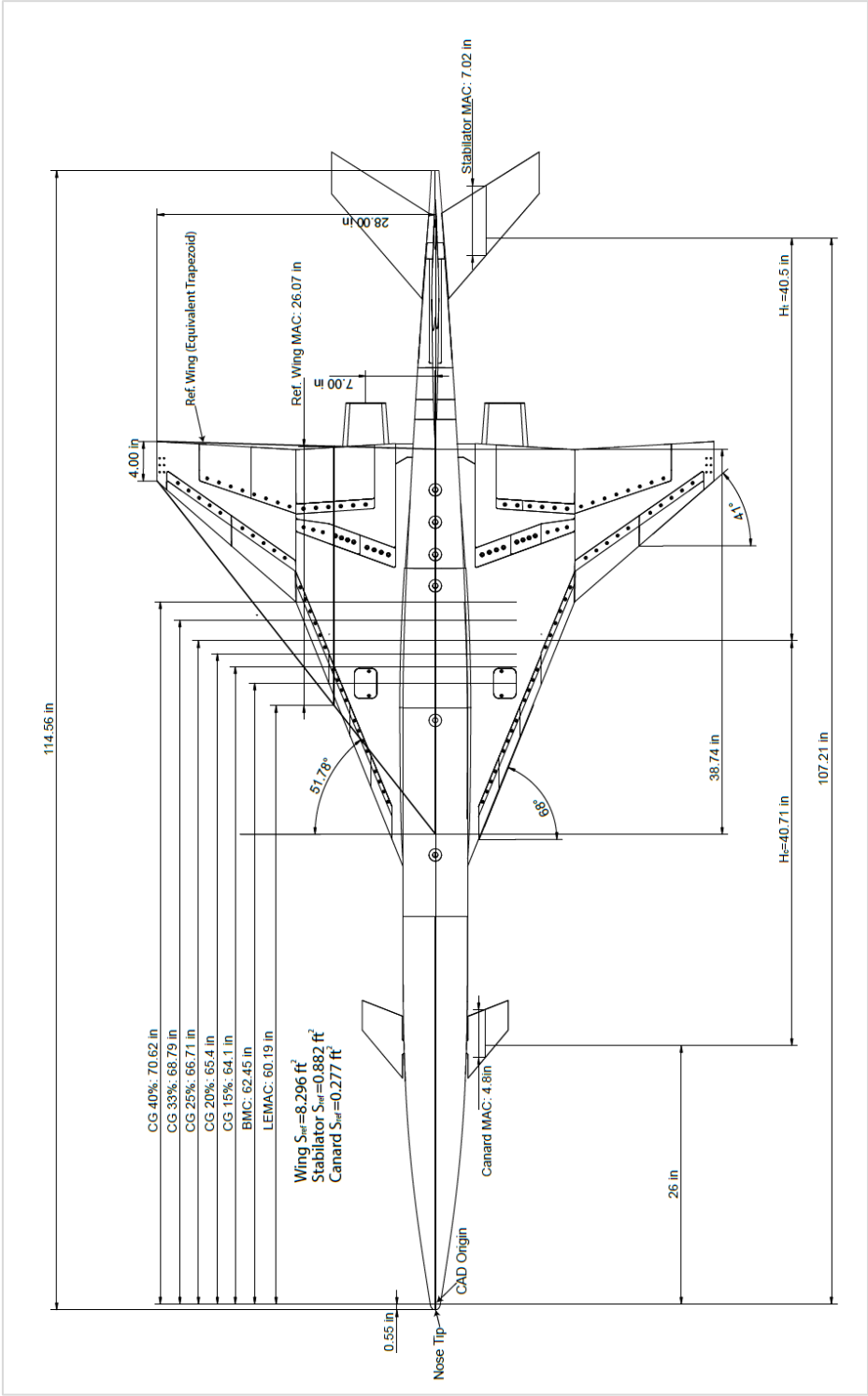

Figure 40- KWT Modular Model, Configuration UW-S-21A Principal Dimensions

External lines of the RSAC “E” version include a number of changes relative to the UW-S-21A “seed”;

- Propulsion pod:
  - Nacelle toe-in
  - Nozzle “clamshell” details
  - Nacelle accessory bulges
  - Engine mounting concept with over-wing ramp fairing

- Lifting surfaces:
  - Thinner airfoil t/c on wing, vertical tail, horizontal tail, and canard
  - Sharper outboard leading edge nose radius, blunter (supercritical section) inboard
  - Wing airfoil camber lines and twist (wash-out) ~ multi-point optimized HSCT wing
  - Modified ventral fin to better match RSAC gear location and max rotation angle

- Fuselage:
  - New area-ruled fuselage, modified body camber line and added flight deck window zone
  - Aft-body and canard “wiping flats” and canard root fairings added
  - Belly fairing for landing gear, ECS packs, RAT, OBIGGS systems volume
  - Wing-body upper surface/trailing edge intersection fillet
  - Nose gear door blister fairing to cover retracted wheels

Figure 41 shows a set of shaded CAD images of the RSAC-E external lines. For integration purposes, the RSAC-E includes geometric wing shapes that anticipate the effect of supersonic cruise and multi-point CFD-based aero optimization, but no CFD optimization has been conducted at this point. The RSAC-E loft should only be considered a “seed” geometry to begin an optimization effort including appropriate internal “packaging” and structural constraints.

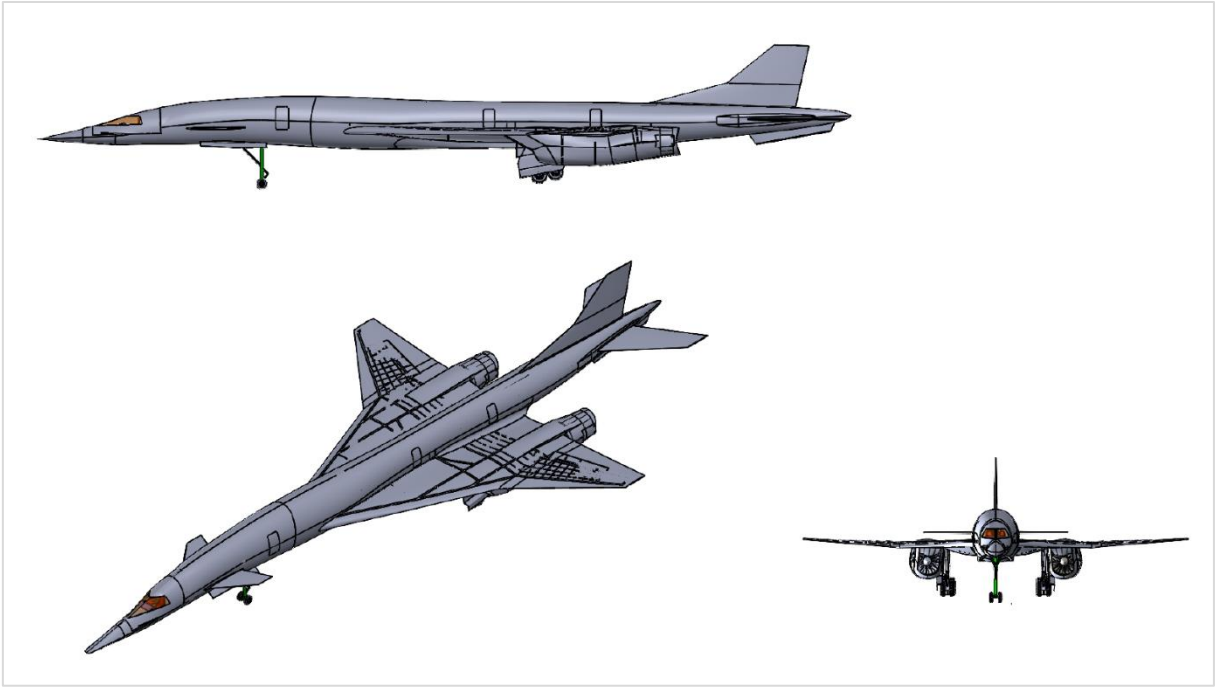

Figure 41- RSAC, December 2024 Status (Version “E”)

As shown in Figure 39, the KWT modular model wings have a number of geometry simplifications that facilitated maximum modularity of the model. These simplifications included; no aerodynamic twist (washout), and airfoil sections with more aft camber than might be optimal for supersonic sections. Washout has a strong influence on Cmo, CLo, and spanwise load distribution which impacts the induced drag in the attached flow regime and wave drag due to lift in the supersonic regime. The Cmo itself can influence the canard and tail deflections needed to trim the airplane at all Mach numbers. The combination of the "flat" (no twist) wing, and the modular model airfoil camber lines, gave the W15 wing a significantly negative value of Cmo for untrimmed low-speed conditions, contributing to the concern for trim drag on the 2015 R-UAV. For the full-scale airplane, the influences of twist vary across the Mach regimes and must be traded off as part of a multi-point shape optimization (including trim and thrust effects) so that a shape considered desirable at cruise could impose an undue penalty at other conditions. The objective of a multi-point optimization is to weight the effects in different Mach regimes in order to find the net best compromise at the airplane level. Representative optimized wing camber and twist shapes from multiple sources (e.g. NASA CP-1999-209691 and paper AIAA-2020-3182) were used to derive shaping trends to apply to lofting the RSAC wing. The first iteration for the RSAC representative wing loft was done in 2021 (Figure 42).

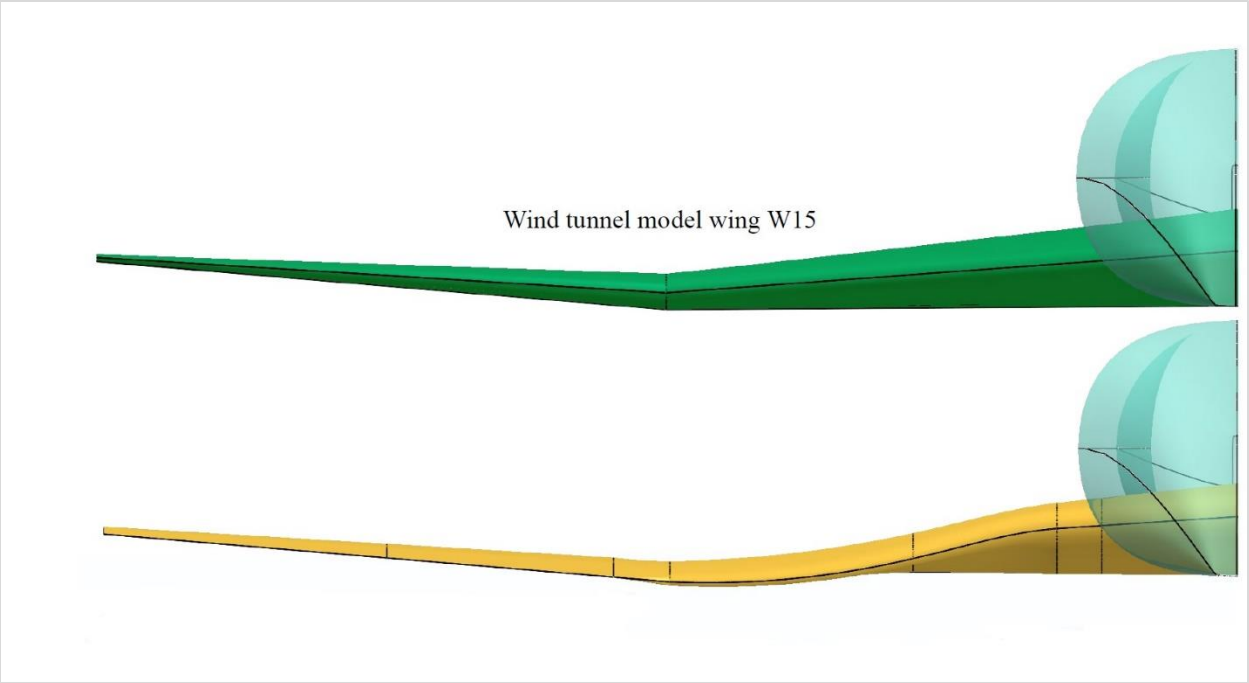

Figure 42- RSAC Representative Optimized Supersonic Wing Shape, 1st Loft Iteration

The RSAC loft was further smoothed and refined incrementally over the next two major configuration cycles (2022-2023). Airfoil leading edge camber and inboard of the sweep break ("crank") the leading-edge nose radius was increased to resemble the "Alternate Cruise Leading Edge" shapes tested in KWT (edge bluntness similar to "supercritical" airfoil sections). The RSAC-E wing loft is designated "RW23". Projected W15 planform is held fixed, as is the 1.5-degree side-of body wing incidence angle, which helps limit the cabin deck angle in cruise. The outboard wing panel sections have a supersonic normal Mach number in cruise and therefore are lofted with sharp leading edges. The outboard panel uses wedge-slab-wedge type supersonic airfoils in order to maximize the depth near the leading and trailing edge flap hinge-lines, and to maximize the torsional stiffness of the outboard panel.

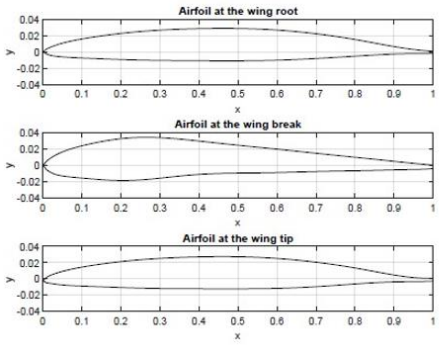

(a) Plot of the W15 Airfoils (thickness exaggerated for clarity)

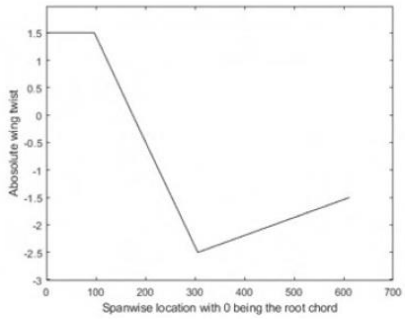

(b) Plot of the twist of the RW23 Wing vs Semi-span

The W15 airfoils and the twist of the RW23 wing

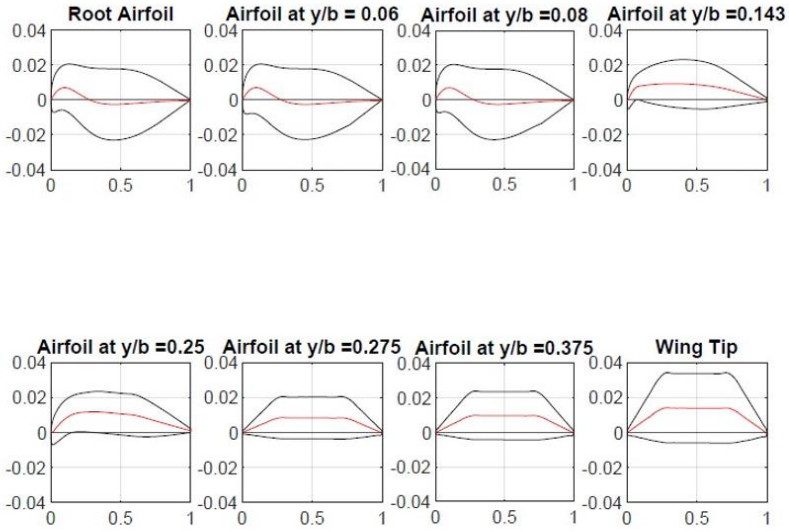

C. Plot of the RW23 airfoils (thickness exaggerated for clarity)

Figure 43- Wing RW23 Loft Elements Compared to W15 Airfoils

External “canoe” fairings to cover dropped hinges or actuators or vertically off-set hinges are not included as the need for these has yet to be determined and would depend on detailed systems and mechanical design trades. Efforts were made on HSCT to keep all actuation internal to the OML to prevent localized kinetic heating at sustained Mach 2.4 conditions. This may not be a favorable trade for the Mach 1.6-1.8 cruise regime proposed for RSAC. With modern actuator technology it may be possible to avoid the large canoe fairings used on Concorde, though it may be required to have smaller fairings over offset hinges. Figure 44 shows an example elevon surface with vertically offset hinges to reduce actuator loads. The larger “canoe” actuator fairings, if needed, can be CFD-optimized and should mainly be a skin friction penalty with negligible net wave drag increase.

Figure 44- Example External Elevon Hinge Fairings (Aft Cover Removed, Mirage 2000)

T

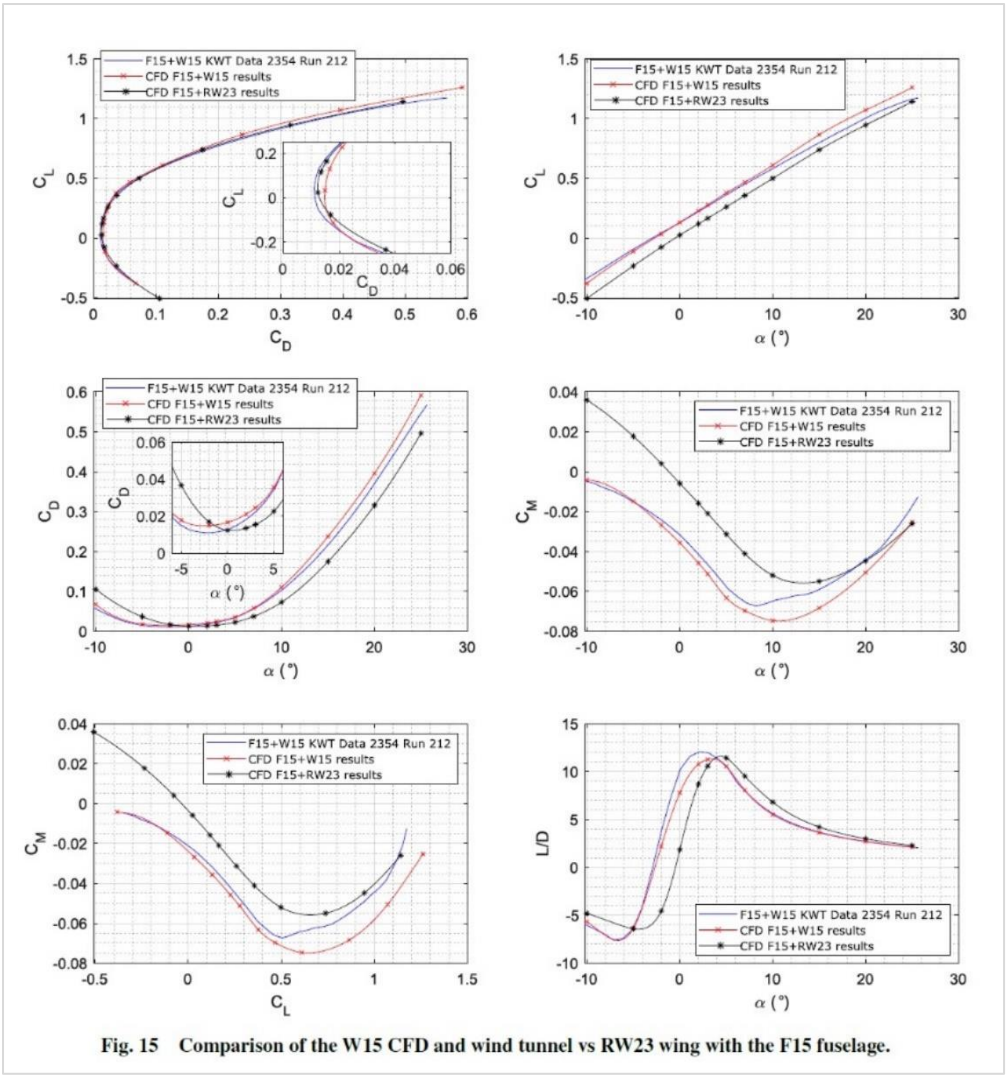

Fig. 15 Comparison of the W15 CFD and wind tunnel vs RW23 wing with the F15 fuselage.

Figure 45- RSAC Wing RW23 Compared to KWT Baseline Wing W15 Longitudinal Coefficients

The incremental effect of the RW23 wing loft relative to the test baseline W15 wing was explored in both vortex lattice methods, and RANS CFD (StarCCM+) for both the wing-alone and wing + body cases. Figure 45 shows the RANS computed differences for the wing +body case.

The modular model's standard fuselage (F15-A15), used for the UW-S-21A configuration, was originally intended to be a generic fuselage for testing a range of slender supersonic concepts. The RSAC needed a realistic, concept-specific fuselage shape appropriate for a full-scale supersonic airliner. The 2021 capstone project class used the simplified lofting tools and wave drag analysis module in OpenVSP to investigate the trends of zero-lift wave drag component of CDo with various body cross-section constraints. Figure 46 shows early results from these trades.

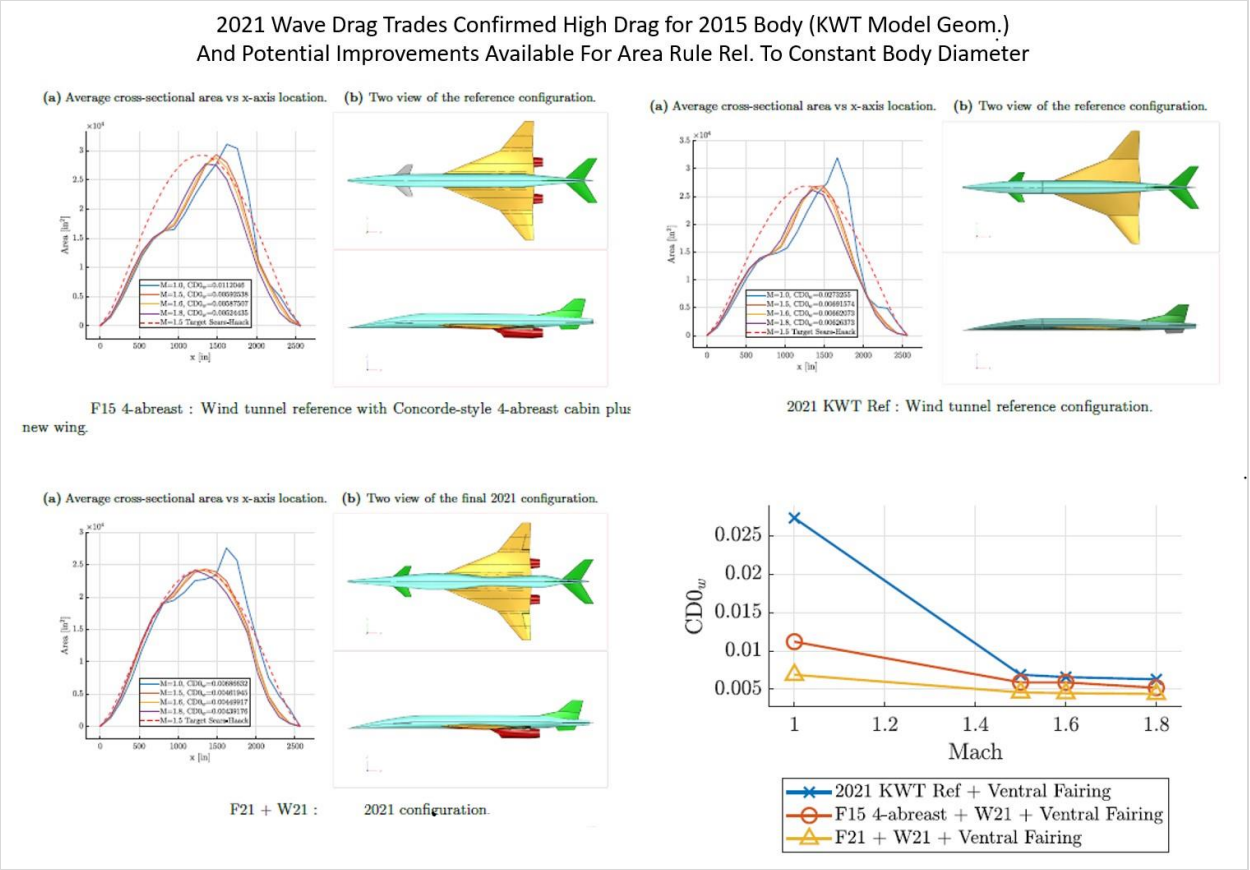

Figure 46- Initial RSAC Area Rule Trades Using OpenVSP

In subsequent years, when it was noted that OpenVSP sometimes gave inconsistent results, systematic comparisons against theoretical solutions and Euler/RANS CFD, were performed with simplified wing and body geometries. OpenVSP results were calibrated against published HSCT wave drag accounting. During the annual major design cycles for RSAC, further trades were done involving dozens of iterations between internal cabin arrangements, landing gear stowage requirements, external loft shapes, and drag assessments using OpenVSP. Figure 47 shows an example of one of the design/evaluate/re-design iterations on body area distributions. Later, details such as wiping flats at the intersection with the all-moving canards and horizontal tail, and a fillet between the aft part of the wing and body were added.

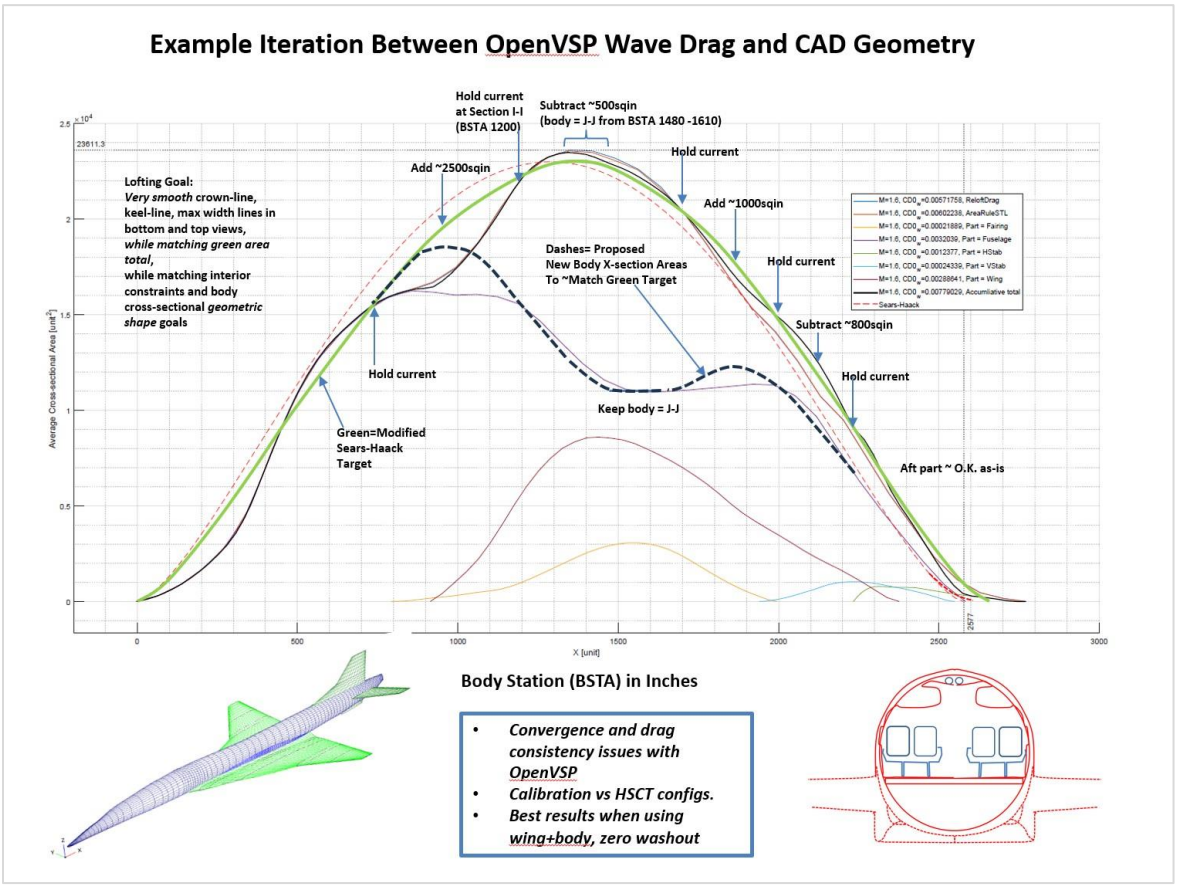

Figure 47- RSAC Body Area-Rule Iteration Example

Estimated body camber effects and preliminary flight deck design concepts were used to define an RSAC-specific nose shape. The flattened "duck-bill" shape of the nose apex (used on the modular model to delay or eliminate "yaw-slice" instability at high alpha), was retained. Wind tunnel testing the area-ruled fuselage shape was necessary to understand the incremental effect that a realistic airliner shape might have relative to the generic F15/A15 fuselage used for most of the SCALOS testing. A near-final iteration on the area-ruled body shape was re-designed to interface with the modular model wing W15 and a duplicate version of the H20L horizontal tail (Figure 48).

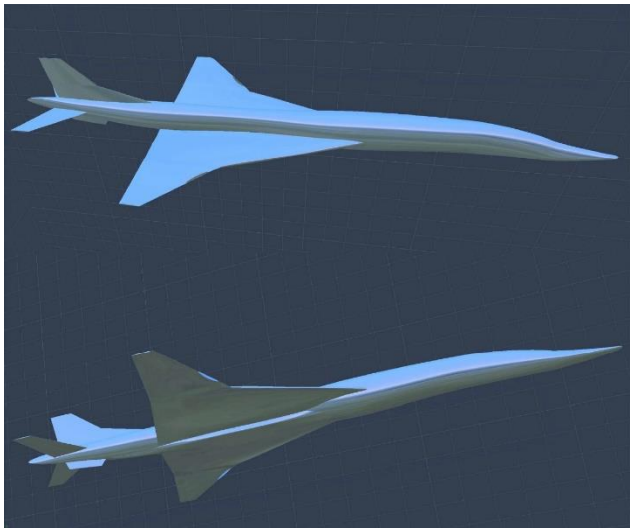

Figure 48- Loft Geometry for the Realistic RSAC Area-Ruled Body with W15 Wing and H20 Tail

Figure 49- SCALOS Modular Model with RSAC Area-Ruled Body, Tested as "UW-S-24A"

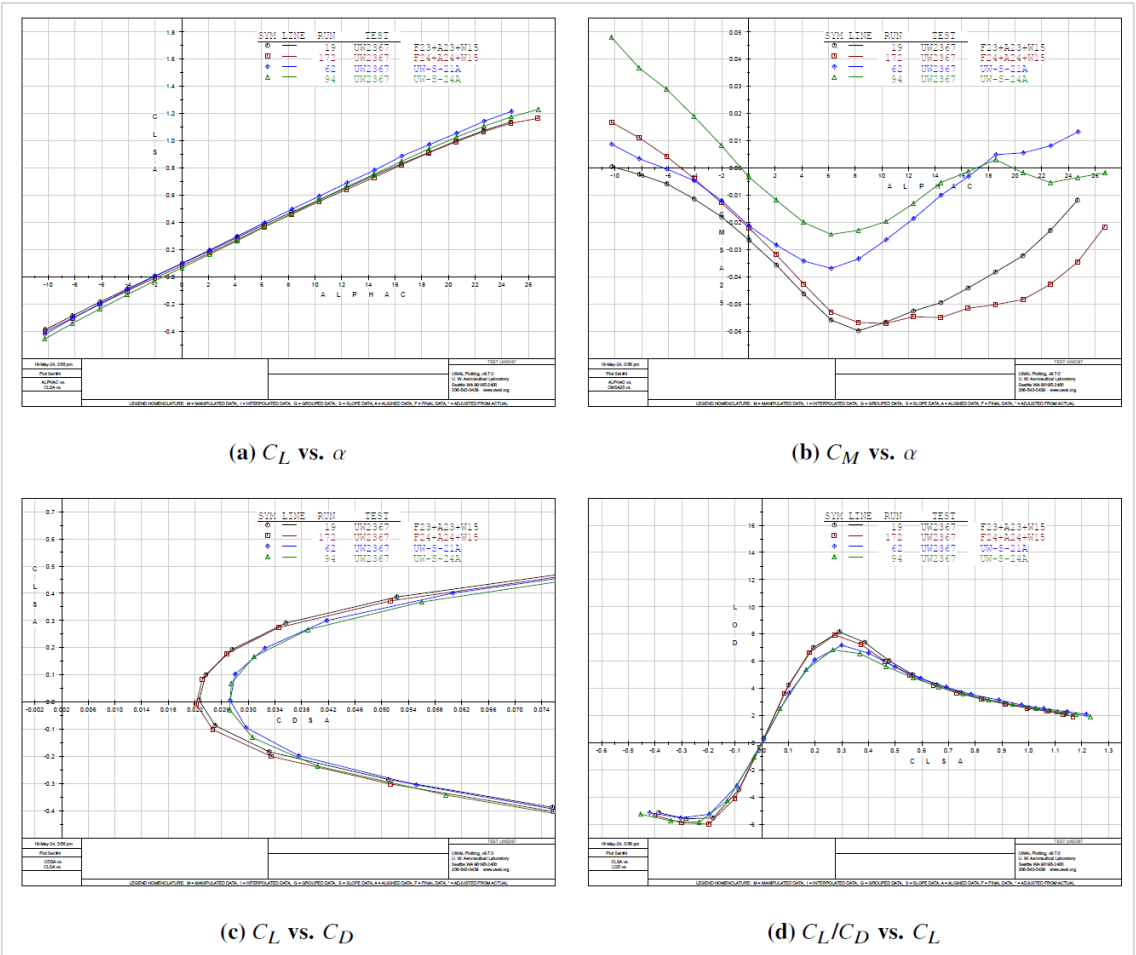

(a) C_L **vs.** α

(b) C_M **vs.** α

(c) C_L **vs.** C_D

(d) C_L/C_D **vs.** C_L

Figure 50- Effects of the RSAC Area-Ruled Body on Longitudinal Aero Coefficients

Preliminary wind tunnel results (with interim corrections) were encouraging, showing the RSAC fuselage caused only a very small loss in clean config lift curve slope and L/Dmax at wind tunnel Reynolds number (< 0.1 units) relative to the baseline modular model's idealized generic slender body of F15/A15. However, this was in untrimmed result and the pitching moment data showed that, as intended, the fuselage camber introduced a positive increase in Cmo of +0.016 and a slightly rotated, more negative dCm/dCL curve at all CL's. Given the more positive Cmo, the trimmed RSAC configuration is expected to show slightly higher net trimmed L/Dmax. Figure 50 shows the effect of the area ruled body one the wing + body, and complete configuration longitudinal aero characteristics.

The UW-S-24A test model still retained the thicker vertical and horizontal tails and canards of the standard SCALOS modular model components. Those components were separately defined with thinner airfoils for the full-scale RSAC and incorporated in the December 2024 geometry, RSAC version E (RSAC-E). RSAC-E also includes minor post-test loft smoothing/re-contouring in the forward body, and a reduced wetted area version of the aft wing-body intersection fillet.

E. Leading and Trailing Edge Devices

Optimizing slender supersonic cruise aircraft for acceptable landing and takeoff (LTO) field-length performance, engine out climb, and 3-point noise certification, requires a careful compromise between the supersonic L/D requirements and subsonic requirements. Maximizing lift at constrained alphas helps to minimize pitch attitude on landing approach, and decrease lift-off speeds on takeoff. At LTO conditions, reducing thrust required on approach and climb-out reduces the noise footprint, so the trimmed low-speed L/D is of first order importance.

Higher sweep, lower aspect ratio planforms that are more point-designed for supersonic flight (e.g. Concorde, Boom Technology's XB-1, low-boom configurations) may rely on letting leading edge flow separate and roll up into stable vortices to generate vortex lift, which decreases the angle of attack necessary to reach a required CL. On configurations with extreme sweep (e.g. HP-115) it is nearly impossible to maintain attached flow anyway, and any leading-edge suction due to attached flow would act in a mostly spanwise direction where it would not do much to offset the high induced drag of the low aspect ratio. On such planforms it is possible for significant increased CL due to vortex lift to result in a net improvement in L/D relative to the attached flow case. But the advantageous increase in CL at alpha due to vortex lift, comes with a significant increase in vortex *drag*. The Polhamus "suction analogy" (NASA-TIM-X-7278) dictates that the increase in lift due to vortex flow comes at the expense of re-orienting the attached flow leading edge suction vector into a direction normal to the plane of the wing. That vortex lift normal force leans progressively rearward as angle of attack increases, significantly degrading drag "polar shape" versus CL.

Higher L/D for better LTO performance and lower airport noise can be achieved primarily by reducing span-loading (higher aspect ratio for a given area), and keeping the flow attached on the more moderately swept edges to prevent loss of leading-edge suction. Higher aspect ratio also increases the lift curve slope, reducing the alpha required to generate a target CL. Reduced outboard wing sweep can provided added span, higher lift curve slope, and direct the attached-flow suction in a more forward direction (provided that the leading vortex formation can be delayed). For this reason, "cranked" planforms have generally been the preferred "best compromise" class of wing planforms since the early 1980's (unless higher sweep and lower aspect ratio are dictated by low sonic boom requirements).

On cranked planforms, increased leading edge nose radius can help delay flow separation on segments of the wingspan that have a subsonic normal Mach during supersonic cruise. On those leading-edge segments with small leading-edge radii or sharp edges, flow separation can be delayed by deflecting leading edge flaps. The leading-edge deflection and delay of vortex flow formation both tend to cause a loss in CL. Trailing edge flap deflections can recover this loss of CL, and provide a more elliptic load distribution for the attached flow conditions, provided excessive canard and tail trim are not required to trim out the nose-down flap moments. Optimization of the low-speed performance involves a complex trade-off of inboard and outboard leading and trailing edge flap deflections with takeoff CL, approach attitude, and climb-out noise due to thrust required and the altitude versus distance trajectory. At intermediate angles of attack, the cranked planforms will inherently have partly attached flow and part-span vortex flow. At higher alphas it is possible to have disorganized separated (stalled) flow, vortex flow, and attached flow. As angle of attack increases, there may be multiple vortex flows that interfere with one another, and smaller secondary or tertiary vortices that form underneath the initial separations. This makes the flow very difficult to predict accurately with most CFD methods. As the vortex separations occur and grow or begin to interfere and break down, the pressure distribution over the wing changes considerably, causing highly non-linear changes to pitching moment and drag due to lift factor $Ke=CD_{Lift}/CL^2$. Different leading edge flap types and combinations of deflections can be more or less effective in delaying or minimizing the pitching moment changes, and maximizing L/D.

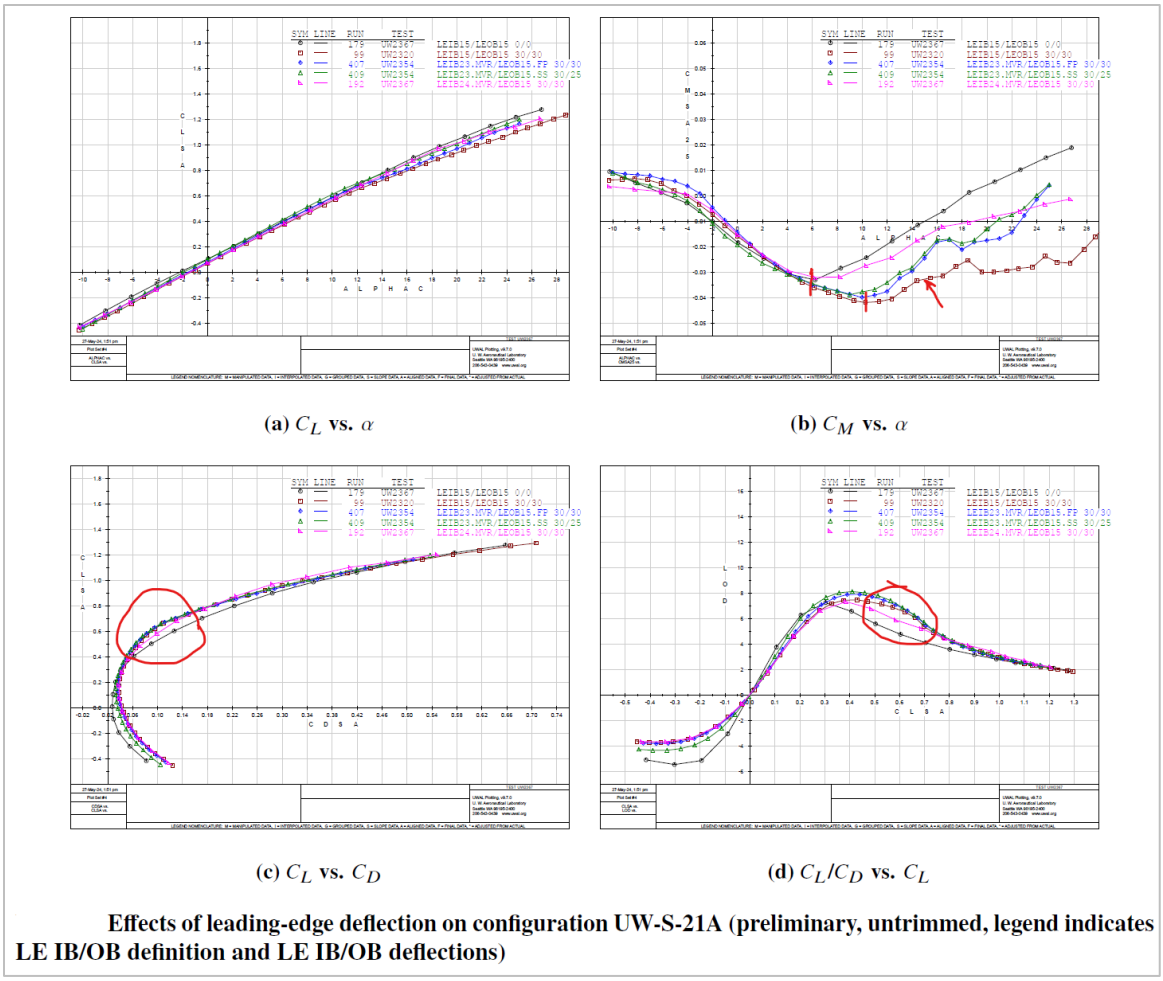

(a) C_L vs. α

(b) C_M vs. α

(c) C_L vs. C_D

(d) C_L/C_D vs. C_L

Effects of leading-edge deflection on configuration UW-S-21A (preliminary, untrimmed, legend indicates LE IB/OB definition and LE IB/OB deflections)

Figure 51- SCALOS KWT Model Leading Edge Flap Deflection Effects

Figure 51 shows example leading edge deflection data for several types on the baseline KWT model configuration with wing W15. Pitch-up is significantly delayed and post pitch-up instability is reduced with the RSAC baseline "droop-nose" type leading edge flaps, simple-hinged near the lower surface of the wing. The L/D is considerably improved in the LTO range of 0.5-0.65 CL, reflecting the improved (more "open") drag polar shape up to that point. This baseline concept for RSAC is shown in Figure 52. A notional actuation method was sketched that would allow the leading-edge segments to be deflected by a linkage attached to rotary gearboxes installed at various points along a rotating shaft that is driven by a power/control unit located in the inboard wing. An angled gear box at the planform break and a series of clutches and back-stops would allow the inboard and outboard deflections to be controlled independently and asymmetric deflections to be stopped.

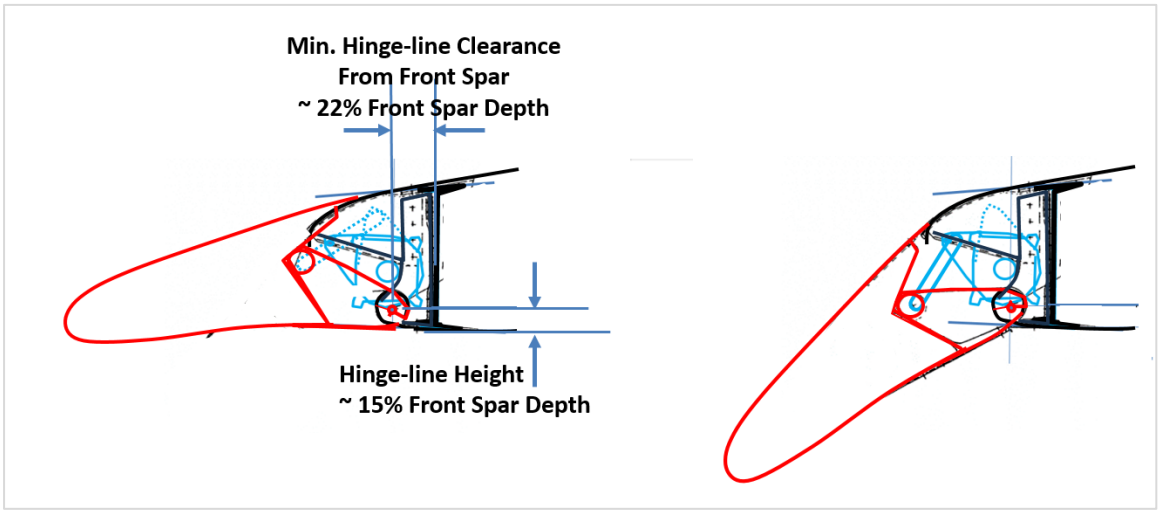

Figure 52- "Droop-Nose", Simple-Hinged Leading-Edge Concept (RSAC Baseline)

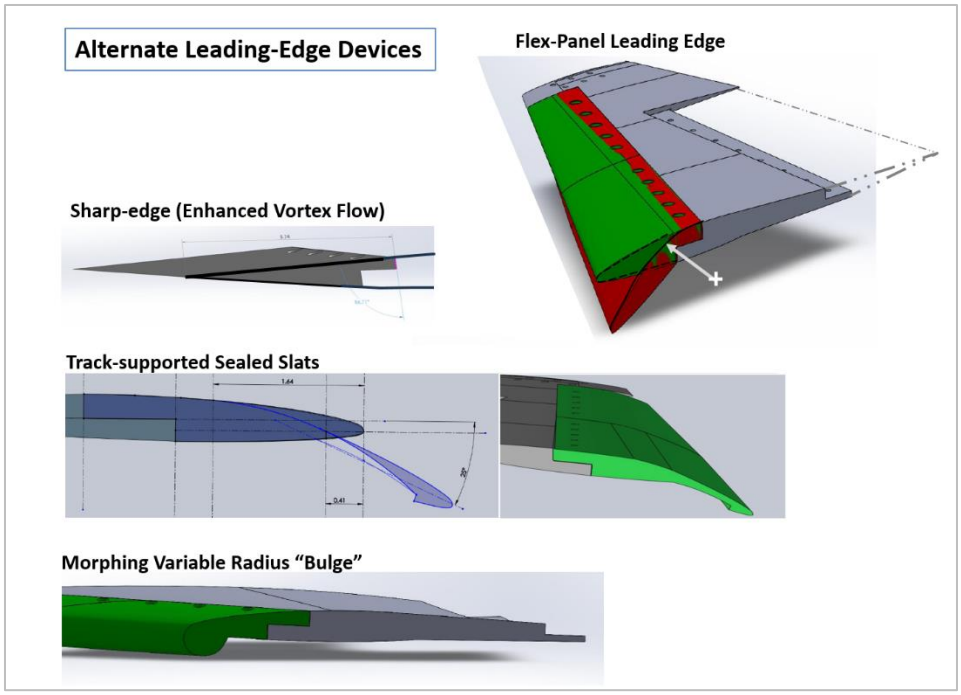

Figure 53- SCALOS Alternate Leading-Edge Concepts

The proposed RSAC baseline leading edge flap concept actuation system would be fundamentally similar in design to that used on several thin-wing fighter aircraft like F-18. The physical dimensions of the system for the outboard-most leading-edge segments would be similar to that for fighter applications due to the minimum thickness wing. While a detailed kinematic model was not developed, the actuation concept sketches were used to determine a minimum set-back distance from the hinge-line to constrain the wing leading edge spar location.

Figure 53 shows alternative leading-edge concepts that were tested for SCALOS, with varying degrees of success. Using one concept on the inboard more highly swept leading edge and another (flex panel or sealed-slats) on the outboard may offer the best combination but this would require more detailed trades. The "morphing" variable-radius type flap for the inboard wing leading edge may have advantages, but the geometry is complex and in both the 2023 and 2024 SCALOS test entries, the as-built 3D printed edge parts did not replicate the results of a similar concept that worked well on a lower sweep delta wing R-UAV in 2009 ("SSQR", a gas-turbine-powered noise shielding flight experiment UAV). The inherently longer outboard chord length for the deployed sealed slat leading edge showed potential advantages compared to the loss in chord that occurs with deployment of the simple hinged concepts.

There is definite benefit for the droop-nose type flap, hinged near the lower surface, compared to a rotary hinge rotating around the mid-thickness of the wing. The lower hinge-line, located slightly aft of the upper surface flap seam, allows the upper trailing edge of the flap to sweep out a larger arc, riding against a curved sealing surface that is part of the fixed portion of the structure on the leading-edge spar.

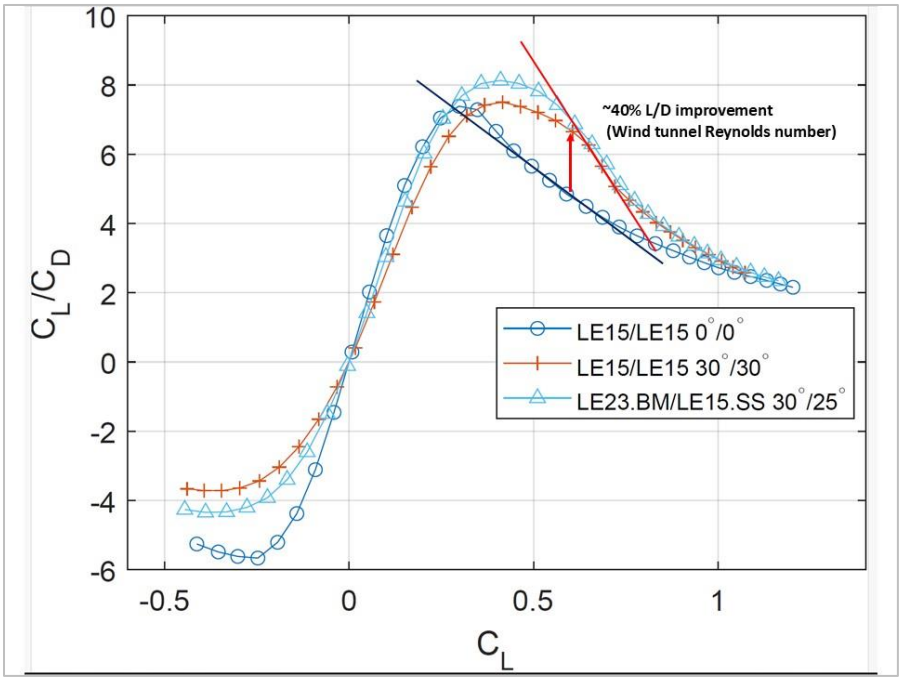

Figure 54- Effectiveness of the Baseline RSAC Flap Concept (IB15/OB15) – L/D

Figure 54 shows the effectiveness of the baseline flap concept, providing a 40% improvement in L/D at 30 degrees deflection inboard and outboard, relative to zero deflection," clean" wing. The comparison with "LE23.BM .." shows an alternate concept using the variable radius "bulge" morphing LE inboard and sealed slats outboard. In both cases, the slope of d(L/D) /dCL is actually much steeper for the deflected edges above 0.65 CL a potential issue for glide path control at or below Vref. Figure 55 shows the effect of the same deflection in terms of axial force (an indicator of "attainable suction")versus alpha.

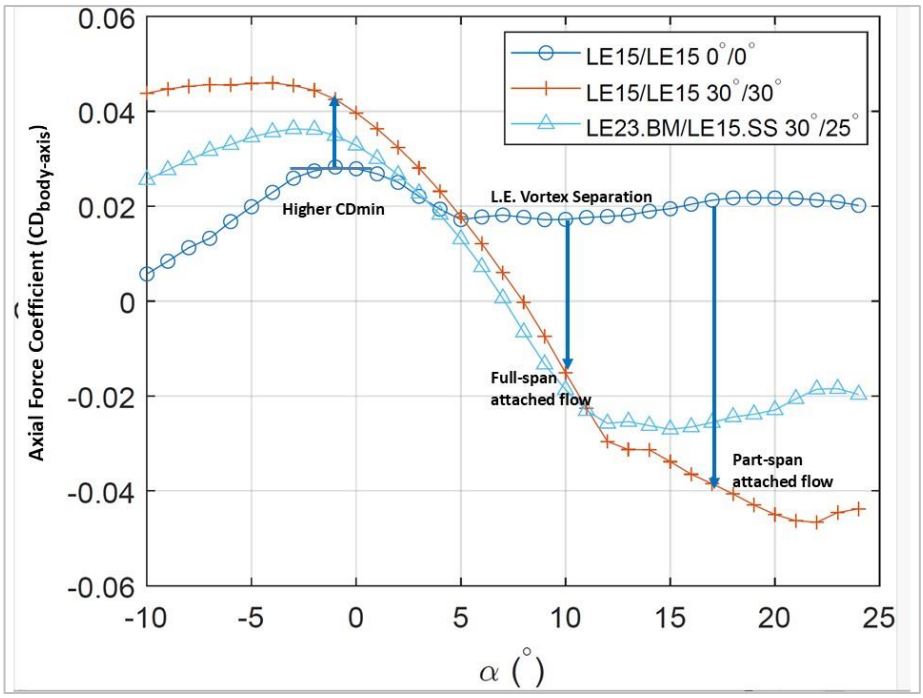

Figure 55- Effect of Baseline RSAC Leading Edge Flap for Attainable Suction

Figure 56 shows the effect of the baseline leading edge flap concept in delaying the pitch-up break in the moment curve, and improving the Cm-alpha stability post pitch-up. While the alternate concept shows good performance for L/Dmax, the L/D and attainable suction trends at the proposed Vref CL of 0.65 (~12 degrees alpha) is essentially the same as the simple-hinged droop-nose baseline concept.

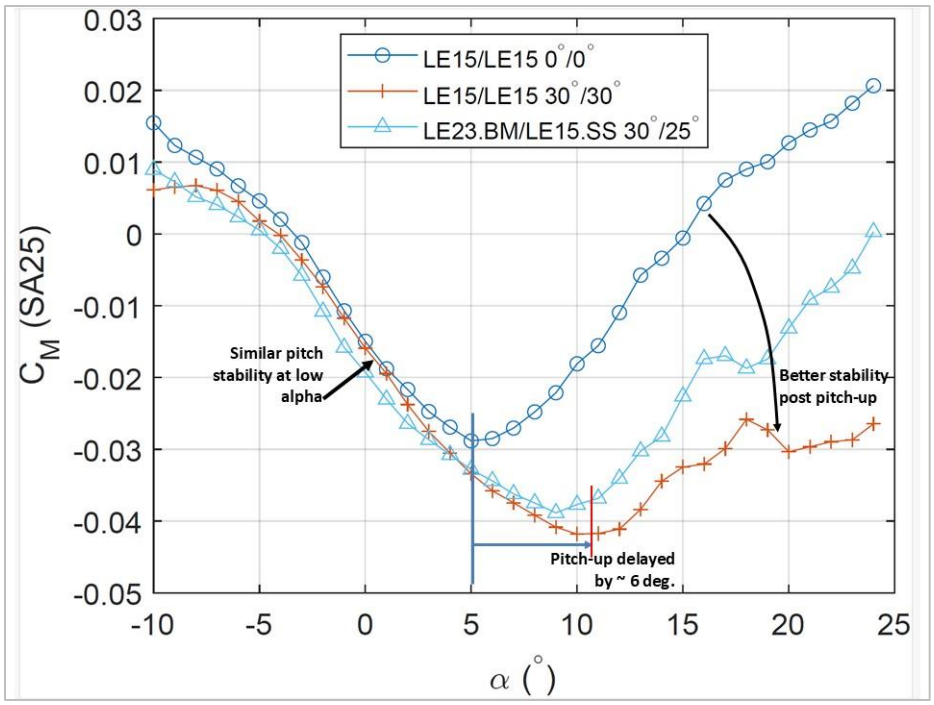

Figure 56- Effectiveness of the Baseline RSAC Flap Concept (IB15/OB15) – Pitch Stability

The shaft-driven gearboxes keep the entire system ahead of the spar (as opposed to the track-supported slats which would require a circular-arc roller track and actuator to pierce the front spar web). Baseline leading edges on the inboard wing would need deflections as high as 60 degrees relative to the hinge-line (30 degrees stream-wise) and would be divided into multiple segments (as on the KWT model parts) to accommodate wing flex and provide redundancy. UW testing of the UW-S-18 configuration in 2018 included the effects of simulated leading edge ice build-up, and the effect of having one leading edge panel missing. In both cases, the effect on the CL curve and CLmax was minimal, with the changes being noted primarily as "lumps" in the pitching moment curve and increased induced drag. On that basis, RSAC assumes that a leading-edge anti-ice system is required only in front of the engine inlets to prevent ice build-up from being ingested and causing engine damage. Leading edges are expected to be deflected on a schedule with Mach number and flight phase (landing, takeoff, climb/descent modes) but not necessarily to vary with alpha. It is possible that "active" leading edge deflections, automatically moving as a function of Mach, alpha, and g load as many fighter aircraft do, would be advantageous, but whether that is a net favorable trade given the added complexity and certification issues would need to be part of a future trade study and possibly flight simulations.

Trailing edge flaps are assumed to be driven by a similar concept with rotary gearboxes and remotely driven torque shafts, similar to several current subsonic airliner trailing edge flap systems. All of the trailing edge segments are assumed available for use as pitch trim, lift flaps, or roll-control devices (i.e. flaperon/elevon/aileron functions).

F. Control Concept

The RSAC assumes a Fly-By-Wire flight control system with coupled engine & autopilot controls similar to 787, A350, and A220/C-series. General control laws and envelope protection logic are assumed to be similar to the C-series which reportedly manages to combine the best features of Boeing and Airbus FBW systems. Control actuation system is assumed to make use of distributed hydraulics and EHA type actuators, brake-by-wire, and steer-by-wire nose gear.

Primary pitch control is via that all-flying horizontal tail, with supplemental pitch control authority from the canard. The "elevon" function of wing trailing edge devices is expected to be used for trim and span-load control. The canard is assumed to be deflected to +/-10 degrees for trim and up to +15/-40 degrees for supplemental pitch control authority. The current horizontal tail was sized for pitch control and forward CG trim on the 2015 R-UAV at model scale and model q. The tail sizing for the full-scale RSAC has not been re-optimized. The tail planform used on RSAC is based on the low trim-drag tail for the UW-S-21A. It is unknown whether this planform would actually be acceptable from the aeroelastic standpoint. It is possible that FEM analysis would show that the span of this tail planform is not sustainable. The earlier horizontal tail planform used on the 2015 R-UAV has been held as a "fall-back" solution if the higher aspect ratio surface proves unworkable. The horizontal tail is one-piece with right and left halves connected in the middle of the body. The canard surfaces are each mounted to side-of-body bearings and actuated from individual machinery compartments inside the fuselage.

The canard and horizontal tail are currently drawn as single-piece surfaces, but the inertia of large control surfaces can make them difficult to move quickly and reverse directions if high bandwidth deflections are required for stability augmentation, gust alleviation/ride quality/structural mode control. Later versions may may need to incorporate separately moving high-rate elevator surfaces on the trailing edges of the lower rate main surface.

Outboard wing trailing edge “aileron” function is assumed to be locked out above [TBD] knots to prevent roll control reversal at high q. The flaperon “droop” function of the outboard wing trailing edge devices are assumed to be used along with outboard leading-edge flaps for “variable camber” function up to Mach 1.5 to keep the thin outboard airfoils operating withing their attached flow “on-design” condition across the altitude/weight/Mach envelope. Downward (positive) deflection of the trailing edge devices for “flap” functions will be limited to 10deg or 15 degrees in order to prevent control saturation and hinge-line flow separation.

Roll control authority will be supplemented by spoiler-slot-deflector devices, which are phased in a primary roll control at transonic and supersonic conditions. Spoiler-slot-deflector (SSD) devices can be fully opened to supplement conventional wing spoilers as speed-brakes for flight path control and to slow the aircraft at supersonic Mach numbers for emergency descent drag. Figure 57 shows a schematic of proposed use of the spoiler-slot-deflector devices that was generated during KWT model test planning (not RSAC-E geometry).

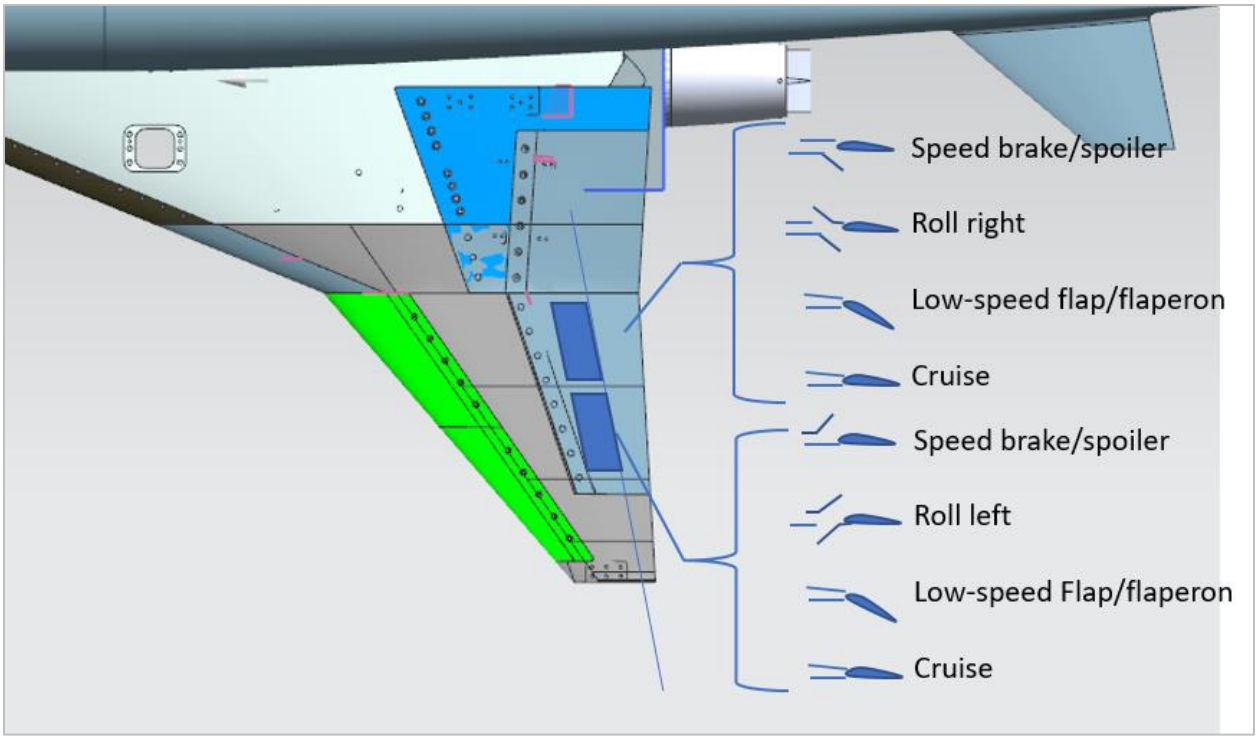

Figure 57- Schematic of Spoiler-Slot-Deflector Use and Outboard Low-Speed Flaperon

Rudder control surface mounted on the vertical tail, is conventionally and would be used as the primary yaw control and yaw/roll damper stabilization. Additional yaw control authority could be obtained by partial deflection of the wing-mounted spoilers.

Alpha/ Beta and roll attitude limiting are anticipated. 3-DOF S&C and 6-DOF flight simulations of RSAC to investigate pitch augmentation, alpha limiting options, and critical pitch control conditions remain to be done at the time of publication due to time, staffing, and funding limits. Complete inertial properties and final corrected wind tunnel data were not available to assess open loop S&C levels at the time of publication. These tasks remain for future work.

Extensive control deflection data has been collected during the SCALOS effort and are now available for more detailed study. Boeing BR&T completed dynamic derivative testing of the UW-S-21A concept for dynamic stability assessments. Dynamic stability will be key to establishing limits of pitch instability.

G. Structures Concept

The RSAC structure is based on N+2 and HSCT examples and lessons-learned (NASA Doc 20000044619, NASA/TP-2005-213533). Figure 58 shows the main integration features of the RSAC and location of key components. Figure 59 shows the main structure elements of RSAC. The structure is primarily carbon fiber (787 spec materials should be good up to Mach 1.8 temperatures in most zones). Selected ribs and leading-edge structure, and hot zones in and around the engine supporting structure would be metallic (presumably titanium, both for thermal environment and stiffness). The main wing box is a tip-to-tip multi-spar structure that carries through under the passenger cabin floor. Immediately ahead of that is the landing gear retract bay which has a single full-depth keel beam running through it to the next major body frame. The multi-spar main box transitions to a dry full-depth large cell honeycomb or "egg crate" structure supporting solid laminate skins. Aeroelastics, and structural mode vibrations/flutter are concerns for the thin lifting surfaces and slender body, but lower risk than on the larger HSCT vehicles because the smaller structure is relatively stiffer, and the RSAC is nearly 100,000lb lighter than Concorde. Predicted weights are based on the N+2 areal weights of major components for the 765-076 and 765-070A concepts, which were in turn predicted with tools calibrated to multiple HSCT detailed finite element models. A manufacturing breakdown for RSAC has not yet been created, but could be expected to be similar to that proposed for HSCT.

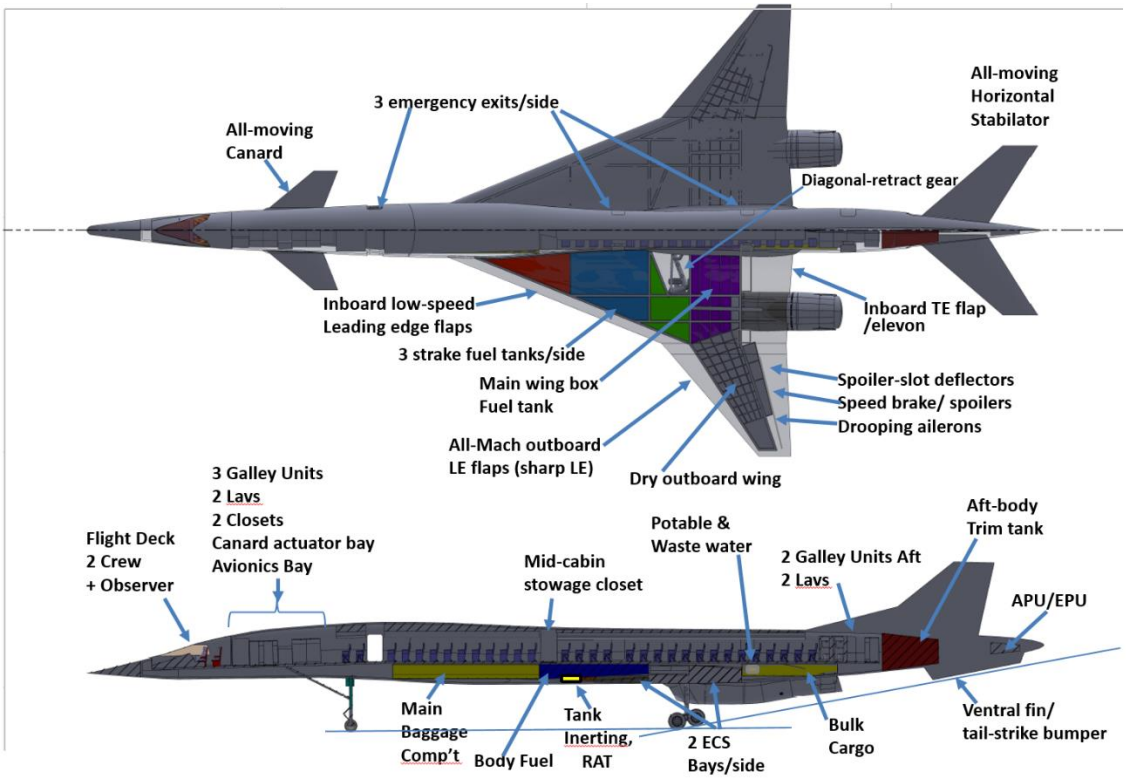

Figure 58- Key Integration Features of the RSAC

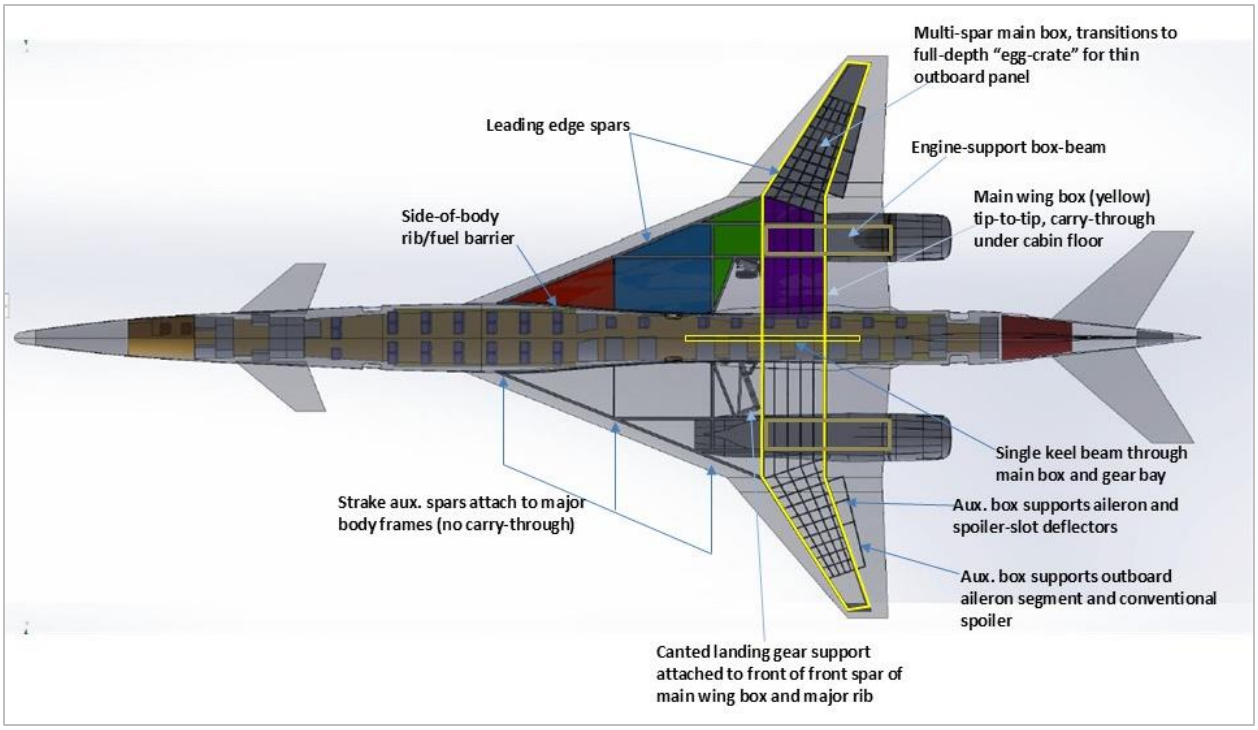

Figure 59- Arrangement of RSAC Major Structure Elements

Figure 60- Iso View of RSAC Primary Structure Concept

H. Fuel System Concept

Figure 61 shows the arrangement of fuel tanks and the maximum fuel capacity (in pounds) for each. Tanks in impact susceptible zones would include wing skin reinforcement (stiffeners) and a rubberized Kevlar (or similar) liner to avoid puncture and hydraulic ram effects.

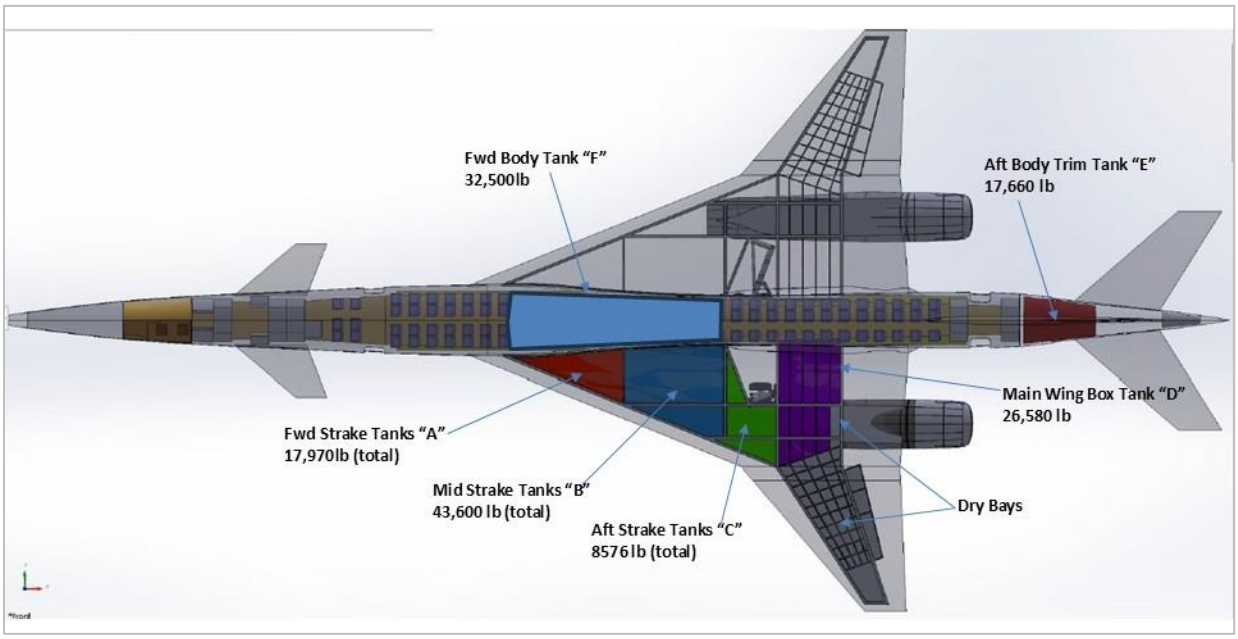

Figure 61- RSAC Fuel Tank Arrangement and Tank Capacities

I. Landing Gear Concept

Design classes, over 4 years, progressively evolved the current landing gear concept for RSAC. The main gear is a composite of features from 767, Concorde, and HSCT landing gears. The gear retracts diagonally into a stow bay in front of the main wing box carry-through. The 4-wheel main gear bogie is tilted by a positioner during retraction to fit in the stowage space. As with Concorde's main gear, the gear shock strut pulls the inner cylinder up during retraction to shorten the main gear leg by 16 inches. This makes the stowed gear length about the same length diagonally as the height of the strut when the loaded aircraft is parked or taxiing. When the main gear is extended and the shock strut fully uncompressed (as on landing approach) the total strut height is about 16 inches longer than when stowed and the bogie sits in a toe-down attitude. The front tire contacts the runway first on touchdown (like 767). The fully compressed gear provides a ground contact angle to the ventral fin/bumper of 10 degrees. The nose gear retracts forward and the nose gear doors include a curved shape that forms a shallow "blister" shaped fairing over the stowed tires. The nose gear length provides a 1-degree nose-up body attitude when the loaded airplane is on the take-off roll. UW experience with R-UAV's of similar wing planform has shown this can smooth the takeoff rotation (especially at forward CG conditions) and potentially decrease ground-roll. The basic gear concept is sketched in Figure 62. Figure 63 shows a cut-away view of the RSAC configuration from below with one gear in retracted position.

Given the close proximity of the engine intakes to the landing gear (Figure 64) engine ingestion of foreign object debris (FOD), especially blown tire tread, is a safety and certification concern. As with the

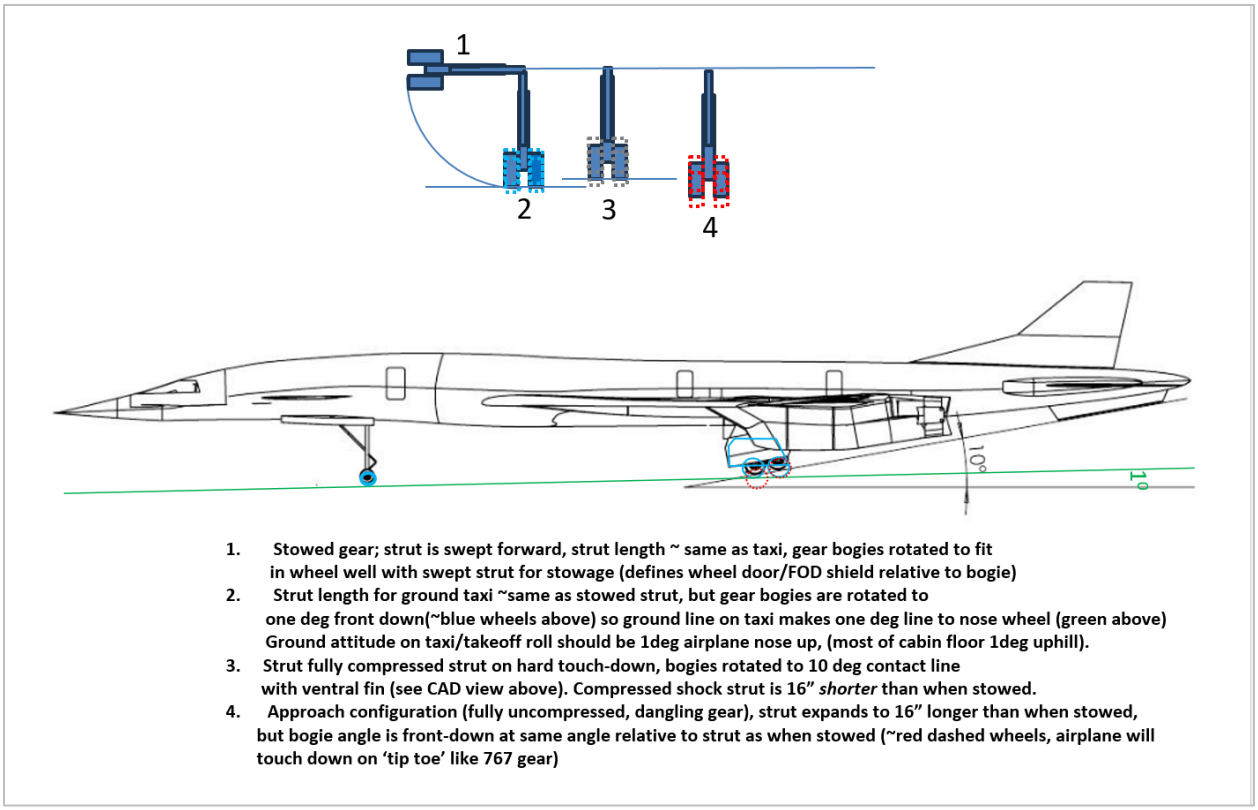

1. Stowed gear; strut is swept forward, strut length ~ same as taxi, gear bogies rotated to fit in wheel well with swept strut for stowage (defines wheel door/FOD shield relative to bogie)
2. Strut length for ground taxi ~same as stowed strut, but gear bogies are rotated to one deg front down(~blue wheels above) so ground line on taxi makes one deg line to nose wheel (green above) Ground attitude on taxi/takeoff roll should be 1deg airplane nose up, (most of cabin floor 1deg uphill).
3. Strut fully compressed strut on hard touch-down, bogies rotated to 10 deg contact line with ventral fin (see CAD view above). Compressed shock strut is 16" *shorter* than when stowed.
4. Approach configuration (fully uncompressed, dangling gear), strut expands to 16" longer than when stowed, but bogie angle is front-down at same angle relative to strut as when stowed (~red dashed wheels, airplane will touch down on 'tip toe' like 767 gear)

Figure 62- RSAC Landing Gear "Shrinking" Shock Strut /Toe-down Bogie Concept

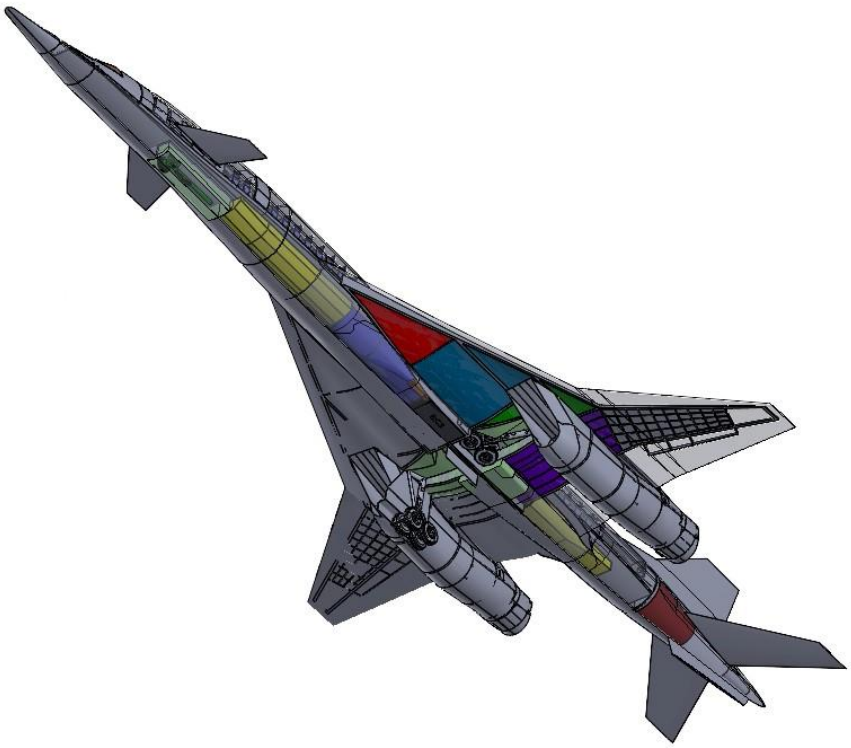

Figure 63- RSAC Main Landing Gear in Extended and Retracted Positions

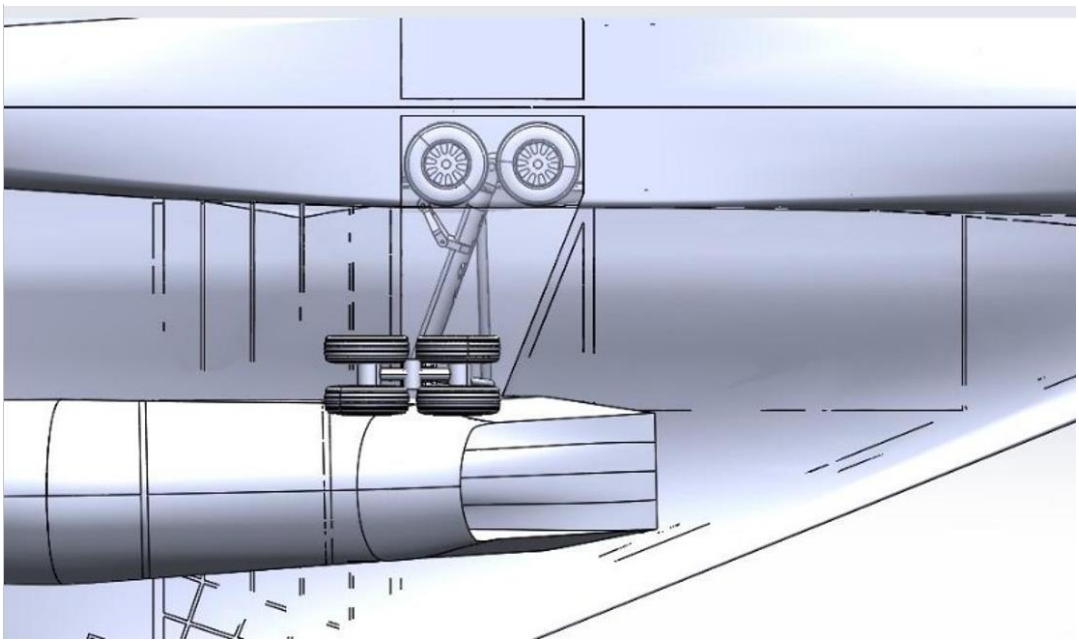

Figure 64- Landing Gear to Engine Intake Proximity

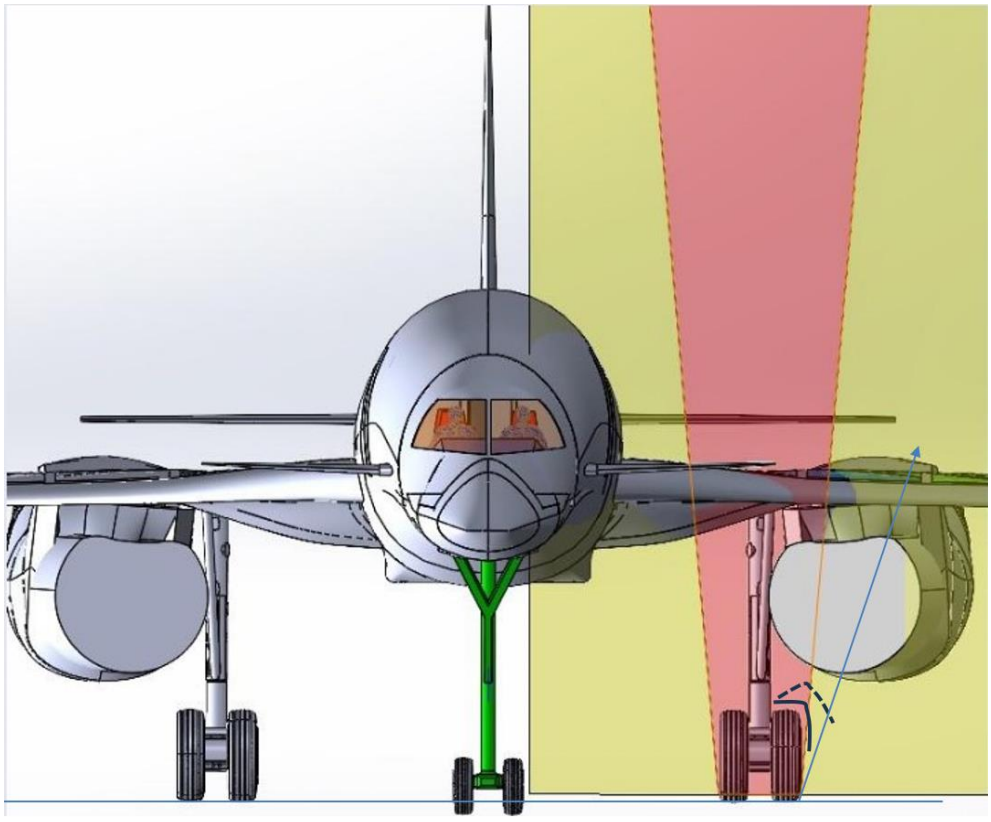

Figure 65- Landing Gear FOD/ Tire Debris High Probability Zone

re-certified Concorde, use of re-treaded tires would be forbidden and tires would be the "NZG" type to protect against side-wall blow-outs and large tread section failures. Lower surface wing skins would be reinforced and fuel tanks in this zone would include self-sealing liners or "bladders" similar to the re-certified Concorde.

After reviewing available literature on tire FOD incidents for Concorde and several other aircraft, it was noted that the majority of wing lower surface impacts seem to occur within a fairly narrow fan-shaped zone to either side of the tire contact point, and within a 10 to 15-degree cone in the forward direction (Figure 65). While it would be impossible to be certain of blocking 100% of tire-generated FOD into the inlets (especially for ricochet trajectories), it seems the vast majority could be deflected by blocking the direct line-of-sight paths from the high probability releases. The objective would be to reduce the total probability of ingesting significant FOD to a similar order as that of subsonic high bypass ratio aircraft which have much larger intake capture areas to contend with and much less clearance between the inlet lower lip and the runway. It is encouraging that, anecdotally, B-1A and B-1B have apparently not particularly suffered from tire FOD issues. Part of the reason Concorde may have had more concern with tire failure incidents is the fact the takeoff speeds for Concorde were very high due to the high wing loading and short span. This essentially made every takeoff a "tire-speed-limited" takeoff--- a case usually only encountered for subsonic aircraft at high altitude airports on hot days. In addition, Concorde had no aft tail and the arm between the ground rotation point and the pitch control surfaces (elevons) was fairly short, which may have increased the load on the tires at the point of takeoff rotation, relative to other aircraft.

Several options were sketched out and considered for means of blocking or deflecting gear-generated FOD from the adjacent RSAC inlets. Several options for landing gear "fenders" were looked at, as these were baselined onto later HSCT designs due to similar concerns (Figure 66).

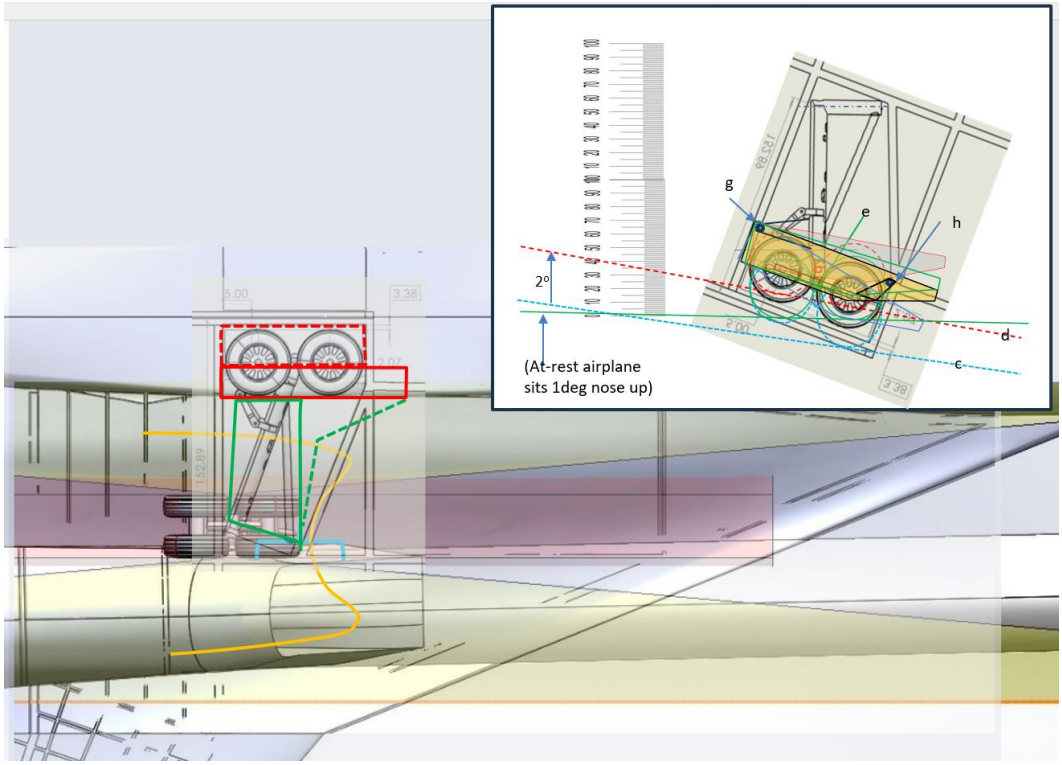

Figure 66- An Example Main Gear Bogie Fender Concept

In the end, the concept which was adopted for RSAC, was to increase the size of the lower portion of the landing gear leg door, extending it downward along-side the wheels, and forward of the front tires (Figure 67). This lower portion would be a separate panel, articulated to move with the bogie, and positioned with the bogie to fit up to the belly fairing on retraction. The added weight of the reinforced and extended leg door and associated positioning linkages was "guesstimated" to be 400 pounds per side. This weight was added to the baseline interior RSAC configuration's weight and balance accounting to assess the rolled-up OEW and center of gravity. The main gear is close enough to the nominal aircraft CG that the change in OEW CG due to this added weight was insignificant and neither was the estimated range penalty. It should be noted that the gear leg cut-out in the lower wing skin was not enlarged for the extended leg door, but rather the section of skin that would have been cut out was simply recessed to form a pocket that the enlarged door panel fits into. When retracted the OML remains flush, and when the gear is lowered the open gear cavity remains the same as it would have been in the typical leg door region. Small wheel cover doors covering 2/3 of the wheel well area remain, hinged to the belly fairing, and remain closed except when the gear is in transit during extension or retraction. This does cause a increase in the wheel well's exposed cavity opening which may be an added airframe noise source to consider for landing approach. The gear bay accommodates tire diameters slightly larger than Concorde's, similar to 767-200 in ACN and 767 MTOW, but with the Concorde's slightly narrower bogie width. Within the time and resources available for the capstone design effort, no detailed kinematic model was created for the landing gear or FOD protection door.

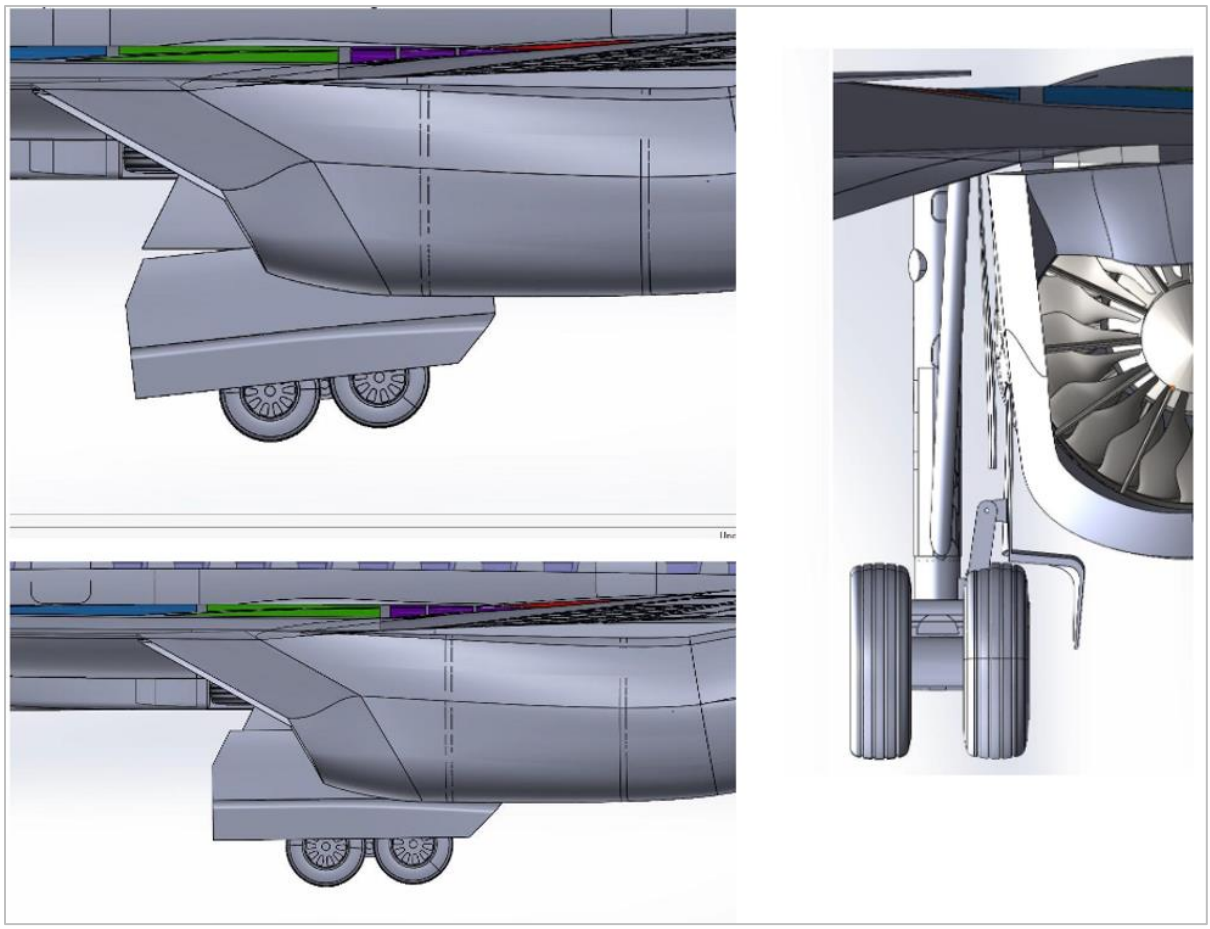

Figure 67- RSAC-E; Articulated Enlarged Gear Door/FOD Deflector Concept

A static CAD model of the RSAC landing gear concept, incorporating a preliminary version of the extended area door for line-of-sight FOD blocking, was used in 2024 to build representative landing gear parts for the UW-S-24 configuration of the SCALOS modular model. Capstone student created the CAD definition and 3D printed the parts, reinforcing the struts with steel rods so they would not deflect at the test airspeeds. Figures 68 and 69 show this landing gear installed in the KWT facility to assess the drag and stability of the deployed gear /FOD doors.

Figure 68- Model UW-S-24 Representation of RSAC With Landing Gear Down

Figure 69- Details of the main landing gear wind tunnel model components

J. Aircraft Systems Concept

The conceptual design and layout of mechanical-electrical and avionics systems for RSAC was beyond the scope of the senior capstone design efforts, and beyond the scope of the overall aerodynamics-centered SCALOS project. However, some thought was necessarily given to systems as needed to understand integration requirements, reasonableness of weights predictions, and to allocate cross-sectional area and volume within the aero OML. It is assumed that actuation would be accomplished using a combination of conventional hydraulics, distributed hydraulics with EHA actuators, and some use of EMA actuators where weight and redundancy requirements permit. The main landing gear would probably be assisted with hydraulic accumulators in order to buffer the hydraulic-electric power demands during low-speed flight operations. Brakes and steering would be electrically signaled and possibly use EMA type actuators. As previously described, leading edge devices (and possibly most trailing edge surfaces) would be actuated by composite torque tubes driven through multiple local rotary gear-boxes by an inboard-mounted power/control unit. Actuation of the canard is assumed to be by redundant linear (EHA) actuators enclosed in a sealed compartment inside the forward cabin. It should be noted that the placement of the canard mechanical equipment enclosure in the RSAC-E is based on a canard spindle location that is farther forward than the intended location shown in the actuation schematic in figure 70. Hinge moment and fail-safe trades can be expected to move the spindle aft, requiring slight movement of the RSAC-E's forward galley and lavatory arrangement. The space allocation for the ganged actuator assembly was scaled from available data for fighter aircraft stabilator and canard actuation. With the exception of the canard system, other actuators are not explicitly shown in the RSAC-E definition.

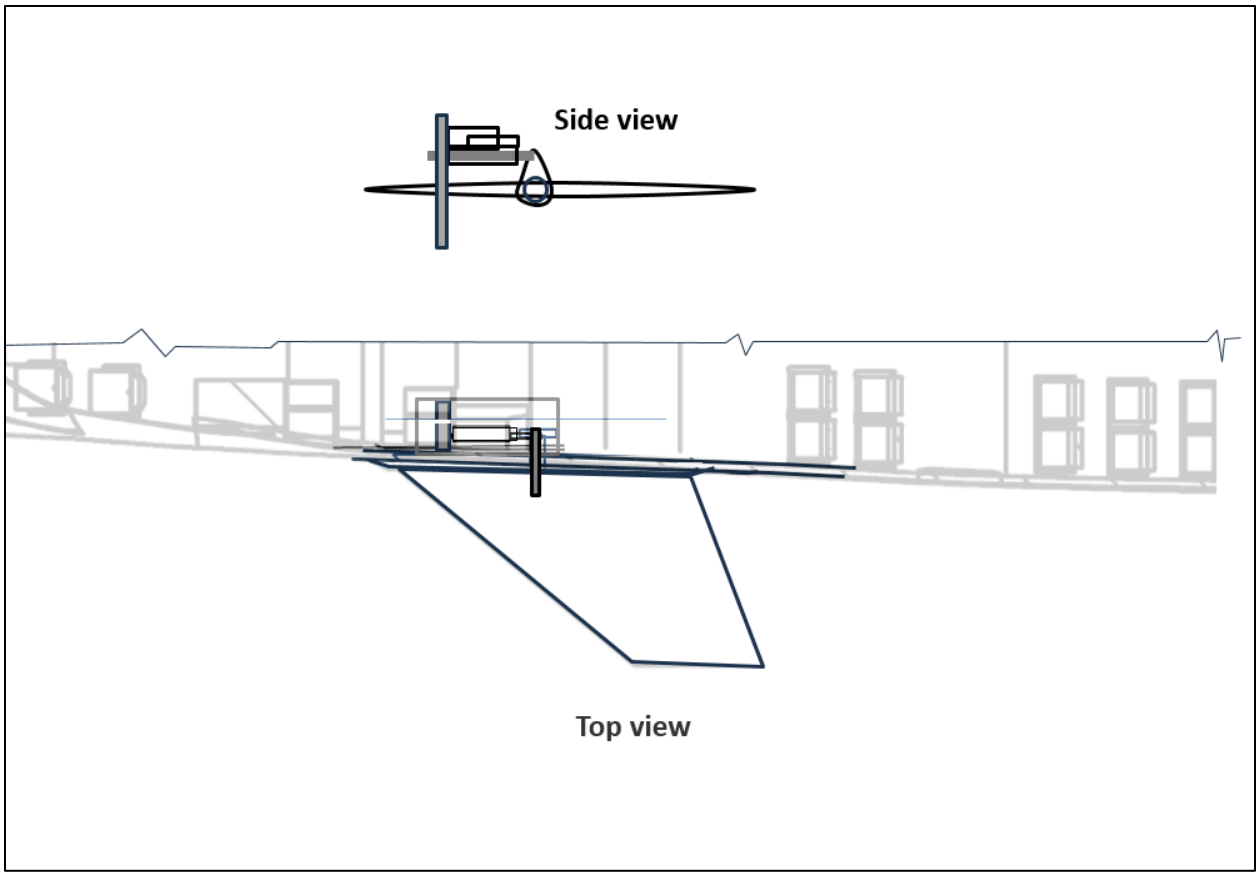

Figure 70- All-flying Canard Actuation / Spatial Integration Concept

The Environmental Control System (ECS), responsible for pressurization, ventilation, and temperature control in the passenger cabin and other pressurized areas in the fuselage, deserves added scrutiny. The thinner air at RSAC cruise altitudes, and kinetic heating due to compressibility effects at cruise Mach numbers up to 1.8 mean that the outside air does not provide as effective a cooling capacity for ECS heat exchangers. Additionally, maintaining cabin pressure at high altitude during the time it takes to slow the airplane from cruise speed and perform an emergency descent argues for a short-term high-flow mode for the pressurization system, possibly with an additional ECS unit for redundancy. These factors indicate the ECS capacity per passenger could be 1.5 to 2x higher than for subsonic aircraft of similar passenger capacity. On faster aircraft such as Concorde and HSCT, flying at even higher altitudes and Mach, it was a good design trade to use the fuel as an ECS heat sink rather than having a conventional subsonic airliner system. Some of the more recent subsonic airliner programs like 787 do not pressurize using engine compressor bleed air, instead relying on electrically powered pumps to pressurize ambient air. This type system is much more reliable but may be heavier and requires additional external air scoops that would increase supersonic drag. The trades involved to choose a particular system for RSAC were beyond the scope of the capstone design effort so a compromise was reached in which physical locations would be allocated for 4 redundant ECS packs with a total physical volume of 1.5x that of the 100-160 passenger A220/C-series aircraft, and individual pack dimensions were roughly based on the EMB-175 system. The ECS unit volume allocation is split between two zones, just forward and just aft to the main wing box carry-through. The present arrangement is merely a “place-holder” and actual trades may indicate that for the cruise Mach number and redundancy requirements of RSAC, some type of hybrid ECS is the best solution. In that case the current space allocation may be over-kill.

Space for the approximate size of tanks for an “OBIGGS” On-Board Inert Gas Generating system required for the nitrogen inerting of empty fuel tank spaces was allocated in the “cheeks” of the landing gear “belly” fairing ahead of the ECS spaces.

An “avionics closet” space is allocated just aft of the flight deck, and electrical/electronic systems spaces exist in the lower lobe of the forward fuselage.

Space is allocated in the tail-cone aft of the horizontal tail, for an APU/EPU system, assumed to be operable in flight at subsonic speeds.

Space is allocated for the potable water and vacuum waste water tanks in the aft lower-lobe at the front of the bulk-cargo stowage space.

The main cargo hold in the forward body has floor-to-ceiling space adequate for incorporation of a low-profile “rolling carpet” conveyer belt system for assistance in loading and unloading passenger bags. The current space allocation for the main cargo hold more than meets the RSAC baggage requirements so volume in the forward portion could be re-allocated if needed for systems space if needed.

K. Payloads /Passenger Accommodations

Considerable effort was spent by the capstone teams on iterating to find a cabin arrangement that would satisfy the goal of having passenger personal space (comfort level) that would be acceptable to the target premium service customer for the expected shorter flight time, but providing minimum body cross-sections for low wave drag. Concorde “got away with” a simple constant section body because the cross-sectional area distribution of the low-span wing and ogee planform provided a fairly low-drag total area distribution. The cabin integration philosophy adopted for RSAC baseline “spec” interior, was to use a

larger seat size based on single aisle first class (e.g. 737 first class, with similar flight times). Use a slightly smaller cabin width from the narrowest cross-section (near the landing gear stowage bay) aft, losing one seat abreast relative to Concorde. Make up for the small seat count loss by using a slightly longer (lower drag) fuselage, and keeping the 4-abreast cross-section in the wider forward cabin, all with the same "spec" seats (Figure 71). The cabin height at the smallest cross-sections would be held to equal or greater than Embraer 175 series (~Concorde cross-section).

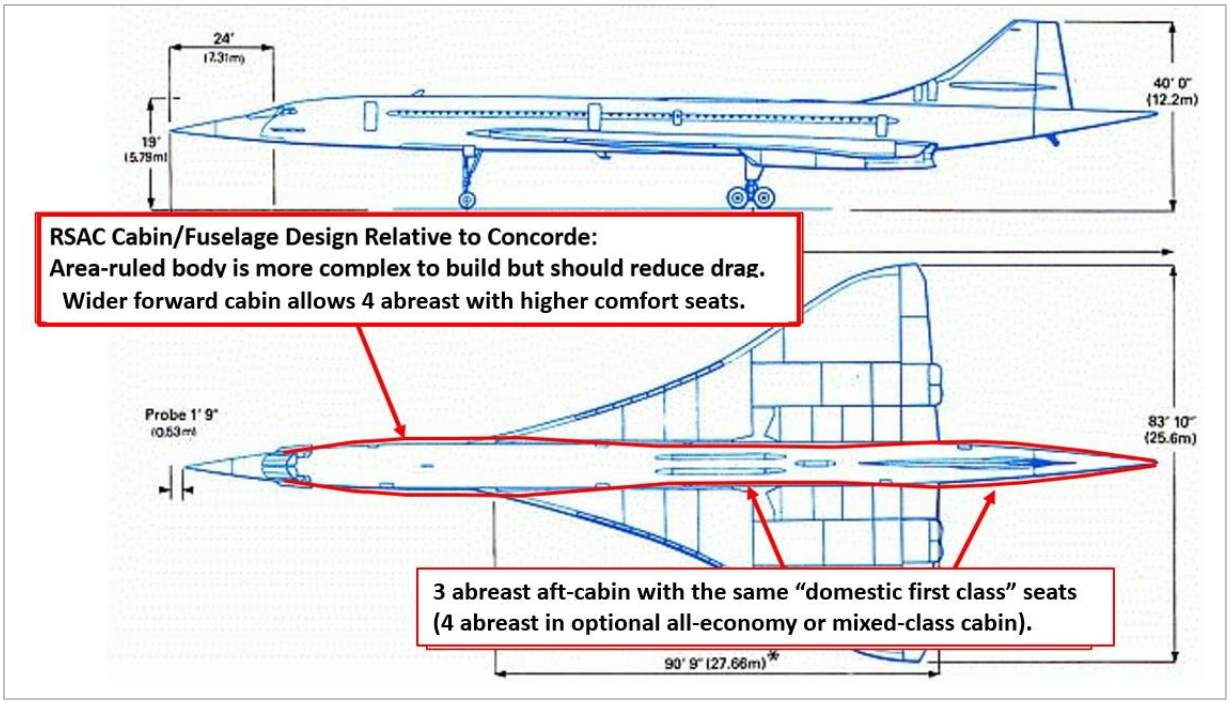

Figure 71- RSAC Cabin Design Philosophy

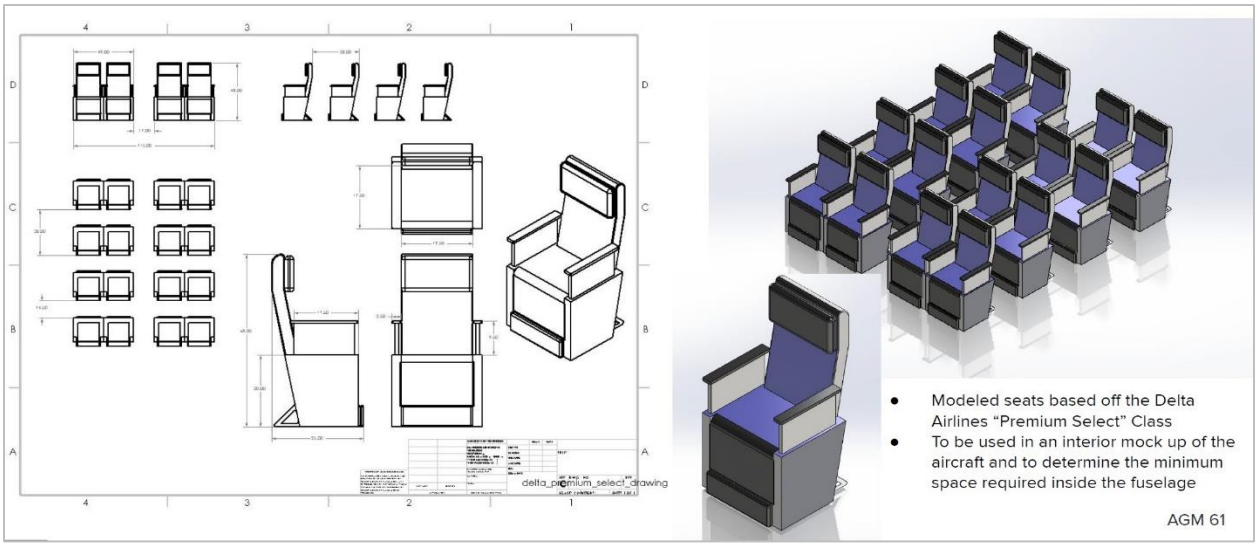

Figure 72- RSAC "Supersonic Business Class" Seat Design

Creating a custom CAD model of the spec interior seat size facilitated trying numerous internal LOPA arrangements during area-rule iterations on the aero OML, and allowed accurate space allocations for development of cross-sections and inboard profile drawings. The "supersonic business class" seat was designed by capstone students based on the overall dimensions of Delta Airlines' "Premium Select" seats (in between premium economy and business class on overseas flights), and 3rd party seat designs such as the Acro Series 7 Lightweight Domestic First/Business class seats (https://acro.aero/product/series-7/). The resulting RSAC "spec" seat is shown in Figure 72.

During design cycle iterations between the external aero shape requirements and internal cabin and lower-lobe volume requirements, several key constraint points emerged. These are shown in Figure 73.

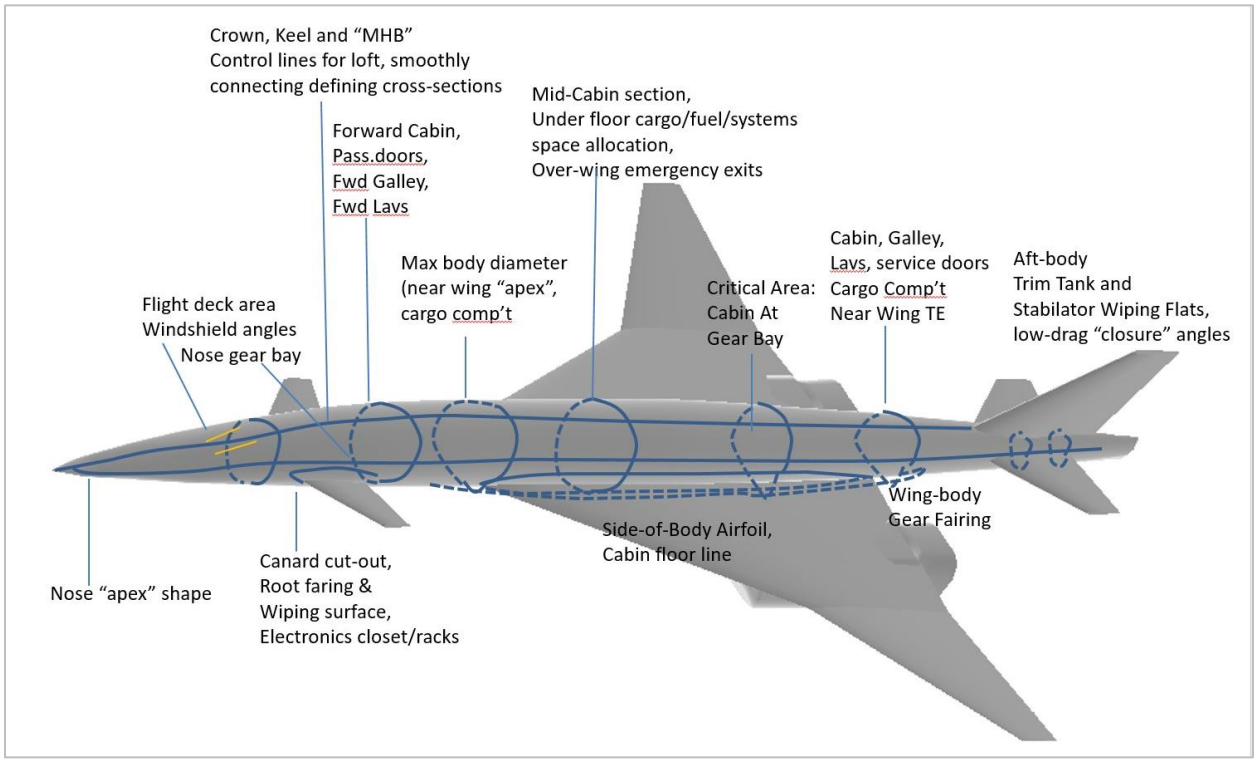

Figure 73- Fuselage: Cabin Defining Cross-Sections and Aero Loft Constraint Points

Cabin cross-sections over the main wing box and just ahead of the landing gear stowage well were particularly challenging because those are areas where the total cross-section of the wing + body are maximum along the oblique Mach cutting planes during wave drag predictions. It is also the region where the physical geometry due to wing box depth and stowed landing gear cross-section are relatively unchangeable, so the burden for minimizing the configuration total maximum area depends heavily on the details of the cabin cross-section. Cabin cross-sections at two example locations are shown in Figure 74.

A secondary goal of the cabin design was that it should provide flexibility to the airlines to reconfigure seating arrangements within the inner mold lines (IML), allowing a high-density all-economy interior, a mixed business and economy cabin, a mixed business/first class interior with lay-flat seats, or an "executive class" interior with lay-flat pod seats and a number of personal cubicles. Layouts of passenger accommodations (LOPA's) were arranged for each of these options, resulting in passenger payload options of 98-103 for the spec interior, 142 for all economy, 45 for mixed first/business, and 36 for the executive cabin.

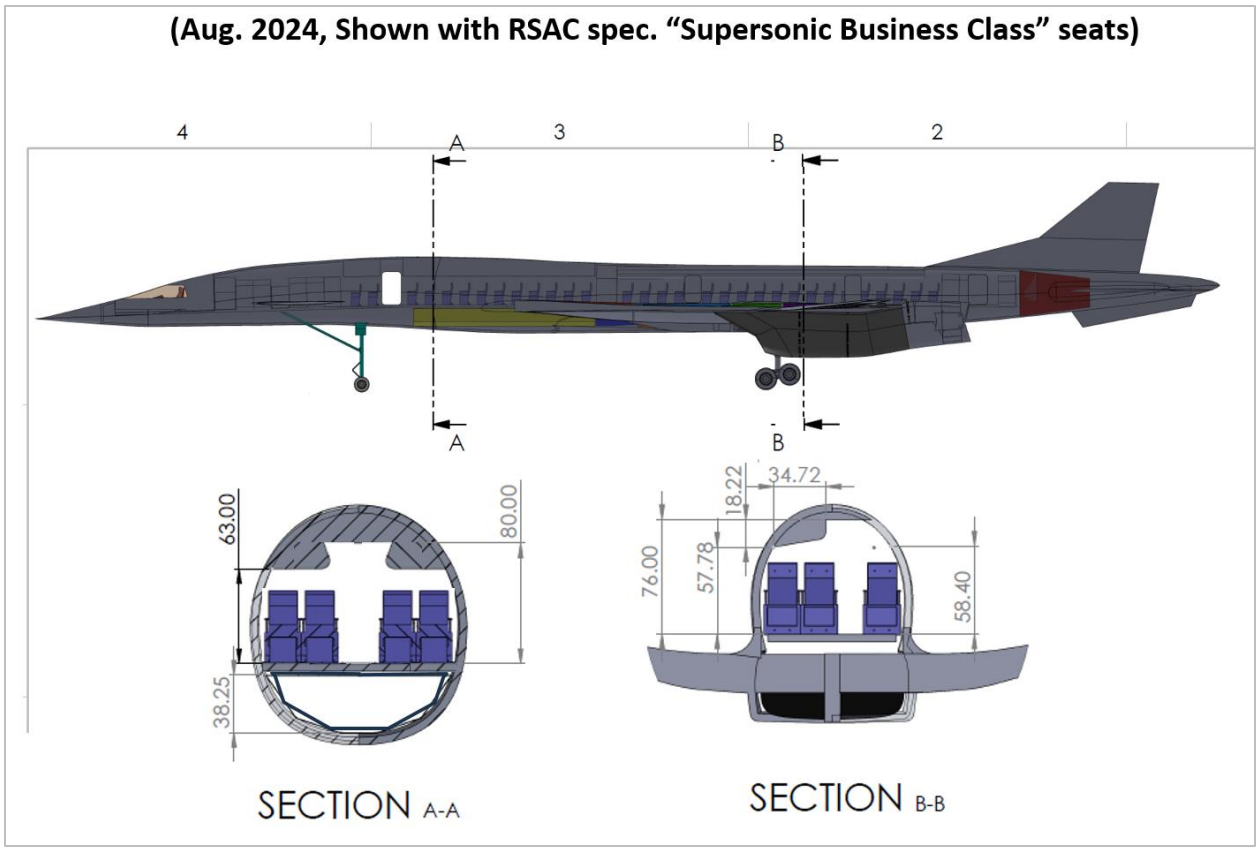

Figure 74- RSAC Cabin Minimum 3, and 4-Abreast Fuselage Cross-Sections

Lavatory and galley accommodations, entry and service doors and emergency egress hatches/ slide-raft locations were chosen with reference other recently certified commercial airliners (e.g. A220/C-series).

An example detailed weight breakdown, and resulting weight and balance checks for several cabin configuration cases are detailed in Section V of this document.

L. Flight Deck

Aside from the passenger cabin versus area distribution trades, and accommodating the stowage of the main landing gear, the definition of the RSAC's nose shape and integration requirements of the flight deck section were given special attention. In spite of ever-evolving improvements in display technology, augmented reality headsets, and XVS/EVS systems for certified aircraft, anecdotal data from pilots of business jet aircraft retain a strong preference for maintaining as much "natural" through-the-window vision as possible to back up electronic systems, particularly for see-and-avoid situations in VMC conditions. Even under IFR controlled conditions, landing approaches in North America are reportedly often flown "VFR" if weather conditions permit. Adding full-time XVS/EVS requirements to transition and currency training specifically for a new supersonic aircraft could also be seen as an added expense *if the configuration is not constrained by stringent low-boom objectives.* The original UW-S-21A configuration's fuselage already had a nose shape that was unconstrained by flight deck or forward window requirements as might be expected of a low-boom design. For the purposes of

the RSAC, it was decided to adopt the design philosophy that a non-drooping nose, designed for maximum through-the-window vision, would be worth incorporating. The plan would be for a large screen HUD type display, overlapping the upper instrument panel, could be used with an external vision system as needed, to fill in “blind spots” in the forward windows. Side windows would be configured to meet FAR vision polar requirements away from the centerline view. As demonstrated during the NASA HSR program, the airplane could be “crabbed” on final approach to view the edge of the runway for flare and touchdown in the event of total failure of the XVS system.

It was recognized that given the geometry of the supersonic aircraft (very long nose) it is advantageous to get the pilots located as far forward as possible. At the same time, the need for a Sears-Hack like area distribution in the far-field, and shallow “entry angles” in the near field place limits on how far forward there is room for a flight deck. Flight deck drawings were compared from available inboard profile drawings of several airliners, business jets, and bombers. The Concorde, with its 1970’s cockpit and 3-person crew was not a suitable reference. It was decided that a good starting point for workable flight deck dimensions would be based on the Dassault Falcon 7X aircraft, a modern, multi-engine, long-range, fly-by-wire aircraft with a state of the art fully electronic flight deck and ergonomic displays. Significantly, the Falcon 7X must accommodate the 2-person crew in comfort on long flights, and pack everything into a business jet space, much smaller than that available for large airliners. Falcon sales brochures and desk-top flight simulator models were used to lay out a preliminary spatial definition of a suitable flight deck (Figure 75).

Figure 75- RSAC Preliminary Flight Deck Design Using CAD and Flight Sim Models

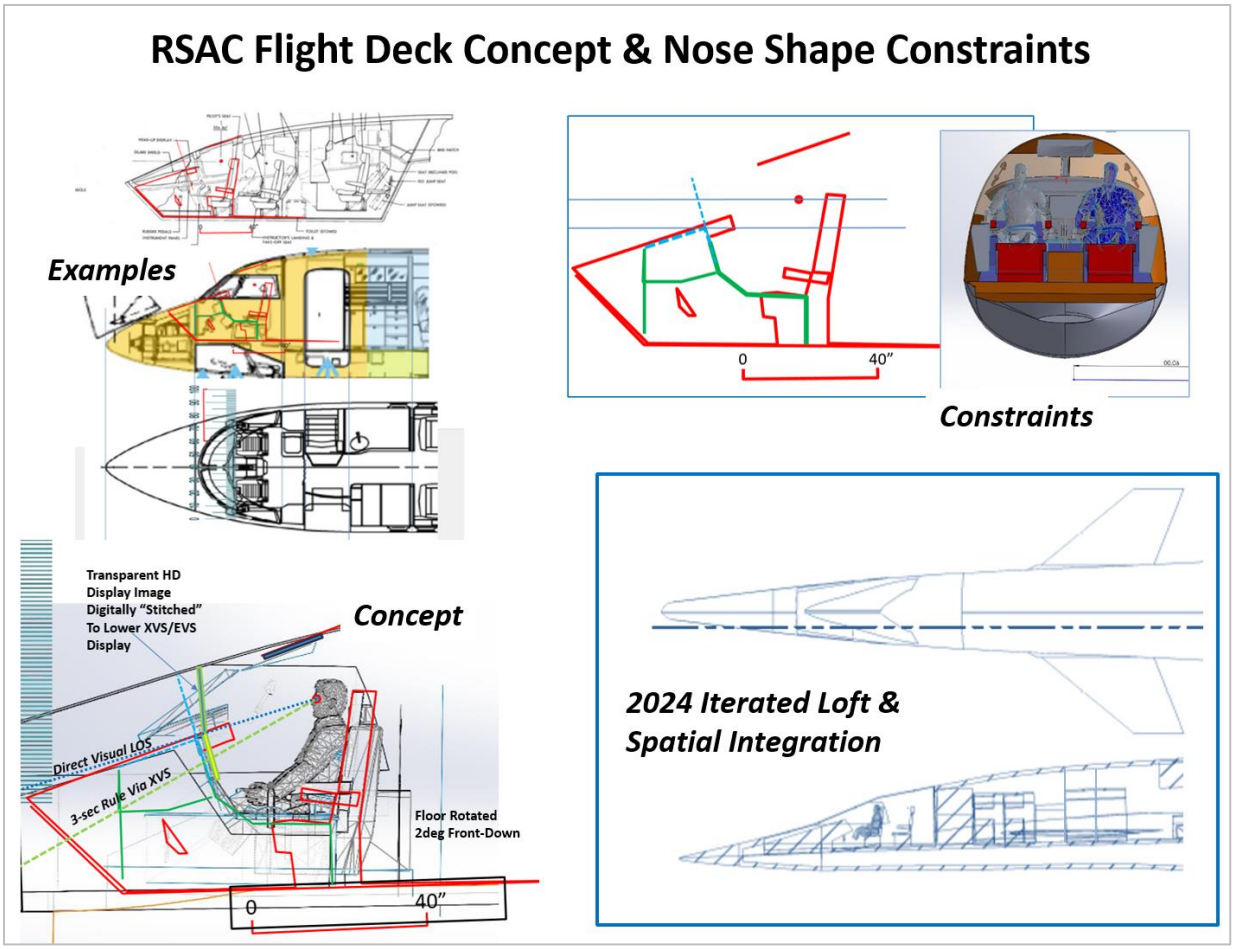

Figure 76- Flight Deck Integration Constraints and External Aero OML Development

Internal dimensional constraints, area distribution requirements, and line-of-sight vison objectives were used to create 3D nose shapes for evaluation during multiple iterations (Figure 76). The design for the area-ruled body that was wind tunnel tested in KWT used the near-final nose shaping. Minor forebody/nose refinements to the windows and body crown-line were done post-test for inclusion in the RSAC-E inboard profile drawings.

Tilting the cockpit floor slightly nose down, and re-arranging the notional display panel configuration allowed the height of the instrument panel to be sculpted out directly in front of each pilot position, and changing the forebody cross-sectional shape to a more "bottom-heavy", super-ellipse provided increased down vision at the pilot locations (using 46" spacing between the seats in flight-position). The FAR standard vision polar outline (Figure 77) was extruded into a 3D solid, projecting forward from the design pilot-eye location to intersect with the OML allowing required window shapes to be compared to the internal geometry (Figure 78).

The resulting RSAC-E proposed nose shape. flight deck layout, and window outlines can potentially satisfy the FAR vision polar at the RSAC's estimated 6-degree nose-up approach attitude. However, an XVS-display covering the upper third of the instrument panel would likely still be needed to satisfy the "3-second rule" for pre-landing view of the touchdown point.

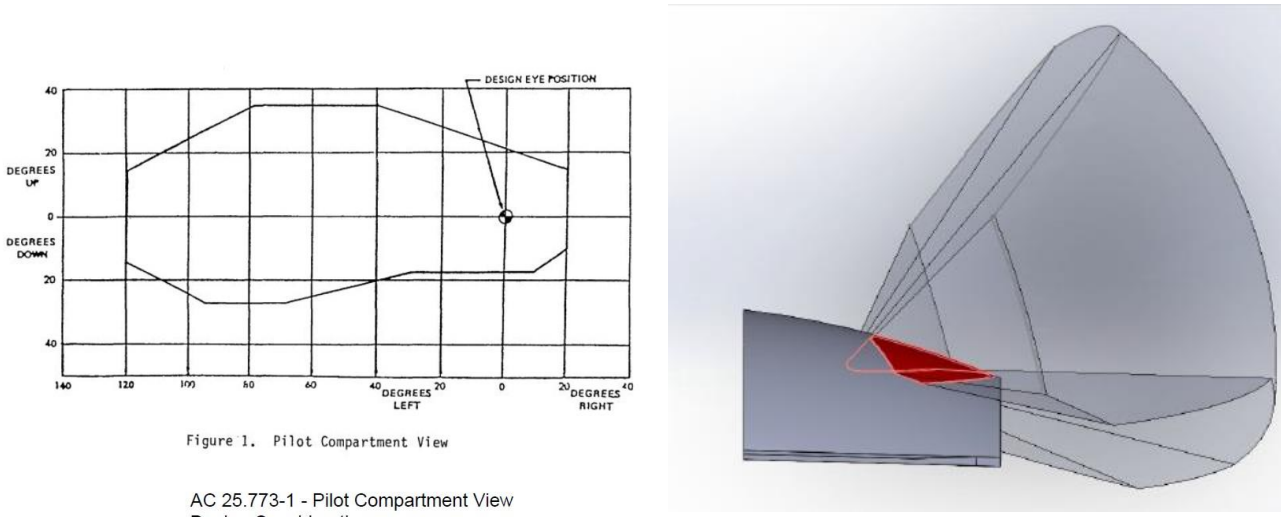

Figure 77- Using a 3D Projection of the FAR Pilot Vision Polar Diagram

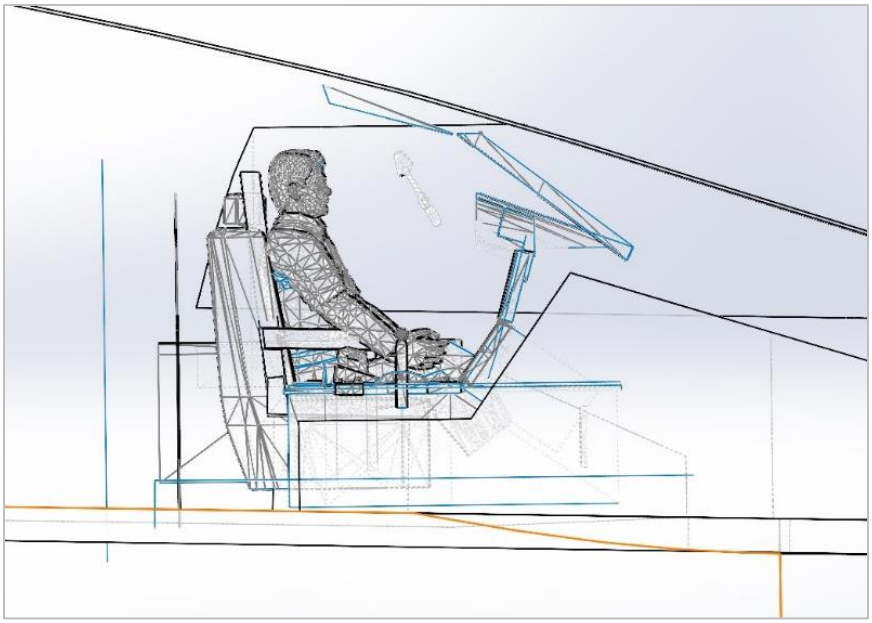

Figure 78- Pilot Station 3D CAD Model

M. Weight and Drag Estimation, Performance Checks

Weight and balance accounting was performed for each example, and the spec interior was checked for CG at minimum flight weight and with 50% payload at Max Landing Weight. Spec interior OEW (Rev. 8, at 100 passengers, before adding FOD door weight) was calculated to be 153,881lbs. As stated earlier, all the lifting surfaces, nacelles, and the fuselage weights were calculated based on the Boeing -070A "N+2" concept areal weights (in turn calibrated to HSCT FEM data and non-modeled weights allowances). The "N+2" systems and engine weights were carried over directly from the published N+2 values, with the exception the two errors were discovered due to a discrepancy between the published configurations. This was corrected for the RSAC's accounting. For RSAC, a more detailed breakdown of lavatory and galley

weights, as well as Standard and Operational items was generated to check against the N+2 published assumptions and provide data for future trade studies. This more detailed breakdown made use of multiple sources including weights data from cabin equipment vendor websites. The resulting weights breakdown for RSAC comprises a "100 point" weight statement. An example detailed weight breakdown, and the resulting weight and balance checks for several cabin configuration cases are detailed in Section V of this document. MEW and OEW build-up summaries are given for the baseline RSAC configuration (based on RSAC-D) in Figures 79 and 80.

RSAC Mfr. Empty Wt. With Spec Interior

RSAC REVISED MASS PROPERTIES				
		XDatum :	At RSAC Nose	At RSAC MAC/4
Item	Item Weight - lbs	Notes & sub totals	Xinches	Xinches
Wing Structure	34260		1559	80
Horizontal Tail Structure	2060		2400	921
Vertical Tail Structure	1470		2320	841
Fuselage Structure Fwd	10860	Forward fuselage	870	-609
	0	Mid-fueslage plug	1473	-6
Fuselage Structure Aft	7439	Aft-fuselage	1913	434
Main Landing Gear	8750	(stowed) down gear moves CG +0.2%	1593	114
Nose Landing Gear	940	(stowed)	680	-799
Forebody Controls (canard)	830		593	-886
Main Structure Sub Total		**66609**		
Inlet Structures & Systems	6020		1723	244
Cowling	1120		1832	353
Pylon	3260		1793	314
Engine/mid-nacelle	30920		1843	364
Nozzle	820		1963	484
Installation (incl. fairings)	2200		1843	364
Engine Accessories, Controls, & Start System	200		1823	344
Propulsion Sub Total		**44540**		
Fuel System	4790	center on mid-wing	1543	64
APU/EPU	290	tail cone	2460	981
Flight Deck / instruments	1260	flight deck	330	-1149
Surface Controls	4500	ave of LE/TE tails	1772	293
Hydraulic Power System	2250	center on landing gear post area	1634	155
Pneumatic System		(n/a; electro-hydraulics only)		
Electrical power	2520	distributed centers	1443	-36
Electronics bay	880	under forward cabin	460	-1019
Fuel Inerting System (02 separators)	140	fwd gear fairing	1380	-99
Cabin & Passenger Accomodations: 101 seat spec interior				
3 abreast forward cabin	483	seating zone 1	723	-756
4 abreast mid-cabin	3542	seating zone 2	1013	-466
3 abreast aft-cabin	4106	seating zone 3	1653	174
optional seating	0	seating zone 4		
Pot./waste water system (2x40gal)	280	aft of fwd cargo bay	1800	321
Forward galley(3)	2040		460	-1019
Aft galley(2)	1360		2123	644
Forward lav(2)	300		613	-866
Mid-lavs	0		1343	-136
Aft lavs (2)	300		2120	641
Other Cabin/ Fixed equipment	6730		1233	-246
Environmental Control System packs (2)	1710	belly fairing fwd of gear well	1460	-19
Ice Protection	310	inboard of front of nacelle	1318	-161
Exterior Markings	610	Awet centroid	1448	-31
Typical Customer Options:				
Load and Handling	130	fwd cargo	980	-499
Internet/other cabin eqpt	250	ctr. On mid cabin	1443	-36
Misc. fixed BFE	200	ctr. On mid cabin	1443	-36
Systems & Fixed Equipment Sub Total		**38981**		
Manufacturer's Empty Weight (MEW) Sub Total		**150130**		

Figure 79- MEW statement for RSAC-D

RSAC OEW and MTOW With Spec Interior

RSAC REVISED MASS PROPERTIES				
		X Datum :	At RSAC Nose	At RSAC MAC/4
Item	Item Weight -lbs	Notes & sub totals	X inches	X inches
Manufacturer's Empty Weight (MEW) Sub Total		**150130**		
Oil & unusable fuel	800		1823	344
Potable water	250		1800	321
Waste water/toilet chemicals	80		1800	321
Flight deck crew (2) and baggage, laptops	400	flight deck	343	-1136
(3) Cabin crewperson & bag (1/35pass.)	500	mid cabin	1293	-186
Flight Provisions, food, drink	760	fwd & aft galleys	1093	-386
Food service items	300	fwd & aft galleys	1093	-386
Cargo liner/restraints aft	85	aft cargo	1940	461
Cargo liner/restraints forward	235	fwd cargo	930	-549
Cockpit/crew emergency equipment	60	fwd crew area	493	-986
Slide-rafts (2) forward	240	2 fwd	785	-694
Slide rafts (2) aft	300	2 aft	1750	271
Standard and Operational Items Sub Total		**4010**		
Operational Empty Weight (OEW)Sub-Total		**154140**		
OEW CG, in from nose		**1547**		
Payload (@101passengers in spec interior):		(4 empty seats in zone2)		
3 abreast forward cabin	1122	seating zone 1	723	-756
4 abreast mid-cabin	7480	seating zone 2	1013	-466
3 abreast aft-cabin	9537	seating zone 3	1653	174
optional seating	0	seating zone 4	0	
Checked bags	2020	main cargo	930	-549
Bulk cargo	303	aft cargo bay	1940	461
Zero Fuel Weight (ZFWT) Sub Total		**174602**		
ZFWT CG, in from nose		**1517**		
Fuel Loaded:		(Max. Tank capacities:)		
Fwd body tank F	27021	32500	1300	-179
Fwd strake tanks A	17973	17973	1233	-246
Mid strake tanks B	43600	43600	1433	-46
Aft strake tank C	8576	8576	1553	74
Wing box tanks D	26578	26578	1693	214
Aft body trim tank E	12650	17660	2193	714
Total Fuel Load		**136398**		
Weight Fully Loaded (Ramp Wt)		**311000**		
CG in Inches From RSAC Nose		**1501**		
CG in %MAC		**31.98**		
Design MTOGW		**310000**		

Figure 80- RSAC-D OEW Statement

Mission performance and aircraft sizing was initially assessed by the 2020 and 2021 capstone classes by adjusting published N+2 aero data and weights, for configuration differences between the 070A concept and the proposed RSAC. In subsequent classes, bottoms-up estimates of RSAC drag were done using spreadsheets and handbook methods. In 2024 as wind tunnel data became available on the most RSAC-like UW-S-24A KWT model, it became possible to derive wind tunnel-based performance inputs that were RSAC-specific. Adjustments were made to the preliminary wind tunnel results to account for residual laminar run areas on the wings and tail, and model excrescences, to extract form factors and residual pressure drag at zero lift. This

allowed the bottoms-up component build-ups of CDo to be calibrated to the measured test data for the clean configuration. The resulting build-up could then be adjusted to full-scale flight Reynolds number conditions, and a full-scale incompressible excrescence drag allowance of 8% added. The wind tunnel polar shape data was used as-is with no attempted scale adjustment. Later refinements accounted for geometry differences between the wind tunnel model and full scale, such as fillet wetted areas, canard and tail surface t/c, etc. RANS CFD analysis of the RSAC's wing RW23 compared to the W15 test wing were used to generate wing geometry corrections (Figure 81).

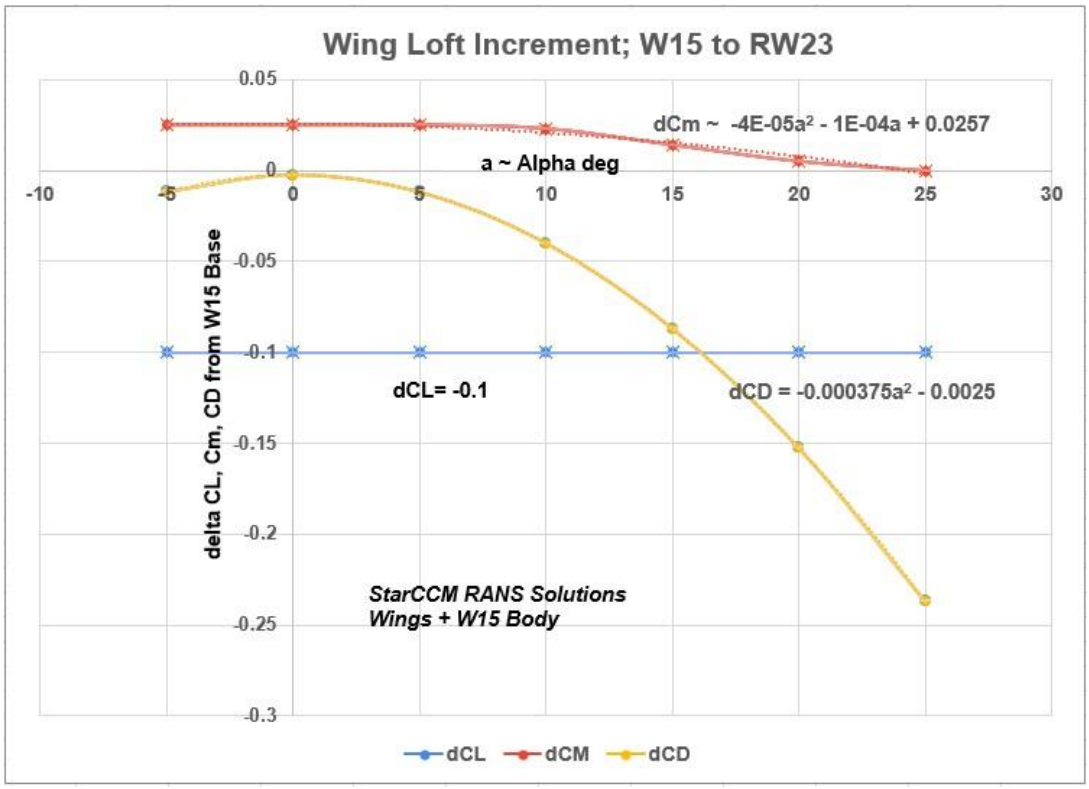

Figure 81- Adjustment for Differences Between W15 KWT Data and RW23

The "polar shape" variation of attainable suction with CL for the "clean wing"was simply modeled by curve fitting the clean configuration drag polar to develop a table of varying induced drag factor Ke, versus CL. An envelope formed by the locus of lowest flaps-deflected drag points vs CL using the available KWT test data, was drawn, and from this a trend of delta Ke for flaps was developed. This allows flap deflection effects to be accounted for at any incompressible flight condition. The drag build-up process for mission performance inputs is outlined in Figure 82. This process was reviewed with NASA in the August 2024 Seattle meeting. Although improved CFD data has since been developed for the adjustment to represent the RW23 wing loft, significant delays in the availability of final corrected UW-S-24A including data for flap effects, trim and landing gear drag were not available in time to update the initial drag estimates, mission performance data, or takeoff/landing assessments. It is hoped that that work can be completed as a follow-on task and used to generate complete RSAC drag polars for external use.

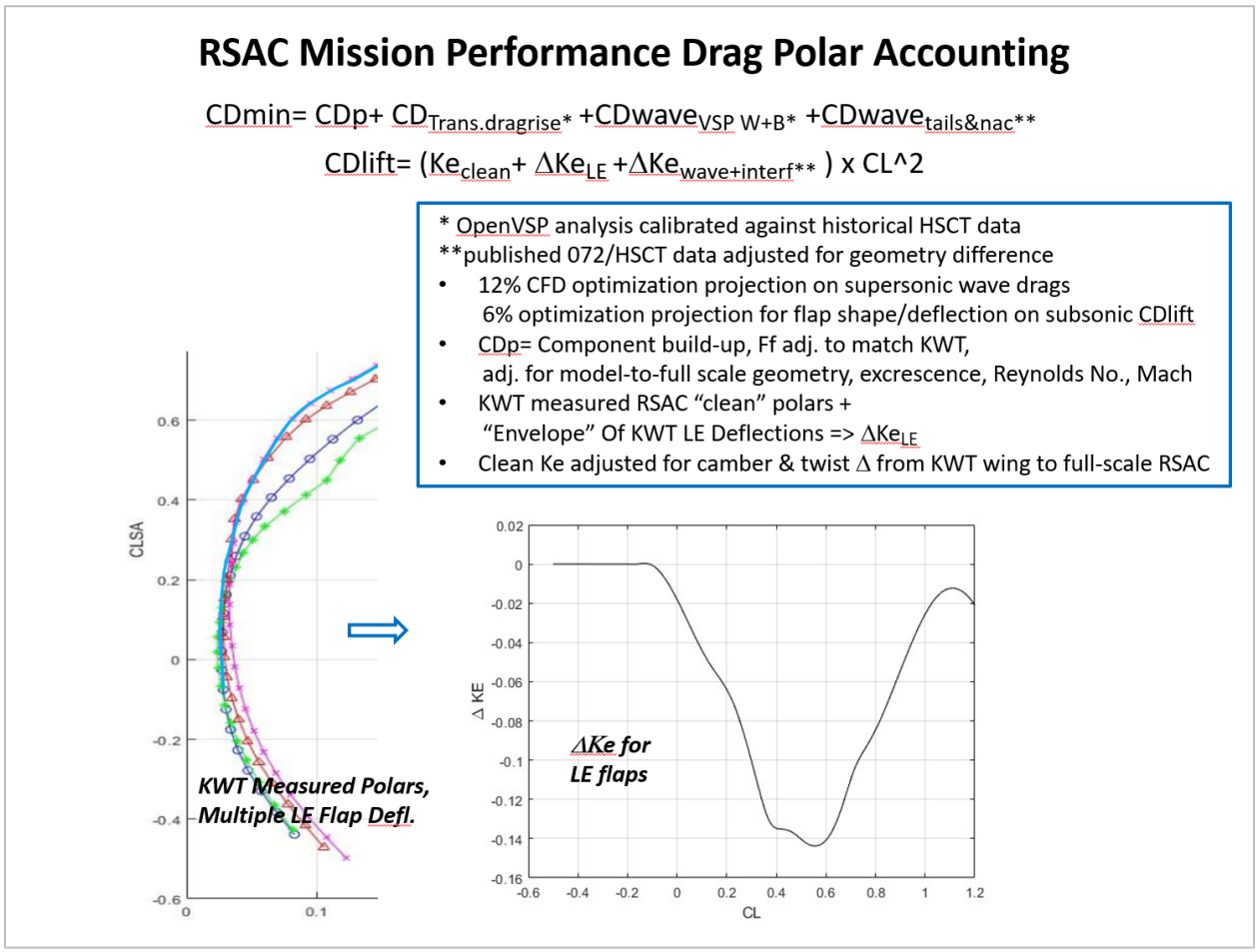

Figure 82- RSAC Drag Build-Up Process

It has been possible to update the transonic and supersonic drag estimates for RSAC. Due to inconsistent results from the OpenVSP wave drag tool, the cruise L/D conditions were checked by doing drag tracking relative the HSCT's "TCA", and the "2015TC" configuration with similar planform, for which other published data was available. The results of this tracking showed that the RSAC -D configuration was slightly high in drag relative to the 070A (Figure 83), and this is consistent with the slight shortfall in range that was estimated by the capstone students in June of 2024 (3860nm). The preliminary drag polars that were used were based on RSAC version D and did not account for some small OML and fuel capacity improvements made since then, incorporated in the RSAC-E in the fall of 2024. A comparison of N+2 study configurations 072B and 070A with the last available cruise L/D for RSAC (D) is shown in Figure 84. The drag levels for the unoptimized RSAC aero configuration include an allowance for expected wave drag improvements due to non-linear multi-point CFD optimization, as noted, consistent with HSCT trends.

RSAC-"D" Cruise Drag Prediction; Tracking From HSCT ("2015TC") Geometry

Scaled to Equal Span Rel. To HSCT ("2015TC"), June 1, 2024 Definition RSAC Has…	RSAC Drag Penalty Relative to HSCT Check Points (Retains HSCT demonstrated non-linear multi-point CFD optimization allowances)
(S_{canard}/S_{wing}); 1.15x	+ 0.17 counts Cdw_{can} => Mach 1.6 Cdw_{can}= 1.23cts + 0.2 counts Cdp_{can} => Mach 1.6 Cdp_{can}= 1.58cts
(S_{horiz}/S_{wing}); 2.0x	+ 1.1 counts CDw_{horiz} => Mach 1.6 Cdp_{horiz}= 2.1cts + 1.567 counts CDp_{horiz} => Mach 1.6 CDp_{horiz}= 3.13cts
($S_{vert.+Ventral}/S_{wing}$); 1.5x	+ 0.78 counts CDw_{vert} => Mach 1.6 Cdw_{vert}=2.2cts + 1.1 counts CDp_{vert} => Mach 1.6 Cdp_{vert}= 3.3cts
Larger Wing TE chord; + 5.85% delta $A_{wet, wing}$	+1.4 counts CDp for delta A_{wet} => Mach 1.6 Cdp_{wing}= 26.8
Nacelle/diverter 20% longer, 80% greater side area, 1.8x A_{wet}	+ 1.75 counts Cdw_{nac} (=>2.63cts $Cdw_{nac+ interf}$ at 0.10 CL) + 2.64 counts Cdp_{nac} =5.94cts
Forebody height ratio = 1.20 Forebody width ratio = 1.22 Mid-body height ratio = 1.18 Mid-body width ratio= 1.12 +10sqft at Mach 1.6-1.8 for thicker wing tip & gear fairing Net faired equiv. body delta Amax= 290sqft => 1.234 A_{max} ratio at constant Mach cut lengths	+ 4.23 counts CDw (at Mach 1.6) =>Total CDw_{W+B} at RSAC Sref is 25.32*.88proj= 22.28cts +14%Awet, total body CDp=27.58 cts
Lifting Length AR ratio= 1.0	Equal CDL+ CDLwave (=> effective "e" at Mach 1.66=0.380, and KE= 0.2885 at RSAC Sref), 0.002885 at CL=0.1 incl. 2.63ct$CDw_{nac+interf}$
Reduced Reynolds Number due to aircraft size (=> 1.0554x CDp)	~+3.5 counts CDp (at Mach 1.6)
Note: Final coefficients x 0.9452 for ratio of scaled Sref's	Net RSAC L/D at CL=0.10 is 8.19 =>123.2cts, ~6cts > -070A Ref. (August 1, 2024 Status)

Figure 83- Check of RSAC Cruise Drag by Comparison using HSCT Data

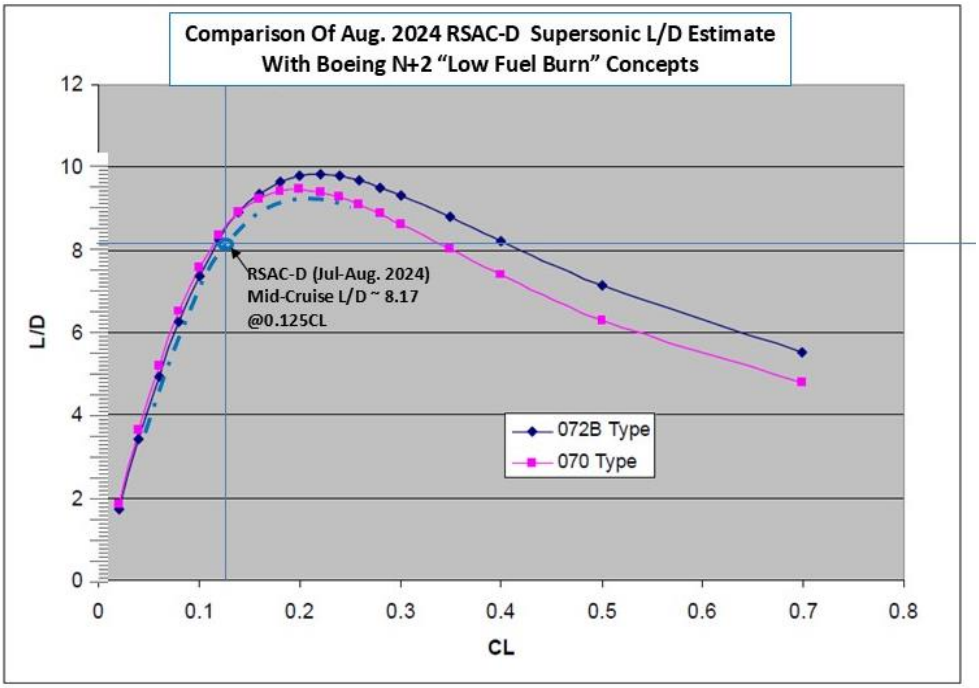

Figure 84- RSAC Projected Supersonic L/D Compared to N+2 Reference Concepts

The landing approach Vref speed, takeoff speed schedules, etc. are all indexed off the “stall speed” for each weight & flap configuration. Because slender aircraft do not “stall” in the conventional sense (that is reach and angle of attack where increasing the angle causes a distinct decrease in lift), the equivalent behavior is for lift level to plateau or gradually decrease. This typically occurs when the leading-edge vortices break down or “burst” at a point ahead of the wing trailing edge. However, on cranked planforms, the interference of multiple vortex systems, disorganized separation on outboard wing panels, or decrease in vortex strength before reaching vortex “burst” cause significant non-linearities in the pitch, yaw, and rolling moments before maximum CL is reached. For this reason, a virtual “stall” speed must be declared (maximum demonstrated lift for certification) based on reaching lateral-directional stability limits, rapid drag divergence, unsteady buffeting flow, or reaching a point where the short-period pitch time-to-double becomes too short to effectively augment with fly-by-wire.

At the time of this publication (December 2024), final corrected wind tunnel data from SCALOS needed to define a declared stall speed and assess the boundaries of instable conditions now exists. However, the planned evaluation of open-loop flight characteristics and augmentation needs fell outside the scope of SCALOS grant time and resources. That said, preliminary results indicate that a declared “stall” speed of 125 knots in landing configuration is probably likely, giving a landing approach Vref of 155 knots as was assumed for sizing the Boeing -070A configuration, and assumed for the RSAC.

Operationally, the normal touchdown speed, after bleed-off during flare, is Vref +gust correction. The corresponding approach speed is Vref + ½ steady wind speed or 5 knots whichever is greater, +gust correction, up to a maximum total of Vref+25 knots. Concorde flew Vref+7 as the normal approach rather than +5 minimum in zero wind, and noise certification tests are done at Vref+10. The speed-limit for approach at many civilian airports is based on ICAO “Category D” approach speed of 165knots = 155Kt Vref+10, so the RSAC’s target Vref of 155 KEAS is about the highest that is reasonable. As discussed previously, the RSAC’s proposed maximum landing weight of 220,000lbs would result in a similar landing payload-range capability as Concorde’s MLW of 245,000 lbs because of the Concorde’s higher MTOW and fuel load.

N. Configuration Development Conclusions

The primary focus of the RSAC conceptual design was for UW capstone senior design classes and graduate students, working with instructors and advisors, to develop a credible “straw horse” representation of a supersonic airliner that could be brought to market within 12 years or so. It is intended to be technically feasible using mostly off-the-shelf technology, requiring technology commercial-use maturation and development efforts not greater than those expended on the 787 or A380 programs a decade or so ago. The sizing and proportions of RSAC’s wing and propulsion components would coincide with those used to define model parts for the SCALOS modular model testing. The RSAC’s external aerodynamic lines (OML, Figure 41) would provide a realistic starting point for those wishing to exercise or further develop aero shape optimization tools. The conceptual internal arrangement would provide representative integration features and “packaging” dimensions /volume allowances to guide the development of OML shape constraints. A detailed weights breakdown, representative propulsion system and structures concepts and engine performance estimates, combined with information from the SCALOS wind tunnel testing database, would provide academia, industry, and researchers with a common non-proprietary point-of-departure for design trades, MDO development, and calibration of various predictive tools. To the maximum extent possible, within the limitations of the academic program and the time and resources of the SCALOS grant program, we believe the above objectives have been achieved. Like all concept level designs, the RSAC-E still contains many “place-holders” and assumptions and is far from the “perfect design”. The RSAC-E does satisfy the original configuration intents (Figure 85).

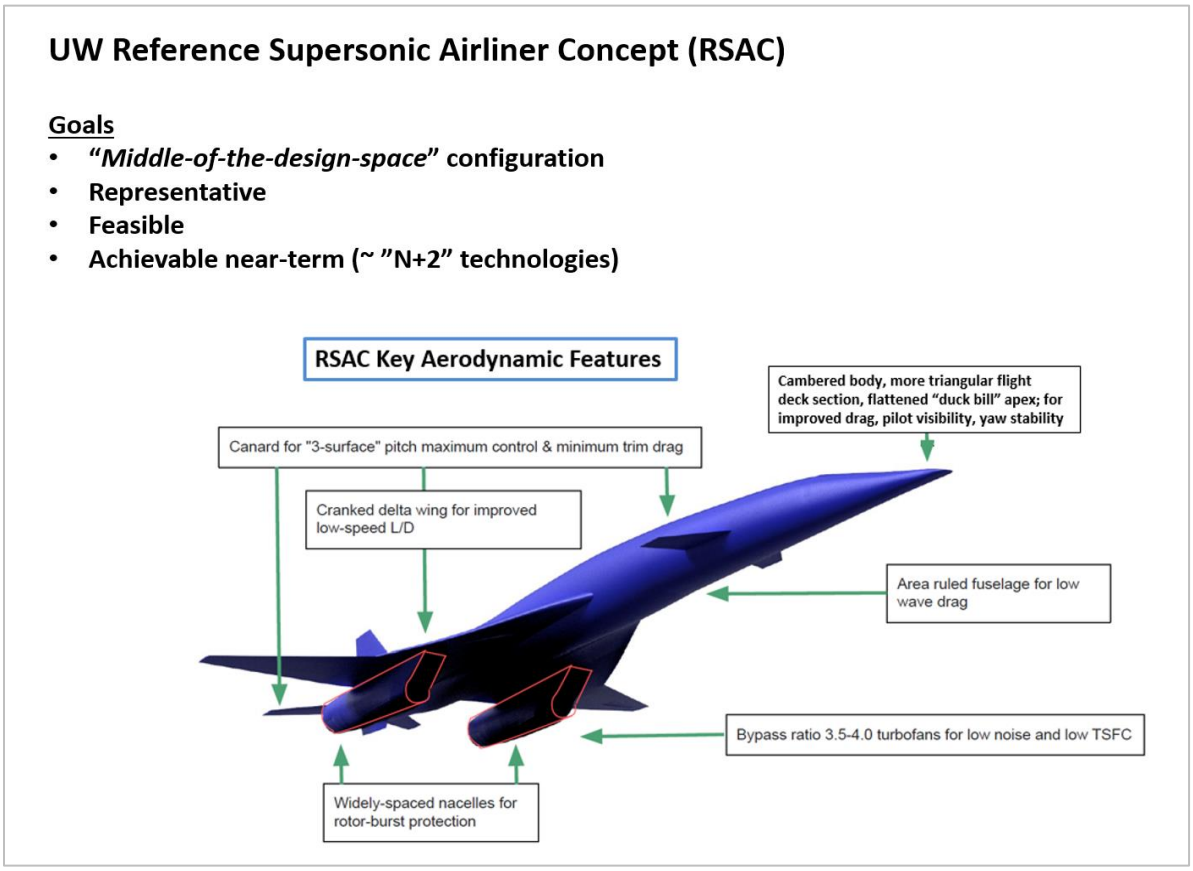

Figure 85- RSAC Conceptual Design

IV. RSAC Final 2024 Configuration Technical Drawings

University of Washington-NASA SCALOS Reference Supersonic Airliner Concept

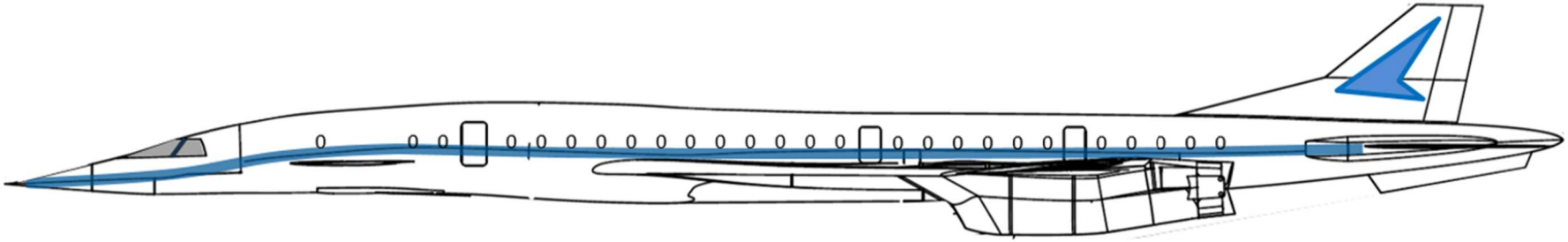

Length overall: 215.8 ft
Wingspan: 102.0 ft
Height: 38.2 ft

Max. Takeoff Weight: 311,000 lb
Empty Weight (spec. interior): 154,140 lb
Maximum Landing Weight: 220,000 lb

Cruise speed: Mach 0.95 (over land)
Mach 1.6 supersonic long-range cruise
Mach 1.8 maximum supersonic cruise (1190 mph)

Passengers: 103 spec. interior "RSAC business class"
(or) 36 RSAC executive seating
(or) 143 all economy seating

Engines: (2) 60,000lb SLST, BPR~3.6, 84"fans
Mixed flow turbofan (MFTF), +variable cycle features
Variable A8/A9 nozzles, low-impact ejectors
FADEC-controlled noise-optimized lapse rate
Low NOx combustors

Range: 3800nm Mach 1.6 mission
(Atlanta-Lisbon)
3600nm Mach 1.8 mission
(New York-Paris)
4350nm subsonic mission
4100nm mixed sub-/supersonic mission
(Vancouver-Tokyo, Chicago-Frankfurt)

Takeoff field length: < 10,000 ft
Landing field length: < 7000 ft
Approach speed Vref: 155 kt

Landing/takeoff noise: Stage 5/ICAO Ch.14
Fuel consumption: ~50% reduction rel. to Concorde
Per passenger CO2 footprint~ subsonic business class
(spec interior, trans-Atlantic service)

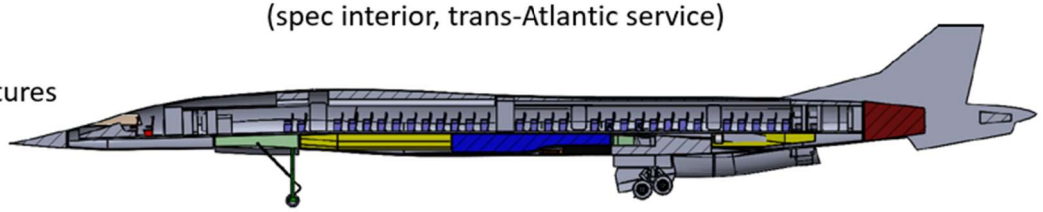

Figure 86- RSAC One-Page Description

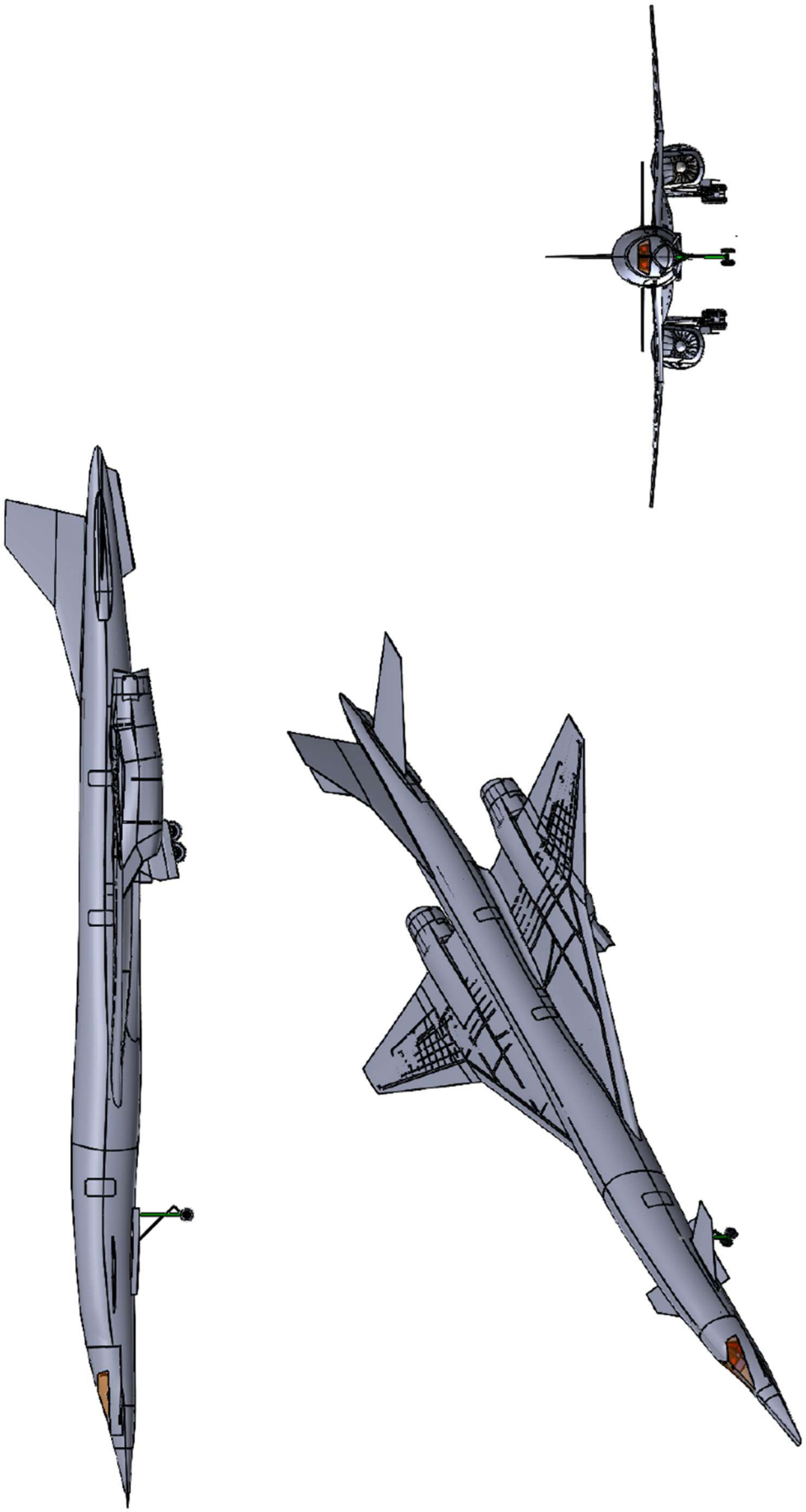

Figure 87- RSAC External Lines

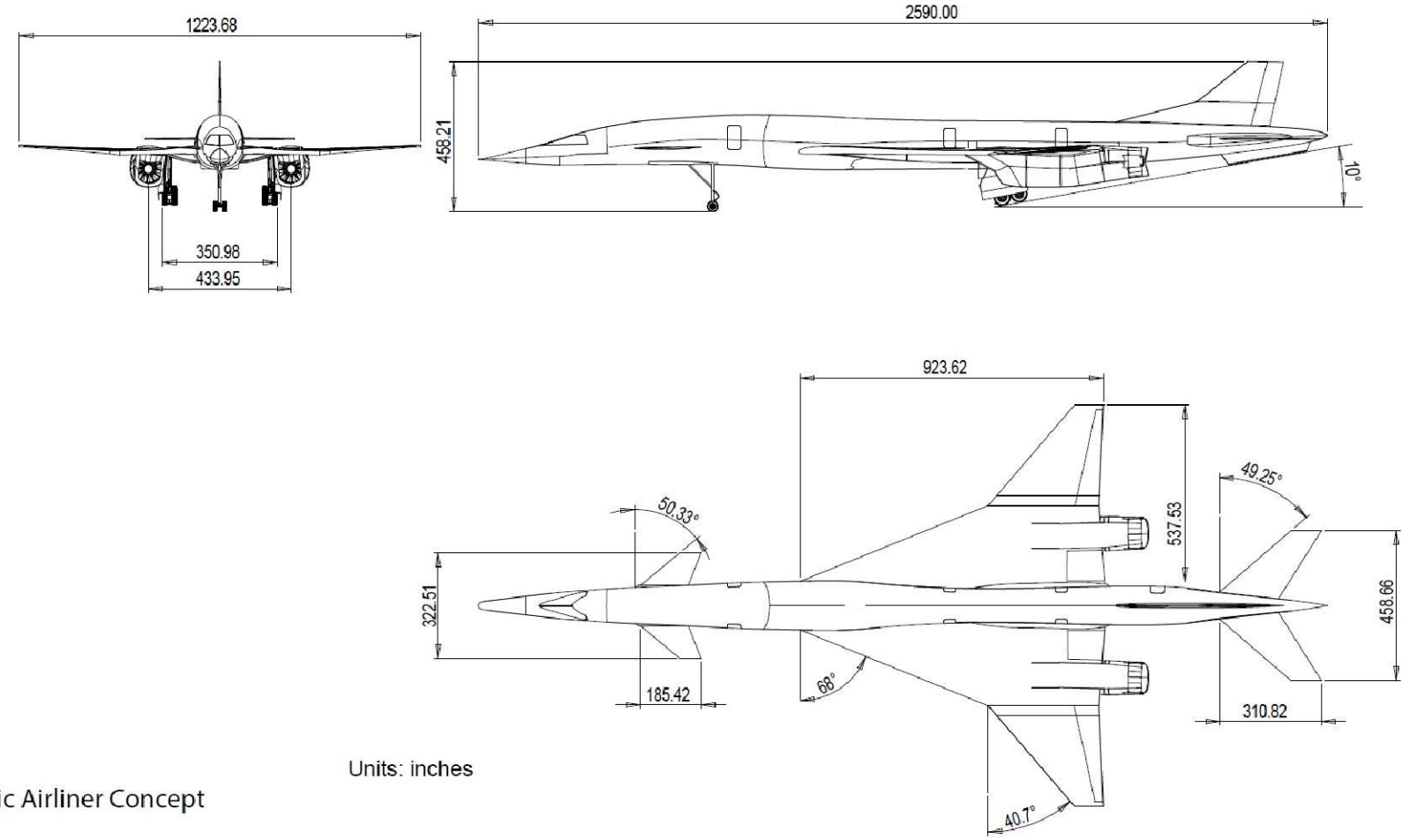

Units: inches

Reference Supersonic Airliner Concept
RSAC Model E
University of Washington, November, 2024

Figure 88- RSAC Principal Dimensions

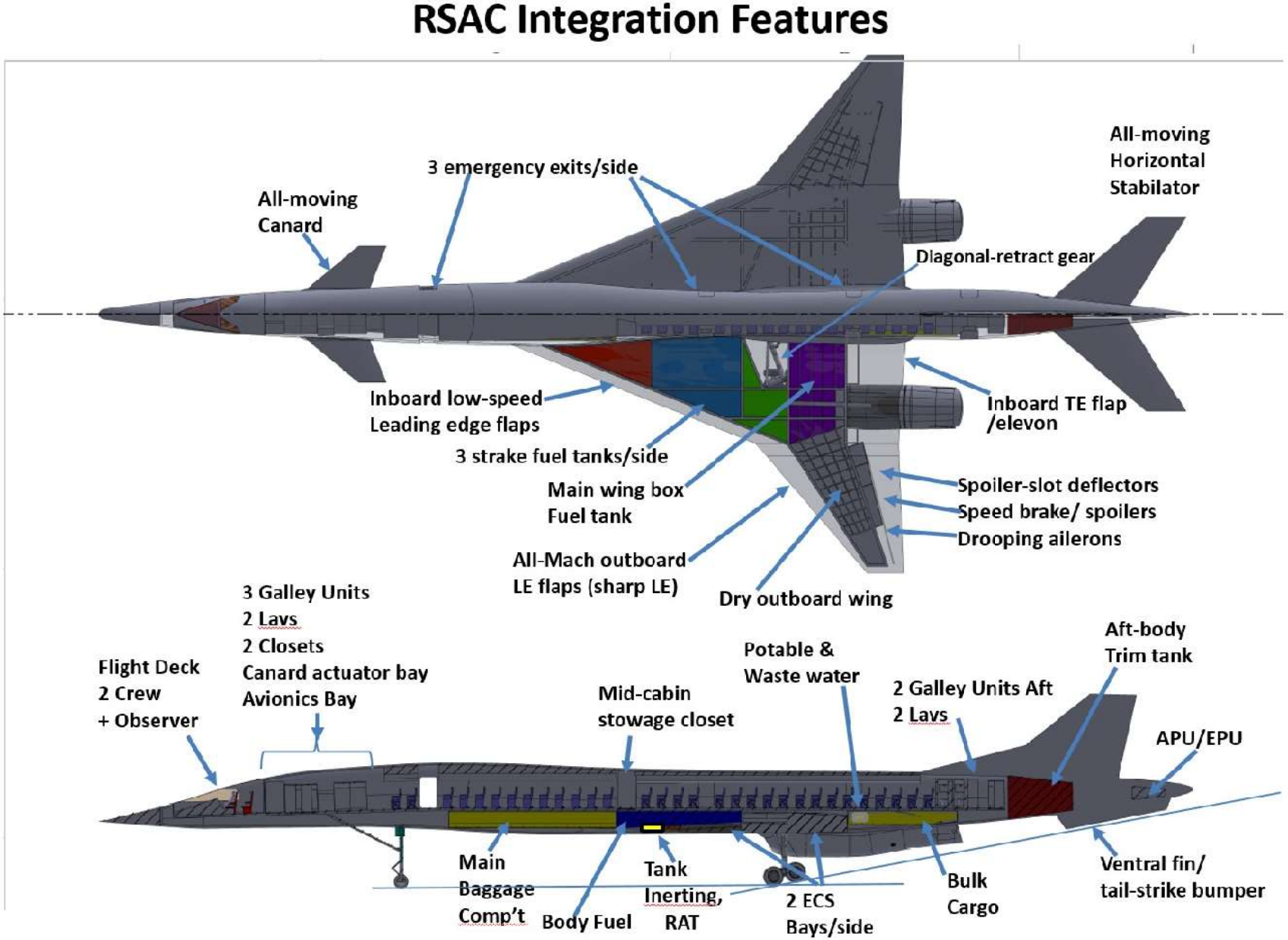

Figure 89- RSAC Internal Features

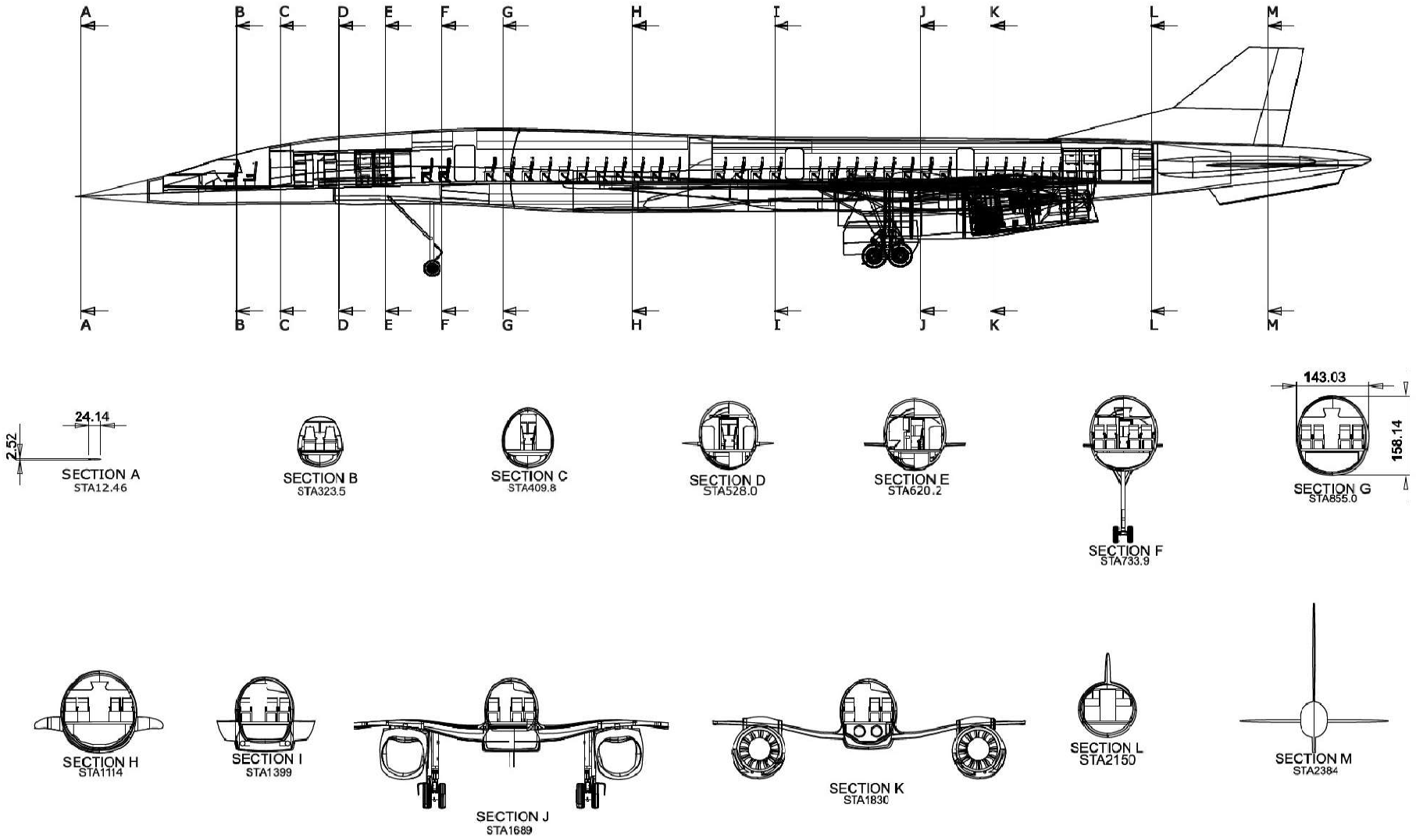

Figure 90- RSAC Inboard Profile Drawing

Units: Inches

Reference Supersonic Airliner Concept
RSAC Model E
University of Washington, November, 2024

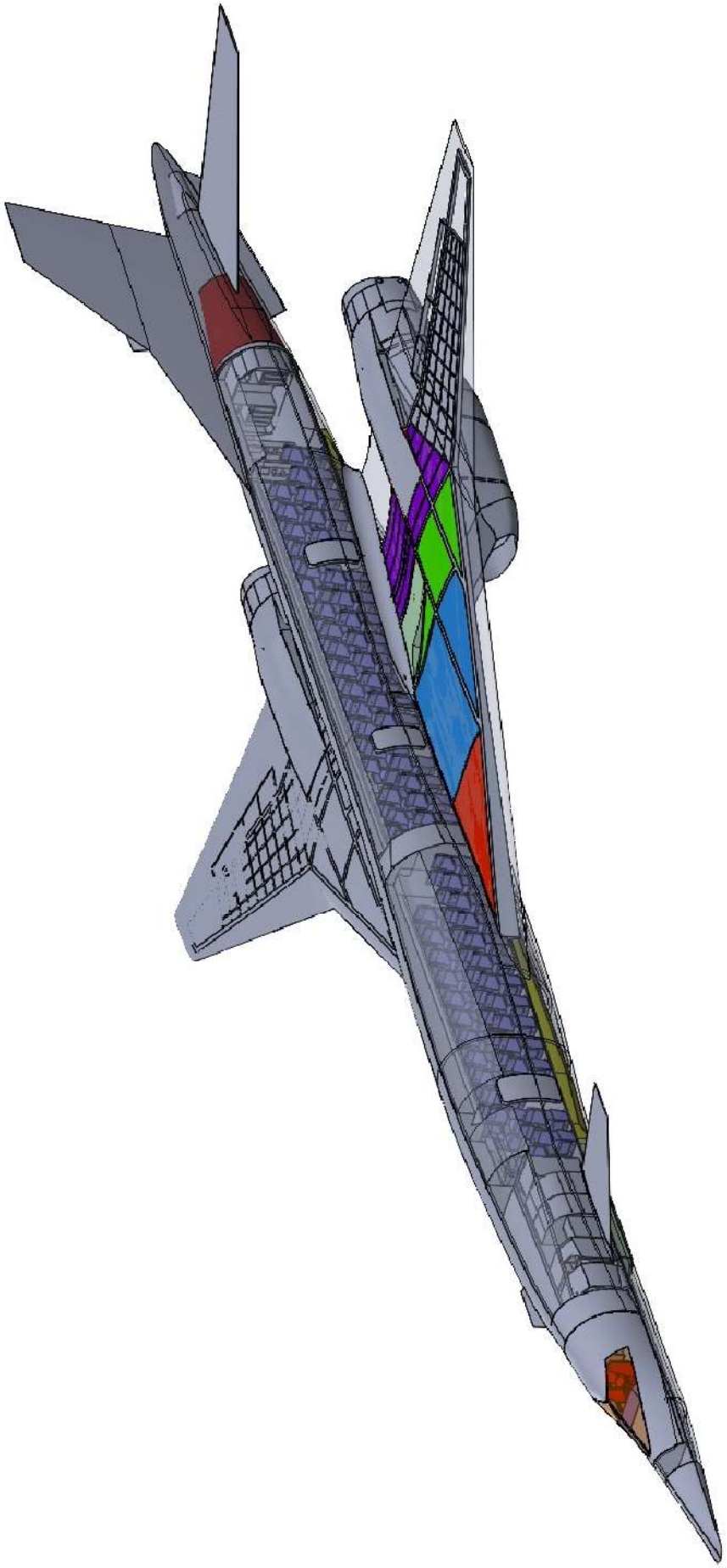

Figure 91- RSAC Cut-Away, Top Iso

Figure 92- RSAC Cut-Away, Bottom Iso

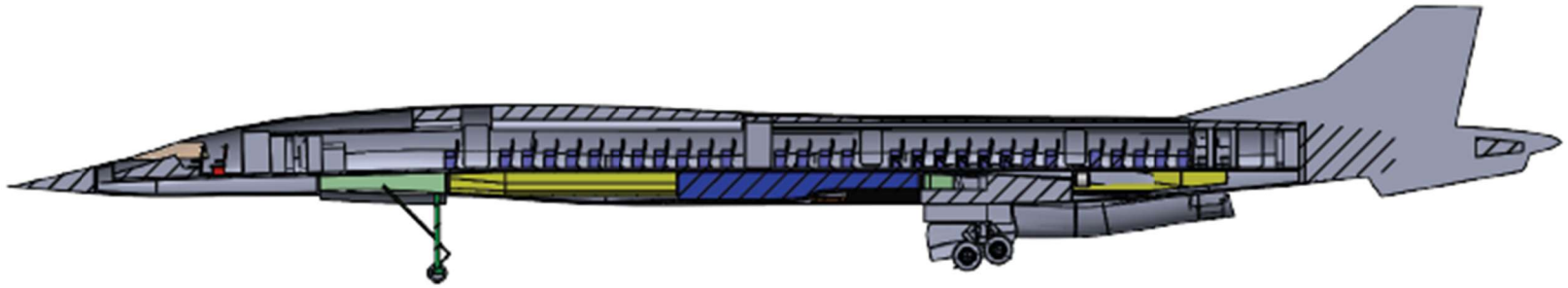

SECTION A-A

Cut through Middle

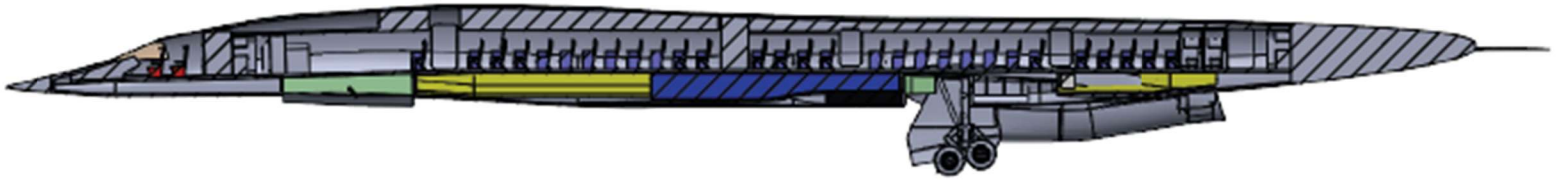

SECTION B-B

Cut through Pilot's view

SECTION D-D

Nacelle Cross-Section

Figure 93- RSAC Shaded Inboard Profile

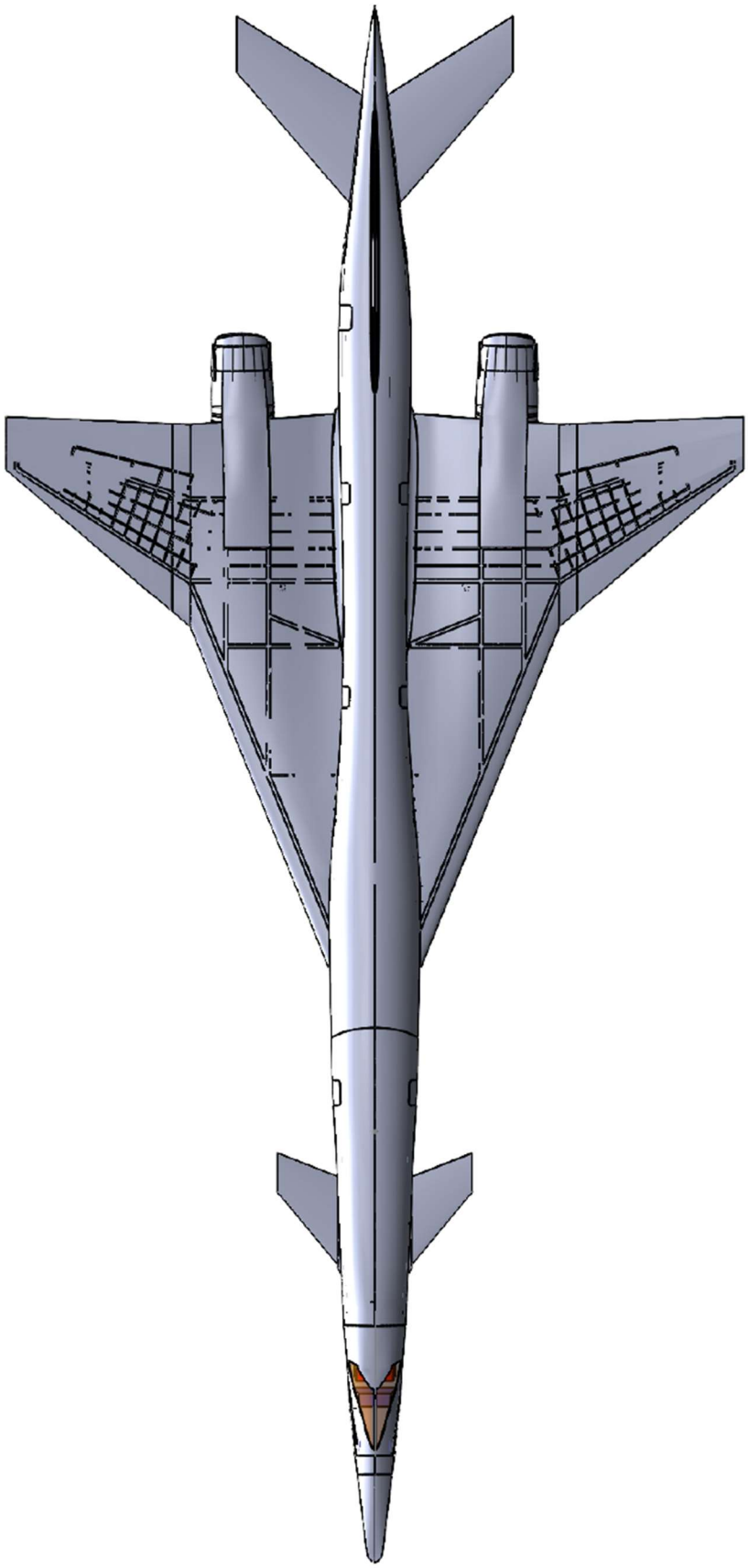

Figure 94- RSAC Shaded Plan View

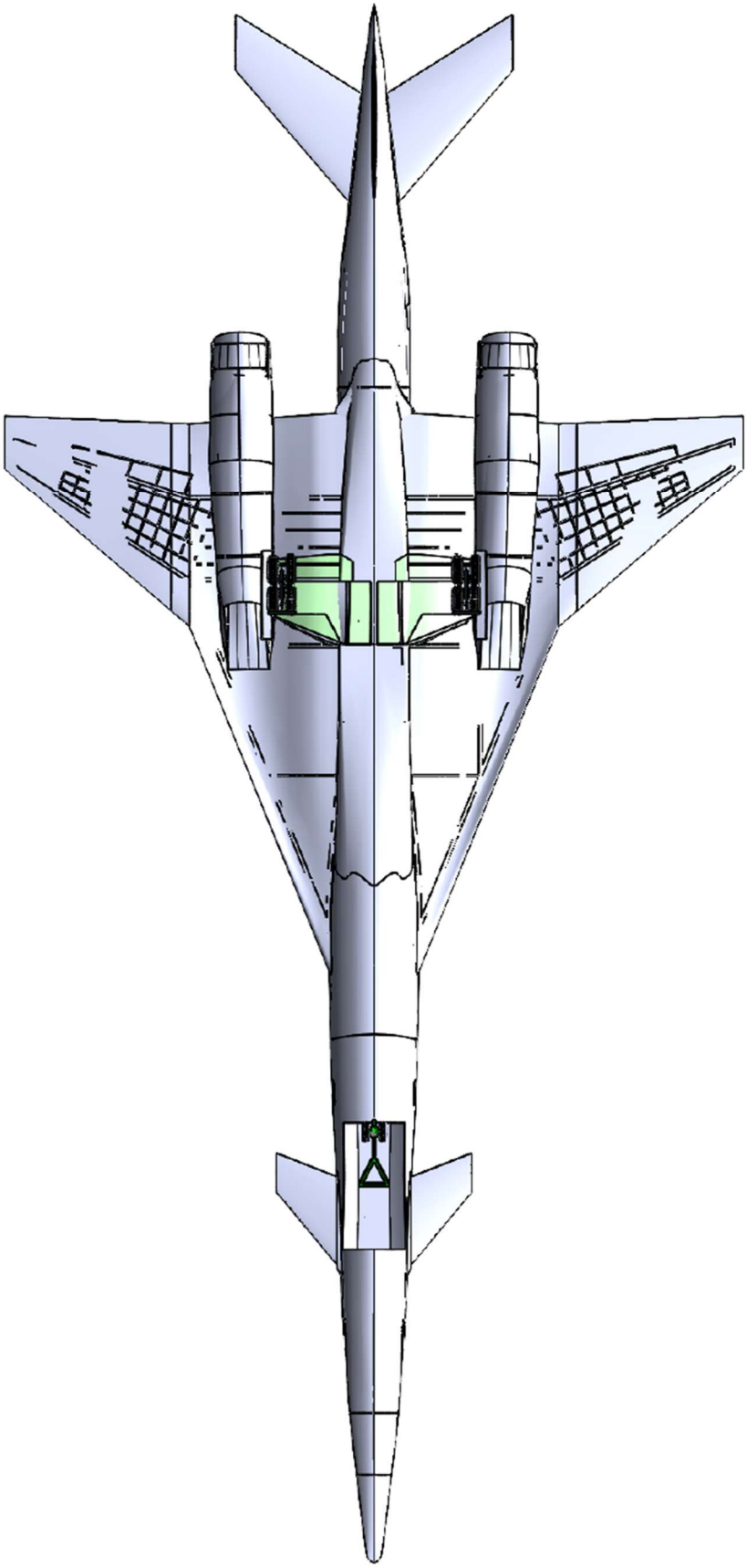

Figure 95- RSAC Shaded Plan Bottom View

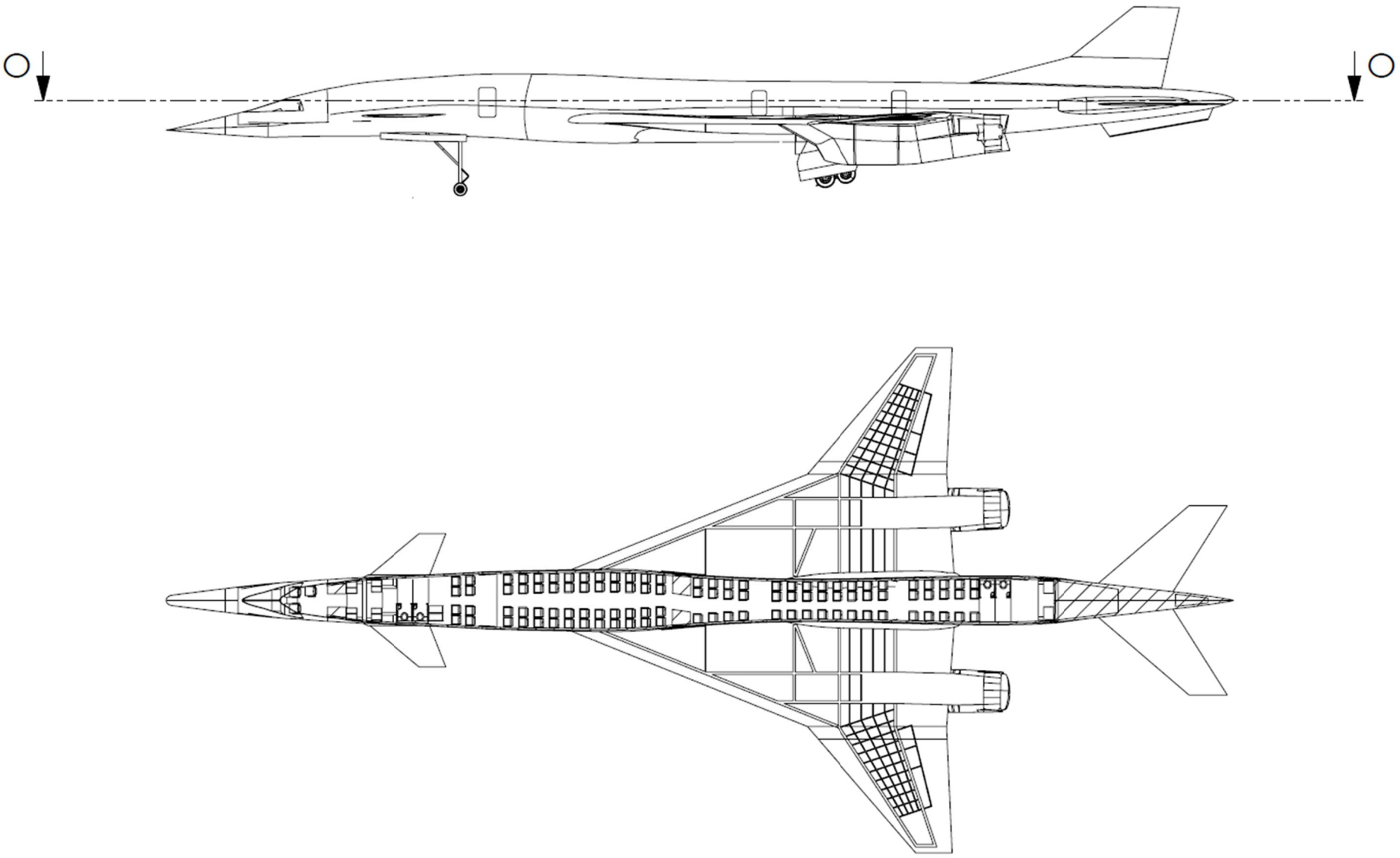

Figure 96- RSAC Sectioned View, Deck Plan

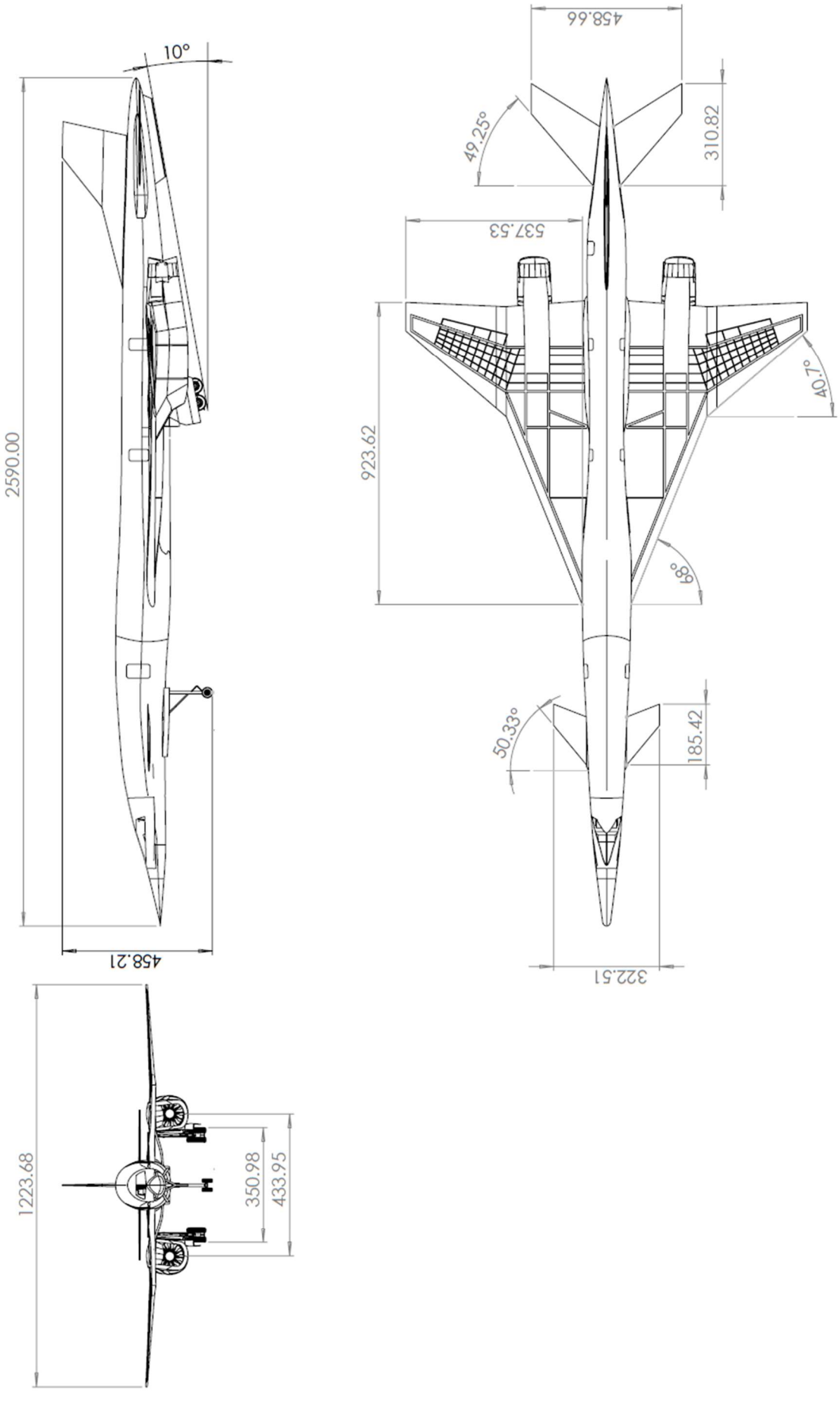

Figure 97- RSAC Basic 3-View, No UW Title Block

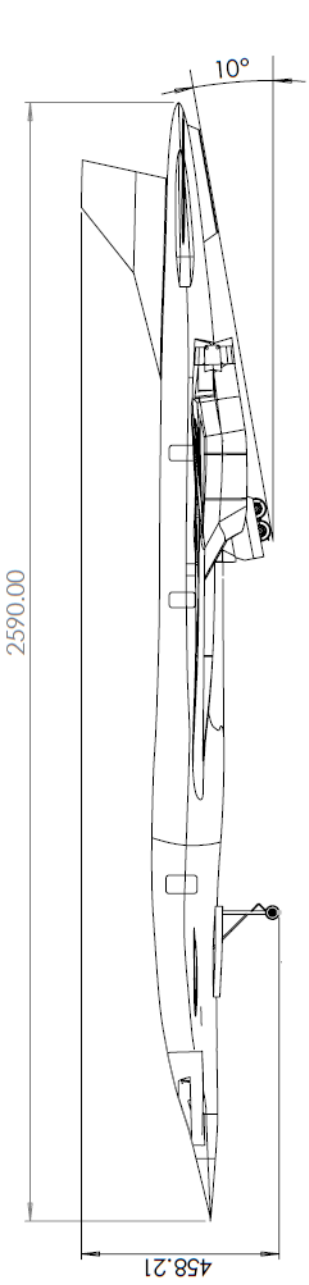
10°
2590.00
458.21

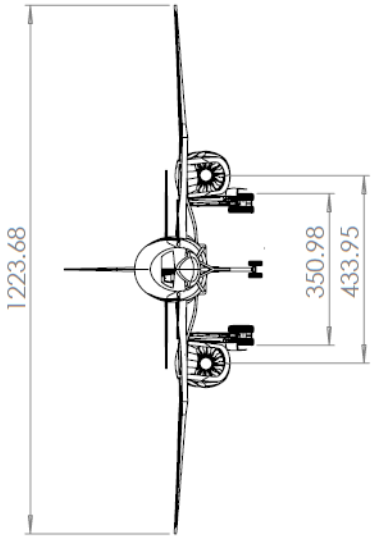
1223.68
350.98
433.95

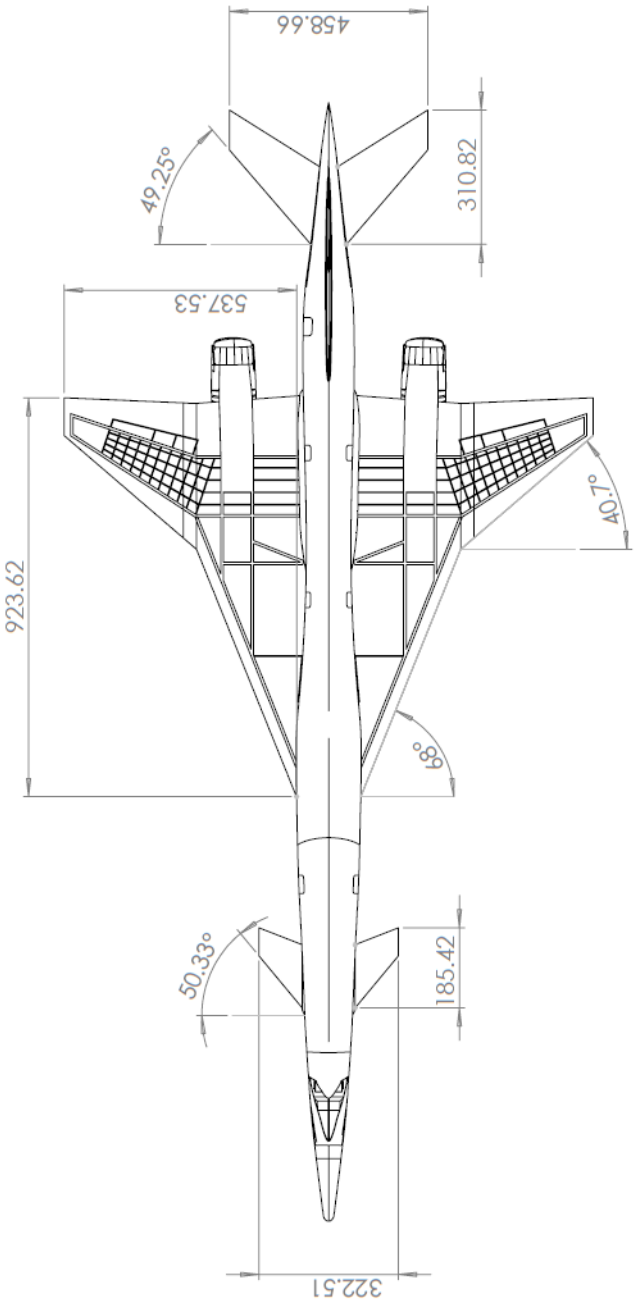
458.66
49.25°
310.82
537.53
923.62
40.7°
8°
50.33°
185.42
322.51

V. RSAC-D Weight & Balance

CG Travel/Fuel Management Checks
Sept, 2024

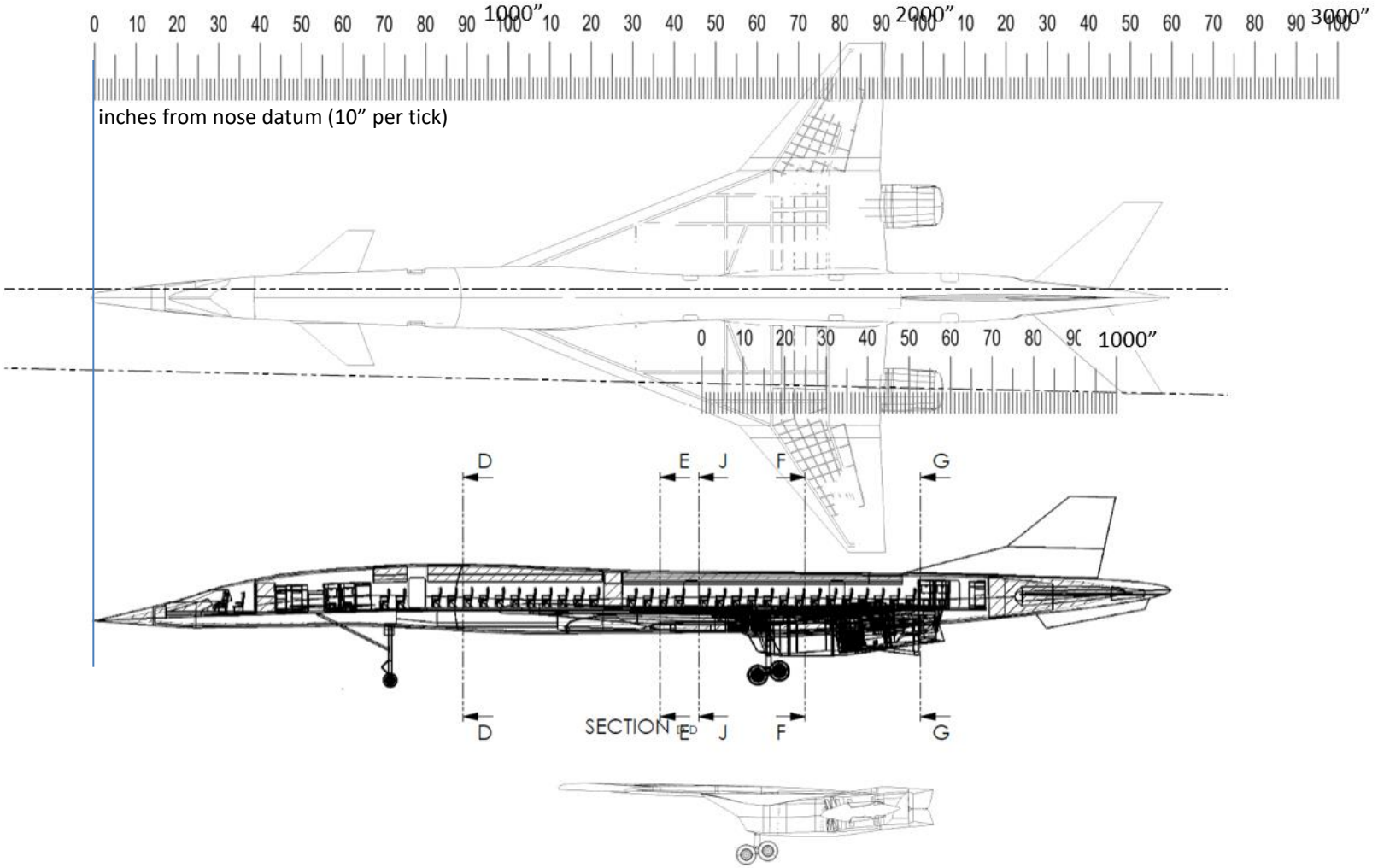
0 10 20 30 40 50 60 70 80 90 100 10 20 30 40 50 60 70 80 90 100 10 20 30 40 50 60 70 80 90 100
1000"
2000"
3000"
inches from nose datum (10" per tick)
0 10 20 30 40 50 60 70 80 90 1000"
D
E
J
F
G
SECTION

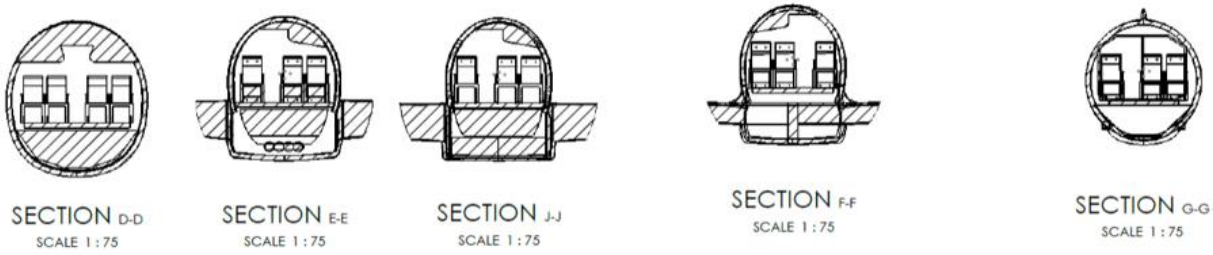
SECTION D-D
SCALE 1 : 75
SECTION E-E
SCALE 1 : 75
SECTION J-J
SCALE 1 : 75
SECTION F-F
SCALE 1 : 75
SECTION G-G
SCALE 1 : 75

RSAC-D LOPA With “Spec” Interior (Missing Aft Over-Wing Escape Hatches)

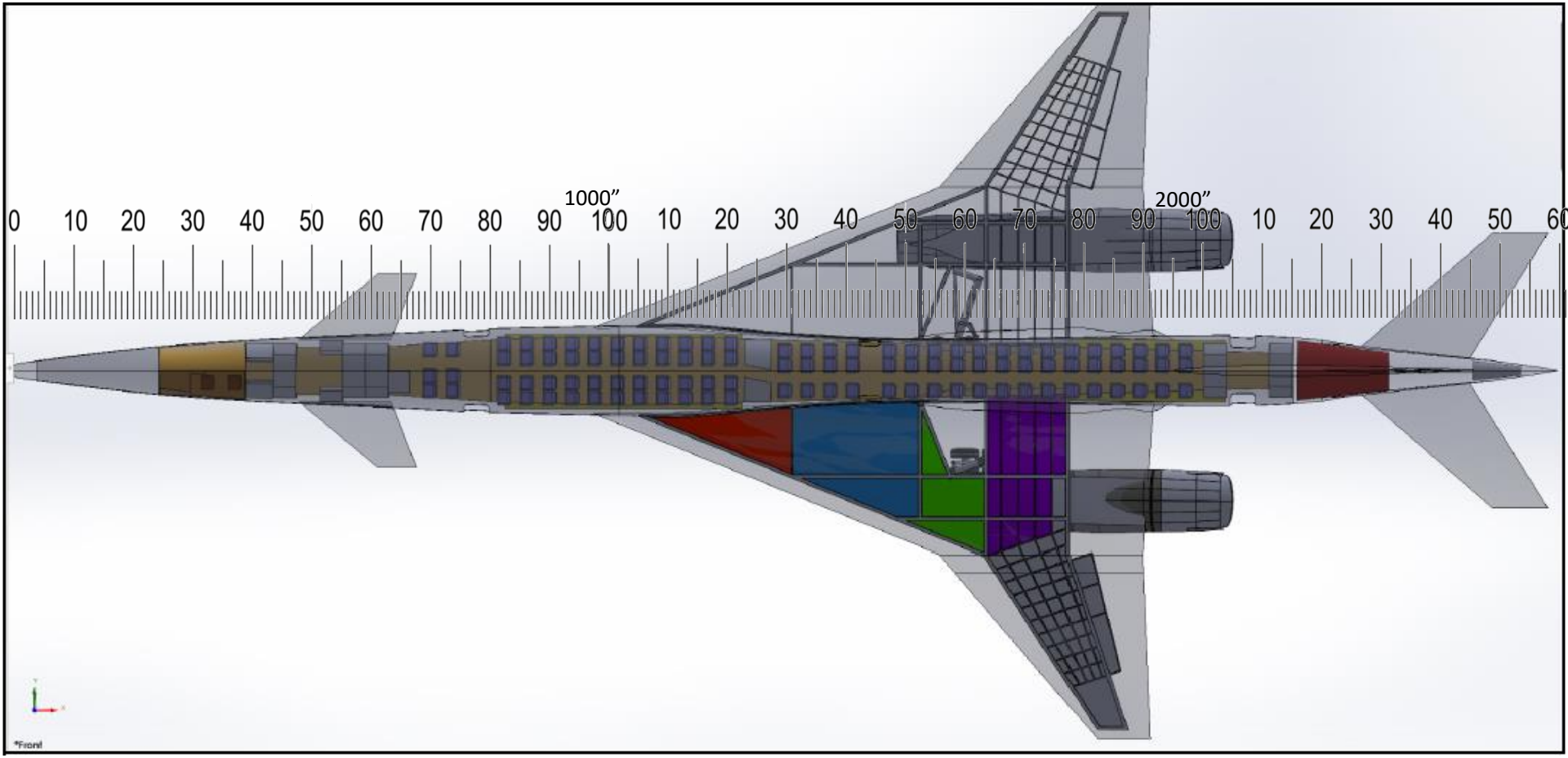

RSAC Mfr. Empty Wt. With Spec Interior

RSAC REVISED MASS PROPERTIES

Item	Item Weight -lbs	Notes & sub totals	X Datum : At RSAC Nose X inches	At RSAC MAC/4 X inches
Wing Structure	34260		1559	80
Horizontal Tail Structure	2060		2400	921
Vertical Tail Structure	1470		2320	841
Fuselage Structure Fwd	10860	Forward fuselage	870	-609
	0	Mid-fueslage plug	1473	-6
Fuselage Structure Aft	7439	Aft-fuselage	1913	434
Main Landing Gear	8750	(stowed) down gear moves CG + 0.2%	1593	114
Nose Landing Gear	940	(stowed)	680	-799
Forebody Controls (canard)	830		593	-886
Main Structure Sub Total		**66609**		
Inlet Structures & Systems	6020		1723	244
Cowling	1120		1832	353
Pylon	3260		1793	314
Engine/mid-nacelle	30920		1843	364
Nozzle	820		1963	484
Installation (incl. fairings)	2200		1843	364
Engine Accessories, Controls, & Start System	200		1823	344
Propulsion Sub Total		**44540**		
Fuel System	4790	center on mid-wing	1543	64
APU/EPU	290	tail cone	2460	981
Flight Deck /instruments	1260	flight deck	330	-1149
Surface Controls	4500	ave of LE/TE tails	1772	293
Hydraulic Power System	2250	center on landing gear post area	1634	155
Pneumatic System		(n/a; electro-hydraulics only)		
Electrical power	2520	distributed centers	1443	-36
Electronics bay	880	under forward cabin	460	-1019
Fuel Inerting System (02 separators)	140	fwd gear fairing	1380	-99
Cabin & Passenger Accomodations: 101 seat spec interior				
3 abreast forward cabin	483	seating zone 1	723	-756
4 abreast mid-cabin	3542	seating zone 2	1013	-466
3 abreast aft-cabin	4106	seating zone 3	1653	174
optional seating	0	seating zone 4		
Pot./waste water system (2x40gal)	280	aft of fwd cargo bay	1800	321
Forward galley(3)	2040		460	-1019
Aft galley(2)	1360		2123	644
Forward lav(2)	300		613	-866
Mid-lavs	0		1343	-136
Aft lavs (2)	300		2120	641
Other Cabin/ Fixed equipment	6730		1233	-246
Environmental Control System packs (2)	1710	belly fairing fwd of gear well	1460	-19
Ice Protection	310	inboard of front of nacelle	1318	-161
Exterior Markings	610	Awet centroid	1448	-31
Typical Customer Options:				
Load and Handling	130	fwd cargo	980	-499
Internet/other cabin eqpt	250	ctr. On mid cabin	1443	-36
Misc. fixed BFE	200	ctr. On mid cabin	1443	-36
Systems & Fixed Equipment Sub Total		**38981**		
Manufacturer's Empty Weight (MEW) Sub Total		**150130**		

RSAC OEW and MTOW With Spec Interior

RSAC REVISED MASS PROPERTIES				
		X Datum :	At RSAC Nose	At RSAC MAC/4
Item	Item Weight -lbs	Notes & sub totals	X inches	X inches
Manufacturer's Empty Weight (MEW) Sub Total		**150130**		
Oil & unusable fuel	800		1823	344
Potable water	250		1800	321
Waste water/toilet chemicals	80		1800	321
Flight deck crew (2) and baggage, laptops	400	flight deck	343	-1136
(3) Cabin crewperson & bag (1/35pass.)	500	mid cabin	1293	-186
Flight Provisions, food, drink	760	fwd & aft galleys	1093	-386
Food service items	300	fwd & aft galleys	1093	-386
Cargo liner/restraints aft	85	aft cargo	1940	461
Cargo liner/restraints forward	235	fwd cargo	930	-549
Cockpit/crew emergency equipment	60	fwd crew area	493	-986
Slide-rafts (2) forward	240	2 fwd	785	-694
Slide rafts (2) aft	300	2 aft	1750	271
Standard and Operational Items Sub Total		**4010**		
Operational Empty Weight (OEW)Sub-Total		**154140**		
OEW CG, in from nose		**1547**		
Payload (@101 passengers in spec interior):		(4 empty seats in zone2)		
3 abreast forward cabin	1122	seating zone 1	723	-756
4 abreast mid-cabin	7480	seating zone 2	1013	-466
3 abreast aft-cabin	9537	seating zone 3	1653	174
optional seating	0	seating zone 4	0	
Checked bags	2020	main cargo	930	-549
Bulk cargo	303	aft cargo bay	1940	461
Zero Fuel Weight (ZFWT) Sub Total		**174602**		
ZFWT CG, in from nose		**1517**		
Fuel Loaded:		(Max.Tank capacities:)		
Fwd body tank F	27021	32500	1300	-179
Fwd strake tanks A	17973	17973	1233	-246
Mid strake tanks B	43600	43600	1433	-46
Aft strake tank C	8576	8576	1553	74
Wing box tanks D	26578	26578	1693	214
Aft body trim tank E	12650	17660	2193	714
Total Fuel Load		**136398**		
Weight Fully Loaded (Ramp Wt)		**311000**		
CG in Inches From RSAC Nose		**1501**		
CG in %MAC		**31.98**		
Design MTOGW		**310000**		

RSAC Weight Sub-Element Details

Details of allowances included in weight items:					
Each passenger seat location includes :	weight in lbs				
Basic IFE screen/remote	4				
Blanket/pillow/pocket contents/headphones	3.5				
Life jacket, bag, safety cards	2				
+ Seat Weight Allowances:	Basic seat;		(Total Weight per Seat Location)		
RSAC Spec. Supersonic Bus. Class	75		80.5	9500	RSAC
Typical Economy	30		35.5	3510	070A
Max Density Economy Seat	22		27.5		
Int'l Business Class (59' min pitch)	135		140.5		
78" pitch lay-flat Int'l First Class	160		165.5	1690	070A
Herringbone light wt cube	280		285.5		
Cubicle/Int'l pod	340		345.5		
Main cargo baggage roller/carpet:	130		@ centroid of main cargo floor	130	in Cargo Compt
(need flat floor & 3" belt, 40" to ceiling)					
Each payload passenger includes :			(Total 210lb/pass)		
Ave pass weight lbs	180		@ seat location		
Ave carry-on bag lbs	7		@ seat location		
Checked bag allowance lbs	20		forward main cargo bay		
Ave. non-bag cargo	3		aft bulk cargo comp't		
Per Pass.-related OEW weights allowances:					
Food & drinks provisions	7.6		760	in Flight Provisions	
Safety Equipment:					
Crew O2, and safety eqpt	60		60		
Escape Slides (lbs each);					
Forward	120		240		
Aft/Over-wing	150		300	(for 2)	
			600	total in Safety Equipment	
Galley empty weights;					
Galley "unit" (1 per 20-25 pass.) - lbs each:	370				
Galley frame/compartments	140				
2 Galley Carts/unit	80				
Galley equipment, coffee makers, ovens	90		680	each galley in pass accom	
Food service items	60		60	each galley in std& ops	
Potable water per passenger	2.5		250	in std and ops, in 40gal capacity tank	
				40 gal capacity waste water tank is empty	
Crew weights:					
Flight deck crew (2) and baggage, laptops	200		400	in standard and ops	
Cabin crewperson & bag (1/35pass.)	168		500	3 attendants, in standard and ops	
Other cabin/fixed equipt.:			6730	in pass accomodtions	
0.75psf carpets	700				
cabin thermal/noise insulation	1500				
0.5psf, ceiling panels, side-walls	1000				
Cabin floor panels	1000				
5.4per ft carry-on stowage bins	1260				
2x40" Closets, stowage lockers	250				
Seat tracks	420				
Cabin partitions	200				
PSU passenger controls	100				
Passenger oxygen system	300				
Cargo compartment liner Forward	250			in cargo	
Cargo compartment liner Aft	50			in cargo	
Basic Lavatory unit - 1 per 18-25 pass.	150		600	4 lavs in cabin accomodations	
Lavatory Chemicals/lav	20		80	for 4 lavs in std and ops	

Fuel Tank Notes: The following filling efficiencies rel. to CAD-measured tank volumes have been applied:			
Vol. filling efficiency/tank	Tank Location	Assumptions	Delta CG %MAC per 15K fuel load in these tanks
1	Fwd body tank F	as-draw is net inside volume	-2
0.95	Fwd strake tanks A	truss-rib wet-wing	-3
0.95	Mid strake tanks B	truss-rib wet-wing	-1
0.85	Aft strake tank C	std. filling efficiency assumes Concorde type liners	0
0.85	Wing box tanks D	std. filling efficiency assumes Concorde type liners	1
1	Aft body trim tank E	as-draw is net inside volume	5

RSAC Spec. Interior

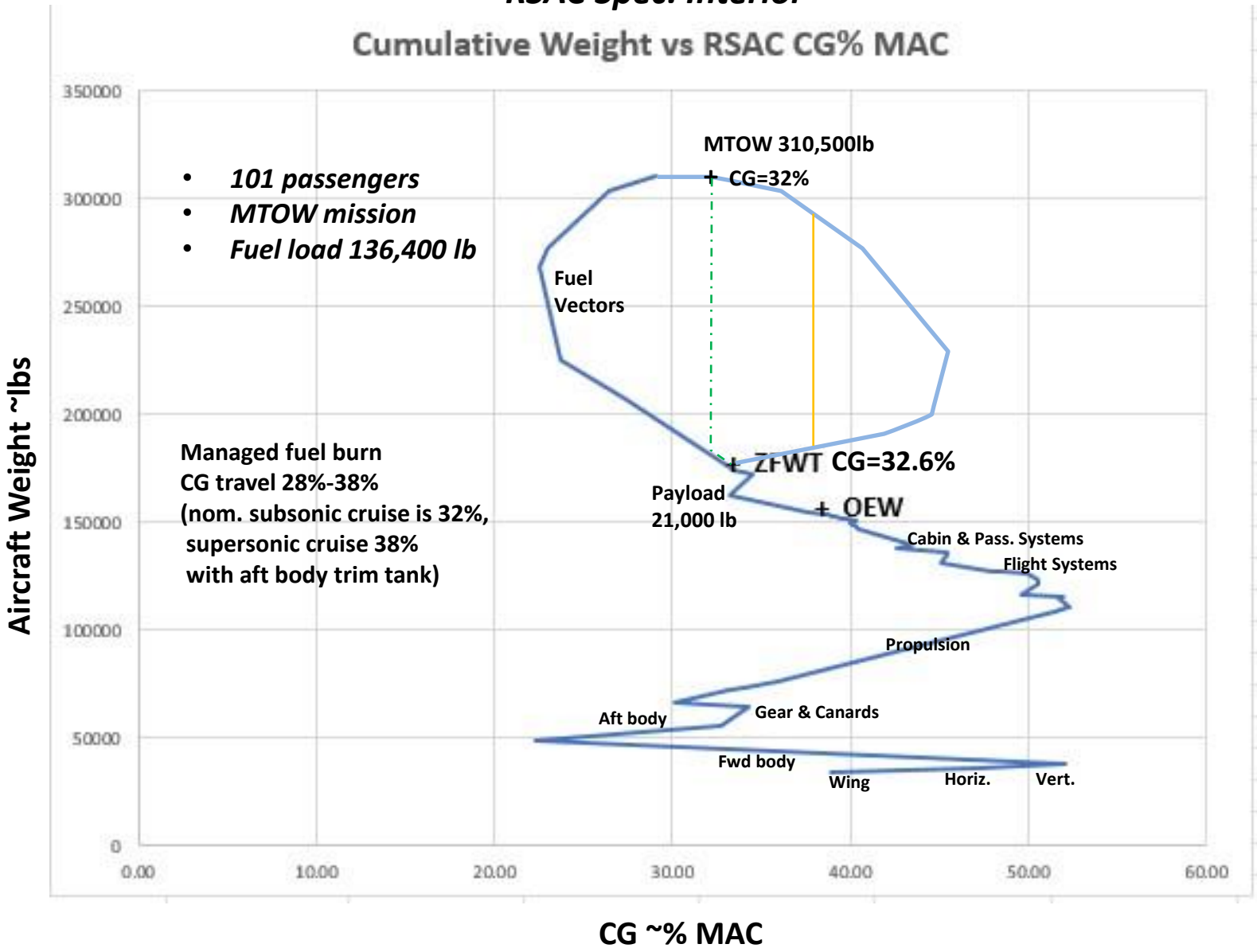

Spec. Interior at 50% Capacity, Max Fuel Load

Cumulative Weight vs RSAC CG% MAC @50% Payload

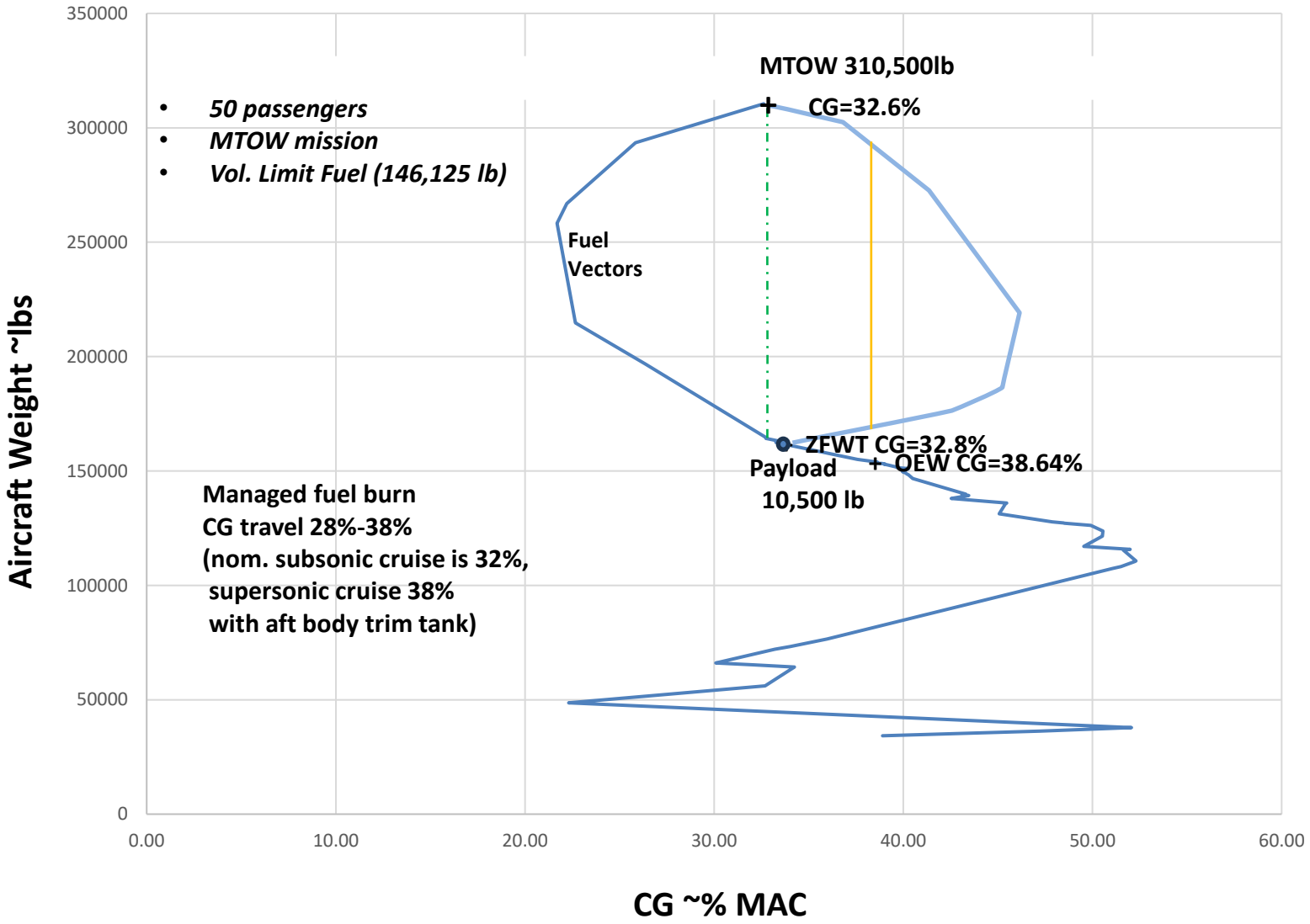

LOPA Seating Zones for Supersonic First/"Executive" Class @ 77-78" Pitch

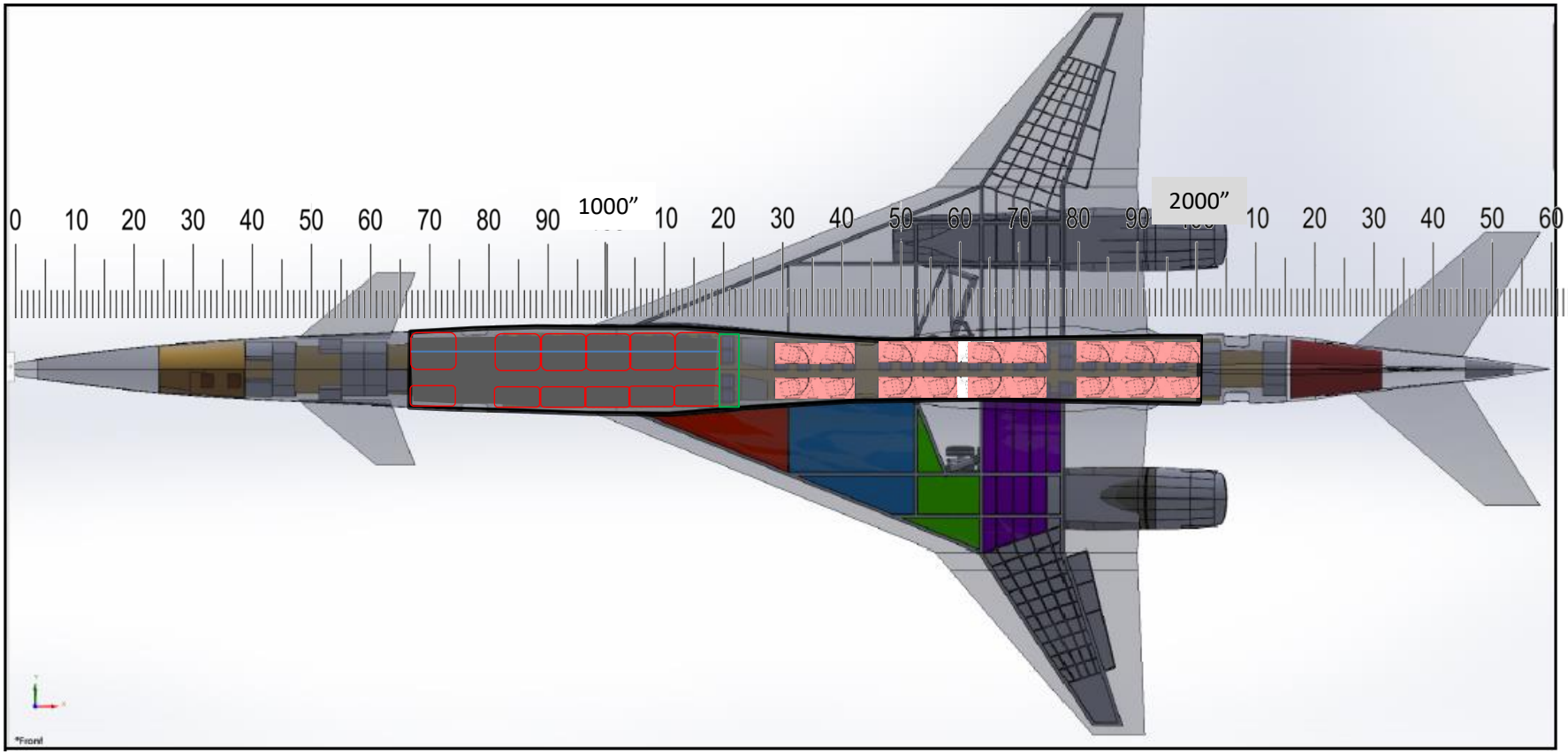

<u>36 Passengers Total</u>

Red: 6 rows @ 3 abreast deep-recline shell seats = 18

White: 9 rows @ 2 abreast angled lay-flat cubes = 18

Green: 1 added pax. services , 1 added stowage closet

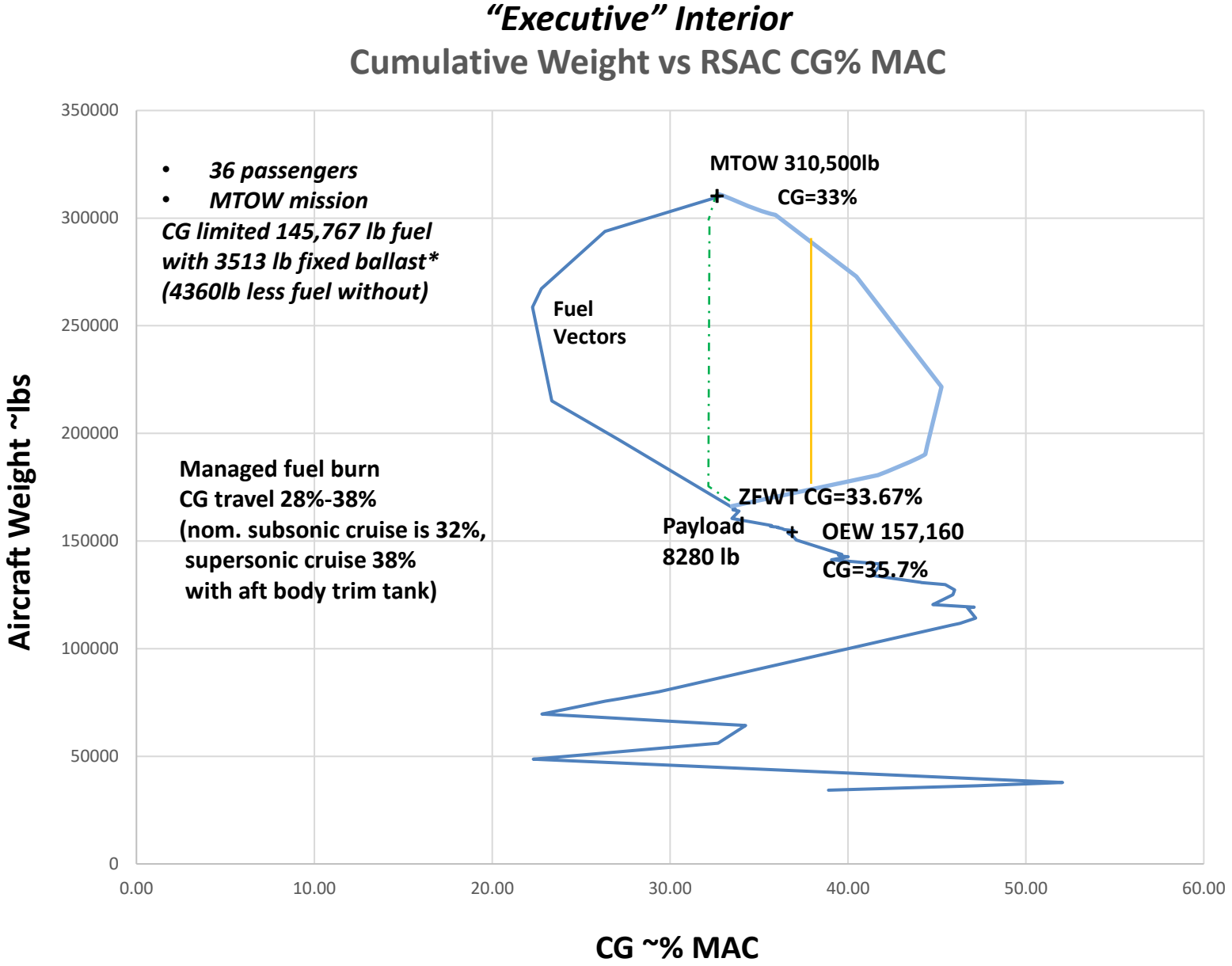
"Executive" Interior
Cumulative Weight vs RSAC CG% MAC
• 36 passengers
• MTOW mission
CG limited 145,767 lb fuel
with 3513 lb fixed ballast*
(4360lb less fuel without)
MTOW 310,500lb
CG=33%
Fuel
Vectors
ZFWT CG=33.67%
Payload
8280 lb
OEW 157,160
CG=35.7%
Managed fuel burn
CG travel 28%-38%
(nom. subsonic cruise is 32%,
supersonic cruise 38%
with aft body trim tank)
Aircraft Weight ~lbs
350000
300000
250000
200000
150000
100000
50000
0
0.00
10.00
20.00
30.00
40.00
50.00
60.00
CG ~% MAC

LOPA Seating Zones for High Density “All Economy” Seating @ 33-34” Pitch

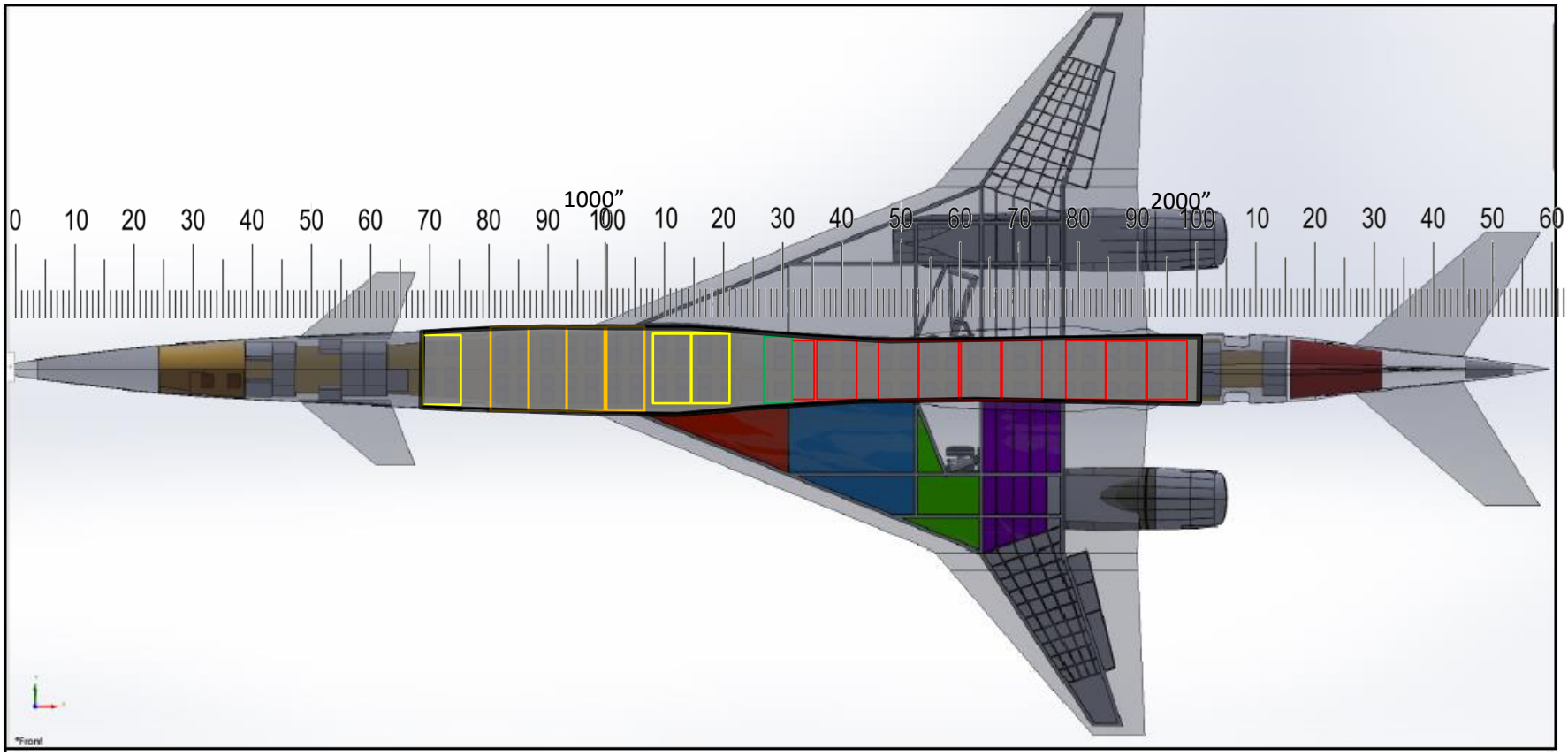

<u>142 Passengers Total</u>

Yellow: 6 rows @ 5 abreast = 30

Orange: 8 rows @ 6 abreast = 48

Red: 16 rows @ 4 abreast = 64

Green: 1 added lav, 1 added ½ galley

Maximum Payload "All Economy" Interior

Cumulative Weight vs RSAC CG% MAC

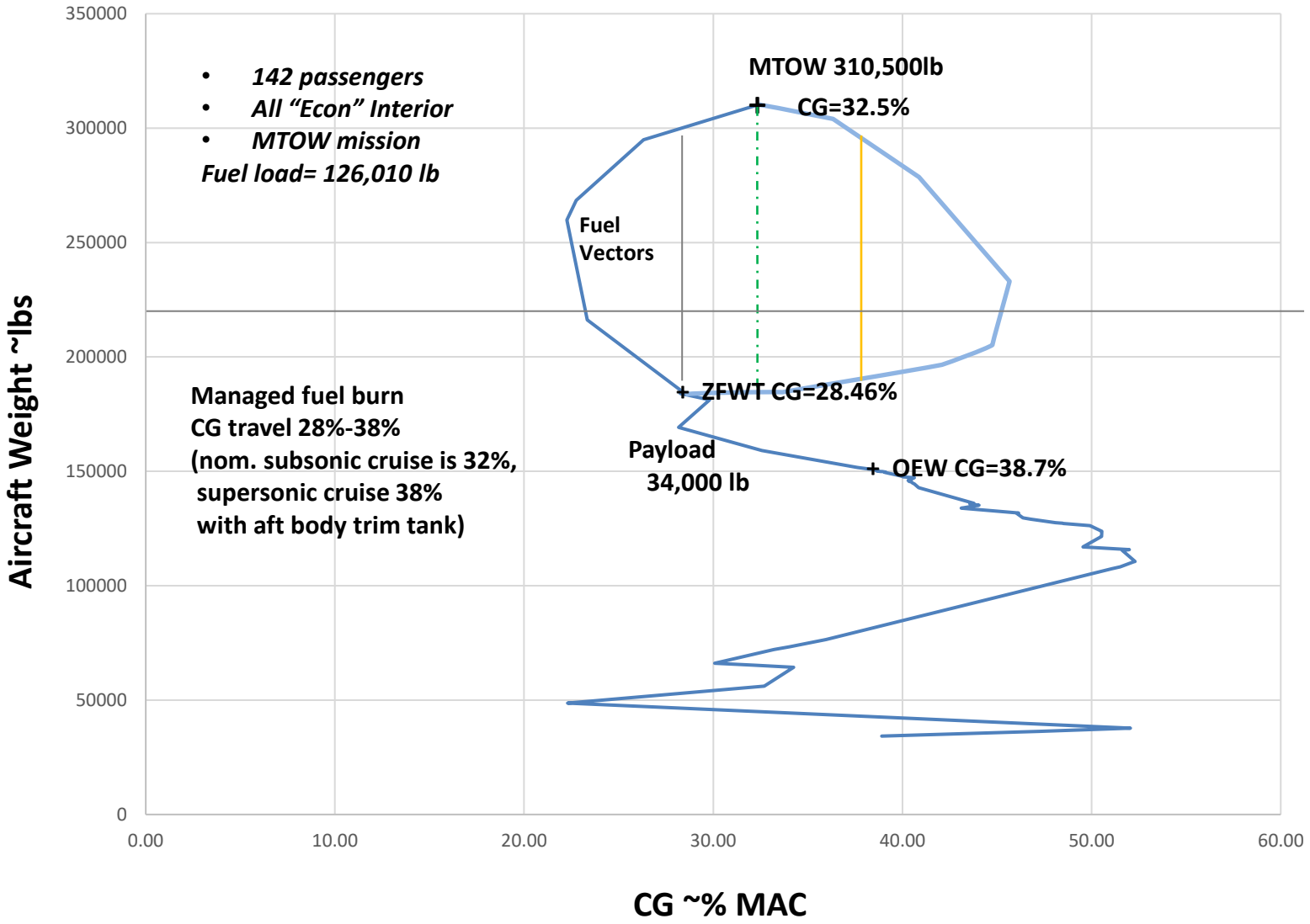

RSAC-E Weight And Balance Study (Sept.2024)

- The RSAC “Spec” baseline interior (~ all “domestic First Class” seating) is 100-104 seats*, matching Concorde’s capacity but at higher comfort level. The maximum capacity interior with all-Economy seating is 142 passengers. With all international First/Business Class lay-flat seats and personal cubicles, the “all Executive” interior holds 36 passengers.
- The target 32-32.5% CG (with gear retracted) is achievable at MTOW for all interior configurations of interest. Gear-down CG is 0.2% MAC aft of the gear-up case.
- *Balanceable* fuel load varies by up to 13.6% (20k lbs) depending on the cabin configuration & payload being carried
- Fuel use management (tank selection vs. mission phase) provides a nominal subsonic cruise CG of 32%MAC and nominal supersonic CG of up to 38%MAC throughout 85-100% of any mission profile without *active* fuel pumping to trim (fuel pumping or emergency dumping from the aft trim tank may still be needed to restore subsonic static margin for unexpected enroute emergency slow-downs to subsonic speeds –needs investigation/simulation)
- Minimum flight weight configuration (factory flight test cases, flight demonstrations, training flights) will need to end the flight with 9000lbs of unusable fuel in the forward strake tanks, plus up to 5000lbs of ballast in the forward cargo bay, in order to maintain the flight CG ahead of the aft-limit for subsonic flight

*Performance estimates were done at nominal 100 passengers, up to 4 seats may be empty, “E” version of RSAC is drawn with 103 seats at minimum 38” pitch. Weight and balance update for estimated weight of the extended “FOD shield” main gear doors has only been performed for the “spec” interior, 100-passenger payload case

Critical Longitudinal S&C Check Conditions*

- Takeoff rotation at 310,500lb, CG at 28.5%CG, 'all econ' interior pitch inertia with 'dumbbell-loaded' fuel (forward CG, max Iyy inertia)
- Go-around at 28%CG at MLW=220,000lb
- High KEAS pull-up at 33.67%CG at 174,880 lb
- Stall recovery at 33.67%CG at 174,880 lb
  - Pitch down acceleration rate
  - Negative Cm with full-down control up to alpha=1.15x alpha Vs or CL_{max}
- Subsonic flight at low alpha/high speed for emergency descent at CG for supersonic cruise at 38% (alpha margin to pitch-up, time to double), time req'd for LE/TE reconfiguration, re-trimming, and fuel CG transfer
- Transonic/low-supersonic Cm "tuck" trim drag optimization with canards, aft-tail, and elevons, including optimum outboard leading and trailing edge flap deflections.

*At the time of release of this report (December 2024), these checks have not yet been completed for the RSAC due to delays in processing wind tunnel and CFD results. It is hoped they will be the subject of follow-on work.

VI. Reference Supersonic Airliner Concept Project Participants

Senior Design Capstone Team 2020:

Avi Soval, Elaine Xiong, Jacob Rork, William Hendrickson, Nico Miguel, Danny Roberts, Seth Timney, Dustin Tabor, Eric Racadag, Si-linLi

Senior Design Capstone Team 2021:

Austin Chandra, Brendan Geffe, Nathan Han, Danny Beeson, Colton Hill,

Anant Kapur, Shelby Lee, Zhangsheng Lian, Pascal Nagata, Anwar Moustafa, Ignacio Re,

Michael Stemen, Vinsensius

Senior Design Capstone Team 2022:

Julia Bailey, Karina Bridgman, Megs Cambra, Michael Chi, Constantine Cooper,

Frank Goess, Rahul Gupta, Matthew Hekman, Josh Ignacio, Noah Inahara, Binyu Long,

Daniel Moore, Anthony Nguyen, Misae Nguyen, Vincent Ning, Connor Stroup,

Berit Syltebo, Daniel Teshome, Parker Timmons

Senior Design Capstone Team 2023:

Alex Arce-Torres, Glenn Berg, Pranav Bhagavatula, Iaroslav Grishin, Jake Li, Alex Martin,

Hayden Nolting, Jacob Price, Aaron Wickenhagen, Kenneth Wiersema

Senior Design Capstone Team 2024:

Chris Browne, Connor Cassidy, Caleb Hadland, Patrick Galvin,

Raiden Egbert, Andrew Truong, Josie Wilson, Anderson Yuan

Graduate Students, TA's, Graduate Summer Hire Interns:

Nicolas Mavriplis, K.Y. Eddie Ting, Kenneth Wiersema, Anwar Moustafa, Avi Soval, Josie Wilson

Professors, Technical Advisors:

Eli Livne, Chet Nelson, Reza Soltani